Trace Element Proxies and Mineral Indicators of Hydrothermal Fluid Composition and Seafloor Massive Sulfide Deposit Formation Processes

by
Guy Nathaniel Evans
B.S., B.A., College of William and Mary, 2010

Submitted in partial fulfillment of the requirements for the degree of
Doctor of Philosophy
at the
MASSACHUSETTS INSTITUTE OF TECHNOLOGY
and the
WOODS HOLE OCEANOGRAPHIC INSTITUTION

June 2017

Author……
Department of Earth, Atmospheric, and Planetary Sciences, MIT &
Department of Geology and Geophysics, WHOI
May 25, 2017

Certified by…….
Margaret K. Tivey
Thesis Supervisor

Accepted by……...
Mark Behn
Chair, Joint Committee for Marine Geology and Geophysics

Trace Element Proxies and Mineral Indicators of Hydrothermal Fluid Composition and Seafloor Massive Sulfide Deposit Formation Processes

By

Guy Nathaniel Evans

THESIS ABSTRACT

This thesis analyzes compositions of seafloor massive sulfide (SMS) deposits and related hydrothermal vent fluids to identify proxies of reaction zone conditions (host-rock lithology, hydrothermal fluid temperature and chemistry). Chapter 2 investigates the morphology, mineralogy, and geochemistry of SMS deposits from six vent fields along the Eastern Lau Spreading Center (ELSC), demonstrating that ELSC SMS deposits record differences in hydrothermal fluid temperature, pH, sulfur fugacity and host-rock lithology related to proximity to the nearby Tonga Subduction Zone. Chapters 3 and 4 focus on partitioning of Co, Ni, Ga, Ag, and In between hydrothermal vent fluids and chalcopyrite lining fluid conduits in black smoker chimneys. Chapter 3 develops secondary ion mass spectrometry (SIMS) as a technique to measure Co, Ni, Ga, Ag, and In in chalcopyrite and identifies a correlation between Ga and In in chalcopyrite and hydrothermal fluid pH. Chapter 4 presents new data on these elements in ELSC hydrothermal fluids that, combined with SIMS analyses of chalcopyrite chimney linings and previously published data on vent fluids from the Manus Basin, provide evidence that supports partitioning of Ag a lattice substitution for Cu. Together, concentrations of Ga, In, and Ag in chalcopyrite provide proxies of hydrothermal fluid pH and metal (i.e., Ag and Cu) contents.

Thesis Supervisor: Dr. Margaret K. Tivey

Title: Senior Scientist, Woods Hole Oceanographic Institution

ACKNOWLEDGEMENTS

The work presented in this thesis could not have been accomplished without a network of professional and personal support. To that end, I would like to acknowledge my advisor, Dr. Margaret K. Tivey, for her mentorship and dedication, and members of my thesis committee: Dr. Jeffrey S. Seewald, Dr. Nobumichi Shimizu, Prof. Shuhei Ono, and Prof. Olivier J. Rouxel for their valuable input and advice to improve the contents of this thesis. Dr. Brian Monteleone's help in developing secondary ion mass spectrometry of trace elements in sulfide minerals and Margaret Sulanowska's help with sample preparation are also greatly acknowledged, as are Dr. Paul R. Craddock and Dr. Jill M. McDermott, my predecessors in the MIT/WHOI Joint Program, whose theses provided significant contributions to the work presented here.

I would also like to acknowledge the captains and crews of the R/V Melville, the R/V Thompson, the R/V Atlantis III, and the R/V Roger Revelle, and the team of the ROV Jason II for their expertise in recovering fluid and SMS deposit samples from active vent fields, as well as chief scientists, Dr. Chris German (AT18-16) and Prof. Anna-Louise Reysenbach (RR1507) for welcoming my participation on research cruises to the Mid-Cayman Rise and Eastern Lau Spreading Center. Work presented in Chapter 2 of this thesis was supported by the National Science Foundation through grants OCE-1038135 to GNE and MKT, OCE-1038124, OCE-0241796, OCE-1233037 to JSS, and OCE-0242088 to CGW. Chapters 3 and 4 were supported by the National Science Foundation through grants OCE-1038135 and NSF Graduate Research Fellowship to GNE and funding from grant NSF OCE-1536480 to MKT. Dr. Nobumichi Shimizu is also gratefully acknowledged for his insights into secondary ion mass spectrometry and picking of mineral grains.

I would like to thank the administrative support of the MIT/WHOI Academic Programs Office including Dr. Jim Yoder, Dr. Margaret K. Tivey, Julia Westwater, Leanor Fraser, Ronni Schwarz, and Kris Kipp for their efforts to ensure the smooth operation of the MIT/WHOI Joint Program, as well as my friends and colleagues within the Joint Program for their comradery and (at times) commiseration. These include especially Dr. Anna Wargula, Dr. Sarah Rosengard, Dr. Evan Howard, Dr. Emily Moberg, Dr. Eleanor Bors, Dr. Alice Alpert, and Dr. Sophie Chu. I would also like to thank those in my community who have offered their love and support to me and my family over these past six years. These include the members and congregation of Hope Fellowship Church in Cambridge and of John Wesley United Methodist Church in Falmouth, especially the members of our fellowship group in Cambridge and Somerville and Ken and Marika Roth in West Falmouth. The same Spirit that causes us to seek knowledge in the farthest reaches and deepest depths also calls us to reach out and welcome strangers into our homes.

I would like to thank my family, including my sister, Catrin Evans, and especially my parents, Dr. Patricia Jue and David Evans, whose experience raising me was a constant reminder that raising a child and completing a Ph.D. thesis is possible. To my son Michito and others who may follow, it is possible, but also very difficult. Please take some time to think about it.

Finally, and most of all, I would like to thank my wife, Kazue, for her consistent love, patience, and support and reminding me of the important things that I might otherwise forget.

DEDICATION

24 April, 2015

View of Ata volcano from the deck of the R/V Roger Revelle,
1920 meters above the Mariner vent field.

Today, dawn greets us with a splendor, a shock of daylight cut through cloud. Before it, a rainstorm curtails its trailing curtain and evaporates in steaming haze. All around, the world rests, an eternity split by sea and sky. Below, a bird — perhaps a gannet— swoops down over the water, looking for fish. And there, rising quite improbably in the east is a volcanic island, a mote of mountain made material, mirage suspended in the morning mist.

And, as if to prove its existence, I take a photograph...

And I sit, rocking on this metal boat, a warm conglomerate of carbon, hydrogen, oxygen… congealed condensate of sky and sea.

TABLE OF CONTENTS

LIST OF TABLES

LIST OF FIGURES

Chapter 1

Introduction

1. Background and Motivation

Seafloor massive sulfide (SMS) deposits are accumulations of metal sulfide and other (e.g., sulfate, oxide, silicate, sulfosalt, rarely carbonate) minerals formed at or near the seafloor by the activity of venting seafloor hydrothermal fluids. Actively forming SMS deposits were first discovered in 1979, coincident with the discovery of high-temperature (380°C ± 30°C) seafloor hydrothermal vents that followed the discovery of lower-temperature (10°C to 17°C) seafloor hydrothermal vents in 1977 (Corliss et al., 1979; Spiess et al., 1980). Since this initial discovery, at least 165 active vent fields hosting SMS deposits have been found in submerged areas of high geothermal heat flux around the world, and 500 to 5,000 are estimated to exist globally (Hannington et al., 2011). Geologic settings include: ultraslow-, slow-, intermediate-, fast-, and ultrafast-spreading mid-ocean ridges, intraoceanic arcs and back-arc basins, transitional island arcs and back-arc rifts, sedimented ridges and related rifts, intracontinental rifts and back-arc rifts, off-axis and intraplate volcanoes, and volcanic rifted margins (see reviews by Hannington et al., 2010; Beaulieu, 2015; Figure 1).

In contrast to the relatively recent discovery of SMS deposits, humans have been mining copper, zinc, and other metals from volcanogenic massive sulfide (VMS) deposits ―likely to be the geologically preserved remnants of ancient SMS deposits―for thousands of years. Archaeological evidence suggests that such mining began in the late-Neolithic Period (a.k.a. Chalcolithic Period) ~7,000 years ago at sites in Anatolia and the Eastern Mediterranean,

becoming more widespread with the advent of the Bronze Age, ~5,000 years ago (Kassianidou and Knapp, 2005). Contemporary mining of VMS deposits occurs in ophiolite belts around the world, where pieces of oceanic crust have been uplifted onto land by geologic processes (Galley et al., 2007; Figure 2). The exact correspondence between modern SMS deposits on the seafloor and ophiolite-hosted massive sulfide deposits is not always clear as some ancient massive sulfide deposits may lack modern seafloor counterparts (Hannington et al., 2010). Nevertheless, there are clear similarities between SMS and VMS deposits with respect to deposit morphology, mineralogy, geochemistry, and (paleo-) tectonic settings (Franklin et al., 2005; Hannington et al., 2005; Hannington et al., 2010). Moreover, mineral textures interpreted to be the geologically preserved remnants of black smoker chimneys have been reported in VMS deposits in Japan (Scott, 1981), Cyprus (Oudin and Constantinou, 1984), the southern Urals (Herrington et al., 1998; Maslennikov et al., 2009), and the Eastern Pontides (Revan et al., 2014). Several of these deposits also contain fossils of hydrothermal vent fauna, including brachiopods, gastropods, mollusks, and worm tubes (see review by Little et al., 1998).

The significance of studies investigating the geochemistry of actively forming SMS deposits lies in the opportunity to directly compare SMS deposits with the hydrothermal fluids from which they form. Such studies provide insight into the formation processes of SMS deposits as well as opportunities to develop proxies of hydrothermal fluid temperature and chemistry based on the mineralogical, geochemical, or isotopic composition of SMS deposits (e.g., Hannington et al., 1995; Tivey, 1995; Tivey et al., 1995; Tivey et al., 1999; Rouxel et al., 2004; Craddock et al., 2010; McDermott et al., 2015; Kawasumi and Chiba, 2017). The overarching goal of the studies presented in this thesis is to compare samples of SMS deposit minerals with the hydrothermal fluids from which they form in order to develop mineralogical

and trace element proxies of hydrothermal fluid temperature and chemistry and host-rock lithology. Particular focus is placed on the mineralogy and trace element contents of black smoker chimneys linings compared with the temperature and chemistry of hydrothermal fluid sample pairs and thermodynamic modelling of fluid speciation and mineral saturation at *in situ* temperatures and pressures.

Figure 1.
Map of seafloor hydrothermal vent locations from the InterRidge database (from Beaulieu, 2010; https://vents-data.interridge.org/)

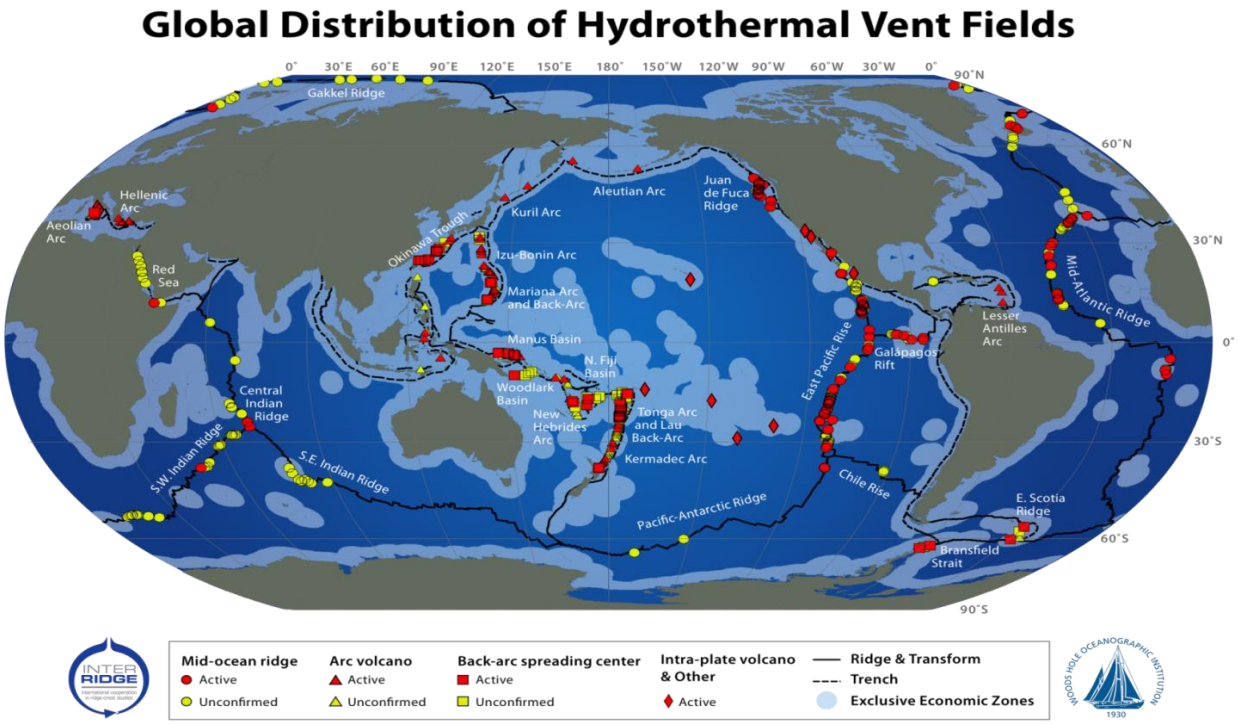

Figure 2.
Map of volcanogenic massive sulfide deposit locations (from Galley, 2007). Red symbols indicate known locations of volcanogenic massive sulfide (VMS) and seafloor massive sulfide (SMS) deposits. Black symbols indicate the locations, names, and estimated tonnages of the 45 most economically important VMS mining districts.

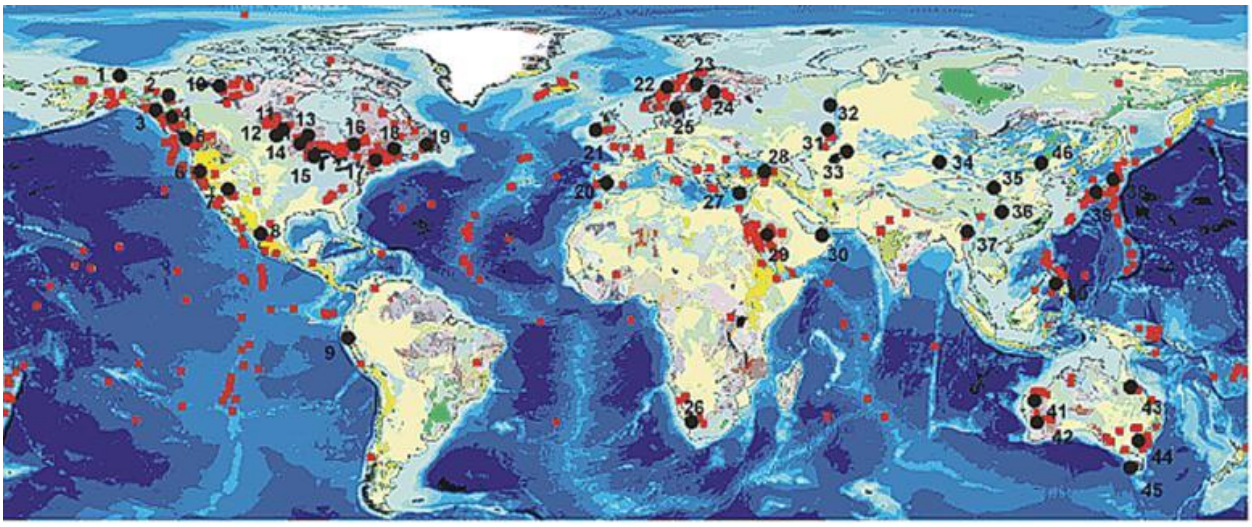

1. Alaska, Brooks Range 33 Mt
2. Finlayson, Yukon 20 Mt
3. Windy Craggy 300 Mt
4. Northern Cordillera 100 Mt
5. Myra Falls 30 Mt
6. Shasta, Klammath 35 Mt
7. Jerome, Arizona 40 Mt
8. Central Mexico 120 Mt
9. Tambo Grande 200 Mt
10. Slave 20-30 Mt
11. Ruttan, Manitoba 70 Mt
12. Flin Flon-Snow Lk 150 Mt
13. Geco-Manitouwadge 60 Mt
14. Sturgeon Lake 35 Mt
15. Ladysmith-Rhineland 80 Mt
16. Abitibi 600 Mt
18. Bathurst 250 Mt
19. Central Nfld. 75 Mt
20. Iberian Pyrite Belt 1000 Mt
21. Avoca 37 Mt
22. Tondheim Norway >100 Mt
23. Skellefte Sweden 70 Mt
24. Outokumpu-Pyhsim 90 Mt
25. Bergslagen-Orijarvi 110 Mt
27. Troodos Cyprus 35 Mt
28. Turkey, Black Sea 200 Mt
29. Saudi Arabia 70 Mt
30. Semail Oman 30 Mt
31. Southern Urals >400 Mt
32. Central Urals >100 Mt
33. Rudny Altai >100 Mt
34-36. China >500 Mt
35. Bawdwin-Laochang >40 Mt
38. Hokuroku Japan 80 Mt
39. Besshi Japan 230 Mt
40. Philippines 65 Mt
41-42. WA >75 Mt
43. Central Queensland
44. Lachlan Fold Belt
45. Mt. Read Tasmania 150 Mt

2. Formation of Seafloor Massive Sulfide Deposits

Seafloor massive sulfide deposits form as reduced and usually acidic metal- and sulfide-rich hydrothermal fluids exit the seafloor and encounter cold, sulfate-rich, oxidized, and alkaline seawater. As hydrothermal fluids cool during upflow and subsequent expulsion from the seafloor, the solubility of metal sulfide minerals decreases. When metal sulfide mineral solubility is exceeded by the concentrations of metals and sulfide in hydrothermal fluids, these minerals become saturated and begin to precipitate. SMS deposit mineralogy is often layered based on differences in the temperature at which different minerals become saturated.

Mixing between hydrothermal fluids and seawater at or near the seafloor can also affect mineral precipitation and SMS deposit formation by accelerating cooling and buffering pH, which promotes metal sulfide precipitation by decreasing solubility, or inhibits metal sulfide precipitation by diluting metal and sulfide concentrations. In addition, sulfate minerals can precipitate from the heating of seawater (anhydrite) or reactions between ions contained in hydrothermal fluid with seawater sulfate. For example, hydrothermal Ba^{2+} can react with seawater sulfate to form barite and hydrothermal Ca^{2+} can react with seawater to form additional anhydrite. Further afield, the reaction of metals contained in hydrothermal fluids with oxygenated seawater leads to the precipitation of oxide or mixed oxide and sulfide deposits, either in the vicinity of SMS deposits or as distal sediments.

Seafloor massive sulfide deposits exhibit a variety of deposit morphology related to the temperature, chemistry, and flow pathways of hydrothermal vent fluids (Figure 3; Tivey, 2007). Black smoker chimneys, which derive their name from the pipe-like shape of the deposit and the black, smoke-like appearance of buoyant hydrothermal fluid laden with sulfide mineral particulate, are formed in two stages from vigorously venting high-temperature (> 300°C) hydrothermal fluids (Figure 4; Haymon, 1983; Goldfarb et al., 1983). First, an anhydrite ($CaSO_4$) matrix containing fine-grained metal sulfide minerals is deposited as venting hydrothermal fluid heats the surrounding seawater (Figure 4). Anhydrite, which exhibits retrograde solubility, precipitates from the calcium (Ca^{2+}) and sulfate (SO_4^{2-}) contained in seawater at ~150°C (Bischoff and Seyfried, 1978). Additional Ca^{2+} may also be contributed by the hydrothermal fluid (Albarede et al., 1981). As hydrothermal fluid becomes physically and chemically insulated from interactions with the surrounding seawater, a layer of chalcopyrite ($CuFeS_2$) or cubanite ($CuFe_2S_3$) ± wurtzite ((Zn, Fe)S) ± pyrite (FeS_2) or pyrrhotite ($Fe_{1-x}S$) is deposited along the

inner lining of the chimney wall. Diffusive and advective interactions between hydrothermal fluids and seawater within the chimney wall lead to further precipitation of metal sulfide minerals and replacement of the previously deposited anhydrite-dominated matrix as chemical conditions become more reduced (Haymon, 1983; Goldfarb et al., 1983; Tivey, 1995).

Figure 3.
Artistic representation of seafloor massive sulfide deposits showing: (A) black smoker chimneys (B) "white smoker" spires (C) flanges (D) diffuse flows (C. (image by C. Kearney after Sarrazin et al. (1999)).

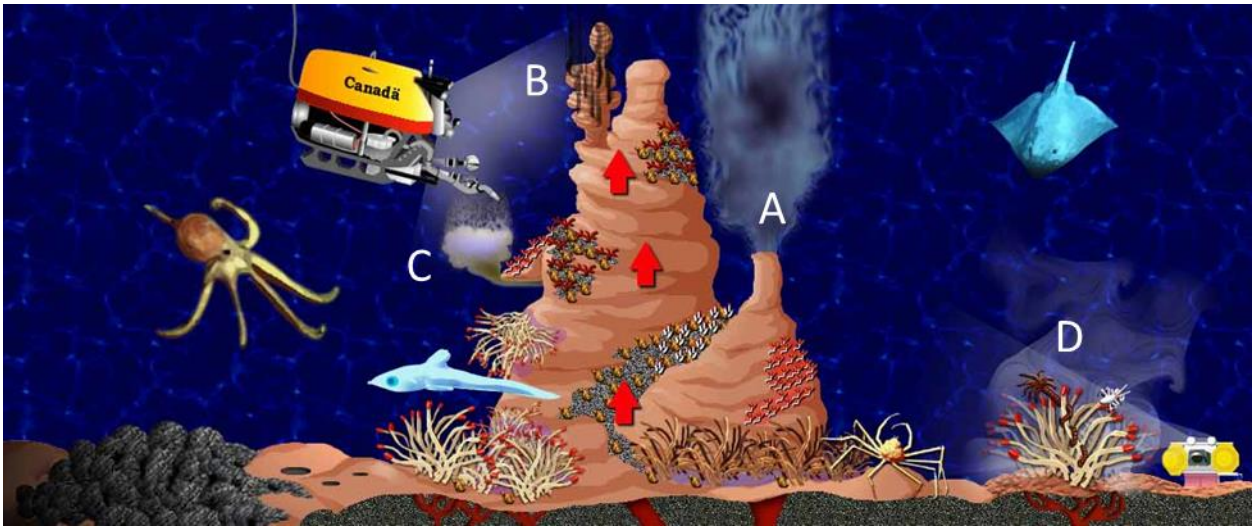

Where hydrothermal fluids vent less vigorously, and are often cooler, beehive-like SMS deposits or "white smoker" spires may also be deposited (e.g., Haymon and Kastner, 1981; Kormas et al., 2006; Figure 5). Where deposits exhibit significant structural stability, horizontal flanges can develop as buoyant hydrothermal fluids are trapped in pools beneath mineral flanges, often spilling upward around the lip of the flange (e.g., Tivey et al., 1999; Figure 6). Low-temperature diffuse venting occurs where hydrothermal fluids have mixed with seawater and/or substantially cooled in the subsurface prior to venting. Such fluids are often not associated with sulfide mineral deposits, but are important habitats for vent field fauna (Figure 3). SMS deposits

can also consist of composite structures exhibiting several types of hydrothermal venting in different areas. Examples include the steep-sided edifices found at vent fields along the Endeavour Segment of the Juan de Fuca Ridge (Tivey et al., 1999; Figure 7) and the large (diameter ≈ 200 m; height ≈ 50 m) massive sulfide mound at the TAG hydrothermal field on the Mid-Atlantic Ridge (Tivey et al., 1995; Humphris and Tivey, 2000; Figure 8).

Figure 4.
Artistic representation of black smoker chimney formation processes (J. Doucette, WHOI Graphic Services, after Haymon, 1983). Stage 1 chimneys (on left) form by heating of seawater and precipitation of an anhydrite-dominated matrix. Stage 2 chimneys (on right) are characterized by precipitation of a metal sulfide inner layer that precipitates from conductively cooled hydrothermal fluids (see text for details).

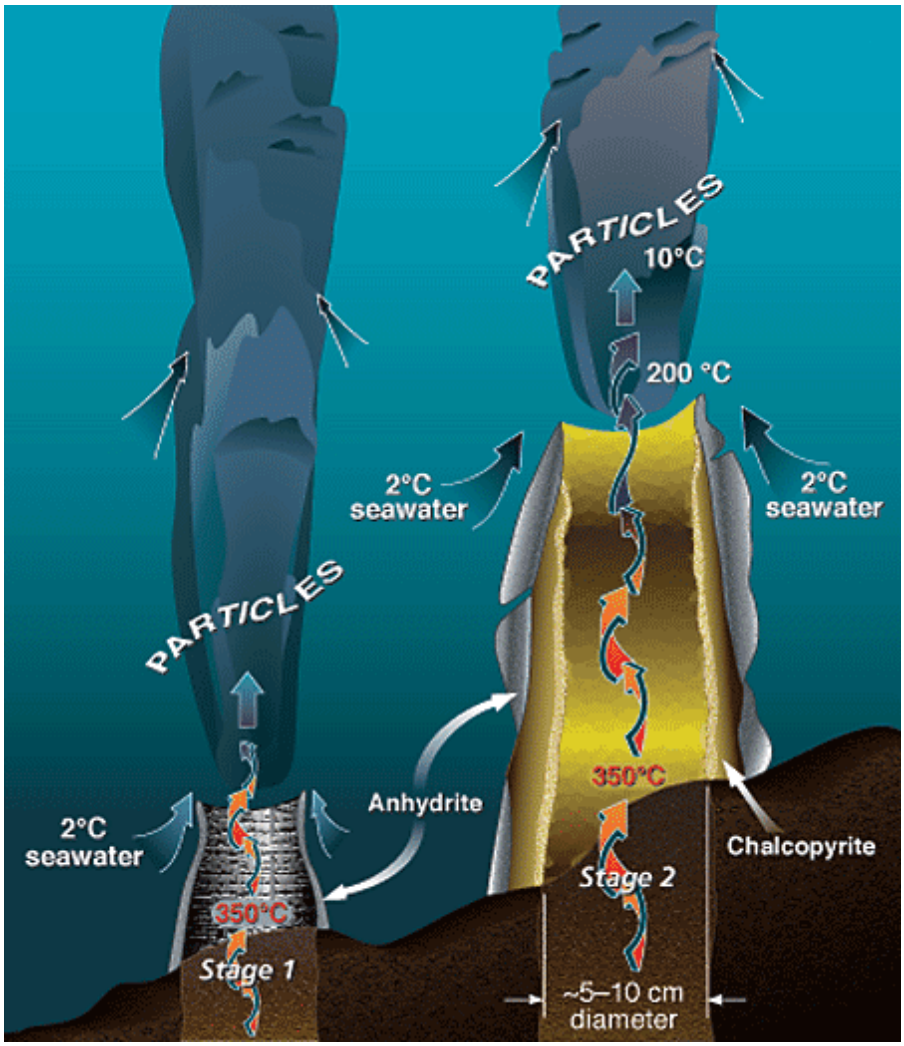

Figure 5.
Schematic drawing of a cross section of a "white-smoker" spire based on deposits collected from the East Pacific Rise (from Kormas et al., 2006).

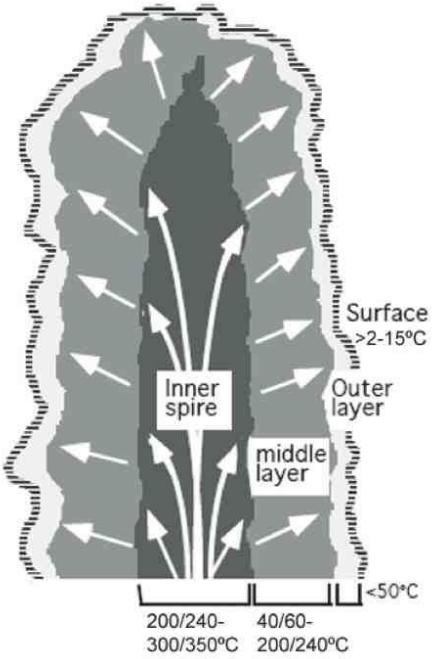

Figure 6.
Schematic drawing of cross section of flange with trapped pool of buoyant fluid (from Tivey, 2007)

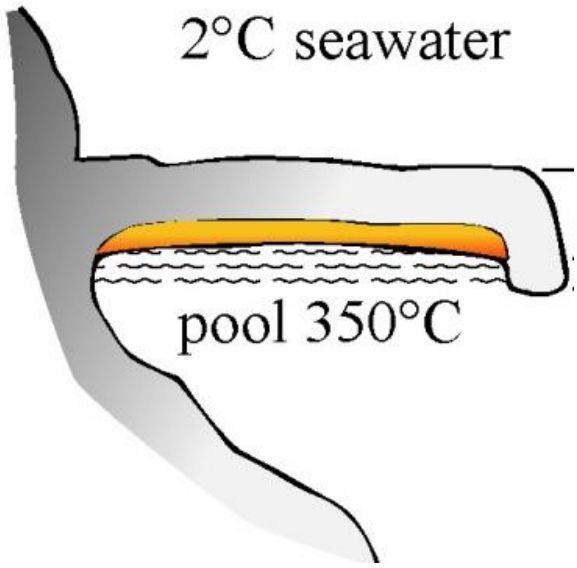

Figure 7.
Schematic drawing of a steep-sided hydrothermal edifice at the Main Endeavour Field on the Juan de Fuca Ridge and associated formation processes (from Tivey et al., 1999).

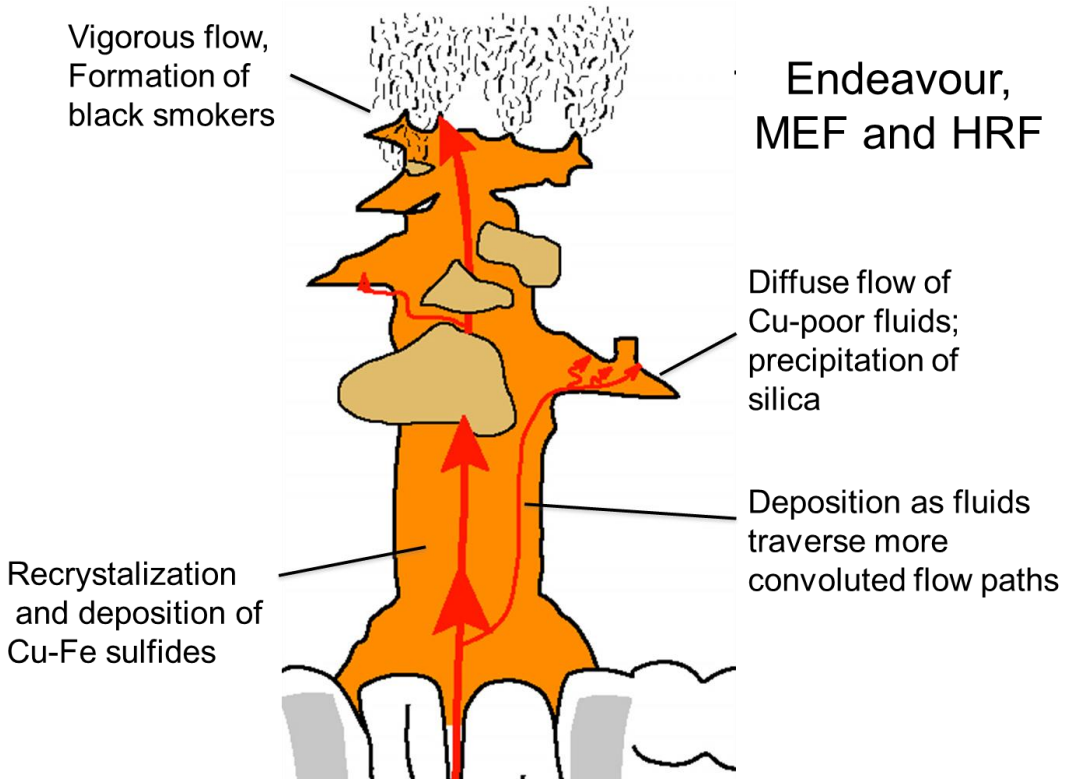

Figure 8.
Schematic drawing of a cross section of the ~200 m diameter hydrothermal mound at the TAG hydrothermal field on the Mid-Atlantic Ridge showing formation processes including direct venting of black smoker fluids and white smoker fluids formed by mixing of black smoker fluids and seawater within the hydrothermal mound (from Humphris and Tivey, 2000).

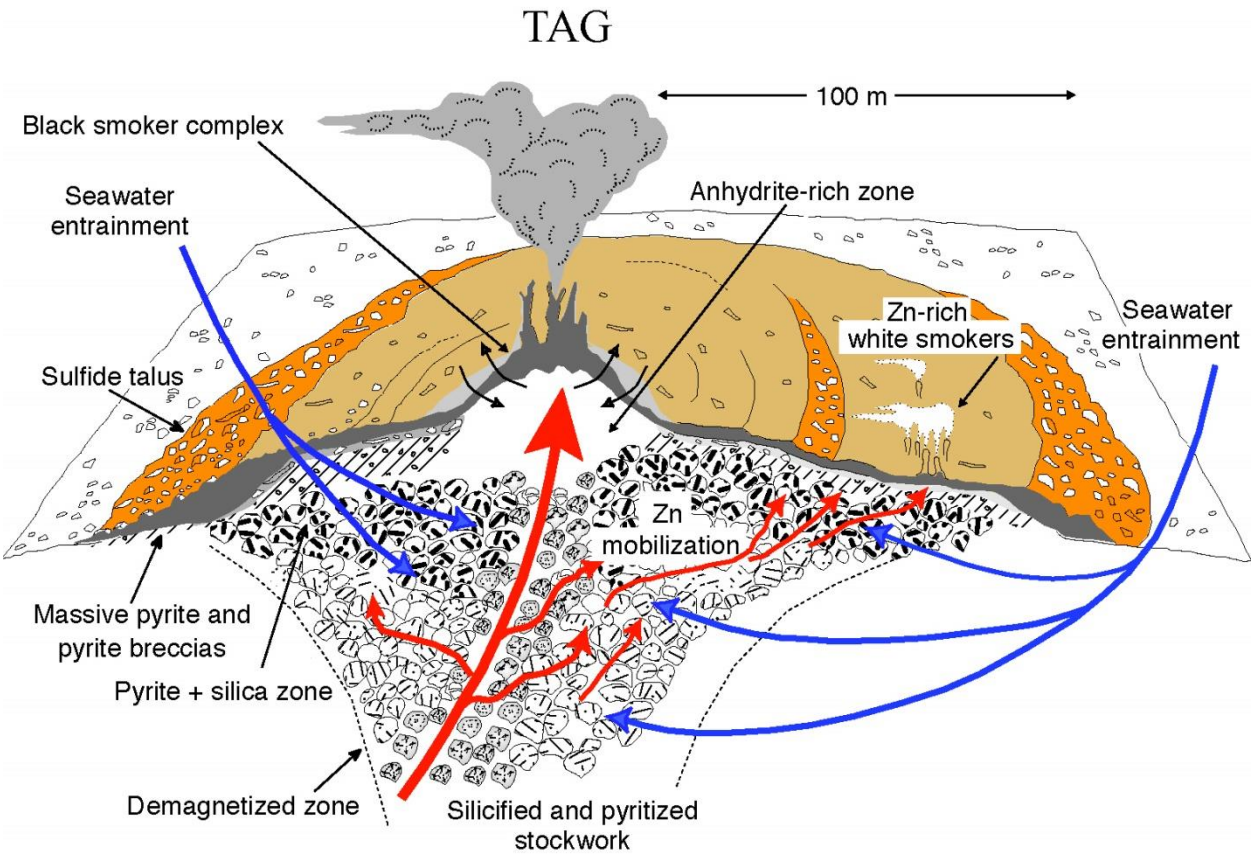

3. Formation of Seafloor Hydrothermal Fluids

The seafloor hydrothermal fluids that vent and form SMS deposits are a type of chemically evolved seawater produced by a series of progressively hotter chemical reactions between seawater and crustal host rock that take place as seawater percolates into the seafloor and is heated by hot rock or magma sourced from the earth's mantle (Alt, 1995). First, low-temperature (< 60°C) reactions between oxidized seawater and ferrous iron (Fe(II)) contained in primary igneous minerals produce secondary alteration minerals containing ferric iron (Fe(III)) and a reduced residual fluid (Alt, 1995; Figure 9). Above ~150°C, Mg^{2+} is removed from this fluid to form Mg-rich smectite (< 200°C) and chlorite (> 200°C) in exchange for H^{+}, Ca^{2+}, and Na^{+} contained in crustal host rocks (Alt, 1995; Figure 9). This process produces an acidic fluid from which Mg has been quantitatively removed (Alt, 1995; Figure 9). Also above ~150°C, precipitation of anhydrite ($CaSO_4$) leads to the removal of Ca and SO_4^{2-}, a process which continues as Ca^{2+} is leached from crustal host rocks (Alt, 1995; Figure 9). At higher temperatures, ion exchange reactions such as albitization ($CaAl_2Si_2O_8$ (anorthite) + $2Na^{+}$ + $4SiO_{2(aq)}$ $\rightarrow 2NaAlSi_3O_8$ (albite) + Ca^{2+}) and reduction of seawater sulfate to sulfide additionally modify hydrothermal fluid chemistry (Alt, 1995; Figure 9). At very high temperatures (~425°C), these hydrothermal fluids then leach metals (e.g., Cu, Fe, Mn, Zn) and reduced sulfur from crustal rocks (e.g., Alt, 1995; Butterfield et al., 2003). Magmatic volatiles (e.g., ^{3}He, CO_2, CH_4, H_2, H_2O, SO_2) can also enter hydrothermal fluids and modify fluid chemistry (e.g., Alt, 1995; Gamo et al., 1997; Reeves et al., 2011; Mottl et al., 2011).

As the temperature of hydrothermal fluids approaches the boiling curve (below the critical point) or two-phase boundary (above the critical point), the density of these fluids rapidly decreases and fluids are buoyant and rise (Norton, 1984; figure 10A). This decrease in density

coincides with maxima in the thermal expansion coefficient and heat capacity and a minimum in kinematic viscosity of water (Norton, 1984; Figures 10B to 10D). As a result, upflow is very rapid and hydrothermal fluids generally do not fully equilibrate, chemically or thermally, with surrounding host rocks as they rise (Norton 1984; Ding and Seyfried, 1994; Von Damm, 1995). Additionally, the dielectric constant of water decreases with temperature, such that charged particles form complexes. Thus, the thermodynamic activity of free ions (including H^+) is much decreased. Thermodynamic fluid modelling must thereby be implemented to calculate the thermodynamic activity of free ions and pH at *in situ* conditions.

Figure 9.
Schematic drawing of a cross section of a hydrothermal circulation cell (Jack Cook, WHOI Graphic Services) showing important chemical reactions and associated additions and removal of components from hydrothermal fluids at increasing temperatures (see text for details).

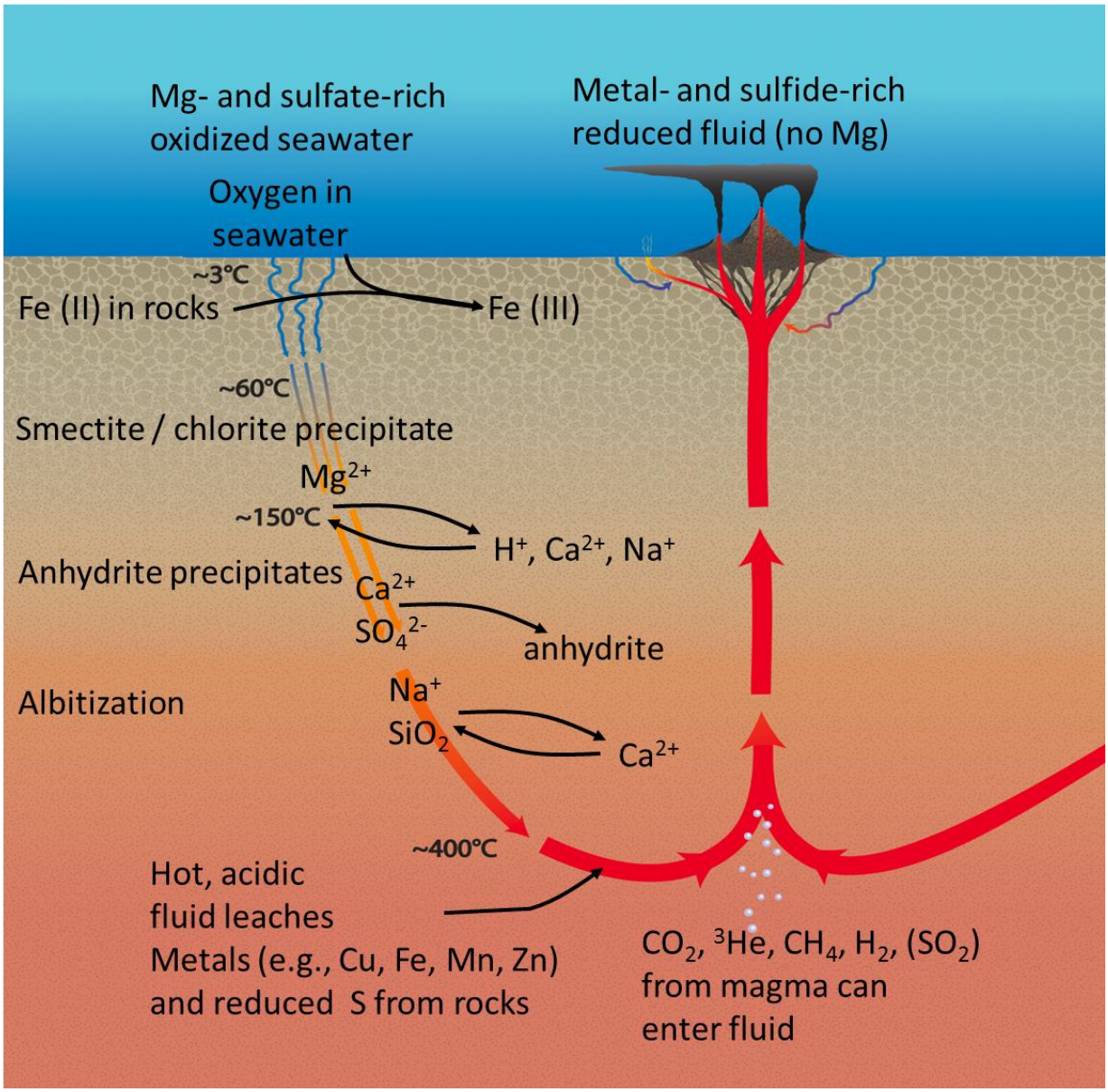

Figure 10.
Contour plots of the physical properties of pure water at temperatures from 0°C to 1000°C and pressures from 0 bar to 1000 bar including the (A) density (ρ), (B) thermal expansion coefficient (α), (C) heat capacity (C_p), (D) kinematic viscosity (υ), and (E) dielectric constant. Hydrothermal fluids are not pure water, but overall patterns in physical properties are thought to be comparable (from Norton, 1984).

Figure 10A. Density of Water as a Function of Temperature and Pressure

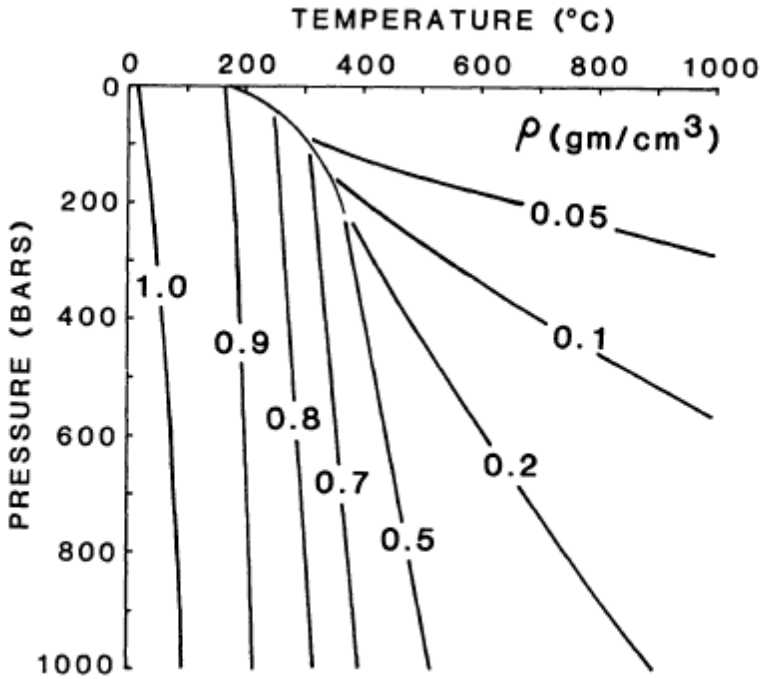

Figure 10B. Thermal Expansion Coefficient of Water as a Function of Temperature and Pressure

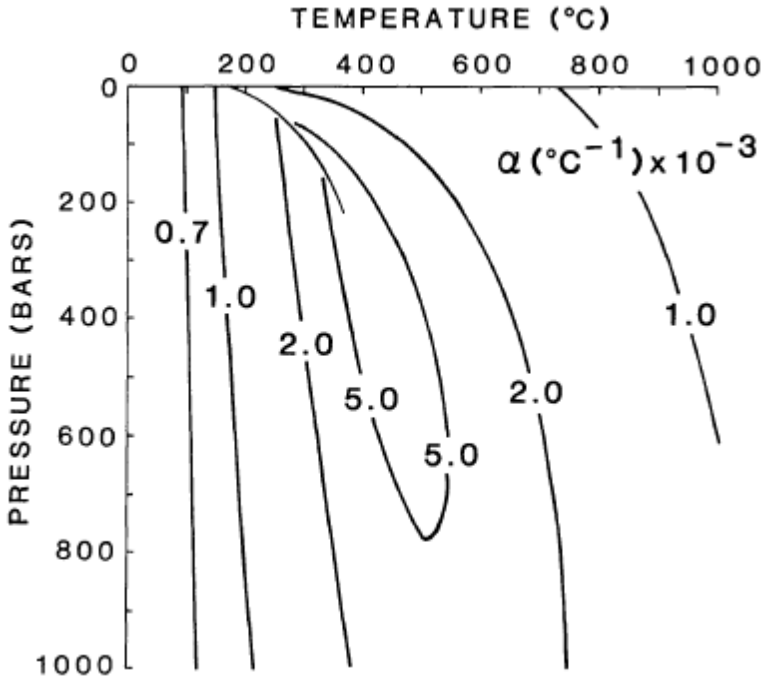

Figure 10C. Heat Capacity of Water as a Function of Temperature and Pressure

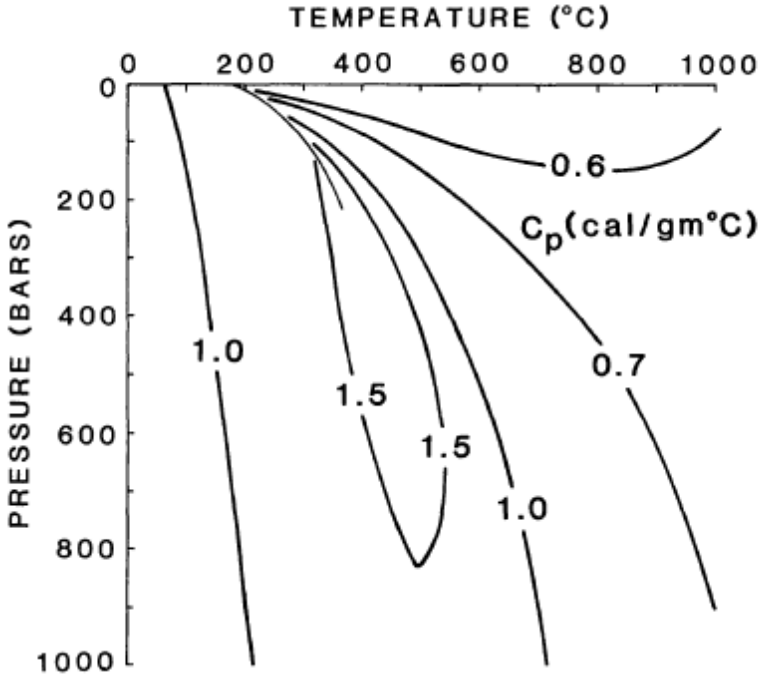

Figure 10D. Kinematic Viscosity of Water as a Function of Temperature and Pressure

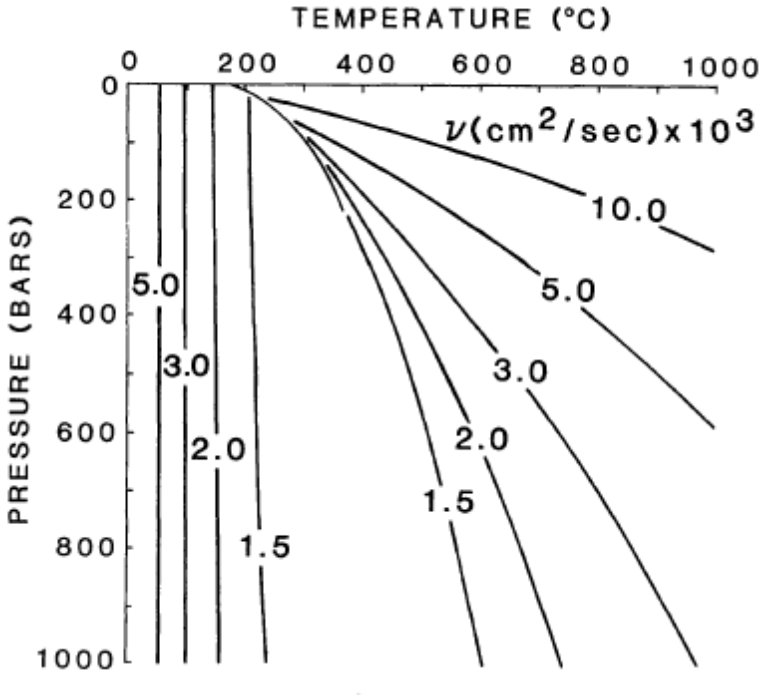

Figure 10E. Dielectric Constant of Water as a Function of Temperature and Pressure

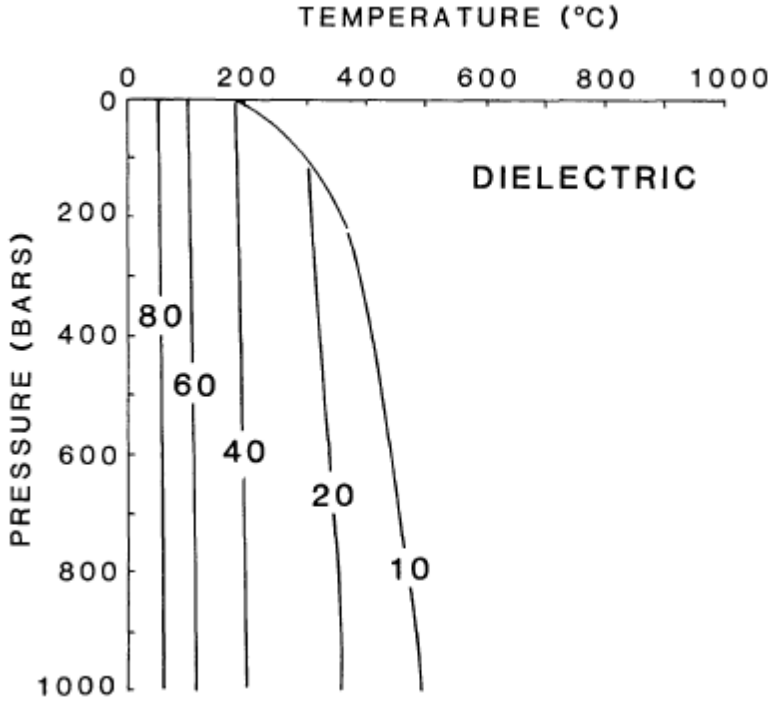

4. Measuring Trace Metals in Hydrothermal Fluids

Despite the potential for directly comparing SMS deposit characteristics with those of hydrothermal fluids and the importance of trace element analyses in the study of VMS and other sulfide ore deposits, relatively few data are available concerning the concentrations of sulfide mineral trace elements in hydrothermal fluids. Ironically, the paucity of data concerning these elements is partially a result of the partitioning of these elements into metal sulfide, as metal sulfide rich particulates precipitate during collection and cooling of the hydrothermal fluid sample (Figure 11). In order to obtain accurate measurements of trace metal contents of the original hydrothermal fluid, these particulate "dregs" fractions must be dissolved and analyzed (Trefry et al. 1994; Table 1). Additionally, metal-rich particulates might also precipitate from the dissolved fraction of the hydrothermal fluid sample during storage. These particulates (a.k.a. "filter" fractions) must also be filtered out, dissolved, and analyzed (Trefry et al. 1994). As with other hydrothermal fluid components, entrainment of seawater during sampling is accounted for by extrapolation to a zero-Mg endmember concentration following the assumption that endmember hydrothermal fluids contain negligible Mg (Von Damm et al., 1985).

Because dregs fractions can be contaminated with small pieces of SMS deposit materials entrained or "cored" during seafloor sampling, or incompletely recovered during shipboard sampling, accurate measurements of trace metals in hydrothermal fluid require that multiple (e.g., at least three) samples be taken from the same vent. However, such intensive sampling is time consuming and generally not performed. In cases where only one or two samples have been obtained (as is the case for all vent fluids analyzed in this thesis) the accuracy of hydrothermal fluid trace metal analyses can be posited (but not confirmed) by comparing vent fluids of similar temperature, pH, and major element compositions from the same vent field.

Figure 11.
Photograph of hydrothermal fluid sampling using the isobaric gas-tight (IGT) sampler described in Seewald et al. (2002) as manipulated by the Jason II remotely operated vehicle (Photograph by Chris German and the Jason Group). To the right is a schematic drawing of the IGT sampling container showing separation of a particulate "dregs" fraction (black) from the liquid "dissolved" fraction (blue). Gases, such as H_2 may also be sampled, while a particulate "filters" fraction may also precipitate from the dissolved fraction (or aliquots thereof) during storage.

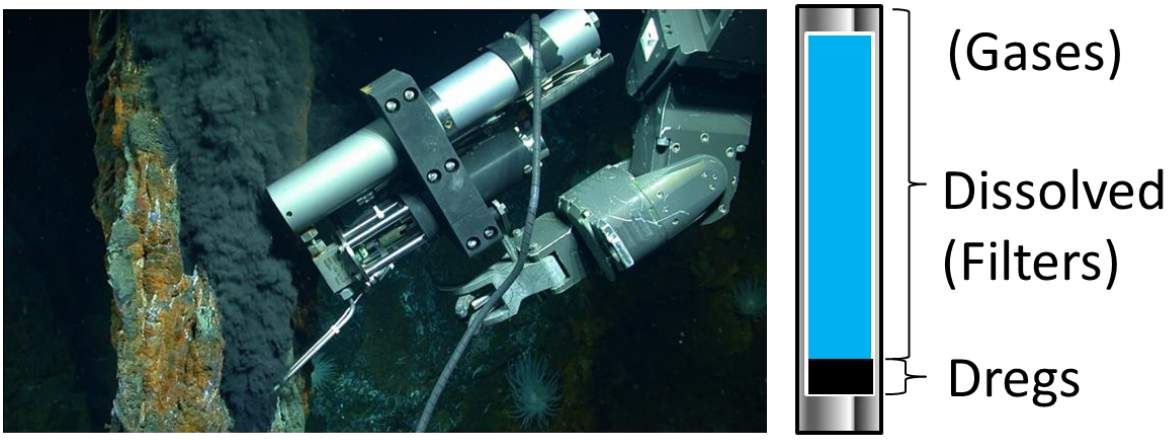

Table 1.
Reproduction of table from Trefry et al. (1994) listing the contribution of precipitates to the total concentration of various metals analyzed in hydrothermal fluids from the southern Juan de Fuca Ridge.

Contribution of Residual Precipitates to Total Concentrations of Trace Metals in Vent Fluids

Element	Range in Amounts of Metal in Precipitates, nmol kg^{-1} Fluid	Contributon of Precipitates as Percent of Total Metal	
		Average	Range
Ag	0.6-19	31	7-77
Cd	1-178	22	<1-58
Co	0.4-74	4	<1-18
Cu	100-2000	24	<1-53
Fe	<500-40,000	<0.1	<1
Mn	<500	<0.1	<0.1
Mo	<1-14	18	2-52
Pb	2.6-288	16	0.5-38
Sb	0.1-1.6	12	1-30
Zn	1300-159,000	19	<1-39

5. Measuring Trace Metals in SMS Deposits

Measurements of trace metals in SMS deposit materials are often performed on bulk mineral samples with distributions of trace elements among various minerals either being inferred by statistical correlations or, where possible, done on individual mineral grains by electron microprobe analysis (EMPA). While use of EMPA enables accurate and non-destructive measurements of trace elements at ~2 μm spatial scales, the relatively high detection limits of this technique (~100s μg/g) severely limit analyses of many trace elements. In particular, investigations of black smoker chimneys have shown that the concentrations of many trace elements in the innermost lining of black smoker chimneys are near or below the detection limits of electron microprobe (e.g., Tivey et al., 1995; Tivey et al., 1999; Craddock, 2009). Techniques offering lower detection limits, such as laser-ablation inductively coupled plasma mass spectrometry (LA-ICPMS), proton microprobe (PIXE), and secondary ion mass spectrometry (SIMS), have also been used to investigate black smoker chimney linings (Butler and Nesbitt, 1999; Ryan, 2001; Layne et al., 2005). Generally, these techniques suffer from a lack of homogeneous matrix-matched reference materials, though some recent progress has been made using standards of synthetic glass, sulfide sinters, or pressed sulfide powder precipitates (Danyushevsky et al., 2011 and papers using these methods; Wohlgemuth-Ueberwasser et al., 2011; Maslennikov et al., 2009). A major focus of this thesis and Chapter 3 in particular is the use of SIMS to measure trace elements in chalcopyrite precipitated along the innermost linings of black smoker chimneys and the construction of SIMS calibration curves by which to quantify trace element concentrations.

6. Overview of Thesis

The presence of actively forming massive sulfide deposits on the seafloor provides a unique opportunity to sample these metal-rich mineral deposits in the direct context of the high temperature (250°C to 400°C) metal-bearing fluids (±seawater) from which they form. Study of these deposits leads to insights into the analogous formation processes that produced hydrothermal sulfide deposits mined on land. These terrestrial deposits are important sources of Ag, Cu, Pb, and Zn, as well as several "critical" metals and metalloids used in advanced materials and electronics (e.g., Co, Ga, Ge, In). Moreover, the chemical contrast between reduced hydrothermal fluids venting at the seafloor and surrounding oxygenated seawater supplies chemical energy that supports robust deep sea ecosystems driven by chemosynthetic metabolisms. Seafloor massive sulfide deposits are important targets for biological prospecting today and may have played an essential role in the origin of life in the deep past (Corliss et al., 1981).

This thesis, entitled "Trace Element Proxies and Mineral Indicators of Hydrothermal Fluid Composition and Seafloor Massive Sulfide Deposit Formation Processes," seeks to determine how seafloor massive sulfide (SMS) deposits record aspects of the chemistry of hydrothermal fluids that, in turn, reflect volcanic, tectonic, and geodynamic processes. The thesis is divided into two parts. The first part, Chapter 2, investigates the morphology, mineralogy, and geochemistry of SMS deposits from six hydrothermal vent fields along the Eastern Lau Spreading Center, a back-arc spreading center dynamically linked to the Tonga Subduction Zone. Additional analyses of mineral-forming elements (e.g., Cu, Zn, Ba, and Pb) and H_2 in associated vent fluids supplement existing data and enable comparisons of SMS deposit samples with thermodynamic calculations of mineral saturation states and fluid speciation at *in situ* conditions.

The second part of the thesis, Chapters 3 and 4, examines the relationship between the trace element content of black smoker chimney linings and the chemistry of the hydrothermal fluids from which they formed. Secondary ion mass spectrometry is developed as a method for measuring trace elements (Co, Ni, Ga, Ag, In) in chalcopyrite, and analyses of trace elements in black smoker chimney linings are combined with new and published analyses of trace elements in corresponding hydrothermal fluids to more closely determine the mechanisms by which these elements are incorporated into chalcopyrite.

Chapter 2: Influences of the Tonga Subduction Zone on Seafloor Massive Sulfide Deposits along the Eastern Lau Spreading Center

Chapter 2 was submitted in August 2016 to *Geochimica et Cosmochimia Acta* with co-authors Dr. Margaret Tivey (Woods Hole Oceanographic Institution (WHOI)), Dr. Jeffrey Seewald (WHOI), and Dr. Geoff Wheat (University of Alaska Fairbanks) and is currently in revision. This chapter presents data on the mineralogy, bulk geochemistry, and electron microprobe analyses of mineral deposit samples collected from six hydrothermal vent fields along the Eastern Lau Spreading Center (ELSC). From north to south, the distance between each of these six vent fields and the Tonga Subduction Zone decreases from 100 km to 40 km.

Seafloor massive sulfide deposits from the basalt-hosted Kilo Moana and TowCam vent fields in the north resemble those found along mid-ocean ridges of similar spreading rates and consist of steep-sided Zn-, Fe-, and Cu-rich edifices, some with small sulfide-rich flanges. Further to the south, SMS deposits at the Tahi Moana-1, ABE and Tu'i Malila vent fields associated with more felsic lithologies exhibit higher concentrations of mantle-incompatible elements (e.g., Ba, Pb, As, and Sb), the presence of barite ($BaSO_4$) and galena (PbS), and a

southward increasing abundance of barite-rich flanges. These differences in the elemental content, mineralogy, and morphology of SMS deposits reflect a southward increase in the abundance of intermediate and felsic igneous rocks closer to the subduction zone (Fouquet et al., 1993; Martinez and Taylor, 2002; Langmuir et al., 2006; Bézos et al., 2009; Escrig et al., 2009).

Magmas along the ELSC close to the Tonga Subduction Zone are lower in temperature than their mid-ocean ridge counterparts and produce greater volumes of porous volcanic rocks (Martinez et al., 2006; Mottl et al., 2011; Sleeper and Martinez 2014). As a result, hydrothermal fluids along this length are typically lower in temperature, higher in pH, and vent at shallower depths than those along mid-ocean ridges with similar spreading rates (Mottl et al., 2011). The moderate pH of hydrothermal fluids results in zinc sulfide minerals precipitating at high temperatures. Deposits are Zn-rich and Cu-poor, Zn sulfides along fluid conduits are poor in trace elements, and Zn concentration in bulk samples exhibit poor correlations with other elements except Cd. An exception to this rule is found at the southernmost Mariner vent field, where Cu-rich deposits are associated with high-temperature, low-pH (< 3 at 25°C) fluids.

Concentrations of Zn in bulk samples collected at the Mariner vent field and at northern vent fields where hydrothermal fluids exhibit pH < 3.5 are significantly correlated with Ag. The exceptionally low pH of hydrothermal fluids at the Mariner vent field is likely caused by localized entrainment of SO_2-rich magmatic volatiles sourced from oxidized magmas (Mottl et al., 2011). Because such magmas form in the regions closest to the subduction zone, even the exceptional hydrothermal fluids and deposits found at the Mariner vent field are closely related to the back-arc geologic setting.

Chapter 3: Trace Element Chemistry of Black Smoker Chimney Linings Measured by Secondary Ion Mass Spectrometry

Chapter 3 focuses on the development of secondary ion mass spectrometry (SIMS) as a method for measuring trace elements (Co, Ni, Ga, Ag, In) in the chalcopyrite linings of black smoker chimneys. These elements are thought to occur as substitutions for Cu and Fe in the chalcopyrite crystal lattice (e.g., Huston et al., 1995). SIMS is chosen as a preferred method because it produces smaller (and shallower) ablation pits in comparison with laser ablation inductively coupled mass spectrometry, and lower detection limits than electron microprobe analyses. Following the use of SIMS to examine the spatial homogeneity and relative abundances of selected trace elements in black smoker chimney linings, handpicked grains of chalcopyrite from selected black smoker chimney linings were digested and analyzed by inductively coupled plasma mass spectrometry and compared with serial dilutions of standard reference solutions. This allowed for the construction of calibration curves by which to derive quantitative measurements of Co, Ni, Ga, Ag, and In in chalcopyrite using SIMS. Linings of black smoker chimneys are generally homogeneous (standard error < 20% of the mean) and trace element concentrations cover a wide enough range to readily distinguish between linings from different vents and deposits. Thus, these measurements may provide useful information about differences in hydrothermal fluid chemistry. Additionally, a correlation is observed between hydrothermal fluid pH and the Ga and In contents of black smoker chimney linings measured by SIMS, providing a potential proxy of hydrothermal fluid pH based on the trace element contents of black smoker chimney linings.

Chapter 4: Trace Element Proxies of Hydrothermal Fluid pH and Metal Content Based on Sample Pairs of Seafloor Hydrothermal Fluids and Chalcopyrite Lining Black Smoker Chimneys

Chapter 4 investigates the behavior of trace elements (Co, Ni, Ga, Ag, In) in "black smoker" chimneys and corresponding hydrothermal vent fluids. SIMS analyses of trace elements in black smoker chimney linings from Chapter 3 are combined with new analyses of these elements in hydrothermal fluids from the Eastern Lau Spreading Center and previously published analyses of hydrothermal fluids from vent fields in the Manus Basin (Craddock, 2009). Thermodynamic modelling is implemented to calculate fluid speciation including the activities of free ions and pH at *in situ* temperatures and pressures. In this chapter, a linear relationship is identified between the Ag concentration of chalcopyrite lining black smoker chimneys and the free ion activity ratio of Ag+ : Cu+ in hydrothermal fluids suggesting regular partitioning of Ag into chalcopyrite as a lattice substitution replacing Cu. When combined with the Ga and In proxy of hydrothermal fluid pH identified in Chapter 3, the concentration of Ag in black smoker chimney linings provides a further proxy for pH and also for concentrations of Ag and Cu in the associated hydrothermal fluids.

References

Albarede, F., Michard, A., Minster, J. F., and Michard, G. (1981) $^{87}Sr/^{86}Sr$ ratios in hydrothermal waters and deposits from the East Pacific Rise at 21 N. *Earth Planet. Sci. Lett.*, ***55*(2)**, 229-236.

Alt, J. C. (1995) Subseafloor Processes in Mid- Ocean Ridge Hydrothermal Systems. In *Seafloor hydrothermal systems: physical, chemical, biological, and geological interactions* (eds. S. E. Humphris, R. A. Zierenberg, L. S. Mullineaux, and R. E. Thomson), American Geophysical Union, Washington, D. C.. pp. 85-114.

Beaulieu, S. E., Baker, E. T., German, C. R., and Maffei, A. (2013) An authoritative global database for active submarine hydrothermal vent fields. *Geochem. Geophys. Geosys.*, ***14*(11)**, 4892-4905.

Beaulieu, S. E., Baker, E. T., and German, C. R. (2015) Where are the undiscovered hydrothermal vents on oceanic spreading ridges?. *Deep Sea Research Part II: Topical Studies in Oceanography*, **121**, 202-212.

Bézos, A., Escrig, S., Langmuir, C. H., Michael, P. J., and Asimow, P. D. (2009) Origins of chemical diversity of back- arc basin basalts: A segment- scale study of the Eastern Lau Spreading Center. *J. Geophys. Res.: Solid Earth*, **114**, *B06212, doi:*10.1029/2008JB005924.

Bischoff, J. L., and Seyfried, W. E. (1978) Hydrothermal chemistry of seawater from 25 degrees to 350 degrees C. *Amer. J. Sci.*, **278(6)**, 838-860.

Butler, I. B. and Nesbitt, R. W. (1999) Trace element distributions in the chalcopyrite wall of a black smoker chimney: insights from laser ablation inductively coupled plasma mass spectrometry (LA–ICP–MS) *Earth Planet. Sci. Lett.*, **167(3)**, 335-345.

Butterfield, D. A., Seyfried Jr., W. E., and Lilley, M. D. (2003) Composition and evolution of hydrothermal fluids. In *Energy and Mass Transfer in Marine Hydrothermal Systems* (eds. P.E. Halbach, V. Tunnicliffe, J. R. Hein), Berlin, Dahlem University Press, **89**, pp. 123-161.

Corliss, J. B., Dymond, J., Gordon, L. I., and Edmond, J. M. (1979) Submarine Thermal Springs on the Galapagos Rift. *Science*, **203**, 16.

Corliss, J. B., Baross, J. A., and Hoffman, S. E. (1981) An Hypothesis Concerning the Relationships Between Submarine Hot Springs and the Origin of Life on Earth. *Oceanologica Acta, Special issue*.

Craddock, P. R. (2009) Geochemical tracers of processes affecting the formation of seafloor hydrothermal fluids and deposits in the Manus back-arc basin. Ph.D. Thesis, MIT/WHOI Joint Program in Oceanography.

Craddock, P. R., Bach, W., Seewald, J. S., Rouxel, O. J., Reeves, E., and Tivey, M. K. (2010) Rare earth element abundances in hydrothermal fluids from the Manus Basin, Papua New Guinea: Indicators of sub-seafloor hydrothermal processes in back-arc basins. *Geochim. Cosmochim Acta*, **74(19)**, 5494-5513.

Danyushevsky, L., Robinson, P., Gilbert, S., Norman, M., Large, R., McGoldrick, P., and Shelley, M. (2011) Routine quantitative multi-element analysis of sulphide minerals by laser ablation ICP-MS: Standard development and consideration of matrix effects. *Geochemistry: Exploration, Environment, Analysis*, **11(1)**, 51-60.

Ding, K., and W.E. Seyfried Jr. (1994) Effect of conductive cooling on chemistry of mid-ocean ridge hydrothermal fluids: Experimental and theoretical constraints. *Mineralogical Magazine* **58A**:231–232.

Escrig, S., Bézos, A., Goldstein, S. L., Langmuir, C. H., and Michael, P. J. (2009) Mantle source variations beneath the Eastern Lau Spreading Center and the nature of subduction components in the Lau basin–Tonga arc system, *Geochem. Geophys. Geosys.*, **10**, *Q04014, doi:*10.1029/2008GC002281.

Fouquet, Y., von Stackelberg, U., Charlou, J. L., Erzinger, J., Herzig, P. M., Mühe, R., and Wiedicke, M. (1993) Metallogenesis in back-arc environments: the Lau Basin example. *Econ. Geol.*, **88(8)**, 2154-2181.

Franklin, J. M., Gibson, H. L., Jonasson, I. R., and Galley, A. G. (2005) Volcanogenic massive sulfide deposits. *Economic Geology 100th Anniversary Volume*, Society of Economic Geologists, Littleton, Colorado, USA, 523-560.

Galley, A. G., Hannington, M. D., and Jonasson, I. R. (2007) Volcanogenic massive sulphide deposits. In *Mineral deposits of Canada: A synthesis of major deposit types, distinct metallogeny, and the evolution of geological provinces, and exploration methods, 5* (ed. W. Goodfellow), St. Johns, Geological Association of Canada, Mineral Deposits Division, Special Publication 5, pp. 141-162.

Gamo, T., Okamura, K., Charlou, J. L., Urabe, T., Auzende, J. M., Ishibashi, J., Shitashima, K., Chiba, H., and Shipboard Scientific Party of the ManusFlux Cruise (1997) Acidic and sulfate-rich hydrothermal fluids from the Manus back-arc basin, Papua New Guinea. *Geology*, **25(2)**, 139-142.

Goldfarb, M. S., Converse, D. R. Holland, H. D. and Edmond, J. M. (1983) The genesis of hot spring deposits on the East Pacific Rise, 21° N, *Economic Geology Monographs*, **5**, 184-197.

Hannington, M. D., Jonasson, I. R., Herzig, P. M., and Petersen, S. (1995) Physical and chemical processes of seafloor mineralization at mid- ocean ridges. In *Seafloor hydrothermal systems: physical, chemical, biological, and geological interactions* (eds. S. E. Humphris, R. A. Zierenberg, L. S. Mullineaux, and R. E. Thomson), American Geophysical Union, Washington, D. C.. pp. 115-157. doi: 10.1029/GM091p0115.

Hannington, M. D., de Ronde, C. D. J., and Petersen, S. (2005) *Sea-floor tectonics and submarine hydrothermal systems. Economic Geology 100th Anniversary Volume.* Society of Economic Geologists, Littleton, Colorado, USA, pp. 111-141.

Hannington, M., Jamieson, J., Monecke, T., and Petersen, S. (2010) Modern sea-floor massive sulfides and base metal resources: Toward an estimate of global sea-floor massive sulfide potential. *Society of Economic Geologists Special Publication*, **15**, 317-338.

Hannington, M., Jamieson, J., Monecke, T., Petersen, S., and Beaulieu, S. (2011) The abundance of seafloor massive sulfide deposits. *Geology*, **39(12)**, 1155-1158.

Haymon, R. M. (1983) Growth history of hydrothermal black smoker chimneys. *Nature*, **301**, 695-698.

Haymon, R. M., and Kastner, M. (1981) Hot spring deposits on the East Pacific Rise at 21 N: preliminary description of mineralogy and genesis. *Earth Planet. Sci. Lett.*, **53(3)**, 363-381.

Humphris, S. E., and Tivey, M. K. (2000) A synthesis of geological and geochemical investigations of the TAG hydrothermal field: Insights into fluid-flow and mixing processes in a hydrothermal system. *Special Papers-Geological Society of America*, 213-236.

Herrington, R.J., Maslennikov, V.V., Spiro, B., Zaykov, V.V., and Little, C.T.S. (1998) Ancient vent chimney structures in the Silurian massive sulphides of the Urals. In *Modern Ocean Floor Processes and the Geological Records. Geol. Soc. London, Special Publications,* **148** (eds. R. A. Mills, K. Harrison), pp. 241–257.

Huston, D. L., Sie, S. H., Suter, G. F., Cooke, D. R., and Both, R. A. (1995) Trace elements in sulfide minerals from eastern Australian volcanic-hosted massive sulfide deposits; Part I, Proton microprobe analyses of pyrite, chalcopyrite, and sphalerite, and Part II, Selenium levels in pyrite; comparison with delta 34 S values and implications for the source of sulfur in volcanogenic hydrothermal systems. *Econ. Geol.*, **90(5)**, 1167-1196.

Kassianidou, V. and Knapp, A. B. (2005) Archaeometallurgy in the Mediterranean: The social context of mining, technology and trade. In *The Archaeology of Mediterranean Prehistory* (eds. E. Blake and A. B. Knapp), John Wiley & Sons, pp. 215-51.

Kawasumi, S., and Chiba, H. (2017) Redox state of seafloor hydrothermal fluids and its effect on sulfide mineralization. *Chem. Geol.*. **451**, 25-37.

Kormas, K. A., Tivey, M. K., Von Damm, K., and Teske, A. (2006) Bacterial and archaeal phylotypes associated with distinct mineralogical layers of a white smoker spire from a deep- sea hydrothermal vent site (9 N, East Pacific Rise) *Environmental Microbiology*, **8(5)**, 909-920.

Langmuir, C. H., Bézos, A., Escrig, S., and Parman, S. W. (2006) Chemical systematics and hydrous melting of the mantle in back-arc basins. In *Back-Arc Spreading Systems: Geological, Biological, Chemical, and Physical Interactions* (eds. D. M. Christie, C. R.

Fisher, S.-M. Lee, and S. Givens) Geophysical Monograph Series, vol. 166, American Geophysical Union, Washington, DC. Pp. pp. 87–146.

Layne, G., Tivey, M. K., and Humphris, S. E. (2005) Trace metal concentrations in common sulfide minerals using SIMS. *Fifteenth Annual V. M. Goldschmidt Conference* Abstracts, A55.

Little, C. T. S., Herrington, R. J., Maslennikov, V. V., and Zaykov, V. V. (1998) The fossil record of hydrothermal vent communities. *Geological Society, London, Special Publications*, **148(1)**, 259-270.

Martinez, F. and Taylor, B. (2002) Mantle wedge control on back-arc crustal accretion. *Nature*. **416**, 417-420.

Martinez, F., Taylor, B., Baker, E. T., Resing, J. A., and Walker, S. L. (2006) Opposing trends in crustal thickness and spreading rate along the back-arc Eastern Lau Spreading Center: Implications for controls on ridge morphology, faulting, and hydrothermal activity. *Earth Planet. Sci. Lett.*, **245(3)**, 655-672.

Maslennikov, V.V., Maslennikova, S.P., Large, R.R., and Danyushevsky, L.V., (2009) Study of trace element zonation in vent chimneys from the Silurian Yaman-Kasy volcanic-hosted massive sulfide deposits (the southern Urals, Russia) using laser ablation inductively coupled plasma mass spectrometry (LA-ICP MS), *Econ. Geol*., **104**, 1111–1141.

McDermott, J. M., Ono, S., Tivey, M. K., Seewald, J. S., Shanks, W. C., and Solow, A. R. (2015) Identification of sulfur sources and isotopic equilibria in submarine hot-springs using multiple sulfur isotopes. *Geochim. Cosmochim. Acta*, **160**, 169-187.

Mottl, M. J., Seewald, J. S., Wheat, C. G., Tivey, M. K., Michael, P. J., Proskurowski, G., McCollom, M., Reeves, E., Sharkey, S., You, C.-F., Chan, L.-H., and Pichler, T. (2011) Chemistry of hot springs along the Eastern Lau Spreading Center. *Geochim. Cosmochim. Acta*, **75(4)**, 1013-1038.

Norton, D. L. (1984) Theory of hydrothermal systems. *Annual Review of Earth and Planetary Sciences*, ***12*(1)**, 155-177.

Oudin, E., Constantinou, G. (1984) Black smoker chimney fragments in Cyprus sulphide deposits. *Nature*, **308**, 349–353.

Reeves, E. P., Seewald, J. S., Saccocia, P., Bach, W., Craddock, P. R., Shanks, W. C., Sylva. S., Walsh, E., Pichler, T., and Rosner, M. (2011) Geochemistry of hydrothermal fluids from the PACMANUS, Northeast Pual and Vienna Woods hydrothermal fields, Manus Basin, Papua New Guinea. *Geochim. Cosmochim. Acta*, **75(4)**, 1088-1123.

Revan, M. K., Genç, Y., Maslennikov, V. V., Maslennikova, S. P., Large, R. R., and Danyushevsky, L. V. (2014) Mineralogy and trace-element geochemistry of sulfide minerals in hydrothermal chimneys from the Upper-Cretaceous VMS deposits of the eastern Pontide orogenic belt (NE Turkey) *Ore Geology Reviews*, **63**, 129-149.

Ryan, C. G. (2001) Developments in dynamic analysis for quantitative PIXE true elemental imaging. *Nuclear Instruments and Methods in Physics Research Section B: Beam Interactions with Materials and Atoms*, **181(1)**, 170-179.

Rouxel, O., Fouquet, Y., and Ludden, J. N. (2004) Subsurface processes at the Lucky Strike hydrothermal field, Mid-Atlantic Ridge: evidence from sulfur, selenium, and iron isotopes. *Geochim. Cosmochim. Acta*, **68(10)**, 2295-2311.

Sarrazin, J., Juniper, S. K., Massoth, G., and Legendre, P. (1999) Physical and chemical factors influencing species distributions on hydrothermal sulfide edifices of the Juan de Fuca Ridge, northeast Pacific. *Marine Ecology Progress Series*, 89-112.

Seewald, J. S., Doherty, K. W., Hammar, T. R., and Liberatore, S. P. (2002) A new gas-tight isobaric sampler for hydrothermal fluids. *Deep Sea Research Part I: Oceanographic Research Papers*, **49(1),** 189-196.

Scott, S.D. (1981) Small chimneys from Japanese Kuroko deposits. In *Seminars on Seafloor Hydrothermal Systems* (eds. R. Goldie, T. J. Botrill), Geosciences Canada. 8, pp. 103–104.

Sleeper, J. D. and Martinez, F. (2014) Controls on segmentation and morphology along the back- arc Eastern Lau Spreading Center and Valu Fa Ridge. *J. Geophys. Res.*, **119(3)**, 1678-1700.

Spiess, F. N., Macdonald, K. C., Atwater, T., Ballard, R., Carranza, A., Cordoba, D., Cox, C., Diaz Garcia, V. M., Francheteau, J., Guerrero, J., Hawkins, J., Haymon, R., Hessler, R., Juteau, T., Kaster, M., Larson, R., Luyendyk, B., Macdougall, J. D., Miller, S., Normark, W., Orcutt, J., Rangin, C. (1980) East Pacific Rise: Hot Springs and Geophysical Experiments. *Science*, **207**, 1421-1433.

Tivey, M. K. (1995) The influence of hydrothermal fluid composition and advection rates on black smoker chimney mineralogy: Insights from modeling transport and reaction. *Geochim. Cosmochim. Acta*, **59(10)**, 1933-1949.

Tivey, M. K., Humphris, S. E., Thompson, G., Hannington, M. D., and Rona, P. A. (1995) Deducing patterns of fluid flow and mixing within the TAG active hydrothermal mound using mineralogical and geochemical data. *J. Geophys. Res.: Solid Earth*, **100(B7)**, 12527-12555.

Tivey, M. K., Stakes, D. S., Cook, T. L., Hannington, M. D., and Petersen, S. (1999) A model for growth of steep- sided vent structures on the Endeavour Segment of the Juan de Fuca

Ridge: Results of a petrologic and geochemical study. *J. Geophys. Res.: Solid Earth*, **104(B10),** 22859-22883.

Tivey, M. K. (2007) Generation of seafloor hydrothermal vent fluids and associated mineral deposits. *Oceanography* **20**, 1 (2007): 50-65.

Trefry, J. H., Butterfield, D. B., Metz, S., Massoth, G. J., Trocine, R. P., and Feely R. A. (1994) Trace metals in hydrothermal solutions from Cleft segment on the southern Juan de Fuca Ridge. *J. Geophys. Res.: Solid Earth.* **99,** 4925–4935.

Von Damm, K. L. (1995) Controls on the chemistry and temporal variability of seafloor hydrothermal fluids. In *Seafloor Hydrothermal Systems: Physical, Chemical, Biological, and Geological Interactions* (eds. S. E. Humphris, R. A. Zierenberg, L. S. Mullineaux, and R. E. Thomson), American Geophysical Union, Washington, D. C., pp. 222-247.

Von Damm, K. L., Edmond, J. M., Grant, B., Measures, C. I., Walden, B., and Weiss, R. F. (1985) Chemistry of submarine hydrothermal solutions at 21° N, East Pacific Rise. *Geochim. Cosmochim. Acta*, **49(11),** 2197-2220.

Wohlgemuth-Ueberwasser, C. C., Viljoen, F., Petersen, S., and Vorster, C. (2015) Distribution and solubility limits of trace elements in hydrothermal black smoker sulfides: An in-situ LA-ICP-MS study. *Geochim. Cosmochim. Acta,* **159**, 16-41.

Chapter 2

Influences of the Tonga Subduction Zone on Seafloor Massive Sulfide Deposits along the Eastern Lau Spreading Center

(This chapter was submitted in August 2016 to *Geochimica et Cosmochimia Acta* and is currently under revision as a co-authored paper with Margaret K. Tivey (Woods Hole Oceanographic Institution (WHOI)), Jeffrey S. Seewald (WHOI), and C. Geoff Wheat (University of Alaska Fairbanks))

ABSTRACT

This study investigates the morphology, mineralogy, and geochemistry of seafloor massive sulfide (SMS) deposits from six back-arc hydrothermal vent fields along the Eastern Lau Spreading Center (ELSC) in the context of endmember vent fluid chemistry and proximity to the Tonga Subduction Zone. Additional analyses of mineral-forming elements (Cu, Zn, Ba, and Pb) and $H_{2\,(aq)}$ in hydrothermal fluids supplement existing data and enable thermodynamic calculations of mineral saturation states at *in situ* conditions.

From north to south, a decrease in distance between the Eastern Lau Spreading Center and the Tonga Subduction Zone correlates with a change in crustal lithology from back-arc basin basalt in the north to mixed andesite, rhyolite, and dacite in the south. Results presented here document southward increases in the abundance of mantle-incompatible elements in hydrothermal fluids (Ba and Pb) and SMS deposits (Ba, Pb, As, and Sb), which is also expressed

in the abundance of barite ($BaSO_4$) and galena (PbS) in SMS deposits. Barite influences deposit morphology, contributing to the formation of horizontal flanges and squat terraces.

From north to south, a regional-scale lowering of hydrothermal reaction zone temperatures leads to lower-temperature, higher-pH vent fluids relative to mid-ocean ridges of similar spreading rates (Mottl et al., 2011). These fluids are Zn- and Cu-poor and vent from Zn-rich, Cu-poor deposits. Locally, higher-temperature and lower pH vent fluids at the southernmost Mariner vent field have been linked to higher reaction zone temperatures and the localized addition of acidic magmatic volatiles (Mottl et al., 2011). These fluids are Zn- and Cu-rich and vent from Cu-rich, Zn-poor and Pb-poor SMS deposits. Thermodynamic calculations indicate that the contrasting metal contents of vent fluids and SMS deposits can be accounted for by vent fluid pH. Wurtzite/sphalerite ((Zn, Fe)S) and galena (PbS) are saturated at higher temperatures in higher-pH, Zn-, Cu-, and Pb-poor ELSC vent fluids, but are undersaturated at similar temperatures in low-pH, Zn- , Cu-, and Pb-rich vent fluids from the Mariner vent field.

Indicators of pH in ELSC SMS deposits include the presence of co-precipitated wurtzite and chalcopyrite along conduit linings in deposits formed from higher pH fluids and different correlations between concentrations of Zn and Ag in bulk geochemical analyses. Significant positive Zn:Ag correlations are found in deposits associated with hydrothermal fluids of pH < 3.6, while weak or negative correlations of Zn:Ag are found in deposits formed from fluids of pH > 3.5 to 4. The mineral linings of open conduit chimneys (minerals present, mol% FeS in (Zn,Fe)S), which precipitate directly from hydrothermal fluids, closely reflect the temperature and sulfur fugacity of sampled hydrothermal fluids. These mineral linings thus can be used as indicators of hydrothermal fluid temperature and composition (pH, metal content, sulfur fugacity).

1. INTRODUCTION

Seafloor massive sulfide (SMS) deposits form as acidic, metal- and sulfide-rich hydrothermal fluids discharge into cold, alkaline, oxygen- and sulfate-rich seawater. Such hydrothermal fluids are produced as a result of rock-dominated hydrothermal reactions that occur along mid-ocean- and back-arc spreading centers when seawater that has percolated into the earth's lithosphere is heated by hot rock or magma sourced from the earth's mantle. The presence of active venting provides the opportunity to directly sample hydrothermal fluids as well as the deposits that are forming either directly from these fluids (e.g., mineral linings of black smoker chimneys) or from mixtures of these fluids with seawater, providing insight into SMS formation. Specifically, SMS deposits are thought to be closely analogous to volcanic-associated massive sulfide deposits, an important class of base-metal ore deposit (Hannington et al., 1995). In this context, the study of active SMS deposits along back-arc spreading centers is especially important as more than 80% of volcanic-associated massive sulfide deposits are thought to have formed in similar geologic settings (Barrie and Hannington, 1999; Franklin et al., 2005; Hannington et al., 2005). Sampling along back-arc spreading centers has revealed a diversity of hydrothermal fluid chemistry and SMS deposit types that can be related to variations in seafloor lithology and the influences of subduction-zone geologic processes (e.g., Hannington et al., 2005 and references therein; Craddock, 2009; Reeves et al., 2011; Mottl et al., 2011).

The Eastern Lau Spreading Center (ELSC) in the Lau back-arc Basin of the southwestern Pacific Ocean (Fig.1) is an ideal setting in which to study the effects of subduction-zone geologic processes on actively forming SMS deposits. From north to south, a near-linear decrease in distance between the ELSC and the adjacent Tofua Volcanic Arc is accompanied by systematic variations in spreading center morphology, spreading rate, and seafloor lithology (Taylor and

Martinez, 2003; Martinez et al., 2006; Ferrini et al., 2008; Bézos et al., 2009; Escrig et al., 2009; Sleeper and Martinez, 2014). In turn, these variations have been linked to differences in hydrothermal fluid chemistry (Fouquet et al., 1993a; Ishibashi et al., 2006; Takai et al., 2008; Mottl et al., 2011), SMS deposits (Fouquet et al., 1993a; Tivey et al., 2005; Ferrini et al., 2008; Takai et al., 2008), and biological communities (Podowski et al., 2009; Beinart et al., 2012; Flores et al., 2012). Analyses by Mottl et al. (2011) of hydrothermal fluids from the vent fields investigated here document systematic regional-scale trends in vent fluid chemistry related to a southward decrease in the temperature of hydrothermal reaction zones, a transition to more felsic lithology with a subducted sediment component closer to the subduction zone, and the distinct chemistry of vent fluids from the Mariner vent field consistent with the addition of acidic magmatic volatiles.

This report provides a systematic overview of the morphology, mineralogy, and geochemistry of SMS deposits from six active hydrothermal vent fields along the ELSC. From north to south, these vent fields are: Kilo Moana, TowCam, Tahi Moana-1, ABE, Tu'i Malila, and Mariner (Fig. 1). This report also presents data on the concentrations of dissolved metals (Cu, Zn, Pb, Ba) and H_2 in hydrothermal fluids collected from these vent fields (Table 1b). These new data are used in conjunction with previously published data from Mottl et al. (2011) to model fluid speciation and mineral saturation at *in situ* conditions. The results of fluid modelling are then compared with the observed mineralogy of paired mineral samples from SMS deposits. Such comparisons provide insight into the formation processes of SMS deposits along the ELSC within the regional geologic context of the Tonga Subduction Zone.

2. GEOLOGIC SETTING

The ELSC is an active back-arc spreading center located in the Lau Basin between the islands of Tonga and Fiji (Fig. 1A). From a regional perspective, the triangular Lau Basin is the northern section of a 2,000 km-long southward-propagating extensional tectonic region that also includes the Kermadec Volcanic Arc and the Taupo Volcanic Zone (Fig. 1A; Parson and Wright, 1996). To the east, the near-parallel lineaments of the Tofua Volcanic Arc and the Tonga Subduction Zone form a 17° angle with the strike of the ELSC and the distance between the ELSC and the Tofua Volcanic Arc decreases from ~100 km in the north to ~40 km in the south. Concurrent with this change in distance to the Tofua Volcanic Arc, the ELSC spans a geomorphologic transition from an axial trough in the north to an axial ridge in the south (von Stackelberg et al., 1985, 1988, 1990; Foucher et al., 1988). Between the latitudes of 20°50'S and 22°40'S, the axial ridge is bathymetrically well-defined and is identified as the Valu Fa Ridge (Fig. 1B); seismic records indicate continuation of the ridge beneath sedimentary cover as far north as 20°20'S (Foucher et al., 1988; Wiedicke and Collier, 1993).

The geomorphologic transition from axial valley to axial ridge (Martinez and Taylor, 2002) is accompanied by a change in crustal lithology from tholeiitic back-arc-basin basalt in the north to mixtures of basaltic andesite, andesite, and rhyodacite in the south (Jenner et al., 1987; Frenzel et al., 1991; Vallier et al., 1991; Fouquet et al., 1993a; Fretzdorff et al., 2006; Langmuir et al., 2006; Bézos et al., 2009; Escrig et al., 2009; Sleeper and Martiner, 2014). Escrig et al. (2009) and Sleeper and Martinez (2014) identify two important sources of geochemical variation along the ELSC. First, a stepwise transition in crustal lithology and isotopic signatures at 20°36'05"S (between the TowCam and Tahi Moana-1 vent fields) is proposed to coincide with the presence of hydrated mantle associated with the Tonga Subduction Zone (Sleeper and

Martinez, 2014). South of this transition zone, subduction zone signatures increase with proximity to the subduction zone and crustal rocks are enriched in elements such as Ba and Pb, which are fluid-mobile and preferentially partition into melts during mantle melting (Escrig et al., 2009; Sleeper and Martinez, 2014). A second-order sinusoidal variation in crustal lithology and isotopic signatures is also identified south of this transition zone and is proposed to represent the influence of hydrated melt diapirs likewise arising from the subducting slab (Escrig et al., 2009; Sleeper and Martinez, 2014). This second-order variation correlates with second-order segmentation of the ELSC and the projected locations of arc volcano clusters (Sleeper and Martinez, 2014). One of these proposed diapirs occurs at 22°12'S, corresponding with a region of enhanced volcanism and the overlapping spreading center that hosts the Mariner vent field as well as the projected location of Ata volcano (Fig. 1B; Escrig et al., 2009; Sleeper and Martiner, 2014). A second proposed hydrated melt diaper occurs at 21°33'S (between the ABE and Tu'i Malila vent fields) (Escrig et al., 2009; Sleeper and Martinez, 2014).

A 460-channel towed seismic survey indicates the presence of two axial magma chambers beneath the ELSC (Harding et al., 2000; Jacobs et al., 2007). The northern magma chamber extends from 20°30'S to 21°30'S at a depth of 1.5 to 2.5 km (avg. 2.34 km) below the seafloor, but does not directly underlie the ABE vent field (Jacobs et al., 2007). In contrast, the southern magma chamber extends from 21°45'S to at least 22°40'S (the end of the survey line), underlying both the Tu'i Malila and Mariner vent fields at a depth of 2.0 to 3.5 km (avg. 2.82 km) below the seafloor (Jacobs et al., 2007). Earlier normal incidence four-channel wide-angle seismic reflection surveys show a rough doubling of this southern magma chamber from a cross-axis width of 0.6 to 2.3 km beneath the central Valu Fa Ridge (south of the Mariner vent field) to

a width of 4 km beneath the overlapping spreading center that surrounds the Mariner vent field (Morton and Sleep, 1985; Collier and Sinha, 1990).

3. METHODS

3.1. Field Sampling

Samples of active and inactive SMS deposits from vent fields along the ELSC were collected during cruises TUIM05MV (2005, R/V Melville) and TN236 (2009, R/V Thompson) using the Jason II remotely operated vehicle. Many of these deposits were sampled along with the hydrothermal fluids that were flowing through them at the time of collection. Hydrothermal fluids were collected in isobaric gas-tight (IGT) samplers (Seewald et al., 2002).

3.2. Fluid Chemistry

Fluid samples were processed on the ship within 24 h of recovery. Shipboard measurements of pH (at 25ºC) were made using a Ag/AgCl combination reference electrode that was calibrated daily. Dissolved H_2 concentration was determined shipboard following a headspace extraction using a gas chromatograph (GC) equipped with a 5Å molecular sieve packed column and a thermal conductivity detector. Total aqueous sulfide ($\Sigma H_2S = H_2S + HS^- + S^{2-}$) was sparged from a sample aliquot acidified with 25 wt% phosphoric acid and precipitated shipboard as Ag_2S in a 5 wt% solution of $AgNO_3$ for subsequent gravimetric measurement in a shore-based laboratory.

An aliquot of each hydrothermal fluid sample that was collected in 2005 was filtered through a 0.45 μm filter into high-density polyethylene bottles that were "hot" acid cleaned and acidified with ultra-pure 6 N HCl to a pH of ~1.8 (Mottl et al., 2011). Another aliquot was

diluted 1:20 with 0.1 N HCl. Solid precipitates were removed from the sampler following complete removal of the fluid by sequentially rinsing with water and acetone and collecting the particles on a 0.45 μm nylon filter. Concentrations of Cu, Zn, Pb, and Ba in filtered aliquots and digested residual particles were analyzed using inductively coupled plasma atomic emission spectrometry (ICP-AES). Total fluid metal concentrations were calculated based on the addition of dissolved-, filter-, and precipitate "dregs" fractions (Trefry et al. 1994). Analytical errors can be estimated based on repeat measurements of the sample solutions and are on the order of 10% for most measurements.

3.3. Deposit Sample Preparation

SMS deposit samples were photographed and air-dried following shipboard recovery and transferred to climate-controlled storage upon arrival at the Woods Hole Oceanographic Institution. Selected samples were then cut and subsampled for petrographic and geochemical study. Sample powders were produced in mild- or hard-steel barrels after which they were split into two subsamples, one for bulk geochemical analyses and a second for mineralogical analysis by x-ray diffraction. Petrographic samples were prepared as polished thin sections and examined under reflected and transmitted light with a petrographic microscope. Sphalerite and wurtzite were identified by crystal morphology and anisotropy under crossed nicols in transmitted light, while pyrite and marcasite were identified by crystal morphology and pleochroism under crossed nicols in reflected light. Following visual inspection and mineralogical description, selected thin sections were carbon-coated and analyzed by electron microprobe.

Powdered samples were selected to be representative of the whole sample and are either radial sections of concentrically layered samples or interior (i.e. unweathered) pieces of visually

homogeneous samples. Where possible, these pieces were separated from whole samples along pre-existing fractures in order to avoid contamination from steel tools. Otherwise, they were cut using a rock saw or separated using a hammer and chisel. Petrographic thin sections are intended to match the mineralogy of sample powders and, in most cases, were cut from pieces or faces made during geochemical subsampling.

3.4. Mineralogy and Geochemistry

Bulk geochemical analyses were conducted by Activation Laboratories, Ltd. in Sudbury, Ontario. Concentrations of As, Au, Ba, Co, Sb, Se, and Zn were measured by instrumental neutron activation analysis, while concentrations of Ag, Ca, Cd, Cu, Fe, Mn, Mo, Pb, and Sr were measured by inductively coupled plasma mass spectrometry (ICP-MS) following sodium peroxide fusion. For samples collected in 2009, analyses of total S by infrared detection on combustion and Si by ICP-OES following sodium peroxide fusion were also conducted; samples were also ground more finely in order to improve digestion of barite and anhydrite. Correlation coefficients between bulk element concentrations in samples from each vent field were calculated using the Matlab script *corrcoef*.

Analysis of sample powders by x-ray diffraction was conducted on a Philips Analytical PW1830 with a copper tube. Electron microprobe analyses of copper-iron-, iron-, and zinc-iron sulfides in areas free of visible inclusions were conducted at the MIT electron microprobe facility using a JEOL JXA-8200. The concentrations of Ag, As, Cd, Co, Cu, Fe, Mn, S, Sb, Se, and Zn were measured using 2(PbSe)$AgBiS_2$, NiAs, $CdS_{40}ZnS_{60}$, Co_9S_8, $CuFeS_2$, MnS, Sb_2S_3, and ZnS reference standards. Count times were 40 s for Cu, Fe, and S; 120 s for Ag, Cd, and Zn; 140 s for Mn; 180 s for Co; and 240 s for As, Sb, and Se.

4. RESULTS

4.1. Hydrothermal Fluid Temperature and pH

Vent fluid exit temperatures and pH presented here include and supplement those from Mottl et al., (2011). Vent fluids from the Kilo Moana vent field collected in 2005 exhibit temperatures of 300°C to 333°C and pH (at 25°C) of 2.9 to 4.0 (Fig. 2; Table 1). Samples collected in 2009 exhibit lower temperatures of 290°C to 304°C and higher pH (at 25°C) of 4.0 to 4.1 (Fig. 2; Table 1). No hydrothermal activity was observed at the Kilo Moana vent field in 2015 (observation from cruise RR1507). For all other vent fields, vent fluid temperatures and pH are comparable for samples collected in 2005 and 2009. Vent fluid temperatures and pH are: 288°C to 320°C, pH(at 25°C) = 3.6 to 4.1 at the TowCam vent field, 286°C to 310°C, pH(at 25°C) = 3.3 to 3.9 at the Tahi Moana-1 vent field, 278°C to 317°C, pH(at 25°C) = 3.9 to 4.6 at the ABE vent field, 178°C to 317°C, pH(at 25°C) = 3.8 to 5.7 at the Tu'i Malila vent field, and 240°C to 363°C, pH(at 25°C) = 2.2 to 2.7 at the Mariner vent field (Fig. 2; Table 1).

4.2. Hydrothermal Fluid Chemistry: Cu, Zn, Ba, Pb, and H_2

The concentrations of vent fluid Cu, Zn, Ba, Pb, and H_2 reported here for all except the Tahi Moana-1 vent field are "endmember" concentrations calculated by extrapolating a least squares linear regression of an individual species plotted against Mg for one to three fluid samples recovered from a given vent orifice, and seawater, to zero-Mg. This method is based on the assumption that high-temperature hydrothermal fluids contain little or no Mg, such that the measured Mg concentration of a hydrothermal fluid sample may be used as a tracer of seawater entrained during sampling (Von Damm et al., 1985).

Endmember concentrations of dissolved Cu in high-temperature hydrothermal fluids from the ELSC are 8 to 11 μmol/kg at the Kilo Moana vent field, 3 to 8 μmol/kg at the TowCam vent field, 4 to 6 μmol/kg at the ABE vent field, and 2 to 16 μmol/kg at the Tu'i Malila vent field (Fig. 2; Tables 1 and S1). Compared to these vent fields, high-temperature fluids at the Mariner vent field exhibit a larger range and higher Cu concentrations of 4 to 171 μmol/kg (Fig. 2; Table 1). Endmember concentrations of dissolved Zn are 58 to 108 μmol/kg at the Kilo Moana vent field, 19 to 74 μmol/kg at the TowCam vent field, 33 to 44 μmol/kg at the ABE vent field, and 7 to 49 μmol/kg at the Tu'i Malila vent field (Fig. 2; Table 1). Endmember Zn concentrations are much higher at the Mariner vent field, covering a range of 242 to 514 μmol/kg (Fig. 2; Table 1).

Average and maximum endmember concentrations of dissolved Ba and Pb in high-temperature hydrothermal fluids increase monotonically from the Kilo Moana to Mariner vent fields (Fig. 2; Table 1 and S1). Endmember Ba concentrations are 22 to 26 μmol/kg at the Kilo Moana vent field, 21 to 34 μmol/kg at the TowCam vent field, 7 to 63 μmol/kg at the ABE vent field, 37 to 77 μmol/kg at the Tu'i Malila vent field, and 44 to 131 μmol/kg at the Mariner vent field (Fig. 2; Table 1). Endmember concentrations of Pb likewise increase from 226 to 402 nmol/kg at the Kilo Moana vent field, to 369 to 515 nmol/kg at the TowCam vent field, 380 to 573 nmol/kg at the ABE vent field, 532 to 786 nmol/kg at the Tu'i Malila vent field, and 751 to 1200 nmol/kg at the Mariner vent field (Fig. 2; Table 1). Endmember concentrations of dissolved H_2 at the Kilo Moana vent field are 220 to 498 μM, while concentrations of dissolved H_2 at all other vent fields are low by comparison with a range of 33 to 198 μM (Fig. 2; Tables 1 and S1).

4.3. Morphology and Mineralogy of Seafloor Massive Sulfide Deposits

ELSC SMS deposits are formed as hydrothermal edifices variously composed of open conduit chimneys, conical and bulbous spires including beehives, disk-shaped flanges, and squat columnar terraces (Fig. 3). In general, the mineralogy of these portions of SMS deposits may be divided into three layers: (1) low-porosity, sulfide-rich inner layers that were adjacent to the highest-temperature hydrothermal fluids, (2) high-porosity middle layers composed of mixtures of sulfide and sulfate minerals that were in contact with pore fluids of intermediate temperature and chemistry, and (3) low-porosity outer layers composed of marcasite, iron-oxyhydroxides, and amorphous silica that were adjacent to cold or slightly warmed seawater and/or diffuse hydrothermal flow. In the case of horizontal flanges, which trap rising hydrothermal fluids, lower-, middle-, and upper layers correspond to the inner-, middle-, and outer layers in chimneys.

Along the ELSC, morphologic variations among SMS deposits within each vent field are characterized by open conduit chimneys (black smokers) venting high-temperature fluids, active spires and diffusers (white smokers and beehives) venting intermediate- and/or high-temperature fluids, and flanges and squat terraces venting intermediate- and/or low-temperature fluids. Among high-temperature deposits, variations between vent fields are expressed in the mineralogy of sulfide-rich inner layers, which are variously composed of cubanite, chalcopyrite, cubanite/chalcopyrite intermediate solid solution (iss), pyrrhotite, pyrite, and wurtzite (Fig. 4A-4H). Among low-temperature deposits, between-field variation is characterized by the presence, absence, and abundance of barite-rich flanges and horizontal deposit structures (Fig. 3, 4).

Elements that occur in deposits as major mineral-forming elements at all vent fields include Ca, Cu, Fe, S, and Zn. Minor amounts of Si are also present, mostly as amorphous silica. Oxygen was not measured, but is present as a mineral-forming element in sulfate and silicate

minerals. Joining this list at the Tahi Moana-1, ABE, Tu'i Malila, and Mariner vent fields are Ba and Pb, both of which reach maximum concentrations in deposits from the Tu'i Malila vent field (Fig. 5). With the exception of the Mariner vent field, Ba and Pb concentrations are higher to the south, while high-temperature SMS deposits at the Mariner vent field are distinctly Cu-rich and Zn-poor compared to other vent fields (Fig. 5). Mineralogical descriptions categorized by vent field and sample type are presented in Table 2. Major and minor element data are shown in Fig. 5, with full presentation of the data in Supplementary Tables 2 and 3.

4.3.1. Kilo Moana and TowCam

SMS deposits at the Kilo Moana and TowCam vent fields are located along the edges of volcanic fissures at Kilo Moana or, in the case of TowCam, small extensional faults that cross-cut shallow volcanic domes (Ferrini et al., 2008). SMS deposits at the Kilo Moana vent field are characterized by ~5 m-tall edifices (Fig. 3A) composed of multiple active and inactive open conduit chimneys and beehive-shaped diffusers. The bases of larger edifices are covered with short skirts of sulfide-rich talus, while shorter edifices rise directly from pillow basalts. Larger edifices also exhibit narrow, disk-shaped protrusions, which are inactive and located below or to the side of active venting on a given edifice. While described as "flanges" on the basis of sample morphology, the presence of trapped pools of buoyant fluid beneath these overhanging ledges, which are a characteristic feature of flanges, was not confirmed during Jason dives (M. K. Tivey, pers. comm.). SMS deposits at the TowCam vent field are characterized by < 5 m–tall edifices composed of active and relict spires. Open conduit chimneys (Fig. 3B) are rare, as are beehive-shaped diffusers. Active and relict spires are cone-shaped and exhibit steep, lumpy sides.

Active spires at the Kilo Moana and TowCam vent fields exhibit anastomosing fluid conduits lined with low porosity layers of either euhedral bladed wurtzite or massive chalcopyrite and minor pyrite (Table 2). These fluid conduits are surrounded by a porous groundmass of intergrown dendritic structures composed of subhedral-to-euhedral sphalerite and wurtzite, euhedral pyrite ± tabular anhydrite, and minor chalcopyrite (Table 2). Within these layers, late stage amorphous silica is also present as < 10 μm coatings on sulfide and sulfate grains. Deposit exteriors are composed of marcasite dendrites coated in a thin layer (< 0.1 mm) of iron-oxyhydroxide and amorphous silica. Relict spires are similar in texture to active spires except that wurtzite grains lining interior conduits are larger with a higher abundance of euhedral grains and alternating marcasite- and wurtzite-dominated layers are more distinct than those observed in active spires (Table 2).

High temperature (~330°C) open conduit chimneys at the Kilo Moana vent field are lined with massive cubanite (Fig. 4A, 4E; Table 2). Minor, interstitial grains of pyrrhotite and wurtzite are also present. In contrast, high temperature (~330°C) open conduit chimneys at the TowCam vent field are lined with massive chalcopyrite intergrown with wurtzite and pyrite (Table 2). At lower temperatures (~300°C), open conduit chimneys at both vent fields are lined with euhedral wurtzite ± pyrite with chalcopyrite (+iss at Kilo Moana) present as inclusions and interstitial grains (Table 2). At the Kilo Moana vent field, the disk-like protrusions on the exteriors of SMS deposits share a similar mineralogy with active spires and are mainly composed of dendritic marcasite, wurtzite, and minor chalcopyrite (Table 2).

4.3.2. Tahi Moana-1, ABE, and Tu'i Malila

Detailed bathymetry and mapping of the Tahi Moana-1 vent field has not been done, but analysis of dive videos and associated depth readings indicate that hydrothermal edifices are located on a low-relief bathymetric high composed of sedimented pillow basalts. A lower resolution bathymetric map presented by Martinez et al. (2006) indicates a NE-SW trend in linear bathymetric features. High-resolution bathymetric mapping and dive videos of the ABE and Tu'i Malila vent fields indicate that SMS deposits are associated with significant N-S and NNE-SSW striking normal faults and brecciated lava flows (Ferrini et al., 2008). At the Tu'i Malila vent field, several volcanic domes are also identified (Ferrini et al., 2008).

SMS deposits at the Tahi Moana-1 vent field are characterized by < 5 m-tall, cone-shaped active and relict spires (Fig. 3C). Open conduit chimneys are rare and only one sample was collected. Spires at the Tahi Moana-1 vent field exhibit flat tops and narrow horizontal flanges that protrude beyond the base of the spires (Fig. 3D). The presence of white microbial mats and scale worms inhabiting these flanges suggests that they are hydrothermally active. However, these flanges have not been directly observed to be trapping pools of buoyant fluid. SMS deposits at the ABE vent field are characterized by 3-5 m-tall, cone-shaped edifices (Fig. 3E) composed of active and relict spires and open conduit chimneys. Pronounced horizontal flanges are found at the base of these edifices, elevated above a substrate of broken sulfide talus or bare a'a-type lava flows. Horizontal flanges are also present as discrete, actively venting structures with neither open conduit chimneys nor active spires (Fig. 3F). SMS deposits at the Tu'i Malila vent field are characterized by 5-10 m-tall edifices composed of horizontal flanges, relict beehives, vertical spires, and open conduit chimneys (Fig. 3G). Individual structures composed entirely of horizontal flanges that reach heights of up to ~12 m are also present in the southern

part of the vent field (Fig. 3H). More sulfide-rich edifices at the Tu'i Malila vent field likewise exhibit an abundance of horizontal flanges (e.g., Fig. 3G).

Hydrothermal edifices at the Tahi Moana-1, ABE, and Tu'i Malila vent fields exhibit similar mineralogy. Anastomosing fluid conduits are lined by low-porosity inner layers of massive chalcopyrite and euhedral pyrite (T > 310°C), or euhedral wurtzite ± chalcopyrite (T < 310°C), surrounded by porous middle layers composed of intergrown dendrites of subhedral-to-euhedral wurtzite and/or sphalerite ± tabular anhydrite or barite (increasing to south), with minor euhedral pyrite, marcasite, chalcopyrite and trace-to-minor galena (Table 2). Outer layers are composed of marcasite dendrites with minor acicular barite (Fig. 4I; Table 2).

Compared to SMS deposits found at the Kilo Moana and TowCam vent fields, SMS deposits at the Tahi Moana-1, ABE, and Tu'i Malila vent fields are characterized by a southward increase in the abundance of barite and horizontal flanges. Lower- and middle layers of flanges at the Tahi Moana-1 vent field are composed of dendritic sphalerite and pyrite with minor chalcopyrite; upper layers are composed of dendritic marcasite and acicular barite (Table 2). At the ABE vent field, flanges are larger and more abundant, trapping pools of lower-temperature buoyant fluids (e.g., Fig. 3F, 141°C). These flanges are barite-rich (Table S2, max. 82 wt%) and are composed of dendritic structures formed by tabular barite and interstitial fine-grained (< 5 μm) pyrite with late-stage amorphous silica filling interstices (Table 2). Barite is abundant throughout the Tu'i Malila vent field and is found in both flanges (Table S2, max. 84 wt%), open conduit chimneys (Table S2, max. 61 wt%), and as a matrix mineral in the middle and outer layers of active and relict spires (Table 2). Flanges at the Tu'i Malila vent field are likewise wide and trap pools of buoyant hydrothermal fluids (e.g., Fig. 3H, 178°C; also Table 1A, fluid sample TM4). Flanges are composed of barite and minor anhydrite with interstitial pyrite, wurtzite, and

sphalerite (Fig. 4K; Table 2). Minor interstitial chalcopyrite and marcasite are also present in upper layers, as is a late-stage coating of amorphous silica that fills interstices (Fig. 4K; Table 2). This coating is especially thick in relict samples.

High-temperature fluids at the Tahi Moana-1 (286°C to 310°C), ABE (278°C to 317°C), and Tu'i Malila (198°C to 312°C) vent fields are associated with open conduit chimneys and venting active spires. At the Tahi Moana-1 vent field, sample J2-450-3-R1, which was in contact with the 310°C fluid TMo5 (Table 1) at the time of collection, is lined with massive chalcopyrite with minor inclusions of < 5 μm euhedral pyrite (Table 2). Minor wurtzite is also present, either as bladed grains or as oleander-leaf twinning in chalcopyrite (Table 2). At the ABE vent field, sample J2-449-6-R1, collected with 317°C fluid A10 (Table 1; same vent as A1), is lined with massive chalcopyrite and euhedral pyrite (Fig.4B, 4F; Table 2). The modal abundance of pyrite increases toward the outside of the sample and minor sphalerite is present near the outer edge (Table 2). Sample J2-449-5-R1, collected with 306°C fluid A11 (Table 1; same vent as A2), is lined with bladed grains of chalcopyrite and wurtzite (Fig. 4C, 4G; Table 2). Trace pyrite is present as inclusions in chalcopyrite and chalcopyrite is also present as oleander-leaf twinning in bladed wurtzite (Table 2). The modal abundance of wurtzite increases toward the outside of the sample (Fig. 4C). Minor anhydrite and trace bornite, digenite, covellite, and galena are present near the outer edge, as are amorphous silica, iron-oxyhydroxides, and clays (Table 2). A relict open conduit sample (J2-136-5-R1) exhibits similar mineralogy to the 306°C sample with a lining composed of massive chalcopyrite, bladed wurtzite, and trace euhedral pyrite. At the Tu'i Malila vent field, sample J2-442-4-R2, which was in contact with 312°C fluid TM11 (Table 1; same vent as TM2) is lined with massive chalcopyrite and euhedral pyrite with minor sphalerite, acicular barite, and trace galena present near the outer edge (Table 2).

SMS deposits at the Tu'i Malila vent field contain comparatively high concentrations of Pb, primarily present as galena (Tables 2 and S2). The most Pb-rich sample, J2-134-9-R1, is an active spire associated with 198°C fluid TM7 (Table 1). This sample is lined with euhedral wurtzite intergrown with chalcopyrite and galena (Fig. 4J; Table 2). Reflected light petrography and x-ray diffraction analyses of samples collected at the Tu'i Malila vent field also indicate the presence of trace galena in both active and relict spires as well as in some open conduit chimneys and active flanges (Table S2).

4.3.3. Mariner

SMS deposits at the Mariner vent field occur in discrete clusters and are surrounded by volcanic domes and brecciated lava flows (Ferrini et al., 2008). Local faults or fissures, if present, are obscured by brecciated lava flows and are not evident in high resolution bathymetry or dive videos (Ferrini et al., 2008). Morphologically, SMS deposits may be divided into four types: short and slender open conduit chimneys, tall columns (Fig. 3I), bulbous edifices, and squat terraces (Fig. 3J). In comparison with other ELSC vent fields, high-temperature deposits at the Mariner vent field are Cu-rich and Zn-poor. Tall columns, open conduits, and bulbous spires are rich in Cu and Ba, while squat terraces are rich in Ba and Zn. At the Mariner vent field, SMS deposits are covered in a ubiquitous coating of orange-brown iron-oxyhydroxides and, where fluids emerge, white microbial mats likely containing abundant elemental sulfur.

High-temperature (311°C to 363°C) fluids at the Mariner vent field are associated with tall columns up to 27 m in height (Fig. 3I; Ferrini et al., 2008) and arrays of slender open conduit chimneys < 5 m in height. High-temperature open conduit chimneys exhibit 0.5 - 2 cm linings of massive chalcopyrite which grade into similarly textured layers of massive bornite-covellite-

digenite (bn-cv-dg) and outer layers of mixed tabular anhydrite and barite supporting minor interstitial sphalerite and chalcopyrite and trace tennantite (Fig. 4D, 4H; Table 2). Alternatively, some portions of outer layers are composed of dendritic pyrite and marcasite (Table 2). Chalcopyrite linings of open conduit chimneys often consist of two chalcopyrite layers of similar texture, one within the other (see Fig. 4D), likely reflecting the growth of new open conduits within the interiors of previous linings. Indeed, field observations of onlapping open conduits on the tops and sides of actively forming edifices and tall columns suggest that the formation of new open conduit chimneys and incorporation of old open conduit chimneys is an important growth mechanism of Mariner deposits. It is also worth noting that the highest temperature fluids and deposits are associated with active phase separation at the seafloor (Mottl et al., 2011).

Intermediate-temperature (150°C to 250°C) fluids at the Mariner vent field are associated with bulbous edifices. These are bulky structures composed of large bulbous domes and supporting columns. The mineralogy of active spires is characterized by a porous groundmass of intergrown dendrites of chalcopyrite and bornite with less-porous outer layers of dendritic pyrite and marcasite with minor chalcopyrite, wurtzite, and acicular barite (Table 2).

Compared to the ABE and Tu'i Malila vent fields, overhanging structures are rare at the Mariner vent field and flanges are small, angular, and fragile. However, some bulbous edifices exhibit small protruding flanges, the upper surfaces of which are adorned with ~5 cm antler-shaped tubes of layered iron-oxyhydroxide and silica. Flanges are composed of dendrites of tabular and acicular barite with interstitial subhedral-to-euhedral sphalerite and subhedral pyrite (Table 2). Amorphous silica is absent from most portions of these structures but present as a minor phase in uppermost layers (Table 2).

Low-temperature (< 150°C) fluids at the Mariner vent field are associated with squat terraces (Fig. 3J) or diffuse flows. Squat terraces are short cylindrical structures < 5 m in height that occur in the periphery of tall columns. These terraces lack horizontal overhangs and fluids emerge from openings beneath and between smaller disk-shaped structures on top of the cylinder. Fluids are generally low in temperature and Mg-rich, with a maximum temperature of 109°C measured in 2009. Samples of squat terraces from the Mariner vent field are composed of a dendritic matrix of tabular barite with interstitial sphalerite, minor pyrite and marcasite, and trace chalcopyrite and tennantite (Fig. 4L; Table 2). The abundance of sphalerite increases toward the interior of the deposit and acicular barite is present toward the exterior (Table 2). Overall, the mineralogy of squat terraces is similar to that of active flanges from the Tu'i Malila and ABE vent fields. However, squat terraces from the Mariner vent field lack the late-stage amorphous silica coating present in active flanges at the ABE and Tu'i Malila vent fields.

4.4. Major, Minor, and Trace Elements in Seafloor Massive Sulfide Deposits

Elements present as major mineral-forming elements in SMS deposits include Cu, Fe, Zn, Pb, Ca, Ba, S, Si, and O (Fig. 5; Table S2). Minor and trace elements present at detectable levels in ELSC SMS deposits include Ag, Au, As, Cd, Co, Mn, Mo, Pb, Sb, Se, and Sr (Fig. 5; Table S3). Electron microprobe analyses for wurtzite and sphalerite in open conduit chimneys range from 3 to 14 mol% FeS at Kilo Moana to 1 to 6 mol% FeS at Mariner (Table 3). Additional results of electron microprobe analyses are presented in Fig. 6 and Table S4.

4.4.1. Copper, Cobalt, and Selenium

Open conduit chimneys are Cu-rich, as are active and relict spires from the Mariner vent field (Fig. 5; Table S2). Open conduit chimneys from the Tu'i Malila vent field are enriched in Cu relative to other Tu'i Malila samples, but contain lower Cu concentrations than open conduit chimneys at other vent fields. Concentrations of Co in bulk samples are only significant in samples from the Kilo Moana and ABE vent fields, with one additional high value in an open conduit chimney from the Tu'i Malila vent field (Fig. 5; Table S3). Concentrations of Se in bulk samples are only significant in samples from the Kilo Moana vent field (Fig. 5; Table S3). Concentrations of Co and Se in bulk samples are significantly and positively correlated with Cu and Fe for samples from the ABE and Tu'i Malila vent fields (at a significance level of $p < 0.05$, where p is the Pearson p-value) (Table 4). Significant and positive correlations also exist between Cu and Se in samples from the Kilo Moana vent field ($r = 0.90$, $n = 18$) and between Fe and Se in samples from the Tahi Moana-1 vent field ($r = 0.63$, $n = 13$) (Table 4).

Electron microprobe analyses (Fig. 6; Table S4) show that high concentrations of Co occur in interior cubanite and iss in open conduit chimneys from the Kilo Moana vent field, and in chalcopyrite along inner layers of open conduit chimneys from the ABE vent field where it is intergrown with pyrite. Elevated Co concentrations also occur intermittently within exterior sphalerite and marcasite, which also host Se, As, Mn, and Cd ± Sb and Ag (Table S4). Occurrences of Se are similar to those of Co. However, elevated concentrations of Se occur within inner-layer chalcopyrite and pyrite in open conduit chimneys from the ABE and Tu'i Malila vent fields even on spots where Co concentrations are low (Table S4). Nevertheless, Co and Se are correlated in bulk samples from these two vent fields (Table 4). For samples from the Mariner vent field, electron microprobe analyses show that Co and Se concentrations are

elevated in interior chalcopyrite and in exterior sphalerite and marcasite as at other vent fields (Fig. 6; Table S4). However bulk concentrations of both Co and Se are low relative to other vent fields and are not significantly correlated (Fig. 5; Table 4; Table S3).

4.4.2. Zinc, Cadmium, and Manganese

Bulk concentrations of Zn, Cd, and Mn are greatest in samples from the TowCam, Tahi Moana-1 and ABE vent fields, with lower concentrations in deposits from the Kilo Moana, Tu'i Malila and Mariner vent fields (Fig. 5; Tables S2 and S3). Compared to the Zn-rich deposits from the TowCam, Tahi Moana-1 and ABE vent fields, deposits from the Kilo Moana vent field are rich in Fe, those from the Tu'i Malila vent field are rich in Ba, and those from the Mariner vent field are rich in Cu and Ba (Fig. 5; Tables S2 and S3). All three of these elements are more abundant in active and relict spires compared to open conduit chimneys from the same vent field (Fig. 5; Tables S2 and S3).

Bulk concentrations of Zn are highest among active and relict spires from the Kilo Moana, TowCam, Tahi Moana-1, and ABE vent fields (Fig. 5; Table S2). In contrast, active and relict spires from the Tu'i Malila and Mariner vent fields are low in Zn, but are instead high in Ba at the Tu'i Malila vent field and in Cu and Ba at the Mariner vent field (Fig. 5; Table S2). Nevertheless, some Tu'i Malila samples do contain high concentrations of Zn, including several open conduit chimneys and a few active and relict spires (Fig. 5; Table S2). High-temperature actively venting deposits at the Mariner vent field are strikingly Zn-poor compared to those from other ELSC vent fields. In contrast, Mariner flanges and squat terraces and one sample from a Ba-rich relict spire contain high concentrations of Zn (Fig. 5; Table S2).

Bulk concentrations of Cd are positively and significantly correlated with Zn for all vent fields (Table 4). Electron microprobe analyses show that Cd concentrations are invariably highest in wurtzite and sphalerite (Fig. 6). However, low (<500 μg/g) concentrations of Cd also occur in chalcopyrite, pyrite, and marcasite (Fig. 6). Electron microprobe analyses for Mn reveal detectable concentrations of Mn in nearly all sphalerite and wurtzite analyzed (Fig. 6; Table S4) with higher Mn concentrations in pyrite and marcasite. Mn is not significantly correlated with Zn in bulk samples. Manganese concentrations in all zinc- and iron sulfide minerals are higher in samples from the TowCam, Tahi Moana-1, ABE, and Tu'i Malila vent fields, compared to samples from the Kilo Moana and Mariner vent fields (Fig. 6).

4.4.3. Barium and Lead

Bulk concentrations of Ba are low in SMS deposits from the Kilo Moana, TowCam and Tahi Moana-1 vent fields and high in deposits from the Tu'i Malila and Mariner vent fields with intermediate concentrations in deposits from the ABE vent field (Fig. 5; Table S2). High concentrations of Ba are associated with the presence of barite, especially among barite-rich flanges from the ABE and Tu'i Malila vent fields and squat terraces from the Mariner vent field.

Bulk concentrations of Pb increase from the Kilo Moana vent field to the Tu'i Malila vent field, where Pb concentration reaches a maximum and galena is observed as an abundant minor phase (Fig. 4J, 5; Table 2, S2). However, concentrations of Pb in samples from the Mariner vent field are low relative to samples from the ABE and Tu'i Malila vent fields, being more similar to concentrations at the TowCam and Tahi Moana-1 vent fields (Fig. 5; Table S2). Concentrations of Pb are positively and significantly correlated with As and Au at all vent fields except Tu'i Malila and Mariner (Table 4). At the Tu'i Malila vent field, Pb is not significantly

correlated with any element, while at Mariner, Pb is only significantly and positively correlated with Sr ($r = 0.90$, $n = 24$) and Se ($r = 0.53$, $n = 24$) and is significantly and negatively correlated with Cu ($r = -0.61$, $n = 24$) and Fe ($r = -0.63$, $n = 24$) (Table 4). Electron microprobe analyses of Pb were attempted, but spectral interferences with S could not be resolved.

4.4.4. Arsenic, Antimony, and Silver

Bulk concentrations of As and Sb increase between the Kilo Moana and Tu'i Malila vent fields (Fig. 5; Table S3). At the Mariner vent field, Sb concentrations are less than those at the Tu'i Malila vent field, while As concentrations are greater (Fig. 5; Table S3). Concentrations of As and Sb are positively and significantly correlated for all vent fields except Kilo Moana, and are also correlated with Au for all vent fields except Mariner (Table 4). In addition, concentrations of As and Ag are positively and significantly correlated for all vent fields except TowCam (Table 4). Bulk concentrations for all of these elements are generally higher in active and relict spires than in open conduits (Fig. 5; Table S3).

Electron microprobe analyses of As and Sb reveal detectable concentrations of As in pyrite, marcasite, and sphalerite, and to a lesser extent in chalcopyrite and wurtzite; Sb concentrations are highest in sphalerite, with lesser concentrations in wurtzite and chalcopyrite (Fig. 6). Detectible concentrations of Sb in marcasite are only found among active flanges from the Tu'i Malila vent field and only a few samples have detectible concentrations of Sb in pyrite (Fig. 6). Concentrations of As and Sb in sphalerite increase from north to south as do concentrations of As in pyrite (Fig. 6). Where detectable (among open conduit chimneys and in active and relict spires from the Mariner vent field), concentrations of As and Sb in chalcopyrite also increase from north to south (Fig. 6). Concentrations of As and Sb in wurtzite are generally

below detection limits with a few exceptions among open conduit chimneys and in active flanges from the Mariner vent field (Fig. 6). Large-grained euhedral wurtzite that lines high-temperature fluid conduits lacks detectable As and Sb.

Bulk concentrations of Ag increase between the Kilo Moana and Tahi Moana-1 vent fields and again between the ABE and Mariner vent fields, with lower concentrations in samples from the Kilo Moana and ABE vent fields (Fig. 5; Table S3). Maximum Ag concentrations are present in samples of barite-rich squat terraces from the Mariner vent field (249 to 639 μg/g) and active flanges from the Tahi Moana-1 vent field (253 to 326 μg/g) (Fig. 5). Electron microprobe analyses reveal elevated concentrations of Ag in inner-layer cubanite, chalcopyrite, and middle-layer bornite, as well as outer-layer sphalerite, wurtzite, and marcasite (Fig. 6; Table S4). On spots with detectable Ag, other trace elements are also present, especially Se and Sb in wurtzite, Co, Se, As, and Sb in sphalerite, and Mn and As in marcasite. Ag is present in pyrite, sphalerite, and marcasite in active flanges from the Tu'i Malila vent field, and in sphalerite and pyrite among barite-rich squat terraces from the Mariner vent field (Fig. 6).

5. DISCUSSION

Analyses of SMS deposits and hydrothermal fluids from six vent fields along the ELSC reveal spatially organized differences, either in the form of north-south gradients or in distinguishing the Mariner vent field from other ELSC vent fields. These patterns mimic those identified by previous investigations of crustal lithology (e.g., Escrig et al., 2009; Sleeper and Martinez, 2014) and hydrothermal fluid chemistry (e.g., Mottl et al., 2011), which likewise point to the influence of enhanced magmatic activity near the Mariner vent field as well as more gradual trends related to the change in distance between the ELSC and the adjacent volcanic arc.

As noted and described in Mottl et al., (2011), hydrothermal fluids from these same vent fields are consistent with a decrease in reaction zone temperature between the Kilo Moana and Tu'i Malila vent fields and a transition toward more felsic lithology closer to the subduction zone. Hydrothermal fluid chemistry at the Mariner vent field is strongly influenced by the addition of acidic magmatic volatiles, which leads to higher-temperature, lower-pH, and metal-rich hydrothermal fluids (Mottl et al., 2011). Here, we identify specific indicators of hydrothermal fluid temperature, pH, sulfur fugacity (fS_2), and trace element content of hydrothermal fluids as expressed by the morphology, mineralogy, and geochemistry of ELSC SMS deposits, placing them within the geologic context of the ELSC and proximal Tonga Subduction Zone.

5.1. Hydrothermal Fluid Chemistry

Previous studies of hydrothermal fluid chemistry have identified two groups of dissolved elements, those that are rapidly and quantitatively released to solution and not controlled by mineral solubility, thus reflecting the elemental content of crustal host rocks, and those that are solubility-controlled by reversible chemical reactions between hydrothermal fluids and minerals within the seafloor (e.g., Mottl and Holland, 1978; Seyfried et al., 1984; Von Damm, 1995). Concentrations of elements in the second group are strongly affected by the temperature and pH of hydrothermal fluids, and concentrations of ligands (e.g., Cl^-). Along most of the ELSC, i.e., north of the Mariner vent field, hydrothermal fluid temperature and pH co-vary with crustal lithology with no evidence of phase separation (Mottl et al., 2011). High-temperature, low-pH vent fluids at the Mariner vent field contrast with this trend, making it possible to more readily distinguish between solubility and lithology-controlled elements. Additionally, Mariner vent

fluids exhibit Cl^- of either less than or greater than seawater and variable dissolved gas contents, attributable to phase separation (Takai et al., 2008; Mottl et al., 2011).

5.1.1 Dissolved Ba and Pb

Results of this study demonstrate that Ba concentrations in ELSC vent fluids increase gradually from north to south (Table 1b; Fig. 2). Furthermore, dissolved Ba concentrations do not correlate with vent fluid temperature or pH (Fig. 7). Concentrations of Pb in ELSC vent fluids likewise increase from north to south, weakly correlating with vent fluid pH only among Mariner vent fluids (Fig. 7). Concentrations of Ba and Pb in igneous rocks collected from the seafloor also increase gradually from north to south (Bézos et al., 2009; Escrig et al., 2009). These positive correlations between fluid and rock chemistry occur despite contrasting fluid temperature and pH (see Fig. 7), and strongly suggest that concentrations of Ba and Pb in ELSC hydrothermal fluids are primarily controlled by Ba and Pb concentrations in crustal host rocks.

The idea that crustal composition affects the concentration of Ba in hydrothermal fluids has been previously proposed (e.g., Hannington and Scott, 1988; Scott et al., 1990; Moore and Stakes, 1990; Fouquet et al., 1991; Bendel et al., 1993; Langmuir et al., 1997). However, high Ba concentrations (Ba > 67 μmol/L) in vent fluids from the ultramafic-hosted Rainbow vent field associated with Ba-poor sepentinized peridotites suggest that crustal lithology may not be the only factor controlling Ba concentrations (Douville, 2002; Andreani et al., 2014).

High concentrations of Pb in vent fluids from the Vai Lili vent field (Pb = 3.8 to 7.0 μmol/kg) are accompanied by high Zn concentrations (Zn = 1.4 to 3.0 mmol/kg) and can be attributed to remobilization of subsurface mineral deposits (Fouquet et al., 1993a). Such a mechanism has also been proposed to explain elevated Zn and other high metal contents in the

TAG white smoker fluids (Tivey et al., 1995) and several of the PACMANUS vent fields in the Manus Basin (Craddock, 2009).

5.1.2 Dissolved Cu and Zn

In contrast to Ba and Pb, dissolved concentrations of Cu and Zn in vent fluids positively correlate with temperature and negatively correlate with pH (Fig. 2; Fig. 7). Furthermore, dissolved concentrations of Cu and Zn exhibit similar patterns across ELSC vent fields as the solubility-controlled components Mn, Fe, and H_2S (Mottl et al., 2011; this paper, Fig. 2; Table 1). Fluid-mineral equilibrium experiments intended to mimic the formation of hydrothermal fluids suggest that lower- temperature water-rock reactions lead to elevated pH and lower H_2S, SiO_2, and metal contents (e.g., Seewald and Seyfried, 1990; Seyfried and Ding, 1995; Seyfried et al., 2002) compared to higher temperature conditions. As discussed in Mottl et al. (2011), hydrothermal fluid chemistry observed from the Kilo Moana to Tu'i Malila vent fields is consistent with regionally lower reaction-zone temperatures along the ELSC compared to mid-ocean spreading centers of similar spreading rate, with a further lowering of reaction zone temperature along the Valu Fa Ridge. Low reaction-zone temperatures have been attributed to shallower seafloor depths, thicker or more porous oceanic crust, and/or lower magma temperatures, all potential results of changes in magma chemistry induced by a flux of hydrous material through the Tonga Subduction Zone (Mottl et al., 2011; Escrig et al., 2009).

The very low pH and very high metal contents of Mariner vent fluids (Fig. 2; Tables 1A, 1B) fall outside the ranges observed in high-temperature water-rock reaction experiments and are attributed to the localized addition of acidic magmatic volatiles enriched in SO_2, CO_2, HCl, and HF combined with the increased solubility of metal sulfide minerals under these conditions

(Mottl et al., 2011). Importantly, the presence of more oxidized magmas and SO_2-rich magmatic volatiles is a consequence of the proximity of the subduction zone (Nilsson and Peach, 1993). Similar trends in hydrothermal fluid chemistry were also observed at the Vai Lili vent field (in 1989; Fouquet et al., 1993a) and in the Manus Basin, where crustal composition differs from basalt at the Vienna Woods vent field to more felsic compositions at the PACMANUS and SuSu Knolls vent fields and anomalously acidic hydrothermal fluids are attributed to acidic magmatic volatiles sourced from evolved felsic magmas (Reeves et al., 2011). In contrast, there is no evidence for the addition of acidic magmatic volatiles in Tu'i Malila vent fluids, despite its location above the same magma reflector (Mottl et al., 2011).

5.1.3 Dissolved Metal Ratios (Fe/Mn, Cu/Zn, Fe/Cu)

Pester et al. (2011) present a geothermometer based on the Fe/Mn ratio of hydrothermal fluids. This thermometer is based on basalt experiments and field data from the basalt-hosted 13°N vent field on the East Pacific Rise and the ultramafic-hosted Rainbow vent field on the Mid-Atlantic Ridge (Pester et al., 2011). Data presented here for vent fluids from the ELSC show no clear relationship between Fe/Mn ratios and vent fluid exit temperatures (Fig. 7). In contrast, vent fluid Fe/Mn ratios negatively correlate with vent fluid pH (Fig. 7). Such a relationship has also been reported among hydrothermal fluids collected along the Mid-Atlantic Ridge (Douville et al., 2002). Interestingly, the slope of the regression between vent fluid pH (at 25°C) and the Fe/Mn ratio is less steep for most ELSC vent than the slope for the northernmost Kilo Moana vent field (Fig. 7). In turn, the slope for Kilo Moana vent fluids is less steep than the slope presented in Douville et al. (2002) for vent fluids from the Mid-Atlantic Ridge. This

suggests an additional control on vent fluid Fe/Mn ratios, perhaps related to host-rock lithology or mineral assemblages.

Ratios of Cu/Zn in ELSC vent fluids are positively correlated with temperature (Fig. 7). This is consistent with the experiments of Seewald and Seyfried (1990), which show that Cu precipitates more readily than Zn during cooling of hydrothermal fluids during upflow, Additionally, ratios of vent fluid Fe/Cu in ELSC hydrothermal fluids are positively correlated with vent fluid $H_{2(aq)}$. This observation is consistent with previous work concluding that Fe/Cu ratios are largely controlled by vent fluid redox state (Seyfried and Ding, 1993; 1995). Indeed, the calculated Fe/Cu ratios of Kilo Moana vent fluids (Fe/Cu = 215 to 405) are in close agreement with values presented in Seyfried and Ding (1993, 1995) for fluids buffered by the pyrite-pyrrhotite-magnetite mineral assemblage while Fe/Cu ratios for other ELSC vent fluids (Fe/Cu = 14 to 146, with the exception of one outlier = 2,456) are in close agreement with values for fluids buffered by the hematite-magnetite-pyrite mineral assemblage (Seyfried and Ding, 1993; 1995).

5.2. Effects of Hydrothermal Fluid Temperature and pH on SMS Deposits.

5.2.1 Thermodynamic Constraints

In order to compare hydrothermal fluid chemistry with the mineralogy of paired chimney linings, thermodynamic modelling of fluid speciation and mineral saturation based on the endmember fluid chemistries of fluid samples KM5, TM2, and MA3 (Table 5) at the measured *in situ* temperatures was conducted using the EQ3/6 software package (Wolery, 1992) and the SUPCRT92 thermodynamic database (Johnson et al., 1992) modified after Tivey (1995). Mineral precipitation was suppressed (acknowledging that fluids along the lining are rapidly replenished;

see Tivey 1995); chalcopyrite and sphalerite were used as indicators of copper-iron sulfide and zinc sulfide saturation, respectively.

Open conduit chimneys collected from the Kilo Moana vent field in 2005 associated with the highest-temperature fluids (T > 320°C, pH (at 25°C) = 2.9 to 4.0) exhibit Cu-rich inner layers (massive cubanite, iss, and chalcopyrite) (Fig. 4A, 4E; Table 2). For KM5, accounting for the effect that precipitation of bottle solids (43.5 μmol/kg Fe, 5.6 μmol/kg Cu, and 30.8 μmol/kg Zn at zero-Mg) would have had on the measured pH of the fluid, the adjusted endmember pH at 25°C is 3.7 (measured pH (at 25°C) = 3.5), the pH at 329°C is 4.4, and the fluid is undersaturated with respect to all sulfide minerals. However, if the pH at the *in situ* temperature is adjusted to 4.6, which corresponds to a pH of 3.8 at 25°C (considered to be within the error of the measurements for pH and the uncertainties associated with the thermodynamic database), then the fluid is saturated with respect to chalcopyrite (thermodynamic data for cubanite and isocubanite are not available), in agreement with the copper-iron sulfide lining of sample J2-137-1-R1, the pair to fluid KM5. With conductive cooling of this fluid (Table 5), calculations indicate that pyrite is saturated at 268°C, sphalerite is saturated at 246°C, and galena is saturated at 189°C (Table 6).

At the ABE and Tu'i Malila vent fields, where pH (at 25°C) = 3.8 to 4.7, open conduit chimneys are lined with chalcopyrite and pyrite in samples corresponding to fluid temperatures >310°C (Fig. 4B, 4F; Table 2), and with chalcopyrite intergrown with wurtzite in samples corresponding to fluid temperatures 300°C to 310°C (Fig. 4C, 4G; Table 2). This suggests that saturation of these fluids with respect to wurtzite occurs at high temperatures in the range 300°C to 310°C. Thermodynamic calculations based on the endmember chemistry of fluid sample TM2 at the measured temperature of 312°C (Table 5) yield an *in situ* pH of 5.6 and

supersaturation with respect to chalcopyrite, pyrite, and sphalerite (Table 6). However, if sulfide minerals are allowed to precipitate, reflecting the possibility of rapid precipitation of sulfide minerals along the chimney wall, pH is lowered; chalcopyrite and pyrite remain supersaturated at the *in situ* temperature of 312°C, while sphalerite is undersaturated. With conductive cooling, sphalerite becomes saturated at 288°C (Table 6). These results are consistent with the observed mineralogy of the highest-temperature chimney linings. If conductive cooling models are continued, galena becomes saturated at 258°C if mineral precipitation is suppressed or 208°C if sulfide mineral precipitation is allowed (Table 6). This is roughly consistent with the observation of galena within the lining of sample J2-134-9-R1 (Fig. 4J), which was venting 198°C fluid TM7 (Table 1) at the time of collection.

At the Mariner vent field, where pH (at 25°C) = 2.2 to 2.7, SMS deposits associated with high-temperature fluids are strikingly Zn-poor and Cu-rich relative to deposits from other ELSC vent fields (Table S2). In contrast with SMS deposits from other vent fields, wurtzite and sphalerite at Mariner are only present near the very outer edges of deposits venting high-temperature fluids, in low-temperature deposits such as squat terraces, or as late stage mineralization in the interior of relict spires, suggesting that zinc sulfide precipitation occurred at relatively low temperatures (Table 2). Accounting for metals precipitated in the bottle (61.4 μmol/kg Fe, 150.8μmol/kg Cu, and 390.0 μmol/kg Zn at zero-Mg) the pH of Mariner MA3 vent fluid would have been 3.0 at 25°C (vs. measured 2.7), resulting in a pH of 4.2 at 363°C (Table 5). Calculations predict that chalcopyrite is saturated at 363°C, pyrite is saturated at 245°C, sphalerite is saturated at 193°C, and galena is saturated at 151°C (Table 6). The calculated saturation temperatures of sphalerite and galena for MA3 are thus much lower than those calculated for KM5 and TM2, despite the significantly higher concentrations of Zn and Pb in

MA3 fluid. This contrast points to the importance of fluid pH in controlling zinc- and lead sulfide solubility.

These calculations illustrate how low-pH fluids lead to the formation of copper-iron sulfide linings at high temperatures with zinc sulfides precipitating at lower temperatures, while higher pH fluids result in co-precipitation of copper-iron and zinc sulfides at high temperatures. The importance of this effect of pH has been highlighted before, particularly for deposits on the Endeavour Segment of the Juan de Fuca Ridge (e.g., Tivey at al., 1999; Kristall et al., 2006, 2011). While not explicitly tested through the application of thermodynamic fluid modelling, differences in the mineralogy of open conduit chimney linings between samples collected at the Kilo Moana vent field in 2005 (copper-iron sulfide) and those collected in 2009 (co-precipitated copper-iron sulfide and zinc-iron sulfide) reflect changes in vent fluids to lower temperature and higher pH in 2009. This supports the hypothesis that chimney lining mineralogy can be a sensitive indicator of hydrothermal fluid temperature and pH.

5.2.2 Incorporation of Trace Elements into Wurtzite/Sphalerite

Seafloor massive sulfide deposits along the ELSC are associated with hydrothermal fluids of both relatively high and low endmember pH and allows for investigation of the incorporation of trace elements into wurtzite and/or sphalerite over a range of pH conditions. Electron microprobe analyses of ELSC SMS samples indicate that wurtzite present along or near fluid conduit linings intergrown with chalcopyrite (indicative of high formation temperatures) contains relatively high concentrations of Cd and Mn, and to a lesser extent Co and Se, but low concentrations of Ag, As, and Sb (Fig. 6; Table S4). In contrast, wurtzite and sphalerite present near the exteriors of deposits (indicative of low formation temperatures) incorporate higher

concentrations of Ag, As, and Sb (As and Ag are also incorporated into exterior marcasite and pyrite, while Ag and to a lesser extent Sb are also incorporated into copper-iron sulfides such as chalcopyrite, regardless of location; Fig. 6). The incorporation of Cd and Mn into high-temperature interior sphalerite and wurtzite and Ag, As, Pb, and Sb into low-temperature exterior sphalerite and wurtzite has been previously noted in deposits from the Main Endeavour Field that also formed from fluids with relatively high pH (pH (at 25°C) = 4.2 to 4.5; Tivey et al., 1999). Thus, the presence of abundant Cd- and Mn-rich, but Ag-, As-, and Sb-poor sphalerite and wurtzite may be indicative of high zinc sulfide formation temperatures and, hence, elevated endmember fluid pH.

Bulk geochemical analyses of deposit samples provide an alternative method for examining the relative distributions of Zn and Ag, As, Pb, and Sb by a comparison of correlation coefficients between different element concentrations. Such correlations have been used in the past to investigate distributions of Ag, As, Pb, Sb, and Au with positive correlations between these elements and Zn attributed to the formation of Ag- and Au-bearing sulfosalts and galena in the Zn-rich lower-temperature portions of deposits (Hannington et al., 1991). A compilation of correlation coefficients for Zn and these elements (as well as Cd) for the full range of sample types present at each of the ELSC vent fields reveals that bulk concentrations of Zn and Ag are positively correlated for samples from the Kilo Moana, Tahi Moana-1, and Mariner vent fields, where the minimum fluid pH is 3.3 or less. However, they are negatively or not significantly correlated for samples from the TowCam, ABE, and Tu'i Malila vent fields, where the minimum fluid pH is 3.6 or greater (Fig. 8). This analysis was repeated on a sulfide-normalized basis to account for the presence of barite and anhydrite with little change in the results for Zn:Ag correlations (Fig. 8).

Poor Zn:Ag correlations for deposits associated with vent fluids of relatively high pH have been previously reported (Tivey et al., 1999; Kristall et al. 2006, 2011). Tivey et al. (1999) observed that correlations of Zn with Ag, as well as of Zn with As, Pb, and Sb, were poor for deposits from the Endeavour Segment of the Juan de Fuca Ridge (pH (at 25°C) = 4.2 to 4.5), and noted that this differed significantly from correlations observed for deposits at other vent fields, such as at the Snakepit vent field (pH (at 23°C) 3.7 to 3.9; Edmond et al., 1995) where bulk concentrations of Zn were positively correlated with Ag ($r = 0.82$), Pb ($r = 0.84$), and Sb ($r = 0.61$) (Fouquet et al., 1993b). Similar poor correlations of Zn with Ag, As, Sb, and Pb were reported by Kristall et al. (2006, 2011) for SMS deposits formed from relatively high pH (pH (at 25°C) = 4.7 to 4.8) vent fluids at the Mothra vent field, also on the Endeavour Segment. The hypothesis proposed to explain the lack of correlation for Endeavour Segment deposits was that Ag, As, Sb, and Pb were not present in zinc sulfide minerals that precipitated at high temperatures owing to high fluid pH such that high-temperature portions of the deposit could be rich in Zn but poor in Ag, As, Sb, and Pb (Tivey et al., 1999; Kristall et al., 2006). Bulk geochemical correlations for samples from ELSC SMS deposits support this hypothesis for correlations between Zn:Ag, Zn:As, and Zn:Pb, with poor correlations at vent fields with fluid pH greater than 3.6 to 4. Furthermore, correlations of Zn:Ag are consistently significant and positive at vent fields with lower pH vent fluids (at the Kilo Moana, Tahi Moana-1, and Mariner vent fields). In contrast, correlations between bulk concentrations of Zn and Sb are not consistently poor for ELSC deposits formed at vent fields that exhibit relatively high pH, and Zn:Sb, Zn:Pb, and Zn:As correlations are not consistently significant and positive at vent fields that exhibit relatively low pH (Fig. 7). Differences in these correlations may in part reflect

precipitation of Pb, As, and Sb in minerals other than wurtzite and sphalerite (e.g., galena and sulfosalts), though sulfosalts are only observed at Mariner vent field and only in a few samples.

Results from the ELSC suggest that correlations between bulk concentrations of Zn and Ag are an indication of the saturation temperature of zinc sulfides, which in turn reflects hydrothermal fluid pH. A poor correlation indicates a relatively high pH (minimum pH > 3.6), while a good correlation reflects deposit formation from relatively low pH (minimum pH < 3.3) vent fluids.

5.2.3. Flanges, Squat Terraces, Barite, and Amorphous Silica

Flanges at the ABE and Tu'i Malila vent fields and squat terraces at the Mariner vent field are composed of barite, which forms the bulk of the mineral content, with interstitial sphalerite and pyrite. Additionally, barite within flanges from the ABE and Tu'i Malila vent fields is coated with late-stage amorphous silica, while barite within squat terraces at Mariner is not (Table 2). Instead, the barite-rich flanges from the Mariner vent field are very small relative to those at the ABE and Tu'i Malila vent fields, and exhibit only minor amorphous silica associated with Fe-oxyhydroxides in exterior layers (Table 2). These observations are consistent with the hypothesis that amorphous silica precipitates at relatively high pH due to the absence of kinetic barriers, strengthening vent structures and enabling the formation of large flanges (Tivey et al., 1999). In contrast, kinetic barriers in low pH fluids inhibit the precipitation of amorphous silica (Fournier, 1985). Without the stability provided by late-stage amorphous silica, flanges at the Mariner vent field are likely to be structurally weak, breaking before they can reach the size of flanges at the ABE or Tu'i Malila vent fields. Although amorphous silica does precipitate at the Kilo Moana, TowCam, and Tahi Moana-1 vent fields, consistent with higher pH compared to

the Mariner vent field, Ba concentrations in hydrothermal fluids and SMS deposits are low. This likely explains the presence of small, sulfide-rich flanges at the Kilo Moana and Tahi Moana-1vent fields, but absence of large barite-rich flanges. The combined role of barite and silica in the formation of large, stable structures has been previously reported (Hannington and Scott, 1988; Tivey et al., 1999).

5.3. Effects of Sulfur Fugacity (fS_2) on SMS Deposits

In addition to temperature and pH, sulfur fugacity (fS_2) is an important parameter that controls the relative stability of sulfide mineral phases. The addition of aqueous H_2 concentrations to the fluid chemistry dataset presented in Mottl et al. (2011) allows for the calculation of the fS_2 at *in situ* temperatures and pressures via the following equations:

$$2H_{2,aq} + S_{2,g} = 2H_2S_{aq} \quad (1)$$

$$fS_{2,g} = K_{eq}\frac{\{H_2S_{aq}\}^2}{\{H_{2,aq}\}^2} \quad (2)$$

where $\{H_2S_{aq}\}$ and $\{H_{2,aq}\}$ are the aqueous activity of H_2S and H_2, respectively, and K_{eq} is the equilibrium constant. For the purpose of these calculations, activity coefficients for H_2S and H_2 were assumed to be unity. The equilibrium constant at *in situ* temperatures and pressures was calculated using thermodynamic data in the SUPCRT92 database (Johnson et al., 1992). Acid dissociation of H_2S in the *in situ* pH range for ELSC vent fluids is calculated to be < 3 % for the highest pH samples (Table S5) allowing the activity of H_2S to be determined directly from the measured total dissolved H_2S concentrations.

Examination of sulfide mineral phase relations in terms of temperature and fS_2 reveals some important trends (Fig. 9). In particular, there is a general increase in the sulfidation state (a function of temperature and fS_2, e.g., Einaudi et al., 2003; Sillitoe and Hedenquist, 2003) of fluids from the Kilo Moana vent field in the north to the Mariner vent field in the south (Fig. 9). Between the Kilo Moana and Tu'i Malila vent fields, this increase is primarily driven by the decrease in H_2 contents of hydrothermal fluids from north to south (Fig. 2; Table 1, S5). Elevated concentrations of H_2S in Mariner vent fluids and low H_2 concentrations (Fig. 2) result in high sulfidation state (Fig. 9). Elevated concentrations of H_2S and low concentrations of H_2 in Mariner vent fluids may reflect the addition of oxidized, sulfur-rich (i.e., SO_2-rich) magmatic volatiles, as has been previously proposed (Mottl et al., 2011). According to the classification proposed by Sillitoe and Hedenquist (2003), SMS deposits along the ELSC range from low-intermediate sulfidation state to intermediate sulfidation state deposits, with an increase in sulfidation state corresponding to increasing proximity to the volcanic arc. Similar patterns are reported in the Manus Basin, where higher sulfidation state deposits are likewise located closer to the volcanic arc (Craddock, 2009).

The mineralogy of open conduit chimney linings from ELSC vent fields closely reflects the temperature and sulfur fugacity of sampled hydrothermal fluids. At Kilo Moana, fluids plot along the pyrite/pyrrhotite boundary and below the chalcopyrite/cubanite boundary on the $\log(fS_2)$ vs. 1000/T(K) phase diagram (Fig.9). As observed in polished section, the linings of high-temperature open conduit chimneys collected in 2005 are composed of massive cubanite with minor–to-trace pyrrhotite (Fig. 4E; Table 2).

While the sulfidation state of fluids collected in 2009 cannot be directly calculated because H_2 has not been measured, it is possible to estimate the sulfidation state based on the H_2

concentrations of similar-temperature fluids collected in 2005. In using the measured H_2 concentration of 306°C fluid KM6 to estimate the fS_2 of 304°C fluid KM9 and in using the measured H_2 concentration of 300°C fluid KM4 to estimate the fS_2 of 290°C fluid KM10, it is shown that the sulfidation state of Kilo Moana vent fluids remains roughly the same, despite a decrease in temperature and fS_2. The lining of sample J2-434-2-R1G, which was collected with fluid KM9, also contains cubanite suggesting that the estimation is appropriate and that sulfidation state is a persistent characteristic of Kilo Moana vent fluids despite changes in temperature, pH, and composition.

Fluids from the TowCam and ABE vent fields show a range of calculated fS_2 that is similar to the range observed at Kilo Moana (Fig. 2). However, fluid temperatures are lower and fluids plot within the pyrite stability field, outside the stability field of pyrrhotite and spanning the boundary between cubanite and chalcopyrite (Fig. 9). In polished section, high-temperature open conduit chimney samples from the TowCam, ABE, and Tu'i Malila vent fields are lined with chalcopyrite and pyrite or chalcopyrite and wurtzite (Fig. 4F); cubanite and pyrrhotite are absent. This is consistent with the higher calculated sulfidation state of these fluids at these lower temperatures.

At the Mariner vent field, high H_2S and low H_2 result in higher fS_2 among high-temperature fluids (Fig. 9). This corresponds to a higher sulfidation state, albeit within the chalcopyrite and pyrite stability fields (Fig. 9). High temperature open conduits at Mariner vent field are lined with chalcopyrite (Fig. 4H). However, the higher sulfidation assemblage of bornite and pyrite is present in mid-layers at slightly lower temperatures, possibly reflecting transformations of these fluids as they cool. Alternatively, bornite may be a secondary mineral formed by alteration of primary chalcopyrite in the presence of seawater. The observations that

massive bornite exhibits similar textures to massive chalcopyrite and occurs primarily near the exteriors of open conduit chimney linings in association with tabular barite and anhydrite (Fig. 4D, 4H; Table 2) support the latter explanation.

The high fS_2 and sulfidation state of hydrothermal fluids at Mariner relative to other ELSC vent fields is likely a reflection of the addition of SO_2-rich magmatic volatiles into the hydrothermal system. Such volatiles are both oxidizing and sulfur-rich, each acting to increase the sulfur content (H_2S) of hydrothermal fluids without increasing H_2. This contrasts with the effect of higher reaction zone temperatures, which increase both H_2S and H_2 concentrations (Seyfried and Ding, 1995; Seyfried et al., 2002).

Sulfidation state also affects the composition of sphalerite and wurtzite. Qualitatively (based on color in transmitted light) and quantitatively (based on electron microprobe analyses), the mol% FeS of wurtzite and sphalerite ((Zn,Fe)S) contained in open conduit chimneys is highest at the Kilo Moana vent field (3 to 14 mol% FeS) and lowest at the Mariner vent field (1 to 6 mol% FeS). Wurtzite and sphalerite in open conduit chimneys from the TowCam (4 to 6 mol% FeS), Tahi Moana-1 (5 to 6 mol% FeS), ABE (2 to 4 mol% FeS), and Tu'i Malila (4 to 9 mol% FeS) vent fields exhibit intermediate concentrations of mol% FeS in (Zn,Fe)S (Table 3). These values match expectations for equilibrium concentrations of Fe in (Zn, Fe)S as a function of fS_2 and temperature based on measured fluid chemistries, suggesting that the FeS content of (Zn, Fe)S lining open conduit chimneys is also a reasonable indicator of hydrothermal fluid temperature and fS_2 and a more sensitive indicator than copper-iron sulfide mineralogy (Fig. 9). Wurtzite and sphalerite in active spires from the Tu'i Malila vent field (10 to 14 mol% FeS), exhibit higher mol% FeS, which is consistent with formation at more reducing conditions within active spires (Table 6). The correspondence of fluid fS_2 and temperature with SMS mineral

assemblages and mol% FeS in (Zn,Fe)S has been previously reported (e.g., Hannington et al., 1995; Kawasumi and Chiba, 2017).

5.4 Effects of Crustal Lithology on SMS Deposits

Concentrations of Ba and Pb in ELSC SMS deposits increase from north to south with the exception of the Mariner vent field, where bulk concentrations of Ba and Pb decrease relative to the Tu'i Malila vent field despite higher concentrations in Mariner vent fluids (Fig. 5; Table S2). These lower concentrations of Ba and Pb in Mariner deposits relative to high concentrations in Mariner fluids are the results of two mechanisms: 1) the lack of amorphous silica that would add structural support to barite-rich flanges and 2) the pH dependence of galena solubility. The presence of galena in samples from the more southerly Vai Lili vent field despite low fluid pH (pH(25°C) = 2) is likely the result of much higher Pb concentrations in Vai Lili fluids (3.8 to 7 μmol/kg at Vai Lili vs. 0.8 to 1.2 μmol/kg at Mariner), possibly as a result of near-surface remobilization of previously precipitated Zn- and Pb-rich sulfide deposits (Fouquet et al., 1993a).

Analyses of ELSC SMS deposits are also consistent with the hypothesis proposed by Langmuir et al. (1997) that barite is a common vent deposit mineral when the corresponding volcanic substrate contains > 50 μg/g Ba, but that no barite or only minor barite is present when the substrate contains < 20 μg/g Ba. Chemical analyses of igneous rock dredged from the ELSC show that rocks containing < 20 μg/g Ba are only found north of 20°29'S, while rocks containing > 50 μg/g Ba are only found south of 20°37'S (Escrig et al., 2009). This places the transition between the zones somewhere in the vicinity, or to the north, of the Tahi Moana-1vent field, consistent with the presence of barite as a trace component in SMS deposits at the

TowCam vent field, as a minor component at the Tahi Moana-1vent field, and as a major component at the ABE, Tu'i Malila, and Mariner vent fields.

Bulk concentrations of As and Sb in SMS deposits also increase from north to south (Fig. 5). However, bulk concentrations of Sb are lower in Mariner SMS deposits than at Tu'i Malia (Fig. 5). This likely reflects the incorporation of Sb into zinc sulfides and the lower abundance of zinc sulfide minerals at Mariner (a result of higher temperature, lower pH fluids). Nevertheless, at the individual mineral level, electron microprobe data show increasing concentrations of As in sphalerite and pyrite and increasing concentrations of Sb in sphalerite from north to south, suggesting that the effects of crustal lithology on As and Sb are partially transmitted to SMS deposits (Fig. 6). As and Sb were only measured in the dissolved portions of fluids, not in the dregs or filters. Concentrations of these elements in the vent deposits suggest however, that concentrations in endmember vent fluids increase from north to south, reflecting regional differences in crustal lithology as described by Escrig et al., 2009 and Sleeper and Martinez (2014).

Concentrations of Co in SMS deposits are higher at Kilo Moana than at other ELSC vent fields, reflecting more mafic lithology (Fig. 5). Electron microprobe analyses show that elevated concentrations of Co are primarily found in the linings and middle layers of open conduit chimneys, but are also present in the middle layers and exteriors of spires and flanges associated with marcasite, pyrite, and sphalerite (Fig. 6; Table S4).

The effects of crustal lithology on ELSC SMS deposits with respect to the proximity of the Tonga Subduction Zone are seen most clearly as a north-to-south increase in mantle-incompatible elements such as Ba, Pb, As, and Sb accompanied by a decrease in mantle-compatible elements such as Co in deposits and, where measured, also in fluids (Fig. 2, 5). In

addition to crustal lithology, the incorporation of these elements into SMS deposits is controlled by deposit-forming processes at the seafloor. This includes the precipitation of Ba and Pb as barite and galena and the incorporation of As, Sb, and Co as trace elements in sulfide minerals.

5.5. Comparison with SMS Deposits at Other ELSC Vent Fields

Of the additional confirmed active vent fields along the ELSC (the Tahi Moana-2, White Church, TELVE, Vai Lili, S'i S'i, Misitelli, and Hine Hina vent fields), detailed mineralogical and geochemical descriptions are only available for SMS deposits from the White Church, Vai Lili and Hine Hina vent fields. Similar to the SMS deposits at the Tu'i Malila vent field, deposits at the White Church vent field are Zn- and Ba-rich and associated with normal faulting (Fouquet et al., 1993a). Chimney morphology is characterized by horizontal layers and deposit mineralogy is dominated by barite and sphalerite with abundant galena and late stage silica (Fouquet et al., 1993a). High-temperature hydrothermal activity was not observed at the White Church vent field in 1989 (Fouquet et al., 1993a). However, numerous hydrothermal plumes located in the same area in 2004 suggest active venting at or near this site (Baker et al., 2006).

High temperature (280°C to 334°C), low pH (pH (at 25°C) = 2) hydrothermal fluids collected in 1989 from the Vai Lili vent field were associated with large, Cu-rich deposits (Fouquet et al., 1993a). These characteristics resemble those of the Mariner vent field. However, no evidence of magmatic volatile addition was found at the Vai Lili vent field and the low fluid pH of Vai Lili vent fluids can be attributed to subsurface deposition of Cu-Fe sulfides and remobilization of Zn-, Cd-, Pb-, and As-rich low-temperature mineral assemblages (Fouquet et al., 1993a). The maximum fluid temperature measured at the Vai Lili vent field in 2005 was 121°C (Tivey et al., 2012), suggesting that this vent field may have been in a waning stage in

1989. Sulfide mineralization at the Hine Hina vent field is associated with advanced argillic alteration (alunite- pyrophyllite-silica) and exhibit negative $\delta^{34}S$ isotopic signatures (Herzig et al., 1998). Hina Hina deposits are thus substantially different from the vent fields studied here, more closely resembling those of the SuSu Knolls vent fields in the Eastern Manus Basin (Yeats et al., 2014; McDermott et al., 2015).

6. CONCLUSION

The influence of the Tonga Subduction Zone on ELSC SMS deposits can be divided into regional and local effects. Regional effects are associated with the decrease, from north to south, in the distance between the ELSC and the Tofua Volcanic Arc and include crustal lithology that is increasingly enriched in mantle-incompatible elements in addition to lower reaction zone temperatures that result from shallower seafloor depths, thicker or more porous crust, and/or lower magma temperatures (Mottl et al., 2011; Escrig et al., 2009).

Lower reaction zone temperatures lead to the formation of higher pH hydrothermal fluids with lower Mn, Fe, and H_2S concentrations (Mottl et al., 2011) and lower Cu, Zn and H_2 concentrations. The elevated fluid pH results in zinc sulfide mineral saturation at higher temperatures, leading to formation of Zn-rich deposits despite low concentrations of Zn in vent fluids. The lower H_2 results in higher sulfidation states, affecting mineral stability in deposits.

The regional gradient in crustal lithology corresponds to a general increase in mantle-incompatible elements in fluids (e.g., Ba, Pb), and in SMS deposits (e.g., Ba, Pb, Sb, As), from north to south. However concentrations of some of these elements in SMS deposits are additionally modified by localized processes of deposit formation, including the stabilization of flanges (Ba) and effects of low pH on zinc- and lead-sulfide mineral saturation and precipitation

(Pb and Sb). Nevertheless, overall results reported here suggest that concentrations of Ba and Pb in hydrothermal fluids, and concentrations of these elements and Sb and As in SMS deposits, do reflect crustal lithology.

Local effects of the Tonga Subduction Zone influence the morphology, mineralogy, and geochemistry of SMS deposits at the Mariner vent field. The large active magma chamber beneath the Mariner vent field along with the associated higher-temperature reaction zone and addition of SO_2-rich magmatic volatiles lead to high vent fluid concentrations of Mn, Fe, and significantly lower pH (Mottl et al., 2011), and high concentrations of Cu and Zn, as well as an increase in the sulfidation state. The low pH prevents saturation of zinc- and lead- sulfide minerals at high temperatures such that high-temperature portions of Mariner SMS deposits are Cu-rich and Zn-poor relative to other ELSC deposits despite high concentrations of zinc in the vent fluids; low temperature portions of Mariner SMS deposits (e.g., small flanges and squat terraces) are Zn-, Pb-, and Ba-rich, and Si-poor.

The SMS deposits along the ELSC also record fluid sulfidation state. Mineral content of open conduit chimney linings shifts from massive cubanite ± pyrrhotite ± wurtzite at the Kilo Moana vent field to massive chalcopyrite ± pyrite ± wurtzite at other ELSC vent fields. The FeS content of zinc sulfides among open conduit chimneys within each vent field also reflects fluid temperature and fS_2, accurately recording an increase in the sulfidation state of hydrothermal fluids and SMS deposits with proximity to the Tonga Subduction zone.

The textural observations and geochemical data for ELSC deposit samples reported here, coupled with fluid analyses presented here for Cu, Zn, Pb, Ba, and H_2, allow more quantitative assessment of the roles that crustal lithology, reaction zone temperature, and local addition of magmatic volatiles play in determining SMS deposit and composition. The mineralogy of

chimney linings and the incorporation of Fe and trace elements into zinc sulfide minerals provide indications of hydrothermal fluid temperature, fS_2, and pH. In addition, the correlation between bulk geochemical concentration of Zn and Ag within a vent field is a useful indicator of hydrothermal fluid pH that holds for all ELSC vent fields, with positive and significant correlation between Zn and Ag reflecting deposition from low pH (minimum pH < 3.3) vent fluids at the Kilo Moana, Tahi Moana-1, and Mariner vent fields, and poor correlation between Zn and Ag reflecting deposition from high pH (minimum pH > 3.6) vent fluids at the TowCam, ABE, and Tu'i Malila vent fields. Analyses reported here demonstrate that the mineralogy and geochemistry of SMS deposits along the ELSC are accurate recorders of hydrothermal fluid chemistry, which can in turn be related to regional and local geologic processes influenced by proximity to the Tonga Subduction Zone.

ACKNOWLEDGEMENTS

We thank the captains and crews of the R/V Melville and the R/V Thompson and the team of the ROV Jason II for their expertise in recovering fluid and SMS deposit samples from active vent fields. Margaret Sulanowska's help with sample preparation is greatly acknowledged. This work was supported by the National Science Foundation [grant numbers OCE-1038135 to GNE and MKT, OCE-1038124, OCE-0241796, OCE-1233037 to JSS, and OCE-0242088 to CGW].

REFERENCES

Andreani, M., Escartin, J., Delacour, A., Ildefonse, B., Godard, M., Dyment, J., Fallick, A. E., and Fouquet, Y. (2014) Tectonic structure, lithology, and hydrothermal signature of the Rainbow massif (Mid- Atlantic Ridge 36° 14′ N). *Geochem. Geophys. Geosys.*, **15(9)**, 3543-3571.

Baker, E. T., Resing, J. A., Walker, S. L., Martinez, F., Taylor, B., and Nakamura, K. I. (2006) Abundant hydrothermal venting along melt- rich and melt- free ridge segments in the Lau back- arc basin. *Geophys. Res. Lett.*, **33(7),** L07308.

Barrie, C. T. and Hannington, M. D. (1999) Classification of volcanic-associated massive sulfide deposits based on host-rock composition. *Rev. Econ. Geol.,* **8**, 1-11.

Beaulieu, S. E., Baker, E. T., and German, C. R. (2015) Where are the undiscovered hydrothermal vents on oceanic spreading ridges?. *Deep Sea Research Part II: Topical Studies in Oceanography*, **121**, 202-212.

Beinart, R. A., Sanders, J. G., Faure, B., Sylva, S. P., Lee, R. W., Becker, E. L., Gartman, A., Luther, G. W., Seewald, J. S., Fisher, C. R., and Girguis, P. R. (2012) Evidence for the role of endosymbionts in regional-scale habitat partitioning by hydrothermal vent symbioses. *PNAS*, **109(47)**, E3241-E3250.

Bendel, V., Fouquet, Y., Auzende, J. M., Lagabrielle, Y., Grimaud, D., and Urabe, T. (1993) The White Lady hydrothermal field, North Fiji back-arc basin, southwest Pacific. *Econ. Geol.*, **88(8)**, 2237-2245.

Bézos, A., Escrig, S., Langmuir, C. H., Michael, P. J., and Asimow, P. D. (2009) Origins of chemical diversity of back-arc basin basalts: A segment-scale study of the Eastern Lau Spreading Center. *J. Geophys. Res.: Solid Earth*, **114**, B06212, doi:10.1029/2008JB005924.

Collier, J. S. and Sinha, M. C. (1990) Seismic images of a magma chamber beneath the Lau Basin back-arc spreading centre. *Nature*, **346**, 646 to 648; doi:10.1038/346646a0.

Craddock, P. R. (2009) Geochemical tracers of processes affecting the formation of seafloor hydrothermal fluids and deposits in the Manus back-arc basin. Ph.D. Thesis, MIT/WHOI Joint Program in Oceanography.

Douville, E., Charlou, J. L., Oelkers, E. H., Bienvenu, P., Colon, C. J., Donval, J. P., Fouquet, Y., Prieur, D., and Appriou, P. (2002) The rainbow vent fluids (36 14′ N, MAR): the influence of ultramafic rocks and phase separation on trace metal content in Mid-Atlantic Ridge hydrothermal fluids. *Chem. Geol.*, **184(1)**, 37-48.

Edmond, J. M., Campbell, A. C., Palmer, M. R., Klinkhammer, G. P., German, C. R., Edmonds, H. N., Elderfield, H., Thompson, G., and Rona, P. (1995) Time series studies of vent fluids from the TAG and MARK sites (1986, 1990) Mid-Atlantic Ridge: a new solution chemistry model and a mechanism for Cu/Zn zonation in massive sulphide orebodies. *Geological Society, London, Special Publications*, **87(1)**, 77-86.

Einaudi, M. T., Hedenquist, J. W., and Inan, E. E. (2003) Sulfidation state of fluids in active and extinct hydrothermal systems: transitions from porphyry to epithermal environments. In

Special Publication-Society of Economic Geologists, **10** (eds. S.F. Simmons, I. Graham). Society of Economic Geologists, pp. 285-314.

Escrig, S., Bézos, A., Goldstein, S. L., Langmuir, C. H., and Michael, P. J. (2009) Mantle source variations beneath the Eastern Lau Spreading Center and the nature of subduction components in the Lau basin–Tonga arc system, *Geochem. Geophys. Geosys.*, **10**, Q04014, doi:10.1029/2008GC002281.

Ferrini, V. L., Tivey, M. K., Carbotte, S. M., Martinez, F. , and Roman, C. (2008) Variable morphologic expression of volcanic, tectonic, and hydrothermal processes at six hydrothermal vent fields in the Lau back-arc basin, *Geochem. Geophys. Geosys.*, **9**, Q07022, doi:10.1029/2008GC002047.

Flores, G. E., Shakya, M., Meneghin, J., Yang, Z. K., Seewald, J. S., Wheat, C. G., Podar, M., and Reysenbach, A.-L. (2012) Inter-field variability in the microbial communities of hydrothermal vent deposits from a back-arc basin. *Geobio.*, **10**: 333–346. doi:10.1111/j.1472-4669.2012.00325.x

Foucher, J. P. and Shipboard Scientific Party (1988) La ride de Valu Fa dans le basin de Lau meridionnal (sud-ouest Pacifique). *Academie des Sciences Comptes Rendues*, **307.2**, 609-616.

Fouquet, Y., von Stackelberg, U., Charlou, J. L., Donval, J. P., Erzinger, J., Foucher, J. P., Herzig, P., Mühe, R., Soakai, S., Wiedicke, M., and Whitechurch, H. (1991) Hydrothermal activity and metallogenesis in the Lau back-arc basin. *Nature*, **349(6312)**, 778-781.

Fouquet, Y., von Stackelberg, U., Charlou, J. L., Erzinger, J., Herzig, P. M., Mühe, R., and Wiedicke, M. (1993a) Metallogenesis in back-arc environments: the Lau Basin example. *Econ. Geol.*, **88(8)**, 2154-2181.

Fouquet, Y., Wafi, A., Cambon, P., Mevel, C., Meyer, G., and Cente, P. (1993b) Tectonic Setting, mineralogical and geochemical zonation in the Snake Pit sulfide deposit (Mid-Atlantic Ridge at 23°N). *Econ. Geol*., **88(8)**, 2018-2036.

Fournier, R. O. (1985) The behavior of silica in hydrothermal solutions. *Rev. Econ. Geol.*, **2**, 45-61.

Franklin, J. M., Gibson, H. L., Jonasson, I. R., and Galley, A. G. (2005) Volcanogenic massive sulfide deposits. *Economic Geology 100th Anniversary Volume*, Society of Economic Geologists, Littleton, Colorado, USA, 523-560.

Frenzel, J. M., Mühe, R., and Stoffers, P. (1990) Petrology of the volcanic rocks from the Lau basin, southwest Pacific. Geol. Jahrb. **92**, 395-479.

Fretzdorff, S., U. Schwarz-Schampera, H. L. Gibson, C.-D. Garbe-Schönberg, F. Hauff, and P. Stoffers (2006) Hydrothermal activity and magma genesis along a propagating backarc basin: Valu Fa Ridge (southern Lau basin), *J. Geophys. Res*., **111**, sB08205, doi:10.1029/2005JB003967.

Hannington, M. D. and Scott, S. D. (1988) Mineralogy and geochemistry of a hydrothermal silica-sulfide-sulfate spire in the caldera of Axial Seamount, Juan de Fuca Ridge. *Can. Mineral.*, **26(3)**, 603-625.

Hannington, M., Herzig, P., Scott, S., Thompson, G., and Rona, P. (1991) Comparative mineralogy and geochemistry of gold-bearing sulfide deposits on the mid-ocean ridges. *Marine Geol.*, **101(1)**, 217-248.

Hannington, M. D., Jonasson, I. R., Herzig, P. M., and Petersen, S. (1995) Physical and chemical processes of seafloor mineralization at mid-ocean ridges. In *Seafloor hydrothermal systems: physical, chemical, biological, and geological interactions* (eds. S. E. Humphris, R. A. Zierenberg, L. S. Mullineaux, and R. E. Thomson), American Geophysical Union, Washington, D. C.. pp. 115-157. doi: 10.1029/GM091p0115.

Hannington, M. D., de Ronde, C. D. J., and Petersen, S. (2005) Sea-floor tectonics and submarine hydrothermal systems. *Economic Geology 100th Anniversary Volume.* Society of Economic Geologists, Littleton, Colorado, USA, 111-141.

Harding, A. J., Kent, G. M., and Collins, J. A. (2000) Initial results from a multichannel seismic survey of the Lau backarc basin, *Eos Trans. AGU*, **81**,abstract T61C-16.

Herzig, P. M., Hannington, M. D., and Arribas Jr, A. (1998) Sulfur isotopic composition of hydrothermal precipitates from the Lau back-arc: implications for magmatic contributions to seafloor hydrothermal systems. *Mineral. Dep.*, *33*(3), 226-237.

Ishibashi, J. -I., Lupton, J. E., Yamaguchi, T., Querellou, J., Nunoura, T., and Takai, K. (2006) Expedition reveals changes in Lau Basin hydrothermal system. *Eos Trans. AGU*, **87(2)**, 13-17.

Jacobs, A. M., Harding, A. J., and Kent, G. M. (2007) Axial crustal structure of the Lau back-arc basin from velocity modeling of multichannel seismic data. *Earth Planet. Sci. Lett.*, **259(3)**, 239-255.

Jenner, G. A., Cawood, P.A., Rautenschlein, M., and White, W. M. (1987) Composition of backarc basin volcanics, Valu Fa Ridge, Lau basin: Evidence for a slab-derived component in their mantle source, *J. Volcanol. Geotherm. Res*., **32**, 209–222.

Johnson, J. W., Oelkers, E. H., and Helgeson, H. C. (1992) SUPCRT92: A software package for calculating the standard molal thermodynamic properties of minerals, gases, aqueous species, and reactions from 1 to 5000 bar and 0 to 1000 C. *Computers Geosci.*, **18(7)**, 899-947.

Kawasumi, S., and Chiba, H. (2017) Redox state of seafloor hydrothermal fluids and its effect on sulfide mineralization. *Chem. Geol.,* **451**, 25-37.

Kristall, B., Kelley, D. S., Hannington, M. D., and Delaney, J. R. (2006) Growth history of a diffusely venting sulfide structure from the Juan de Fuca Ridge: A petrological and geochemical study. *Geochem. Geophys. Geosys*., **7(7),** doi:10.1029/2005GC001166

Kristall, B., Nielsen, D., Hannington, M. D., Kelley, D. S., and Delaney, J. R. (2011) Chemical microenvironments within sulfide structures from the Mothra Hydrothermal Field: Evidence from high-resolution zoning of trace elements. *Chem. Geol.,* **290(1)**, 12-30.

Langmuir, C., Humphris, S., Fornari, D., Van Dover, C., Von Damm, K., Tivey, M. K., Colodner, D., Charlou, J.-L., Desonie, D., Wilson, C., Fouquet, Y., Klinkhammer, G., Bougault, H., (1997) Hydrothermal vents near a mantle hot spot: the Lucky Strike vent field at 37 °N on the Mid-Atlantic Ridge. *Earth Planet. Sci. Lett.*, **148(1)**, 69-91.

Langmuir, C. H., Bézos, A., Escrig, S., and Parman, S. W. (2006) Chemical systematics and hydrous melting of the mantle in back-arc basins. In *Back-Arc Spreading Systems: Geological, Biological, Chemical, and Physical Interactions* (eds. D. M. Christie, C. R. Fisher, S.-M. Lee, and S. Givens) Geophysical Monograph Series, vol. 166, American Geophysical Union, Washington, DC. 87–146.

Martinez, F. and Taylor, B. (2002) Mantle wedge control on back-arc crustal accretion. *Nature,* **416**, 417-420.

Martinez, F., Taylor, B., Baker, E. T., Resing, J. A., and Walker, S. L. (2006) Opposing trends in crustal thickness and spreading rate along the back-arc Eastern Lau Spreading Center: Implications for controls on ridge morphology, faulting, and hydrothermal activity. *Earth Planet. Sci. Lett.*, **245(3)**, 655-672.

McDermott, J. M., Ono, S., Tivey, M. K., Seewald, J. S., Shanks, W. C., and Solow, A. R. (2015) Identification of sulfur sources and isotopic equilibria in submarine hot-springs using multiple sulfur isotopes. *Geochim. Cosmochim. Acta*, *160*, 169-187.

Moore, W. S. and Stakes, D. (1990) Ages of barite-sulfide chimneys from the Mariana Trough. *Earth Planet. Sci. Let.*, **100(1)**, 265-274.

Morton, J. L. and Sleep, N. H. (1985) Seismic reflections from a Lau Basin magma chamber. In *Geology and Offshore Resources of Pacific Island Arcs-Tonga Region* (eds. D. W. Scholl and T. L. Vallier). Circum-Pacific Council for Energy and Mineral Resources, Houston, pp. 441-453.

Mottl, M. J. and Holland, H. D. (1978) Chemical exchange during hydrothermal alteration of basalt by seawater. I. Experimental results for major and minor components of seawater. *Geochim. Cosmochim. Acta*, **42**, 1103-1115.

Mottl, M. J., Seewald, J. S., Wheat, C. G., Tivey, M. K., Michael, P. J., Proskurowski, G., McCollom, M., Reeves, E., Sharkey, S., You, C.-F., Chan, L.-H., and Pichler, T. (2011) Chemistry of hot springs along the Eastern Lau Spreading Center. *Geochim Cosmochim. Acta*, **75(4)**, 1013-1038.

Nilsson, K. and Peach, C. L. (1993) Sulfur speciation, oxidation state, and sulfur concentration in backarc magmas. *Geochim. Cosmochim. Acta* , ***57*(15)**, 3807-3813.

Parson, L. M. and Wright, I. C. (1996) The Lau-Havre-Taupo back-arc basin: A southward-propagating, multi-stage evolution from rifting to spreading. *Tectonophysics*, **263(1)**, 1-22.

Pester, N. J., Rough, M., Ding, K., and Seyfried, W. E. (2011) A new Fe/Mn geothermometer for hydrothermal systems: Implications for high-salinity fluids at 13 N on the East Pacific Rise. *Geochim. Cosmochim. Acta*, ***75*(24)**, 7881-7892.

Podowski, E. L., Moore, T. S., Zelnio, K. A., Luther, G. W., and Fisher, C. R. (2009) Distribution of diffuse flow megafauna in two sites on the Eastern Lau Spreading Center, Tonga. *Deep Sea Research Part I: Oceano. Res. Papers*, **56(11)**, 2041-2056.

Reeves, E. P., Seewald, J. S., Saccocia, P., Bach, W., Craddock, P. R., Shanks, W. C., Sylva. S., Walsh, E., Pichler, T., and Rosner, M. (2011) Geochemistry of hydrothermal fluids from the PACMANUS, Northeast Pual and Vienna Woods hydrothermal fields, Manus Basin, Papua New Guinea. *Geochim. Cosmochim. Acta*, **75(4)**, 1088-1123.

Ryan, W. B. F., Carbotte, S. M., Coplan, J. O., O'Hara, S., Melkonian, A., Arko, R., Weissel, R. A., Ferrini, V., Goodwillie, A., Nitsche, F., Bonczkowski, J., and Zemsky, R. (2009) Global Multi-Resolution Topography synthesis, *Geochem. Geophys. Geosys.*, **10**, Q03014, doi:10.1029/2008GC002332.

Sack, R. O., and Ebel, D. S. (2006) Thermochemistry of sulfide mineral solutions. In *Reviews in mineralogy and geochemistry*, **61(1)** (ed. D.J. Vaughan). Geochemical Society and Mineralogical Society of America. 265-364.

Scott, S. D., Chase, R. L., Hannington, M. D., Michael, P. J., McConachy, T. F. and Shea, G.T. (1990) Sulfide deposits, tectonics, and petrogenesis of Explorer Ridge, Northeast pacific Ocean. In *Ophiolites, Oceanic Crustal Analogues* (eds. J. Malpas et al.), Cyprus Geol. Surv. Dep., Nicosia, pp. 719-733.

Seewald, J. S. and Seyfried, W. E. (1990) The effect of temperature on metal mobility in subseafloor hydrothermal systems: constraints from basalt alteration experiments. *Earth Planet. Sci. Lett.*, **101(2)**, 388-403.

Seewald, J. S., Doherty, K. W., Hammar, T. R., and Liberatore, S. P. (2002) A new gas-tight isobaric sampler for hydrothermal fluids. *Deep Sea Research Part I: Oceanographic Research Papers*, **49(1),** 189-196.

Seyfried, W. E. and Ding, K. (1993) The effect of redox on the relative solubilities of copper and iron in Cl-bearing aqueous fluids at elevated temperatures and pressures: an experimental study with application to subseafloor hydrothermal systems. *Geochim. Cosmochim. Acta*, **57(9)**, 1905-1917.

Seyfried, W. E. and Ding, K. (1995) Phase equilibria in subseafloor hydrothermal systems: A review of the role of redox, temperature, pH and dissolved Cl on the chemistry of hot spring fluids at mid-ocean ridges. In *Seafloor Hydrothermal Systems: Physical, Chemical, Biological, and Geological Interactions* (eds. S. E. Humphris, R. A. Zierenberg, L. S. Mullineaux, and R. E. Thomson), American Geophysical Union, Washington, D. C., 248-272.

Seyfried W. E. Jr., Janecky, D. R., and Mottl M. J. (1984) Alteration of the oceanic crust: implications for geochemical cycles of lithium and boron. *Geochim. Cosmochim. Acta*, **48**, 557-569.

Seyfried, W. E., Ding, K., and Rao, B. (2002) Experimental calibration of metastable plagioclase–epidote-fluid equilibria at elevated temperatures and pressures: applications to the chemistry of hydrothermal fluids at mid-ocean ridges. In *Water-rock Interactions, Ore Deposits, and Environmental Geochemistry: A Tribute to David A. Crerar.* (eds. R. Hellman and S.A. Wood). The Geochemical Society, pp. 257-278.

Sillitoe, R. H. and Hedenquist, J. W. (2003) Linkages between volcanotectonic settings, ore-fluid compositions, and epithermal precious metal deposits. In *Special Publication-Society of Economic Geologists*, **10** (eds. S.F. Simmons, I. Graham). Society of Economic Geologists. Pp. 315-343.

Smith, W. H. and Sandwell, D. T. (1997) Global sea floor topography from satellite altimetry and ship depth soundings. *Science*, **277(5334)**, 1956-1962.

Sleeper, J. D. and Martinez, F. (2014) Controls on segmentation and morphology along the back- arc Eastern Lau Spreading Center and Valu Fa Ridge.. *Res.*, **119(3)**, 1678-1700.

Stoffers, P., Worthington, T. J., Schwarz-Schampera, U., Hannington, M. D., Massoth, G. J., Hekinian, R., Schmidt, M., Lundsten, L. J., Evans, L. J., Vaiomo'unga, R., and Kerby, T. (2006) Submarine volcanoes and high-temperature hydrothermal venting on the Tonga arc, southwest Pacific. *Geology*, **34(6)**, 453-456.

Takai, K., Nunoura, T., Ishibashi, J.-I., Lupton, J., Suzuki, R., Hamasaki, H., Ueno, Y., Kawagucci, S., Gamo, T., Suzuki, Y., Hirayama, H., and Horikoshi, K. (2008) Variability in the microbial communities and hydrothermal fluid chemistry at the newly discovered

Mariner hydrothermal field, southern Lau Basin. J. *Geophys. Res*., **113**, G02031, doi:10.1029/2007JG000636.

Taylor, B. and Martinez, F. (2003) Back-arc basin basalt systematics. *Earth Planet. Sci. Lett.*, **210(3)**, 481-497.

Tivey, M. K. (1995) The influence of hydrothermal fluid composition and advection rates on black smoker chimney mineralogy: Insights from modeling transport and reaction. *Geochim. Cosmochim. Acta*, **59(10)**, 1933-1949.

Tivey, M. K., Humphris, S. E., Thompson, G., Hannington, M. D., and Rona, P. A. (1995). Deducing patterns of fluid flow and mixing within the TAG active hydrothermal mound using mineralogical and geochemical data. *J. Geophys. Res.*, **100(B7)**, 12527-12555.

Tivey, M. K., Stakes, D. S., Cook, T. L., Hannington, M. D., and Petersen, S. (1999) A model for growth of steep-sided vent structures on the Endeavour Segment of the Juan de Fuca Ridge: Results of a petrologic and geochemical study. *J. Geophys. Res: Solid Earth*, **104(B10),** 22859-22883.

Tivey, M. K., Craddock, P. R., Seewald, J. S., Ferrini, V.L., Kim, S., Mottl, M., Sterling, N.A., Reysenbach, A., and Wheat, C. G. (2005, December) Characterization of six vent fields within the Lau Basin. In *AGU Fall Meeting Abstracts* (Vol. 1, p. 0477).

Tivey, M. K., Becker, E., Beinart, R., Fisher, C. R., Girguis, P. R., Langmuir, C. H., Michael, P. J., and Reysenbach, A. L. (2012). Links from mantle to microbe at the Lau Integrated Study Site: Insights from a back-arc spreading center. *Oceanography*, **25**, 62–77.

Trefry, J. H., Butterfield, D. B., Metz, S., Massoth, G. J., Trocine, R. P., and Feely R. A. (1994) Trace metals in hydrothermal solutions from Cleft segment on the southern Juan de Fuca Ridge. *J. Geophys. Res.***99,** 4925–4935.

Vallier, T. L., Jenner, G. A., Frey, F. A., Gill, J. B., Davis, A. S., Volpe, A. M., Hawkins, J. W., Morris, J. D., Cawood, P. A., Morton, J. L., Scholl, D. W., Rautenschlein, M., White, W. M., Williams, R. W., Stevenson, A. J., and White, L., D. (1991) Subalkaline andesite from Valu Fa Ridge, a back-arc spreading center in southern Lau Basin: petrogenesis, comparative chemistry, and tectonic implications. *Chem. Geol.*, **91(3)**, 227-256.

Von Damm, K. L. (1995) Controls on the chemistry and temporal variability of seafloor hydrothermal fluids. In *Seafloor Hydrothermal Systems: Physical, Chemical, Biological, and Geological Interactions* (eds. S. E. Humphris, R. A. Zierenberg, L. S. Mullineaux, and R. E. Thomson), American Geophysical Union, Washington, D. C., 222-247.

Von Damm, K. L., Edmond, J. M., Grant, B., Measures, C. I., Walden, B., and Weiss, R. F. (1985) Chemistry of submarine hydrothermal solutions at 21° N, East Pacific Rise. *Geochim. Cosmochim. Acta*, **49(11),** 2197-2220.

von Stackelberg, U. and Shipboard Scientific Party (1985) Hydrothermal sulfide deposits in back-arc spreading centers in the southwest Pacific, Bundesanstalt für Geowissenschaften und Rohstoffe, **Circular 2**, 3-14.

von Stackelberg, U. and Shipboard Scientific Party (1988) Active hydrothermalism in the Lau Back-arc Basin (SW Pacific): First results from the SONNE 48 cruise (1987). *Mar. Min.*, **7**, 431-442.

von Stackelberg, U., Marchig, V., Müller, P., and Weiser, T. (1990) Hydrothermal mineralization in the Lau and North Fiji Basins. *Geol. Jahrb., Reihe D*, **92**, 547-613.

Wiedicke, M. and Collier, J. (1993) Morphology of the Valu Fa spreading ridge in the southern Lau Basin. *J. Geophys. Res: Solid Earth*, **98(B7)**, 11769-11782.

Wolery, T. J. (1992) EQ3/6: A software package for geochemical modeling of aqueous systems: package overview and installation guide (version 7.0). Livermore, CA: Lawrence Livermore National Laboratory.

Yeats, C. J., Parr, J. M., Binns, R. A., Gemmell, J. B., and Scott, S. D. (2014) The SuSu Knolls Hydrothermal Field, Eastern Manus Basin, Papua New Guinea: An Active Submarine High-Sulfidation Copper-Gold System. *Econ, Geol.*, **109(8)**, 2207-2226.

TABLES and FIGURES

Table 1. Endmember concentrations of mineral-forming elements and major vent fluid parameters of ELSC hydrothermal fluids.

Fluid	Year	[a,b]T	[a,c]pH	[a]Cl	[a]H_2S	[a]Mn	[a]Fe	[d]Fe	[d]Cu	[d]Zn	[d]Pb	[d]Ba	H2
		°C	25°C	mm	mm	µm	µm	µm	µm	µm	nm	µm	µM
KM1	2005	333	3.6	580	5.7	510	2480	2480	8	58	270	24	310
KM2	2005	332	3.6	570	5.5	690	3140	3200	NM	NM	310	24	220
KM3	2005	321	2.9	580	6.6	730	3810	3840	9	74	310	26	360
KM4	2005	300	3.2	570	5.5	520	2280	2470	11	NM	230	25	480
KM5	2005	329	3.5	580	6.4	720	2890	2900	11	108	NM	NM	360
KM6	2005	306	3.6	590	5.6	680	2960	3120	10	60	400	22	440
KM8	2005	333	4.0	580	5.6	550	2520	2560	NM	64	390	NM	500
KM9	2009	304	4.1	570	3.5	210	530	NM	NM	NM	NM	NM	NM
KM10	2009	290	3.9	570	3.9	190	590	NM	NM	NM	NM	NM	NM
TC1	2005	328	4.1	530	4.9	390	260	310	4	19	370	34	130
TC3	2005	320	4.0	530	4.7	400	260	270	3	49	430	34	180
TC4	2005	316	4.1	530	5.0	410	280	280	5	61	500	21	150
TC5	2005	302	3.7	550	4.6	330	320	340	7	53	NM	25	110
TC6	2005	288	3.9	550	3.8	390	340	370	4	50	430	28	NM
TC7	2005	288	4.0	530	5.3	370	290	310	8	74	520	29	200
TC9	2009	320	3.6	560	4.8	330	210	NM	NM	NM	NM	NM	NM
TMo1	2009	306	3.3	580	3.1	590	330	NM	NM	NM	NM	NM	NM
TMo2	2009	298	3.9	580	4.1	300	230	NM	NM	NM	NM	NM	NM
TMo3	2009	286	3.7	560	3.2	730	280	NM	NM	NM	NM	NM	NM
TMo5	2009	310	3.7	560	3.3	350	250	NM	NM	NM	NM	NM	NM
A1	2005	309	4.3	530	3.6	460	260	270	6	36	390	37	60
A2	2005	309	4.1	540	3.1	480	270	260	5	44	380	7	NM
A4	2005	278	4.4	590	2.9	270	160	NM	NM	NM	NM	NM	50
A5	2005	290	4.5	550	3.2	290	160	170	4	33	380	63	100
A8	2005	308	4.5	550	3.0	300	160	NM	NM	NM	NM	NM	80
A9	2005	295	4.6	590	2.7	290	130	160	NM	37	570	26	100
A10	2009	317	3.9	540	3.9	410	150	NM	NM	NM	NM	NM	NM
A11	2009	306	4.0	550	2.7	280	80	NM	NM	NM	NM	NM	NM
A12	2009	297	4.0	590	3.0	350	140	NM	NM	NM	NM	NM	NM
TM1	2005	279	4.5	650	2.4	430	200	220	16	48	530	51	50
TM2	2005	312	4.4	650	2.4	410	210	220	7	28	570	39	50
TM4	2005	178	5.7	630	1.2	330	140	NM	NM	NM	NM	NM	120
TM5	2005	265	4.6	650	2.4	440	200	NM	NM	NM	NM	NM	40
TM6	2005	265	4.4	650	2.4	400	220	230	2	18	560	37	100
TM7	2005	198	5.0	640	2.2	410	200	NM	NM	NM	NM	NM	NM
TM8	2005	229	4.4	640	2.2	380	140	NM	11	7	790	77	110
TM10	2005	274	4.1	640	2.1	380	230	270	4	49	NM	NM	70
TM11	2009	315	3.8	650	2.8	370	150	NM	NM	NM	NM	NM	NM
TM12	2009	284	4.2	640	2.8	310	180	NM	NM	NM	NM	NM	NM
MA1	2005	334	2.5	620	6.1	5940	11230	11420	171	467	860	77	50
MA2	2005	311	2.6	620	4.3	6280	11210	11270	105	514	750	44	30
MA3	2005	363	2.7	610	9.6	5730	12960	13120	156	336	1130	75	130
MA5	2005	249	2.6	530	4.6	5440	10450	10550	96	321	860	97	60
MA6	2005	240	2.7	530	6.5	4870	10670	10680	4	242	1200	131	180
MA8	2009	359	2.4	470	17.8	3860	9420	NM	NM	NM	NM	NM	NM
MA9	2009	338	2.3	540	8.9	5200	12550	NM	NM	NM	NM	NM	NM
MA11	2009	356	2.2	NM	11.8	4390	11570	NM	NM	NM	NM	NM	NM
MA12	2009	350	2.3	560	10.8	4630	13080	NM	NM	NM	NM	NM	NM

for Table 1:

Endmember compositions are based on fluid samples listed in Supplementary Table S1. Analytical errors for metal analyses of individual fluid samples are estimated at ±10% and ±10 µmol/kg for measurements of Mn and Fe. Uncertainties resulting from differential sampling of hydrothermal fluids cannot be quantified.

[a] 2005 values from Mottl et al. (2011)
[b]T is maximum temperature measured at the seafloor during sampling.
[c]pH is reported as measured at 25°C
[d] includes redigested bottle solids
mm = mmol/kg fluid, µm = µmol/kg fluid, µM = µmol/L fluid, NM = not measured
KM = Kilo Moana, TC = TowCam, TMo = Tahi Moana-1, A = ABE, TM = Tu'i Malila, MA = Mariner

Table 2. Mineral textures of SMS deposit samples from the Kilo Moana (KM), TowCam (TC), Tahi Moana-1 (TMo), ABE (A), Tu'i Malila (TM), and Mariner (MA) vent fields categorized by sample type.

KM	OC	Three layers: (1) Linings (~330°C): massive cb with minor po, grades outward to iss and cp. Euhedral py near boundary with middle layer. Linings (~300°C): euhedral wz with cp or iss as inclusions or interstitial grains. (2) Middle layers: matrix of ~1 cm tabular anh with interstitial wz, sp, py, cp (variable grain size and texture). (3) Outer layers: dendritic mc, outer coating of FeOOH and amsi
KM	AS	Porous middle layers surround anastomosing fluid conduits. Inner layers: euhedral wz or massive cp and minor py. Middle layers: dendritic wz, py, and mc with minor cp. Late-stage amsi (< 10 µm coating). From interior to exterior, the abundance of wz decreases and the abundance of mc increases.
KM	RS	Porous layers surround anastomosing fluid conduits. Inner layers: euhedral wz, minor cp and mc. Middle layers: euhedral-subhedral wz, euhedral-subhedral mc. Outer layers: mc dendrites.
KM	AF	Lower and middle layers: alternating layers of dendritic mc intergrown with wz (size: 20-30 µm), minor interstitial cp. Upper layer: mc dendrites (< 4 mm).
KM	RF	Lower layer: 1-2 mm euhedral wz, minor cp. Middle layer: euhedral wz (50 to 200 µm) intergrown with euhedral py, dendritic wz, and minor interstitial cp. Upper layer: mc dendrites (< 4 mm). Late-stage amsi.
TC	OC	Two samples: (1^{st}) (matches geochem.) Lining: massive cp intergrown with wz and py. (2^{nd}) Lining: euhedral wz intergrown with cp. Middle layers of both: euhedral-subhedral wz and py, minor anh and cp. Outer layers: mc dendrites.
TC	AS	Porous middle layers surround anastomosing fluid conduits. Linings: 50 µm – 400 µm subhedral-euhedral wz and 5 – 30 µm cp and py. Alternatively, ~1 mm-long, inward-facing dendrites of < 100 µm wz and cp. Middle layers: dendritic matrix of wz and py, minor cp. Also, interstitial anh far from fluid conduits and late-stage amsi (< 10 µm coating). Outer layers: < 1 mm layer of py and mc dendrites. Late-stage amsi (< 10 µm coating)
TC	RS	Porous middle layers surround anastomosing fluid conduits. Dendritic matrix of euhedral-to-subhedral wz, sp, py, minor cp. Outer layers: (~1 mm) mc dendrites, minor ba.
TMo	OC	Three layers: (1) Lining (310°C): massive cp with < 5 µm inclusions of euhedral py, minor bladed wz, oleander-leaf twinning. (2) Middle layer: cp, wz, py (grain size variable up to 200 µm), interstitial tabular anh. (3) Outer layer: anh up to 500 µm; fine-grained w, py, cp; py and mc dendrites (< 500 µm) .
TMo	AS	Porous middle layers surround anastomosing fluid conduits. Dendritic matrix of subhedral sp, minor py, cp, trace ga. Outer layers: (~1 mm) mc dendrites, minor acicular ba.
TMo	RS	no polished section.
TMo	AF	Dendritic matrix of subhedral sp, py, and minor cp. Upper layer: acicular ba, mc dendrites.
A	OC	Two layers: (1) Lining (317°C): massive cp with 100 – 500 µm inclusions of euhedral py. Lining (306°C): intergrown blades of cp and wz; oleander-leaf twinning of cp in wz; trace py in cp. (2) Outer layers: sp, minor anh, trace bn, dg, cv, ga.
A	AS	Porous middle layers surround anastomosing fluid conduits. Linings: euhedral wz and/or cp. Middle layers dendritic matrix of wz, sp, minor mc and euhedral py, trace-to-minor ba, and trace ga. Outer layers: mc dendrites, minor acicular ba.
A	RS	Porous middle layers surround anastomosing fluid conduits. Linings: inward-facing dendritic sphalerite. Middle layers: wz, py, cp (< 50 µm), and minor ba. Lathe-shaped voids suggest dissolution of ba. Outer layers: mc dendrites.
A	AF	Dendritic matrix of tabular ba (< 100 µm) with interstitial, fine-grained (< 5 µm) sulfides. Only py positively identified, using secondary electron microscope. Late-stage interstitial amsi
TM	OC	Lining (312°C): massive cp and euhedral py (100 – 200 µm). Lining: (279°C) bladed wz, intergrown with lesser interstitial cp and py. Outer layers: tabular anh and minor interstitial sp, acicular ba, and trace ga.
TM	AS	Porous middle layers surround anastomosing fluid conduits. Linings: thin rims of massive sp, trace-to-minor cp. Middle layers: tabular ba with interstitial py, sp, wz, trace-to-minor ga. Outer layers: dendritic mc and acicular ba. Lining of J2-134-9-R1 (T = 198°C) is euhedral wz, minor interstitial cp and ga.
TM	RS	Porous middle layers surround anastomosing fluid conduits filled with tabular ba (< 1 mm). Linings: thin rims of massive wz/sp, trace-to-minor cp, py, ga. Middle layers: ba lathes and interstitial py, sp, wz, trace-to-minor cp, ga. Outer layers: dendritic mc, acicular ba, FeOOH.
TM	AF	Lower layer: dendritic matrix of tabular ba and interstitial sp. Middle layer: dendritic matrix of tabular ba, minor anh, and interstitial py and sp. Upper layer: subhedral sp with thin mc rims, minor cp. Late-stage interstitial amsi

TM	RF	Dendritic matrix of tabular ba (2 to 3mm), interstitial euhedral-subhedral sp and minor py. Late-stage amsi (13 wt%).
MA	OC	Three layers: (1) Linings: massive cp, often doubled. (2) Middle layers: massive bn-cv-dg (0-14% bn). Alternatively, dendritic cp and bn. (3) Outer layers: tabular anh, ba, and fine-grained interstitial sp, cp. trace tn. Alternatively, dendritic py and mc.
MA	AS	Porous inner layers surround anastomosing fluid conduits. Inner layers: cp and bn dendrites (0-9% bn). Outer layers: dendritic py and mc, lesser cp replacing wz, acicular ba.
MA	RS	Porous middle layers surround anastomosing fluid conduits. Linings: massive cp with inward-facing sp dendrites. Middle layers: dendritic ba, interstitial sp, mc (< 5 μm); bn-cv-dg replacing cp. Outer layers: dendritic mc.
MA	AF	Dendritic matrix of tabular and acicular ba with interstitial euhedral-subhedral sp and py. Minor amsi In upper layer.
MA	ST	Dendritic matrix of tabular ba and interstitial euhedral-subhedral sp . Minor mc/py, trace cp and tn. Acicular ba near exterior.
MA	RF	Dendritic matrix of tabular ba and interstitial euhedral-subhedral sp. Minor cp and py intergrown with sp.

Sample types are: open conduit chimneys (OC), active spires (AS), relict spires (RS), active flanges (AF), relict flanges (RF), and squat terraces (ST).
Mineral types are: amorphous silica (amsi), anhydrite (anh), barite (ba), bornite (bn), cubanite (cb), chalcopyrite (cp), chalcopyrite-cubanite intermediate solid solution (iss), covellite (cv), digenite (dg), iron- oxyhydroxides (FeOOH), galena (ga), marcasite (mc), pyrite (py), pyrrhotite (po), sphalerite (sp), tennantite (tn), and wurtzite (wz).

Table 3: Summary of electron microprobe analyses of mol% FeS in wurtzite and sphalerite.
KM = Kilo Moana, TC = TowCam, TMo = Tahi Moana-1, A = ABE, TM = Tu'i Malila, MA = Mariner
OC = open conduit chimneys, AS = active spires, RS = relict spires .AF = active flanges, n = number of spots measured

		n=	min.	max.	mean
KM	OC	9	3	14	8
	AS	6	5	11	9
	RS	3	7	8	7
TC	OC	3	4	6	5
	AS	15	5	10	6
	RS	6	4	7	6
TMo	OC	9	5	6	5
	AS	6	1	3	2
	RS	5	2	8	4
A	OC	10	2	4	3
	AS	6	3	6	5
	RS	3	1	4	2
TM	OC	11	4	9	6
	AS	6	10	14	12
	AF	7	1	7	3
	RS	6	1	2	1
MA	OC	4	1	6	3
	AS	4	1	7	4
	AF	7	0	0	0
	RS	5	0	2	1

Table 4. Tables of Pearson Correlation coefficients calculated based on bulk geochemical analysis of all SMS deposits samples at each vent field. Borders indicate significance at Pearson p-value, $p < 0.05$.

Kilo Moana, n = 18

	Cu	Fe	Co	Se	Zn	Cd	Mn	Pb	As	Sb	Ag	Au	Mo	Ca	Sr	Ba
Fe	0.12															
Co	0.03	0.18														
Se	0.90	0.10	0.30													
Zn	-0.44	-0.52	-0.49	-0.58												
Cd	-0.38	-0.50	-0.43	-0.51	0.97											
Mn	-0.33	0.11	-0.19	-0.20	0.10	0.06										
Pb	-0.49	0.05	-0.36	-0.43	0.23	0.11	0.87									
As	-0.50	0.10	-0.33	-0.43	0.13	0.08	0.70	0.73								
Sb	-0.42	-0.51	-0.51	-0.57	0.92	0.84	0.19	0.37	0.30							
Ag	-0.47	-0.18	-0.56	-0.57	0.50	0.37	0.43	0.77	0.63	0.64						
Au	-0.55	-0.08	-0.45	-0.56	0.53	0.45	0.71	0.88	0.73	0.62	0.90					
Mo	-0.11	0.20	-0.20	-0.13	-0.10	-0.10	0.41	0.31	0.59	0.00	0.19	0.28				
Ca	0.04	-0.44	0.46	0.25	-0.40	-0.35	-0.28	-0.39	-0.25	-0.42	-0.40	-0.46	-0.15			
Sr	0.02	-0.43	0.49	0.26	-0.38	-0.33	-0.24	-0.36	-0.29	-0.41	-0.40	-0.43	-0.18	0.97		
Ba	-0.11	0.49	0.78	0.09	-0.30	-0.26	-0.02	-0.11	-0.06	-0.30	-0.31	-0.18	0.05	-0.12	-0.10	
S	-0.05	0.83	-0.18	-0.18	-0.03	-0.04	0.26	0.27	0.35	0.00	0.15	0.26	0.33	-0.81	-0.80	0.34

ABE, n = 16

	Cu	Fe	Co	Se	Zn	Cd	Mn	Pb	As	Sb	Ag	Au	Mo	Ca	Sr	Ba
Fe	0.63															
Co	0.66	0.66														
Se	0.68	0.71	0.69													
Zn	-0.49	-0.52	-0.55	-0.40												
Cd	-0.19	-0.48	-0.50	-0.27	0.86											
Mn	-0.72	-0.10	-0.44	-0.60	0.36	0.08										
Pb	-0.37	0.09	-0.16	-0.34	0.15	-0.07	0.57									
As	-0.69	-0.05	-0.30	-0.58	0.24	-0.05	0.91	0.74								
Sb	-0.83	-0.33	-0.45	-0.69	0.40	0.12	0.85	0.70	0.93							
Ag	-0.64	-0.23	-0.30	-0.65	-0.07	-0.20	0.68	0.48	0.80	0.81						
Au	-0.75	-0.18	-0.37	-0.65	0.17	-0.07	0.86	0.73	0.96	0.95	0.87					
Mo	-0.63	-0.22	-0.40	-0.48	0.61	0.34	0.69	0.81	0.78	0.79	0.40	0.72				
Ca	0.63	0.37	0.55	0.34	-0.53	-0.46	-0.51	-0.24	-0.46	-0.56	-0.39	-0.46	-0.50			
Sr	0.36	0.19	0.27	0.28	-0.72	-0.62	-0.52	-0.25	-0.45	-0.46	-0.19	-0.30	-0.58	0.74		
Ba	-0.29	-0.39	-0.16	-0.25	-0.42	-0.40	-0.10	-0.03	-0.02	0.11	0.42	0.22	-0.24	-0.14	0.44	
S	0.24	0.42	0.12	0.29	0.25	0.15	0.09	0.11	0.04	-0.09	-0.25	-0.15	0.14	0.02	-0.31	-0.59

TowCam, n = 10

	Cu	Fe	Co	Se	Zn	Cd	Mn	Pb	As	Sb	Ag	Au	Mo	Ca	Sr	Ba
Fe	0.74															
Co	0.47	0.28														
Se	0.33	0.20	0.13													
Zn	-0.57	-0.62	0.10	-0.29												
Cd	-0.10	-0.16	0.19	-0.31	0.80											
Mn	-0.55	0.08	-0.32	-0.19	0.02	-0.20										
Pb	-0.42	-0.14	-0.11	-0.29	0.16	-0.08	0.63									
As	-0.41	0.12	-0.28	-0.10	0.07	-0.07	0.81	0.85								
Sb	-0.41	-0.17	-0.01	-0.07	0.28	0.07	0.42	0.83	0.79							
Ag	-0.13	0.12	0.11	0.38	-0.29	-0.63	0.58	0.55	0.55	0.41						
Au	-0.46	-0.08	-0.18	0.03	0.16	-0.08	0.59	0.85	0.90	0.90	0.58					
Mo	-0.33	-0.05	-0.05	0.46	0.00	-0.26	0.60	0.59	0.66	0.60	0.72	0.69				
Ca	-0.25	-0.45	-0.22	-0.40	-0.12	-0.32	-0.29	-0.26	-0.44	-0.23	-0.27	-0.31	-0.54			
Sr	-0.25	-0.43	-0.22	-0.39	-0.15	-0.36	-0.27	-0.21	-0.39	-0.17	-0.22	-0.25	-0.49	1.00		
Ba	-0.19	-0.08	-0.17	-0.16	-0.21	-0.30	0.37	0.75	0.52	0.53	0.39	0.55	0.57	-0.14	-0.08	
S	0.35	0.65	0.21	-0.01	0.14	0.54	0.18	0.04	0.33	0.08	-0.13	0.11	-0.03	-0.73	-0.75	-0.26

Tu'i Malila, n = 24

	Cu	Fe	Co	Se	Zn	Cd	Mn	Pb	As	Sb	Ag	Au	Mo	Ca	Sr	Ba
Fe	0.82															
Co	0.65	0.78														
Se	0.42	0.71	0.73													
Zn	0.12	0.07	0.10	-0.23												
Cd	0.26	0.13	0.16	-0.19	0.93											
Mn	-0.06	-0.02	-0.14	-0.36	0.31	0.14										
Pb	-0.11	0.02	-0.14	-0.09	-0.01	-0.12	0.37									
As	-0.25	-0.24	-0.46	-0.33	0.33	0.26	0.13	0.08								
Sb	-0.25	-0.22	-0.38	-0.22	0.51	0.46	0.02	0.12	0.68							
Ag	-0.47	-0.47	-0.49	-0.35	0.18	0.04	0.10	0.23	0.66	0.61						
Au	-0.56	-0.41	-0.54	-0.36	0.23	0.12	0.04	0.00	0.71	0.59	0.72					
Mo	0.25	0.22	0.08	-0.15	0.61	0.69	0.14	-0.03	0.44	0.20	-0.02	0.22				
Ca	0.40	0.66	0.64	0.79	-0.10	0.03	-0.24	-0.10	-0.34	-0.24	-0.35	-0.33	0.03			
Sr	-0.21	-0.36	-0.18	-0.04	-0.08	-0.09	-0.08	-0.06	-0.02	0.22	0.32	0.12	-0.32	-0.09		
Ba	-0.41	-0.31	-0.38	-0.23	-0.55	-0.51	-0.29	-0.02	0.03	-0.18	-0.03	0.13	-0.20	-0.27	-0.51	
S	0.63	0.70	0.65	0.48	0.62	0.61	0.17	-0.01	-0.02	0.18	-0.14	-0.16	0.39	0.46	0.09	-0.84

Tahi Moana-1, n = 13

	Cu	Fe	Co	Se	Zn	Cd	Mn	Pb	As	Sb	Ag	Au	Mo	Ca	Sr	Ba
Fe	0.43															
Co	-0.14	0.34														
Se	0.39	0.63	0.61													
Zn	-0.47	-0.11	0.02	0.09												
Cd	-0.21	0.25	0.44	0.72	0.56											
Mn	-0.38	0.27	-0.10	-0.35	0.29	-0.13										
Pb	-0.44	0.07	0.00	-0.24	0.66	0.03	0.72									
As	-0.56	0.10	0.07	-0.11	0.79	0.29	0.65	0.79								
Sb	-0.55	0.24	0.48	0.36	0.73	0.64	0.35	0.62	0.65							
Ag	-0.36	0.11	-0.01	-0.03	0.84	0.25	0.56	0.90	0.87	0.72						
Au	-0.50	-0.03	-0.01	-0.15	0.84	0.22	0.58	0.95	0.82	0.74	0.96					
Mo	-0.36	0.04	-0.15	-0.31	0.43	-0.01	0.64	0.43	0.71	0.19	0.48	0.40				
Ca	-0.04	-0.59	-0.16	-0.45	-0.70	-0.54	-0.46	-0.58	-0.69	-0.63	-0.75	-0.64	-0.48			
Sr	-0.15	-0.23	0.02	-0.41	-0.46	-0.56	0.13	-0.05	-0.19	-0.31	-0.26	-0.23	0.21	0.46		
Ba	-0.13	0.04	-0.12	-0.28	0.14	-0.26	0.46	0.24	0.45	0.03	0.32	0.19	0.77	-0.25	0.51	
S	-0.02	0.77	0.53	0.65	0.27	0.58	0.19	0.15	0.37	0.56	0.24	0.17	0.09	-0.63	-0.44	-0.08

Mariner, n = 24

	Cu	Fe	Co	Se	Zn	Cd	Mn	Pb	As	Sb	Ag	Au	Mo	Ca	Sr	Ba
Fe	0.82															
Co	0.30	0.33														
Se	-0.34	-0.28	-0.12													
Zn	-0.69	-0.66	-0.32	0.52												
Cd	-0.61	-0.59	-0.28	0.19	0.89											
Mn	-0.18	0.01	-0.10	-0.16	-0.10	-0.07										
Pb	-0.61	-0.63	-0.32	0.53	0.36	0.08	0.08									
As	-0.51	-0.42	-0.31	0.15	0.53	0.55	0.40	0.35								
Sb	-0.25	-0.09	-0.16	0.25	0.22	0.14	0.24	0.21	0.64							
Ag	-0.53	-0.66	-0.28	0.09	0.73	0.88	-0.07	0.09	0.56	0.08						
Au	0.20	-0.12	-0.07	0.16	-0.07	-0.17	0.02	0.25	0.25	0.41	-0.04					
Mo	0.47	0.33	0.53	-0.27	-0.33	-0.21	0.15	-0.42	-0.06	0.06	-0.15	0.44				
Ca	0.11	0.09	0.25	-0.12	-0.38	-0.33	-0.10	-0.33	-0.50	-0.29	-0.31	-0.22	0.11			
Sr	-0.48	-0.56	-0.22	0.38	0.05	-0.18	-0.06	0.90	0.13	0.06	-0.07	0.25	-0.37	0.00		
Ba	-0.36	-0.26	0.02	-0.41	0.39	0.64	0.34	-0.30	0.36	0.07	0.58	-0.33	0.07	-0.26	-0.49	
S	0.49	0.73	0.16	0.32	-0.17	-0.30	-0.21	-0.32	-0.25	0.05	-0.48	-0.11	0.05	0.11	-0.35	-0.48

Table 5. Model fluid compositions[a] used in EQ3/6 calculations.

Property	Units	KM5	TM2	MA3
[b]T	°C	329	312	363
[c]pH	(25°C)	3.8	4.35	2.95
Cl^-	mmol/kg	584	653	605
[d]Na^+	mmol/kg	492	513	439
Ca^{2+}	mmol/kg	34.0	47.5	43.8
K^+	mmol/kg	16.3	43.6	36.9
SiO_2,aq	mmol/L	21.7	14.6	15.1
[e]CO_2,aq	mmol/L	7.46	13.0	39.8
HS^-	mmol/L	6.3	2.5	9.3
Mn^{2+}	µmol/kg	718	406	5723
Fe^{2+}	µmol/kg	2894	210	12991
Cu^+	µmol/kg	10.9	7	156
Zn^{2+}	µmol/kg	108	28	334
[f]Pb^{2+}	nmol/kg	329	571	1135
[f]Ba^{2+}	µmol/kg	23	39	74.9
H_2, aq	µmol/kg	359	46.1	131
Mg^{2+}	mmol/kg	0	0	0
HSO_4^-	mmol/kg	0	0	0
O_2, aq	mmol/L	0	0	0

[a] Models represent zero-Mg endmember concentrations reported in Mottl et al. (2011) with the addition of new data for Fe, Cu, Zn, Pb, Ba, and H_2 (this paper).

[b] Maximum measured temperature at the seafloor.

[c]pH at 25°C. Differences in pH from measured values (Table 1a) reflect adjustment to what pH would be prior to precipitation of bottle solids. However, the pH of fluid KM5 was increased by 0.1 to achieve saturation with respect to chalcopyrite at 329°C (see text).

[d]Na^+ has been modified to achieve charge balance.

[e] $CO_{2,\,aq}$ was not measured directly for fluid sample KM5. Model value is from fluid sample KM3, chosen on the basis of similar temperature, Cl^-, and Na^+.

[f] Ba^{2+} and Pb^{2+} were not measured directly for fluid sample KM5 ([Cl] = 584mM). Model values are the mean concentrations of fluid samples KM1, KM2, and KM6 (mean [Cl] =583mM).

Table 6. Results of EQ3/6 fluid modelling for conductive cooling of model vent fluids showing saturation temperature of chalcopyrite (CP), pyrite (PY), sphalerite (SP), and galena (GA).

KM5, mineral precipitation suppressed[a]			
T(°C)	pH	(fO_2)	(fS_2)
329	4.6	-31.0	-9.8
329		(CP)	
300	4.3	-33.7	-10.7
268		(PY)	
250	4.0	-39.0	-12.5
246		(SP)	
200	3.9	-45.3	-14.6
189		(GA)	
150	3.8	-53.0	-17.2
100	3.8	-62.6	-20.5
50	3.8	-74.9	-24.8
25	3.8	-82.6	-27.4

MA3, mineral precipitation suppressed[a]			
T(°C)	pH	(fO_2)	(fS_2)
363	4.2	-27.1	-7.6
363[c]		(CP)	
350	4.0	-28.2	-8.0
300	3.4	-32.8	-9.6
250	3.1	-38.1	-11.3
245		(PY)	
200	3.0	-44.4	-13.4
193		(SP)	
151		(GA)	
150	3.0	-52.1	-16.0
100	3.0	-61.7	-19.3
50	2.9	-74.1	-23.6
25	3.0	-81.8	-26.2

TM2, mineral precipitation suppressed[a]			
T(°C)	pH	(fO_2)	(fS_2)
312	5.6	-30.7	-9.4
312		(CP)	
312		(PY)	
312		(SP)	
300	5.5	-31.5	-10.0
258		(GA)	
250	5.0	-36.7	-11.6
200	4.7	-42.8	-13.7
150	4.5	-50.4	-16.3
100	4.3	-59.7	-19.5
50	4.3	-71.8	-23.8
25	4.3	-79.2	-26.5

TM2, mineral precipitation allowed[b]			
T(°C)	pH	(fO_2)	(fS_2)
312	5.4	-31.3	-9.9
312		(CP)	
312		(PY)	
300	5.3	-32.4	-10.3
288		(SP)	
250	4.7	-37.9	-12.3
208		(GA)	
200	4.3	-44.5	-14.7
150	4.0	-52.3	-17.4
100	3.9	-61.9	-20.8
50	3.8	-74.4	-25.2
25	3.8	-82.1	-27.9

[a] Closed system equilibrium model in which sulfide mineral precipitation is suppressed.
[b] Closed system equilibrium model in which sulfide mineral precipitation is allowed.
[c] Chalcopyrite is slightly undersaturated in the range 355°C-294°C

Figure 1. (A) Regional geology of the Eastern Lau Spreading Center (ELSC) (from Stoffer et al. (2006)). NLSC = Northern Lau Spreading Center; CLSC = Central Lau Spreading Center; ELSC = Eastern Lau Spreading Center; VFR = Valu Fa Ridge; TVZ = Taupo Volcanic Zone.) (B) Locations of confirmed and inferred active vent fields along the ELSC. Confirmed active vent fields are: (1) Kilo Moana (20°03'09"S, 176°08'02"W, 2620 meters below sea level (mbsl)), (2) TowCam (20°19'00"S, 176°08'12"W, 2700 mbsl)), (3) Tahi Moana-1 (20°41'59"S, 176°10'58"W, 2260 mbsl), (4) ABE (20°45'48"S, 176°11'30"W, 2220 mbsl), (5) Tahi Moana-2 (1870 mbsl), (6) White Church (1960 mbsl), (7) Tu'i Malila (21°59'21"S, 176°34'04"W, 1870 mbsl), (8) TELVE (1760 mbsl), (9) Mariner (22°10'49"S, 176°36'05"W, 1910 mbsl)) and Vai Lili (1764 mbsl) vent fields, (10) Si'i Si'i (1950 mbsl), (11) Misiteli (2050 mbsl), (12) Hine Hina (1900 mbsl). Vent locations from Beaulieu et al., (2010) and references therein. Base map bathymetry from Smith and Sandwell (1997) and Martinez et al. (2006) accessed via GeoMapApp (Ryan et al., 2009).

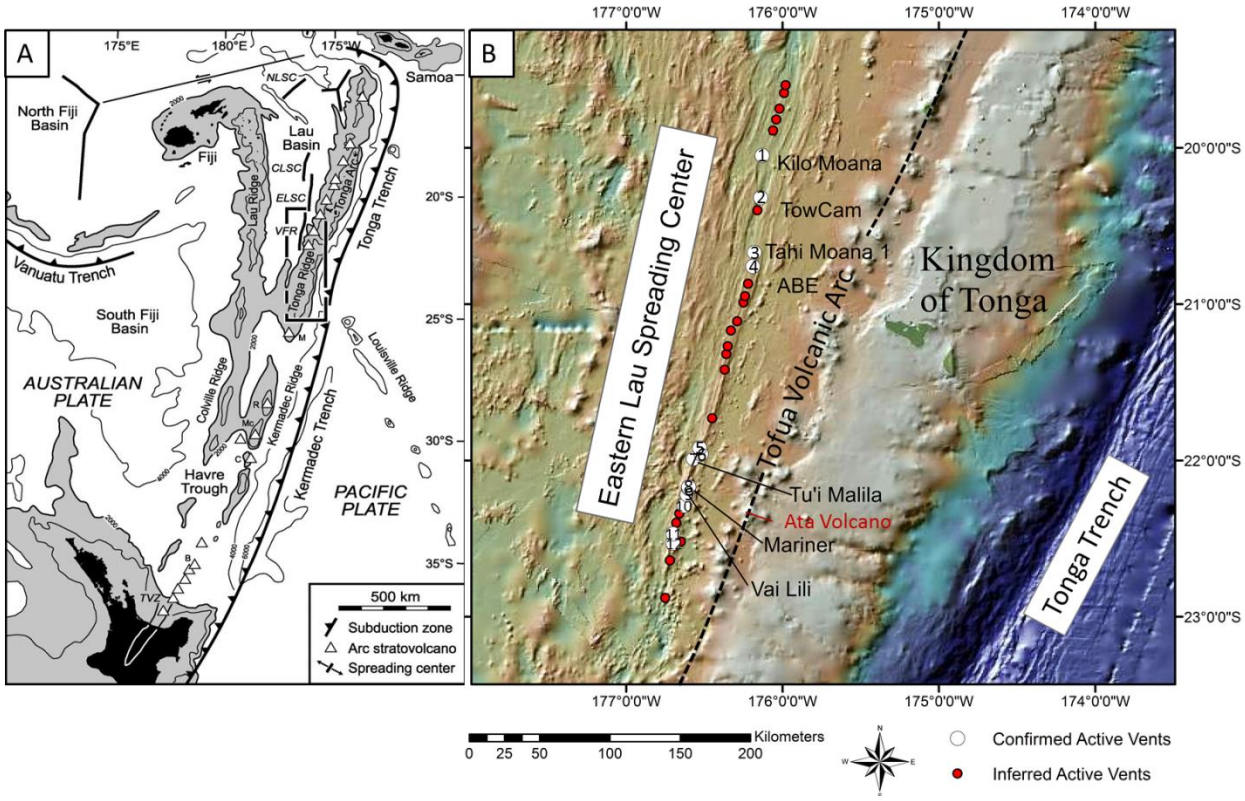

Figure 2. Temperature and endmember fluid chemistry of ELSC hydrothermal fluids. Concentrations of Fe, Cu, Zn, Pb, and Ba include redigested bottle solids (see text). Maximum measured temperature, pH at 25°C, zero-Mg chlorinity and H_2S (by gravimetric analysis, = grav) are from Mottl et al. (2011). Log(fS_2) at *in situ* temperatures and pressures was calculated using the SUPCRT92 database. (mm = mmol/kg fluid; µm = µmol/L fluid; nm = nmol/kg fluid). KM = Kilo Moana, TC = TowCam, TMo = Tahi Moana-1, A = ABE, TM = Tu'i Malila, MA = Mariner

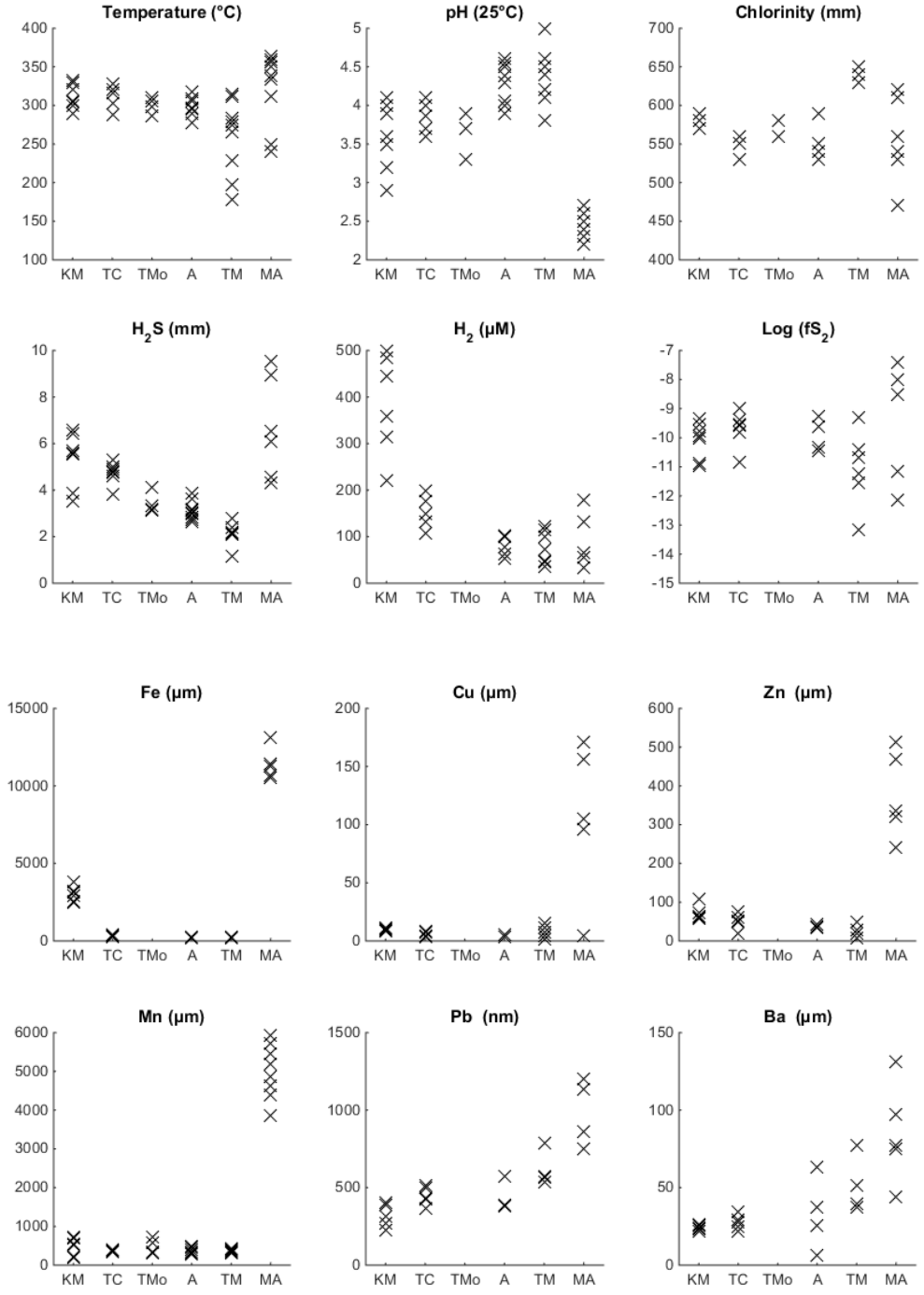

Figure 3. Photographs of ELSC SMS deposits taken by Jason II ROV. Morphologies include: (A) >5 m edifice at Kilo Moana, (B) <5 m edifice at TowCam with three open conduit chimneys, (C) <5 m edifice and (D) close up of narrow sulfide-rich flange near base at Tahi Moana-1, (E) ~5 m edifice and (F) nearby barite-rich flange, T = 141°C, at ABE (G) 5-10 m edifice at Tu'i Malila with spires offset by barite-rich flanges, (H) low-lying barite-rich flanges at Tu'i Malila, T = 178°C, (I) ~20 m copper-rich columns at Mariner and (J) barite-rich squat terraces at Mariner.

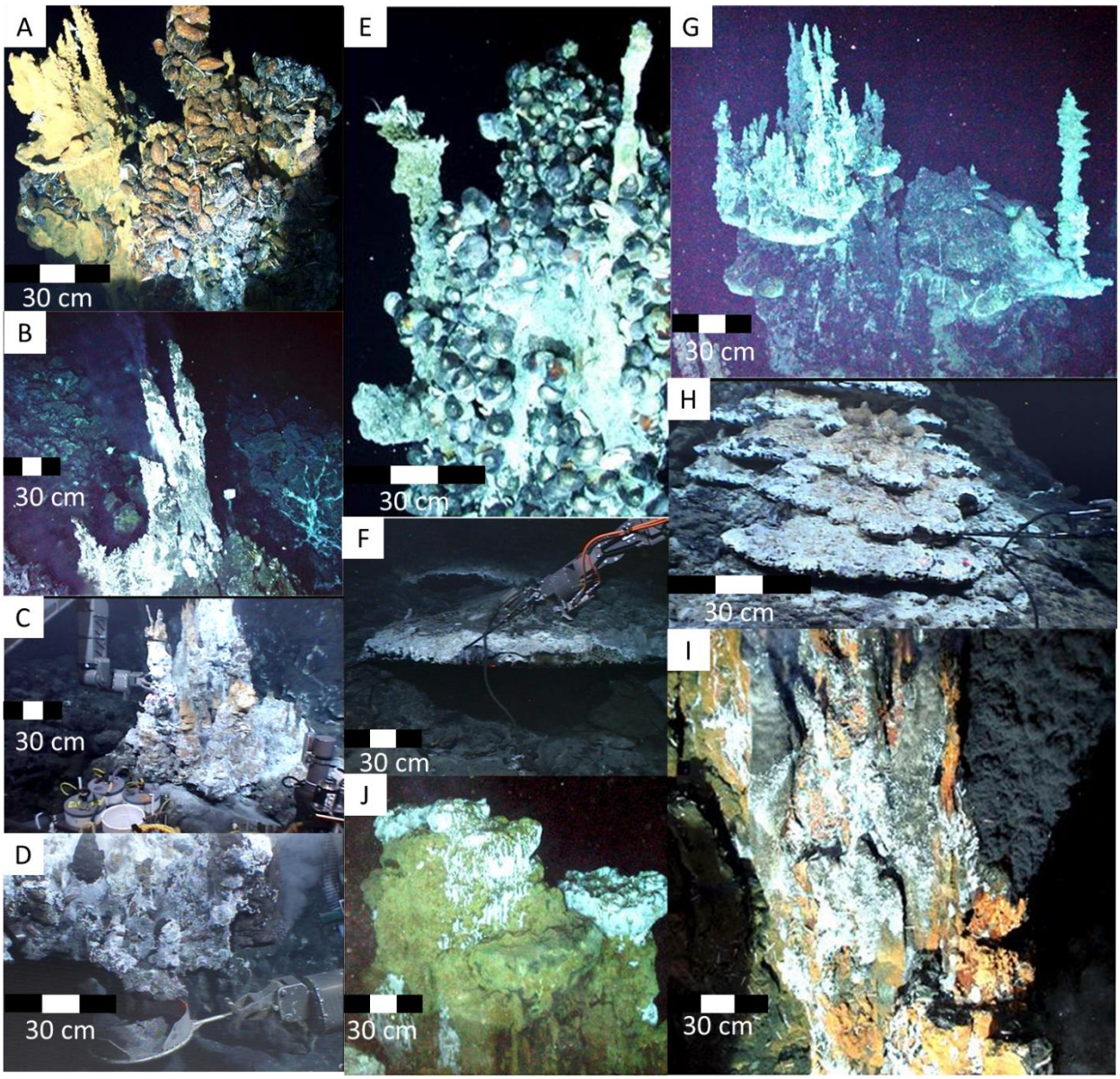

Figure 4. Images of polished sections. (A-D) Open conduit chimneys (VF = vent fluid; SW = seawater): (A) J2-137-1-R1; pair with Kilo Mana fluid KM5, T=329°C (B) J2-449-6-R1; pair with ABE fluid A10, T=317°C (C) J2-449-5-R1; pair with ABE fluid A11, T=306°C (D) J2-437-3-R2; pair with Mariner fluid MA9, T=338°C . (E-H) Close ups of open conduit chimney linings in (A-D). Labels indicate paired fluid samples. Lining mineralogy: (E) massive cubanite (cb) with minor pyrrhotite (po), (F) massive chalcopyrite (cp) with minor pyrite (py), (G) intergrown cp and wurtzite (wz), (H) massive cp with minor bornite (bn) toward exterior. (I) J2-128-5-R1, exterior of active spire from ABE composed of marcasite dendrites, minor sphalerite (sp) toward interior and minor barite (ba) and amorphous silica (amsi) toward exterior. (J) J2-134-9-R1, interior of active spire from Tu'i Malila lined with euhedral wurtzite with cp inclusions (wz(cp)) and interstitial galena (ga) and cp. (K) J2-442-12-R2, active flange from Tu'i Malila composed of ba with interstitial wz(cp) and py, plus late-stage amorphous silica coating. (L) J2-135-5-R1, squat terrace from Mariner composed of dendrites of ba and interstitial sp. Light gray material in vent field area of images E, G, and K is residual carbon coat from electron microprobe analyses

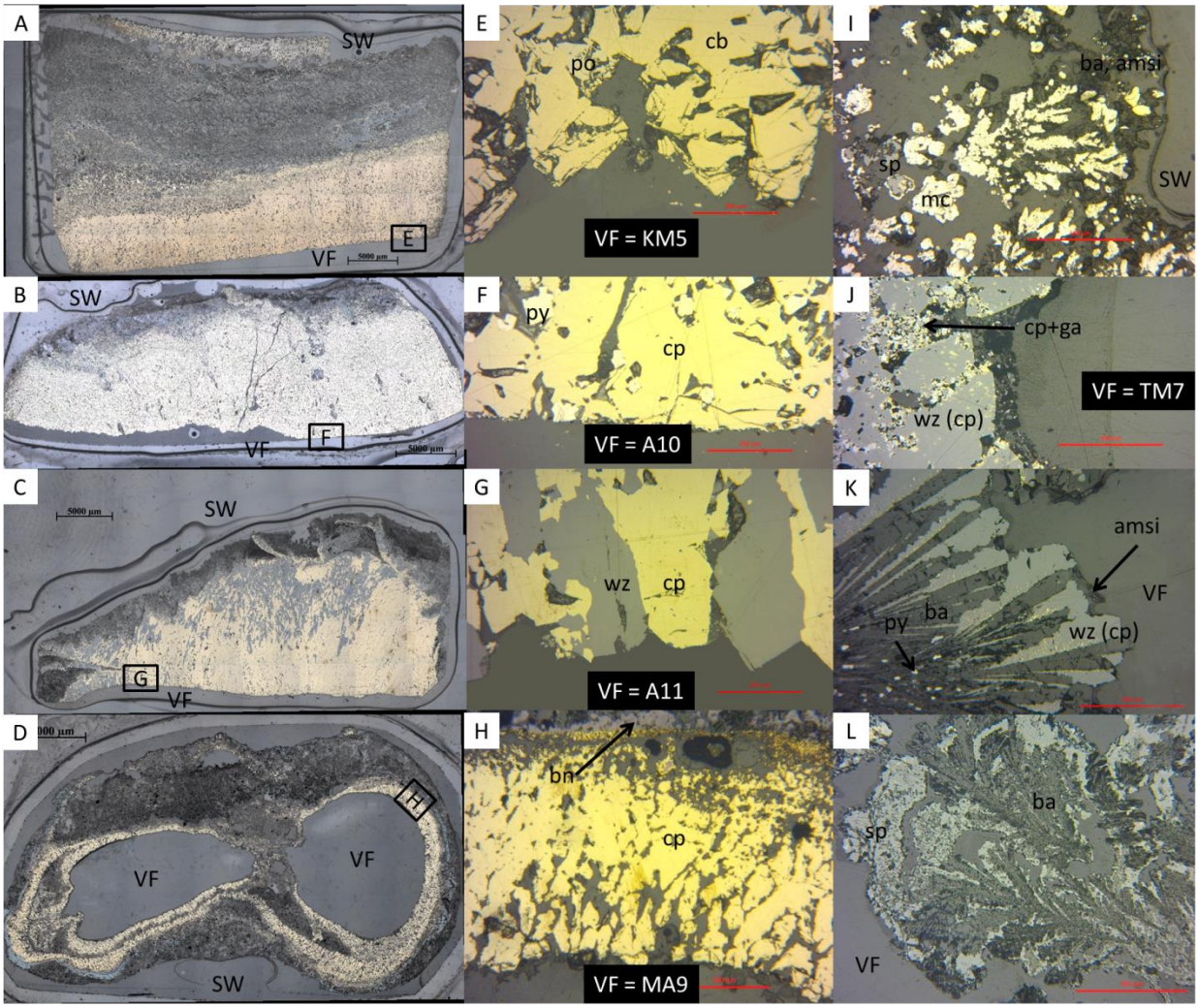

Figure 5. Elemental contents of bulk sample powders. KM = Kilo Moana, TC = TowCam, TMo = Tahi Moana-1, A = ABE, TM = Tu'i Malila, MA = Mariner.

Symbology and Number of Samples for Bulk Geochemical Analysis

		KM	TC	TMo	A	TM	MA
○	open conduit chimneys	7	1	1	4	5	7
Δ	active spires	5	7	6	6	5	3
▽	relict spires	4	2	2	4	11	8
+	active flange and squat terraces	1	0	4	2	2	5
×	relict flanges	1	0	0	0	1	1
◊	total for median	18	10	13	16	24	24

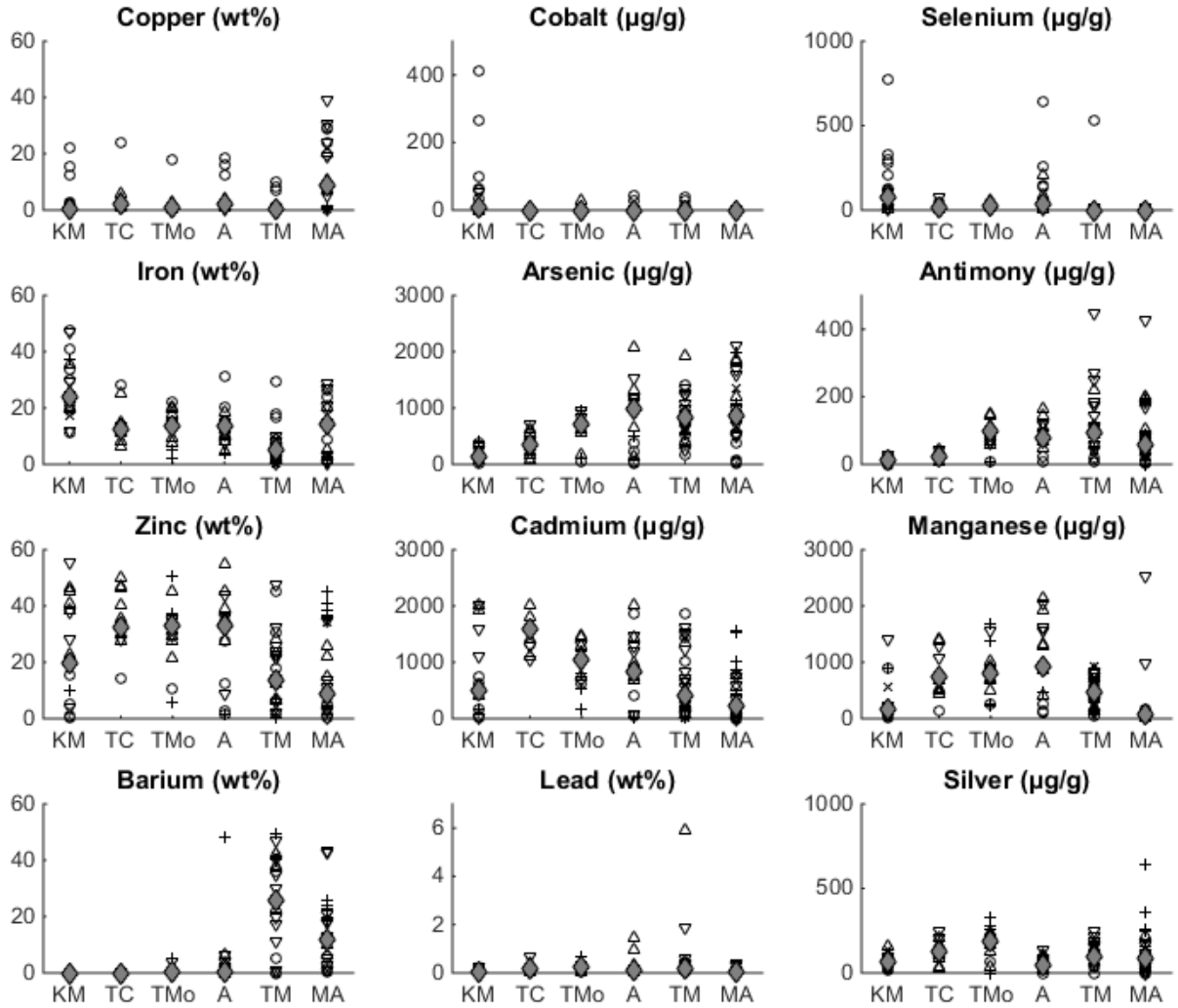

Figure 6. Trace element concentrations (µg/g) measured by electron microprobe: open conduit chimneys (○), active spires (Δ), relict spires (▽), active flanges and squat terraces (+), and relict flanges (×). Values below detection limit not shown. KM = Kilo Moana, TC = TowCam, TMo = Tahi Moana-1, A = ABE, TM = Tu'i Malila, MA = Mariner

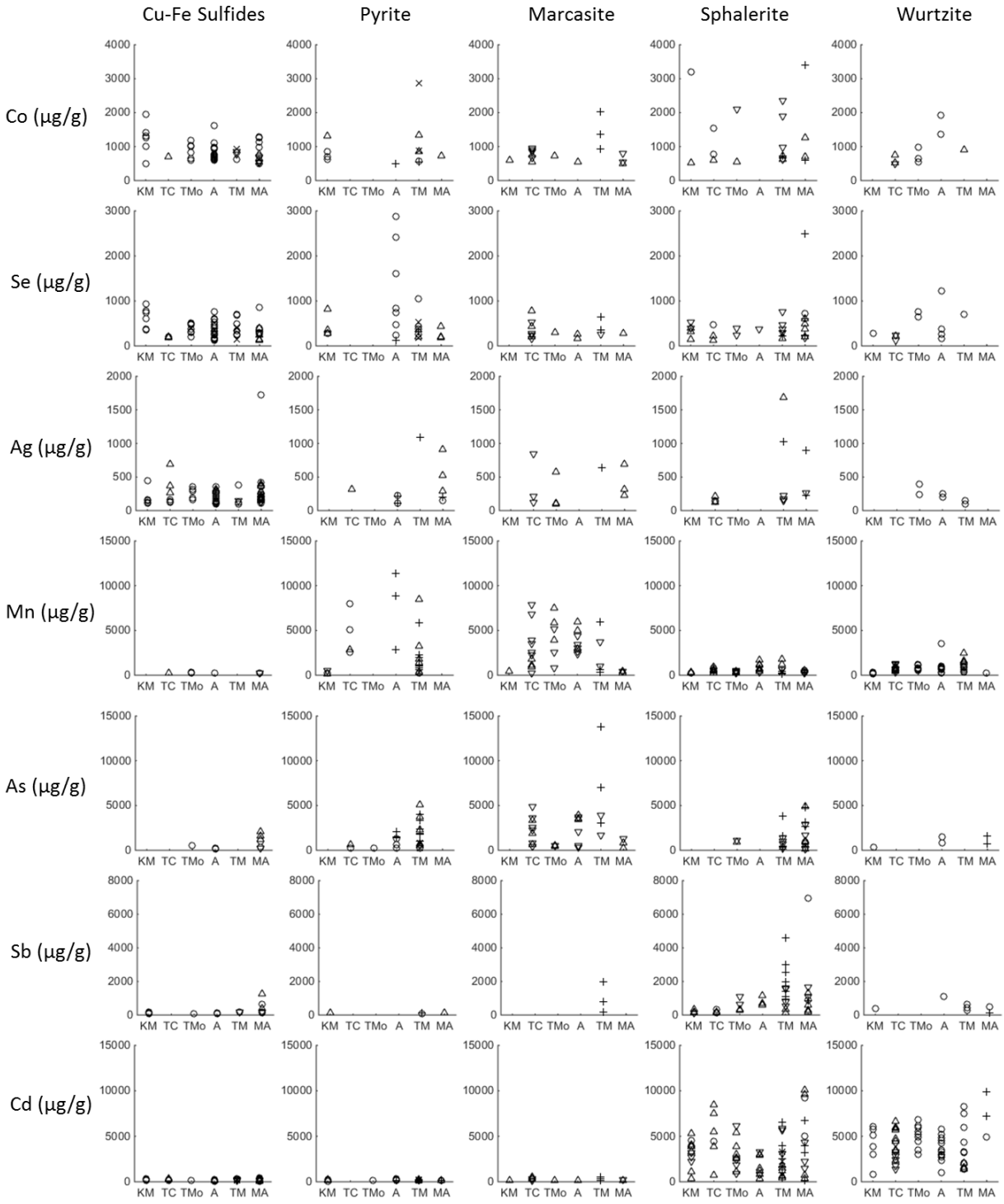

.

Figure 7. Bivariate plots of vent fluid temperature, pH (at 25°C), and metal contents. KM ‘05 = Kilo Moana (collected in 2005), KM ‘09 = Kilo Moana (collected in 2009),TC = TowCam, TMo = Tahi Moana-1, A = ABE, TM = Tu’i Malila, MA = Mariner.

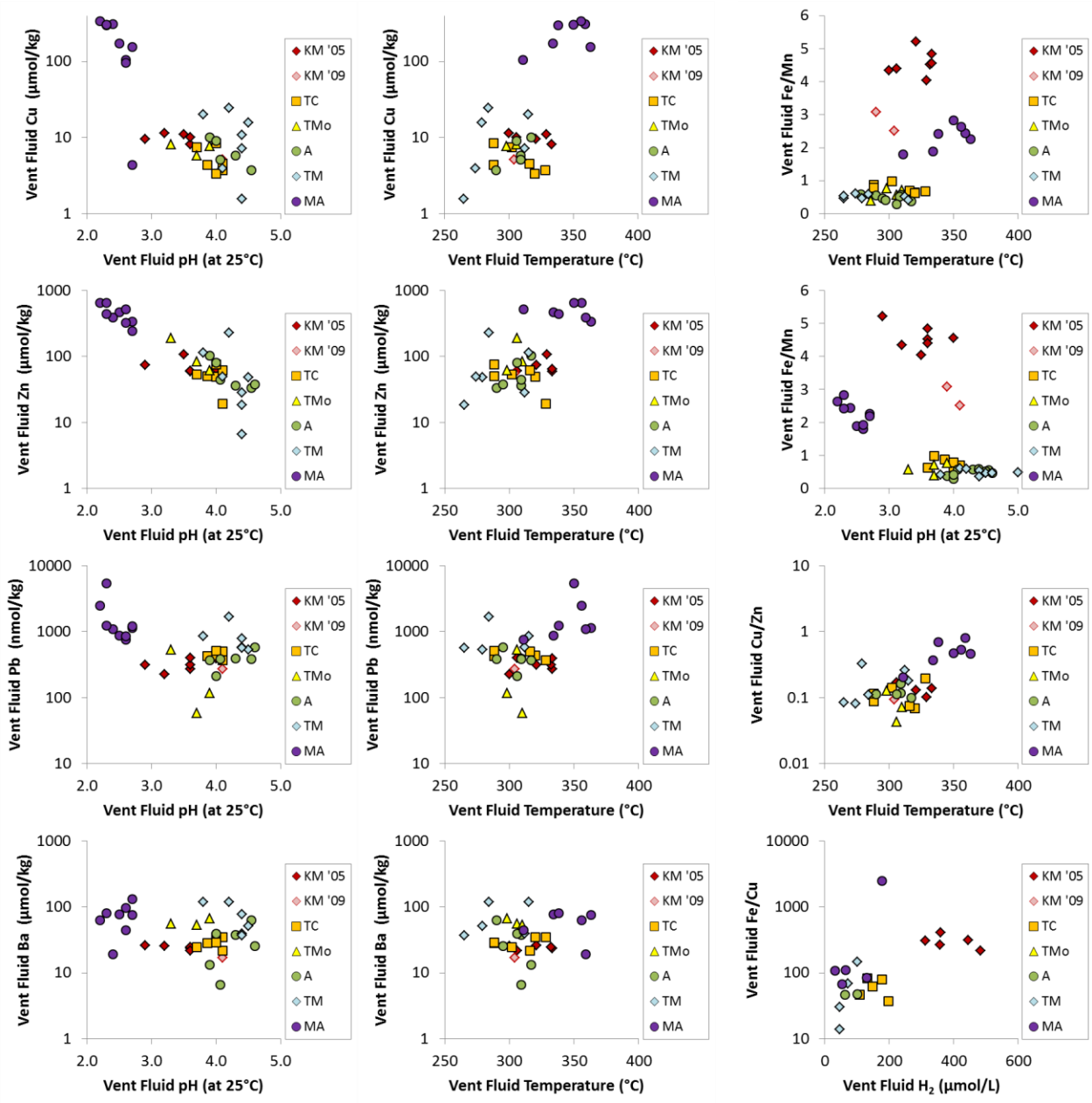

Figure 8. Correlation coefficients between concentrations of Zn and Ag, Cd, Pb, As, and Sb in bulk samples (bulk) and on a sulfide normalized basis (sulfide). Black bars are considered statistically significant ($p < 0.1$). (n = number of samples; pH (25°C) is the minimum pH of high-temperature fluids as measured at 25°C.

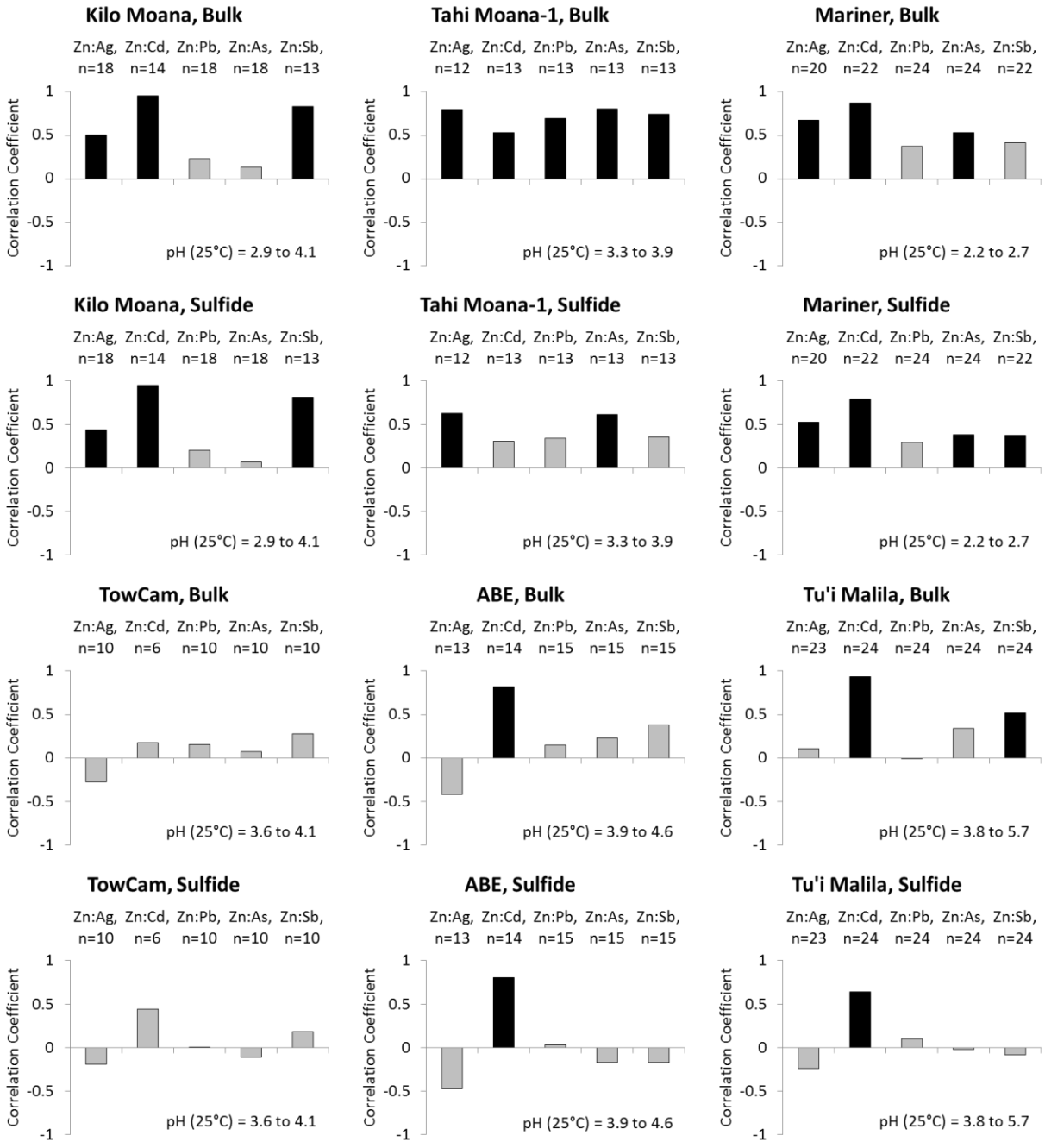

Figure 9. High-temperature ELSC hydrothermal fluids on log(fS_2) vs. 1000/T(K) diagram: KM = Kilo Moana, TC = TowCam, A = ABE, TM = Tu'i Malila, MA = Mariner. Positions of Kilo Moana fluids collected in 2009 (KM '09) is estimated based on the $H_{2,aq}$ concentrations of similar-temperature fluids collected in 2005. Sulfidation states as defined in Sillitoe and Hedenquist (2003) are delineated by equilibrium sulfidation reactions between minerals. Background mineral phase diagram (solid lines; pressure = 1 bar) and isochores of mole% FeS of sphalerite in equilibrium with pyrite and/or pyrrhotite (stippled lines) are reproduced from figures in Sack and Ebel (2006).

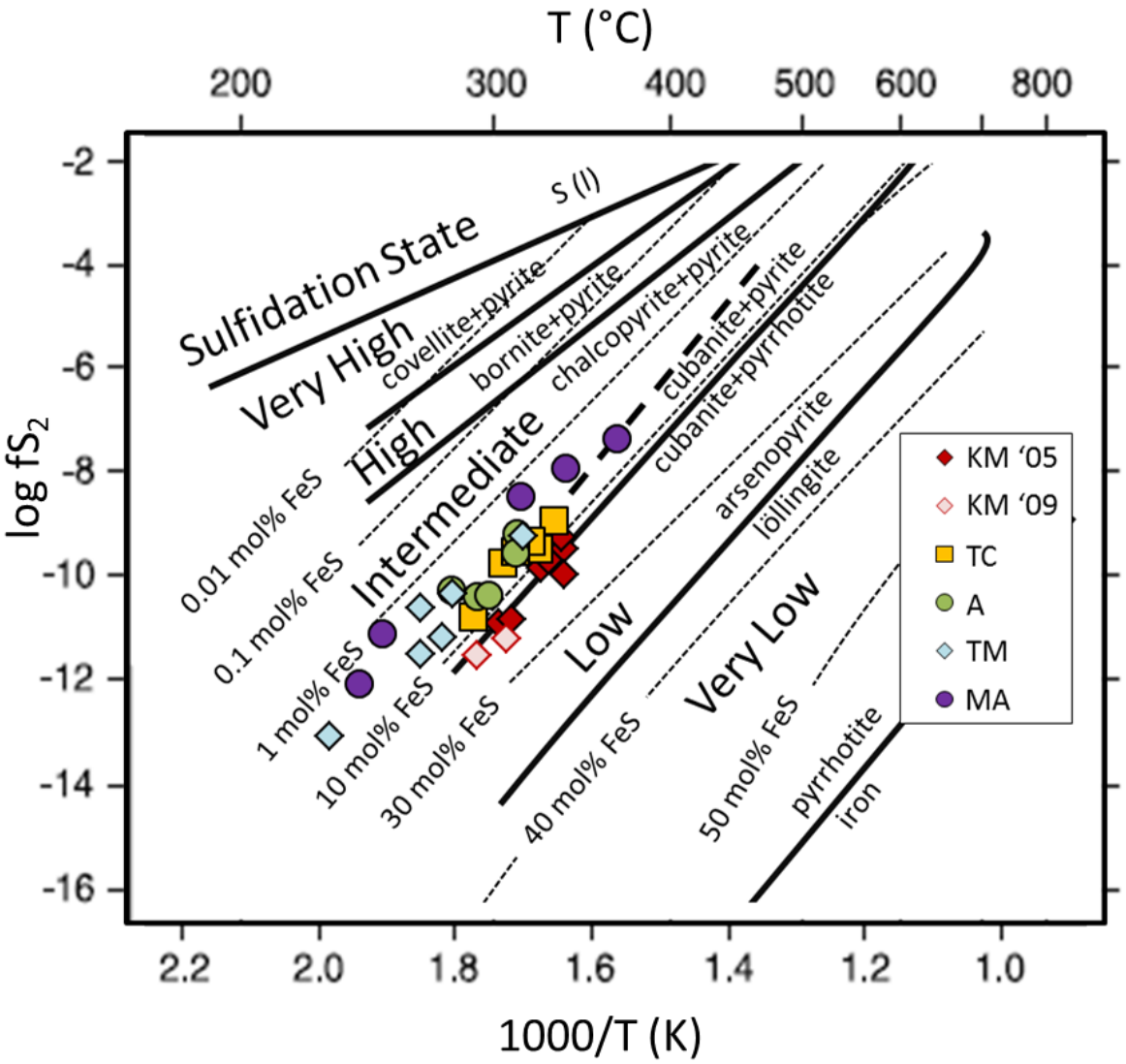

SUPPLEMENTARY MATERIAL

Table S1a. Trace metal and hydrogen concentrations of Kilo Moana hydrothermal fluids

			ICPAES										GC
	Mg mm	[c]pH 25°C	[a]Fe µm	[c]Fe µm	Cu µm	[c]Cu µm	Zn µm	[c]Zn µm	Pb nm	[c]Pb nm	Ba µm	[c]Ba µm	H_2 µM
KM1													
J2-124-MR	3.8	3.6	2200		9		66		270		24		
J2-124-MG	2.1	3.5	2500	2500	9	9	66	68	260	270	19	19	
J2-124-IGT3	1.7	3.6	2300	2300	2	7	14	51	60	270	25	25	320
J2-124-IGT4	1.6	3.6	2500	2500	2	7	11	51	50	240	25	25	280
Endmember			2500	2500		8		58		270		24	310
standard error			100	100		1		4		10		2	
KM4													
J2-125-IGT2	2.2	3.1	2200	2400	0.4	11	21		10	220	24	24	470
J2-125-IGT5	3.7	3.2	2100		1		73		130		10		440
Endmember			2300	2500		11				230		25	480
KM6													
J2-137-IGT3	3.0	3.7	2800		0.1		1				11		420
J2-137-IGT5	2.9	3.6	2800	3000	1	9	49	56	230	380	18	20	430
Endmember			3000	3100		10		60		400		22	450
KM2													
J2-125-IGT7	2.8	3.6	3000	3000	5		20		90	300	23	23	210
Endmember			3100	3200						310		24	220
KM3													
J2-125-IGT1	2.4	2.9	3600	3700	3	9	33	70	100	300	25	25	340
Endmember			3800	3800		9		74		310		26	360
KM5													
J2-137-IGT1	1.5	3.5	2800		2		12		60		23		350
J2-137-IGT2	2.0	3.5	2700	2800	5	11	73	104	710		13		350
Endmember			2900	2900		11		108					360
KM8													
J2-137-IGT8	1.8	4.0	2400	2500	9		59	62	310	380	19		480
Endmember			2500	2600				64		390			500

Table S1b. Trace metal and hydrogen concentrations of TowCam hydrothermal fluids

			ICPAES										GC
	Mg	[c]pH	[a]Fe	[c]Fe	Cu	[c]Cu	Zn	[c]Zn	Pb	[c]Pb	Ba	[c]Ba	H_2
	mm	25°C	µm	µm	µm	µm	µm	µm	nm	nm	µm	µm	µM
TC1													
J2-126-IGT2	2.0	4.1	260	330	5		40		290	430	28	28	130
J2-126-IGT3	1.5	4.1	250	260	1	4	8	18	60	290	38	38	130
Endmember			260	310		4		19		370		34	130
TC3													
J2-126-IGT7	5.2	4.5	230	260	1		9		80	320	21		160
J2-127MR	1.5	4.1	230	230	3	3	49	49	480	480	30	30	
J2-127MG	0.7	4.0	270	270	3	3	46	46	410	420	37	37	
Endmember			260	270		3		49		430		34	180
standard error			10	10									
TC4													
J2-126-IGT6	2.3	4.1	270	270	4	4	58	59	460	480	21	21	140
Endmember			280	280		5		61		500		21	150
TC5													
J2-127-IGT1	3.3	3.6	310	330	1		74		140		18	20	110
J2-127-IGT2	3.5	3.7	300	320	1	7	19	50	100		26	26	100
Endmember			320	340		7		53				25	110
TC6													
J2-127-IGT5	2.2	4.0	330	380	1	4	22	59	240	380	31	31	
J2-127-IGT6	2.6	4.0	320	320	2	4	31	36	330	440	22	22	
Endmember			340	370		4		50		430		28	
TC7													
J2-139-IGT5	1.5	4.1	290	310	5	9	71	75	520		28	31	190
J2-139-IGT6	2.2	4.2	270	290	6	8	65	69	440	490	22	24	190
Endmember			290	310		8		74		520		29	200

Table S1c. Trace metal and hydrogen concentrations of ABE hydrothermal fluids

			ICPAES										GC
	Mg	[c]pH	[a]Fe	[c]Fe	Cu	[c]Cu	Zn	[c]Zn	Pb	[c]Pb	Ba	[c]Ba	H_2
	mm	25°C	µm	µm	µm	µm	µm	µm	nm	nm	µm	µm	µM
A1													
J2-128-IGT7	4.0	4.5	240	250									54
J2-128-IGT8	2.3	4.4	250	260	3	6	26	34	240	370	35	36	65
Endmember			260	270		6		36		390		37	63
A2													
J2-128-MR	44.6	6.4	40		2		11		80		1		
J2-128-MG	2.9	4.3	250	250	5	5	41	42	360	360	6	6	
J2-136-MR	2.4	4.3	260		5		37		340		7		
Endmember			270	260		5		44		380		7	
A4													
J2-129-IGT3	2.5	4.4											52
J2-129-IGT4	9.7	5.1											43
Endmember													54
A5													
J2-129-IGT5	1.7	4.5	160	190	1	4	10	32	190	370	55	61	94
J2-129-IGT6	4.1	4.9	130	140	1	3	6		120		17		97
Endmember			160	170		4		33		380		63	101
A8													
J2-136-IGT5	1.9	4.5											76
Endmember													78
A9													
J2-136-IGT6	2.8	4.6	130	170	3		30	35	390	540	6	24	89
J2-136-IGT4	7.1	4.9	110	120									95
Endmember			130	160				37		570		26	101

Table S1d. Trace metal and hydrogen concentrations of Tu'i Malila hydrothermal fluids

			ICPAES										GC
	Mg	[c]pH	[a]Fe	[c]Fe	Cu	[c]Cu	Zn	[c]Zn	Pb	[c]Pb	Ba	[c]Ba	H_2
	mm	25°C	µm	µm	µm	µm	µm	µm	nm	nm	µm	µm	µM
TM1													
J2-132-IGT1	5.5	4.5	180	200	1	14	7	43	110	480	7	46	43
Endmember			200	220		16		48		530		51	48
TM2													
J2-132-IGT3	2.2	4.4	220	220	3	10	19	30	360	660	19	38	44
J2-134-MR	1.9	4.3	190	200	4	4	24	24	430	440	16		
J2-134-MG	2.5	4.3	180		4		22		440		13		
Endmember			210	220		7		28		570		39	46
TM4													
J2-132-IGT5	26.0	5.7											62
Endmember													122
TM5													
J2-132-IGT6	11.7	4.6											27
Endmember													35
TM6													
J2-134-IGT3	2.5	4.4	210	220	0.3	1	14	18	440	540	17	35	94
J2-134-IGT6	2.6	4.4	200		3		3		110		14		98
Endmember			220	230		2		18		560		37	101
TM8													
J2-138-IGT2	3.3	4.5	130	160	bdl	10	3	6	420	740	57	73	109
J2-138-IGT4	2.6	4.4	130		0.1		3		160		35		108
Endmember			140	170		11		7		790		77	115
TM10													
J2-138-IGT7	3.2	4.4	210	250	1	4	32	46	800		85		68
J2-138-IGT8	2.2	4.2	230		1		11		290		65		70
Endmember			230	270		4		49					73

Table S1e. Trace metal and hydrogen concentrations of Mariner hydrothermal fluids

			ICPAES										GC
	Mg	[c]pH	[a]Fe	[c]Fe	Cu	[c]Cu	Zn	[c]Zn	Pb	[c]Pb	Ba	[c]Ba	H_2
	mm	25°C	µm	µm	µm	µm	µm	µm	nm	nm	µm	µm	µM
MA1													
J2-130-MR	4.2	2.8	10400		145		418		1370		128		
J2-130-MG	18.3	2.5	6900		69		167		690		70		
J2-130-IGT1	2.7	2.5	10800	10900	10	209	27	475	100	640	22	67	48
J2-130-IGT2	3.5	2.5	10600	10600	2	113	10	404	30	990	37	79	55
Endmember			11200	11400		171		467		860		77	55
MA2													
J2-131-IGT7	13.3	2.6	7900	7900	6		33		130	680	9	38	24
J2-131-IGT8	8.9	2.7	9800	9800	bdl	88	7	428	20	520	7	32	29
Endmember			11200	11300		106		515		750	bdl	44	33
MA3													
J2-131-IGT3	2.5	2.7	12200		24	154	36	245	180	870	18	58	130
J2-131-IGT4	1.9	2.7	12600	12700	0.1	146	2	399	10	1300	37	85	130
Endmember			13000	13100		156		336		1130		75	130
MA5													
J2-135-IGT7	5.9	2.6	8800	8800	0.4		68		300	690	18	68	60
J2-135-IGT8	4.2	2.6	10100	10200		89	11	296	50	860	22	107	60
Endmember			10400	10500		97		322		860		97	70
MA6													
J2-135-IGT1	3.7	2.7	9900	9900		4	16	225	80	1120	22	122	170
Endmember			10700	10700		4		242		1200		131	180

for Supplementary Table S1:

Analytical errors for metal analyses of individual fluid samples are estimated at ±10% and ±10 µmol/kg for measurements of Mn and Fe.
[a] from Mottl et al. (2011)
[b]pH is reported as measured at 25°C
[c] includes redigested bottle solids
mm = mmol/kg fluid, µm = µmol/kg fluid, µM = µmol/L fluid, bdl = below detection limit
KM = Kilo Moana, TC = TowCam, TMo = Tahi Moana-1, A = ABE, TM = Tu'i Malila, MA = Mariner
ICPAES = inductively coupled plasma atomic emission spectroscopy, GC = gas chromatography

Table S2. Major element contents, calculated mineral weight percent, and identification of minerals by optical microscopy and x-ray diffraction for SMS deposit samples from the Kilo Moana (KM), TowCam (TC), Tahi Moana-1 (TMo), ABE (A),

Vent Field	Sample	Sample ID	Fluid	T	Cu	Fe	Zn	Pb	Ca	Ba	S	Si	O	CP	BN	PY/MC	WZ/SP	FeS	GA	AN	BA	SI	HM	TOTAL	Mineral ID	Mineral ID
unit				(°C)	wt %	wt %	wt %	wt %	wt %	wt%	%*	%	wt%	wt%	wt%	wt%	wt%	wt%	wt%	wt%	wt%	wt%	wt%	wt%	major (minor) {trace}	major (minor) {trace}
method					ICP-MS	ICP-MS	INAA	ICP-MS	ICP-MS	INAA	IR/calc.	ICP-OES	calc.	calc.	calc.	calc.	calc.	calc.	calc.	calc.	calc.	calc.	calc.	calc.	XRD	Optical Petrography
detection limit					2µg/g	0.05%	50µg/g	0.8µg/g	0.01%	50µg/g	0.01%	0.0														
KM	oc	J2-125-6-R1	KM3	321	22	30	0.2	0.00	1.4	0.0	34 *	...	2	64	0	22	<1	…	0	5	0	...	0	91	cp (an, py) {wz}	cb, iss, cp (py, mc) {wz}
KM	oc	J2-137-1-R1	KM5	329	16	41	0.2	0.00	0.0	0.0	45 *	...	0	45	0	58	<1	…	0	<1	0	...	0	103	cp (po)	py, cp, po
KM	oc	J2-137-1-R1A	KM5	329	12	21	20	0.01	2.7	0.0	34 *	...	4	36	0	22	29	…	0	9	0	...	0	96	sp, cp (an)	cb, iss, cp, wz, sp, py, mc (po, an, hm)
KM	oc	J2-137-2-R1	KM6	306	2.0	19	5	0.01	11	0.0	25 *	...	17	6	0	37	8	…	0	37	0	...	0	88	an, py (cp) {sp}	an, py (cp, wz)
KM	oc	J2-137-6-R1A			1.2	48	1.2	0.03	0.0	0.0	47 *	...	3	3	0	83	2	…	0	<1	0	...	11	100	py, mc (cp) {wz, po}	
KM	oc	J2-137-6-R1B			2.5	11	0.4	0.00	16	0.0	13 *	...	25	7	0	19	<1	…	0	54	0	...	0	80	an (cp)	
KM	oc	J2-434-2-R1G	KM9	304	0.4	34	16	0.18	0.2	0.0	43	1.1	0	1	0	60	23	6	<1	<1	0	2	0	93	wz (sp) {mc, py}	mc, wz {cp}
KM	as	J2-124-2-R1A2			0.4	23	39	0.08	0.0	0.0	39 *	...	0	1	0	50	57	…	0	<1	0	...	0	108	wz (py) {mc}	wz, py/mc {cp}
KM	as	J2-124-2-R1D			0.1	36	23	0.17	0.0	0.0	41 *	...	1	<1	0	71	34	…	<1	0	0	...	4	109	wz (py) {mc}	
KM	as	J2-124-5-R1-C2	KM4	300	0.4	24	41	0.10	0.1	0.0	37 *	...	0	1	0	50	61	…	<1	<1	0	...	0	112	wz (py) {mc}	
KM	as	J2-124-5-R1CH			0.4	20	47	0.05	0.1	0.0	35 *	...	0	1	0	42	69	…	0	<1	0	...	0	112	wz (py)	wz (py, mc) {cb, iss, am.si.}
KM	as	J2-124-5-R1-CM			0.4	20	45	0.04	0.1	0.0	35 *	...	0	1	0	41	67	…	0	<1	0	...	0	109	wz (py)	
KM	rs	J2-125-11-R1A			0.5	12	55	0.07	0.0	0.0	34 *	...	0	1	0	25	82	…	0	<1	0	...	0	109	sp (wz) {py}	
KM	rs	J2-125-11-R1B			0.0	47	4	0.06	0.0	0.0	47 *	...	3	0	0	85	6	…	0	<1	0	...	11	101	py, mc (sp,wz)	
KM	rs	J2-125-3-B1			0.3	24	38	0.25	0.1	0.0	36 *	...	0	<1	0	52	56	…	<1	<1	0	...	0	108	wz {py,mc}	wz, py, mc {cp}
KM	rs	J2-125-7-R1			0.7	29	28	0.06	0.1	0.0	42 *	...	0	2	0	62	42	…	0	<1	0	...	0	106	sp (wz,py) {mc}	
KM	af	J2-436-2-R1			0.2	37	10	0.23	0.1	0.0	48	0.3	0	<1	0	79	14	0	<1	<1	0	<1	0	94	sp, py (mc) {wz}	mc, wz {cb}
KM	rf	J2-124-3-R1			0.4	17	20	0.23	0.0	0.0	30 *	...	0	1	0	36	30	…	<1	<1	0	...	0	68	wz (mc) {py}	wz, mc (si) {cb}

Sample types are: open conduit chimneys (oc), active spires (as), relict spires (rs), active flanges (af), relict flanges (rf), and squat terraces (st).

For Si, non-measurements are marked with "…"

* S values for samples from 2005 were calculated by assuming that iron not present as chalcopyrite or hematite is present as FeS2 (PY/MC).

Low weight totals are attributed to incomplete digestion of sulfate minerals.

High weight totals are attributed to contamination from mild steel barrels or Fe present as the FeS component of (Zn,Fe)S.

Mineral Abreviations are: chalcopyrite (CP), bornite (BN), pyrite (PY), marcasite (MC), wurtzite (WZ), sphalerite (SP), galena (GA), anhydrite (AN), barite (BA), amorphous silica (SI), and hematite (HM).

Major mineral contents are calculated from bulk geochemistry as follows :

2005 Cu as CP (CuFeS2)
Remaining Fe as PY/MC (FeS2), additional S not accounted for by CP, WZ/SP, or GA added to mass balance.
Zn as Fe-free WZ/SP (ZnS).
Pb as GA (PbS).
Ba as BA (BaSO4), additional S and O added to mass balance.
Ca as AN (CaSO4), additional S and O added to mass balance.
FeS and SI contents of 2005 samples cannot be calculated and are marked with "…".

2009 Similar to 2005. However, Si and reduced S were measured directly.
Following distribution of reduced S as Fe-free WZ/SP (ZnS) and GA (PbS) based on Zn and Pb, remaining Cu, Fe, and reduced S distributed:
between CP and BN if excess Cu versus Fe relative to (CuFeS2)
between CP and PY/MC (FeS2) and/or FeS with distribution between FeS2 and FeS determined by molar ratio of remaining unassign Fe and reduced S.
Where Cu (mol%) exceeds Fe (mol%), the mass percent of FeS2 cannot be calculated and is marked with "…"
Si as SI (SiO2), O added to mass balance.

Mineral contents as determined by XRD and microscopy are also listed. Major minerals (>5%), Minor minerals (1-5%), Trace minerals (<1%).
Additional minerals not described in weight totals are: cubanite (cb), chalcopyrite-cubanite solid solution (iss), pyrrhotite (po), covellite (cv), digenite (dg), and tennantite (tn).

Table S2 cont. Major element contents, calculated mineral weight percent, and identification of minerals by optical microscopy and x-ray diffraction for SMS deposit samples from the TowCam (TC), Tahi Moana-1 (TMo), and ABE (A) vent fields.

Vent Field	Sample Type	Sample ID	Fluid	T	Cu	Fe	Zn	Pb	Ca	Ba	S	Si	O	CP	BN	PY/MC	WZ/SP	FeS	GA	AN	BA	SI	HM	TOTAL	Mineral ID	Mineral ID
unit				(°C)	wt %	wt %	wt %	wt %	wt %	wt%	%*	%	wt%	wt%	wt%	wt%	wt%	wt%	wt%	wt%	wt%	wt%	wt%	wt%	major (minor) {trace}	major (minor) {trace}
method					ICP-MS	ICP-MS	INAA	ICP-MS	ICP-MS	INAA	IR/calc.	ICP-OES	calc.	calc.	calc.	calc.	calc.	calc.	calc.	calc.	calc.	calc.	calc.	calc.	XRD	Optical Petrography
detection limit					2µg/g	0.05%	50µg/g	0.8µg/g	0.01%	50µg/g	0.01%	0.0														
TC	oc	J2-126-7-B1			24	28	14	0.01	0.0	0.0	35 *	...	0	70	0	15	21	…	0	0	0	...	0	106	cp (sp)	
TC	as	J2-126-5-R1	TC3	320	2.3	15	35	0.41	0.1	0.0	35 *	...	0	7	0	28	53	…	<1	<1	0	...	0	87	sp (wz) {py,mc,cp}	wz, py, mc (cp)
TC	as	J2-127-1-R1C	TC5	302	1.8	12	47	0.40	0.1	0.0	36 *	...	0	5	0	22	70	…	<1	<1	0	...	0	97	sp (cp) {py,mc}	wz, mc (cp)
TC	as	J2-127-1-R2			6	11	40	0.05	0.1	0.0	33 *	...	0	17	0	13	60	…	0	<1	0	...	0	91	sp (py, cp) {wz}	
TC	as	J2-127-4-R1	TC7	288	1.0	6	46	0.07	3.0	0.0	30 *	...	5	3	0	11	69	…	0	10	0	...	0	93	wz (an) {cp}	wz, py, an (cp) {si}
TC	as	J2-127-5-R1			0.6	8	27	0.12	10	0.0	23 *	...	16	2	0	16	41	…	<1	33	0	...	0	92	an (wz) {py}	
TC	as	J2-139-1-R1A			3.9	25	30	0.19	0.2	0.0	40 *	...	0	11	0	47	45	…	<1	<1	0	...	0	103	sp {cp, py, wz, mc}	sp, wz, mc, cp
TC	as	J2-139-1-R1B			3.2	13	50	0.29	0.0	0.0	34 *	...	0	9	0	21	75	…	<1	<1	0	...	0	105	wz {cp, py/mc}	
TC	rs	J2-126-5-R2			0.8	13	28	0.70	0.2	0.5	29 *	...	1	2	0	26	42	…	<1	<1	<1	...	0	70	wz (py) {mc,cp,si}	wz, py, mc (an, cp)
TC	rs	J2-127-3-R1			1.2	14	28	0.12	0.1	0.0	28	10.1	0	3	0	22	42	3	<1	<1	0	22	0	92	wz, sp (py){an}	
TMo	oc	J2-450-3-R1	TMo5	310	18	22	11	0.01	2.5	0.2	32	1.3	4	52	0	12	16	<1	0	8	<1	3	0	91	cp, an {sp, wz, py}	cp, wz, py, an, (si)
TMo	as	J2-444-4-R1			1.0	8	45	0.34	0.4	0.3	31	1.5	1	3	0	13	68	<1	<1	1	<1	3	0	88	sp {py, cp}	wz, mc (an, cp, si) {ba}
TMo	as	J2-444-10-R1			0.7	14	27	0.21	5	1.3	33	2.3	8	2	0	27	41	<1	<1	16	2	5	0	93	sp (an, py) {cp}	
TMo	as	J2-444-22-R1A			1.1	20	33	0.27	0.1	0.4	39	1.0	0	3	0	40	49	0	<1	<1	<1	2	0	95	sp (cp) {py}	mc, wz (cp)
TMo	as	J2-444-22-R1B			3.0	9	22	0.05	11	0.1	29	1.2	17	9	0	13	32	<1	0	36	<1	3	0	92	sp an {cp, py, tr}	
TMo	as	J2-444-23-R1			0.3	20	30	0.26	0.1	1.2	38	0.7	1	<1	0	43	44	0	<1	<1	2	1	0	90	sp {py, ba, mc}	mc, wz, py (cp, ba)
TMo	as	J2-444-23-R2			0.4	18	35	0.24	0.1	0.0	34	0.3	0	1	0	23	52	7	<1	<1	0	<1	0	84	sp (py) {cp, mc}	wz, mc, py (cp)
TMo	rs	J2-444-17-R1			1.0	12	36	0.26	0.1	0.0	33	4.4	0	3	0	24	53	0	<1	<1	0	9	0	90	sp (wz) {py, hal}	
TMo	rs	J2-445-10-R1			0.8	15	30	0.26	0.1	3.8	31	4.4	2	2	0	26	44	2	<1	<1	6	9	0	90	sp (ba)	
TMo	af	J2-444-13-R2			1.5	5	51	0.30	0.1	0.6	30	1.3	0	4	0	6	76	1	<1	<1	1	3	0	91	sp {cp, ba}	
TMo	af	J2-445-4-R1			0.8	13	36	0.64	0.2	5	29	0.7	3	2	0	11	53	8	<1	<1	9	2	0	84	sp {ba,py,cp}	
TMo	af	J2-445-6-R2			1.0	14	37	0.49	0.2	0.0	33	0.8	0	3	0	22	55	3	<1	<1	0	2	0	85	sp (py) {ba, cp}	
TMo	af	J2-445-7-R1			0.3	1.9	5	0.02	27	0.1	26	0.3	43	<1	0	<1	8	2	0	91	0	<1	0	101	an {py,sp}	
A	oc	J2-128-3-R1	A1	309	18	21	2.8	0.11	7	0.0	25 *	...	11	53	0	9	4	…	<1	23	0	...	0	89	cp, an {py,sp}	
A	oc	J2-136-5-B1			19	15	28	0.00	0.0	0.0	31 *	...	0	48	3	…	41	…	0	0	0	...	0	92	cp (wz)	wz, cp (py, bn) {si}
A	oc	J2-449-5-R1	A11	306	13	16	13	0.01	8	0.0	29	0.9	12	36	0	5	19	2	0	26	0	2	0	91	an, cp, sp	cp, wz, an (py) {bn, dg,cv, si}
A	oc	J2-449-6-R1	A10	317	16	32	1.5	0.02	1.6	0.3	37	0.9	3	46	0	35	2	2	0	5	<1	2	0	91	cp (py) {an}	cp, py (sp, an) {bn, ba}
A	as	J2-128-5-R1A			1.2	10	39	0.29	0.1	0.0	31 *	...	0	3	0	19	58	…	<1	<1	0	...	0	81	sp {ba, cp, py}	sp, py, mc, cp, an (si,ba)
A	as	J2-128-5-R1B			2.0	14	35	0.22	0.1	0.0	34 *	...	0	6	0	27	53	…	<1	<1	0	...	0	85	sp (py) {cp}	
A	as	J2-128-8-R1			4	8	45	0.13	0.1	0.0	32 *	...	0	12	0	10	68	…	<1	<1	0	...	0	89	sp {cp, py, wz}	
A	as	J2-129-3-R1	A5	290	1.4	11	28	0.94	0.2	6	26 *	...	3	4	0	21	41	…	1	<1	11	...	0	78	sp (wz) {ba, cp, py}	wz, ba, py, mc (cp, si)
A	as	J2-136-5-R1A	A9	298	2.2	4	55	0.05	0.1	0.0	32 *	...	0	6	0	5	82	…	0	<1	0	...	0	93	sp (wz) {cp, ga}	
A	as	J2-136-5-R1B	A9	298	0.8	19	33	1.46	0.1	4	38 *	...	2	2	0	38	49	…	2	<1	6	...	0	98	sp {ba, py, cp}	
A	as	J2-128-1-R2			1.2	10	39	0.35	0.1	2.6	0 *	...	1	3	0	19	58	…	0	<1	4	...	0	86		
A	rs	J2-128-1-R2			0.2	15	8	0.21	0.2	7	21 *	...	3	<1	0	32	13	…	<1	<1	11	...	0	55	ba (py, wz) {si}	
A	rs	J2-128-8-R2			2.0	10	37	0.18	0.8	2.2	30 *	...	2	6	0	19	54	…	<1	3	4	...	0	85	sp (wz) {cp, ba, py}	
A	rs	J2-129-1-R3			0.9	7	36	0.13	0.1	3.9	26 *	...	2	3	0	14	54	…	<1	<1	7	...	0	77	sp {cp, py, ba}	sp, py, mc (ba, cp, si, an, hm)
A	rs	J2-136-6-R1			1.5	14	44	0.11	0.1	1.6	37 *	...	1	4	0	27	65	…	<1	<1	3	...	0	99	sp {py, ba}	
A	af	J2-128-2-R1			0.0	4	1.2	0.08	0.5	48	5 *	...	23	<1	0	8	2	…	0	2	82	...	0	93	ba {py, ga}	ba (mc, wz)

Table S2 cont. Major element contents, calculated mineral weight percent, and identification of minerals by optical microscopy and x-ray diffraction for SMS deposit samples from the Tu'i Malila (TM) vent field.

Vent Field	Sample Type	Sample ID	Fluid	T	Cu	Fe	Zn	Pb	Ca	Ba	S	Si	O	CP	BN	PY/MC	WZ/SP	FeS	GA	AN	BA	SI	HM	TOTAL	Mineral ID	Mineral ID
unit				(°C)	wt %	wt %	wt %	wt %	wt %	wt%	%*	%	wt%	wt%	wt%	wt%	wt%	wt%	wt%	wt%	wt%	wt%	wt%	wt%		major (minor) {trace}	major (minor) {trace}
method					ICP-MS	ICP-MS	INAA	ICP-MS	ICP-MS	INAA	IR/calc.	ICP-OES	calc.	calc.	calc.	calc.	calc.	calc.	calc.	calc.	calc.	calc.	calc.	calc.		XRD	Optical Petrography
detection limit					2µg/g	0.05%	50µg/g	0.8µg/g	0.01%	50µg/g	0.01%	0.0															
TM	oc	J2-132-14-R1	TM5	265	10	18	18	0.03	0.7	5	29 *	...	3	30	0	19	26	…	0	2	8	...	0	86	sp, cp (py) {ba, an}	
TM	oc	J2-134-7-R1A	TM6	265	1.5	9	45	0.18	0.3	0.1	32 *	...	0	4	0	16	67	…	<1	<1	<1	...	0	87	wz, sp (py) {cp}	wz, py, cp (an, ba, si) {ga, tn}
TM	oc	J2-134-7-R1B	TM6	265	0.2	9	6	0.14	0.3	36	13 *	...	17	<1	0	19	9	…	<1	<1	61	...	0	89	ba (wz) {py}	
TM	oc	J2-134-7-R1C	TM6	265	8	16	30	0.05	0.6	0.0	34 *	...	1	24	0	20	45	…	0	2	0	...	0	91	wz, py (cp) {an, ga}	
TM	oc	J2-442-4-R2	TM11	315	7	30	1.3	0.01	7	0.4	41	0.4	11	20	0	50	2	0	0	23	<1	<1	0	95	cp, py, an	cp, py (wz, ba, an, si)
TM	as	J2-132-13-R1			1.0	2.2	28	0.17	0.2	26	17 *	...	12	3	0	3	42	…	<1	<1	44	...	0	92	sp, ba {cp, ga}	
TM	as	J2-134-9-R1	TM7	198	1.1	9	12	6	0.1	23	17 *	...	11	3	0	16	18	…	7	<1	39	...	0	84	ba (wz) {cp, ga}	ba,an, wz, py,mc ga (cp, hm, si)
TM	as	J2-138-7-R1A			0.1	5	6	0.07	0.2	42	9 *	...	20	<1	0	10	9	…	0	<1	71	...	0	91	ba {py, sp}	ba, py (sp, ga)
TM	as	J2-138-7-R1B			0.1	5	6	0.09	0.2	42	9 *	...	20	<1	0	11	9	…	<1	<1	71	...	0	92	ba {py, sp, ga}	
TM	as	J2-442-9-R1			0.2	1.6	7	0.48	0.6	38	18	2.0	19	<1	0	3	11	0	<1	2	65	4	0	84	ba {sp}	ba, sp, py (an, cp, ga)
TM	rs	J2-132-15-R1			0.7	6	24	0.04	0.1	25	19 *	...	12	2	0	12	36	…	0	<1	42	...	0	93	sp (ba) {py, ga}	
TM	rs	J2-132-9-R2			0.5	5	14	0.04	0.1	35	12 *	...	16	1	0	9	21	…	0	<1	59	...	0	91	ba (sp)	
TM	rs	J2-134-8-R1			1.2	8	26	0.40	5	11	22 *	...	13	3	0	15	38	…	<1	17	19	...	0	92	sp, wz (ba) {cp, py, ga}	
TM	rs	J2-134-8-R2			0.4	10	22	1.9	0.2	20	22 *	...	10	1	0	20	32	…	2	<1	34	...	0	90	sp, wz (ba) {py, ga}	
TM	rs	J2-138-10-R1			0.1	1.3	1.9	0.37	0.1	47	2.4 *	...	22	<1	0	3	3	…	<1	<1	80	...	0	85	ba {sp, ga}	
TM	rs	J2-138-2-R1A			0.4	7	48	0.40	0.1	0.7	31 *	...	0	1	0	13	71	…	<1	<1	1	...	0	87	sp {py, wz}	ba, wz, mc, py (cp, si) {ga}
TM	rs	J2-138-2-R1B			0.1	6	6	0.13	0.1	40	9 *	...	19	<1	0	12	9	…	<1	<1	68	...	0	89	ba {py, sp}	
TM	rs	J2-447-5-R2			0.4	0.5	14	0.30	0.1	30	17	7.1	14	1	0	<1	20	0	<1	<1	51	15	0	88	ba, sp	ba, an, si, sp (cp, py)
TM	rs	J2-447-7-R2			1.1	4	33	0.34	0.1	17	27	0.9	8	3	0	6	49	0	<1	<1	29	2	0	89	sp (ba, py) {cp}	sp, ba, cp, py (hm, ac)
TM	rs	J2-447-9-R2-H			0.3	4	22	0.42	0.1	26	24	0.6	12	<1	0	8	32	0	<1	<1	44	1	0	86	ba, sp, py, an (cp)	
TM	rs	J2-447-9-R2-M			0.4	4	23	0.59	0.4	26	24	0.6	13	1	0	8	34	0	<1	1	44	1	0	90		
TM	af	J2-132-8-R1	TM4	178	0.1	1.6	0.6	0.03	0.2	49	2.1 *	...	23	<1	0	3	<1	…	0	<1	84	...	0	87	ba {sp, ga}	ba, (sp, py, si) {ga}
TM	af	J2-138-5-R1			0.1	5	7	0.02	0.1	40	9 *	...	19	<1	0	10	10	…	0	<1	68	...	0	89	ba {py, sp}	
TM	rf	J2-447-5-R1			0.1	0.1	1.9	0.35	0.1	41	13	5.9	19	<1	0	<1	3	0	<1	<1	70	13	0	86	ba (sp)	ba, si, sp, py (cp)

Table S2 cont. Major element contents, calculated mineral weight percent, and identification of minerals by optical microscopy and x-ray diffraction for SMS deposit samples from the Mariner (MA) vent field.

Vent Field	Sample Type	Sample ID	Fluid	T	Cu	Fe	Zn	Pb	Ca	Ba	S		Si	O	CP	BN	PY/MC	WZ/SP	FeS	GA	AN	BA	SI	HM	TOTAL	Mineral ID	Mineral ID
unit				(°C)	wt %	wt %	wt %	wt %	wt %	wt%	%*		%	wt%	wt%	wt%	wt%	wt%	wt%	wt%	wt%	wt%	wt%	wt%	wt%	major (minor) {trace}	major (minor) {trace}
method					ICP-MS	ICP-MS	INAA	ICP-MS	ICP-MS	INAA	IR/calc.		ICP-OES	calc.	calc.	calc.	calc.	calc.	calc.	calc.	calc.	calc.	calc.	calc.	calc.	XRD	Optical Petrography
detection limit					2µg/g	0.05%	50µg/g	0.8µg/g	0.01%	50µg/g	0.01%		0.0														
MA	oc	J2-130-1-R2	MA1	334	29	20	1.2	0.00	6	6	25	*	...	11	61	12	…	2	…	0	19	9	...	0	103	cp (an) {ba}	cp, bn, an (sp, ba)
MA	oc	J2-131-1-R1	MA2	311	29	19	0.1	0.00	6	0.8	24	*	...	10	59	14	…	<1	…	0	21	1	…	0	95	cp (an)	
MA	oc	J2-437-3-R2-H	MA9	338	24	26	5	0.06	0.9	2.7	33		0.1	3	69	0	9	7	1	0	3	5	<1	0	94	cp (an) {sp, ba, wz, ga}	cp, py, an, sp, ba (bn, mc) {tn}
MA	oc	J2-437-3-R2-M	MA9	338	20	24	5	0.06	2.4	2.9	32		0.1	5	57	0	10	7	3	0	8	5	<1	0	90	cp (an) {sp, ba, wz, ga}	
MA	oc	J2-437-3-R2-M	MA9	338	19	20	0.1	0.00	8	0.6	28		0.2	14	56	0	<1	<1	3	0	29	<1	<1	0	87	an, cp	
MA	oc	J2-439-8-R1	MA11	356	24	29	2.8	0.05	0.1	3.0	34		0.0	2	69	0	13	4	2	0	<1	5	0	0	94	cp {ba, sp}	cp, py (sp, bn, ba) {dg}
MA	oc	J2-448-8-R1	MA12	350	7	9	0.5	0.01	21.1	0.6	26		0.1	34	19	0	2	<1	2	0	72	1	<1	0	97	an (cp) {py}	an, cp (sp, py)
MA	as	J2-131-7-R1			11	20	26	0.08	0.4	7	31	*	...	4	30	0	24	38	…	0	1	11	...	0	105	cp, sp (wz, ba) {py}	cp, wz, py, mc, ba, an
MA	as	J2-439-13-R2			21	14	15	0.13	0.3	10	28		0.0	5	43	9	…	22	0	<1	<1	17	0	0	91	sp ba (cp)	cp, bn, sp, ba (an, mc) {ga}
MA	as	J2-'439-4-R1			11	5	22	0.21	3.0	13	25		0.3	11	13	9	…	33	0	<1	10	22	<1	0	89	sp (ba) {cp}	
MA	rs	J2-131-3-RB1			5	14	13	0.00	0.1	19	22	*	...	9	15	0	20	20	…	0	<1	32	...	0	87	ba, sp, cp	sp, ba, cp, mc, si
MA	rs	J2-131-8-R1A			31	27	4	0.02	0.1	5	31	*	...	4	75	7	…	5	…	0	<1	9	...	5	101	cp {sp, ba}	cp (sp, ba) {py}
MA	rs	J2-131-8-R1B			19	21	7	0.03	0.1	13	28	*	...	6	54	0	10	10	…	0	<1	22	...	0	96	cp (sp) {ba, py}	
MA	rs	J2-131-8-R1C			5	15	11	0.11	0.5	21	22	*	...	11	14	0	22	17	…	<1	2	36	...	0	90	ba (sp, py) {cp}	ba, mc, sp (py, cp, si)
MA	rs	J2-446-1-R3			0.6	3	35	0.32	0.2	18	27		0.0	8	2	0	6	52	0	<1	<1	30	0	0	90	sp (ba)	
MA	rs	J2-448-10-R1			39	15	0.1	0.01	0.0	1.1	23		0.2	1	34	44	…	<1	0	0	<1	2	<1	0	79	cp	bn, cp (ac)
MA	rs	J2-448-5-R1			0.1	0.5	4	0.33	0.1	43	15		2.3	20	<1	0	<1	5	0	<1	<1	73	5	0	83	ba (sp)	
MA	rs	J2-448-6-R1			0.1	0.9	2.6	0.42	0.3	43	15		2.4	21	<1	0	2	4	0	<1	<1	73	5	0	84	ba {sp}	ba, si, (py, sp, hm)
MA	af	J2-439-3-R1			0.1	2.8	45	0.27	0.3	11	29		0.0	6	<1	0	6	68	0	<1	<1	19	0	0	92	sp (ba) {tn}	
MA	af	J2-448-2-R1			0.0	2.5	39	0.28	0.3	18	27		0.0	9	0	0	5	57	0	<1	<1	31	0	0	94	sp (ba)	
MA	st	J2-131-4-R1			0.7	0.2	36	0.00	0.2	23	18	*	...	11	<1	<1	…	53	…	0	<1	38	...	0	92	sp (ba) {ga}	
MA	st	J2-135-5-RB1H	MA4/7	<100	0.4	0.2	41	0.07	0.2	24	20	*	...	11	<1	<1	0	61	…	0	<1	41	...	0	102	sp, ba	sp, ba
MA	st	J2-135-5-RB1M	MA4/7	<100	0.2	0.2	36	0.09	0.3	26	18	*	...	13	<1	<1	0	54	…	<1	<1	44	...	0	98	sp, ba	sp, ba
MA	rf	J2-446-1-R1			0.6	2.5	34	0.27	0.1	20	25		0.0	9	2	0	4	51	0	<1	<1	33	0	0	90	sp (ba)	

Table S3. Minor and trace element contents of SMS deposit samples from the Kilo Moana (KM), TowCam (TC), Tahi Moana-1 (TMo), ABE (A), Tu'i Malila (TM), and Mariner (MA) vent fields. Sample types are: open conduit chimneys (oc), active spires (as), relict spires (rs), active flanges (af), relict flanges (rf), and squat terraces (st). bdl = below detection limits.

Vent Field	Sample Type	Sample ID	Ag	Cd	Mn	Mo	Pb	Sr	As	Au	Co	Sb	Se
unit			µg/g	µg/g	µg/g	µg/g	µg/g	µg/g	µg/g	ng/g	µg/g	µg/g	µg/g
method			ICP-MS	ICP-MS	ICP-MS	ICP-MS	ICP-MS	ICP-MS	INAA	INAA	INAA	INAA	INAA
detection limit			5 µg/g	2 µg/g	3 µg/g	1 µg/g	0.8 µg/g	3 µg/g	0.5 µg/g	2 ng/g	1 µg/g	2 µg/g	3 µg/g
KM	oc	J2-125-6-R1	21	9	80	9	22	160	6	200	31	bdl	770
KM	oc	J2-137-1-R1	19	9	25	68	2	18	3	180	63	bdl	330
KM	oc	J2-137-1-R1A	59	750	42	99	120	240	120	2700	57	16	280
KM	oc	J2-137-2-R1	48	180	42	53	150	970	210	1000	100	3	110
KM	oc	J2-137-6-R1A	13	37	150	37	300	25	86	1500	410	bdl	210
KM	oc	J2-137-6-R1B	12	26	52	27	16	2500	6	350	270	bdl	300
KM	oc	J2-434-2-R1G	84	610	880	200	1800	23	370	7100	bdl	9	130
KM	as	J2-124-2-R1A2	110	> 2000	180	36	830	3	160	7000	4	15	bdl
KM	as	J2-124-2-R1D	160	420	230	61	1700	bdl	190	9200	2	13	bdl
KM	as	J2-124-5-R1-C2	97	1900	180	42	970	4	180	7200	bdl	22	bdl
KM	as	J2-124-5-R1CH	63	> 2000	130	48	510	10	91	4400	bdl	16	bdl
KM	as	J2-124-5-R1-CM	62	> 2000	130	50	430	7	87	4600	bdl	15	22
KM	rs	J2-125-11-R1A	74	> 2000	130	31	710	3	110	3800	bdl	28	15
KM	rs	J2-125-11-R1B	24	27	230	42	640	8	97	1100	bdl	bdl	bdl
KM	rs	J2-125-3-B1	96	1600	1400	49	2500	24	270	10500	55	18	110
KM	rs	J2-125-7-R1	93	1100	180	56	610	12	320	5600	9	17	63
KM	af	J2-436-2-R1	100	180	910	88	2300	7	420	8700	8	9	79
KM	rf	J2-124-3-R1	140	420	560	37	2300	10	200	7400	bdl	15	30
TC	oc	J2-126-7-B1	130	1300	130	46	100	7	99	780	3	11	41
TC	as	J2-126-5-R1	210	1400	1400	140	4100	5	570	4800	bdl	25	8
TC	as	J2-127-1-R1C	120	> 2000	670	140	4000	12	610	9800	bdl	44	26
TC	as	J2-127-1-R2	20	> 2000	450	130	490	6	220	1300	bdl	22	29
TC	as	J2-127-4-R1	39	> 2000	510	24	660	270	63	810	bdl	6	bdl
TC	as	J2-127-5-R1	100	1100	530	20	1200	1100	170	2700	bdl	23	bdl
TC	as	J2-139-1-R1A	89	1800	1400	100	1900	16	570	5000	bdl	23	bdl
TC	as	J2-139-1-R1B	160	> 2000	800	170	2900	3	330	5000	5	34	17
TC	rs	J2-126-5-R2	210	1300	1300	280	7000	79	710	9700	bdl	44	8
TC	rs	J2-127-3-R1	240	1000	1100	280	1200	18	400	5800	bdl	22	71

Table S3 cont. Minor and trace element contents of SMS deposit samples from the Tahi Moana-1 (TMo) and ABE (A) vent fields. Sample types are: open conduit chimneys (oc), active spires (as), relict spires (rs), active flanges (af), relict flanges (rf), and squat terraces (st). bdl = below detection limits.

Vent Field	Sample Type	Sample ID	Ag	Cd	Mn	Mo	Pb	Sr	As	Au	Co	Sb	Se
unit			µg/g	µg/g	µg/g	µg/g	µg/g	µg/g	µg/g	ng/g	µg/g	µg/g	µg/g
method			ICP-MS	ICP-MS	ICP-MS	ICP-MS	ICP-MS	ICP-MS	INAA	INAA	INAA	INAA	INAA
detection limit			5 µg/g	2 µg/g	3 µg/g	1 µg/g	0.8 µg/g	3 µg/g	0.5 µg/g	2 ng/g	1 µg/g	2 µg/g	3 µg/g
TMo	oc	J2-450-3-R1	68	630	270	30	140	240	45	330	bdl	6	44
TMo	as	J2-444-4-R1	230	1000	810	120	3400	130	580	8800	bdl	114	20
TMo	as	J2-444-10-R1	130	740	1000	210	2100	810	610	4200	bdl	69	21
TMo	as	J2-444-22-R1A	190	1100	920	110	2700	200	810	5800	bdl	99	29
TMo	as	J2-444-22-R1B	40	1300	490	41	460	750	150	1800	bdl	56	34
TMo	as	J2-444-23-R1	170	1500	690	90	2600	540	710	5400	26	143	53
TMo	as	J2-444-23-R2	240	1400	720	67	2400	10	640	6700	4	148	41
TMo	rs	J2-444-17-R1	180	1300	850	190	2600	11	830	5700	bdl	63	23
TMo	rs	J2-445-10-R1	210	700	1600	310	2600	960	940	5200	bdl	73	14
TMo	af	J2-444-13-R2	280	1200	250	150	3000	160	960	8100	bdl	98	30
TMo	af	J2-445-4-R1	330	550	1400	160	6400	1100	890	11000	bdl	103	13
TMo	af	J2-445-6-R2	250	800	1700	110	4900	25	900	9000	bdl	100	17
TMo	af	J2-445-7-R1	bdl	170	230	14	180	930	93	580	bdl	7	< 0.8
A	oc	J2-128-3-R1	37	48	120	18	1100	240	390	700	42	23	250
A	oc	J2-136-5-B1	17	1900	260	21	30	18	22	49	bdl	6	130
A	oc	J2-449-5-R1	bdl	410	250	9	140	480	33	130	bdl	6	150
A	oc	J2-449-6-R1	bdl	32	140	10	190	220	240	170	27	7	640
A	as	J2-128-5-R1A	49	1400	1300	130	2900	100	1000	2600	bdl	108	58
A	as	J2-128-5-R1B	27	830	1900	94	2200	14	980	1900	5	71	89
A	as	J2-128-8-R1	22	1000	860	96	1300	7	660	1100	bdl	78	39
A	as	J2-129-3-R1	95	740	1300	140	9400	51	1300	3100	4	145	bdl
A	as	J2-136-5-R1A	13	> 2000	410	100	520	9	150	380	bdl	50	210
A	as	J2-136-5-R1B	100	680	2200	240	14600	58	2100	4700	bdl	163	bdl
A	rs	J2-128-1-R2	130	80	2000	66	2070	73	1500	3300	bdl	117	bdl
A	rs	J2-128-8-R2	89	1500	1600	89	1800	58	1200	2700	3	125	bdl
A	rs	J2-129-1-R3	72	1200	930	120	1300	41	1100	2200	bdl	92	bdl
A	rs	J2-136-6-R1	86	1300	1600	71	1100	48	1200	2700	bdl	120	30
A	af	J2-128-2-R1	97	6	480	8	750	370	490	2300	bdl	77	bdl

Table S3 cont. Minor and trace element contents of SMS deposit samples from the Tui' Malila (TM) vent fields. Sample types are: open conduit chimneys (oc), active spires (as), relict spires (rs), active flanges (af), relict flanges (rf), and squat terraces (st). bdl = below detection limits.

Vent Field	Sample Type	Sample ID	Ag	Cd	Mn	Mo	Pb	Sr	As	Au	Co	Sb	Se
unit			µg/g	µg/g	µg/g	µg/g	µg/g	µg/g	µg/g	ng/g	µg/g	µg/g	µg/g
method			ICP-MS	ICP-MS	ICP-MS	ICP-MS	ICP-MS	ICP-MS	INAA	INAA	INAA	INAA	INAA
detection limit			5 µg/g	2 µg/g	3 µg/g	1 µg/g	0.8 µg/g	3 µg/g	0.5 µg/g	2 ng/g	1 µg/g	2 µg/g	3 µg/g
TM	oc	J2-132-14-R1	40	1000	560	97	280	62	880	1400	bdl	90	bdl
TM	oc	J2-134-7-R1A	49	1900	800	140	1800	36	530	2600	14	53	bdl
TM	oc	J2-134-7-R1B	110	76	710	49	1400	190	1400	7000	bdl	110	bdl
TM	oc	J2-134-7-R1C	42	1400	600	46	500	49	380	780	29	16	bdl
TM	oc	J2-442-4-R2	bdl	59	35	15	130	530	160	110	36	6	530
TM	as	J2-132-13-R1	150	1400	140	130	1700	100	1900	7800	bdl	220	bdl
TM	as	J2-134-9-R1	130	240	850	26	59200	21	800	2700	bdl	120	bdl
TM	as	J2-138-7-R1A	95	68	440	18	710	180	860	5100	bdl	87	bdl
TM	as	J2-138-7-R1B	100	71	470	19	930	220	870	5600	bdl	96	bdl
TM	as	J2-442-9-R1	62	190	180	15	4800	5700	400	4400	bdl	87	bdl
TM	rs	J2-132-15-R1	64	1200	300	75	350	69	900	8500	bdl	140	4
TM	rs	J2-132-9-R2	98	720	340	34	400	140	720	7500	bdl	110	bdl
TM	rs	J2-134-8-R1	96	1500	610	80	4000	350	660	5000	4	110	bdl
TM	rs	J2-134-8-R2	190	560	840	89	18600	84	1300	11200	bdl	270	bdl
TM	rs	J2-138-10-R1	69	65	95	8	3700	360	270	2800	bdl	42	bdl
TM	rs	J2-138-2-R1A	110	1500	810	24	4000	8	900	6300	bdl	250	bdl
TM	rs	J2-138-2-R1B	92	99	670	15	1300	88	810	4700	bdl	91	bdl
TM	rs	J2-447-5-R2	160	260	730	6	3000	2200	970	4300	bdl	59	4
TM	rs	J2-447-7-R2	170	1600	320	28	3400	3700	1300	5100	bdl	450	19
TM	rs	J2-447-9-R2-H	220	840	410	35	4200	4300	1100	9100	bdl	190	11
TM	rs	J2-447-9-R2-M	250	640	480	36	5900	3400	1200	9400	bdl	170	10
TM	af	J2-132-8-R1	160	10	110	5	340	130	530	4100	bdl	79	bdl
TM	af	J2-138-5-R1	52	240	290	19	200	120	550	3700	bdl	48	bdl
TM	rf	J2-447-5-R1	57	14	940	1	3500	3800	350	2300	bdl	23	bdl

Table S3 cont. Minor and trace element contents of SMS deposit samples from the Mariner (MA) vent field. Sample types are: open conduit chimneys (oc), active spires (as), relict spires (rs), active flanges (af), relict flanges (rf), and squat terraces (st). bdl = below detection limits.

Vent Field	Sample Type	Sample ID	Ag	Cd	Mn	Mo	Pb	Sr	As	Au	Co	Sb	Se
unit			µg/g	µg/g	µg/g	µg/g	µg/g	µg/g	µg/g	ng/g	µg/g	µg/g	µg/g
method			ICP-MS	ICP-MS	ICP-MS	ICP-MS	ICP-MS	ICP-MS	INAA	INAA	INAA	INAA	INAA
detection limit			5 µg/g	2 µg/g	3 µg/g	1 µg/g	0.8 µg/g	3 µg/g	0.5 µg/g	2 ng/g	1 µg/g	2 µg/g	3 µg/g
MA	oc	J2-130-1-R2	24	47	140	130	1	250	380	4700	3	46	bdl
MA	oc	J2-131-1-R1	9	5	130	9	7	250	18	900	bdl	4	bdl
MA	oc	J2-437-3-R2-H	bdl	87	25	27	590	520	560	1800	bdl	34	bdl
MA	oc	J2-437-3-R2-M	28	100	27	27	550	590	520	1800	bdl	38	bdl
MA	oc	J2-437-3-R2-M	bdl	bdl	160	9	21	860	53	460	bdl	11	bdl
MA	oc	J2-439-8-R1	bdl	44	13	31	500	470	530	690	1	23	11
MA	oc	J2-448-8-R1	bdl	12	38	22	53	1500	71	390	1	7	3
MA	as	J2-131-7-R1	71	760	99	30	770	58	1200	3000	bdl	110	bdl
MA	as	J2-439-13-R2	120	270	27	6	1300	1200	1900	3300	bdl	200	bdl
MA	as	J2-'439-4-R1	220	550	40	56	2100	2200	1800	9500	bdl	200	6
MA	rs	J2-131-3-RB1	170	590	980	43	41	41	1600	4600	bdl	430	bdl
MA	rs	J2-131-8-R1A	19	110	22	15	240	66	530	1300	bdl	79	bdl
MA	rs	J2-131-8-R1B	39	170	52	21	250	74	700	1800	3	87	bdl
MA	rs	J2-131-8-R1C	78	350	12000	48	1100	79	2100	2900	bdl	190	bdl
MA	rs	J2-446-1-R3	98	750	38	7	3200	2700	1700	3600	bdl	170	14
MA	rs	J2-448-10-R1	96	bdl	83	70	51	280	510	12100	bdl	39	bdl
MA	rs	J2-448-5-R1	41	14	91	bdl	3300	4000	840	3500	bdl	20	bdl
MA	rs	J2-448-6-R1	110	15	2500	8	4200	4400	980	4100	bdl	68	bdl
MA	af	J2-439-3-R1	260	860	120	3	2700	1600	1100	4700	bdl	190	19
MA	af	J2-448-2-R1	160	430	98	1	2800	2400	870	2600	bdl	89	14
MA	st	J2-131-4-R1	640	1500	40	17	30	42	2000	bdl	bdl	12	bdl
MA	st	J2-135-5-RB1H	360	1600	26	15	710	60	950	bdl	bdl	bdl	bdl
MA	st	J2-135-5-RB1M	250	1000	20	15	930	50	750	bdl	bdl	bdl	bdl
MA	rf	J2-446-1-R1	180	770	81	4	2700	2400	1300	5100	bdl	180	14

Table S4. Electron microprobe data for SMS deposit samples from the Kilo Moana (KM), TowCam (TC), Tahi Moana-1 (TMo), ABE (A), Tu'i Malila (TM), and Mariner (MA) vent fields. Sample types are: open conduit chimneys (oc), relict open conduit chimneys (ro), active spires (as), relict spires (rs), active flanges (af), relict flanges (rf), breccias (br), and squat terraces (st). Minerals are: cubanite (cb), chalcopyrite (cp), pyrite (py), marcasite (mc), sphalerite (sp), wurtzite (wz), bornite (bn), and covellite (cv). "Position" represents location of electron microprobe spot relative to the presumed fluid conduits, identified by mineralogical texture. * Pb analyses are considered unreliable because interferences with S could not be resolved. "…" = below detection limits.

SulfideID	Vent Field	Sample Type	Mineral	Position	Fe	Cu	Zn	Pb*	S	Co	Se	Ag	Mn	As	Sb	Cd	TOTAL
unit					wt%					0.1 mg/g							wt%
detection limit					0.08	0.055	0.11		0.007	5	1.5	1	4	2	1	1	
J2-137-1-R1	KM	oc	cb	lining	40	22	0.2	0.2	36	...	...	1	...	...	...	2	99
J2-137-1-R1	KM	oc	cb	lining	39	23	0.3	0.1	36	...	...	1	...	...	...	2	99
J2-137-1-R1	KM	oc	cb	lining	41	23	0.1	0.1	35	13	...	1	...	...	...	2	99
J2-137-1-R1	KM	oc	cb	middle	41	23	0.3	0.2	36	10	4	...	...	...	1	2	101
J2-137-1-R1	KM	oc	cb	middle	40	23	...	0.2	36	...	4	...	...	...	...	2	99
J2-137-1-R1	KM	oc	cb	middle	41	24	...	0.1	35	14	7	...	...	...	1	2	99
J2-137-1-R1	KM	oc	cb	middle	41	23	0.1	0.1	35	13	...	...	...	...	1	2	99
J2-137-1-R1	KM	oc	cb	middle	42	22	0.2	0.1	35	20	9	2	...	...	...	2	100
J2-137-1-R1	KM	oc	cb/cp	middle	35	27	0.1	0.2	36	...	8	1	...	...	2	1	98
J2-137-1-R1	KM	oc	cp	middle	31	31	0.4	0.2	36	...	6	1	...	...	...	3	98
J2-137-1-R1	KM	oc	cp	middle	31	32	1.3	0.1	36	...	...	4	...	...	...	4	99
J2-137-1-R1	KM	oc	py	middle	47	...	...	0.2	53	7	3	...	...	...	...	...	100
J2-137-1-R1	KM	oc	py	middle	47	0.1	...	0.2	53	...	...	...	...	...	...	...	100
J2-137-1-R1	KM	oc	py	exterior	46	...	...	0.3	53	8	...	...	...	...	...	...	100
J2-137-1-R1	KM	oc	py	exterior	47	...	0.4	0.3	53	6	...	...	...	...	...	2	100
J2-137-1-R1	KM	oc	sp	middle	14	0.9	50	0.1	34	...	...	...	...	...	...	39	100
J2-137-1-R1	KM	oc	sp	middle	9	0.2	57	0.1	34	32	...	...	...	...	...	46	101
J2-137-1-R1	KM	oc	wz	middle	12	0.7	52	0.1	34	...	...	...	...	...	...	60	100
J2-137-1-R1	KM	oc	wz	middle	9	0.3	56	0.1	34	...	...	...	...	...	...	30	100
J2-137-1-R1	KM	oc	wz	middle	8	0.3	58	0.1	34	...	3	...	...	...	...	58	100
J2-137-1-R1	KM	oc	wz	middle	3.0	0.3	65	0.1	33	...	...	...	...	3	...	8	101
J2-137-1-R1	KM	oc	wz	middle	7	0.1	57	0.1	34	...	...	...	...	...	...	51	99
J2-137-1-R1	KM	oc	wz	middle	6	0.4	59	0.1	33	...	...	...	...	...	4	39	99
J2-124-5-R1	KM	as	py	middle	45	0.1	0.7	0.2	53	...	3	...	...	...	1	2	99
J2-124-5-R1	KM	as	py	middle	46	...	1.3	0.2	52	13	8	...	...	...	...	2	99
J2-124-5-R1	KM	as	py	middle	47	0.1	0.4	0.3	53	...	4	...	...	...	...	1	101
J2-124-5-R1	KM	as	mc	exterior	46	0.2	0.5	0.3	53	...	...	...	...	...	...	2	99
J2-124-5-R1	KM	as	mc	exterior	46	...	...	0.3	52	6	...	...	...	...	...	...	99
J2-124-5-R1	KM	as	mc	exterior	46	...	0.5	0.3	53	...	...	...	4	...	...	1	100
J2-124-5-R1	KM	as	sp	middle	11	0.4	55	0.3	34	...	...	...	...	...	3	53	101
J2-124-5-R1	KM	as	sp	middle	9	...	57	0.2	34	...	...	...	...	...	1	39	100
J2-124-5-R1	KM	as	sp	middle	11	0.4	54	0.3	34	...	...	...	...	...	...	33	100
J2-124-5-R1	KM	as	sp	middle	10	...	55	0.2	34	...	2	...	...	...	...	41	100
J2-124-5-R1	KM	as	sp	middle	5	1.2	61	0.2	34	5	4	...	...	...	...	4	101
J2-124-5-R1	KM	as	sp	middle	10	0.5	55	0.3	34	...	3	...	...	...	2	11	100
J2-125-3-B1	KM	rs	py	middle	46	...	2.2	0.4	53	...	...	...	...	...	...	...	102
J2-125-3-B1	KM	rs	py	middle	47	...	...	0.3	54	...	...	...	...	...	...	...	101
J2-125-3-B1	KM	rs	py	exterior	46	...	...	0.3	54	...	...	...	5	...	...	...	100
J2-125-3-B1	KM	rs	sp	lining	8	...	60	0.2	34	...	5	...	...	...	...	28	102
J2-125-3-B1	KM	rs	sp	middle	7	...	61	0.2	34	...	4	...	...	...	...	32	102
J2-125-3-B1	KM	rs	sp	middle	7	...	60	0.2	34	...	...	...	...	...	1	23	101

Table S4 cont. Electron microprobe data for SMS deposit samples from the TowCam (TC) vent field

SulfideID	Vent Field	Sample Type	Mineral	Position	Fe	Cu	Zn	Pb*	S	Co	Se	Ag	Mn	As	Sb	Cd	TOTAL
unit					wt%					0.1 mg/g							wt%
detection limit					0.08	0.055	0.11		0.007	5	1.5	1	4	2	1	1	
J2-139-2-R1	TC	oc	cp	lining	31	34	...	0.2	35	...	...	2	...	...	...	2	101
J2-139-2-R1	TC	oc	cp	lining	31	34	...	0.2	35	...	...	1	...	...	...	3	100
J2-139-2-R1	TC	oc	cp	lining	31	34	0.4	0.2	35	...	2	1	...	...	...	3	101
J2-139-2-R1	TC	oc	py	lining	47	0.2	...	0.3	54	...	...	...	51	...	...	...	102
J2-139-2-R1	TC	oc	py	middle	48	0.4	0.3	0.2	53	...	...	...	...	...	...	...	102
J2-139-2-R1	TC	oc	py	middle	45	...	1.9	1.7	52	...	...	...	26	2	...	...	101
J2-139-2-R1	TC	oc	py	middle	46	...	...	0.4	53	...	...	...	80	...	...	...	100
J2-139-2-R1	TC	oc	sp	middle	4	0.2	63	0.2	33	15	5	1	6	...	3	45	102
J2-139-2-R1	TC	oc	sp	middle	5	0.3	62	0.2	34	8	5	2	9	...	1	45	102
J2-126-5-R1	TC	as	cp	lining	31	34	...	0.2	35	...	2	3	...	...	...	3	100
J2-126-5-R1	TC	as	cp	lining	31	33	0.4	0.2	34	...	2	4	...	...	...	3	100
J2-126-5-R1	TC	as	py	lining	47	...	...	0.3	53	...	...	3	28	6	...	...	101
J2-126-5-R1	TC	as	mc	middle	46	0.1	...	0.4	53	...	2	...	11	7	...	3	99
J2-126-5-R1	TC	as	mc	middle	46	0.1	0.2	1.0	52	8	8	...	18	33	...	5	100
J2-126-5-R1	TC	as	mc	middle	47	...	0.1	0.3	53	6	4	...	9	19	...	4	101
J2-126-5-R1	TC	as	sp	middle	5	0.1	60	0.2	33	...	...	...	9	...	...	39	100
J2-126-5-R1	TC	as	sp	middle	7	0.5	57	0.2	33	...	...	...	...	...	1	7	98
J2-126-5-R1	TC	as	sp	middle	7	0.1	59	0.2	33	6	...	...	9	...	...	38	100
J2-126-5-R1	TC	as	wz	lining	7	...	60	0.2	33	...	...	...	8	...	...	34	101
J2-126-5-R1	TC	as	wz	lining	6	...	60	0.2	33	...	...	...	10	...	...	47	101
J2-126-5-R1	TC	as	wz	lining	5	...	61	0.2	34	...	...	...	5	...	...	24	100
J2-127-4-R1	TC	as	cp	lining	31	34	0.5	0.2	35	...	...	...	...	...	...	...	102
J2-127-4-R1	TC	as	cp	lining	30	34	0.9	0.2	35	7	...	3	...	...	...	...	100
J2-127-4-R1	TC	as	cp	lining	30	26	6	0.3	37	...	...	7	...	...	...	3	99
J2-127-4-R1	TC	as	sp	middle	7	...	59	0.1	33	...	...	...	4	...	...	55	100
J2-127-4-R1	TC	as	sp	middle	7	...	59	0.2	33	...	2	1	7	...	2	75	101
J2-127-4-R1	TC	as	sp	middle	7	0.1	59	0.2	34	...	...	2	5	...	...	84	100
J2-127-4-R1	TC	as	wz	lining	7	0.1	60	0.1	34	...	...	...	7	...	...	44	101
J2-127-4-R1	TC	as	wz	lining	10	2.3	53	0.1	34	...	...	...	5	...	...	57	100
J2-127-4-R1	TC	as	wz	lining	7	...	59	0.1	34	...	...	...	5	...	...	67	100
J2-127-4-R1	TC	as	wz	lining	5	...	60	0.1	34	5	2	...	7	...	...	58	100
J2-127-4-R1	TC	as	wz	lining	6	...	58	0.1	33	...	...	...	7	...	...	60	99
J2-127-4-R1	TC	as	wz	lining	5	...	60	0.2	34	7	...	...	6	...	...	35	100
J2-126-5-R2	TC	rs	mc	lining	46	...	0.8	0.7	52	...	...	...	68	5	...	1	100
J2-126-5-R2	TC	rs	mc	lining	47	0.2	...	0.3	52	10	2	...	...	8	...	...	100
J2-126-5-R2	TC	rs	mc	lining	47	0.2	...	0.2	52	9	2	...	...	25	...	...	100
J2-126-5-R2	TC	rs	mc	middle	44	...	1.3	2.6	52	...	2	8	23	5	...	3	100
J2-126-5-R2	TC	rs	mc	exterior	46	...	...	0.4	53	...	...	2	79	...	...	...	101
J2-126-5-R2	TC	rs	mc	exterior	45	...	0.1	0.3	53	...	...	...	35	22	...	2	99
J2-126-5-R2	TC	rs	mc	exterior	45	...	0.2	0.3	52	9	5	...	25	49	...	1	98
J2-126-5-R2	TC	rs	mc	exterior	44	...	0.2	0.3	53	7	3	1	39	36	...	...	98
J2-126-5-R2	TC	rs	wz	lining	7	...	59	0.2	34	...	...	...	12	...	...	28	101
J2-126-5-R2	TC	rs	wz	lining	7	0.2	60	0.2	33	...	...	...	13	...	...	33	101
J2-126-5-R2	TC	rs	wz	middle	4	...	63	0.2	33	...	...	...	7	...	...	14	101
J2-126-5-R2	TC	rs	wz	middle	5	0.1	62	0.2	34	...	2	...	...	...	...	24	101
J2-126-5-R2	TC	rs	wz	middle	6	0.1	60	0.2	33	...	...	...	7	...	...	42	100
J2-126-5-R2	TC	rs	wz	middle	6	0.1	60	0.1	33	...	...	...	8	...	...	18	100

Table S4 cont. Electron microprobe data for SMS deposit samples from the Tahi Moana-1 (TMo) vent field

SulfideID	Vent Field	Sample Type	Mineral	Position	Fe	Cu	Zn	Pb*	S	Co	Se	Ag	Mn	As	Sb	Cd	TOTAL
unit					wt%					0.1 mg/g							wt%
detection limit					0.08	0.055	0.11		0.007	5	1.5	1	4	2	1	1	
J2-450-3-R1	TMo	oc	cp	lining	30	34	...	0.2	35	10	...	2	...	...	...	...	100
J2-450-3-R1	TMo	oc	cp	lining	30	34	...	0.1	35	7	4	2	...	...	...	...	98
J2-450-3-R1	TMo	oc	cp	middle	30	34	0.1	0.2	35	10	5	4	...	...	...	...	100
J2-450-3-R1	TMo	oc	cp	middle	30	35	...	0.1	35	8	5	3	...	5	...	...	100
J2-450-3-R1	TMo	oc	cp	middle	30	35	...	0.1	35	12	2	2	...	...	...	1	100
J2-450-3-R1	TMo	oc	cp	middle	30	34	0.3	0.2	35	...	3	2	...	...	...	...	100
J2-450-3-R1	TMo	oc	cp	middle	30	34	0.1	0.2	35	10	3	2	...	...	...	...	100
J2-450-3-R1	TMo	oc	cp	exterior	29	35	0.1	0.1	35	6	5	3	...	...	...	...	100
J2-450-3-R1	TMo	oc	py	middle	46	0.2	...	0.3	54	...	...	...	...	...	...	...	100
J2-450-3-R1	TMo	oc	py	middle	45	0.1	1.0	0.3	52	...	...	...	...	2	...	1	98
J2-450-3-R1	TMo	oc	py	middle	47	0.4	0.4	0.2	54	...	...	...	...	2	...	2	102
J2-450-3-R1	TMo	oc	wz	lining	6	0.2	61	0.1	34	6	6	4	8	...	...	44	101
J2-450-3-R1	TMo	oc	wz	lining	6	0.1	58	0.2	34	...	...	...	11	...	...	55	99
J2-450-3-R1	TMo	oc	wz	middle	5	0.6	62	0.2	34	...	8	2	5	...	...	30	101
J2-450-3-R1	TMo	oc	wz	middle	6	...	59	0.2	34	...	...	...	12	...	...	62	100
J2-450-3-R1	TMo	oc	wz	middle	6	0.2	59	0.1	34	...	...	...	7	...	...	52	99
J2-450-3-R1	TMo	oc	wz	middle	5	0.1	60	0.1	33	...	...	...	8	...	...	60	100
J2-450-3-R1	TMo	oc	wz	middle	5	...	61	0.1	34	...	...	...	6	...	...	34	100
J2-450-3-R1	TMo	oc	wz	exterior	5	...	59	0.1	33	5	...	...	7	...	...	49	99
J2-450-3-R1	TMo	oc	wz	exterior	5	...	60	0.2	33	10	...	...	8	...	...	68	99
J2-444-4-R1	TMo	as	mc	middle	44	0.2	1.3	0.3	53	...	...	6	75	5	...	...	100
J2-444-4-R1	TMo	as	mc	exterior	45	...	0.9	0.5	53	...	3	...	40	4	...	1	100
J2-444-4-R1	TMo	as	mc	exterior	45	...	0.6	0.4	53	7	...	1	58	5	...	1	100
J2-444-4-R1	TMo	as	sp	middle	2.3	0.2	64	0.1	33	...	...	...	...	...	...	30	101
J2-444-4-R1	TMo	as	sp	middle	1.4	0.8	64	0.6	33	...	...	...	...	9	3	11	100
J2-444-4-R1	TMo	as	sp	middle	2.3	0.4	65	0.2	33	6	...	...	...	...	3	38	101
J2-444-4-R1	TMo	as	sp	middle	2.0	0.1	65	0.2	33	...	...	...	...	...	...	27	101
J2-444-4-R1	TMo	as	sp	middle	1.8	0.4	65	0.2	33	...	...	...	5	...	3	26	101
J2-444-4-R1	TMo	as	sp	middle	2.7	0.3	64	0.2	33	...	...	...	...	...	...	54	101
J2-444-17-R1	TMo	rs	cp	middle	31	33	...	0.2	35	...	...	...	...	...	...	...	100
J2-444-17-R1	TMo	rs	mc	middle	46	...	...	0.4	54	...	...	...	26	...	...	...	100
J2-444-17-R1	TMo	rs	mc	exterior	45	...	1.0	1.0	53	...	...	...	8	6	...	...	100
J2-444-17-R1	TMo	rs	mc	exterior	43	...	3	0.7	52	...	...	...	52	...	...	...	100
J2-444-17-R1	TMo	rs	sp	middle	5	1.4	60	0.3	34	...	...	...	4	...	7	18	100
J2-444-17-R1	TMo	rs	sp	middle	3.2	0.1	61	0.1	33	...	2	...	...	...	...	61	98
J2-444-17-R1	TMo	rs	sp	middle	4	0.2	60	0.2	34	...	...	...	5	...	...	61	99
J2-444-17-R1	TMo	rs	sp	middle	8	0.8	57	0.2	33	21	...	...	...	...	...	24	99
J2-444-17-R1	TMo	rs	sp	exterior	2.3	0.7	62	0.5	33	...	4	...	...	11	11	9	99

Table S4 cont. Electron microprobe data for SMS deposit samples from the ABE (A) vent field

SulfideID	Vent Field	Sample Type	Mineral	Position	Fe	Cu	Zn	Pb*	S	Co	Se	Ag	Mn	As	Sb	Cd	TOTAL
unit					wt%					0.1 mg/g							wt%
detection limit					0.08	0.055	0.11		0.007	5	1.5	1	4	2	1	1	
J2-449-5-R1	A	oc	cp	lining	31	34	...	0.1	36	...	3	...	...	...	1	2	101
J2-449-5-R1	A	oc	cp	lining	30	34	0.2	0.2	35	9	3	1	...	...	...	2	101
J2-449-5-R1	A	oc	cp	lining	31	34	...	0.1	35	7	...	1	...	...	...	2	100
J2-449-5-R1	A	oc	cp	lining	30	33	...	0.1	35	11	2	1	...	...	...	2	99
J2-449-5-R1	A	oc	cp	lining	30	34	0.2	0.1	35	6	2	...	...	...	...	2	100
J2-449-5-R1	A	oc	cp	lining	30	34	...	0.1	35	9	...	...	...	...	...	2	99
J2-449-5-R1	A	oc	cp	lining	31	34	0.1	0.1	35	8	3	...	...	...	...	2	101
J2-449-5-R1	A	oc	cp	middle	31	34	0.1	0.1	36	7	2	2	...	...	...	1	101
J2-449-5-R1	A	oc	cp	middle	30	34	...	0.1	36	9	3	...	...	...	...	1	100
J2-449-5-R1	A	oc	cp	middle	29	34	...	0.1	35	...	8	2	...	...	...	1	99
J2-449-5-R1	A	oc	cp	middle	30	34	...	0.1	35	10	5	...	...	...	...	2	100
J2-449-5-R1	A	oc	cp	middle	30	34	0.1	0.1	35	6	3	...	...	...	...	1	99
J2-449-5-R1	A	oc	cp	middle	31	34	...	0.1	35	6	...	...	...	...	...	2	100
J2-449-5-R1	A	oc	cp	middle	30	34	0.1	0.1	36	10	5	...	...	...	...	1	99
J2-449-5-R1	A	oc	cp	exterior	30	34	0.2	0.1	35	10	4	1	...	...	...	2	100
J2-449-5-R1	A	oc	cp	exterior	30	34	...	0.1	35	10	...	3	...	...	...	...	100
J2-449-5-R1	A	oc	cp	exterior	30	34	1.8	0.1	35	8	5	3	...	3	...	2	101
J2-449-5-R1	A	oc	cp	exterior	30	34	...	0.1	35	9	3	2	...	...	...	2	100
J2-449-5-R1	A	oc	wz	lining	3.2	...	63	0.1	34	19	...	2	35	15	11	...	101
J2-449-5-R1	A	oc	wz	lining	3.0	...	63	0.2	34	14	12	3	8	8	...	23	101
J2-449-5-R1	A	oc	wz	lining	4	...	64	0.1	34	...	2	...	10	...	...	35	102
J2-449-5-R1	A	oc	wz	middle	2.9	...	64	0.1	34	...	...	...	11	...	...	29	101
J2-449-5-R1	A	oc	wz	middle	2.9	...	64	0.1	34	...	...	...	9	...	...	30	101
J2-449-5-R1	A	oc	wz	middle	3.2	...	64	0.1	34	...	2	...	9	...	...	31	102
J2-449-5-R1	A	oc	wz	middle	2.1	0.1	64	0.1	34	...	...	...	...	...	...	10	100
J2-449-5-R1	A	oc	wz	middle	3.0	...	63	0.1	33	...	...	...	7	...	...	27	99
J2-449-5-R1	A	oc	wz	exterior	3.3	0.1	62	0.1	33	...	...	...	10	...	...	35	100
J2-449-5-R1	A	oc	wz	exterior	3.4	...	64	0.1	34	...	...	...	9	...	...	33	101
J2-449-5-R1	A	oc	cv	exterior	3.5	71	...	0.1	24	...	5	4	...	3	...	1	99
J2-449-6-R1	A	oc	cp	lining	31	34	0.1	0.1	34	...	6	...	...	...	...	1	99
J2-449-6-R1	A	oc	cp	lining	30	34	...	0.2	34	...	2	...	...	...	...	...	99
J2-449-6-R1	A	oc	cp	lining	30	33	...	0.2	34	...	4	...	...	...	...	...	98
J2-449-6-R1	A	oc	cp	middle	31	34	...	0.2	35	...	6	...	...	...	...	1	99
J2-449-6-R1	A	oc	cp	middle	31	34	...	0.1	34	7	...	...	...	...	...	...	100
J2-449-6-R1	A	oc	cp	middle	31	34	...	0.2	34	...	4	...	...	...	...	...	100
J2-449-6-R1	A	oc	cp	middle	30	34	...	0.1	35	16	...	2	...	...	...	2	100
J2-449-6-R1	A	oc	cp	exterior	30	34	...	0.2	34	...	...	...	...	...	...	...	99
J2-449-6-R1	A	oc	cp	exterior	30	34	...	0.2	35	...	...	...	...	...	...	...	99
J2-449-6-R1	A	oc	py	lining	46	0.3	...	0.2	53	...	8	...	...	...	...	2	100
J2-449-6-R1	A	oc	py	lining	46	0.4	...	0.2	53	...	29	...	...	6	...	2	100
J2-449-6-R1	A	oc	py	lining	47	0.2	...	0.2	54	...	2	2	...	3	...	2	101
J2-449-6-R1	A	oc	py	middle	46	0.1	...	0.2	53	...	5	...	...	...	...	3	99
J2-449-6-R1	A	oc	py	middle	46	0.3	...	0.3	53	...	7	...	...	...	...	2	100
J2-449-6-R1	A	oc	py	middle	46	0.5	...	0.2	53	...	16	...	...	13	...	2	100
J2-449-6-R1	A	oc	py	middle	46	0.8	...	0.2	53	...	24	2	...	...	...	2	100
J2-449-6-R1	A	oc	py	exterior	46	1.1	...	0.2	54	...	...	1	...	...	...	2	101

Table S4 cont. Electron microprobe data for SMS deposit samples from the ABE (A) vent field

SulfideID	Vent Field	Sample Type	Mineral	Position	Fe	Cu	Zn	Pb*	S	Co	Se	Ag	Mn	As	Sb	Cd	TOTAL
unit					wt%					0.1 mg/g							wt%
detection limit					0.08	0.055	0.11		0.007	5	1.5	1	4	2	1	1	
J2-129-3-R1	A	as	cp	lining	30	33	0.8	0.2	35	...	...	3	...	...	...	2	99
J2-129-3-R1	A	as	cp	lining	29	35	1.1	0.1	35	...	...	3	...	...	...	...	100
J2-129-3-R1	A	as	cp	lining	30	34	1.7	0.1	35	...	...	1	...	...	...	1	101
J2-129-3-R1	A	as	mc	middle	47	...	0.4	0.3	53	...	2	...	30	39	...	...	101
J2-129-3-R1	A	as	mc	exterior	45	...	...	0.2	52	...	...	...	50	34	...	...	99
J2-129-3-R1	A	as	mc	exterior	45	...	2.4	0.6	53	5	3	...	59	36	...	1	102
J2-129-3-R1	A	as	sp	lining	3.1	...	63	0.2	33	...	...	...	7	...	...	30	100
J2-129-3-R1	A	as	sp	lining	6	3.2	58	0.3	33	...	...	...	11	...	...	12	101
J2-129-3-R1	A	as	sp	lining	4	0.1	64	0.1	33	...	...	...	12	...	...	29	101
J2-129-3-R1	A	as	sp	middle	4	1.2	61	0.3	33	...	...	...	6	...	12	14	100
J2-129-3-R1	A	as	sp	middle	4	0.8	63	0.3	33	...	...	...	...	...	7	3	101
J2-129-3-R1	A	as	sp	middle	6	2.2	58	0.3	34	...	...	...	17	...	6	8	101
J2-129-1-R3	A	rs	mc	middle	46	...	0.5	0.3	53	...	...	...	44	3	...	...	100
J2-129-1-R3	A	rs	mc	middle	47	...	...	0.4	53	...	...	...	23	21	...	...	101
J2-129-1-R3	A	rs	mc	exterior	41	...	6	1.6	51	...	...	...	30	5	...	...	100
J2-129-1-R3	A	rs	mc	exterior	39	0.1	8	2.9	49	...	...	...	34	38	...	...	100
J2-129-1-R3	A	rs	mc	exterior	45	...	...	0.5	53	...	...	...	27	...	...	...	99
J2-129-1-R3	A	rs	sp	lining	4	0.3	64	0.1	33	...	4	...	...	...	...	33	101
J2-129-1-R3	A	rs	sp	middle	1.3	...	66	0.2	34	...	...	...	...	...	...	8	101
J2-128-2-R1	A	af	py	middle	44	0.1	0.3	0.5	53	...	...	...	114	14	...	...	99
J2-128-2-R1	A	af	py	middle	45	...	...	0.4	53	...	...	1	29	15	...	2	99
J2-128-2-R1	A	af	py	middle	43	...	0.1	0.5	54	...	...	2	89	21	...	2	99
J2-136-5-B1	A	ro	cp	lining	31	34	...	0.2	35	...	...	1	...	...	...	1	100
J2-136-5-B1	A	ro	cp	lining	30	35	...	0.2	34	7	...	...	...	...	...	3	100
J2-136-5-B1	A	ro	cp	lining	31	34	...	0.2	35	...	...	...	...	...	...	2	100
J2-136-5-B1	A	ro	cp	middle	30	34	1.2	0.2	35	...	...	...	...	...	...	1	100
J2-136-5-B1	A	ro	cp	middle	30	34	0.4	0.2	35	...	2	...	...	...	...	...	99
J2-136-5-B1	A	ro	cp	middle	30	34	0.2	0.2	35	7	2	...	...	...	...	...	100
J2-136-5-B1	A	ro	wz	lining	4	...	61	0.2	33	...	...	...	6	...	...	45	99
J2-136-5-B1	A	ro	wz	lining	4	0.3	61	0.2	33	...	...	...	...	...	...	57	99
J2-136-5-B1	A	ro	wz	middle	3.5	...	62	0.2	33	...	3	...	7	...	...	42	100
J2-136-5-B1	A	ro	wz	middle	4	...	62	0.2	33	...	4	...	6	...	...	53	100
J2-136-5-B1	A	ro	wz	middle	4	...	62	0.2	33	...	...	...	7	...	...	49	100

Table S4 cont. Electron microprobe data for SMS deposit samples from the Tu'i Malila (TM) vent field

SulfideID	Vent Field	Sample Type	Mineral	Position	Fe	Cu	Zn	Pb*	S	Co	Se	Ag	Mn	As	Sb	Cd	TOTAL
unit					wt%					0.1 mg/g							wt%
detection limit					0.08	0.055	0.11		0.007	5	1.5	1	4	2	1	1	
J2-134-7-R1	TM	oc	cp	lining	29	34	0.3	0.2	35	...	...	1	...	...	...	2	99
J2-134-7-R1	TM	oc	cp	lining	30	35	0.3	0.2	35	6	...	...	...	...	...	3	100
J2-134-7-R1	TM	oc	cp	lining	29	35	0.6	0.2	36	...	...	4	...	...	...	2	100
J2-134-7-R1	TM	oc	mc	exterior	47	0.1	...	0.3	53	...	...	...	...	...	...	...	101
J2-134-7-R1	TM	oc	mc	exterior	47	0.3	...	0.3	53	...	...	...	...	...	...	...	101
J2-134-7-R1	TM	oc	wz	lining	6	...	60	0.2	34	...	...	...	7	...	...	32	101
J2-134-7-R1	TM	oc	wz	lining	7	...	60	0.1	33	...	...	...	6	...	...	43	101
J2-134-7-R1	TM	oc	wz	lining	6	0.1	61	0.1	34	...	...	2	4	...	...	44	101
J2-134-7-R1	TM	oc	wz	middle	9	0.1	58	0.2	34	...	...	...	12	...	...	33	101
J2-134-7-R1	TM	oc	wz	middle	7	0.1	59	0.2	33	...	...	...	8	...	...	21	100
J2-134-7-R1	TM	oc	wz	middle	8	...	59	0.2	34	...	...	...	10	...	...	14	100
J2-134-7-R1	TM	oc	wz	middle	9	0.6	57	0.2	34	...	...	...	6	...	3	15	100
J2-442-4-R2	TM	oc	cp	lining	30	34	0.2	0.1	36	...	...	...	...	...	2	3	99
J2-442-4-R2	TM	oc	cp	lining	29	34	0.2	0.1	35	...	7	...	...	...	...	3	100
J2-442-4-R2	TM	oc	cp	lining	29	35	0.1	0.2	35	...	3	...	...	...	...	3	100
J2-442-4-R2	TM	oc	cp	lining	29	34	0.2	0.1	36	...	5	...	...	...	...	2	98
J2-442-4-R2	TM	oc	cp	middle	29	34	...	0.2	35	...	3	...	...	...	...	2	99
J2-442-4-R2	TM	oc	cp	middle	29	35	...	0.2	36	...	7	...	...	...	...	2	100
J2-442-4-R2	TM	oc	cp	exterior	29	34	...	0.1	35	...	2	...	...	...	...	2	99
J2-442-4-R2	TM	oc	py	lining	45	0.1	...	0.3	54	...	...	...	...	...	...	...	99
J2-442-4-R2	TM	oc	py	lining	46	0.1	...	0.2	54	6	3	...	...	...	1	...	101
J2-442-4-R2	TM	oc	py	lining	46	0.5	...	0.2	53	...	4	...	...	...	...	2	100
J2-442-4-R2	TM	oc	py	lining	46	0.8	...	0.2	53	...	4	...	...	...	...	...	100
J2-442-4-R2	TM	oc	py	middle	45	0.2	...	0.3	54	...	...	...	...	2	...	...	99
J2-442-4-R2	TM	oc	py	middle	46	0.2	...	0.2	53	...	...	...	...	...	...	1	100
J2-442-4-R2	TM	oc	py	exterior	46	0.1	...	0.2	53	...	10	...	...	...	...	2	100
J2-442-4-R2	TM	oc	wz	exterior	4	0.7	60	0.1	33	...	7	...	...	...	...	83	99
J2-442-4-R2	TM	oc	wz	exterior	6	4	55	0.2	33	...	...	...	10	...	6	60	99
J2-442-4-R2	TM	oc	wz	exterior	4	0.7	60	0.1	33	...	...	...	4	...	4	75	99
J2-134-9-R1	TM	as	py	lining	44	...	...	0.5	53	13	2	...	85	5	...	2	98
J2-134-9-R1	TM	as	py	lining	46	...	0.9	0.3	53	...	...	...	...	7	...	2	101
J2-134-9-R1	TM	as	py	middle	46	...	...	0.3	53	9	...	...	18	51	...	2	100
J2-134-9-R1	TM	as	py	exterior	45	...	...	0.3	54	...	...	...	32	22	...	1	100
J2-134-9-R1	TM	as	py	exterior	45	...	...	0.4	53	...	...	...	14	38	...	...	99
J2-134-9-R1	TM	as	sp	lining	10	0.7	55	0.3	34	6	...	...	12	...	3	5	100
J2-134-9-R1	TM	as	sp	lining	12	...	53	0.2	34	7	...	...	18	...	...	18	99
J2-134-9-R1	TM	as	sp	lining	14	5	46	0.4	34	...	2	17	13	...	1	6	99
J2-134-9-R1	TM	as	wz	lining	12	0.1	54	0.2	34	...	...	...	14	...	...	14	101
J2-134-9-R1	TM	as	wz	lining	13	0.1	52	0.2	34	9	...	...	25	...	...	21	100
J2-134-9-R1	TM	as	wz	lining	13	...	53	0.2	34	...	...	...	16	...	...	16	100

Table S4 cont. Electron microprobe data for SMS deposit samples from the Tu'i Malila (TM) vent field

SulfideID	Vent Field	Sample Type	Mineral	Position	Fe	Cu	Zn	Pb*	S	Co	Se	Ag	Mn	As	Sb	Cd	TOTAL
unit					wt%					0.1 mg/g							wt%
detection limit					0.08	0.055	0.11		0.007	5	1.5	1	4	2	1	1	
J2-447-7-R2	TM	rs	cp	lining	31	35	...	0.2	35	8	...	2	...	...	2	...	102
J2-447-7-R2	TM	rs	cp	lining	31	35	...	0.2	35	...	...	...	...	...	...	1	102
J2-447-7-R2	TM	rs	cp	lining	31	35	...	0.2	35	9	...	...	...	...	...	2	101
J2-447-7-R2	TM	rs	mc	middle	44	...	...	0.3	54	...	...	...	37	17	...	...	99
J2-447-7-R2	TM	rs	mc	exterior	46	0.4	...	0.5	53	...	...	...	10	39	...	...	100
J2-447-7-R2	TM	rs	mc	exterior	46	0.1	1.1	0.5	53	...	3	...	37	...	...	...	101
J2-447-7-R2	TM	rs	sp	lining	1.2	0.4	66	0.2	33	23	5	1	...	10	16	57	102
J2-447-7-R2	TM	rs	sp	lining	0.9	0.2	67	0.2	33	6	4	...	...	...	5	58	102
J2-447-7-R2	TM	rs	sp	exterior	1.4	0.5	65	0.4	33	10	3	2	...	14	15	11	101
J2-447-7-R2	TM	rs	sp	exterior	2.3	0.7	62	0.3	33	19	8	2	6	7	8	31	100
J2-132-8-R1	TM	af	py	middle	45	...	...	0.8	53	...	...	107	8	...	...	...	100
J2-132-8-R1	TM	af	py	middle	45	...	...	1.2	53	...	...	...	10	40	...	...	100
J2-132-8-R1	TM	af	py	middle	45	...	...	0.4	54	...	...	38	20	18	...	1	100
J2-132-8-R1	TM	af	py	middle	44	0.2	...	1.1	53	...	...	11	12	11	1	...	99
J2-132-8-R1	TM	af	py	middle	45	0.6	...	0.6	54	...	...	42	23	24	...	2	100
J2-132-8-R1	TM	af	mc	middle	45	...	...	0.3	53	9	...	6	59	30	2	2	101
J2-132-8-R1	TM	af	mc	middle	46	...	...	1.8	52	14	4	...	...	70	8	3	101
J2-132-8-R1	TM	af	mc	exterior	44	0.4	0.2	3.7	50	20	6	...	6	138	20	5	101
J2-132-8-R1	TM	af	sp	exterior	7	2.0	55	0.4	33	...	...	...	4	4	46	4	98
J2-138-7-R1	TM	af	sp	middle	1.9	0.4	65	0.3	33	...	...	10	...	...	20	25	101
J2-138-7-R1	TM	af	sp	middle	1.8	0.6	65	0.2	33	...	...	...	...	...	14	16	101
J2-138-7-R1	TM	af	sp	middle	3.3	2.4	59	2.2	33	...	...	...	...	38	25	10	100
J2-442-12-R2	TM	af	py	middle	44	0.4	0.3	0.3	54	6	3	38	59	34	...	2	100
J2-442-12-R2	TM	af	py	middle	47	...	...	0.3	...	...	...	...	6	18	...	3	100
J2-442-12-R2	TM	af	py	middle	45	...	...	1.1	...	...	...	...	10	18	...	2	100
J2-442-12-R2	TM	af	sp	middle	1.2	0.3	66	0.2	...	...	...	...	...	...	11	33	101
J2-442-12-R2	TM	af	sp	middle	3.1	0.9	63	0.2	33	7	2	...	...	4	10	65	101
J2-442-12-R2	TM	af	sp	middle	2.1	1.2	62	0.3	33	...	...	...	...	16	30	40	99
J2-132-10-R1	TM	br	cp	middle	30	34	...	0.2	35	...	4	...	...	...	...	2	100
J2-132-10-R1	TM	br	cp	middle	30	34	...	0.2	35	9	4	...	...	...	...	2	100
J2-132-10-R1	TM	br	cp	middle	31	34	...	0.2	35	...	...	...	...	...	...	3	100
J2-132-10-R1	TM	br	py	middle	47	0.1	...	0.3	53	9	2	...	...	...	...	3	101
J2-132-10-R1	TM	br	py	middle	47	0.1	0.6	0.3	52	29	4	...	...	9	...	2	100
J2-132-10-R1	TM	br	py	middle	48	...	...	0.3	53	...	5	...	...	2	...	1	101
J2-132-10-R1	TM	br	sp	middle	2.3	0.1	64	0.1	33	...	...	...	4	...	...	33	100
J2-132-10-R1	TM	br	sp	middle	1.4	0.1	65	0.2	33	...	3	...	...	...	...	23	100
J2-132-10-R1	TM	br	sp	middle	3.3	...	63	0.2	33	...	...	...	...	...	...	17	100

Table S4 cont. Electron microprobe data for SMS deposit samples from the Mariner (MA) vent field

SulfideID	Vent Field	Sample Type	Mineral	Position	Fe	Cu	Zn	Pb*	S	Co	Se	Ag	Mn	As	Sb	Cd	TOTAL
unit					wt%					0.1 mg/g							wt%
detection limit					0.08	0.055	0.11		0.007	5	1.5	1	4	2	1	1	
J2-130-1-R1	MA	oc	cp	middle	30	33	0.1	0.1	36	...	...	4	...	...	...	...	99
J2-130-1-R1	MA	oc	cp	middle	29	34	...	0.2	35	...	...	4	...	...	...	...	99
J2-130-1-R1	MA	oc	cp	exterior	30	34	...	0.1	35	...	...	2	...	...	...	...	100
J2-130-1-R1	MA	oc	py	exterior	45	0.2	...	0.7	54	...	...	2	...	...	...	...	99
J2-130-1-R1	MA	oc	py	exterior	46	0.1	...	0.3	54	...	...	...	...	...	...	...	100
J2-130-1-R1	MA	oc	wz	middle	3.4	0.4	62	0.2	34	...	...	...	...	...	5	50	100
J2-130-1-R1	MA	oc	bn	middle	12	59	...	0.1	30	...	...	3	...	...	...	...	100
J2-130-1-R1	MA	oc	bn	middle	9	63	...	0.1	28	13	...	...	...	...	...	...	101
J2-130-1-R1	MA	oc	bn	exterior	11	62	...	0.0	27	...	...	...	...	...	1	4	100
J2-130-1-R1	MA	oc	bn/cv	middle	9	64	...	0.1	28	...	...	...	...	...	...	...	100
J2-130-1-R1	MA	oc	bn/cv	middle	9	62	...	0.1	29	...	...	17	...	...	...	...	100
J2-130-1-R2	MA	oc	cp	lining	29	34	...	0.1	35	10	4	...	...	...	...	...	99
J2-130-1-R2	MA	oc	cp	lining	29	35	...	0.1	35	13	3	...	...	...	...	1	100
J2-130-1-R2	MA	oc	cv	lining	4	70	0.4	0.1	25	11	9	...	...	3	1	4	100
J2-130-1-R2	MA	oc	cv	lining	6	66	0.2	0.1	26	5	3	...	...	...	...	2	99
J2-130-1-R2	MA	oc	cv	lining	4	68	0.2	0.1	26	...	...	1	...	...	...	2	98
J2-437-3-R2	MA	oc	cp	lining	30	34	...	0.2	35	...	...	2	...	...	...	2	100
J2-437-3-R2	MA	oc	cp	lining	31	35	...	0.2	35	...	...	...	...	...	...	2	100
J2-437-3-R2	MA	oc	cp	lining	30	34	...	0.1	35	...	3	...	...	...	...	3	100
J2-437-3-R2	MA	oc	cp	lining	30	34	0.5	0.2	35	...	...	...	...	...	...	...	100
J2-437-3-R2	MA	oc	cp	exterior	30	34	...	0.2	35	...	...	4	...	...	2	...	100
J2-437-3-R2	MA	oc	cp	exterior	30	34	...	0.2	35	7	...	2	...	...	...	...	100
J2-437-3-R2	MA	oc	cp	exterior	30	34	0.3	0.2	35	6	3	...	...	10	6	...	100
J2-437-3-R2	MA	oc	py	exterior	48	...	...	0.2	53	...	...	...	...	...	...	2	101
J2-437-3-R2	MA	oc	py	exterior	48	...	...	0.4	53	...	...	...	...	...	...	...	101
J2-437-3-R2	MA	oc	sp	exterior	3.4	1.2	60	0.2	33	...	7	...	...	9	70	92	99
J2-437-3-R2	MA	oc	sp	exterior	6	1.2	58	0.3	33	...	...	...	5	7	9	50	100

Table S4 cont. Electron microprobe data for SMS deposit samples from the Mariner (MA) vent field

SulfideID	Vent Field	Sample Type	Mineral	Position	Fe	Cu	Zn	Pb*	S	Co	Se	Ag	Mn	As	Sb	Cd	TOTAL
unit					wt%					0.1 mg/g							wt%
detection limit					0.08	0.055	0.11		0.007	5	1.5	1	4	2	1	1	
J2-131-7-R1	MA	as	cp	lining	31	35	...	0.2	35	...	...	2	...	...	...	2	102
J2-131-7-R1	MA	as	cp	lining	31	34	...	0.2	34	5	...	...	...	...	...	...	100
J2-131-7-R1	MA	as	cp	middle	31	34	...	0.2	35	8	4	...	...	...	...	1	101
J2-131-7-R1	MA	as	cp	exterior	41	23	0.9	0.2	35	...	...	2	...	...	...	1	100
J2-131-7-R1	MA	as	cp	exterior	39	25	0.8	0.2	35	...	...	1	...	...	...	1	101
J2-131-7-R1	MA	as	mc	middle	47	0.5	...	0.3	53	...	3	2	...	3	...	1	100
J2-131-7-R1	MA	as	mc	exterior	47	0.1	0.3	0.3	52	5	...	7	...	8	...	1	100
J2-131-7-R1	MA	as	mc	exterior	48	...	...	0.2	53	...	...	3	5	...	...	...	101
J2-131-7-R1	MA	as	sp	middle	6	0.2	60	0.3	33	...	6	...	5	11	13	7	101
J2-131-7-R1	MA	as	sp	exterior	23	1.0	41	0.2	34	7	4	...	6	...	6	101	100
J2-131-7-R1	MA	as	sp	exterior	7	0.3	59	0.2	33	12	5	...	...	9	3	3	101
J2-439-13-R2	MA	as	cp	middle	31	35	...	0.2	35	...	...	...	...	16	13	...	101
J2-439-13-R2	MA	as	cp	middle	30	35	...	0.2	35	...	...	4	...	21	4	...	100
J2-439-13-R2	MA	as	cp	middle	30	35	0.1	0.2	35	5	...	3	...	12	...	...	101
J2-439-13-R2	MA	as	py	exterior	47	0.1	1.0	0.4	53	7	2	9	...	...	1	2	102
J2-439-13-R2	MA	as	py	exterior	47	...	...	0.3	54	7	4	5	...	...	1	1	101
J2-439-13-R2	MA	as	py	exterior	47	...	0.7	0.3	54	...	2	3	...	...	...	1	101
J2-439-13-R2	MA	as	sp	middle	1.8	2.7	61	0.5	32	...	...	...	...	48	2	96	100
J2-439-13-R2	MA	as	sp	exterior	1.1	0.1	66	0.8	33	...	2	...	...	...	...	...	101
J2-439-13-R2	MA	as	bn	middle	11	62	...	0.2	27	...	...	2	...	...	...	2	100
J2-439-13-R2	MA	as	bn	middle	11	64	0.1	0.2	27	...	2	2	...	...	...	...	102
J2-439-13-R2	MA	as	bn	middle	12	62	...	0.1	27	...	...	...	...	...	...	...	101
J2-439-13-R2	MA	as	bn	middle	12	64	...	0.1	26	...	...	4	...	...	...	...	102
J2-131-3-RB1	MA	rs	cp	lining	30	33	...	0.2	35	5	3	1	...	3	...	1	98
J2-131-3-RB1	MA	rs	cp	lining	31	33	0.1	0.2	34	7	...	1	...	3	2	...	99
J2-131-3-RB1	MA	rs	cp	lining	31	33	...	0.2	35	5	...	2	...	...	2	...	99
J2-131-3-RB1	MA	rs	mc	exterior	46	0.2	...	0.3	53	...	...	...	...	...	...	3	99
J2-131-3-RB1	MA	rs	mc	exterior	46	0.1	...	0.3	53	5	...	...	...	...	...	2	99
J2-131-3-RB1	MA	rs	mc	exterior	46	...	...	0.3	53	8	...	...	...	13	...	3	99
J2-131-3-RB1	MA	rs	sp	lining	2.2	0.5	63	0.2	33	...	...	...	...	...	11	43	99
J2-131-3-RB1	MA	rs	sp	middle	0.6	...	66	0.1	33	...	...	...	...	...	...	15	100
J2-131-3-RB1	MA	rs	sp	middle	1.2	0.6	64	0.3	32	...	...	...	...	28	...	23	99
J2-131-3-RB1	MA	rs	sp	exterior	1.2	0.6	63	0.4	33	...	2	3	...	17	17	43	99
J2-437-7-R1	MA	af	wz	middle	...	1.6	64	0.3	32	...	...	...	...	7	1	72	99
J2-437-7-R1	MA	af	wz	middle	0.2	1.7	63	0.4	33	...	...	...	...	16	...	99	99
J2-437-7-R1	MA	st	py	middle	46	0.5	0.7	0.6	52	...	...	2	...	...	...	2	101
J2-437-7-R1	MA	st	sp	middle	0.5	0.7	66	0.2	33	34	25	9	...	27	8	68	102
J2-437-7-R1	MA	st	sp	middle	...	1.4	64	0.4	33	...	...	2	...	48	...	32	100
J2-437-7-R1	MA	st	sp	middle	0.4	1.3	64	0.2	33	...	2	...	...	31	...	40	99
J2-437-7-R1	MA	st	sp	middle	...	...	65	0.3	33	6	6	...	...	4	...	2	99

Table S5. Log(fS2) of ELSC hydrothermal fluids as calculated at approximate in situ temperature (T_ref) and pressure (P_ref). The calculated ratio of HS- to H2S at in situ conditions is also calculated in order to justify the approximation H2S = Total S-2, which is used to simplify calculation of log (fS2). TMo = Tahi Moana; A = ABE.

unit	T (°C)	pH (25°C)	H2S,aq (mM)	H2,aq (µM)	Tref (°C)	Pref (bar)	HS-/H2S	Log (fS2)
KM1	333	3.6	6.0	313	330	260	0%	-9.6
KM2	332	3.6	5.4	220	330	260	0%	-9.3
KM3	321	2.9	6.4	359	320	260	0%	-9.9
KM4	300	3.2	5.4	483	300	260	0%	-11.0
KM5	325	3.5	6.3	359	325	260	0%	-9.8
KM6	306	3.6	5.4	445	300	260	0%	-10.9
KM8	333	4.0	5.5	498	330	260	0%	-10.0
KM9	304	4.1	3.5	*445	300	260	0%	-11.3
KM10	290	3.9	3.9	**483	290	260	0%	-11.6
TC1	328	4.1	4.8	132	330	270	0%	-9.0
TC3	320	4.0	4.9	177	320	270	0%	-9.5
TC4	316	4.1	4.9	149	320	270	0%	-9.4
TC5	302	3.7	4.5	108	300	270	0%	-9.8
TC7	288	4.0	3.7	198	290	270	0%	-10.9
TC8	308	4.1	5.2	138	310	270	0%	-9.6
A1	309	4.3	3.6	63.1	310	210	3%	-9.2
A4	278	4.4	2.8	54	280	210	3%	-10.3
A5	290	4.5	3.1	101	290	210	3%	-10.5
A8	308	4.5	2.9	78	310	210	3%	-9.6
A9	295	4.6	2.6	101	295	210	3%	-10.4
TM1	279	4.5	2.3	48	280	190	3%	-10.4
TM2	312	4.4	2.5	46	310	190	3%	-9.3
TM4	178	5.7	1.2	122	…	…	…	…
TM5	265	4.6	2.3	35	265	190	3%	-10.7
TM6	265	4.4	2.4	101	265	190	3%	-11.6
TM7	198	5.0	2.1	135	200	190	3%	-14.6
TM8	229	4.4	2.1	115	230	190	3%	-13.2
TM10	274	4.2	2.0	73.2	270	190	3%	-11.3
MA1	334	2.5	6.2	55	330	190	0%	-8.0
MA2	311	2.6	4.2	33	310	190	0%	-8.5
MA3	363	2.7	9.3	131	360	190	0%	-7.4
MA5	249	2.6	4.5	65	250	190	0%	-11.2
MA6	240	2.7	6.4	179	240	190	0%	-12.1

* H2,aq of KM9 was not measured, but estimated based on the H2,aq content of KM6

** H2,aq of KM10 was not measured, but estimated based on the H2,aq content of KM4

Chapter 3

Trace Element Chemistry of Black Smoker Chimney Linings Measured by Secondary Ion Mass Spectrometry

1. INTRODUCTION

Deep-sea hydrothermal vents are unique locations in which metal-rich seafloor massive sulfide deposits can be sampled in direct contact with deposit-forming seafloor hydrothermal fluids. Particularly relevant for the purpose of understanding the effects of hydrothermal fluid temperature and chemistry on mineral deposit composition are the mineral linings of open conduit black smoker chimneys, which precipitated directly from vigorously venting high-temperature fluids.

Black smoker chimneys are deposited in two stages (Haymon, 1983; Goldfarb et al., 1983). First, mixing between hydrothermal fluids and seawater leads to the precipitation of an initial pipe-like structure composed of an anhydrite ($CaSO_4$) dominated matrix that contains interstitial grains of various metal sulfide minerals. Second, a massive sulfide mineral layer is deposited on the interior of the chimney following physical and chemical separation of hydrothermal fluids and seawater by the initial chimney wall. Above ~250°C, this massive sulfide lining typically contains chalcopyrite ($CuFeS_2$) and/or cubanite ($CeFe_2S_3$). Because this second-stage massive sulfide layer is precipitated directly from venting hydrothermal fluids with little chemical interaction with surrounding seawater, the mineralogy and geochemistry of this innermost layer closely reflect the temperature and chemistry of venting hydrothermal fluids.

Previous studies have noted a close correspondence between the mineralogy of this massive sulfide layer and the temperature, sulfur fugacity, and pH of venting hydrothermal fluids (e.g., Tivey, 1995; Tivey et al., 1999; Kawasumi and Chiba, 2017). However, these mineralogical indicators only distinguish between broad ranges of temperature and chemical composition. The trace element contents of black smoker chimney linings have the potential to provide additional information and constraints on hydrothermal fluid temperature and composition. This has been demonstrated for the Fe content of zinc sulfides such as sphalerite and wurtzite (e.g., Hannington et al., 1995; Kawasumi and Chiba, 2017). However, the homogeneity and concentrations of trace elements in these deposits at small spatial scales and the relationships between trace element concentrations and hydrothermal fluid temperature and chemistry are not well-known.

Investigations of trace elements in black smoker chimneys using electron microprobe have shown that the concentrations of many trace elements in the innermost lining of black smoker chimneys are near or below detection limits (e.g., Tivey et al., 1995; Tivey et al., 1999; Craddock, 2009). Laser-ablation inductively coupled plasma mass spectrometry (LA-ICPMS), proton microprobe (PIXE), and secondary ion mass spectrometry (SIMS), which offer significantly lower detection limits than electron microprobe, have also been used to investigate black smoker chimney linings (Butler and Nesbitt, 1999; Ryan, 2001; Layne et. al, 2005). However, these studies have been hampered by a lack of homogeneous sulfide reference materials and results are reported in relative rather than absolute quantities (Butler and Nesbitt, 1999; Layne et. al, 2005). More recently, some studies have measured trace elements in sulfide minerals using LA-ICPMS calibrated against pressed sulfide powder precipitates, sulfide sinters,

or synthetic glass standards, (Maslennikov et al., 2009; Wohlgemuth-Ueberwasser et al., 2011; Danyushevsky et al., 2011 and papers using these methods).

This study uses SIMS to examine the homogeneity and relative abundances of trace elements in black smoker chimney linings and investigate the intriguing possibility that mineral trace element contents reflect hydrothermal fluid temperature and chemistry, thereby providing trace element proxies of deposit formation conditions. The samples investigated in this study include black smoker chimney samples collected as sample pairs with the hydrothermal fluids that were venting through them at the time of collection. In this way, the trace element concentrations of black smoker chimney linings can be directly compared with the temperature, pH, Cl, H_2S, of the hydrothermal fluids from which they formed as well as host-rock lithology and geologic settings. While other minerals (e.g., wurtzite, pyrite) are present in the linings of some of these samples, the focus of this chapter is on the trace element contents of chalcopyrite, which is the most common lining mineral for black smoker chimneys venting high-temperature (> 250°C) fluids. Some additional samples have also been included for the purpose of establishing calibration curves by which to quantify SIMS measurements. To construct SIMS calibration curves on the basis of matrix-matched standards, grains of chalcopyrite (and cubanite) were picked from a subset of the samples measured by SIMS, then digested, and analyzed by ICP-MS against serial dilutions of external standard solutions. All black smoker chimney samples used for the construction of SIMS calibration curves exhibit monomineralic massive chalcopyrite linings.

2. SAMPLE DESCRIPTION

The black smoker chimney samples examined in this study were obtained from the dry storage repository of the Woods Hole Oceanographic Institution Seafloor Sample Laboratory (Table 1). Black smoker chimney samples were originally collected from active vent fields between 17°34'S and 17°37'S on the southern East Pacific Rise (AT-03, Leg 28), the Main Endeavour Field on the Juan de Fuca Ridge (AII-118, Leg 22; AT-03, Leg30), the Lucky Strike vent field on the Mid-Atlantic Ridge (DIVA1), the Beebe / Piccard vent field on the Mid-Cayman Rise (AT18-16), the Vienna Woods, Fenway, Satanic Mills, Roman Ruins, Roger's Ruins, Suzette, and North Su vent fields in the Manus Basin (MGLN06MV), and the Tahi Moana-1, ABE, Tu'i Malila and Mariner vent fields on the Eastern Lau Spreading Center (TN236; RR1507).

The black smoker chimney samples chosen for this study formed from fluids exhibiting a range of temperature (274°C to 395°C), pH (pH (at 25°C) = 2.3 – 4.4), and metal concentrations, located within vent fields from a variety of geologic settings including back-arc basins (Lau Basin and Manus Basin), and fast-spreading (southern East Pacific Rise), intermediate-spreading (Endeavour Segment of the Juan de Fuca Ridge) , slow-spreading (Lucky Strike), and ultraslow spreading (Mid-Cayman Rise) mid-ocean ridges. Hydrothermal fluid temperature, pH, and metal content to some extent covary, with higher temperature fluids usually more acidic and metal-rich (Seyfried and Seewald, 1990; Seyfried et al., 1991; Seyfried and Ding, 1995). However, samples from several of the vent fluids from Manus Basin from the Mariner vent field in the Lau Basin are additionally affected by the influence of acidic SO_2-rich magmatic volatiles, which lead to lower pH and higher metal contents at a given temperature (Reeves et al., 2011; Mottl et al., 2011). Conversely, vent fluids from the Main Endeavour Field on the Juan de Fuca Ridge exhibit

higher pH measured at 25°C because of buffering by sediment-derived NH_3 (Lilley et al., 1993), though the calculated pH at *in situ* temperatures (~350°C) is comparabile to other basalt-hosted, mid-ocean ridge vent fields (Tivey et al., 1999).

Samples used in this study include two from the Main Endeavour Field, one collected before and the other immediately after the seismic swarm and inferred event that occurred in 1999 (Johnson et al., 2000). This event led to a temporary decrease in the chlorinity and pH (at 25°C) and an increase in the temperature of hydrothermal fluids venting at the Main Endeavour Field (Seyfried et al., 2003). Sample Alv3474-3-1 examined in this study was collected from the Sully deposit in 1999 on cruise AT-03, Leg 30. Compared with other vents at the Main Endeavour Field, hydrothermal fluids from the Sully deposit collected in 1999 exhibit low chlorinity (Seyfried et al., 2003). Sample Alv1931 was collected from the Main Endeavour Field in 1987 on cruise A118, Leg 22 (J. Baross, Chief Scientist). The exact location of this sample and its relationship with venting fluids is unknown.

Table 1. (opposite)
Samples used in this study are from the southern East Pacific Rise (S. EPR), the Juan de Fuca Ridge (JdF), the Mid-Atlantic Ridge (MAR), the Mid-Cayman Rise (MCR), the Manus Spreading Center (MSC), the PACMANUS (PAC) and SuSu Knolls (SuSu) vent fields of the Eastern Manus Basin (EMB), and the Eastern Lau Spreading Center (ELSC). The innermost linings of these chimneys are composed of chalcopyrite (cp) ± cubanite (cb), wurtzite (wz), and/or pyrite (py). Samples used in the SIMS calibration curves are marked with an "X". Those that were attempted but ultimately not used are marked with an "O". The pH of hydrothermal vent fluids is the shipboard measurement taken at 25°C. Fluid pH at *in situ* temperatures is calculated with EQ3/6 software (Wolery, 1992). Concentrations of Cl and H_2S are both endmember concentrations extrapolated to zero-Mg. This follows the assumption that hydrothermal fluids contain negligible Mg (Von Damm et al., 1985). All sample and fluid names are as labeled in the original references and sample archive. References for fluid chemistry are as follows: S. EPR (K.L. Von Damm, unpublished data), MEF (Seyfried et al., 2003), MCR (McDermott, 2015), EMB (Reeves et al., 2011), ELSC (Mottl et al., 2011; Seewald, 2017). References from host-rock lithology are: S. EPR (Krasnov et al., 1997), Lucky Strike (Langmuir et al., 1997), MEF (Karsten et al., 1990), MCR (Elthon et al., 1995), EMB (Binns and Scott, 1993; Kamenetsky et al., 2001; Sinton et al, 2003), ELSC (Jenner et al., 1987; Frenzel et al., 1990; Vallier et al., 1991; Fouquet et al., 1993; Martinez and Taylor, 2002; Langmuir et al., 2006; Bézos et al., 2009; Escrig et al., 2009)

Table 1.

Sample ID	Vent Field	Lithology	Region	Lining Mineral	Callibration Curve	Fluid Pair	T (°C)	pH (at 25°C)	pH (in situ)	Cl (mmol/kg)	H_2S (mmol/kg)
Alv3299-6-1	17 34'S	basalt	S. EPR	cp	X	Hobbes	349	3.2		481	9.0
Alv3288-5-1a	17 37'S	basalt	S. EPR	cp		Simon	337	3.4		751	3.5
Alv3296-2-2a	17 37'S	basalt	S. EPR	cp	O	Maggie					
Alv3296-3	17 37'S	basalt	S. EPR	cp	X	Wally	314	3.4		752	6.5
Alv3296-5-1a	17 37'S	basalt	S. EPR	cp	O	Homer	347	3.3		591	3.7
Alv1931	Main Endeavour Field (pre-event)	E-MORB	JdF	cp	X						
Alv3474-3-1	Main Endeavour Field (post-event)	E-MORB	JdF	cp	X	Sully99	379	3.6	4.3	39.0	20
Alv3480-4	Main Endeavour Field (post-event)	E-MORB	JdF	cp							
DV1-5B	Lucky Strike	E-MORB	MAR	cp							
J2-613-16-R1	Beebe / Piccard	basalt	MCR	cb		BB5	395	3.3	5.0	351	0.0
J2-207-1-R1	Vienna Woods	basalt	MSC	cp/wz		VW1	282	4.4	5.1	691	1.4
J2-210-7-R2	Fenway	felsic	EMB, PAC	cp							
J2-216-16-R1	Fenway	felsic	EMB, PAC	cp		F3	358	2.7	3.9	562	18.8
J2-214-3-R1	Satanic Mills	felsic	EMB, PAC	cp	O	SM3	288	2.5	3.0	503	10.2
J2-208-1-R1	Roman Ruins	felsic	EMB, PAC	cp		RMR1	314	2.3	2.8	632	7.5
J2-213-6-R1	Roger's Ruins	felsic	EMB, PAC	cp		RGR1	320	2.7		648	3.6
J2-217-2-R1	Suzette	felsic	EMB, SuSu	cp	O	SZ1	303	3.8	4.2	626	1.8
J2-217-10-R1	Suzette	felsic	EMB, SuSu	cp		SZ2	274	3.6	4.0	684	1.8
J2-219-2-R1	Suzette	felsic	EMB, SuSu	cp							
J2-223-1-R1	North Su	felsic	EMB, SuSu	cp		NS3	300	3.4	3.9	673	3.4
J2-227-10-R1	North Su	felsic	EMB, SuSu	cp							
J2-450-3-R1	Tahi Moana 1	felsic	ELSC	cp/wz		TMo5	310	3.7	4.6	555	3.3
J2-449-5-R1	ABE	felsic	ELSC	cp/wz		A11	306	4.0	5.2	552	2.7
J2-449-6-R1	ABE	felsic	ELSC	cp/py		A10	317	3.9	5.1	543	3.9
J2-815-5-R1	ABE	felsic	ELSC	cp/wz		A16	300	4.0	5.2	546	3.7
J2-442-4-R2	Tu'i Malila	felsic	ELSC	cp/py		TM11	315	3.8	4.5	653	2.5
J2-819-4-R2	Tu'i Malila	felsic	ELSC	cp/wz		TM15	269	3.9		598	2.3
J2-437-3-R2	Mariner	felsic	ELSC	cp	X	MA9	338	2.3	3.2	541	8.9
J2-817-4-R2	Mariner	felsic	ELSC	cp		MA15	354	3.0	3.8	557	3.1

3. METHODS

In preparation for SIMS analysis, black smoker chimney samples were cut, mounted in epoxy, polished to 1 μm grit with diamond and/or alumina abrasives, and gold coated. For the purpose of generating SIMS calibration curves, a subset of the black smoker chimneys analyzed with SIMS were also picked for chemical digestion and analysis by ICP-MS against external reference standards (Fig. 1). To ensure that samples in this subset did not contain visible inclusions of minerals other than chalcopyrite, polished sections of the same samples were examined under a reflected light petrographic microscope. Picked grains were obtained from the innermost linings of black smoker chimneys (within < 1 mm from the main fluid conduit) by coarse crushing with an agate motor and pestle followed by careful picking with non-metal tools. Sample grains were then individually examined under a Leica Stereo Zoom 6 Photo microscope and transferred to a separate container in order to ensure minimally tarnished samples of purest possible chalcopyrite.

Figure 1. (On left) Photomicrograph of sample J2-207-1-R1 following SIMS measurements and removal of gold coating showing scale of SIMS spots relative to lining composed of intergrown chalcopyrite (yellow) and wurtzite (gray). The fluid conduit adjascent to chimney lining has been filled with epoxy. (On right) Non-metal tools are used to collect mineral grains from the inner lining of black smoker chimney sample J2-213-6-R1. Mineral grains were later picked to ensure purest possible chalcopyrite.

3.1. Secondary Ion Mass Spectrometry (SIMS)

Trace element analyses were obtained using the Cameca IMS 1280 ion microprobe located in the Northeast National Ion Microprobe Facility at the Woods Hole Oceanographic Institution. Secondary ion intensity ratios against $^{63}Cu^{16}O^{+}$ were measured for $^{59}Co^{+}$, $^{60}Ni^{+}$, $^{69}Ga^{+}$, $^{109}Ag^{+}$, $^{113}In^{+}$, and $^{115}In^{+}$. The intensity of $^{54}Fe^{16}O^{+}$ varied more than $^{63}Cu^{16}O^{+}$ and $^{63}Cu^{16}O^{+}$ was selected as a normalizing ratio. Detection limits were set at three standard deviations above the mean secondary ion intensity measured on background mass 54.7. This was evaluated to be 0.25 counts per second (cps) or 5×10^{-5} cps / cps $^{63}Cu^{16}O^{+}$. Quantitative determination limits were set at ten standard deviations above the mean secondary ion intensity measured on the background mass 54.7. This was evaluated to be 0.6 counts per second (cps) or 1.2×10^{-4} cps / cps $^{63}Cu^{16}O^{+}$. Machine settings, typical secondary ion intensities and associated errors for $^{63}Cu^{16}O^{+}$, detection limits, and determination limits are listed in Table 2. Typical mass resolving power was ~10,000. Scans of the relevant masses and potential interferences at this resolution are shown in Figure 2.

Table 2. Machine settings, typical secondary ion intensities, and associated errors for secondary ion mass spectrometry (SIMS) analyses of Co, Ni, Ga, Ag, and In in chalcopyrite. cps = counts per second.

Source	duoplasmatron O_2-
Primary Beam Current	10 nA
Secondary Accelerating Voltage	10 kV
Energy Offset	none
Field Aperture	22 x 22 µm
Raster Area	20 x 20 µm
Spot Diameter	40 µm
Mass Resolving Power	~10,000
Number of Cycles	10
Pre-sputter time	300 s
Integration Time, Trace elements and background	10 s
Integration Time ($^{63}Cu^{16}O$, $^{54}Fe^{16}O$, $^{64}Zn^{16}O$)	5 s
Secondary Ion Intensity on $^{63}Cu^{16}O$ (1000 cps)	5 to 10
Relative Standard Deviation of Ion Intensity on $^{63}Cu^{16}O$	10%
Counting Errors on $^{63}Cu^{16}O$ (%)	0.5%
Secondary Ion Intensity on background mass 54.7 (cps)	< 0.1
Detection Limit (background + 3 × standard deviation)	0.25 cps (5×10^{-5} cps / $^{63}Cu^{16}O$ cps)
Detection Limit (background + 10 × standard deviation)	0.6 cps (1.2×10^{-4} cps / $^{63}Cu^{16}O$ cps)

Figure 2. Plots of mass vs. secondary ion intensity over the relevant mass intervals for $^{59}Co^{+}$, $^{60}Ni^{+}$, $^{69}Ga^{+}$, $^{63}Cu^{16}O^{+}$, $^{109}Ag^{+}$, $^{113}In^{+}$, and $^{115}In^{+}$ at a mass resolving power of ~10,000 as measured on chalcopyrite in black smoker chimney sample Alv3299-6-1 from the southern East Pacific Rise . Actual masses of target ion and those of potential interferences are also identified (Berglund and Wieser, 2011).

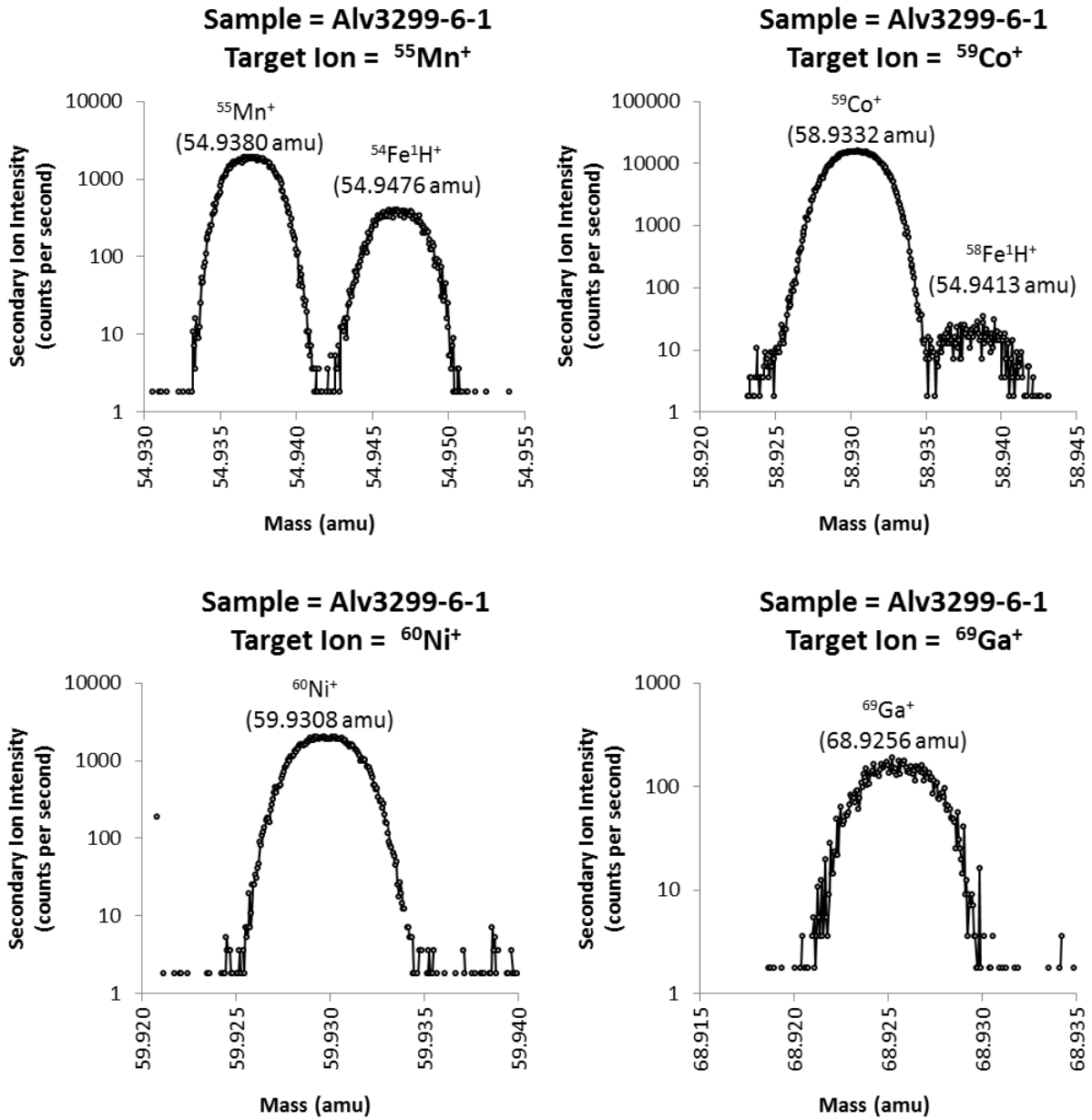

Figure 2 cont.

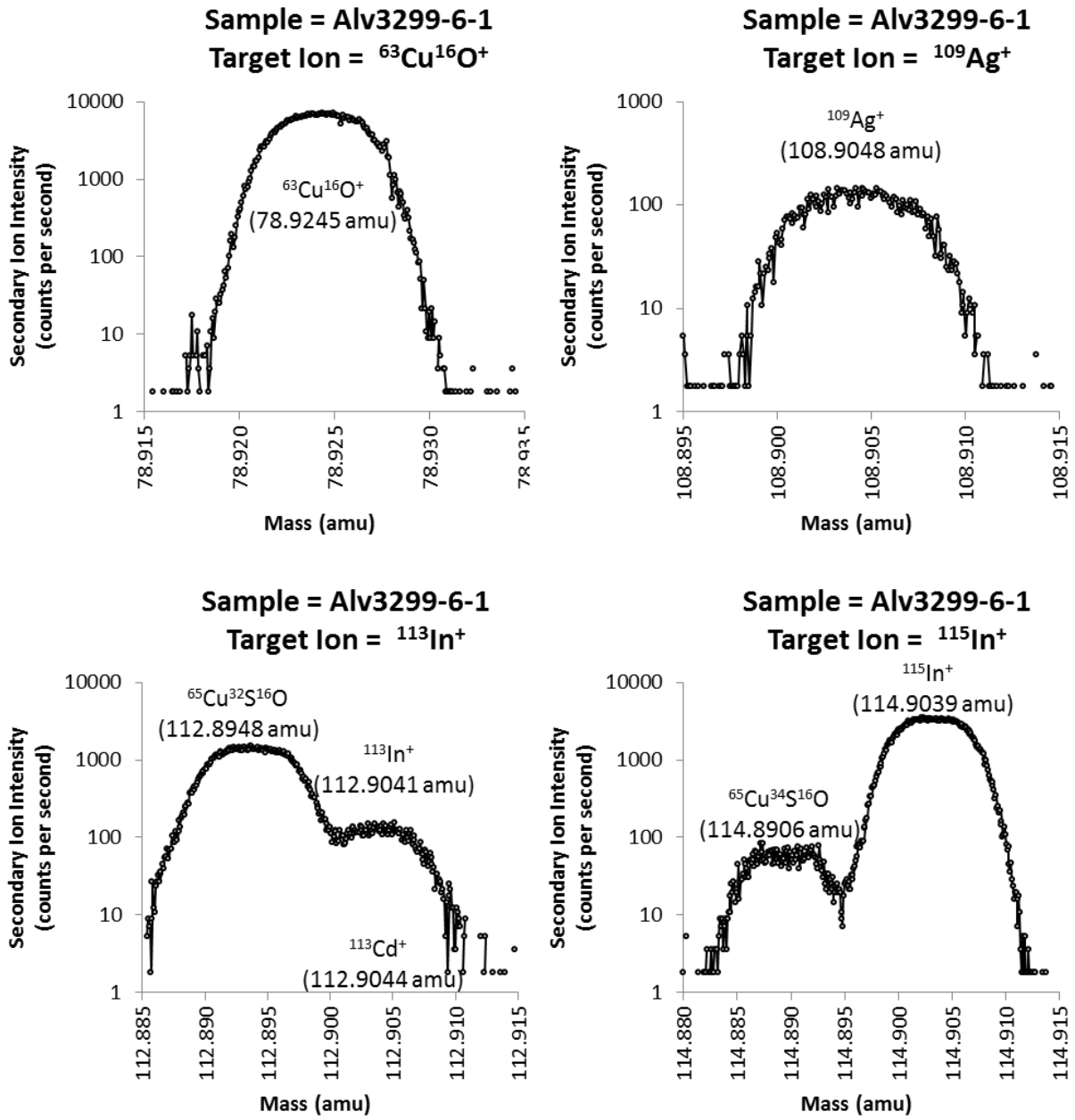

During some sessions, In was measured on mass 113 rather than mass 115. Potential mass interferences between Cd and In on mass 113 could not be resolved. However, these peaks are confidently identified as $^{113}In^{+}$ (largely free of $^{113}Cd^{+}$ interference) because the ratio of intensities measured on these two peaks for multiple samples is identical, within error, to the natural ^{113}In / ^{115}In isotopic abundance ratio (^{113}In / ^{115}In = 0.043406, (Berglund and Wieser, 2011); data used for regression provided in Supplementary Table S1). For the purposes of reporting results in this chapter and making comparisons between samples, measurements of In on mass 113 are reposted as estimated counts on mass 115. Measurements of $^{75}As^{+}$ and $^{74}Ge^{+}$ were also conducted during some sessions. However, $^{75}As^{+}$ was found to be heterogeneous in chalcopyrite and ion intensities for $^{74}Ge^{+}$ were below detection limits.

Measurements of $^{54}Fe^{16}O^{+}$ and $^{64}Zn^{16}O^{+}$ were done to monitor for possible wurtzite and/or pyrite inclusions. Likely ablation of mineral inclusions was particularly notable in black smoker chimney linings composed of intergrown chalcopyrite and wurtzite and spots with anomalously high $^{64}Zn^{16}O^{+}$ intensities were removed from the dataset prior to further analysis.

For each black smoker chimney sample, sample means and standard errors were calculated over the total number of measurements on that sample in each analysis session. Reported trace element ratios obtained during different sessions were then normalized by reference to common samples analyzed during multiple sessions (Fig. 3A and 3B). During each session, a black smoker chimney sample shown to be homogeneous with respect to several of the trace elements of interest was used as a provisional standard to monitor machine stability using the sample-standard bracketing method (typically five sample spots bracketed by two standard spots). The standard error of counts ratios measured on these provisional standards during a given session was generally < 15% of the mean counts ratio.

Figure 3. Repeat measurements of the same elements in the same samples during multiple sessions allows for cross-calibration and normalization of results between sessions. Figure 1A compares the results for Co, Ag, and In for common samples analyzed during the October, 2016 (x-axis) and December, 2015 (y-axis) sessions (Supplementary Table S2). Figure 1B compares the results for Co, Ni, and Ga for common samples analyzed during the September, 2016 (x-axis) and October, 2016 (y-axis) sessions (Supplementary Table S3).

Figure 3A

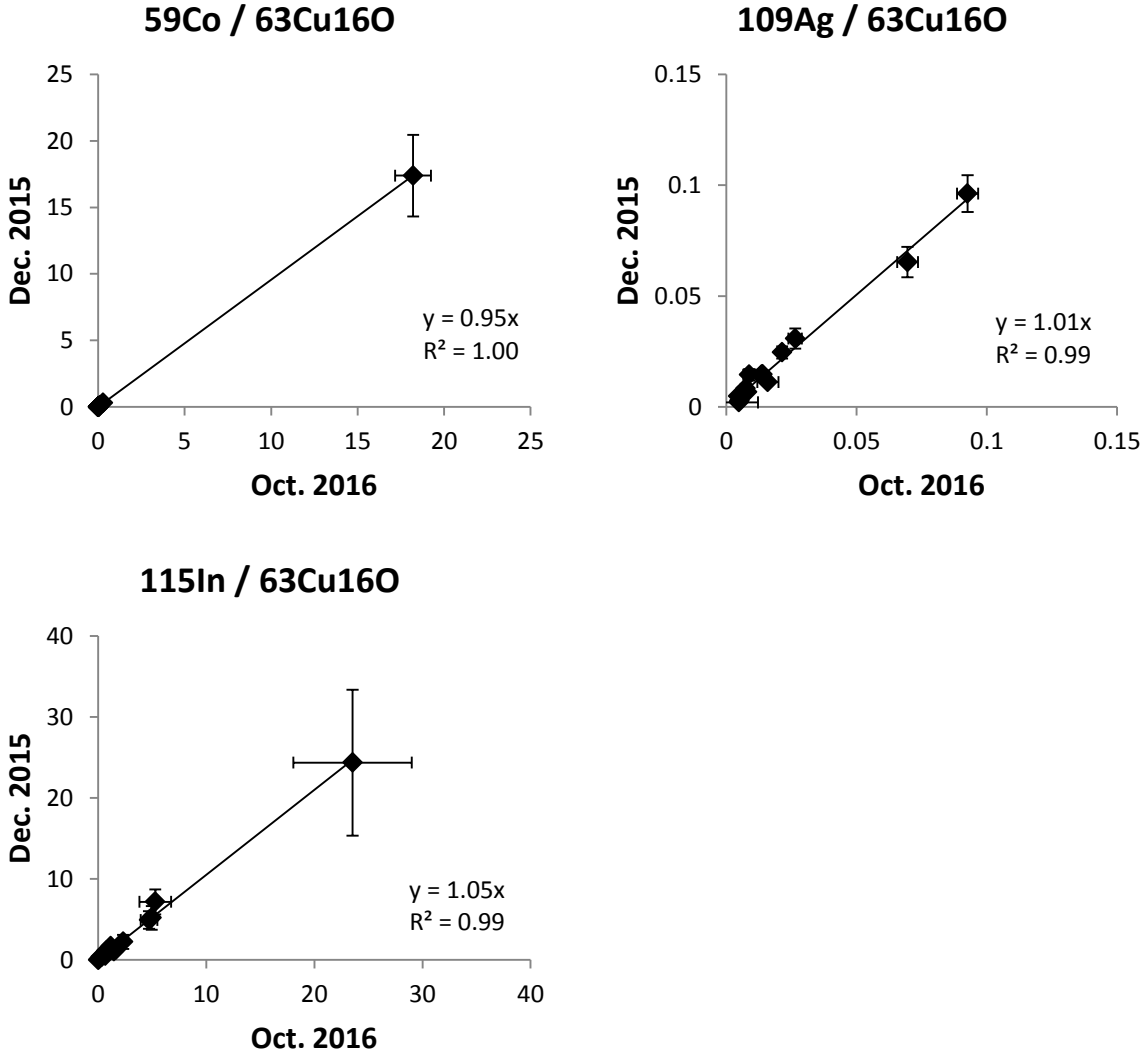

Figure 3B

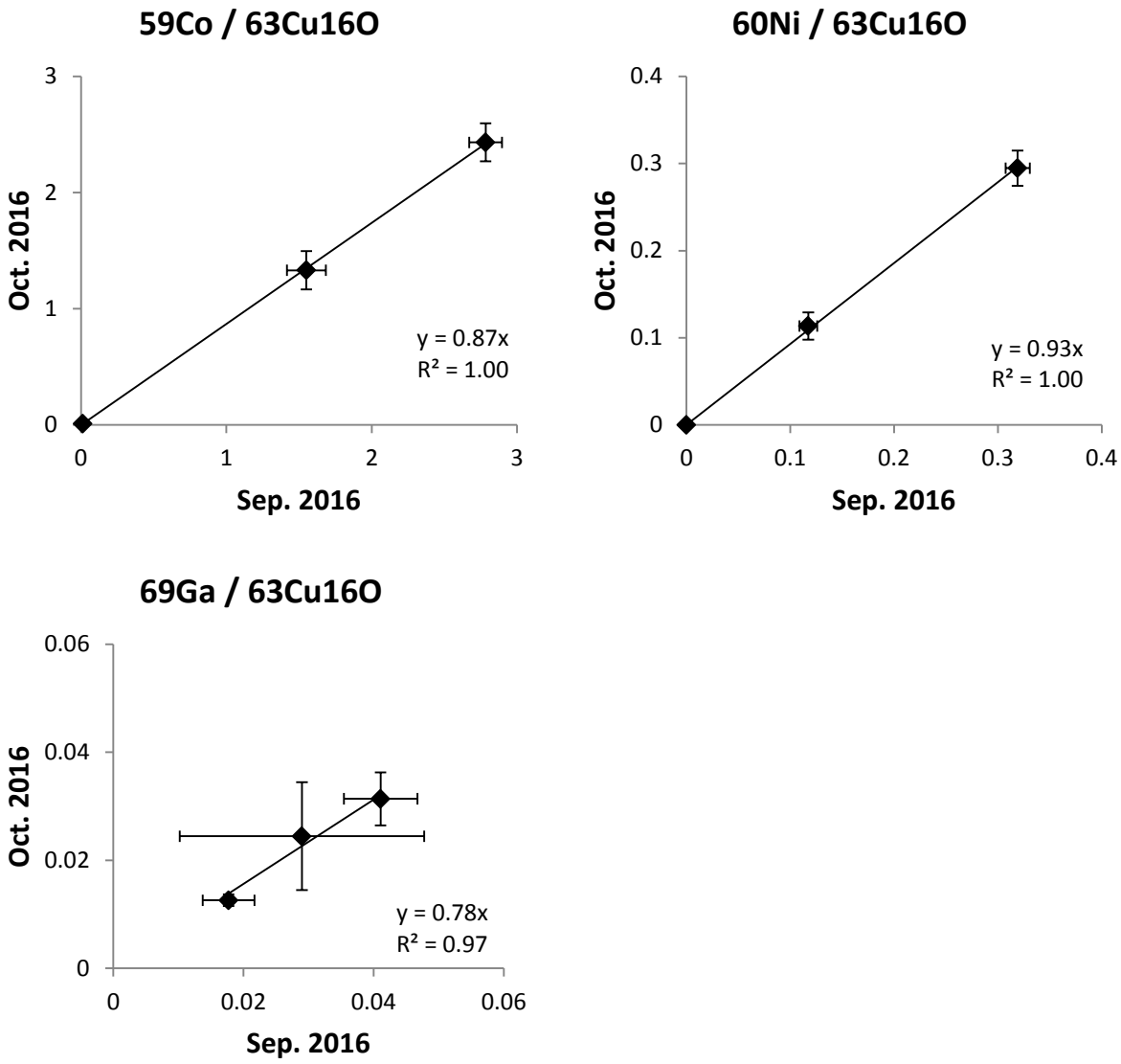
59Co / 63Cu16O
Oct. 2016
Sep. 2016
y = 0.87x
R² = 1.00
60Ni / 63Cu16O
Oct. 2016
Sep. 2016
y = 0.93x
R² = 1.00
69Ga / 63Cu16O
Oct. 2016
Sep. 2016
y = 0.78x
R² = 0.97

3.2. Digestion and ICP-MS Analysis of Picked Chalcopyrite Grains

Immediately after weighing, samples of picked chalcopyrite grains were digested in reverse *aqua regia* (1 part 12 N HCl : 3 parts 16 N HNO_3, by volume) in acid-cleaned Savillex digestion vials and diluted in 30 mL of 5 wt.% HNO_3 before being transferred to Teflon-coated bottles. All reagents are analytical-grade Optima® brand (Thermo Fisher Scientific, Waltham, USA). Milli-Q water was obtained from the Plasma Mass Spectrometry Facility at the Woods Hole Oceanographic Institution.

Major and trace element analyses of digested chalcopyrite (and cubanite) picks were obtained using the Element 2 (Thermo Fisher Scientific, Waltham, USA) in the Plasma Mass Spectrometry Facility at the Woods Hole Oceanographic Institution. Sample solutions were prepared for measurement by ICP-MS by further diluting aliquots of the 30 mL sample dilutions with 5 wt. % HNO3 containing 1 ng/g Sc and Y as internal spikes to a strength of ~2 μg/g Cu for trace element analyses and a strength of ~50 ng/g Cu for major element analyses. Samples were measured against serial dilutions of Specpure® plasma solutions (Sb, As, Ba, Bi, Cd, Ca, Cr, Co, Cu, Ga, Ge, Au, Fe, In, Pb, Mn, Mo, Ni, Se, Si, Ag, Sr, S, Te, Tl, Sn, V, Zn) in 5 wt% analytical grade Optima® brand HNO_3 likewise containing 1 ng/g Sc and Y as internal spikes. All solution masses were weighed to a precision of 0.1 mg. Mass and machine settings for ICP-MS analyses were: Sc45, Y89, Ba137, Ba138, Pb208, Bi209 (low resolution = 300) ; Sc45, Cr52, Mn55, Fe56, Co59, Ni60, Cu63, Cu65, Zn66, Zn68, Ga69, Y89, Mo96, Ag107, Ag109, In115, Sn118, Ba137, Ba138, Au197, Bi209 (medium resolution = 4000). Underlining indicates elements used as internal spikes. The Element 2 was fitted with Ni cones.

The creation of two standard dilution series allowed for estimation of ICP-MS analytical errors by examining the reproducibility of measurements between the two series. These errors

are a function of element concentration in the measured sample solution and the dilution factor of the measured sample solution relative to the original sample. Analytical errors can also be estimated by comparing repeat measurements of the same sample solution. These errors are similar to those calculated by considering differences between measurements of the two standard solutions series and are on the order of 10% for most measurements.

3.3. Principal Component Analysis

To identify the major compositional variables that distinguish black smoker chimneys from different vent fields as well as covariances between different trace elements, principal components and correlations coefficients of the log-transformed SIMS count ratios were calculated using the MATLAB code pca. In order to investigate whether or not these compositional variations might be related to certain hydrothermal fluid parameters, principal components and correlation coefficients were also calculated for an expanded dataset that included the reciprocal absolute temperature (1/K), pH (at 25°C), and log-transformed endmember concentrations of Cl and H_2S for all black smoker chimney samples collected with fluid sample pairs.

4. RESULTS

The small spot size and low detection limits of SIMS enable measurements of trace elements abundances in chalcopyrite present along the innermost linings of black smoker chimney linings, i.e. grains that most likely reflect the chemical and physical parameters of collected hydrothermal fluid sample pairs. By obtaining multiple spots on a single sample, it is possible to evaluate the abundance and homogeneity of trace elements in each sample. For the

purposes of this paper, the abundance and homogeneity of trace elements in each sample is approximated by the means and standard errors (1σ) of SIMS analyses reported as the ratio of counts on each trace element to counts on $^{63}Cu^{16}O$.

4.1. Abundance of Trace Elements in Black Smoker Chimney Linings

Analyses of Co, Ag, and In were conducted using SIMS on 29 black smoker samples of which 22 were also analyzed for Ni and Ga. Trace element counts ratios are above detection limits for most samples and elements and span many orders of magnitude for each element (Fig. 4A – 4F).

Count ratios of $^{59}Co/^{63}Cu^{16}O$ range six orders of magnitude, from 1.2×10^{-5} to 1.7×10^{1}, while count ratios of $^{60}Ni/^{63}Cu^{16}O$ range five orders of magnitude, from 1.4×10^{-5} to 1.3×10^{0}. Count ratios of $^{59}Co/^{63}Cu^{16}O$ and $^{60}Ni/^{63}Cu^{16}O$ are generally higher in black smoker chimney samples from basalt-hosted vent fields than in those from felsic-hosted back-arc vent fields in the Lau and Manus Basins with the exception of samples from SuSu Knolls, which exhibit intermediate Co and Ni concentrations. Additionally, the abundances of Co and Ni covary in basalt-hosted and SuSu Knolls samples, with the highest concentrations of both Co and Ni present in sample J2-613-16-R1 from the Beebe / Piccard vent field on the Mid-Cayman Rise (Fig. 4B, 4C). Count ratios of Co and Ni are low in samples from felsic-hosted systems other than SuSu Knolls and do not covary (Fig. 5A). Arranged in descending order concentrations of Co and Ni are: Mid-Cayman Rise > southern East Pacific Rise ~ Main Endeavour Field (post-event) > SuSu Knolls > Eastern Lau Spreading Center ~ Manus Spreading Center ~ Eastern Manus Basin ~ Main Endeavour Field (pre-event).

Count ratios of ^{55}Mn /$^{63}Cu^{16}O$, ^{69}Ga /$^{63}Cu^{16}O$ and ^{115}In/$^{63}Cu^{16}O$ each cover 2-3 orders of magnitude with ^{55}Mn /$^{63}Cu^{16}O$ ranging from 9.4×10^{-4} to 6.3×10^{-1}, ^{69}Ga /$^{63}Cu^{16}O$ ranging from 1.0×10^{-2} to 2.6×10^{0} and ^{115}In/$^{63}Cu^{16}O$ ranging from 1.3×10^{-2} to 2.5×10^{1}. Count ratios of ^{109}Ag /$^{63}Cu^{16}O$ cover less than two orders of magnitude and range from 1.5×10^{-3} to 9.6×10^{-2}. The abundances of Ga and In weakly covary and Ga is typically more abundant in black smoker chimney linings from felsic-hosted vent systems (Fig. 5B).Count ratios of Mn, Ag, and In exhibit no obvious association with the lithology of host rocks or geologic settings.

4.2. Homogeneity of Trace Elements in Black Smoker Chimney Linings

The homogeneity of trace elements in black smoker chimney linings was evaluated by calculating the standard error of the SIMS count ratios, reported as a percentage of the mean counts ratio. The extent of trace element homogeneity varies widely between samples. However, relative standard errors (1σ) for the majority of samples lie between 5% and 25% for Mn, Co, Ni, and Ag and between 5% and 50% for Ga and In (Fig. 6). The median relative standard errors for all black smoker chimney samples examined in this study are: Mn (21%), Co (40%), Ni (14%), Ga (29%), Ag (24%), and In (35%). For Co, relative standard errors negatively correlate with the ^{59}Co/$^{63}Cu^{16}O$ counts ratio. If only the 12 samples containing > 1 μg/g Co are considered, the median relative standard error for Co is reduced from 40% over the entire sample set to just 13% (conversion from SIMS counts ratios to concentration is described in Section 4. 3.). Relative standard errors of other trace elements do not correlate with counts ratios.

Figure 4. Means and standard errors (1σ) of SIMS measurements for each sample over the number of spots indicated ("n = [number of spots]" or "NM" if not measured) reported as a ratio of counts per second (cps) measured on the target mass to counts per second measured on $^{63}Cu^{16}O$ during the same cycle: (A) ^{55}Mn / $^{63}Cu^{16}O$, (B) ^{59}Co / $^{63}Cu^{16}O$, (C) ^{60}Ni / $^{63}Cu^{16}O$, (D) ^{69}Ga / $^{63}Cu^{16}O$, (E) ^{109}Ag / $^{63}Cu^{16}O$, (F) ^{115}In / $^{63}Cu^{16}O$ (Data in Supplementary Table S4). Values are displayed on a log scale. Detection limits (5×10^{-5} cps / cps $^{63}Cu^{16}O$) and determination limits (1.2×10^{-4} cps / cps $^{63}Cu^{16}O$) as determined on the background mass, 54.7 are also marked. Samples and values used for SIMS calibration curves are shaded in gray.

Figure 4A

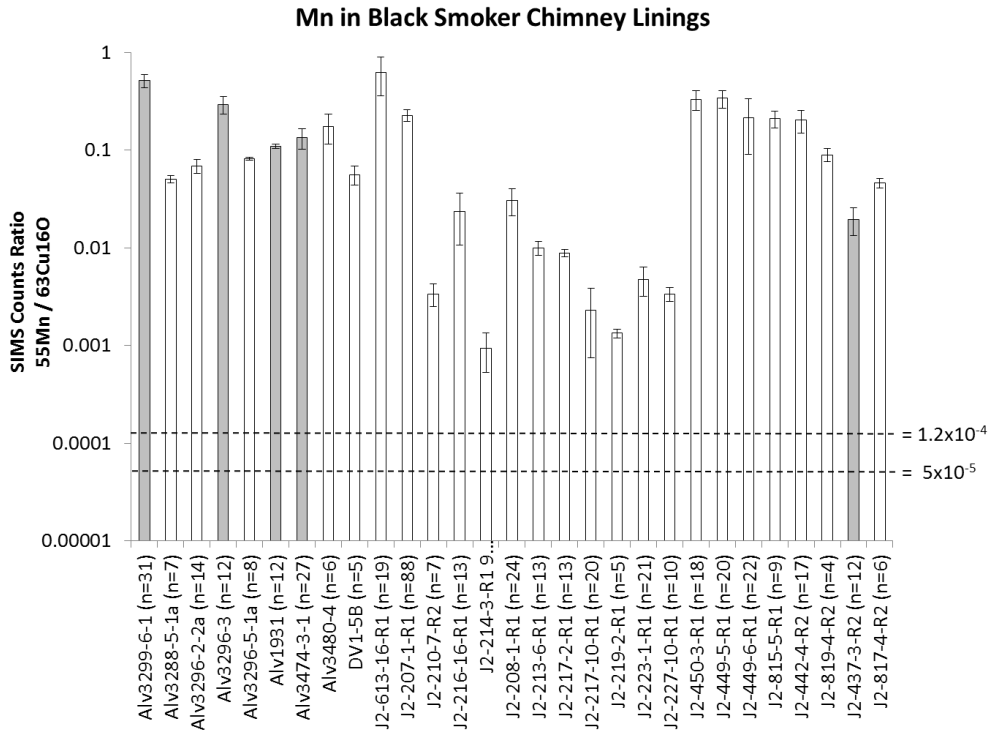

Figure 4B

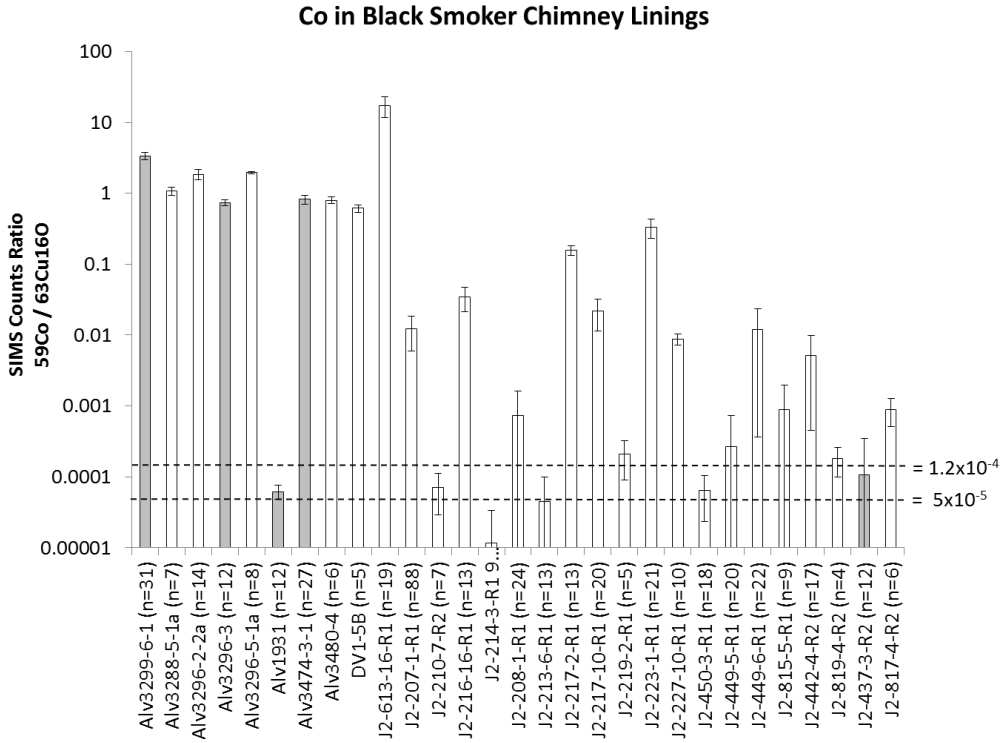

Figure 4C

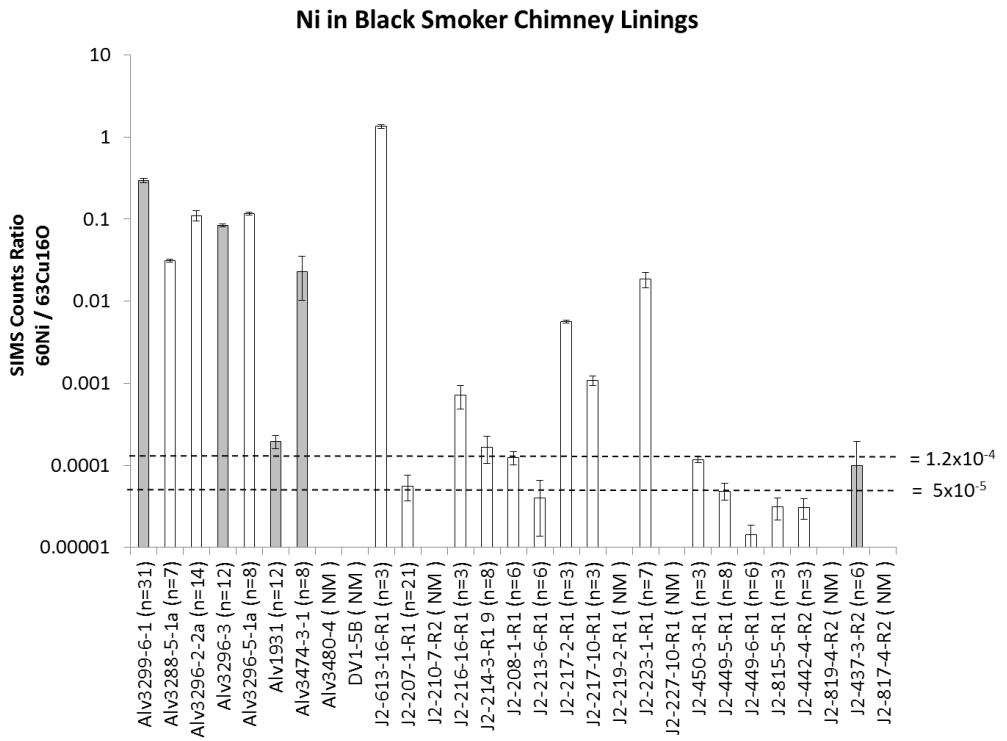

Figure 4D

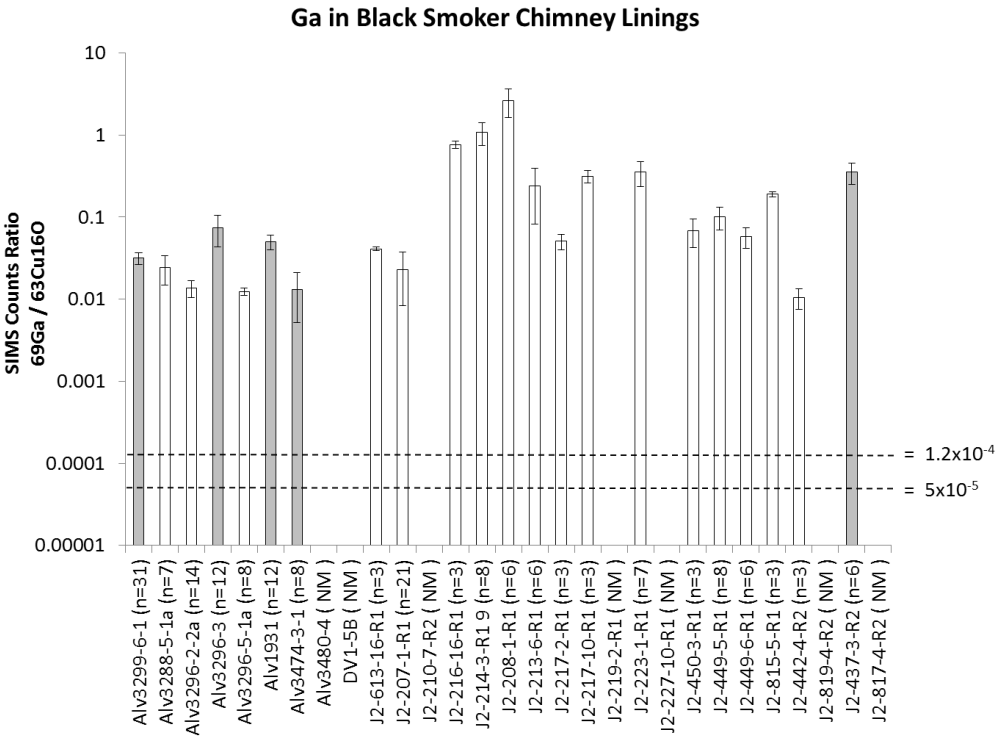

Figure 4E

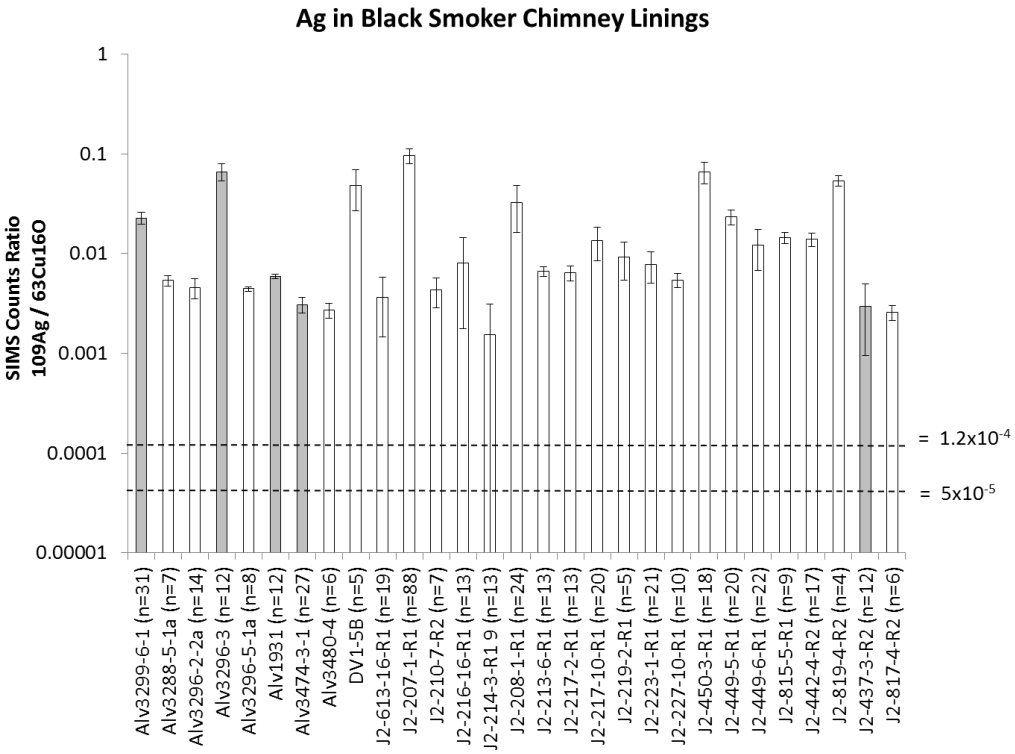

Figure 4F

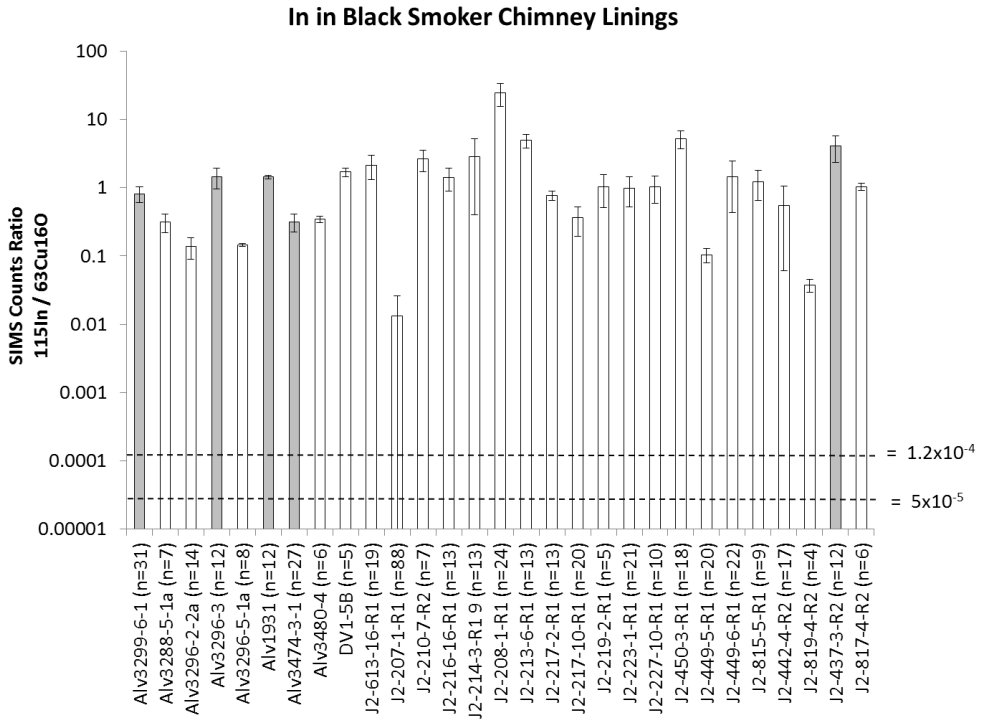
In in Black Smoker Chimney Linings
SIMS Counts Ratio
115In / 63Cu16O
100
10
1
0.1
0.01
0.001
0.0001
0.00001
= 1.2x10-4
= 5x10-5
Alv3299-6-1 (n=31)
Alv3288-5-1a (n=7)
Alv3296-2-2a (n=14)
Alv3296-3 (n=12)
Alv3296-5-1a (n=8)
Alv1931 (n=12)
Alv3474-3-1 (n=27)
Alv3480-4 (n=6)
DV1-5B (n=5)
J2-613-16-R1 (n=19)
J2-207-1-R1 (n=88)
J2-210-7-R2 (n=7)
J2-216-16-R1 (n=13)
J2-214-3-R1 9 (n=13)
J2-208-1-R1 (n=24)
J2-213-6-R1 (n=13)
J2-217-2-R1 (n=13)
J2-217-10-R1 (n=20)
J2-219-2-R1 (n=5)
J2-223-1-R1 (n=21)
J2-227-10-R1 (n=10)
J2-450-3-R1 (n=18)
J2-449-5-R1 (n=20)
J2-449-6-R1 (n=22)
J2-815-5-R1 (n=9)
J2-442-4-R2 (n=17)
J2-819-4-R2 (n=4)
J2-437-3-R2 (n=12)
J2-817-4-R2 (n=6)

Figure 5. Bivariate plots on a log vs. log scale showing comparison of SIMS measurements for (A) ^{59}Co / $^{63}Cu^{16}O$ vs. ^{60}Ni / $^{63}Cu^{16}O$ and (B) ^{69}Ga / $^{63}Cu^{16}O$ vs. ^{115}In / $^{63}Cu^{16}O$.

Figure 5A

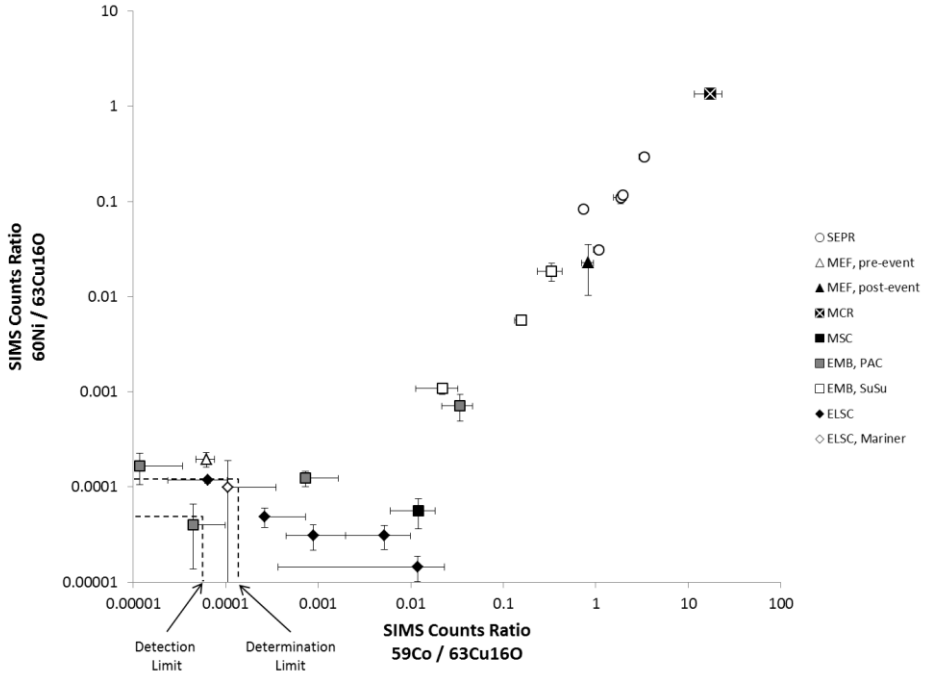

Figure 5B

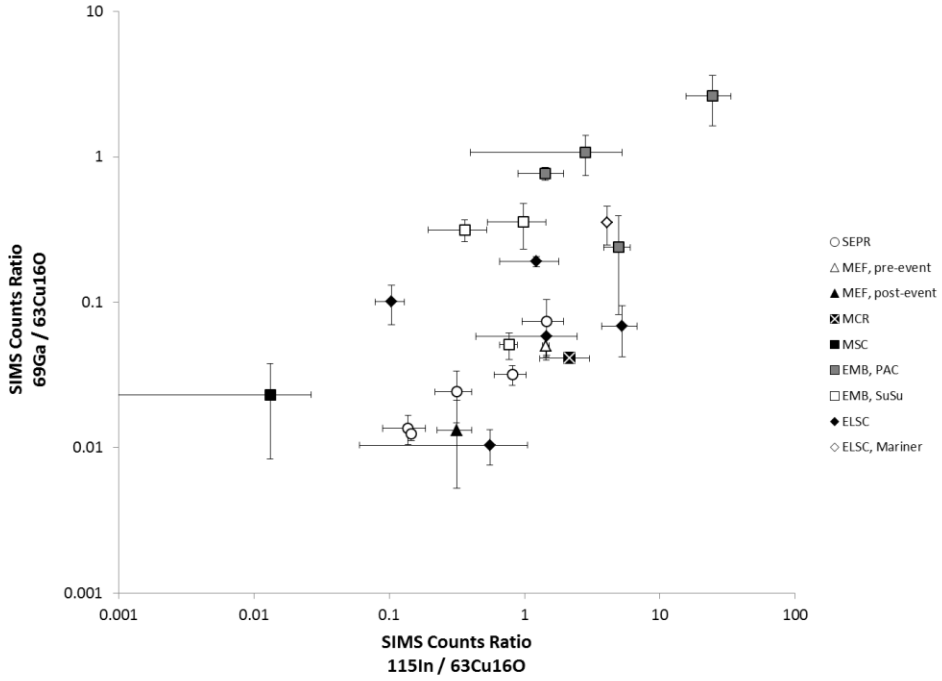

Figure 6. Histograms of the relative standard errors (1σ) of SIMS measurements reported as a percentage of the mean. For Co, samples are separated between those containing >1 μg/g Co (white) and those containing < 1 μg/g Co (gray).

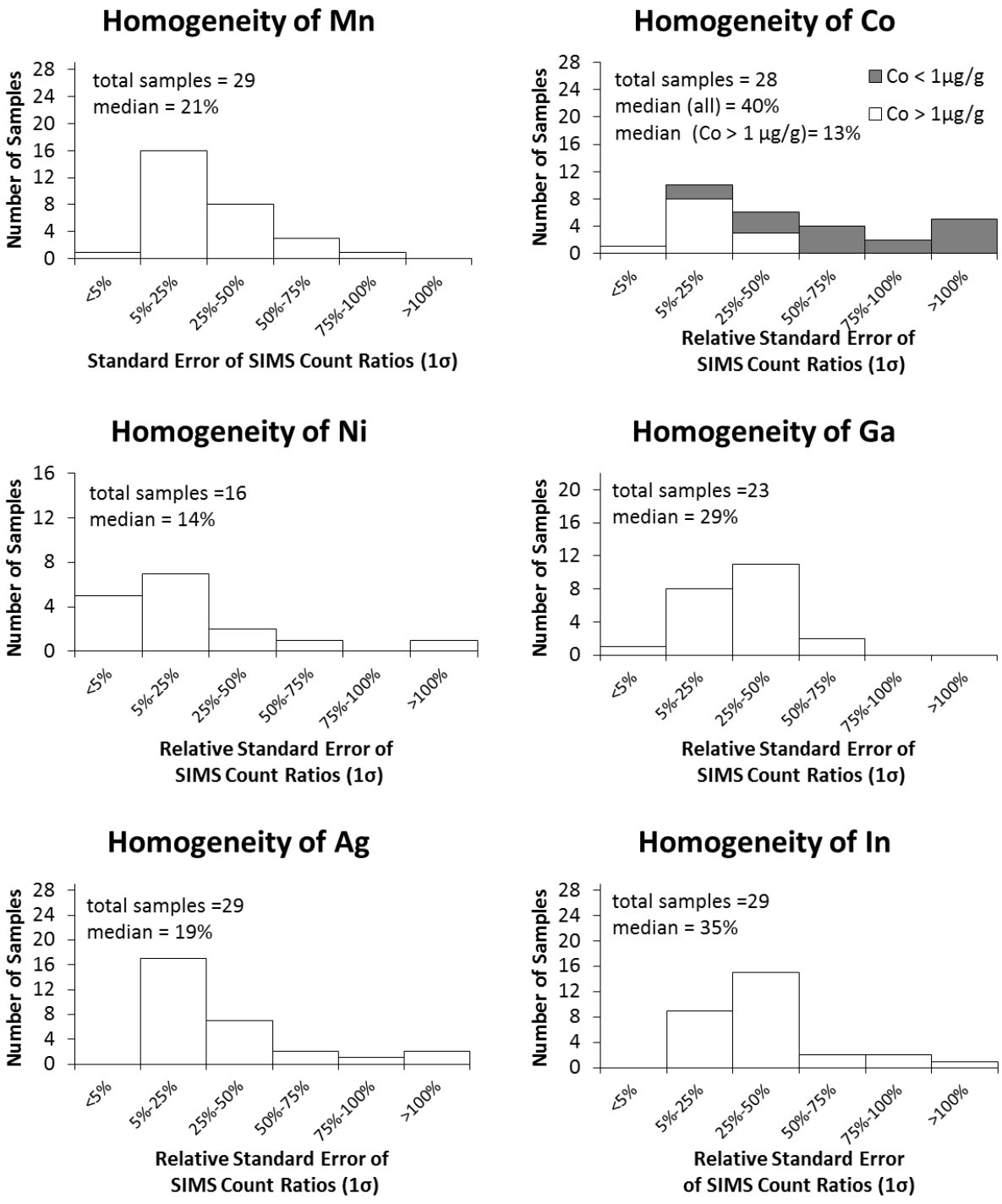

4.3. Trace Elements in Chalcopyrite Lining Picks

Analyses of major element concentrations in picked chalcopyrite and cubanite grains from the innermost linings of black smoker chimneys measured by ICP-MS exhibit overall reproducibility. Total recovery ranges between 86 ± 6 wt% and 108 ± 5 wt% with the exception of one sample with low recovery (63 ± 3 wt %; see Table 2). Analyses of other elements in this sample (e.g., Ca, Ba, Si) are not anomalous. Following the assumption that differences in mass balance are primarily caused by the inefficient or unrecorded transfer of small sample grains between different laboratory containers, reported major and trace element mass fractions have been normalized to 100% recovery.

In general, concentrations are consistent between different picks of the same sample and different digestions of the same pick (Table 2). Trace element concentrations do vary widely between samples of different black smoker chimneys both within a given vent field and between vent fields. Ranges of trace element concentrations in picked grains of chalcopyrite and cubanite analyzed by solution ICP-MS are: Mn (6 – 43 μg/g) Co (0.3 μg/g – 150 μg/g), Ni (30 μg/g – 1120 μg/g), Ga (0.3 μg/g – 40.4 μg/g), Ag (100 μg/g – 2900 μg/g), In (5.9 μg/g – 77 μg/g).

Reported concentrations of Ag include a correction to account for loss of Ag in a concentration stock solution of mixed element standards during storage. Thus, absolute values should be taken with caution. Briefly, a discrepancy was observed between the Ag calibration curves generated by two different dilution series of the same concentrated stock solution of mixed element standards created several months apart. No discrepancy was observed in the calibration curves of other elements or the calibration curve of the earlier created dilution series measured during two different analysis sessions. Comparison of the two calibration curves was indicative of a loss of Ag in the concentrated stock solution with Ag photoreduction being the

most likely cause. Measurements of Ag have been adjusted to correct for the discrepancy between the two calibration curves and to reflect Ag concentrations calibrated against the earlier created dilution series (i.e., the one least affected by possible Ag photoreduction). Further details are presented in Appendix A.

4.4. Trace Element Concentrations of Black Smoker Chimneys

By combining measurements of Co, Ni, Ga, Ag, and In obtained by SIMS and those obtained by ICP-MS, it is possible to develop SIMS calibration curves (Fig. 7A-F). A calibration curve for Mn was also attempted, but was not successful (Fig. 7A). Samples chosen for the construction of SIMS calibration curves are indicated in Table 1 and Figures 4A – 4F. SIMS analyses and ICP-MS analyses of multiple picks from these samples yield consistent results. An exception to this rule is sample J2-437-3-R2, which was included in order to extend the Ga and In calibration curves to higher concentrations despite the analysis of only one aliquot of picked grains.

Calibration curves for the full range of trace element concentrations are drawn for Co, Ni, and Ag by least squares linear regression (Figures, 7B, 7C, 7E). Calibration curves can also be drawn for Ga and In, albeit only within a limited concentration range (Figures 7D, 7F). By using these calibration curves, it is then possible to convert SIMS count ratios to concentrations of Co, Ni, Ga, Ag, and In (Fig. 7B – 7F). Reported uncertainties of trace element concentrations reflect only the uncertainties derived from multiple SIMS analysis and do not reflect the additional uncertainties associated with the slopes of the calibration curves. The reasoning behind this presentation is to maintain focus on the extent of natural variability of trace element concentrations within each sample rather than propagating artifacts of the analysis. Uncertainties

in the slopes of the calibration curves were estimated by serially removing one sample from the dataset and recalculating the regression line. As a percent of the originally calculated calibration curve, the range of slopes for the recalculated calibration curves is: 4.6% for Co, 4.4% for Ni, 4.1% for Ga, 7.9% for Ag, and 33.5% for In. The slope of the In calibration curve is especially sensitive to sample J2-437-3-R2, which defines the high-concentration end of the calibration curve. Otherwise, the uncertainty in the slope of the In calibration curve is limited to 5.7%.

Using these calibration curves, the trace element contents of black smoker chimneys measured by SIMS can be converted to concentration units. The trace element contents of the black smoker chimney samples investigated here cover the following ranges: Co (below detection limit (bdl) to 760 μg/g), Ni (bdl – 480 μg/g), Ga (bdl – 48 μg/g), Ag (60 μg/g – 3800 μg/g), In (bdl – 270 μg/g). Detection limits for Ni (20 μg/g) are high relative to other elements and are caused by uncertainties in the concentrations of Ni measured by ICP-MS for picked grains.

Table 3. Results of ICP-MS analyses of picked chalcopyrite grains from selected black smoker chimney linings. Uncertainties in sample mass are estimated by propagation of weighing errors. Uncertainties in element concentrations estimated by comparison between two sets of standard solutions and by comparison of repeat measurements of the same sample solution. Samples chosen for inclusion in the SIMS calibration curves are marked in bold. Levels of tarnish indicates as "none" for no visible tarnish, "minor" for dark yellow or brown tarnish, and "tarnish" for blue or black tarnish.

Sample	Tarnish	Mass (mg)	Total (wt%)	Cu (wt%)	Fe (wt%)	Zn (wt%)	S (wt%)
3296-3 pick A1	minor	11.88 ± 0.05	86 ± 6	32 ± 3	40 ± 5	0.17 ± 0.05	28 ± 3
3296-3 pick A2	minor	8.81 ± 0.02	96 ± 5	28 ± 2	35 ± 4	0.13 ± 0.04	37 ± 3
3296-3 pick B1	minor	14.63 ± 0.03	89 ± 5	30 ± 2	36 ± 5	0.13 ± 0.05	34 ± 3
3296-3 pick B2	minor	13.04 ± 0.03	95 ± 6	35 ± 3	35 ± 5	0.12 ± 0.04	30 ± 3
3299-6-1 pick A	none	20.01 ± 0.03	90 ± 5	31 ± 2	38 ± 4	0.44 ± 0.05	31 ± 3
3299-6-1 pick B1	none	7.75 ± 0.08	95 ± 6	30 ± 2	37 ± 5	0.37 ± 0.22	33 ± 3
3299-6-1 pick B2	none	10.07 ± 0.03	93 ± 5	27 ± 2	35 ± 5	0.07 ± 0.04	38 ± 3
3299-6-1 pick C	none	4.60 ± 0.04	99 ± 6	30 ± 2	37 ± 5	0.7 ± 0.3	32 ± 3
Alv1931 pick A1	none	3.68 ± 0.05	106 ± 7	31 ± 2	36 ± 5	0.3 ± 0.3	33 ± 3
Alv1931 pick A2	none	5.10 ± 0.10	95 ± 6	29 ± 2	34 ± 5	0.09 ± 0.03	37 ± 3
Alv1931 pick A3	none	16.02 ± 0.03	63 ± 3	31 ± 2	36 ± 3	0.07 ± 0.03	34 ± 2
Alv3474-3-1 pick A1	none	10.5 ± 0.4	99 ± 5	28 ± 2	42 ± 4	bdl ± bdl	30 ± 3
Alv3474-3-1 pick A2	none	15.25 ± 0.04	91 ± 5	30 ± 2	36 ± 5	bdl ± bdl	35 ± 3
Alv3474-3-1 pick A3	none	11.17 ± 0.04	108 ± 5	25 ± 2	48 ± 4	bdl ± bdl	27 ± 2
J2-213-6-R1 pick A	minor	18.54 ± 0.06	90 ± 5	30 ± 2	36 ± 5	bdl ± bdl	33 ± 3
J2-214-3-R1 pick A	tarnish	6.76 ± 0.04	90 ± 5	30 ± 2	36 ± 5	bdl ± bdl	34 ± 3
J2-214-3-R1 pick C	tarnish	4.78 ± 0.10	97 ± 5	31 ± 2	35 ± 4	1.0 ± 0.3	34 ± 3
J2-437-3-R2 pick A	minor	2.0 ± 0.20	90 ± 5	29 ± 2	40 ± 5	0.04 ± 0.01	31 ± 3

Sample	Mn (μg/g)	Co (μg/g)	Ni (μg/g)	Ga (μg/g)	Ag (μg/g)	In (μg/g)
3296-3 pick A1	34 ± 5	41 ± 4	50 ± 23	1.43 ± 0.03	2700 ± 170	20.7 ± 2.3
3296-3 pick A2	22 ± 5	35 ± 3	40 ± 21	1.24 ± 0.02	2500 ± 160	16.3 ± 1.9
3296-3 pick B1	22 ± 5	38 ± 3	40 ± 22	1.38 ± 0.02	2900 ± 180	17.2 ± 2.0
3296-3 pick B2	23 ± 5	30 ± 3	40 ± 21	1.07 ± 0.04	2300 ± 140	15.9 ± 1.9
3299-6-1 pick A	13 ± 5	150 ± 13	110 ± 26	0.67 ± 0.08	490 ± 30	6.7 ± 1.3
3299-6-1 pick B1	13 ± 5	140 ± 12	110 ± 25	0.56 ± 0.08	880 ± 60	6.4 ± 1.2
3299-6-1 pick B2	43 ± 5	130 ± 11	120 ± 24	0.53 ± 0.07	850 ± 60	9.1 ± 1.4
3299-6-1 pick C	17 ± 6	150 ± 13	110 ± 26	0.56 ± 0.08	660 ± 40	6.8 ± 1.3
Alv1931 pick A1	12 ± 6	bdl ± bdl	40 ± 22	1.07 ± 0.05	270 ± 20	10.5 ± 1.5
Alv1931 pick A2	33 ± 5	0.73 ± 0.24	bdl ± bdl	0.93 ± 0.05	270 ± 14	20.0 ± 1.5
Alv1931 pick A3	12 ± 2	0.80 ± 0.23	bdl ± bdl	1.194 ± 0.010	290 ± 20	17.5 ± 1.8
Alv3474-3-1 pick A1	12 ± 5	46 ± 4	bdl ± bdl	0.34 ± 0.08	130 ± 11	6.2 ± 1.1
Alv3474-3-1 pick A2	18 ± 5	48 ± 4	bdl ± bdl	0.49 ± 0.08	150 ± 12	6.6 ± 1.2
Alv3474-3-1 pick A3	13 ± 5	42 ± 4	bdl ± bdl	0.37 ± 0.07	130 ± 10	5.9 ± 1.1
J2-213-6-R1 pick A	18 ± 5	0.7 ± 0.3	30 ± 21	3.3 ± 0.10	330 ± 23	37 ± 4
J2-214-3-R1 pick A	18 ± 5	0.5 ± 0.3	bdl ± bdl	40.4 ± 2.5	140 ± 11	77 ± 6
J2-214-3-R1 pick C	6 ± 5	0.32 ± 0.28	bdl ± bdl	23.7 ± 1.4	100 ± 9	45 ± 4
J2-437-3-R2 pick A	46 ± 6	0.54 ± 0.10	bdl ± bdl	6.40 ± 0.09	137 ± 4	36.4 ± 1.2

Figure 7. Calculated SIMS calibration curves for Mn, Co, Ni, Ga, Ag, and In constructed by comparing ICP-MS measurements of these elements in aliquots of picked chalcopyrite grains (x-axis) and SIMS measurements of these same elements (y-axis). Separate points are plotted for each aliquot of picked grains using a single SIMS value for each black smoker chimney sample. Samples included in the regression used to calculate the calibration curve are marked in black. These correspond to the samples in bold in Table 3. Regression lines are calculated through these points without taking into account sample errors. Additional samples measured by ICP-MS and SIMS but not included in construction of the calibration curves are marked in white.

Figure 7A

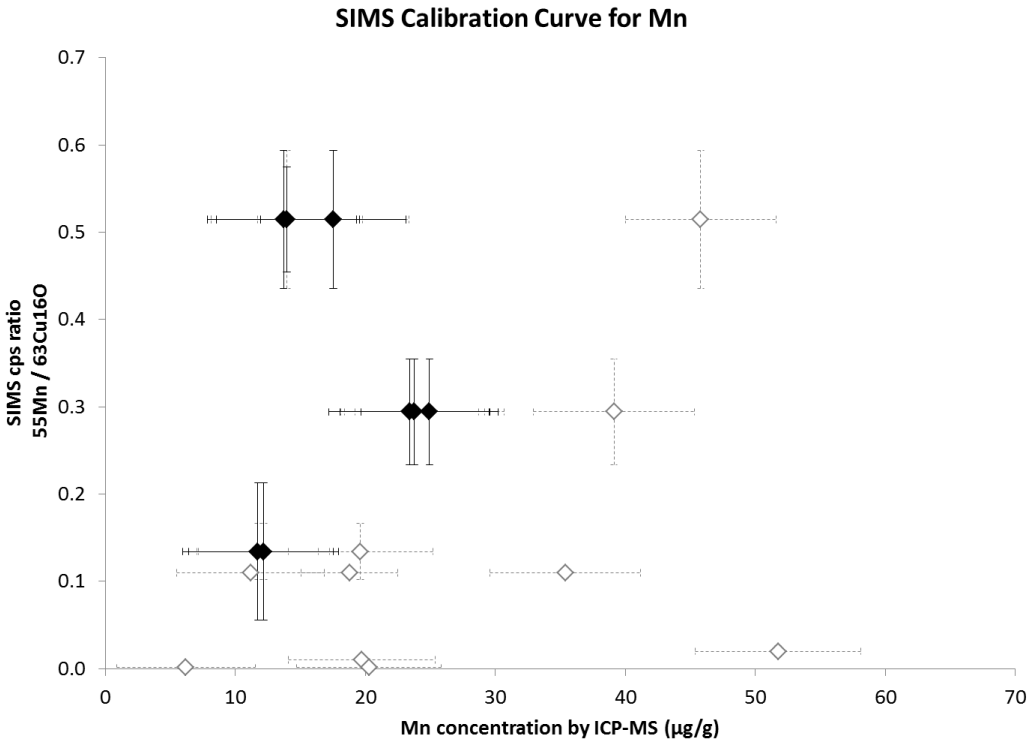

Figure 7B

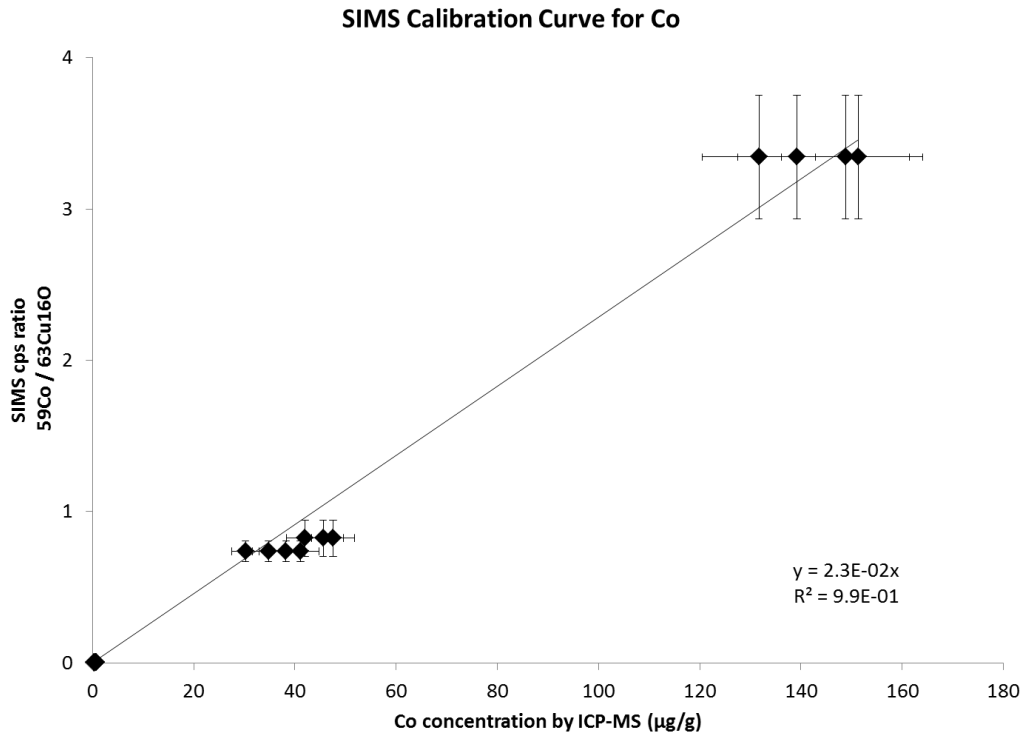

Figure 7C

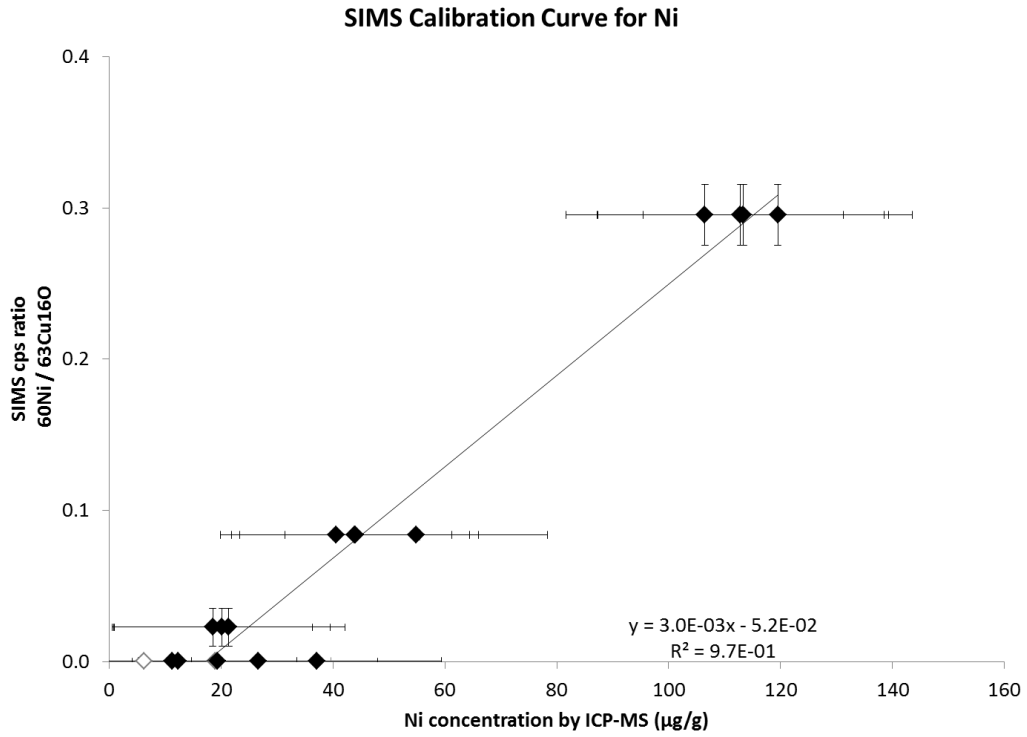

Figure 7D

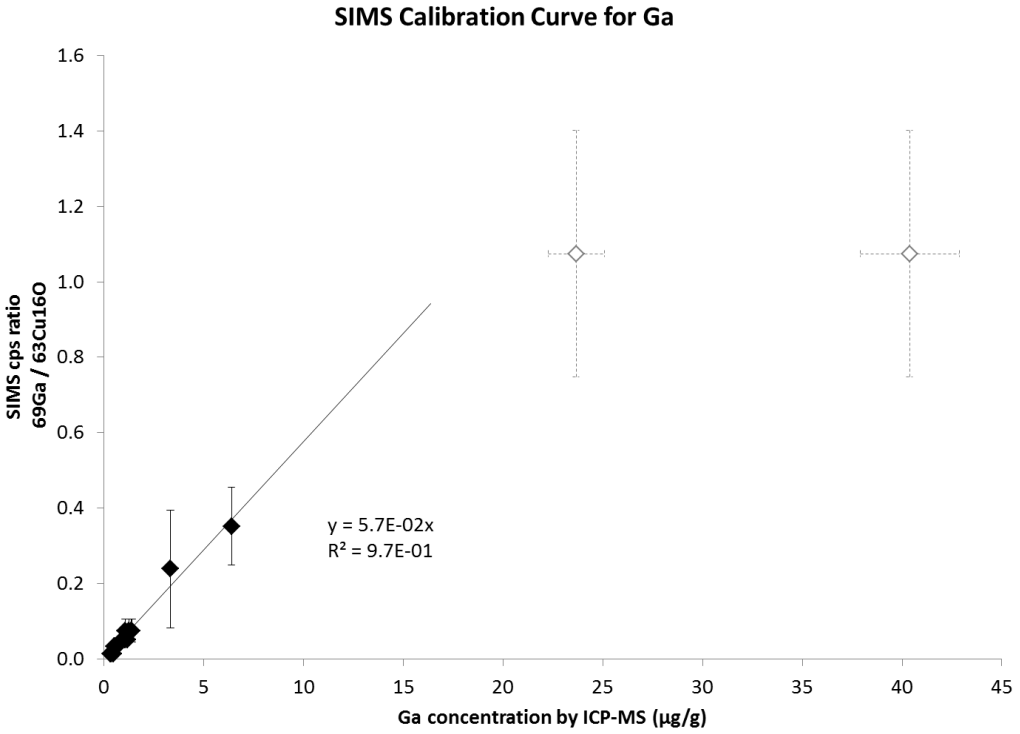

Figure 7E

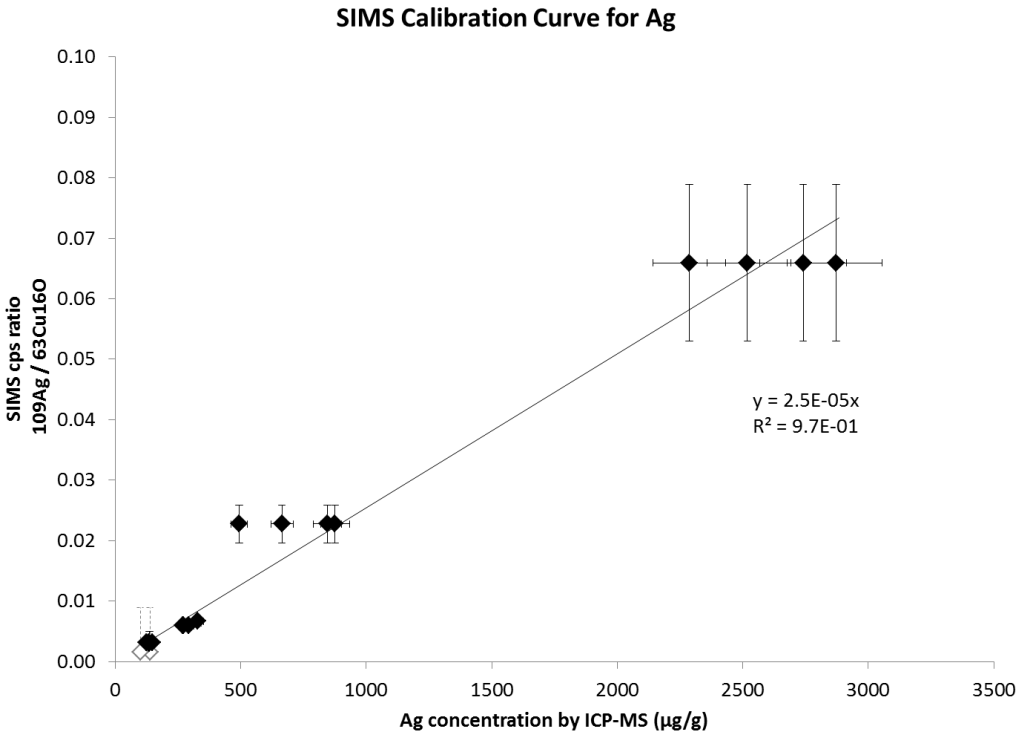

Figure 7F

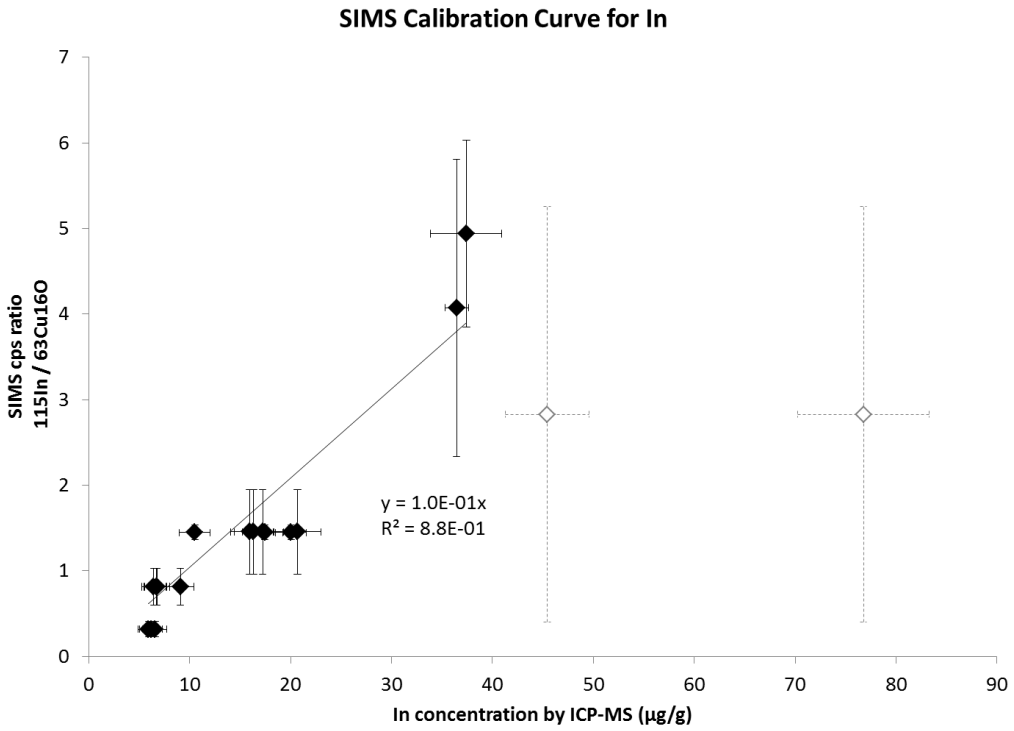
SIMS Calibration Curve for In
SIMS cps ratio
115In / 63Cu16O
In concentration by ICP-MS (µg/g)
y = 1.0E-01x
R² = 8.8E-01
0
1
2
3
4
5
6
7
0
10
20
30
40
50
60
70
80
90

Table 4. SIMS measurements converted to concentration units by use of the calibration curves displayed in Figures 7B to 7F. Values are plotted in µg/g on a linear scale. Samples used for constructing SIMS calibration curves are highlighted in bold. Also indicated are the detection limit, equivalent to 5×10^{-5} cps / $^{63}Cu^{16}O$ cps, and the determination limit, equivalent to 1.2×10^{-4} cps / $^{63}Cu^{16}O$ cps. Indicated sample errors are derived entirely from variation between SIMS spots and do not represent propagated errors from the calibration curves. For Ni, high detection limits (20 µg/g) are caused by uncertainties in ICP-MS measurements. Concentrations lower than 20 µg/g are measureable by SIMS, but cannot be calibrated with the current technique. bdl = below detection limit. NM = not measured.

Sample ID	Vent Field	Co (µg/g)	Ni (µg/g)	Ga (µg/g)	Ag (µg/g)	In (µg/g)
Detection Limit		2 ng/g	20 µg/g	0.9 ng/g	2 µg/g	0.5 ng/g
Determination Limit		5 ng/g	120 µg/g	2 ng/g	5 µg/g	1.2 ng/g
Alv3299-6-1	**EPR, 17 34'S**	**147 ± 18**	**116 ± 22**	**bdl**	**890 ± 120**	**8.8 ± 2.3**
Alv3288-5-1a	EPR, 17 37'S	47 ± 6	25 ± 15	bdl	211 ± 25	3.4 ± 1.0
Alv3296-2-2a	EPR, 17 37'S	81 ± 13	52 ± 20	bdl	180 ± 40	1.5 ± 0.5
Alv3296-3	**EPR, 17 37'S**	**32 ± 3**	**43 ± 16**	**1.4 ± 0.6**	**2600 ± 500**	**16 ± 5**
Alv3296-5-1a	EPR, 17 37'S	86 ± 3	55 ± 16	bdl	174 ± 9	1.57 ± 0.08
Alv1931	**MEF (pre-event)**	**2.7 ng/g ± 0.6 ng/g**	**bdl**	**0.9 ± 0.2**	**232 ± 12**	**15.6 ± 0.9**
Alv3474-3-1	**MEF (post-event)**	**36 ± 5**	**22 ± 19**	**bdl**	**121 ± 22**	**3.4 ± 1.0**
Alv3480-4	MEF (post-event)	35 ± 4	NM	NM	106 ± 18	3.7 ± 0.4
DV1-5B	Lucky Strike	27 ± 3	NM	NM	1900 ± 800	18 ± 3
J2-613-16-R1	Beebe	760 ± 250	480 ± 40	bdl	140 ± 90	23 ± 9
J2-207-1-R1	Vienna Woods	0.53 ± 0.27	bdl	bdl	3800 ± 700	bdl
J2-210-7-R2	Fenway	3.1 ng/g ± 3.1 ng/g	NM	NM	170 ± 60	28 ± 10
J2-216-16-R1	Fenway	1.5 ± 0.6	bdl	NM	320 ± 250	15 ± 6
J2-214-3-R1	Satanic Mills	bdl	bdl	20 ± 6	60 ± 60	31 ± 26
J2-208-1-R1	Roman Ruins	32 ng/g ± 40 ng/g	bdl	48 ± 18	1300 ± 600	265 ± 100
J2-213-6-R1	**Roger's Ruins**	**bdl**	**bdl**	**4.4 ± 2.9**	**260 ± 30**	**53 ± 12**
J2-217-2-R1	Suzette	6.9 ± 1.0	bdl	bdl	250 ± 40	8.3 ± 1.2
J2-217-10-R1	Suzette	1.0 ± 0.5	bdl	5.8 ± 1.0	530 ± 200	3.9 ± 1.8
J2-219-2-R1	Suzette	9 ng/g ± 5 ng/g	NM	NM	360 ± 150	11 ± 6
J2-223-1-R1	North Su	15 ± 4	bdl	6.5 ± 2.2	300 ± 100	11 ± 5
J2-227-10-R1	North Su	0.38 ± 0.07	NM	NM	210 ± 30	11 ± 5
J2-450-3-R1	Tahi Moana-1	2.8 ng/g ± 1.7 ng/g	bdl	1.3 ± 0.5	2600 ± 600	57 ± 17
J2-449-5-R1	ABE	12 ng/g ± 20 ng/g	bdl	1.8 ± 0.6	920 ± 160	1.1 ± 0.3
J2-449-6-R1	ABE	0.5 ± 0.5	bdl	1.1 ± 0.3	470 ± 210	16 ± 11
J2-815-5-R1	ABE	39 ng/g ± 47 ng/g	bdl	3.5 ± 0.3	570 ± 70	13 ± 6
J2-442-4-R2	Tu'i Malila	0.2 ± 0.2	bdl	bdl	540 ± 80	6 ± 5
J2-819-4-R2	Tu'i Malila	8 ng/g ± 4 ng/g	NM	NM	2110 ± 250	bdl
J2-437-3-R2	**Mariner**	**5 ng/g ± 11 ng/g**	**bdl**	**6.4 ± 1.9**	**120 ± 80**	**44 ± 19**
J2-817-4-R2	Mariner	39 ng/g ± 17 ng/g	NM	NM	100 ± 20	11.2 ± 1.3

4.5. Principal Component Analysis

Principal component analysis conducted on the log-transformed dataset of SIMS counts ratios reveals that trace element concentrations of black smoker chimney linings are spread along two principal components that together account for 90.2% of the total variance (Table 5A). The first principal component, which contributes 79.7% of the total variance, is strongly associated with Co and Ni concentrations. The second principal component, which contributes 10.6% of the total variance, is strongly associated with concentrations of In and secondarily Ga and Ni. Correlation coefficients calculated on the same dataset reveal significant positive correlations between Co and Ni ($r = 0.86$; $p = 2.6\times10^{-7}$, where r is the Pearson correlation coefficient and p is the Pearson p-value) and between Ga and In ($r = 0.63$; $p = 1.6\times10^{-3}$) (Table 5B; see Fig. 5A and 5B).

Principal components and correlation coefficients can also be evaluated in the context of commonly measured hydrothermal fluid parameters such as temperature, pH, and concentrations of H_2S, and Cl. Following the addition of these hydrothermal fluid parameters and calculation of principal components and correlation coefficients over the expanded dataset, the two primary principal components identified from the SIMS dataset are maintained (Table 6A). The first principal component associated with concentrations of Co and Ni accounts for 71.2% of the total variance. The second principal component associated with In, and seondarily Ga and Ni, accounts 14.6% of the total variance. It is also associated with fluid pH. In addition to the significant positive correlation between Co and Ni identified previously, Co and Ni are both positively correlated with hydrothermal fluid temperature, while concentrations of Ga and In are positively correlated with each other and negatively correlated with fluid pH (Table 6B). Bivariate plots of Co and Ni against fluid temperature and Ga and In against fluid pH reveal

broad correlating trends, particularly between concentrations of In and fluid pH (Figures 8A – 8D). Concentrations of Co covary with temperature, particularly among samples with relatively high concentrations of Co, from the Mid-Cayman Rise, southern East Pacific Rise, and SuSu Knolls.

Table 5. Principal components (A) and Pearson correlation coefficients (B) calculated for the log-transformed SIMS counts ratios of 59Co, 60Ni, 69Ga, 109Ag, and 115In using the MATLAB code pca. Also indicated is the percent of total variance accounted for by each principal component (A). Significant correlations (Pearson's $p < 0.05$) are enclosed in boxes (B). (Inputs and outputs to principal component analysis in Supplementary Table S5)

Table 5A

	Principal Components				
	pca-1	pca-2	pca-3	pca-4	pca-5
LogCo	0.8	-0.2	0.5	-0.3	-0.1
LogNi	0.6	0.5	-0.4	0.4	0.3
LogGa	-0.2	0.5	0.4	-0.4	0.6
LogAg	-0.1	-0.2	0.6	0.7	0.3
LogIn	-0.1	0.7	0.4	0.2	-0.6
	Percent of Total Variance				
	79.7	10.6	4.8	2.7	2.3

Table 5B

	Pearson Correlation Coefficients			
	LogCo	LogNi	LogGa	LogAg
LogNi	0.9			
LogGa	-0.5	-0.4		
LogAg	-0.2	-0.3	0.0	
LogIn	-0.4	-0.2	0.6	0.0

Table 6. Principal components (A) and Pearson correlation coefficients (B) calculated for an expanded dataset including the log-transformed SIMS counts ratios of 59Co, 60Ni, 69Ga, 109Ag, and 115In and the hydothermal fluid parameters: temperature (1/K), pH (at 25°C), Cl (log 10), H2S (log 10) . Also indicated is the percent of total variance accounted for by each principal component. (Inputs and outputs to principal component analysis in Supplementary Table S6)

Table 6A

	Principal Components								
	pca-1	pca-2	pca-3	pca-4	pca-5	pca-6	pca-7	pca-8	pca-9
1/K	0.0	0.0	0.0	0.0	0.0	0.0	0.0	0.0	1.0
pH	0.0	-0.5	-0.1	0.0	0.2	0.1	0.8	0.0	0.0
LogCl	0.0	0.0	0.1	0.0	0.0	0.0	0.0	1.0	0.0
LogH2S	-0.1	0.1	0.9	-0.1	0.1	-0.2	0.2	-0.1	0.0
LogCo	0.7	-0.2	0.2	0.4	-0.4	0.0	0.0	0.0	0.0
LogNi	0.6	0.4	-0.1	-0.4	0.5	0.1	0.1	0.0	0.0
LogGa	-0.1	0.4	0.1	0.1	-0.3	0.8	0.2	0.0	0.0
LogAg	0.0	-0.2	0.2	0.6	0.7	0.3	-0.3	0.0	0.0
LogIn	-0.1	0.5	-0.2	0.6	0.1	-0.5	0.4	0.0	0.0
	Percent of Total Variance								
	71.2	14.5	4.7	3.9	2.7	2.0	1.0	0.0	0.0

Table 6B

	Pearson Correlation Coefficients							
	1/K	pH	LogCl	LogH2S	LogCo	LogNi	LogGa	LogAg
pH	0.4							
LogCl	0.6	0.2						
LogH2S	0.3	-0.3	0.5					
LogCo	-0.5	0.2	0.0	-0.4				
LogNi	-0.5	-0.1	-0.2	-0.4	0.9			
LogGa	0.2	-0.7	0.0	0.4	-0.5	-0.3		
LogAg	0.3	0.3	0.4	0.1	-0.1	-0.3	-0.1	
LogIn	-0.2	-0.7	-0.3	0.1	-0.3	-0.1	0.6	-0.1

Figure 8. Bivariate plots of vent fluid parameters and trace elements in black smoker chimney linings including: (A) vent fluid temperature vs. ^{59}Co / $^{63}Cu^{16}O$, (B) vent fluid temperature vs. ^{60}Ni / $^{63}Cu^{16}O$, (C) vent fluid pH vs. ^{69}Ga / $^{63}Cu^{16}O$, (D) vent fluid pH vs. ^{115}In / $^{63}Cu^{16}O$.

Figure 8A

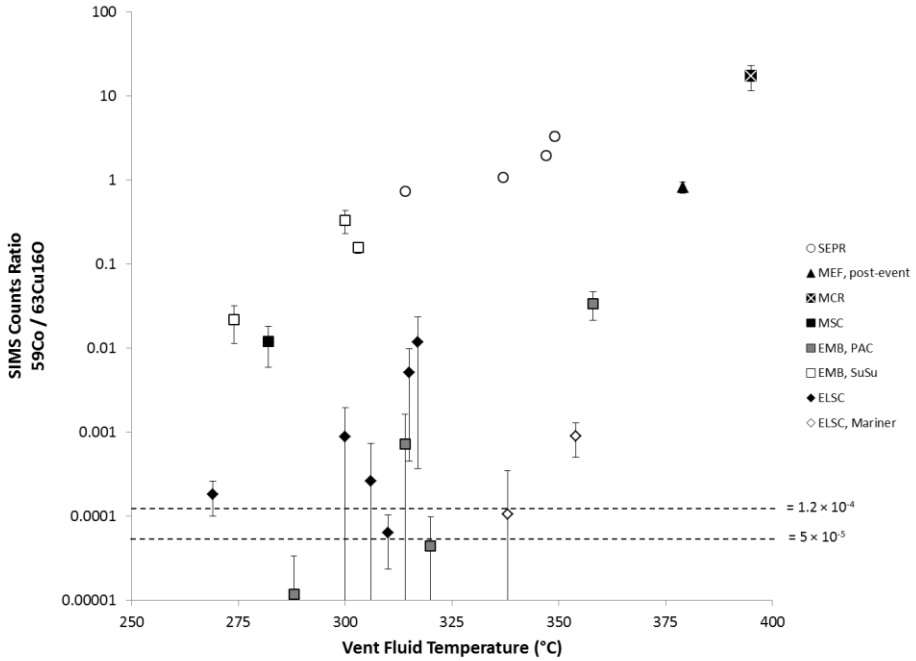

Figure 8B

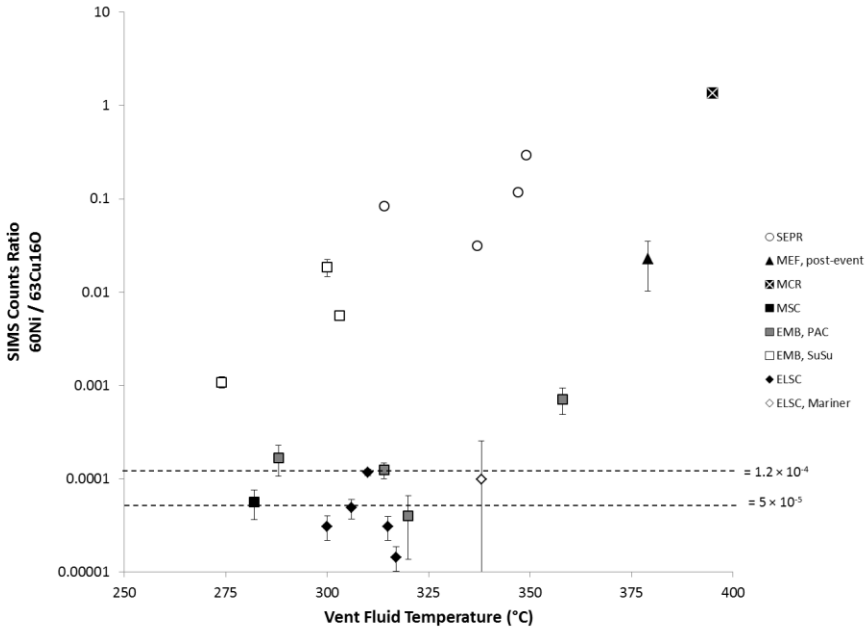

Figure 8C

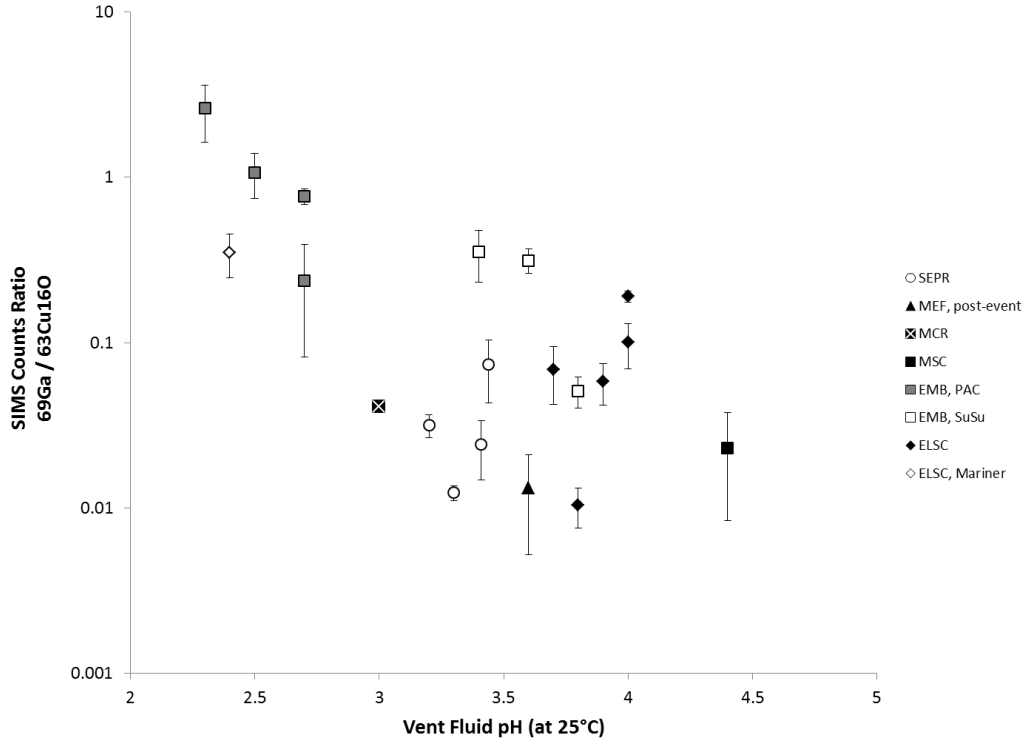

Figure 8D

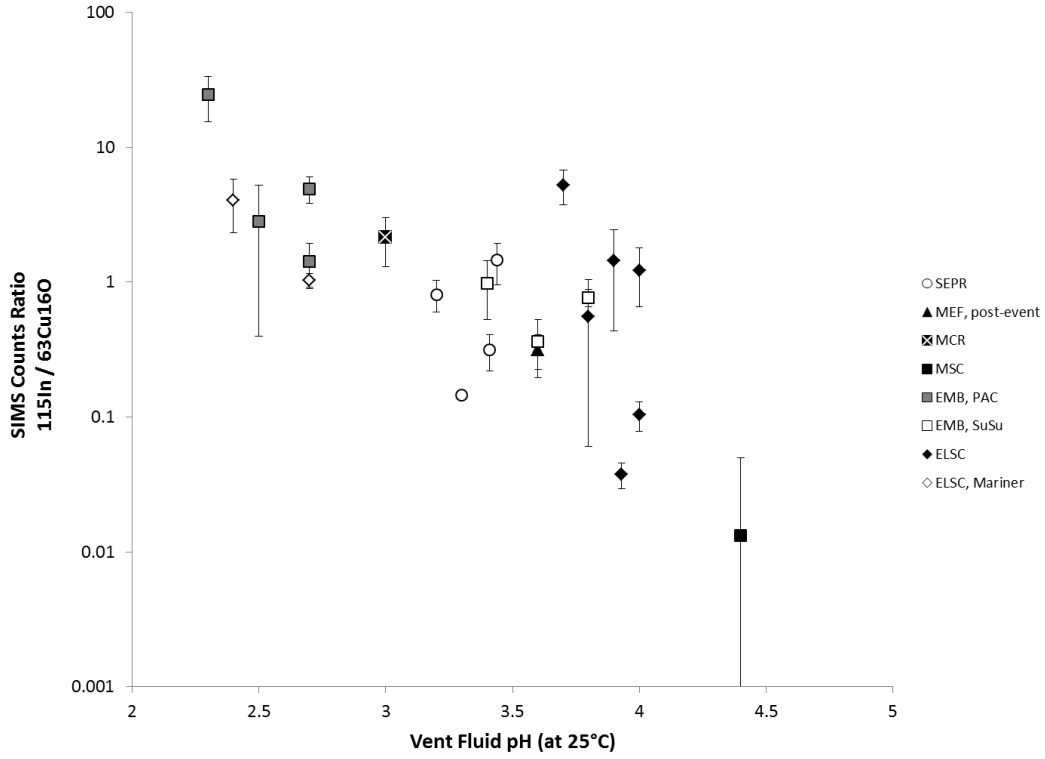

5. DISCUSSION

This study demonstrates the utility of secondary ion mass spectrometry (SIMS) for measuring trace element concentrations in black smoker chimney linings. The variation of trace element concentrations between samples is much larger than the heterogeneity observed within a single sample (Fig. 4A – 4F; Table 4). Therefore, it is possible that the trace element concentrations of black smoker chimney linings contain measureable and meaningful signals that may, in turn, reflect physical and chemical properties of hydrothermal fluid chemistry and/or the conditions and processes through which these mineral linings are deposited. A subset of these samples are sufficiently homogeneous with respect to Co, Ni, Ga, Ag, and In and collectively cover a wide enough range of concentrations to be used in defining SIMS calibration curves by which to quantify measurements. In addition, many of the black smoker chimney linings examined in this study were deposited by fluids of known temperature and chemical composition, allowing for further investigation of the geochemical processes that control trace element concentrations in black smoker chimney linings.

5.1. Evaluation of Calibration Curves

Construction of the calibration curves presented here requires quantitative comparison of SIMS analyses of the innermost 100 μm of a black smoker chimney lining with solution ICP-MS analyses of chalcopyrite grains picked from the innermost 1 mm of a different section of the same sample, usually 1-10 cm apart (Fig. 1). Thus, samples chosen for inclusion in the calibration curves must be homogeneous with respect to the desired trace elements at μm-, mm-, and cm-scales. Additionally, picked grains should be not be tarnished or contain inclusions of other sulfide minerals. While the use of SIMS allows for analyses at small spatial scales and

removal of measurements thought to result from mineral inclusions following the analysis, the same level of control is not possible for the picked grains of chalcopyrite analyzed by solution ICP-MS. The lack of inclusions is especially important for elements which preferentially partition into sphalerite or wurtzite relative to chalcopyrite, such as such as Mn, Ga, and In (Cook and Ciobanu, 2015).

The samples ultimately used in constructing SIMS calibration curves are black smoker chimneys that exhibit monomineralic chalcopyrite linings and from which both reproducible SIMS measurements and untarnished (or mildly tarnished) chalcopyrite grains could be obtained. These samples incude: Alv3296-3 and Alv3299-6-1 from the southern East Pacific Rise, Alv1931 and Alv 3474-3-1 from the Main Endeavour Field on the Juan de Fuca Ridge, J2, 213-6-R1 from the Roger' sRuins vent field in the Eastern Manus Basin, and J2-437-3-R2 from the Mariner vent field on the Eastern Lau Spreading Center. Sample J2-214-3-R1 from Satanic Mills vent field in the Manus Basin was also evaluated by SIMS and ICP-MS, but ultimately excluded from the calibration curve because only tarnished chalcopyrite grains could be picked and because SIMS measurements of Ag were heterogeneous (Fig. 4E).

Of the various trace elements investigated in this study, Ag and In are both thought to occur as lattice substitutions in chalcopyrite (Ag for Cu, In for Fe; Huston et al., 1995). This determination is based on four criteria: (1) the crystal chemistry of the host mineral, (2) experimental studies on the solubilities of the elements of interest in the host mineral, (3) the presence or absence of minerals that contain major concentrations of the elements of interest, and (4) variations in the level of the elements of interest between and within samples (Huston et al., 1995). Extending this logic to the data presented here and considering the overall reproducability of measurements within individual black smoker chimney samples, it is likely that Co, Ni, and

Ga also occur as lattice substitutions in chalcopyrite. A main factor that may affect the quality of developed SIMS calibration curves is the extent of homogeneity with respect to the element at mm- to cm-scales. Small amounts of zinc sulfide contamination in aliquots of picked chalcopyrite grains could also explain the uncertainty of the Ga and In calibration curves at higher concentrations. However, arguments against this explaniation include the lack of significant correlations between Zn and any of these elements in ICP-MS analyses of picked grains and the absense of intergrown wurtzite or sphalerite observable under the petrographic microscope. Alternatively, Ga and In could be less homogeneously distributed in chaclopyrite chimney linings than Co, Ni, or Ag. This explanation is supported by SIMS analyses where the standard errors calculated over multiple spots are typically greater for Ga and In than for Co, Ni, and Ag.

The occurance of Mn in chalcopyrite, whether as a lattice substitution or as inclusions is not well known. The concentrations of Mn measured here are low (typically < 50 μg/g, Table 4) and attempts to develop a SIMS calibration curve for Mn were unsuccessful (Fig. 7A). High detection limits for Ni are caused by uncertainties in the concentrations of Ni measured by ICP-MS for picked grains measured by ICP-MS, which become increasingly important at low Ni concentrations. This may be an artifact of Ni cones used in the Element 2 which interfere with Ni measurements at low concentrations. Subsequent analyzes of Ni should make use of Pt cones.

5.2. Trace Element Concentrations

To date, few studies have provided quantitative analyses of trace element concentrations in black smoker chimney linings using microanalytical techniques with low detection limits. Wohlgemuth-Ueberwasser et al. (2015) used LA-ICPMS to analyze 27 black smoker chimney samples for a number of trace elements including As, Sb, Se, Te, and Au, none of which are

treated here. Comparable data do exist for the trace element contents of chalcopyrite from the inner wall of fossilized black smoker chimney linings from the Yaman-Kazy deposit in the Southern Urals with the results: Co (0.1 μg/g to 5.97 μg/g), Ni (0.2 μg/g to 0.9 μg/g), Ag (7 μg/g to 584 μg/g) ("Chp2" in Maslennikov et al., 2009). Average concentrations of the same elements in chalcopyrite from the inner linings (Zone B) of fossil chimneys from Çayeli and Kutlular volcanogenic massive sulfide (VMS) deposits in the Eastern Pontide orogenic belt are: Co (0.24 μg/g to 2.19 μg/g), Ni (0.12 μg/g to 2.04 μg/g), Ag (14.4 μg/g to 98.19 μg/g) (Revan et al., 2014). Analyses of trace elements in chalcopyrite from the Wocan hydrothermal field on the Carlsberg Ridge obtained by LA-ICP-MS yield average concentrations of: Co (0.1 μg/g), Ni (0.39 μg/g), Ga (22.7 μg/g), Ag (65.3 μg/g), In (13.3 μg/g) (Wang et al., 2017).

The concentrations of trace elements in the chalcopyrite linings of black smoker chimneys investigated in this study are comparable to those reported previously, but cover a wider range of trace element concentrations (Table 4). This is consistent with the examination of black smoker chimneys from a variety of geologic settings, including basalt-hosted vent fields along fast-, intermediate-, slow-, and ultraslow spreading mid-ocean ridges and basalt-hosted and felsic-hosted systems along back-arc spreading centers and volcanic zones (Table 1). Additionally, the samples investigated here are associated with a wide range of hydrothermal fluid parameters, e.g., pH (at 25°C) = 2.3 to 4.4 and temperature = 274°C to 395°C (Table 1).

Notably, the low Co and Ni contents of fossil chimneys from the Yaman-Kazy, Çayeli, and Kutlular deposits are comparable to black smoker chimneys from felsic-hosted vent fields in the Lau and Manus back-arc Basins. The Yaman-Kazy deposit is thought to have formed in a narrow pull-apart extensional zone in a Silurian marginal sea, while the Late Cretaceous Çayeli, and Kutlular deposits are thought to have formed in an island arc setting; all of these deposits are

associated with rhyolite-dacite lavas (Maslennikov et al., 2009, Revan et al., 2014). The similarity in trace element content between chalcopyrite from active and fossil black smoker chimneys associated with similar lithology suggests that at least some trace element signatures may be geologically preserved. Concentrations of Co and Ni are similarly low in chalcopyrite from the presumably basalt-hosted Wocan deposit, which contrasts with the majority of basalt-hosted mid-ocean ridge samples investigated here, but is comparable to concentrations in chimneys from the basalt-hosted Vienna Woods vent field and the pre-event Main Endeavour Field (Table 4). Additional data from a greater number of vent fields is needed to better investigate the relationships between vent fluid chemistry, host rock lithology, and black smoker trace element content. This is an area ripe for further study.

5.3. Controls on Trace Element Concentrations

Principal compoenet analysis highlights two types of geochemical variability among black smoker chimney deposits (Tables 5A and 6A). The first type concerns the concentrations of Co and Ni (Fig. 4B, 4C; Fig. 5A, Table 4). Black smoker chimneys from non-sedimented, basalt-hosted vent fields such as the Mid-Cayman Rise and southern East Pacific Rise have higher concentrations of Co and Ni than black smoker chimneys from the felsic-hosted vent fields of Manus Basin and Lau Basin, while samples from the basalt-hosted Vienna Woods field exhibit intermediate Co and Ni concentrations. The chalcopyrite linings of black smoker chimneys collected from the Main Endeavour Field on the Juan de Fuca Ridge following the 1999 event and the Lucky Strike vent field on the Mid-Atlantic Ridge exhibit higher concentrations of Co than back-arc basin samples and lower Co concentrations than most of the southern East Pacific Rise samples. However, the chalcopyrite lining of sample Alv1931,

collected from the Main Endeavour Field prior to the 1999 event exhibits low concentrations of Co and Ni, comparable to back-arc basin samples. For samples from basalt-hosted vent fields, concentrations of Co and Ni also correlate with vent fluid temperature (Table 6B, Figures 8A and 8B). The association of higher Co and Ni concentrations with more mafic lithology and higher temperatures has been previously recognized and is generally attributed to higher concentrations of these elements in mafic and ultramafic rocks and elevated Co concentrations in high-temperature fluids (Hannington et al., 1991; Hannington et al., 1995; Hannington et al., 2005). Alternatively, Co has been shown to prefferentially partition into isocubanite or Fe-rich intermediate solid solution over chalcopyrite (Rouxel et al., 2004). Data presented here suggests that Ni may partition similarly to Co. Moreover, electron microprobe data show that the composition of sample J2-613-16-R1, which has the highest Co and Ni concentrations of the black smoker chimney linings in this study is compositionally intermediate between stoichiometric chalcopyrite ($CuFeS_2$) and isocubanite ($CuFe_3S_4$) (Fig. 9).

The second source of geochemical variability is related to concentrations of In and secondarily Ga (Tables 5B and 6B, Fig. 5B). Concentrations of these elements broadly correlate, with concentrations of In most highly correlated with fluid pH (Table 6B, Fig. 8D). Studies of In^{3+} speciation under hydrothermal conditions highlight the importance of hydroxide (OH^-) complexes (Wood and Samson, 2006). Figure 10A shows the prevalence of such complexes at 20°C, 1 bar pressure, 1 M $NaClO_4$, total sulfide = 0.01 M. This provides a possible mechanism for the observed pH dependence of In in black smoker chimney linings. Figure 10B shows the aquous speciation of In^{3+} at 25°C and 1 bar pressure as a function of pH and Cl^- concentration.

Figure 9. Plot of Cu and Fe in CuFe sulfide lining of sample J2-613-16-R1 from the Beebe/Piccard vent field on the Mid-Cayman Rise measured by electron microprobe. Results reported as weight percent normalized to total = Cu (wt%) + Fe (wt%) + S (wt%).

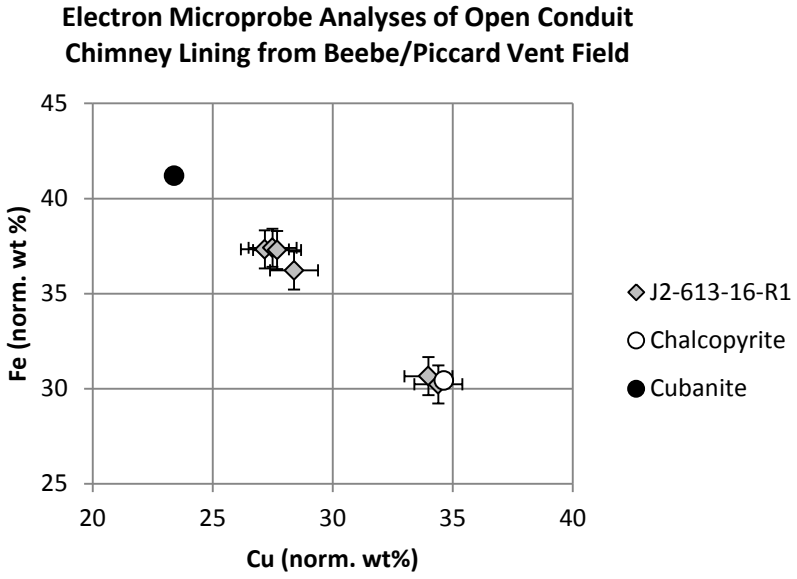

Figure 10. Plots from Wood and Samson (2006) showing (A) the abundance of aquous In^{3+} complexes contributing to the solubility of $In_2S_3(s)$ as a function of pH at (A) the aqueous speciation of In^{3+} vs. the log concentration of In^{3+} aqueous complexes at 20°C, 1 bar pressure, 1 M $NaClO_4$, total sulfide = 0.01 M and (B) the aqueous specitation of In^{3+} as a function of pH and log Cl^- concentration at 25°C and 1 bar pressure. Red line highlights the concentration of In^{3+} as a function of pH. Dashed box outlines approximate compositional range of typical black smoker hydrothermal fluids.

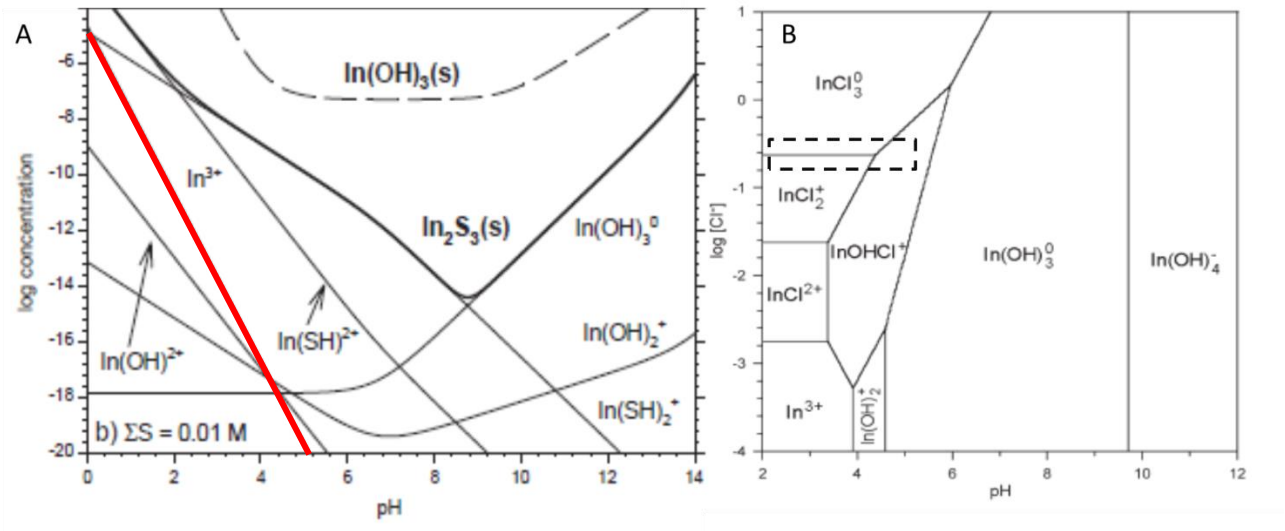

If it is assumed that In occurs in chalcopyrite by regualrly partitioning and substitution of Fe^{3+} in the chalcopyrite lattice, then, according to the theoretical description of trace element partitioning proposed by McIntire (1963), the following partitioning equation can be written:

$$D_{hf,cp} = \frac{\frac{\{In^{3+}\}_{hf}}{\{Fe^{3+}\}_{hf}}}{\frac{\{In^{3+}\}_{cp}}{\{Fe^{3+}\}_{cp}}}$$

where $D_{hf,cp}$ is the partition coefficient between hydrothermal fluid (hf) and chalcopyrite (cp) , $\{In^{3+}\}_{hf}$ and $\{Fe^{3+}\}_{hf}$ are the activities of In^{3+} and Fe^{3+} in the hydrothermal fluid, respectively, and $\{In^{3+}\}_{cp}$ and $\{Fe^{3+}\}_{cp}$ are the thermodynamic activities of In^{3+} and Fe^{3+} in chalcopyrite. The activity and thus concentration of In in chalcopyrite is therefore related to the activity of In^{3+} in the corresponding hydrothermal fluid. At higher pH (and higher OH^- activity), In would primarily be present as hydroxide complexes and the activity of the free ion $\{In^{3+}\}$ in the hydrothermal fluid would be low relative to the total In concentration (Wood and Samson, 2006; Charlotte Ashworth, personal communcation). The In concentration in chalcopyrite chimney linings would thus be low. Conversely, at lower pH, the activity of the free ion, $\{In^{3+}\}$, in hydrothermal fluids would be higher relative to the total In concentration than at higher pH, and chalcopyrite formed from these fluids would contain greater concentrations of In. Analogous reasoning can be used to explain the correlation between hydrothermal fluid pH and Ga, for which hydroxide (OH^-) complexes are likewise important (Wood and Samson, 2006; Fig. 11).

Few reliable data are available for the concentrations of In in seafloor hydrothermal fluids or natural fluids more generally (Douville et al., 2002; Wood and Samson, 2006). Thus, the factors influencing total In concentration cannot by evaluated at this time. Additionally, new experimental data indicate that the activity of In^{3+} at low pH is strongly controlled by chloride

complexes for which the appropriate thermodynamic data have not been published (Charlotte Ashworth, personal communcation). Nevertheless, the observed strong negative correlation between the In concentration in chalcopyrite chimney linings and hydrothermal fluid pH presents the intriguing possibility of In in chalcopyrite as a proxy of hydrothermal fluid pH.

Figure 11. Reproduction of plots in Wood and Samson (2006) of pH vs. the log concentration of aqueous Ga complexes contributing to the solubility of GaOOH at 200°C and 300°Cat vapor saturated pressures using the thermodynamic data of Benézéth et al., (1997). Red lines highlight the concentration of Ga^{3+} as a function of pH.

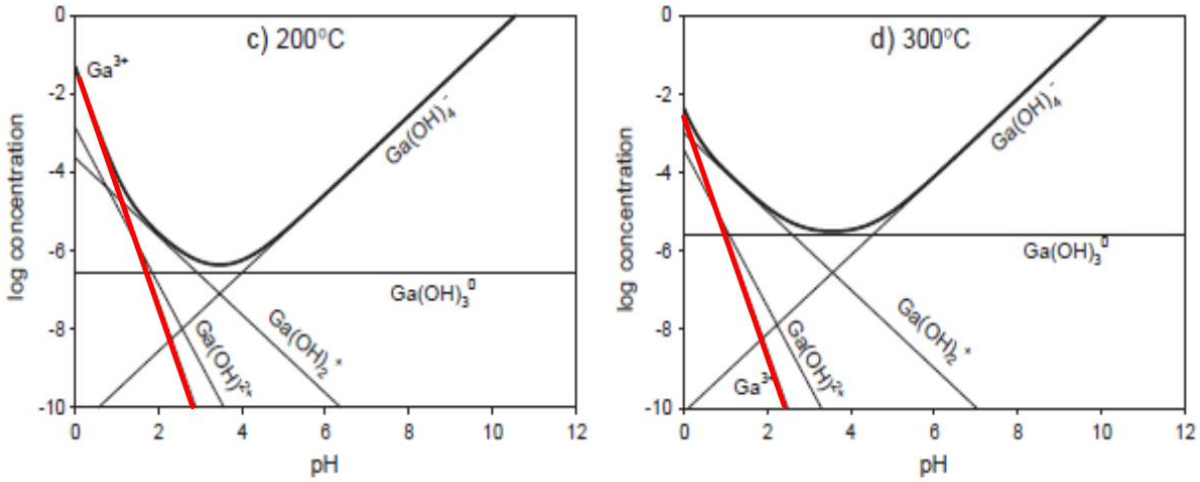

5.4. Main Endeavour Field

The two samples examined in this study from the Main Endeavour Field provide a particularly interesting case study by which to evaluate the potential for black smoker chimney linings to record changes in hydrothermal fluid temperature and/or chemistry. Chalcopyrite lining the conduit of sample Alv3474-3-1, which was collected shortly after the 1999 event, contains higher concentrations of Co and Ni and lower concentrations of Ga, Ag, and In than chalcopyrite lining the conduit of sample Alv1931, collected before the 1999 event. Fluids collected in 1999, when Alv3474-1-3 was collected, exhibit lower chlorininty, lower pH, higher concentrations of Fe and Zn and similar concentrations of Cu as those collected in 1987, when

Alv1931 was sampled (Seyfried et al., 2003; Butterfield and Massoth, 1994). Concentrations of Co, Ni, and Ag were not measured in fluid sampled in 1984, 1987, or 1988. However, fluids collected in 1999 from the Dante deposit in 1999 exhibit higher concentrations of Co and Ni and lower concentrations of Ag than fluids collected in 2000 from the same deposit. These changes in hydrothermal fluid chemistry are thought to represent a partial recovery toward the pre-event state (Seyfried et al., 2003). In light of this, it is intriguing to find similar patterns of trace elements (i.e. higher Co and Ni, lower Ag) in the post-1999 event chimney lining relative to the pre-event black smoker chimney lining (Table 4). Considering the number of samples recovered from the Main Endeavour Field and the relative wealth of knowledge about the distribution and history hydrothermal activity at this site, the examination of trace elements in black smoker chimney linings recovered from the Main Endeavour Field presents a particularly promising avenue for future research into the relationship between hydrothermal activity and mineral deposit geochemistry.

6. CONCLUSION

This study has used secondary ion mass spectrometry (SIMS) to measure concentrations of Co, Ag, and In at high spatial resolutions (spot size = ~40 μm) and low detection limits (2 ng/g; 2 μg/g, and 0.5 ng/g, respectively) in chalcopyrite along the innermost (~100s μm) linings of fluid conduits in 29 black smoker samples; 22 of these samples were also analyzed for Ni and Ga. Chimney samples represent a variety of geologic settings (e.g., fast-, intermediate-, slow-, and ultraslow-spreading mid-ocean ridges, and back-arc spreading centers) and hydrothermal fluid conditions (e.g., pH(25°C) = 2.3 to 4.4 and temperature = 274°C to 395°C), allowing for comparisons between the trace element content of black smoker chimney linings and

hydrothermal fluid parameters for different geologic settings. Accomplishments of this study include the development of SIMS as a technique for measuring Co, Ni, Ga, Ag, and In concentrations in chalcopyrite and the identification of patterns between the concentrations of these elements and hydrothermal fluid parameters, which present possible trace element proxies of deposit formation conditions.

Homogeneous distributions of Co, Ni, Ga, Ag, and In in samples are consistent with the presence of these elements primarily as lattice substitutions. Concentrations of Co and Ni covary with high concentrations of these elements assocaited with high-temperature vent fluids from basalt-hosted mid-ocean ridge vent fields. Concentrations of In and secondarily Ga covary with hydrothermal fluid pH, providing a possible proxy.

Calibration curves developed by comparing SIMS measurements of Co, Ni, Ga, Ag, and In in the monomineralic chalcopyrite linings of selected black smoker chimney linings with solution ICP-MS analyses of digested picked grains of the same samples are constrained within 5% for Co, Ni, Ga, and In and within 10% for Ag, allowing for quantification of SIMS data. Additionally, several of the natural chalcopyrite samples investigated in this study are homogeneous with respect to Co, Ni, Ga, Ag, and In and my be suitable for use as calibration standards in geochemical analysis. Further refinement of the calibration curves presented here could be achieved by cross-calibration with other microanalytical techniques such as LA-ICPMS, especially as the development of and routine use of standard reference materials for sulfide analyses improves.

Overall, this study demonstrates the potential of SIMS to quantitatively measure Co, Ni, Ga, Ag, and In (and other trace elements) in chalcopyrite. Once SIMS calibration curves have been established and calibration standards identified, this technique is viable for a range of

applications in which analyses of chalcopyrite at similarly fine spatial scales and low detection limits are desired. Immediate applications include the analysis of trace elements along the innermost linings of other black smoker chimneys or within the small grains of chalcopyrite present in the interiors of chimney walls with the intent of testing and continuing to search for geochemical proxies of hydrothermal fluid temperature and chemistry.

REFERENCES

Benézéth, P., Diakonov, I. I., Pokrovski, G. S., Dandurand, J. L., Schott, J., and Khodakovsky, I. L. (1997) Gallium speciation in aqueous solution. Experimental study and modelling: Part 2. Solubility of α-GaOOH in acidic solutions from 150 to 250 C and hydrolysis constants of gallium (III) to 300 C. *Geochim. Cosmochim. Acta*, **61(7)**, 1345-1357.

Berglund, M., and Wieser, M. E. (2011) Isotopic compositions of the elements 2009 (IUPAC Technical Report) *Pure and Applied chemistry*, **83(2)**, 397-410.

Bézos, A., Escrig, S., Langmuir, C. H., Michael, P. J., and Asimow, P. D. (2009) Origins of chemical diversity of back- arc basin basalts: A segment- scale study of the Eastern Lau Spreading Center. *J. Geophys. Res.: Solid Earth*, **114**, *B06212, doi:*10.1029/2008JB005924.

Binns, R. A. and Scott, S. D. (1993) Actively forming polymetallic sulfide deposits associated with felsic volcanic rocks in the eastern Manus back-arc basin, Papua New Guinea. *Econ. Geol.*, *88*(8), 2226-2236.

Butler, I. B. and Nesbitt, R. W. (1999) Trace element distributions in the chalcopyrite wall of a black smoker chimney: insights from laser ablation inductively coupled plasma mass spectrometry (LA–ICP–MS) *Earth Planet. Sci. Lett.*, **167(3)**, 335-345.

Butterfield, D. A., and Massoth, G. J. (1994) Geochemistry of north Cleft segment vent fluids: Temporal changes in chlorinity and their possible relation to recent volcanism. *J. Geophys. Res.: Solid Earth*, **99(B3)**, 4951-4968.

Cook, N. J., Ciobanu, C. L., Pring, A., Skinner, W., Shimizu, M., Danyushevsky, L., Melcher, F., and Melcher, F. (2009) Trace and minor elements in sphalerite: A LA-ICPMS study. *Geochim. Cosmochim. Acta*, **73(16),** 4761-4791.

Craddock, P. R. (2009) Geochemical tracers of processes affecting the formation of seafloor hydrothermal fluids and deposits in the Manus back-arc basin. Ph.D. Thesis, MIT/WHOI Joint Program in Oceanography.

Danyushevsky, L., Robinson, P., Gilbert, S., Norman, M., Large, R., McGoldrick, P., and Shelley, M. (2011) Routine quantitative multi-element analysis of sulphide minerals by laser ablation ICP-MS: Standard development and consideration of matrix effects. *Geochemistry: Exploration, Environment, Analysis*, **11(1)**, 51-60.

Douville, E., Charlou, J. L., Oelkers, E. H., Bienvenu, P., Colon, C. J., Donval, J. P., Fouquet, Y., Prieur, D., and Appriou, P. (2002) The rainbow vent fluids (36 14′ N, MAR): the influence of ultramafic rocks and phase separation on trace metal content in Mid-Atlantic Ridge hydrothermal fluids. *Chem. Geol.*, **184(1)**, 37-48.

Elthon, D., Ross, D. K., and Meen, J. K. (1995) Compositional variations of basaltic glasses from the Mid- Cayman Rise Spreading Center. *J. Geophys. Res.: Solid Earth*, **100(B7)**, 12497-12512.

Escrig, S., Bézos, A., *Goldstein*, S. L., Langmuir, C. H., and Michael, P. J. *(*2009*)* Mantle source variations beneath the Eastern Lau Spreading Center and the nature of subduction components in the Lau basin–Tonga arc system, *Geochem. Geophys. Geosys.*, **10**, *Q04014, doi:*10.1029/2008GC002281.

Fouquet, Y., von Stackelberg, U., Charlou, J. L., Erzinger, J., Herzig, P. M., Mühe, R., and Wiedicke, M. (1993) Metallogenesis in back-arc environments: the Lau Basin example. *Econ. Geol.*, **88(8)**, 2154-2181.

Frenzel, J. M., Mühe, R., and Stoffers, P. (1990) Petrology of the volcanic rocks from the Lau basin, southwest Pacific. *Geol. Jahrb*. **92**, 395-479.

Goldfarb, M. S., Converse, D. R. Holland, H. D. and Edmond, J. M. (1983) The genesis of hot spring deposits on the East Pacific Rise, 21° N, Econ. Geol. Monogr., **5**, 184-197.

Hannington, M., Herzig, P., Scott, S., Thompson, G., and Rona, P. (1991) Comparative mineralogy and geochemistry of gold-bearing sulfide deposits on the mid-ocean ridges. *Marine Geology*, ***101*(1-4)**, 217-248.

Hannington, M. D., Jonasson, I. R., Herzig, P. M., and Petersen, S. (1995) Physical and chemical processes of seafloor mineralization at mid- ocean ridges. In *Seafloor hydrothermal systems: physical, chemical, biological, and geological interactions* (eds. S. E. Humphris, R. A. Zierenberg, L. S. Mullineaux, and R. E. Thomson), American Geophysical Union, Washington, D. C.. pp. 115-157. doi: 10.1029/GM091p0115.

Hannington, M. D., de Ronde, C. D. J., and Petersen, S. (2005) *Sea-floor tectonics and submarine hydrothermal systems. Economic Geology 100th Anniversary Volume.* Society of Economic Geologists, Littleton, Colorado, USA, 111-141.

Haymon, R. M. (1983) Growth history of hydrothermal black smoker chimneys. *Nature*, **301**, 695-698.

Huston, D. L., Sie, S. H., Suter, G. F., Cooke, D. R., and Both, R. A. (1995) Trace elements in sulfide minerals from eastern Australian volcanic-hosted massive sulfide deposits; Part I, Proton microprobe analyses of pyrite, chalcopyrite, and sphalerite, and Part II, Selenium levels in pyrite; comparison with delta 34 S values and implications for the source of sulfur in volcanogenic hydrothermal systems. *Econ. Geol.*, **90(5)**, 1167-1196.

Jenner, G. A., Cawood, P.A., Rautenschlein, M., and White, W. M. (1987) Composition of backarc basin volcanics, Valu Fa Ridge, Lau basin: Evidence for a slab-derived component in their mantle source, *J. Volcanol. Geotherm. Res*., **32**, 209–222.

Johnson, H. P., Hutnak, M., Dziak, R. P., Fox, C. G., Urcuyo, I., Cowen, J. P., Nabelek, J., and Fisher, C. (2000) Earthquake-induced changes in a hydrothermal system on the Juan de Fuca mid-ocean ridge. *Nature*, **407(6801)**, 174-177.

Kamenetsky, V. S., Binns, R. A., Gemmell, J. B., Crawford, A. J., Mernagh, T. P., Maas, R., and Steele, D. (2001) Parental basaltic melts and fluids in eastern Manus backarc basin: Implications for hydrothermal mineralization. *Earth Planet. Sci. Lett.*, **184(3)**, 685-702.

Karsten, J. L., Delaney, J. R., Rhodes, J. M., and Liias, R. A. (1990) Spatial and temporal evolution of magmatic systems beneath the Endeavour Segment, Juan de Fuca Ridge: Tectonic and petrologic constraints. *J. Geophys. Res.: Solid Earth*, **95(B12)**, 19235-19256.

Kawasumi, S. and Chiba, H. (2017) Redox state of seafloor hydrothermal fluids and its effect on sulfide mineralization. *Chemical Geology*. **451**, 25-37.

Krasnov, S., Poroshina, I., Cherkashev, G., Mikhalsky, E., and Maslov, M. (1997) Morphotectonics, volcanism and hydrothermal activity on the East Pacific Rise between 21 12′ S and 22 40′ S. *Marine Geophysical Researches*, **19(4)**, 287-317.

Langmuir, C., Humphris, S., Fornari, D., Van Dover, C., Von Damm, K. L., Tivey, M. K., Colodner, D., Charlou, J. –L. Desonie, D., Wilson, C., and Fouquet, Y. (1997) Hydrothermal vents near a mantle hot spot: the Lucky Strike vent field at 37 N on the Mid-Atlantic Ridge. *Earth Planet. Sci. Lett.*, **148(1-2)**, 69-91.

Langmuir, C. H., Bézos, A., Escrig, S., and Parman, S. W. (2006) Chemical systematics and hydrous melting of the mantle in back-arc basins. In *Back-Arc Spreading Systems: Geological, Biological, Chemical, and Physical Interactions* (eds. D.M. Christie, C.R.

Fisher, S.-M. Lee, and S. Givens) Geophysical Monograph Series, vol. 166, American Geophysical Union, Washington, DC. 87–146.

Layne, G., Tivey, M. K., and Humphris, S. E. (2005) Trace metal concentrations in common sulfide minerals using SIMS. *Fifteenth Annual V. M. Goldschmidt Conference* Abstracts, A55.

Lilley, M. D., Butterfield, D. A., Olson, E. J., Lupton, J. E., Macko, S. A., and McDuff, R. E. (1993) Anomalous CH_4 and $NH4^+$ concentrations at an unsedimented mid-ocean-ridge hydrothermal system. *Nature*, **364(6432)**, 45-47.

Martinez, F. and Taylor, B. (2002) Mantle wedge control on back-arc crustal accretion. *Nature*. **416**, 417-420.

Maslennikov, V. V., Maslennikova, S. P., Large, R. R., and Danyushevsky, L. V. (2009) Study of trace element zonation in vent chimneys from the Silurian Yaman-Kasy volcanic-hosted massive sulfide deposit (Southern Urals, Russia) using laser ablation-inductively coupled plasma mass spectrometry (LA-ICPMS) *Econ. Geol.*, **104(8)**, 1111-1141.

McDermott, J. M. (2015) Geochemistry of deep-sea hydrothermal vent fluids from the Mid-Cayman Rise, Caribbean Sea. Ph.D. Thesis, MIT/WHOI Joint Program in Oceanography.

McIntire, W. L. (1963) Trace element partition coefficients—a review of theory and applications to geology. *Geochim. Cosmochim. Acta*, **27(12)**, 1209-1264.

Mottl, M. J., Seewald, J. S., Wheat, C. G., Tivey, M. K., Michael, P. J., Proskurowski, G., McCollom, M., Reeves, E., Sharkey, S., You, C.-F., Chan, L.-H., and Pichler, T. (2011) Chemistry of hot springs along the Eastern Lau Spreading Center. *Geochim Cosmochim. Acta*, **75(4)**, 1013-1038.

Reeves, E. P., Seewald, J. S., Saccocia, P., Bach, W., Craddock, P. R., Shanks, W. C., Sylva. S., Walsh, E., Pichler, T., and Rosner, M. (2011) Geochemistry of hydrothermal fluids from the PACMANUS, Northeast Pual and Vienna Woods hydrothermal fields, Manus Basin, Papua New Guinea. *Geochim. Cosmochim. Acta*, **75(4)**, 1088-1123.

Revan, M. K., Genç, Y., Maslennikov, V. V., Maslennikova, S. P., Large, R. R., and Danyushevsky, L. V. (2014) Mineralogy and trace-element geochemistry of sulfide minerals in hydrothermal chimneys from the Upper-Cretaceous VMS deposits of the eastern Pontide orogenic belt (NE Turkey) *Ore Geology Reviews*, **63**, 129-149.

Rouxel, O., Fouquet, Y., and Ludden, J. N. (2004) Copper isotope systematics of the Lucky Strike, Rainbow, and Logatchev sea-floor hydrothermal fields on the Mid-Atlantic Ridge. *Econ. Geol.*, **99(3)**, 585-600.

Ryan, C. G. (2001) Developments in dynamic analysis for quantitative PIXE true elemental imaging. *Nuclear Instruments and Methods in Physics Research Section B: Beam Interactions with Materials and Atoms*, **181(1)**, 170-179.

Seewald, J. S. (2017) Chemical composition of hydrothermal fluids collected on RV/Roger Revelle RR1507 in the Eastern Lau Spreading Center and Valu Fa Ridge, April-May 2015 (Functional microbial dynamics of vent deposits project) Biological and Chemical Oceanography Data Management Office (BCO-DMO) Dataset version 2017-01-13 http://lod.bco-dmo.org/id/dataset/674750 (accessed, May 2017).

Seewald, J. S., and Seyfried, W. E. (1990) The effect of temperature on metal mobility in subseafloor hydrothermal systems: constraints from basalt alteration experiments. *Earth Planet. Sci. Lett.*, **101(2-4)**, 388-403.

Seyfried, W. E. and Ding, K. (1995) Phase equilibria in subseafloor hydrothermal systems: A review of the role of redox, temperature, pH and dissolved Cl on the chemistry of hot spring fluids at mid- ocean ridges. In *Seafloor Hydrothermal Systems: Physical, Chemical, Biological, and Geological Interactions* (eds. S. E. Humphris, R. A. Zierenberg, L. S. Mullineaux and R. E. Thomson), American Geophysical Union, Washington, D. C., pp. 248-272.

Seyfried, W. E., Ding, K., and Berndt, M. E. (1991) Phase equilibria constraints on the chemistry of hot spring fluids at mid-ocean ridges. *Geochim. Cosmochim. Acta*, **55(12)**, 3559-3580.

Seyfried, W. E., Seewald, J. S., Berndt, M. E., Ding, K., and Foustoukos, D. I. (2003) Chemistry of hydrothermal vent fluids from the Main Endeavour Field, northern Juan de Fuca Ridge: Geochemical controls in the aftermath of June 1999 seismic events. *J. Geophys. Res.: Solid Earth*, *108*(B9).

Sinton, J. M., Ford, L. L., Chappell, B., and McCullouch, M. T. (2003) Magma genesis and mantle heterogeneity in the Manus back-arc basin, Papua New Guinea. *J. Petrol.*, **44(1)**, 159-195.

Tivey, M. K. (1995) The influence of hydrothermal fluid composition and advection rates on black smoker chimney mineralogy: Insights from modeling transport and reaction. *Geochim. Cosmochim. Acta*, **59(10)**, 1933-1949.

Tivey, M. K., Stakes, D. S., Cook, T. L., Hannington, M. D., and Petersen, S. (1999) A model for growth of steep- sided vent structures on the Endeavour Segment of the Juan de Fuca Ridge: Results of a petrologic and geochemical study. *J. Geophys. Res: Solid Earth*, **104(B10),** 22859-22883.

Vallier, T. L., Jenner, G. A., Frey, F. A., Gill, J. B., Davis, A. S., Volpe, A. M., Hawkins, J. W., Morris, J. D., Cawood, P. A., Morton, J. L., Scholl, D. W., Rautenschlein, M., White, W. M., Williams, R. W., Stevenson, A. J., and White, L., D. (1991) Subalkaline andesite

from Valu Fa Ridge, a back-arc spreading center in southern Lau Basin: petrogenesis, comparative chemistry, and tectonic implications. *Chem. Geol.*, **91(3)**, 227-256.

Von Damm, K. L., Edmond, J. M., Grant, B., Measures, C. I., Walden, B., and Weiss, R. F. (1985) Chemistry of submarine hydrothermal solutions at 21° N, East Pacific Rise. *Geochim. Cosmochim. Acta*, **49(11),** 2197-2220.

Wohlgemuth-Ueberwasser, C. C., Viljoen, F., Petersen, S., and Vorster, C. (2015) Distribution and solubility limits of trace elements in hydrothermal black smoker sulfides: An in-situ LA-ICP-MS study. *Geochim. Cosmochim. Acta*, **159**, 16-41.

Wolery, T. J. (1992) EQ3/6: A software package for geochemical modeling of aqueous systems: package overview and installation guide (version 7.0) Livermore, CA: Lawrence Livermore National Laboratory.

Wood, S. A. and Samson, I. M. (2006) The aqueous geochemistry of gallium, germanium, indium and scandium. *Ore Geology Reviews*, *28*(1), 57-102.

Appendix A

ICP-MS standard solutions were created by serial dilution of a major element and minor element stock solution prepared from Specpure® plasma solutions. Major element and minor element stock solutions, standard solutions prepared by serial dilution, and dilutions of digested samples have a matrix of 5wt% HNO_3 that contained ~1 ng/g Sc and ~1 ng/g Y as internal spikes.

The major element stock solution contained:

825 ng/g Cu	952 ng/g Zn	0.93 ng/g Sc
1079 ng/g Fe	952 ng/g S	0.93 ng/g Y

in 5wt% HNO_3

The precision of these concentrations is ~3 ng/g for Cu, Fe, Zn, and S and 0.03ng/g for Sc and Y.

The minor element stock solution contained:

948 ng/g Sb	1043 ng/g Ga	948 ng/g Se
901 ng/g As	806 ng/g Ge	948 ng/g Si
996 ng/g Ba	948 ng/g Au	948 ng/g Ag
901 ng/g Bi	948 ng/g In	996 ng/g Sr
948 ng/g Cd	948 ng/g Pb	901 ng/g Te
948 ng/g Ca	948 ng/g Mn	948 ng/g Tl
996 ng/g Cr	995 ng/g Mo	1043 ng/g Sn
901 ng/g Co	1090 ng/g Ni	901 ng/g V

0.92 ng/g Sc
0.92 ng/g Y

The precision of these concentrations is 5 ng/g for minor elements and 0.03 ng/g for Sc and Y.
On 14 November 2016, the following standard solutions were prepared by serial dilution.

	Target major element concentration	Target minor element concentration	Major element dilution factor	Minor Element dilution factor	Sc, Y Spike concentration
2A	100 ng/g	10 ng/g	9.91	97.6	0.93 ng/g
2B	50 ng/g	5 ng/g	20.3	187.	0.93 ng/g
2C	10 ng/g	1 ng/g	99.9	984.	0.93 ng/g
2D	5 ng/g	0.5 ng/g	210.	1930	0.93 ng/g
2E	1 ng/g	0.1 ng/g	927.	9120	0.93 ng/g
2F	0.5 ng/g	0.05 ng/g	2200	20300	0.93 ng/g

These standard solutions were analyzed on 15, 16, 17 November 2016.

On 13 January 2017, an additional set of standard solutions were prepared by serial dilution.

	Target major element concentration	Target minor element concentration	Major element dilution factor	Minor Element dilution factor	Sc, Y Spike concentration
3A	100 ng/g	10 ng/g	10.0	97.4	0.94 ng/g
3B	50 ng/g	5 ng/g	19.3	193.	0.94 ng/g
3C	10 ng/g	1 ng/g	96.6	936.	0.94 ng/g
3D	5 ng/g	0.5 ng/g	190.	1890	0.94 ng/g
3E	1 ng/g	0.1 ng/g	959.	9300	0.94 ng/g
3F	0.5 ng/g	0.05 ng/g	1870	18700	0.94 ng/g

These standards were analyzed on 17 January 2017. The standard solutions prepared on 14 November 2016 were also analyzed.

During the 17 January 2017 session, a discrepancy was noted between the Ag counts per second measured in the 3A-3F standard solution series and the Ag counts per second measured in the 2A-2F standard solution series. These are shown on the following graphs.

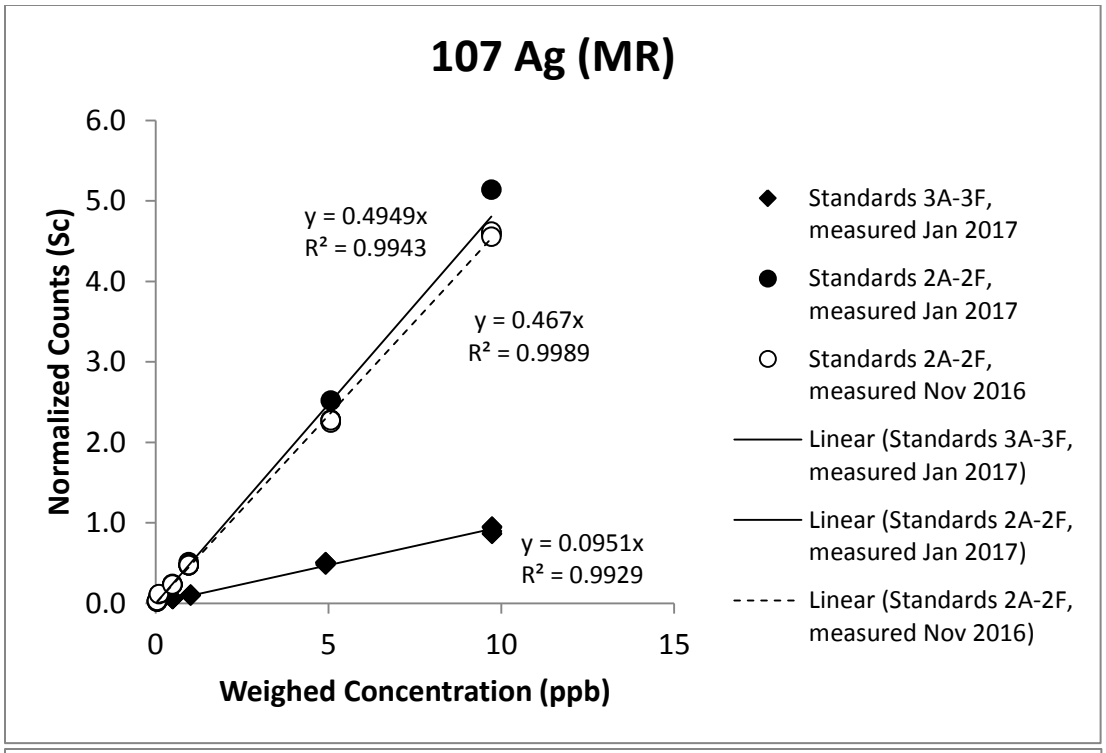
107 Ag (MR)
Normalized Counts (Sc)
Weighed Concentration (ppb)
y = 0.4949x
R² = 0.9943
y = 0.467x
R² = 0.9989
y = 0.0951x
R² = 0.9929
Standards 3A-3F, measured Jan 2017
Standards 2A-2F, measured Jan 2017
Standards 2A-2F, measured Nov 2016
Linear (Standards 3A-3F, measured Jan 2017)
Linear (Standards 2A-2F, measured Jan 2017)
Linear (Standards 2A-2F, measured Nov 2016)

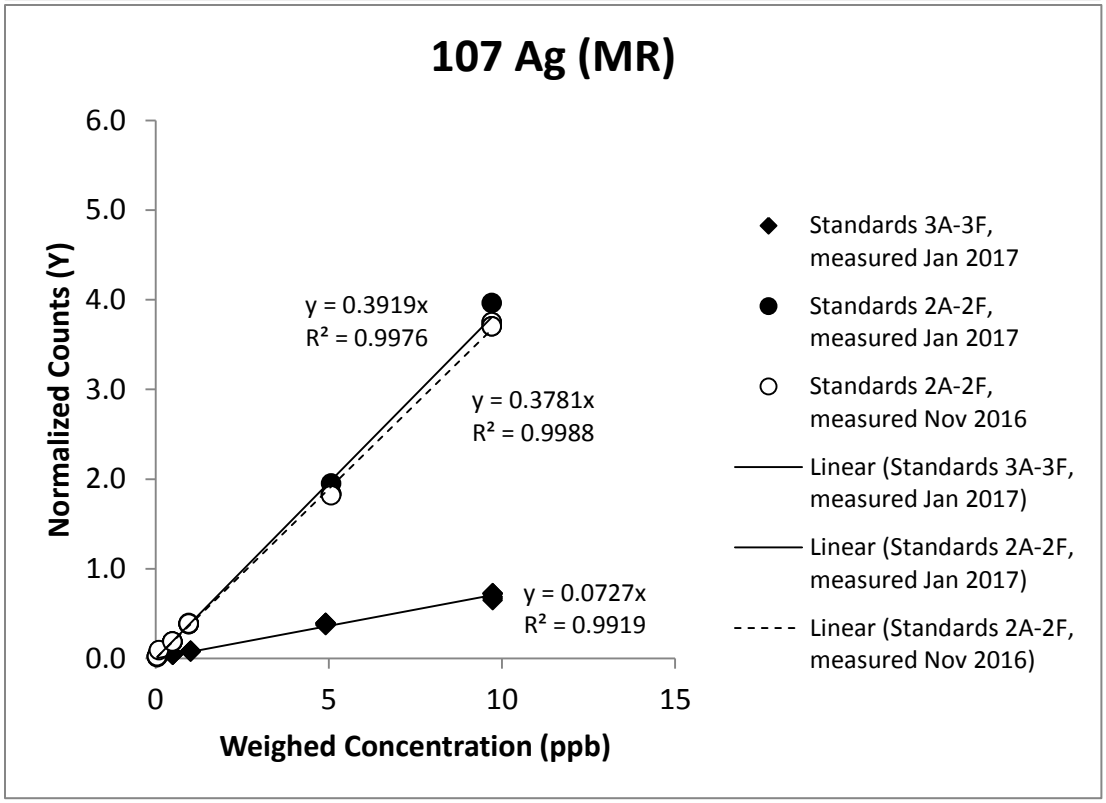
107 Ag (MR)
Normalized Counts (Y)
Weighed Concentration (ppb)
y = 0.3919x
R² = 0.9976
y = 0.3781x
R² = 0.9988
y = 0.0727x
R² = 0.9919
Standards 3A-3F, measured Jan 2017
Standards 2A-2F, measured Jan 2017
Standards 2A-2F, measured Nov 2016
Linear (Standards 3A-3F, measured Jan 2017)
Linear (Standards 2A-2F, measured Jan 2017)
Linear (Standards 2A-2F, measured Nov 2016)

Measurements of Ag in standard solutions 2A-2F completed in January 2017 gave the same results (within error) as those completed in November 2016. Measurements of Ag in standard solutions 3A-3F were much lower than expected and all dilutions are lower by the same factor (5.2±0.2). Because no change was observed in the 2A-2F solutions and all 3A-3F solutions were affected by the same ratio, the most likely explanation is that there was a loss in Ag from the minor element stock solution prior to serial dilution. Because no other elements were affected, this suggests a process unique to Ag. One possibility is photo-reduction of Ag caused by exposure of the minor element stock solution to light during storage. The 2A-2F solutions were not affected by this process, possibly because they are much more diluting than the stock solution or because they were stored in a dark cabinet.

Hypothesis: Ag in the minor element stock solution precipitated due to photo-reduction that occurred between the time at which the 2A-2F series of standard dilutions was created (November) and the time at which the 3A-3F series of standard solutions was created (January). The same process did not affect the 2A-2F standard solutions either because they were stored in the dark (unknown) or because they are more dilute. It is not known whether or not photo-reduction and precipitation of Ag occurred in the period between creation of the minor element stock solution and creation of the 2A-2F series of standard solutions is unknown. However, this period was less than one day.

If uncorrected, calculated values of Ag concentrations in standard solutions 2A-2F and all other samples measured against standard solutions 3A-3F are overestimated.

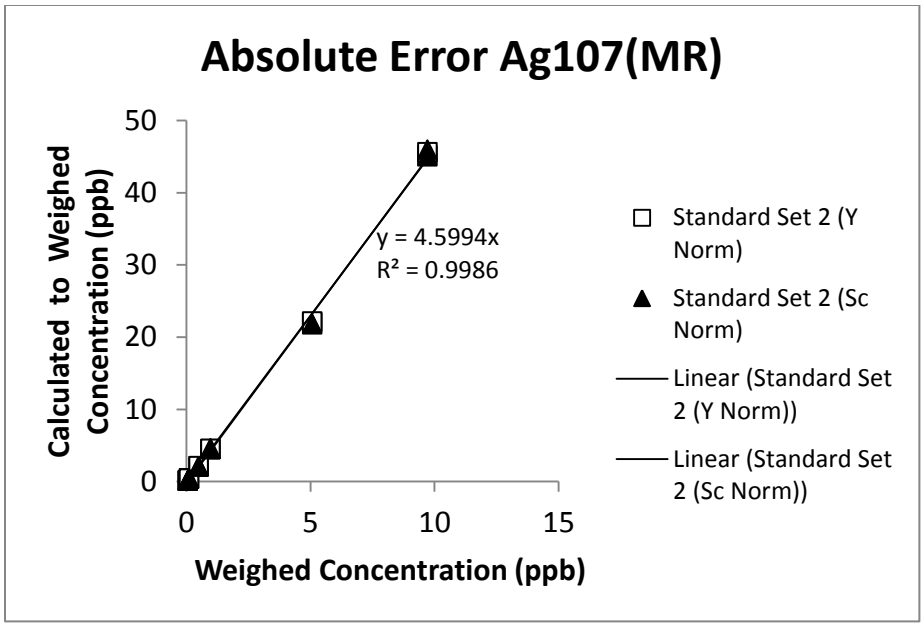

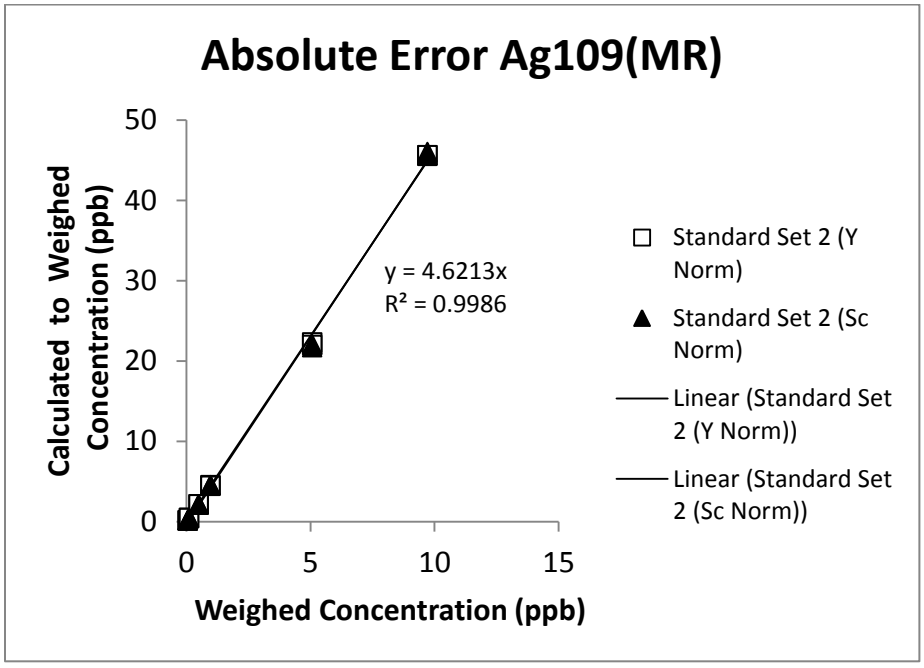

To correct, all values of Ag concentrations calculated by comparison to the 3A-3F standard solutions should be divided by a factor of 5.2±0.2 (or the slope of the 2A-2F line divided by the 3A-3F line). This can be validated by plotting difference between the calculated concentrations of the 2A-2F standard solutions and weighed concentrations of the 2A-2F standard solution series as a function of the weighed concentration of the 2A-2F standard solutions. This should by

symmetrical around zero and close to zero. This procedure assumes that only the 3A-3F series of standard solutions were significantly affected by photo-reduction of Ag and that the weighed concentrations of the 2A-2F standard solutions are accurate. It is not possible to definitively demonstrate that this assumption is correct, but at least makes all measurements comparable between sessions.

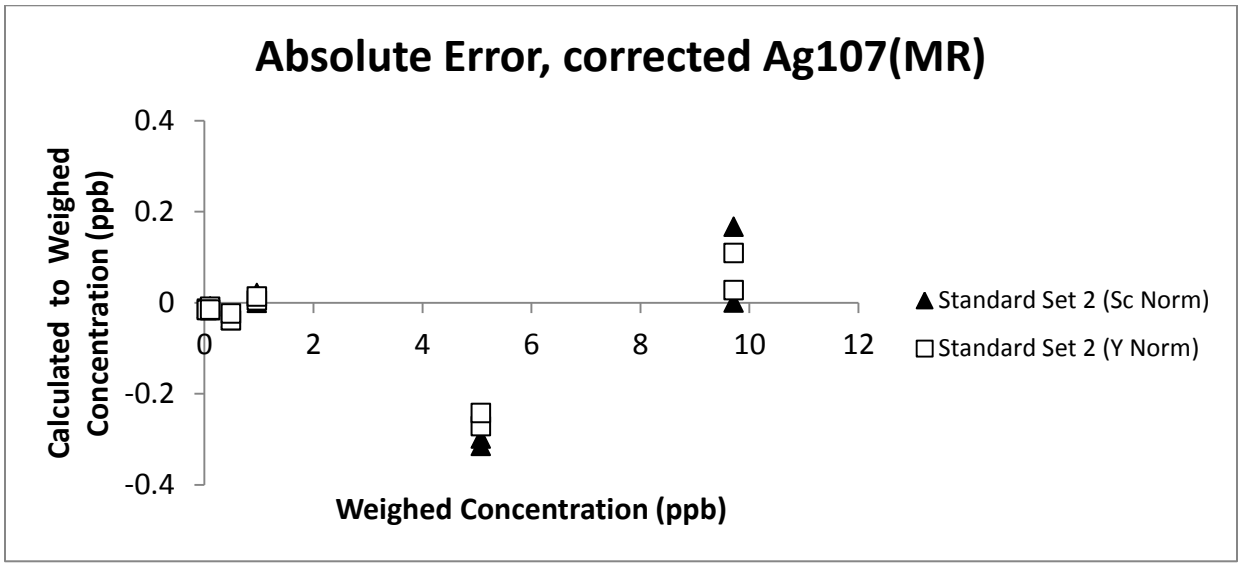

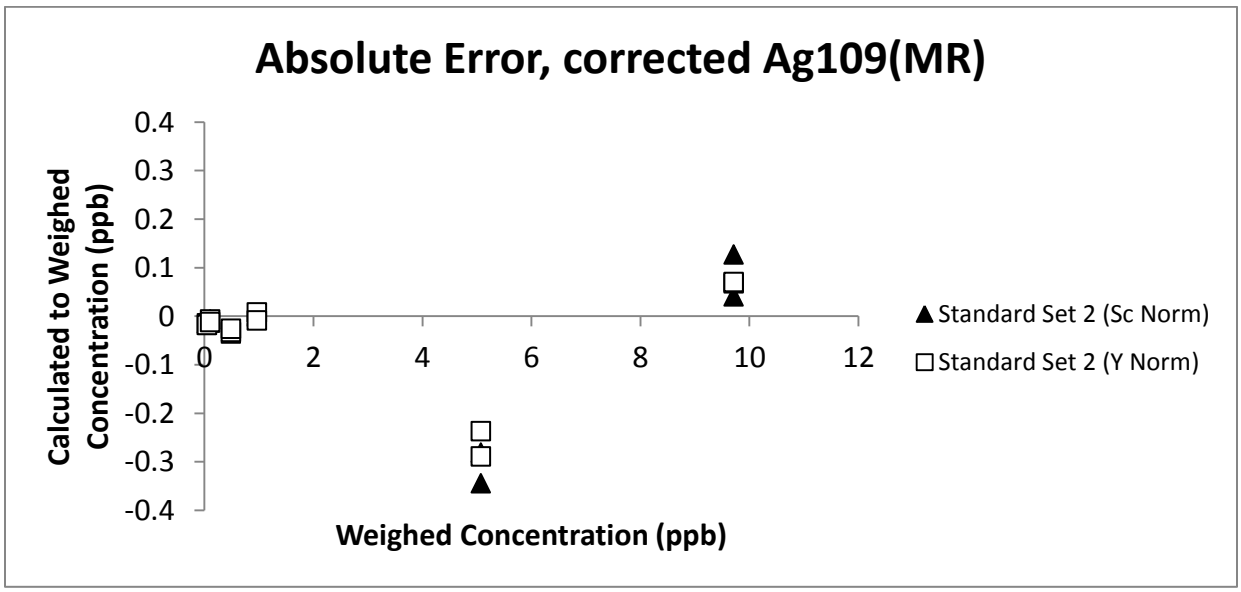

SUPPLEMENTARY MATERIAL

Supplementary Table S1: Data for Linear Regression of $^{113}In/^{115}In$

			113In / 63Cu16O			115In / 63Cu16O		
Sample	Date	n=	Sample Mean	±	Standard Error (1σ)	Sample Mean	±	Standard Error (1σ)
J2-207-1-R1	Sep-16	16	4.88E-04	±	7.02E-05	9.60E-04	±	3.13E-04
3288-5-1a	Sep-16	7	1.25E-02	±	3.99E-03	2.84E-01	±	8.60E-02
3296-2-2a	Sep-16	11	6.32E-03	±	7.43E-04	1.36E-01	±	1.78E-02
3296-3	Sep-16	12	5.61E-02	±	2.02E-02	1.31E+00	±	4.46E-01
3296-5-1a	Sep-16	8	5.64E-03	±	4.19E-04	1.32E-01	±	7.03E-03
3299-6-1	Sep-16	12	3.78E-02	±	2.41E-03	8.75E-01	±	4.70E-02
Alv1931	Sep-16	12	5.31E-02	±	8.86E-03	1.31E+00	±	7.83E-02
Alv3474-3-1	Sep-16	8	1.24E-02	±	2.42E-03	2.86E-01	±	6.19E-02
MASS-1	Sep-16	11	2.65E-02	±	6.18E-03	5.66E-01	±	1.11E-01
J2-207-1-R1	Oct-16	5	5.28E-04	±	6.60E-05	6.67E-04	±	3.74E-05
J2-208-1-R1	Oct-16	6	1.05E+00	±	2.46E-01	2.35E+01	±	5.47E+00
J2-213-6-R1	Oct-16	6	1.87E-01	±	2.48E-02	4.71E+00	±	7.63E-01
J2-214-3-R1	Oct-16	6	2.42E-01	±	6.45E-02	5.28E+00	±	1.47E+00
J2-216-16-R1	Oct-16	3	7.26E-02	±	1.34E-02	1.63E+00	±	3.01E-01
J2-217-10-R1	Oct-16	3	1.09E-02	±	2.56E-03	2.45E-01	±	6.01E-02
J2-217-2-R1	Oct-16	7	1.23E-02	±	2.92E-03	2.96E-01	±	4.12E-02
J2-223-1-R1	Oct-16	7	3.46E-02	±	5.55E-03	7.53E-01	±	1.28E-01
3296-2-2a	Oct-16	3	3.73E-03	±	5.64E-04	8.54E-02	±	1.18E-02
3299-6-1	Oct-16	19	2.76E-02	±	3.80E-03	6.82E-01	±	8.03E-02
J2-437-3-R2	Oct-16	6	1.48E-01	±	2.64E-02	3.30E+00	±	6.14E-01
J2-442-4-R2	Oct-16	3	2.46E-02	±	8.04E-04	6.60E-01	±	3.08E-02
J2-449-5-R1	Oct-16	8	3.47E-03	±	5.94E-04	7.82E-02	±	1.28E-02
J2-449-6-R1	Oct-16	6	4.03E-02	±	2.73E-02	1.17E+00	±	3.79E-01
J2-450-3-R1	Oct-16	3	2.20E-01	±	3.71E-03	4.95E+00	±	7.21E-02
J2-613-16-R1	Oct-16	3	1.03E-01	±	2.07E-03	2.31E+00	±	5.49E-02
J2-815-5-R1	Oct-16	3	6.44E-02	±	9.27E-03	1.46E+00	±	1.64E-01

Supplementary Table S2: Data for Figure 3A

Sample	Date	n=	55Mn	59Co	109Ag	115In	115In
			Sample Mean of Counts Ratio over 63Cu16O				
J2-207-1-R1	Oct. 2016	5	1.97E-01	1.04E-02	9.26E-02	5.28E-04	6.67E-04
J2-208-1-R1	Oct. 2016	6	2.29E-02	4.93E-05	2.64E-02	1.05E+00	2.35E+01
J2-213-6-R1	Oct. 2016	6	8.98E-03	5.05E-05	6.48E-03	1.87E-01	4.71E+00
J2-214-3-R1	Oct. 2016	6	1.96E-03	2.93E-05	4.83E-03	2.42E-01	5.28E+00
J2-216-16-R1	Oct. 2016	3	2.10E-02	3.26E-02	8.04E-03	7.26E-02	1.63E+00
J2-217-10-R1	Oct. 2016	3	1.24E-03	1.36E-02	1.59E-02	1.09E-02	2.45E-01
J2-217-2-R1	Oct. 2016	7	5.96E-03	9.73E-02	4.60E-03	1.23E-02	2.96E-01
J2-223-1-R1	Oct. 2016	7	4.60E-03	2.89E-01	7.45E-03	3.46E-02	7.53E-01
J2-442-4-R2	Oct. 2016	3	1.95E-01	3.77E-03	1.35E-02	2.46E-02	6.60E-01
J2-449-5-R1	Oct. 2016	8	2.91E-01	3.25E-05	2.14E-02	3.47E-03	7.82E-02
J2-449-6-R1	Oct. 2016	6	1.24E-01	6.71E-03	8.80E-03	4.03E-02	1.17E+00
J2-450-3-R1	Oct. 2016	3	3.07E-01	6.80E-05	6.95E-02	2.20E-01	4.95E+00
J2-613-16-R1	Oct. 2016	3	5.87E-01	1.82E+01	5.01E-03	1.03E-01	2.31E+00
J2-815-5-R1	Oct. 2016	3	1.90E-01	3.74E-05	1.39E-02	6.44E-02	1.46E+00

Sample	Date	n=	55Mn	59Co	109Ag	115In	115In
			Standard Error 1 sigma				
J2-207-1-R1	Oct. 2016	5	3.84E-03	3.90E-04	4.04E-03	6.60E-05	3.74E-05
J2-208-1-R1	Oct. 2016	6	1.77E-03	1.15E-05	2.57E-03	2.46E-01	5.47E+00
J2-213-6-R1	Oct. 2016	6	1.52E-03	3.73E-05	4.62E-04	2.48E-02	7.63E-01
J2-214-3-R1	Oct. 2016	6	3.63E-04	7.31E-06	7.24E-03	6.45E-02	1.47E+00
J2-216-16-R1	Oct. 2016	3	4.17E-03	2.63E-03	7.75E-04	1.34E-02	3.01E-01
J2-217-10-R1	Oct. 2016	3	1.07E-04	6.77E-04	4.07E-03	2.56E-03	6.01E-02
J2-217-2-R1	Oct. 2016	7	2.07E-04	4.34E-03	3.29E-04	2.92E-03	4.12E-02
J2-223-1-R1	Oct. 2016	7	1.16E-03	2.69E-02	1.07E-03	5.55E-03	1.28E-01
J2-442-4-R2	Oct. 2016	3	3.04E-03	7.35E-04	1.63E-03	8.04E-04	3.08E-02
J2-449-5-R1	Oct. 2016	8	4.46E-02	4.92E-06	1.56E-03	5.94E-04	1.28E-02
J2-449-6-R1	Oct. 2016	6	5.09E-02	5.96E-03	2.37E-03	2.73E-02	3.79E-01
J2-450-3-R1	Oct. 2016	3	9.41E-03	7.97E-06	3.99E-03	3.71E-03	7.21E-02
J2-613-16-R1	Oct. 2016	3	2.42E-01	1.04E+00	1.56E-03	2.07E-03	5.49E-02
J2-815-5-R1	Oct. 2016	3	3.87E-03	7.01E-06	6.47E-04	9.27E-03	1.64E-01

Supplementary Table S2: Data for Figure 3A cont.

Sample	Date	n=	55Mn	59Co	109Ag	115In	115In
			Sample Mean of Counts Ratio over 63Cu16O				
J2-207-1-R1	Dec. 2015	30	2.24E-01	1.08E-02	9.62E-02	8.10E-04	1.82E-02
J2-208-1-R1	Dec. 2015	5	3.34E-02	4.12E-05	3.08E-02	1.09E+00	2.44E+01
J2-213-6-R1	Dec. 2015	7	1.00E-02	2.30E-05	6.72E-03	2.20E-01	4.94E+00
J2-214-3-R1	Dec. 2015	6	2.06E-03	1.27E-05	2.08E-03	3.20E-01	7.18E+00
J2-216-16-R1	Dec. 2015	5	2.38E-02	2.81E-02	6.67E-03	5.57E-02	1.25E+00
J2-217-10-R1	Dec. 2015	6	2.63E-03	1.98E-02	1.12E-02	1.84E-02	4.13E-01
J2-217-2-R1	Dec. 2015	6	6.72E-03	1.08E-01	4.85E-03	1.66E-02	3.73E-01
J2-223-1-R1	Dec. 2015	10	4.42E-03	3.02E-01	8.32E-03	4.99E-02	1.12E+00
J2-442-4-R2	Dec. 2015	7	1.82E-01	4.53E-03	1.45E-02	2.29E-02	5.13E-01
J2-449-5-R1	Dec. 2015	6	3.47E-01	2.68E-05	2.46E-02	3.88E-03	8.70E-02
J2-449-6-R1	Dec. 2015	5	2.61E-01	4.55E-03	1.45E-02	7.53E-02	1.69E+00
J2-450-3-R1	Dec. 2015	10	3.06E-01	5.04E-05	6.54E-02	2.32E-01	5.21E+00
J2-613-16-R1	Dec. 2015	6	6.39E-01	1.74E+01	2.88E-03	9.96E-02	2.23E+00
J2-815-5-R1	Dec. 2015	6	2.08E-01	5.72E-04	1.46E-02	4.76E-02	1.07E+00

Sample	Date	n=	55Mn	59Co	109Ag	115In	115In
			Standard Error 1 sigma				
J2-207-1-R1	Dec. 2015	30	2.68E-02	1.09E-03	8.32E-03	2.02E-04	4.53E-03
J2-208-1-R1	Dec. 2015	5	6.49E-03	6.31E-06	4.54E-03	4.02E-01	9.01E+00
J2-213-6-R1	Dec. 2015	7	1.47E-03	9.20E-06	5.74E-04	4.86E-02	1.09E+00
J2-214-3-R1	Dec. 2015	6	2.05E-04	6.04E-06	2.11E-04	6.86E-02	1.54E+00
J2-216-16-R1	Dec. 2015	5	1.26E-02	2.54E-03	6.65E-04	9.10E-03	2.04E-01
J2-217-10-R1	Dec. 2015	6	1.55E-03	3.67E-03	7.62E-04	4.76E-03	1.07E-01
J2-217-2-R1	Dec. 2015	6	5.09E-04	4.17E-03	3.50E-04	4.89E-03	1.10E-01
J2-223-1-R1	Dec. 2015	10	1.17E-03	3.14E-02	2.10E-03	1.85E-02	4.14E-01
J2-442-4-R2	Dec. 2015	7	1.03E-02	6.66E-04	1.26E-03	8.63E-03	1.94E-01
J2-449-5-R1	Dec. 2015	6	3.86E-02	1.12E-05	2.71E-03	1.12E-03	2.51E-02
J2-449-6-R1	Dec. 2015	5	6.33E-02	4.51E-03	2.58E-03	5.17E-03	1.16E-01
J2-450-3-R1	Dec. 2015	10	3.13E-02	7.17E-06	6.88E-03	6.54E-02	1.47E+00
J2-613-16-R1	Dec. 2015	6	1.59E-01	3.06E+00	5.16E-04	3.82E-02	8.56E-01
J2-815-5-R1	Dec. 2015	6	4.00E-02	9.18E-04	1.85E-03	1.85E-02	4.15E-01

Supplementary Table S3: Data for Figure 3B

Sample	Date	n=	55Mn	59Co	60Ni	69Ga	109Ag	113In	115In
			Sample Mean of Counts Ratio over 63Cu16O						
J2-207-1-R1	Sep. 2016	16	2.35E-01	1.13E-02	6.08E-05	2.90E-02	1.05E-01	4.88E-04	9.60E-04
3296-2-2a	Sep. 2016	11	6.96E-02	1.55E+00	1.17E-01	1.77E-02	5.17E-03	6.32E-03	1.36E-01
3299-6-1	Sep. 2016	12	5.55E-01	2.78E+00	3.19E-01	4.11E-02	2.54E-02	3.78E-02	8.75E-01

Sample	Date	n=	55Mn	59Co	60Ni	69Ga	109Ag	113In	115In
			Standard Error 1 sigma						
J2-207-1-R1	Sep. 2016	16	1.45E-02	8.40E-04	2.10E-05	1.88E-02	5.68E-03	7.02E-05	3.13E-04
3296-2-2a	Sep. 2016	11	7.08E-03	1.34E-01	8.64E-03	3.99E-03	5.91E-04	7.43E-04	1.78E-02
3299-6-1	Sep. 2016	12	3.45E-02	1.12E-01	1.17E-02	5.65E-03	9.22E-04	2.41E-03	4.70E-02

Sample	Date	n=	55Mn	59Co	60Ni	69Ga	109Ag	113In	115In
			Sample Mean of Counts Ratio over 63Cu16O						
J2-207-1-R1	Oct. 2016	5	1.97E-01	1.04E-02	5.46E-05	2.44E-02	9.26E-02	5.28E-04	6.67E-04
3296-2-2a	Oct. 2016	3	5.75E-02	1.33E+00	1.14E-01	1.26E-02	3.77E-03	3.73E-03	8.54E-02
3299-6-1	Oct. 2016	19	4.40E-01	2.43E+00	2.95E-01	3.14E-02	2.21E-02	2.76E-02	6.82E-01

Sample	Date	n=	55Mn	59Co	60Ni	69Ga	109Ag	113In	115In
			Standard Error 1 sigma						
J2-207-1-R1	Oct. 2016	5	3.84E-03	3.90E-04	9.23E-06	9.99E-03	4.04E-03	6.60E-05	3.74E-05
3296-2-2a	Oct. 2016	3	7.31E-03	1.66E-01	1.56E-02	1.08E-03	4.65E-04	5.64E-04	1.18E-02
3299-6-1	Oct. 2016	19	4.57E-02	1.64E-01	2.02E-02	4.90E-03	2.39E-03	3.80E-03	8.03E-02

Supplementary Table S4: Data for Figures 4A - 4F

SIMS data, n = number of spots on a given sample, NM = not measured

Vent Field	Sample	Vent Fluid	pH	pH	59Co/63Cu16O			60Ni/63Cu16O			69Ga/63Cu16O			109Ag/63Cu16O			115In/63Cu16O		
		degC	25C	in situ	n	Average	Error (1σ)	n	Average	Error (1σ)	n	Average	Error (1σ)	n	Average	Error (1σ)	n	Average	Error (1σ)
EPR, 17 34'S	Alv3299-6-1	349	3.2		31	3.34E+00 ±	4.07E-01	31	2.95E-01 ±	2.02E-02	31	3.17E-02 ±	5.02E-03	31	2.27E-02 ±	3.15E-03	31	8.13E-01 ±	2.13E-01
EPR, 17 37'S	Alv3288-5-1a	337	3.4		7	1.07E+00 ±	1.30E-01	7	3.12E-02 ±	1.25E-03	7	2.42E-02 ±	9.43E-03	7	5.37E-03 ±	6.35E-04	7	3.14E-01 ±	9.51E-02
EPR, 17 37'S	Alv3296-2-2a				14	1.85E+00 ±	2.94E-01	14	1.10E-01 ±	1.56E-02	14	1.36E-02 ±	3.12E-03	14	4.55E-03 ±	1.03E-03	14	1.38E-01 ±	4.88E-02
EPR, 17 37'S	Alv3296-3	314	3.4		12	7.37E-01 ±	6.76E-02	12	8.38E-02 ±	3.32E-03	12	7.38E-02 ±	3.05E-02	12	6.59E-02 ±	1.29E-02	12	1.45E+00 ±	4.93E-01
EPR, 17 37'S	Alv3296-5-1a	347	3.3		8	1.97E+00 ±	6.73E-02	8	1.17E-01 ±	4.72E-03	8	1.24E-02 ±	1.23E-03	8	4.43E-03 ±	2.31E-04	8	1.46E-01 ±	7.78E-03
MEF (pre-event)	Alv1931				12	6.18E-05 ±	1.39E-05	12	1.95E-04 ±	3.43E-05	12	5.02E-02 ±	1.03E-02	12	5.92E-03 ±	3.16E-04	12	1.45E+00 ±	8.66E-02
MEF (post-event)	Alv3474-3-1	379	3.6	4.3	27	8.24E-01 ±	1.19E-01	8	2.27E-02 ±	1.24E-02	8	1.32E-02 ±	7.94E-03	27	3.08E-03 ±	5.55E-04	27	3.16E-01 ±	9.05E-02
MEF (post-event)	Alv3480-4				6	7.98E-01 ±	8.94E-02		NM			NM		6	2.70E-03 ±	4.55E-04	6	3.45E-01 ±	3.43E-02
Lucky Strike	DV1-5B				5	6.14E-01 ±	7.37E-02		NM			NM		5	4.81E-02 ±	2.11E-02	5	1.71E+00 ±	2.43E-01
Beebe	J2-613-16-R1	395	3.0	5.0	19	1.74E+01 ±	5.77E+00	3	1.35E+00 ±	6.62E-02	3	4.11E-02 ±	1.91E-03	19	3.64E-03 ±	2.18E-03	19	2.16E+00 ±	8.56E-01
Vienna Woods	J2-207-1-R1	282	4.4	5.1	88	1.21E-02 ±	6.14E-03	21	5.60E-05 ±	1.95E-05	21	2.31E-02 ±	1.47E-02	88	9.56E-02 ±	1.65E-02	88	1.32E-02 ±	3.68E-02
Fenway	J2-210-7-R2				7	7.09E-05 ±	4.16E-05		NM			NM		7	4.29E-03 ±	1.44E-03	7	2.63E+00 ±	9.31E-01
Fenway	J2-216-16-R1	358	2.7	3.9	13	3.41E-02 ±	1.26E-02	3	7.11E-04 ±	2.21E-04	3	7.68E-01 ±	7.97E-02	13	8.10E-03 ±	6.32E-03	8	1.42E+00 ±	5.22E-01
Satanic Mills	J2-214-3-R1	288	2.5	3.0	27	1.18E-05 ±	2.22E-05	8	1.67E-04 ±	6.04E-05	8	1.07E+00 ±	3.27E-01	27	1.55E-03 ±	7.35E-03	27	2.83E+00 ±	2.43E+00
Roman Ruins	J2-208-1-R1	314	2.3	2.8	24	7.28E-04 ±	9.11E-04	6	1.24E-04 ±	2.32E-05	6	2.62E+00 ±	9.93E-01	24	3.25E-02 ±	1.61E-02	11	2.45E+01 ±	9.01E+00
Roger's Ruins	J2-213-6-R1	320	2.7		13	4.4E-05 ±	5.4E-05	6	4.0E-05 ±	2.6E-05	6	2.4E-01 ±	1.6E-01	13	6.6E-03 ±	7.6E-04	13	4.9E+00 ±	1.1E+00
Suzette	J2-217-2-R1	303	3.8	4.2	13	1.57E-01 ±	2.32E-02	3	5.64E-03 ±	2.31E-04	3	5.10E-02 ±	1.08E-02	13	6.44E-03 ±	1.12E-03	8	7.69E-01 ±	1.15E-01
Suzette	J2-217-10-R1	274	3.6	4.0	20	2.18E-02 ±	1.05E-02	3	1.08E-03 ±	1.50E-04	3	3.15E-01 ±	5.28E-02	20	1.35E-02 ±	5.01E-03	9	3.61E-01 ±	1.67E-01
Suzette	J2-219-2-R1				5	2.08E-04 ±	1.17E-04		NM			NM		5	9.16E-03 ±	3.78E-03	5	1.04E+00 ±	5.31E-01
North Su	J2-223-1-R1	300	3.4	3.9	21	3.34E-01 ±	1.01E-01	7	1.85E-02 ±	3.87E-03	7	3.55E-01 ±	1.22E-01	21	7.70E-03 ±	2.64E-03	17	9.83E-01 ±	4.54E-01
North Su	J2-227-10-R1				10	8.77E-03 ±	1.50E-03		NM			NM		10	5.43E-03 ±	8.63E-04	10	1.04E+00 ±	4.49E-01
Tahi Moana 1	J2-450-3-R1	310	3.7	4.6	18	6.39E-05 ±	4.01E-05	3	1.18E-04 ±	9.17E-06	3	6.85E-02 ±	2.62E-02	18	6.60E-02 ±	1.60E-02	18	5.26E+00 ±	1.53E+00
ABE	J2-449-5-R1	306	4.0	5.2	20	2.65E-04 ±	4.67E-04	8	4.86E-05 ±	1.14E-05	8	1.00E-01 ±	3.06E-02	20	2.34E-02 ±	4.07E-03	20	1.04E-01 ±	2.51E-02
ABE	J2-449-6-R1	317	3.9	5.1	22	1.18E-02 ±	1.15E-02	6	1.44E-05 ±	4.26E-06	6	5.83E-02 ±	1.63E-02	22	1.21E-02 ±	5.35E-03	22	1.45E+00 ±	1.01E+00
ABE	J2-815-5-R1	300	4.0	5.2	9	8.81E-04 ±	1.08E-03	3	3.09E-05 ±	9.18E-06	3	1.91E-01 ±	1.47E-02	9	1.45E-02 ±	1.90E-03	9	1.22E+00 ±	5.68E-01
Tu'i Malila	J2-442-4-R2	315	3.8	4.5	17	5.17E-03 ±	4.72E-03	3	3.06E-05 ±	8.65E-06	3	1.04E-02 ±	2.85E-03	17	1.38E-02 ±	2.07E-03	17	5.55E-01 ±	4.95E-01
Tu'i Malila	J2-819-4-R2	269	3.9		4	1.82E-04 ±	8.17E-05		NM			NM		4	5.38E-02 ±	6.38E-03	4	3.75E-02 ±	8.07E-03
Mariner	J2-437-3-R2	338	2.4	3.2	12	1.06E-04 ±	2.44E-04	6	9.93E-05 ±	1.54E-04	6	3.52E-01 ±	1.04E-01	12	2.95E-03 ±	2.00E-03	12	4.07E+00 ±	1.74E+00
Mariner	J2-817-4-R2	354	2.7	3.8	6	8.95E-04 ±	3.88E-04		NM			NM		6	2.57E-03 ±	4.32E-04	6	1.04E+00 ±	1.23E-01

Supplementary Table S5

Input to pca (SIMS data only)					
Sample	log (59Co / 63Cu16O)	log (60Ni / 63Cu16O)	log (69Ga / 63Cu16O)	log (109Ag / 63Cu16O)	log (115In / 63Cu16O)
Alv3299-6-1	0.52	-0.53	-1.50	-1.64	-0.09
Alv3288-5-1a	0.03	-1.51	-1.62	-2.27	-0.50
Alv3296-2-2a	0.27	-0.96	-1.87	-2.34	-0.86
Alv3296-3	-0.13	-1.08	-1.13	-1.18	0.16
Alv3296-5-1a	0.29	-0.93	-1.91	-2.35	-0.84
Alv1931	-4.21	-3.71	-1.30	-2.23	0.16
Alv3474-3-1	-0.08	-1.64	-1.88	-2.51	-0.50
J2-613-16-R1	1.24	0.13	-1.39	-2.44	0.33
J2-207-1-R1	-1.92	-4.25	-1.64	-1.02	-1.88
J2-216-16-R1	-1.47	-3.15	-0.11	-2.09	0.15
J2-214-3-R1	-4.93	-3.78	0.03	-2.81	0.45
J2-208-1-R1	-3.14	-3.91	0.42	-1.49	1.39
J2-213-6-R1	-3.21	-4.40	-0.62	-1.06	0.69
J2-217-2-R1	-0.80	-2.25	-1.29	-2.19	-0.11
J2-217-10-R1	-1.66	-2.97	-0.50	-1.87	-0.44
J2-223-1-R1	-0.48	-1.73	-0.45	-2.11	-0.01
J2-450-3-R1	-4.19	-3.93	-1.16	-1.18	0.72
J2-449-5-R1	-3.58	-4.31	-1.00	-1.63	-0.98
J2-449-6-R1	-1.93	-4.84	-1.23	-1.92	0.16
J2-815-5-R1	-3.05	-4.51	-0.72	-1.84	0.09
J2-442-4-R2	-2.29	-4.51	-1.98	-1.86	-0.26
J2-437-3-R2	-3.98	-4.00	-0.45	-2.53	0.61

Output from pca (SIMS data only)					
Correlation Coefficients	log (59Co / 63Cu16O)	log (60Ni / 63Cu16O)	log (69Ga / 63Cu16O)	log (109Ag / 63Cu16O)	log (115In / 63Cu16O)
log (59Co / 63Cu16O)	1.00	0.86	-0.52	-0.16	-0.37
log (60Ni / 63Cu16O)	0.86	1.00	-0.38	-0.33	-0.18
log (69Ga / 63Cu16O)	-0.52	-0.38	1.00	0.05	0.63
log (109Ag / 63Cu16O)	-0.16	-0.33	0.05	1.00	0.00
log (115In / 63Cu16O)	-0.37	-0.18	0.63	0.00	1.00
Pearson P value	log (59Co / 63Cu16O)	log (60Ni / 63Cu16O)	log (69Ga / 63Cu16O)	log (109Ag / 63Cu16O)	log (115In / 63Cu16O)
log (59Co / 63Cu16O)	1.00	0.00	0.01	0.47	0.09
log (60Ni / 63Cu16O)	0.00	1.00	0.08	0.14	0.43
log (69Ga / 63Cu16O)	0.01	0.08	1.00	0.84	0.00
log (109Ag / 63Cu16O)	0.47	0.14	0.84	1.00	1.00
log (115In / 63Cu16O)	0.09	0.43	0.00	1.00	1.00
Principle Components	pca-1	pca-2	pca-3	pca-4	pca-5
log (59Co / 63Cu16O)	0.76	-0.21	0.51	-0.31	-0.14
log (60Ni / 63Cu16O)	0.62	0.48	-0.43	0.37	0.25
log (69Ga / 63Cu16O)	-0.15	0.51	0.35	-0.43	0.64
log (109Ag / 63Cu16O)	-0.05	-0.18	0.55	0.75	0.32
log (115In / 63Cu16O)	-0.10	0.66	0.35	0.16	-0.63
	pca-1	pca-2	pca-3	pca-4	pca-5
Contribution to total variance (%)	79.65	10.56	4.83	2.70	2.26

Supplementary Table S6

Input to pca (SIMS and fluid data)					SIMS count ratio over 63Cu16O (log 10)				
Sample	1/K	pH	log(mmol Cl)	log(umol H2S)	log (59Co / 63Cu16O)	log (60Ni / 63Cu16O)	log (69Ga / 63Cu16O)	log (109Ag / 63Cu16O)	log (115In / 63Cu16O)
Alv3299-6-1	1.61E-03	3.20	2.68	0.95	0.52	-0.53	-1.50	-1.64	-0.09
Alv3288-5-1a	1.64E-03	3.41	2.88	0.54	0.03	-1.51	-1.62	-2.27	-0.50
Alv3296-3	1.70E-03	3.44	2.88	0.81	-0.13	-1.08	-1.13	-1.18	0.16
Alv3296-5-1a	1.61E-03	3.30	2.77	0.57	0.29	-0.93	-1.91	-2.35	-0.84
J2-207-1-R1	1.80E-03	4.40	2.84	0.15	-1.92	-4.25	-1.64	-1.02	-1.88
J2-208-1-R1	1.70E-03	2.30	2.80	0.88	-3.14	-3.91	0.42	-1.49	1.39
J2-213-6-R1	1.69E-03	2.70	2.81	0.56	-3.21	-4.40	-0.62	-1.06	0.69
J2-214-3-R1	1.78E-03	2.50	2.70	1.01	-4.93	-3.78	0.03	-2.81	0.45
J2-216-16-R1	1.58E-03	2.70	2.75	1.27	-1.47	-3.15	-0.11	-2.09	0.15
J2-217-10-R1	1.83E-03	3.60	2.84	0.26	-1.66	-2.97	-0.50	-1.87	-0.44
J2-217-2-R1	1.74E-03	3.80	2.80	0.26	-0.80	-2.25	-1.29	-2.19	-0.11
J2-223-1-R1	1.74E-03	3.40	2.83	0.53	-0.48	-1.73	-0.45	-2.11	-0.01
J2-437-3-R2	1.64E-03	2.30	2.73	0.95	-3.98	-4.00	-0.45	-2.53	0.61
J2-442-4-R2	1.70E-03	3.80	2.81	0.40	-2.29	-4.51	-1.98	-1.86	-0.26
J2-449-5-R1	1.73E-03	4.00	2.74	0.44	-3.58	-4.31	-1.00	-1.63	-0.98
J2-449-6-R1	1.69E-03	3.90	2.73	0.59	-1.93	-4.84	-1.23	-1.92	0.16
J2-450-3-R1	1.71E-03	3.70	2.74	0.52	-4.19	-3.93	-1.16	-1.18	0.72
J2-613-16-R1	1.50E-03	3.30	2.55	-1.93	1.24	0.13	-1.39	-2.44	0.33
J2-815-5-R1	1.74E-03	4.00	2.74	0.57	-3.05	-4.51	-0.72	-1.84	0.09

Output from pca (SIMS and fluid data)									
Correlation Coefficients	1/K	pH	log(mmol Cl)	log(umol H2S)	log (59Co / 63Cu16O)	log (60Ni / 63Cu16O)	log (69Ga / 63Cu16O)	log (109Ag / 63Cu16O)	log (115In / 63Cu16O)
1/K	1.00	0.35	0.55	0.31	-0.51	-0.54	0.23	0.30	-0.23
pH	0.35	1.00	0.17	-0.32	0.21	-0.08	-0.65	0.33	-0.69
log(mmol Cl)	0.55	0.17	1.00	0.48	-0.03	-0.20	-0.03	0.40	-0.26
log(umol H2S)	0.31	-0.32	0.48	1.00	-0.41	-0.37	0.37	0.11	0.14
log (59Co / 63Cu16O)	-0.51	0.21	-0.03	-0.41	1.00	0.86	-0.51	-0.12	-0.31
log (60Ni / 63Cu16O)	-0.54	-0.08	-0.20	-0.37	0.86	1.00	-0.31	-0.28	-0.08
log (69Ga / 63Cu16O)	0.23	-0.65	-0.03	0.37	-0.51	-0.31	1.00	-0.11	0.60
log (109Ag / 63Cu16O)	0.30	0.33	0.40	0.11	-0.12	-0.28	-0.11	1.00	-0.08
log (115In / 63Cu16O)	-0.23	-0.69	-0.26	0.14	-0.31	-0.08	0.60	-0.08	1.00
Pearson P value	1/K	pH	log(mmol Cl)	log(umol H2S)	log (59Co / 63Cu16O)	log (60Ni / 63Cu16O)	log (69Ga / 63Cu16O)	log (109Ag / 63Cu16O)	log (115In / 63Cu16O)
1/K	1.00	0.14	0.01	0.20	0.03	0.02	0.35	0.21	0.33
pH	0.14	1.00	0.48	0.18	0.39	0.73	0.00	0.16	0.00
log(mmol Cl)	0.01	0.48	1.00	0.04	0.89	0.42	0.91	0.09	0.28
log(umol H2S)	0.20	0.18	0.04	1.00	0.08	0.12	0.12	0.66	0.56
log (59Co / 63Cu16O)	0.03	0.39	0.89	0.08	1.00	0.00	0.02	0.62	0.20
log (60Ni / 63Cu16O)	0.02	0.73	0.42	0.12	0.00	1.00	0.20	0.25	0.73
log (69Ga / 63Cu16O)	0.35	0.00	0.91	0.12	0.02	0.20	1.00	0.66	0.01
log (109Ag / 63Cu16O)	0.21	0.16	0.09	0.66	0.62	0.25	0.66	1.00	0.73
log (115In / 63Cu16O)	0.33	0.00	0.28	0.56	0.20	0.73	0.01	0.73	1.00
Principle Components	pca-1	pca-2	pca-3	pca-4	pca-5	pca-6	pca-7	pca-8	pca-9
1/K	0.00	0.00	0.00	0.00	0.00	0.00	0.00	0.00	1.00
pH	0.04	-0.52	-0.11	0.03	0.15	0.11	0.83	0.00	0.00
log(mmol Cl)	0.00	-0.02	0.08	0.02	0.02	0.02	0.00	1.00	0.00
log(umol H2S)	-0.13	0.13	0.91	-0.15	0.07	-0.22	0.23	-0.06	0.00
log (59Co / 63Cu16O)	0.74	-0.16	0.24	0.42	-0.43	-0.01	-0.04	-0.02	0.00
log (60Ni / 63Cu16O)	0.63	0.41	-0.08	-0.39	0.50	0.10	0.12	0.01	0.00
log (69Ga / 63Cu16O)	-0.14	0.44	0.10	0.13	-0.26	0.80	0.23	-0.01	0.00
log (109Ag / 63Cu16O)	-0.04	-0.18	0.19	0.56	0.68	0.28	-0.27	-0.05	0.00
log (115In / 63Cu16O)	-0.08	0.55	-0.21	0.56	0.07	-0.46	0.35	0.03	0.00
	pca-1	pca-2	pca-3	pca-4	pca-5	pca-6	pca-7	pca-8	pca-9
Contribution to total variance (%)	71.16	14.55	4.72	3.86	2.73	1.98	0.96	0.04	0.00

Chapter 4

Trace Element Proxies of Hydrothermal Fluid pH and Metal Content Based on Sample Pairs of Seafloor Hydrothermal Fluids and Chalcopyrite Lining Black Smoker Chimneys

1. INTRODUCTION

The metal sulfide linings of black smoker chimney deposits that form in association with focused vents of high-temperature seafloor hydrothermal fluids provide a unique opportunity to sample paired mineral and fluid samples in order to quantitatively investigate the relationships between mineral trace element chemistry and the temperature and chemistry of deposit-forming hydrothermal fluids. Especially interesting is the opportunity to sample and measure the major and trace metal contents of venting hydrothermal fluids, an aspect of hydrothermal fluid chemistry that is unavailable for inactive or fossil hydrothermal systems. This paper presents new data on the major and trace metal chemistry of hydrothermal fluids from the Kilo Moana, Tahi Moana-1, ABE, Tu'i Malila, and Mariner vent fields on the Eastern Lau Spreading Center. These new data, as well as existing data on major element and trace metal chemistry in seafloor hydrothermal fluids, are then combined with trace metal concentration data for chalcopyrite that lines related black smoker chimneys (from Chapter 3 of this thesis) to provide quantitative insights into the partitioning of trace metals from vent fluids into solids. Furthermore, this comparison allows for investigation of the extents to which these trace element signatures in black smoker chimney linings can be used as proxies for hydrothermal fluid chemistry, including pH and trace metal concentrations.

Table 1. (opposite)
Black smoker chimney and hydrothermal fluid samples used in this study, from the southern East Pacific Rise (S. EPR), the Main Endeavour Field (MEF) on the Juan de Fuca Ridge (JdF), the Mid-Cayman Rise (MCR), the Manus Spreading Center (MSC), the PACMANUS (PAC) and SuSu Knolls (SuSu) areas of the Eastern Manus Basin (EMB) and the Eastern Lau Spreading Center (ELSC). Vent fields are hosted in basalt, enriched mid-ocean ridge basalts (E-MORB) or felsic host rocks including andesites, rhyolites, and dacites. Chimneys are lined with chalcopyrite (cp), cubanite (cb), co-deposited chalcopyrite and wurtzite (cp/wz), or co-deposited chalcopyrite and pyrite (cp/py). Samples from vent fields thought to be influenced by acidic magmatic volatiles are enclosed in boxes. All sample and fluid names are as labeled in the original references and sample archive. References for fluid chemistry are as follows: S. EPR (K.L. Von Damm, unpublished data), MEF (Seyfried et al., 2003), MCR (McDermott, 2015), EMB (Reeves et al., 2011), ELSC (Mottl et al., 2011; Seewald, 2017). References from host-rock lithology are: S. EPR (Krasnov et al., 1997), Lucky Strike (Langmuir et al., 1997), MEF (Karsten et al., 1990), MCR (Elthon et al., 1995), EMB (Binns and Scott, 1993; Kamenetsky et al., 2001; Sinton et al, 2003), ELSC (Jenner et al., 1987; Frenzel et al., 1990; Vallier et al., 1991; Fouquet et al., 1993; Martinez and Taylor, 2002; Langmuir et al., 2006; Bézos et al., 2009; Escrig et al., 2009)

Table 1

Sample ID	Fluid Pair	Year	Vent Field	Region	Lithology	Lining Mineral	T (°C)	pH (at 25°C)	pH (in situ)	Cl (mmol/kg)	H_2S (mmol/kg)
Alv3299-6-1	Hobbes	1998	17 34'S	S. EPR	basalt	cp	349	3.2		481	9.0
Alv3288-5-1a	Simon	1998	17 37'S	S. EPR	basalt	cp	337	3.4		751	3.5
Alv3296-2-2a	Maggie	1998	17 37'S	S. EPR	basalt	cp					
Alv3296-3	Wally	1998	17 37'S	S. EPR	basalt	cp	314	3.4		752	6.5
Alv3296-5-1a	Homer	1998	17 37'S	S. EPR	basalt	cp	347	3.3		591	3.7
Alv1931		1987	MEF	JdF	E-MORB	cp					
Alv3474-3-1	Sully99	1999	MEF	JdF	E-MORB	cp	379	3.6	4.3	39.0	20
Alv3480-4		1999	MEF	JdF	E-MORB	cp					
J2-613-16-R1	BB5	2013	Beebe / Piccard	MCR	basalt	cb	395	3.0	5.0	351	0.0
J2-207-1-R1	VW1	2006	Vienna Woods	MSC	basalt	cp/wz	282	4.4	5.1	691	1.4
J2-210-7-R2		2006	Fenway	EMB, PAC	felsic	cp					
J2-216-16-R1	F3	2006	Fenway	EMB, PAC	felsic	cp	358	2.7	3.9	562	18.8
J2-214-3-R1	SM3	2006	Satanic Mills	EMB, PAC	felsic	cp	288	2.5	3.0	503	10.2
J2-208-1-R1	RMR1	2006	Roman Ruins	EMB, PAC	felsic	cp	314	2.3	2.8	632	7.5
J2-213-6-R1	RGR1	2006	Roger's Ruins	EMB, PAC	felsic	cp	320	2.7		648	3.6
J2-217-2-R1	SZ1	2006	Suzette	EMB, SuSu	felsic	cp	303	3.8	4.2	626	1.8
J2-217-10-R1	SZ2	2006	Suzette	EMB, SuSu	felsic	cp	274	3.6	4.0	684	1.8
J2-219-2-R1		2006	Suzette	EMB, SuSu	felsic	cp					
J2-223-1-R1	NS3	2006	North Su	EMB, SuSu	felsic	cp	300	3.4	3.9	673	3.4
J2-227-10-R1		2006	North Su	EMB, SuSu	felsic	cp					
	KM9	2009	Kilo Moana	ELSC	basalt	cb	304	4.1			3.5
	TMo1	2009	Tahi Moana 1	ELSC	felsic		306	3.7			3.1
	TMo2	2009	Tahi Moana 1	ELSC	felsic		298	3.9			4.1
J2-450-3-R1	TMo5	2009	Tahi Moana 1	ELSC	felsic	cp/wz	310	3.7	4.6	555	3.3
J2-449-6-R1	A10	2009	ABE	ELSC	felsic	cp/py	317	3.9	5.1	543	3.9
J2-449-5-R1	A11	2009	ABE	ELSC	felsic	cp/wz	306	4.0	5.2	552	2.7
	A13	2015	ABE	ELSC	felsic		283	4.3			3.5
	A14	2015	ABE	ELSC	felsic		300	4.0			3.7
	A15	2015	ABE	ELSC	felsic		290	4.4			3.1
J2-815-5-R1	A16	2015	ABE	ELSC	felsic	cp/wz	300	4.0	5.2	546	3.7
J2-442-4-R2	TM11	2009	Tu'i Malila	ELSC	felsic	cp/py	315	3.8	4.5	653	2.8
	TM12	2009	Tu'i Malila	ELSC	felsic		284	4.2			2.8
	TM13	2015	Tu'i Malila	ELSC	felsic		262	3.9			2.4
	TM14	2015	Tu'i Malila	ELSC	felsic		290	4.0			2.3
J2-819-4-R2	TM15	2015	Tu'i Malila	ELSC	felsic	cp/wz	269	3.9		598	2.3
	TM16	2015	Tu'i Malila	ELSC	felsic		251	3.9			2.0
	TM17	2015	Tu'i Malila	ELSC	felsic		258	3.9			2.1
	TM19	2015	Tu'i Malila	ELSC	felsic		232	4.2			2.2
	MA8	2009	Mariner	ELSC	felsic		359	2.4			17.8
J2-437-3-R2	MA9	2009	Mariner	ELSC	felsic	cp	338	2.4	3.2	541	8.9
	MA11	2009	Mariner	ELSC	felsic		328	2.2			11.8
	MA12	2009	Mariner	ELSC	felsic		350	2.3			10.8
	MA14	2015	Mariner	ELSC	felsic		319	2.4			3.7
J2-817-4-R2	MA15	2015	Mariner	ELSC	felsic	cp	354	2.7	3.8	557	3.1
	MA17	2015	Mariner	ELSC	felsic		362	2.8			17.5
	MA19	2015	Mariner	ELSC	felsic		308	2.6			7.0
	MA20	2015	Mariner	ELSC	felsic		344	2.7			8.8
	MA21	2015	Mariner	ELSC	felsic		345	2.7			9.6

2. GEOLOGIC SETTINGS OF FLUIDS AND CHIMNEYS

Vent fluids analyzed as part of this study are all from the Eastern Lau Spreading Center (ELSC, Fig. 1). Data for these vent fluids are combined with data for vent fluids from the Manus Basin, Juan de Fuca Ridge (Main Endeavour Field), and the Mid-Cayman Rise (Beebe / Piccard vent field) to encompass a range of hydrothermal system reaction zone conditions (lithology, temperature, pressure, presence/absence of magmatic volatiles; see Table 1).

Samples of hydrothermal vent fluids considered in this paper were collected from the Kilo Moana, Tahi Moana-1, ABE, Tu'i Malila, and Mariner vent fields on cruise TN236 (2009, R/V Thompson) and cruise RR1507 (2015, R/V Roger Revelle). Black smoker chimney linings were collected as sample pairs with hydrothermal fluid samples at the Tahi Moana-1, ABE, Tu'i Malila, and Mariner vent fields. These black smoker chimney linings are composed of massive chalcopyrite ± euhedral wurtzite or pyrite. Along the length of the ELSC, there is a lithologic transition from tholeiitic back-arc-basin basalt in the north to mixtures of basaltic andesite, andesite, and rhyodacite in the south (Jenner et al., 1987; Frenzel et al., 1990; Vallier et al., 1991; Fouquet et al., 1993; Martinez and Taylor, 2002; Langmuir et al., 2006; Fretzdorff et al., 2006; Bézos et al., 2009; Escrig et al., 2009; Sleeper and Martinez, 2014). The Kilo Moana vent field is located in the north and is associated with basalt, the Tahi Moana-1 and ABE vent fields occur in a geomorphologic and lithologic transition zone, while the Tu'i Malila and Mariner vent fields occur on the Valu Fa Ridge where host rocks are more felsic in composition (Fig. 1; Mottl et al., 2011).

Figure 1. Map of vent field locations along the Eastern Lau Spreading Center. Active vents in white have been confirmed to exist by submersible while active vents in red are inferred to exist based on water column chemistry. Vent field locations, activity, and confirmed status are as listed in the InterRidge database (Beulieu et al., 2010). Background bathymetric data are from Taylor (2006) accessed through GeoMapApp (http://www.geomapapp.org/). Data have been rendered using ArcGIS, version 10.2.2.

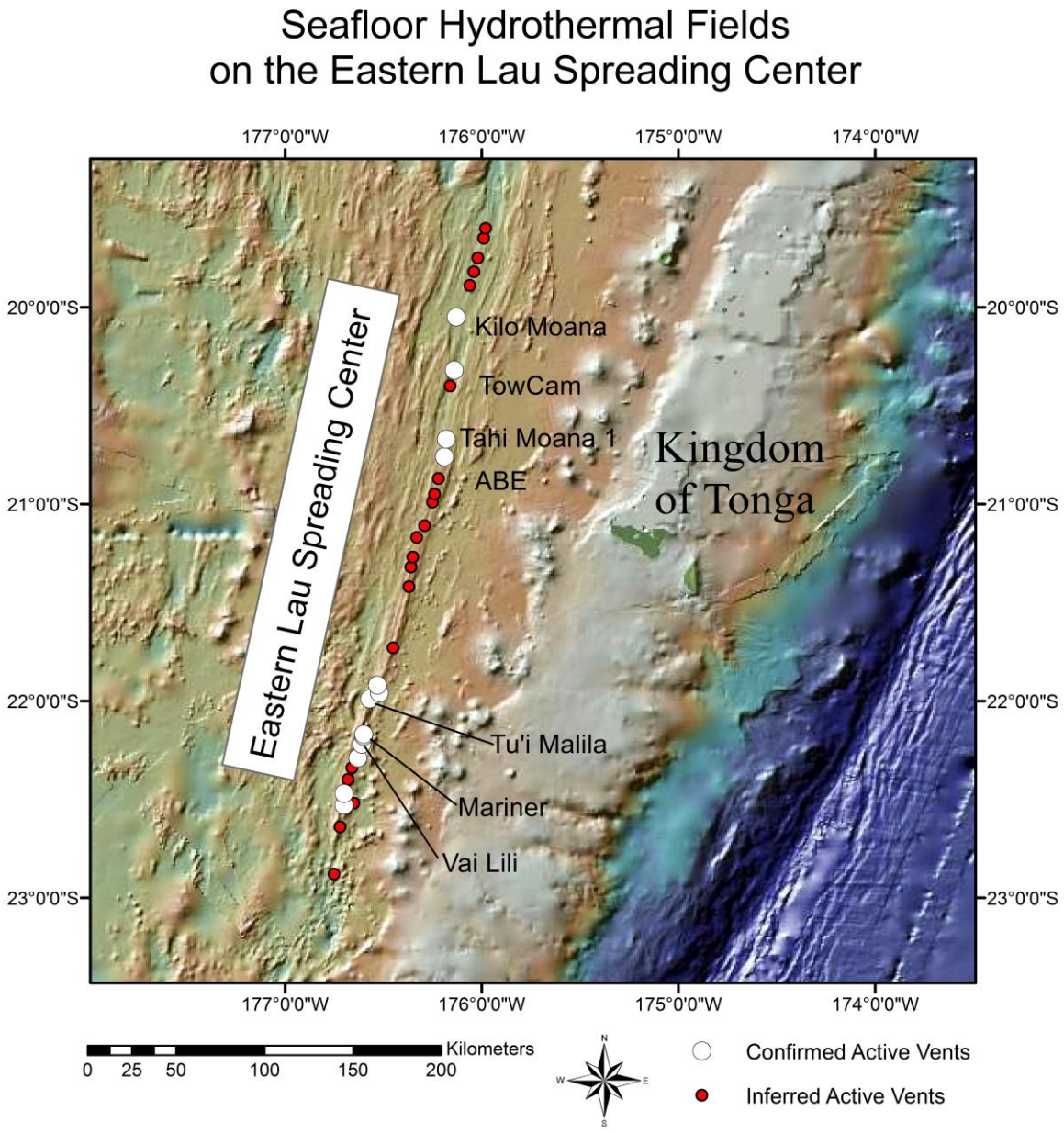

Other existing vent fluid data considered are from the Manus Basin, located in the Bismarck Sea within the territorial waters of Papua New Guinea (Fig. 2). The complex back-arc extension and spreading centers of the Manus Basin are dynamically linked to the New Britain Subduction Zone (Taylor, 1979; Davies et al., 1987; Martinez and Taylor, 1996). Near the center of the Manus Basin, dominantly basaltic lavas erupt along the Manus Spreading Center (Both et al., 1986; Sinton et al., 2003), which hosts the Vienna Woods vent field. Toward the eastern end of the Manus Basin, andesite-rhyolite lavas erupt along a series of *en echelon* neovolcanic ridges that accommodate rifting and extension of previously deposited crust associated with the New Ireland arc (Sinton et al., 2003; Martinez and Taylor, 2006). Hydrothermal venting occurs on the Pual Ridge in the PACMANUS area and at SuSu Knolls, where black smoker and additional acid-sulfate fluids vent from the tops and sides of three volcanic domes: Suzette, North Su, and South Su (Craddock, 2009; Reeves et al., 2011; Seewald et al., 2015). The focus of this paper is exclusively on black smoker fluids. The low pH of vent fluids at the PACMANUS and SuSu Knolls vent fields are attributed to buffering from argillic alteration assemblages and/or the addition of SO_2–rich acidic magmatic volatiles (Reeves et al., 2011; Seewald et al., submitted). In addition, the variability of base metal concentrations in some of these fluids is attributed to remobilization of previously deposited metal sulfides (e.g., Roman Ruins and Roger's Ruins), which leads to locally enriched concentrations of Zn, Pb, Cd, Ag, As, and Sb in venting hydrothermal fluids (Craddock, 2009). The black smoker chimney lining from the Vienna Woods vent field examined in this study is composed of intergrown euhedral wurtzite and chalcopyrite. Black smoker chimney linings from the PACMANUS and SuSu Knolls vent fields are all composed of massive chalcopyrite.

Figure 2. Map of vent field locations in the Manus Basin with inset highlighting vent field locations in the Eastern Manus Basin.Active vents in white and inactive vents in black have been confirmed to exist by submersible while active vents in red are inferred to exist based on water column chemistry. Vent field locations, activity, and confirmed status are as listed in the InterRidge database (Beaulieu et al., 2010). Background bathymetric data are from Taylor (2006) accessed through GeoMapApp (http://www.geomapapp.org/). Data have been rendered using ArcGIS, version 10.2.2.

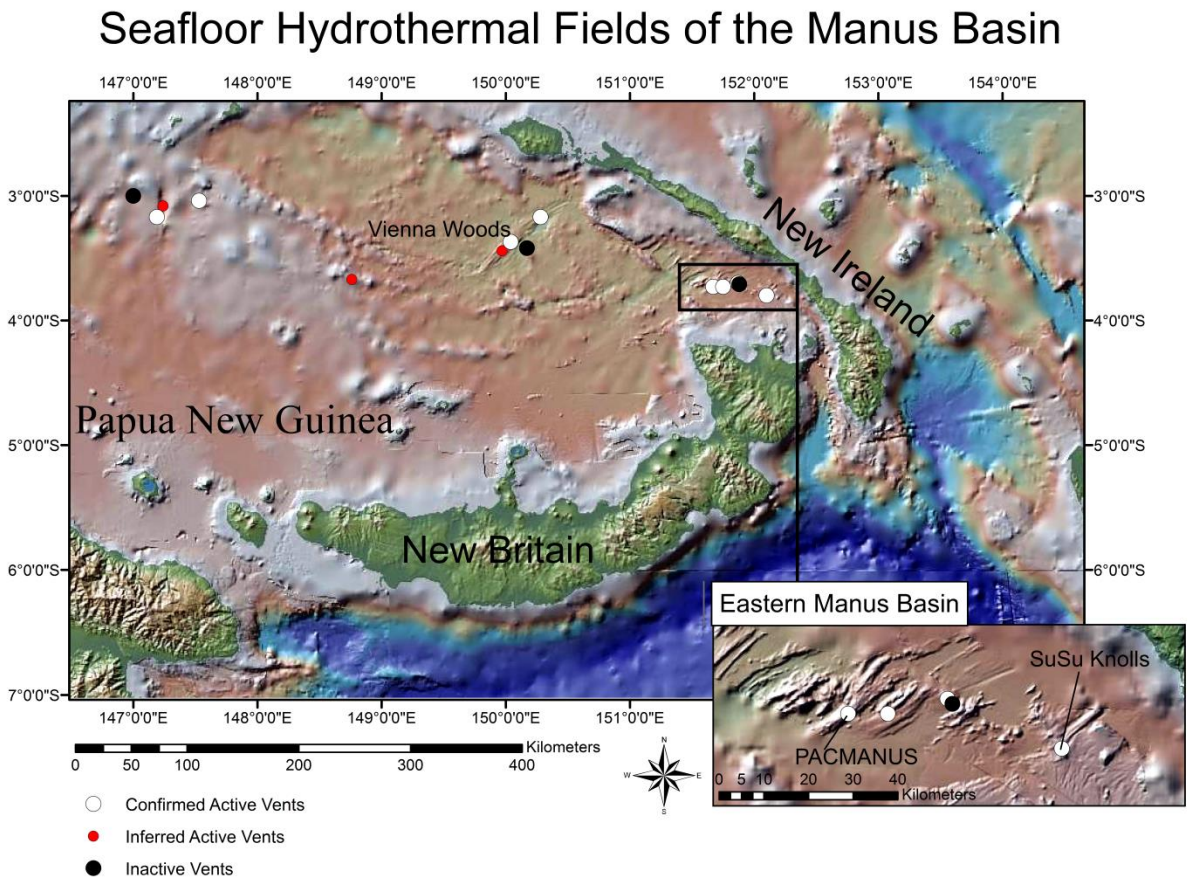

Additional black smoker chimney samples examined in this study include those collected from vent fields between 17°34'S and 17°37'S on the southern East Pacific Rise, the Main Endeavour Field on the Juan de Fuca Ridge, and the Beebe / Piccard vent field on the Mid-Cayman Rise. Inclusion of these samples adds to the diversity of geologic settings represented in the sample suite, specifically ultrafast- (southern East Pacific Rise), intermediate- (Juan de Fuca Ridge), and ultraslow- (Mid-Cayman Rise) spreading mid-ocean ridges. Existing data for fluid pairs of samples from the southern East Pacific Rise (K.L. Von Damm, unpublished data) do not include trace element concentrations. Data for hydrothermal vent fluids from the and Main Endeavour Field from 1999 and the Beebe / Piccard vent field in 2012 are more extensive and include data for Ag, Co, Cu, Fe, and Ni for vent fluids at the Main Endeavour Field and data for Co, Cu, and Fe for fluids from the Beebe / Piccard vent field (Seyfried et al., 2003; McDermott, 2015).

The three samples from the Main Endeavour Field were collected prior to (Alv1931) and immediately following (Alv3474-3-1 and Alv3480-4) the seismic swarm and inferred event that occurred in 1999 (Johnson et al., 2000). This event led to changes in the temperature and chemistry of hydrothermal fluids venting at the Main Endeavour Field including a temporary decrease in chlorinity and pH (at 25°C) and an increase in temperature (Seyfried et al., 2003).

3. METHODS

3.1. Sample Collection

Hydrothermal fluid samples were collected from active hydrothermal vents along the Eastern Lau Spreading Center in 2009 (TN236) and 2015 (RR1507) using the ROV Jason II. One to three fluid samples from each vent were collected in 150 mL isobaric gas-tight (IGT) samplers (Seewald et al., 2002). Temperatures were measured with a thermocouple mounted on the IGT sampler inlet snorkel. Following shipboard recovery, fluid samples were analyzed for pH using a Ag/AgCl combination reference electrode that was calibrated daily. Aliquots for major element and trace metal analysis were transferred to acid-washed high-density polyethylene (HDPE) Nalgene™ bottles. Aliquots for trace metal analysis were acidified with analytical-grade Optima™ HCl prior to storage. In many fluid samples, a precipitate "dregs" fraction formed upon initial collection and cooling of the sample. This was recovered from the inside of the IGT sampling bottle and collected on a 0.22 μm pore-size, 44 mm diameter Nylon filter by rinsing with Milli-Q filtered water and high-purity acetone.

3.2. Digestion of Dregs and Filter Fractions

Dissolved aliquots of hydrothermal fluid samples intended for minor and trace element analysis by inductively coupled plasma mass spectrometry were filtered into HDPE Nalgene™ bottles through 0.22 μm pore-size, 22 mm diameter Nuclepore® nylon filters. This was done to remove additional precipitates (a.k.a. "filter" fraction) that might have formed from the "dissolved" fraction still remaining in solution during the time between shipboard collection and laboratory analysis. Syringes, filters, filter units, and handling equipment were all acid-cleaned

with 5 wt% analytical grade Optima® HNO_3 (Fisher Scientific) prepared by dilution in Milli-Q filtered water. Visible particles sticking to the sides of laboratory vessels were transferred with the aid of Milli-Q filtered water and high-purity ethanol.

Precipitate filter and dregs fractions were digested in reverse *aqua regia* (three parts 16 N are analytical grade Optima® HNO_3 to 1 part 12 N are analytical grade Optima® HCl by volume) in Savillex™ digestion vials and left at 70°C until dry. Samples were then brought up in 5 mL are analytical grade Optima® HNO_3 to remove any remaining HCl and left to dry a second time. Finally, these samples were brought up in 30 mL 5wt% are analytical grade Optima® HNO_3 and stored in HDPE Nalgene® prior to further analysis.

3.3. Major and Trace Element Analysis

Analyses of major elements (Na, K, Li, Ca, Mg) were conducted on diluted samples of the "dissolved" fractions of hydrothermal fluids by ion chromatography (Seewald, 2017). Dilution factors were 1000x for Na and Cl and 150x for K, Li, and Mg. Analyses of minor elements (Fe, Mn) and trace elements (Cr, Co, Ni, Cu, Zn, Ga, Rb, Mo, Ag, Cd, In, Sn, Cs, Au, and Pb) were carried out on diluted samples of "dissolved" fractions and digested "filter" and "dregs" fractions using the Element 2 inductively coupled plasma mass spectrometer (ICP-MS) in the Plasma Mass Spectrometry Facility at the Woods Hole Oceanographic Institution. For the purposes of ICP-MS analysis, samples were diluted with 5 wt% HNO_3 containing 1ng/g dilutions of Specpure ® plasma standard solutions as internal spikes. For samples collected in 2009, elements used as internal spikes were Sc, In, and Bi. For samples collected in 2015, Sc and Y spikes were used, which allowed for In analysis. Dilution factors were generally 1000x for minor

elements and 100x for trace elements. Results from ICP-MS were calibrated against a six-point calibration curve composed of serial dilutions of Specpure ® plasma solutions (for dregs and filter fractions: Sb, As, Ba, Bi, Cd, Ca, Cr, Co, Cu, Ga, Ge, Au, Fe, In, Pb, Mn, Mo, Ni, Se, Si, Ag, Sr, S, Te, Tl, Sn, V, Zn; for dissolved fractions: Sb, Al, Cd, Cr, Cs, Co, Cu, Au, Fe, Mn, Mo, Ni, Pb, Rb, Ag, Tl, U, Zn) in 5 wt% analytical grade Optima® brand HNO_3. For trace element analyses of dissolved fractions, 4.6807 mmol/kg NaCl was added to the serial dilution series to approximate a matrix of 100x-diluted seawater. For dregs and filters samples collected in 2009, mass and machine settings for ICP-MS analyses were: Sc45, In115, Ba137, Ba138, Pb208, Bi209 (low resolution = 300); Sc45, Mn55, Fe56, Co59, Ni60, Cu63, Cu65, Zn66, Zn68, Rb85, Mo96, Ag107, Ag109, In115, Cs133, Au197, Bi209 (medium resolution = 4000). For dregs and filters samples collected in 2015, mass and machine settings were: Sc45, Y89, Ba137, Ba138, Pb208, Bi209 (low resolution = 300) ; Sc45, Cr52, Mn55, Fe56, Co59, Ni60, Cu63, Cu65, Zn66, Zn68, Ga69, Y89, Mo96, Ag107, Ag109, In115, Sn118, Ba137, Ba138, Au197, Bi209 (medium resolution = 4000). Underlining indicates elements used as internal spikes.

3.4. Calculation of Trace Metal Concentrations in Hydrothermal Fluids

In order to obtain the comprehensive chemical composition of a hydrothermal fluid, the dregs-, filter-, and dissolved fractions must each be considered in the analysis (Trefry et al., 1994; Metz and Trefry, 2000). This was done by calculating the contribution of each of these fractions to the original hydrothermal fluid sample for each element and summing the total. Following mathematical reconstitution of the original fluid samples, the compositions of endmember hydrothermal fluids prior to mixing are obtained by extrapolating to zero-Mg composition by

projecting a linear regression forced through the composition of seawater through the measured sample compositions and onto the zero-Mg axis (Fig. 3A to 3D). This method follows the assumption that hydrothermal fluids contain negligible Mg and that measured Mg concentrations are thus attributable to entrainment of seawater prior to or during collection of samples (Von Damm et al., 1985). While this method in generally effective, significant uncertainty arise as mineral deposit particles can be accidentally entrained during sampling and recovery of dregs and filter fractions can be incomplete. In cases where multiple fluid samples have been taken from the same vent, the quality of fluid sampling can be confirmed if multiple samples extrapolate to similar zero-Mg endmember concentrations. Alternatively, likely sampling artifacts can be identified if multiple samples extrapolate to extremely different endmember compositions. In cases where only one fluid sample has been taken from a given vent, it may not be possible to determine the quality of fluid sampling. However, the likely quality of fluid sampling can in some cases be inferred by comparison with vent fluid samples from the same vent field that exhibit similar temperature, pH, chlorinity, etc.

Figure 3. Plots of measured concentrations of Mg vs. (A) Mn, (B) Fe, (C) Cu, and (D) Ag in hydrothermal fluid samples from the Tu'i Malila vent field analyzed by considering dissolved fractions only (hollow symbols) and by combining analyses of dissolved, dregs, and filters fractions (filled symbols). Samples marked in red exhibit anomalously high concentrations of Cu, Fe, and Ag, and are thought to be contaminated by entrained particles of SMS deposit materials. Following removal of these samples from the analysis, endmember concentrations of hydrothermal fluids are calculated by projection of a linear regression line forced through the composition of seawater onto the y-axis (i.e. zero-Mg).

Figure 3A

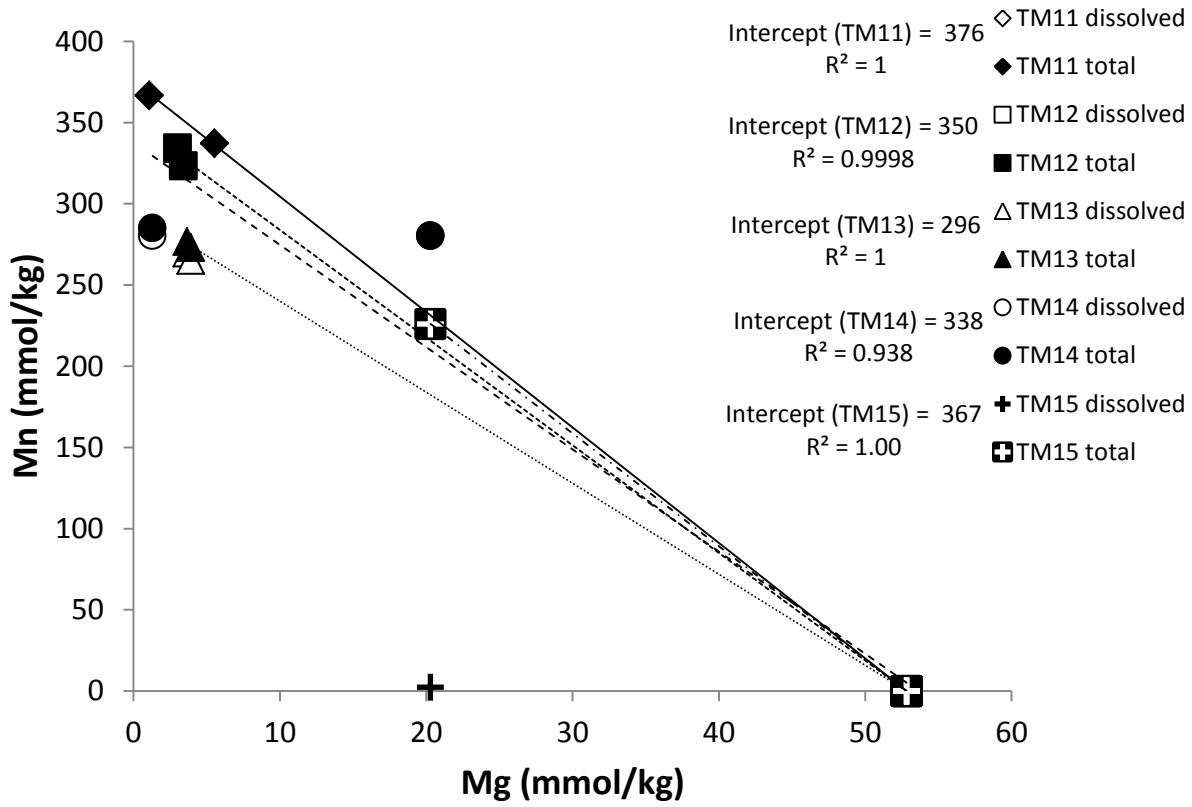

Figure 3B

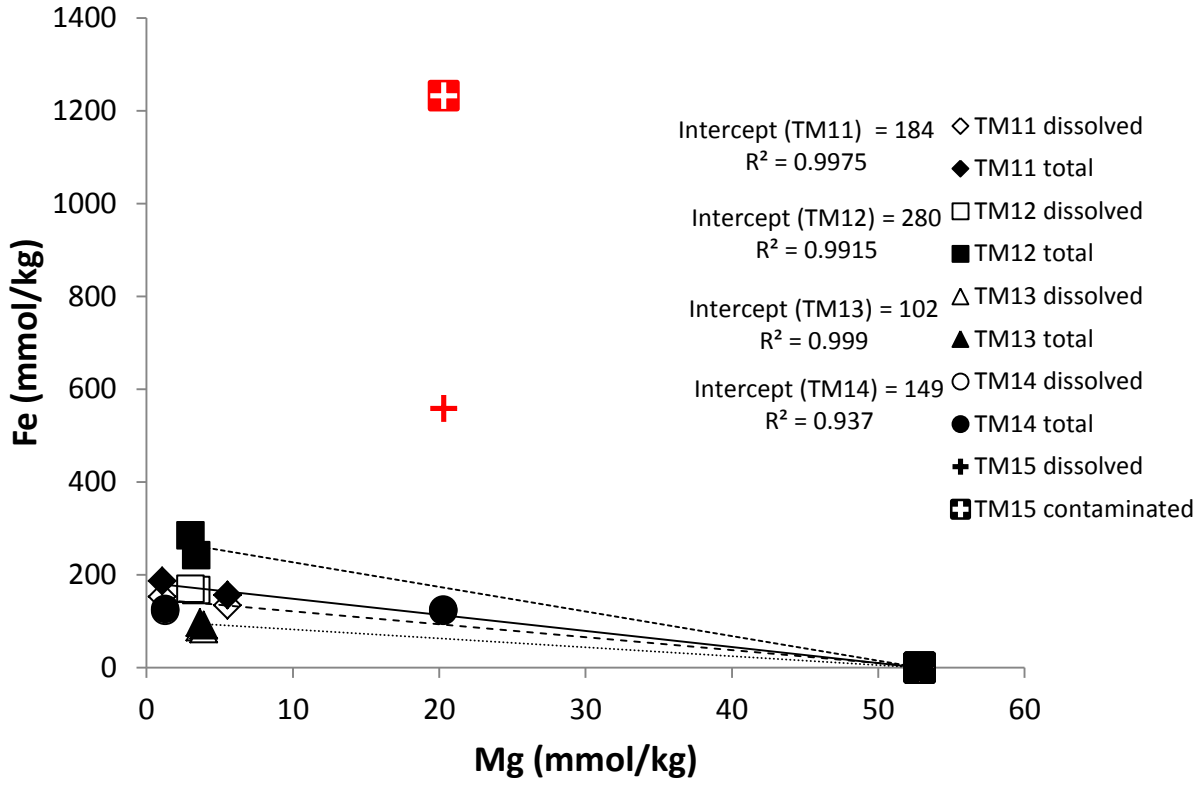
1400
1200
1000
800
600
400
200
0
Fe (mmol/kg)
0
10
20
30
40
50
60
Mg (mmol/kg)
Intercept (TM11) = 184
R² = 0.9975
Intercept (TM12) = 280
R² = 0.9915
Intercept (TM13) = 102
R² = 0.999
Intercept (TM14) = 149
R² = 0.937
TM11 dissolved
TM11 total
TM12 dissolved
TM12 total
TM13 dissolved
TM13 total
TM14 dissolved
TM14 total
TM15 dissolved
TM15 contaminated

Figure 3C

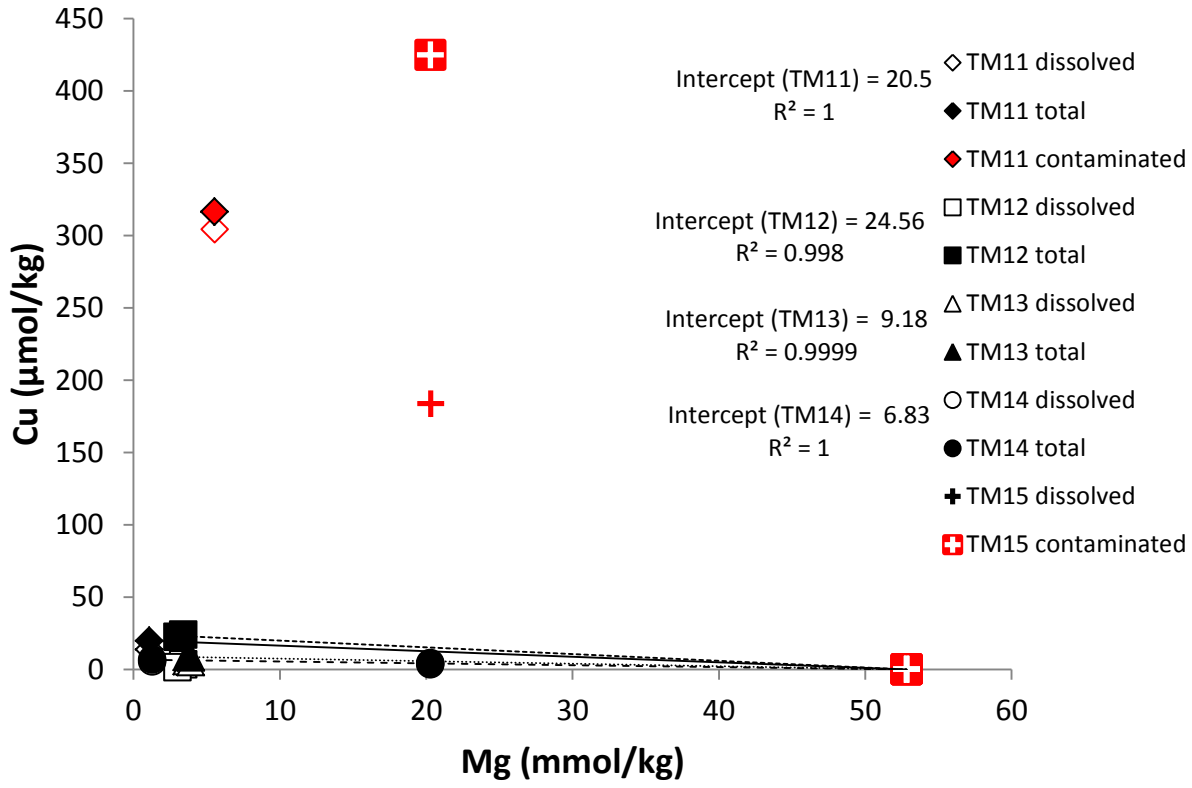
Cu (µmol/kg)
Mg (mmol/kg)
0
50
100
150
200
250
300
350
400
450
0
10
20
30
40
50
60
Intercept (TM11) = 20.5
R² = 1
Intercept (TM12) = 24.56
R² = 0.998
Intercept (TM13) = 9.18
R² = 0.9999
Intercept (TM14) = 6.83
R² = 1
TM11 dissolved
TM11 total
TM11 contaminated
TM12 dissolved
TM12 total
TM13 dissolved
TM13 total
TM14 dissolved
TM14 total
TM15 dissolved
TM15 contaminated

Figure 3D

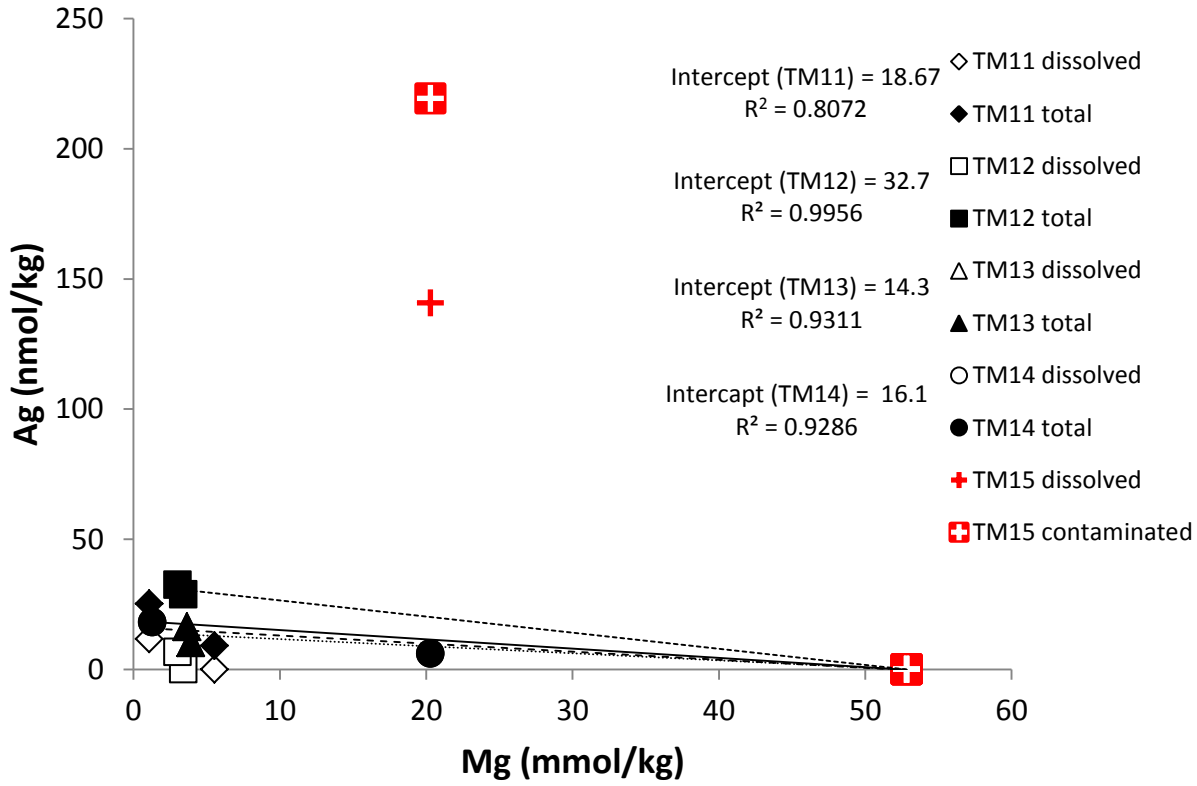
250
200
150
100
50
0
Ag (nmol/kg)
0
10
20
30
40
50
60
Mg (mmol/kg)
Intercept (TM11) = 18.67
R² = 0.8072
Intercept (TM12) = 32.7
R² = 0.9956
Intercept (TM13) = 14.3
R² = 0.9311
Intercapt (TM14) = 16.1
R² = 0.9286
TM11 dissolved
TM11 total
TM12 dissolved
TM12 total
TM13 dissolved
TM13 total
TM14 dissolved
TM14 total
TM15 dissolved
TM15 contaminated

3.5. Trace Element Analysis of Black Smoker Chimney Linings

The Co, Ni, Ga, Ag, and In contents of chalcopyrite precipitated along the innermost linings of black smoker chimney linings were analyzed by secondary ion mass spectrometry (SIMS) using the Cameca 1280 Ion Microprobe in the Northeast National Ion Microprobe Facility at the Woods Hole Oceanographic Institution. Details of these analyses and calibration against picked grains of chalcopyrite analyzed by ICP-MS are found in Chapter 3 of this thesis.

3.6. Fluid Chemical Modelling

To compare measured trace element chemistry of black smoker chimney linings with the relevant hydrothermal fluid chemistry at *in situ* temperatures and pressures, the activities of aqueous complexes and free ions (including *in situ* pH) were calculated using the EQ3/6 software package (Wolery, 1992) and thermodynamic data from SUPCRT92 (Johnson et al., 1992) modified as described by Tivey et al. (1999) and Tivey (2004). Additionally, thermodynamic data for the chloride complexes of Co, Ni, and In, and hydroxide complexes of Ga and In were obtained from the SLOP07 database available at http://geopig3.la.asu.edu:8080/GEOPIG pigopt1.html (Shock et al., 1997; Sverjensky et al., 1997). The dissociation reaction constants for select complexes are listed in Table 2.

Table 2. Tabulated base 10 logarithm of the equilibrium reaction coefficients (K) for the dissociation of aqueous complexes as calculated by SUPCRT (Johnson et al., 1992) for temperatures from 25°C to 350°C and 250 bar pressure and used in EQ3/6 calculations of fluid speciation (Wolery, 1992). Data sources for the thermodynamic data used in SUPCRT calculations are listed in the right-hand column (D&S92 is Ding and Seyfried, 1992).

Table 2. Log K for EQ3/6 input

	Log K at pressure = 250 bar, temperature =								
Reaction	25°C	50°C	75°C	100°C	175°C	250°C	300°C	350°C	Citation
[Ag(HS)2-] = [Ag+] + 2[HS-]	-17.617	-16.208	-15.073	-14.146	-12.255	-11.289	-11.076	-11.389	SUPCRT92
[AgCl,aq] = [Ag+] + [Cl-]	-3.262	-3.076	-2.946	-2.858	-2.789	-2.970	-3.269	-3.913	SUPCRT92
[AgCl2-] = [Ag+] + 2[Cl-]	-5.214	-4.884	-4.661	-4.519	-4.432	-4.741	-5.192	-6.069	SUPCRT92
[AgCl3-2] = [Ag+] + 3[Cl-]	-4.979	-4.399	-3.999	-3.731	-3.462	-3.751	-4.225	-5.110	SUPCRT92
[AgCl4-3] = [Ag+] + 4[Cl-]	-3.565	-2.671	-2.120	-1.812	-1.817	-2.669	-3.579	-4.898	SUPCRT92
[CaCl+] = [Ca+2] + [Cl-]	0.720	0.653	0.536	0.384	-0.223	-1.030	-1.730	-2.770	SUPCRT92
[CaCl2,aq] = [Ca+2] + 2[Cl-]	0.706	0.717	0.623	0.452	-0.393	-1.675	-2.873	-4.771	SUPCRT92
[CoCl+] = [Co+2] + [Cl-]	-3.276	-3.230	-3.238	-3.285	-3.604	-4.161	-4.714	-5.616	SUPCRT92
[CuCl,aq] = [Cu+] + [Cl-]	-2.250	-2.250	-2.750	-3.000	-3.750	-4.500	-5.000	-5.500	D&S92
[CuCl2-] = [Cu+] + 2[Cl-]	-5.225	-4.701	-4.331	-4.076	-3.785	-4.003	-4.419	-5.249	SLOP07
[CuCl3-2] = [Cu+] + 3[Cl-]	-5.569	-4.758	-4.193	-3.808	-3.370	-3.640	-4.143	-5.069	SLOP07
[FeCl+] = [Fe+2] + [Cl-]	0.182	0.105	-0.019	-0.176	-0.782	-1.575	-2.262	-3.288	SUPCRT92
[FeCl2,aq] = [Fe+2] + 2[Cl-]	2.930	2.190	1.460	0.723	-1.480	-3.690	-5.160	-6.630	D&S92
[Ga(OH)+2] + [H+] = [Ga+3] + [H2O]	-11.241	-10.673	-10.283	-10.021	-9.755	-10.040	-10.518	-11.419	SLOP07
[HCl,aq] = [H+] + [Cl-]	0.630	0.725	0.738	0.691	0.328	-0.306	-1.008	-2.153	SUPCRT92
[In(OH)+2] + [H+] = [In+3] + [H2O]	-9.812	-9.442	-9.184	-9.007	-8.827	-9.056	-9.454	-10.246	SLOP07
[KCl,aq] = [K+] + [Cl-]	1.543	1.335	1.147	0.969	0.459	-0.093	-0.570	-1.354	SUPCRT92
[MnCl+] = [Mn+2] + [Cl-]	-0.277	-0.565	-0.878	-1.203	-2.232	-3.368	-4.260	-5.481	SUPCRT92
[NaCl,aq] = [Na+] + [Cl-]	0.809	0.720	0.617	0.506	0.119	-0.379	-0.846	-1.642	SUPCRT92
[NiCl+] = [Ni+2] + [Cl-]	0.516	0.404	0.259	0.091	-0.513	-1.272	-1.927	-2.918	SLOP07

4. RESULTS

4.1. Hydrothermal fluids from the Eastern Lau Spreading Center

A total of 62 fluid samples were collected from 34 vents (13 in 2009 and 21 in 2015) at five different vent fields (five vent fields in 2009 and three vent fields in 2015) along the Eastern Lau Spreading Center (ELSC). Of these samples, 47 contained low concentrations of Mg (< 10 mmol/kg) indicative of low extents of mixing (< 20%) with seawater. The measured compositions of fluid samples analyzed for this study are presented in Tables 3A to 3D. The calculated zero-Mg endmember compositions of low-Mg vent fluids are presented in Tables 4A to 4B. Endmember concentrations of selected elements for vent fluids from the Eastern Lau Spreading Center and Manus Basin are additionally presented in Figure 4. The separate contributions of the dissolved-, filter-, and dregs fractions to each fluid sample are supplied in Supplementary Tables S1 to S3. Plots of linear regressions are supplied in Appendix A.

4.1.1. Major Fluid Parameters

The measured temperatures, pH, and zero-Mg endmember concentrations of major ions (Na, Li, K, Ca) for vent fluids presented in this study from the Kilo Moana, Tahi Moana-1, ABE, Tu'i Malila, and Mariner vent fields overlap values previously reported by Mottl et al., (2011) and Chapter 2 of this thesis. The general characteristics of ELSC vent fluids and inferred vent fluid formation processes are discussed in Mottl et al. (2011) and are not addressed further here.

4.1.2. Mn, Fe, Cu, In

Zero-Mg endmember concentrations of Mn, Fe, and Cu are significantly greater in fluids collected from the Mariner vent field than those collected from other ELSC vent fields (Table 4A; Fig. 4A). Within individual vent fluid samples, Mn and Fe are dominantly contained in the dissolved fraction in contrast to Cu, which is variably contained in the dregs fraction. Because of the use of ^{115}In as an internal spike during ICP-MS analysis, concentrations of In in vent fluid samples were only measured in the dregs and filter fractions of fluids collected in 2015 from the ABE, Tu'i Malila, and Mariner vent fields. As with Mn, Fe, and Cu, endmember In concentrations are higher in vent fluids collected from the Mariner vent field compared to vent fluids from the ABE and Tu'i Malila vent fields (Table 4B, Fig. 4C).

Endmember Mn concentrations for low-Mg vent fluids from the Mariner vent field range from 3,700 ± 120 μmol/kg (MA17) to 6090 ± 50 μmol/kg (MA13). In comparison, endmember Mn concentrations for vent fluids from the Kilo Moana, Tahi Moana-1, ABE, and Tu'i Malila vent fields are lower, but similar to each other and range from 215 ± 1 μmol/kg (KM9) to 580 ± 2 μmol/kg (TMo1).

Endmember concentrations of Fe in Mariner vent fluids range from 6,730 ± 70 μmol/kg to 14,000 ±300 μmol/kg. Endmember concentrations of Fe in other ELSC vent fluids range from Fe = 248 ± 3 μmol/kg to 370 ± 30 μmol/kg for the Tahi Moana-1 vent field, Fe = 67 ±3 μmol/kg to 340 μmol/kg for the ABE vent field, and Fe = 102 ± 3 μmol/kg to 500 ±140 μmol/kg for the Tu'i Malila vent field. The endmember Fe concentration of fluid KM9 from the Kilo Moana vent field is somewhat higher, at 1100 ±110 μmol/kg.

Endmember Cu concentrations for low-Mg vent fluids from the Mariner vent field range from 109 ± 1 μmol/kg to 1100 ± 800 μmol/kg while endmember concentrations of Cu for fluids from Kilo Moana, Tahi Moana-1, and ABE vent fields range from 4 ± μmol/kg (A16) to 75 μmol/kg (A14). Endmember Cu concentrations of fluids from the Tu'i Malila vent field are slightly higher and range from 6.8 ± 0.03 μmol/kg to 25 ± 1 μmol/kg. Endmember In concentrations for low-Mg fluids from the Mariner vent field range from 84 ± 3 nmol/kg to 240 ± 50 nmol/kg while endmember In concentrations for ABE and Tu'i Malila vent fluids range from 30 ± 15 nmol/kg to 57 ± 3 nmol/kg.

4.1.3. Zn, Cd, Ag, Ga

Endmember concentrations of Zn, Cd, Ag, and Ga are generally higher in the low-pH, high-temperature fluids from the Mariner vent field than in fluids from other ELSC vent fields (Table 4A, 4B; Fig. 4B, 4C). While several fluid samples from the Tu'i Malila vent field also exhibit high concentrations of these elements, these high concentrations are not constrained by multiple fluid samples and could represent sampling artifacts. With the exception of these outliers (TM16 and TM17 for Zn, TM19 for Ag, MA14 for Ga and Ag) strong correlations are observed between endmember concentrations of Zn and Cd ($r = 0.95$), Ag ($r = 0.81$), Ga ($r = 0.87$) and endmember Zn concentrations also correlate with vent fluid temperature ($r = 0.70$).

Endmember Zn concentrations for fluids from the Mariner vent field range from 300 μmol/kg (MA18) to 1800 ± 100 μmol/kg (MA14). Endmember Cd concentrations of Mariner vent fluids range from 230 nmol/kg (MA18) to 1,560 ± 40 μmol/kg (MA14). Endmember Ag concentrations for Mariner vent fluids range from 40 ± 28 nmol/kg to 100 ± 14 nmol/kg.

Endmember Ga concentrations for Mariner vent fluids range from 90 ± 13 nmol/kg to 280 ± 20 nmol/kg.

Endmember Zn concentrations from the Kilo Moana, Tahi Moana-1, ABE, and Tu'i Malila vent fields are highly variable and range from 37 ± 1μmol/kg (A16) to 960 μmol/kg (TM16). Endmember Cd concentrations range from 31 nmol/kg (A10) to 1,600 ±700 nmol/kg. Endmember Ag concentrations range from below detection limits (A16) to 520 nmol/kg (TM19). Endmember Ga concentrations are < 15 nmol/kg for fluids from the Kilo Moana and Tahi Moana-1 vent fields. Endmember Ga concentrations range from 6 nmol/kg to 114 nmol/kg at the ABE vent field and 6 ± 4 nmol/kg to 91 nmol/kg at the Tu'i Malila vent field.

4.1.4. Co and Ni

Endmember Co concentrations are similar for vent fluids from the Tahi Moana-1 (Co = 110 ± 8 nmol/kg to 160 ± 28 nmol/kg) and ABE (Co = 73 ±1 nmol/kg to 180 ±18 nmol/kg) vent fields and are higher for vent fluids from the Tu'i Malila (Co = 100 ± 15 nmol/kg to 240 nmol/kg) and Mariner vent field (Co = 200 ± 20 nmol/kg to 500 ±130 nmol/kg) (Table 4A; Fig. 4B, 4C). The endmember Co concentration of fluid KM9 from Kilo Moana vent field is higher, 560 ± 50 nmol/kg.

Endmember Ni concentrations are highest in fluids from the Mariner vent field with a range of 120 ±50 nmol/kg to 1,100 ± 600 nmol/kg (Table 4A; Fig. 4B, 4C). Endmember Ni concentrations range from 76 ± 3 nmol/kg to 700 ± 200 nmol/kg at the Tu'i Malila vent field, 110 nmol/kg to 570 nmol/kg at the ABE vent field, and 200 ± 140 nmol/kg to 700 ± 140 nmol/kg at the Tahi Moana-1 vent field (Table 4A; Fig. 4B, 4C). The endmember Ni concentration of fluid KM9 from Kilo Moana vent field is 100 ± 06 nmol /kg (Table 4A; Fig. 4B, 4C).

4.2. Aqueous Speciation

Thermodynamic modelling of fluid speciation using EQ3/6 indicates that ions will be more greatly complexed at *in situ* temperatures than at 25°C. This leads to higher pH at *in situ* temperatures compared to the pH measured at 25°C and a decrease in the activity of free ions relative to total elemental concentrations. The pH, log fO2 and log fS2 of modelled fluids at in situ temperatures and 250 bar are presented in Table 6. According to the thermodynamic calculations, Cu, Fe, Co, Ag, and In are dominantly present as chloride complexes while Ni is split between free ions and chloride complexes and Ga is predominantly present as hydroxide complexes.

Table 3. Measured temperatures and fluid chemistry for hydrothermal fluid samples from the Kilo Moana (KM), Tahi Moana-1 (TMo), ABE (A), Tu'i Malila (TM), and Mariner (MA) vent fields. One or two samples were collected in IGT samplers of each "fluid" defined by fluid emanating from a particular vent and values reflect summation of the dissolved, dregs, and filter fractions. Temperature was measured by a thermocouple mounted to the IGT sampler snorkel, pH was measured shipboard by a daily calibrated Ag/AgCl combination reference electrode, Mg, Na, Li, and K were measured by ion chromatography, and all other elements were measured by ICP-MS. Temperature, pH, Mg are from Seewald (2017), Mn and Fe concentrations for KM9, TMo1, TMo2, TMo5, A10, A11, TM11, TM12, MA8, MA9, MA10, MA11, and MA12 are from C. G. Wheat, pers. comm. Components that were not measured are labelled with "NM".

Table 3A.Measured Fluid Chemistry (1 of 4)

Fluid	Sample	max T	pH	Mg	Cr	Mn	Fe	Co	Ni	Cu	Zn	Ga
		°C	25°C	mmol/kg	nmol/kg	umol/kg	umol/kg	nmol/kg	nmol/kg	umol/kg	umol/kg	nmol/kg
KM9	J2-434-IGT1	301	4.1	2.5	1500	200	990	490	200	5	38	5
KM9	J2-434-IGT4	304	5.0	3.0	NM	200	1200	580	17	5	68	NM
TMo1	J2-444-IGT1	297	3.3	2.9	8500	550	380	140	760	15	230	11
TMo1	J2-444-IGT6	306	3.7	2.4	1100	560	320	130	500	8	180	18
TMo2	J2-444-IGT3	298	4.4	4.6	1100	270	220	170	320	6	56	3
TMo2	J2-444-IGT4	297	3.9	1.0	1100	290	250	130	72	8	170	20
TMo5	J2-450-IGT4	309	3.7	1.4	590	390	280	120	640	6	80	1
TMo5	J2-450-IGT6	310	3.8	2.0	630	380	260	100	60	6	79	2
A10	J2-449-IGT5	317	4.4	2.1	4200	420	160	77	100	10	98	10
A11	J2-449-IGT1	306	4.0	2.5	3500	280	100	70	220	5	77	8
A11	J2-449-IGT6	312	3.9	2.1	710	450	160	70	120	12	77	4
A13	J2-815-IGT7	283	5.0	12.8	3300	320	150	94	2200	4	85	87
A13	J2-815-IGT8	283	4.3	2.3	1400	450	2900	110	550	110	3000	140
A14	J2-815-IGT1	288	5.1	16.8	1800	250	1800	150	1400	250	5500	94
A14	J2-815-IGT3	300	4.0	1.9	1400	400	330	170	380	72	420	80
A15	J2-815-IGT2	290	4.9	8.1	930	170	94	130	480	7	49	53
A15	J2-815-IGT4	279	4.4	1.9	1600	250	120	100	390	9	96	75
A16	J2-815-IGT5	262	4.6	1.7	890	250	63	59	250	5	35	63
A16	J2-815-IGT6	263	4.5	1.7	420	250	68	130	140	3	37	57
TM11	J2-442-IGT3	313	4.1	5.5	1400	340	160	100	420	320	86	9
TM11	J2-442-IGT4	315	3.8	1.1	4900	370	190	81	860	20	120	2
TM12	J2-442-IGT1	284	4.3	3.4	7700	320	240	110	220	24	110	14
TM12	J2-442-IGT6	268	4.2	3.0	7000	330	280	110	180	22	310	87
TM13	J2-819-IGT6	260	3.9	4.3	290	280	97	150	52	9	83	55
TM13	J2-819-IGT8	262	3.9	3.6	280	270	92	160	140	8	75	67
TM14	J2-819-IGT4	214	4.0	1.5	260	280	120	170	55	4	57	67
TM14	J2-819-IGT5	290	3.9	1.7	330	290	130	170	72	7	89	63
TM15	J2-819-IGT2	269	5.0	22.0	920	230	1200	210	550	420	3500	190
TM16	J2-819-IGT3	251	3.9	5.5	290	390	590	170	67	16	880	79
TM16	J2-819-IGT7	242	4.2	6.7	380	340	320	150	70	5	110	59
TM17	J2-819-IGT4B	258	3.9	3.1	680	270	530	180	220	22	770	98
TM17	J2-819-IGT5B	257	4.0	4.4	310	250	300	80	63	10	550	69
TM18	J2-819-IGT2B	296	4.6	10.4	5100	96	160	150	460	4	47	67
TM18	J2-819-IGT7B	232	5.4	36.9	540	250	160	150	110	13	370	74
TM19	J2-819-IGT6B	232	4.2	3.0	550	250	190	230	140	7	130	75
TM20	J2-819-IGT3B	138	5.3	33.4	240	120	120	140	45	24	150	51

Table 3B. Measured Fluid Chemistry (2 of 4)

Fluid	Sample	max T	pH	Mg	Cr	Mn	Fe	Co	Ni	Cu	Zn	Ga
		°C	25°C	mmol/kg	nmol/kg	umol/kg	umol/kg	nmol/kg	nmol/kg	umol/kg	umol/kg	nmol/kg
MA8	J2-437-IGT1	359	2.6	5.6	NM	3600	9100	340	65	290	350	NM
MA8	J2-437-IGT3	359	2.4	3.8	NM	3500	10800	640	170	1800	380	NM
MA9	J2-437-IGT5	338	2.4	6.7	2000	3800	9500	200	370	250	460	100
MA9	J2-437-IGT6	336	2.3	3.2	NM	5000	15900	170	360	300	340	NM
MA10	J2-439-IGT1	109	5.2	48.1	NM	7	3600	83	160	260	17600	NM
MA11	J2-439-IGT6	328	2.2	3.7	2900	4100	11100	270	190	320	600	205
MA12	J2-446-IGT3	350	2.3	2.9	600	49	150	14	76	59	140	41
MA12	J2-446-IGT6	350	2.3	3.5	2700	4200	11500	290	580	280	600	160
MA13	J2-816-IGT5	140	2.6	20.4	210	4100	1500	120	270	19	2300	49
MA13	J2-816-IGT6	78	2.6	18.1	590	4300	1700	150	970	5	1100	70
MA14	J2-817-IGT5	318	2.4	2.6	640	5300	6400	210	250	100	1600	280
MA14	J2-817-IGT6	319	2.3	2.8	1100	5200	6300	190	770	100	1800	240
MA15	J2-817-IGT2	354	3.0	12.7	940	3400	9400	260	270	200	330	150
MA15	J2-817-IGT4	345	2.7	1.4	1800	4300	12500	210	290	220	350	160
MA16	J2-817-IGT1	363	5.8	6.8	2800	4200	12400	220	1600	180	530	110
MA16	J2-817-IGT8	364	2.7	2.1	2100	4400	13700	260	550	210	330	140
MA17	J2-817-IGT5B	360	2.9	8.0	690	3100	13900	590	510	3700	740	170
MA17	J2-817-IGT6B	362	2.8	8.1	1700	3300	9700	360	470	440	550	190
MA18	J2-818-IGT4	300	2.7	12.8	970	3700	9000	210	510	110	170	90
MA18	J2-818-IGT5	300	4.3	35.5	1500	1500	3900	170	700	99	290	91
MA19	J2-818-IGT2	308	2.9	15.6	1100	3400	8400	290	1000	630	400	140
MA19	J2-818-IGT3	297	2.6	9.4	1500	3900	9400	230	720	430	460	190
MA20	J2-818-IGT6	344	2.6	NM	1100	4900	11500	180	380	190	520	160
MA20	J2-818-IGT8	342	2.7	2.7	1200	4800	10900	200	470	120	310	130
MA21	J2-818-IGT7	345	2.7	2.8	1200	4200	11600	240	330	270	460	170
MA21	J2-818-M1		3.4	22.8	350	2600	7200	160	200	110	180	55

Table 3C. Measured Fluid Chemistry (3 of 4)

Sample	max T	pH	Mg	Mo	Ag	Cd	In	Sn	Sb	Au	Pb
	°C	25°C	mmol/kg	nmol/kg	nmol/kg	nmol/kg	nmol/kg	nmol/kg	nmol/kg	nmol/kg	nmol/kg
J2-434-IGT1	301	4.1	2.5	170	47	29	NM	NM	1676	0	160
J2-434-IGT4	304	5.0	3.0	150	51	83	NM	NM	1700	NM	350
J2-444-IGT1	297	3.3	2.9	130	52	210	NM	NM	21	0	1000
J2-444-IGT6	306	3.7	2.4	65	30	180	NM	6	49	1	510
J2-444-IGT3	298	4.4	4.6	110	45	47	NM	6	28	0	110
J2-444-IGT4	297	3.9	1.0	72	41	170	NM	5	51	0	510
J2-450-IGT4	309	3.7	1.4	50	26	92	NM	2	33	0	57
J2-450-IGT6	310	3.8	2.0	39	25	94	NM	1	21	0	55
J2-449-IGT5	317	4.4	2.1	43	13	30	NM	3	49	0	350
J2-449-IGT1	306	4.0	2.5	73	8	30	NM	2	14	0	300
J2-449-IGT6	312	3.9	2.1	66	2	44	NM	2	23	0	110
J2-815-IGT7	283	5.0	12.8	1300	19	130	53	72	45	840	370
J2-815-IGT8	283	4.3	2.3	1300	63	3200	42	23	430	1800	7800
J2-815-IGT1	288	5.1	16.8	1800	62	7000	42	52	2200	3000	8500
J2-815-IGT3	300	4.0	1.9	1300	9	590	53	97	170	800	530
J2-815-IGT2	290	4.9	8.1	770	0	68	41	56	1600	4400	470
J2-815-IGT4	279	4.4	1.9	99	49	120	20	42	98	230	1100
J2-815-IGT5	262	4.6	1.7	980	0	57	43	130	49	300	690
J2-815-IGT6	263	4.5	1.7	810	0	48	35	40	38	1000	430
J2-442-IGT3	313	4.1	5.5	310	9	61	NM	3	39	0	350
J2-442-IGT4	315	3.8	1.1	100	25	81	NM	86	29	NM	1200
J2-442-IGT1	284	4.3	3.4	120	29	53	NM	NM	25	1	2400
J2-442-IGT6	268	4.2	3.0	110	33	470	NM	NM	50	NM	730
J2-819-IGT6	260	3.9	4.3	860	16	180	NM	34	44	2200	680
J2-819-IGT8	262	3.9	3.6	1200	10	130	41	41	46	1800	51
J2-819-IGT4	214	4.0	1.5	1000	6	110	44	39	52	0	770
J2-819-IGT5	290	3.9	1.7	1100	18	150	42	68	50	2900	820
J2-819-IGT2	269	5.0	22.0	1400	220	6900	53	86	1700	5200	5000
J2-819-IGT3	251	3.9	5.5	1300	110	1500	43	40	150	2800	2900
J2-819-IGT7	242	4.2	6.7	1000	0	230	39	67	51	1700	390
J2-819-IGT4B	258	3.9	3.1	1200	130	1300	45	44	67	2800	3300
J2-819-IGT5B	257	4.0	4.4	1100	65	1000	37	33	160	2200	3000
J2-819-IGT2B	296	4.6	10.4	1300	0	120	39	40	54	1200	300
J2-819-IGT7B	232	5.4	36.9	1100	2	1300	45	45	55	4400	1100
J2-819-IGT6B	232	4.2	3.0	1100	500	120	48	46	440	8300	11000
J2-819-IGT3B	138	5.3	33.4	910	8	320	34	40	52	3000	880

Table 3D. Measured Fluid Chemistry (4 of 4)

Sample	max T	pH	Mg	Mo	Ag	Cd	In	Sn	Sb	Au	Pb
	°C	25°C	mmol/kg	nmol/kg	nmol/kg	nmol/kg	nmol/kg	nmol/kg	nmol/kg	nmol/kg	nmol/kg
J2-437-IGT1	359	2.6	5.6	170	33	270	NM	NM	1654	NM	710
J2-437-IGT3	359	2.4	3.8	320	67	270	NM	NM	1680	1	1300
J2-437-IGT5	338	2.4	6.7	210	58	390	NM	NM	1664	1	1100
J2-437-IGT6	336	2.3	3.2	2000	1600	10300	NM	NM	25	1	338400
J2-439-IGT1	109	5.2	48.1	2000	1500	10300	NM	NM	26	3	342000
J2-439-IGT6	328	2.2	3.7	210	55	290	NM	NM	1714	1	2300
J2-446-IGT3	350	2.3	2.9	35	10	72	NM	6	50	1	710
J2-446-IGT6	350	2.3	3.5	160	90	460	NM	NM	92	2	5100
J2-816-IGT5	140	2.6	20.4	790	950	2500	36	42	100	880	5400
J2-816-IGT6	78	2.6	18.1	1300	36	130	48	350	46	1600	11900
J2-817-IGT5	318	2.4	2.6	350	14	1500	140	110	120	1800	1200
J2-817-IGT6	319	2.3	2.8	1000	67	1400	170	57	150	3500	3200
J2-817-IGT2	354	3.0	12.7	1200	29	300	82	64	110	2300	1300
J2-817-IGT4	345	2.7	1.4	1400	66	330	85	75	91	960	1300
J2-817-IGT1	363	5.8	6.8	540	78	550	74	61	160	2000	1500
J2-817-IGT8	364	2.7	2.1	1100	26	280	84	130	870	2500	2600
J2-817-IGT5B	360	2.9	8.0	840	76	260	150	43	180	23000	470
J2-817-IGT6B	362	2.8	8.1	1500	100	430	100	110	56	26700	6200
J2-818-IGT4	300	2.7	12.8	1000	81	180	77	48	110	1200	490
J2-818-IGT5	300	4.3	35.5	1100	74	290	67	44	210	2700	460
J2-818-IGT2	308	2.9	15.6	2000	78	350	230	78	260	6600	3900
J2-818-IGT3	297	2.6	9.4	1200	70	440	170	92	310	1900	1000
J2-818-IGT6	344	2.6	NM	1200	110	440	100	56	91	2600	1900
J2-818-IGT8	342	2.7	2.7	1100	33	290	75	48	160	1400	970
J2-818-IGT7	345	2.7	2.8	1100	55	460	110	100	180	1400	760
J2-818-M1		3.4	22.8	1000	17	170	39	35	60	150	660

Table 4. (opposite)
Endmember fluid compositions calculated by extrapolation of the fluid data presented in Table 3 to zero-Mg concentration. Where multiple samples are available, uncertainties are estimated by the range of endmember fluid concentrations calculated for each sample. Components that were not measured are labelled "NM". Those affected by contamination of the sample by entrained particles are labelled "cont". Samples for which recovery of the element is thought to be incomplete are labeled with "inc".

Table 4A. Endmember Fluid Compositions (1 of 2)

Fluid	Number of Samples	min. Mg	max. T	min. pH	Cr	Mn	Fe	Co	Ni	Cu	Zn	Ga
		mmol/kg	°C	25°C	nmol/kg	umol/kg	umol/kg	nmol/kg	nmol/kg	umol/kg	umol/kg	nmol/kg
KM9	2	2.5	304	4.1	1600 ± NM	215 ± 1	1100 ± 110	560 ± 50	100 ± 96	5 ± 0	60 ± 16	5 ± NM
TMo1	2	2.4	306	3.3	1100 ± NM	580 ± 2	370 ± 30	146 ± 6	700 ± 140	8 ± NM	220 ± 27	15 ± 4
TMo2	2	1.0	298	3.9	1180 ± 50	293 ± 1	248 ± 3	160 ± 28	200 ± 140	8 ± 1	120 ± 50	10 ± 8
TMo5	2	1.4	310	3.7	630 ± 24	396 ± 5	278 ± 7	110 ± 8	400 ± 300	6 ± 0	83 ± 0	2 ± 0
A10	1	2.1	317	4.4	4400 ± NM	440 ± NM	170 ± NM	80 ± NM	110 ± NM	10 ± NM	100 ± NM	10 ± NM
A11	2	2.1	312	3.9	740 ± NM	400 ± 90	140 ± 30	73 ± 1	180 ± 50	9 ± 3	80 ± 0	6 ± 2
A13	2	2.3	283	4.3	1400 ± NM	450 ± 28	200 ± NM	115 ± 6	570 ± NM	5 ± NM	110 ± NM	110 ± NM
A14	2	1.9	300	4.0	1500 ± NM	400 ± 24	340 ± NM	180 ± 18	400 ± NM	75 ± NM	430 ± NM	83 ± NM
A15	2	1.9	290	4.4	1400 ± 260	240 ± 27	120 ± 4	130 ± 30	500 ± 90	9 ± 0	80 ± 20	73 ± 6
A16	2	1.7	263	4.5	700 ± 240	258 ± 3	67 ± 3	100 ± 40	200 ± 60	4 ± 1	37 ± 1	62 ± 3
TM11	2	1.1	315	3.8	3000 ± 1700	376 ± 1	180 ± 8	100 ± 15	700 ± 200	20 ± NM	110 ± 16	6 ± 4
TM12	2	3.0	284	4.2	7900 ± 400	350 ± 4	280 ± 22	117 ± 1	210 ± 22	25 ± 1	200 ± 110	50 ± 40
TM13	2	3.6	262	3.9	309 ± 7	296 ± 1	102 ± 3	167 ± 6	110 ± 50	9 ± 0	85 ± 4	66 ± 7
TM14	2	1.5	290	3.9	360 ± 40	300 ± 80	150 ± 30	200 ± 50	77 ± 5	7 ± 0	91 ± 1	80 ± 22
TM15	1	22.0	269	5.0	1500 ± NM	370 ± NM	cont. ± NM	cont ± NM	890 ± NM	cont ± NM	cont ± NM	cont ± NM
TM16	2	5.5	251	3.9	370 ± 50	410 ± 19	500 ± 140	180 ± 8	76 ± 3	12 ± 6	960 ± NM	80 ± 11
TM17	2	3.1	258	3.9	500 ± 190	280 ± 8	400 ± 120	140 ± 50	200 ± 80	17 ± 6	700 ± 110	90 ± 15
TM18	2	10.4	296	4.6	670 ± NM	310 ± 18	200 ± 130	440 ± NM	140 ± NM	15 ± 3	400 ± 160	91 ± NM
TM19	1	3.0	232	4.2	580 ± NM	260 ± NM	200 ± NM	240 ± NM	150 ± NM	7 ± NM	130 ± NM	79 ± NM
TM20	1	33.4	138	5.3	600 ± NM	290 ± NM	290 ± NM	cont ± NM	99 ± NM	cont ± NM	380 ± NM	130 ± NM
MA8	2	3.8	359	2.4	NM ± NM	3820 ± 28	11000 ± 900	500 ± 160	120 ± 50	1100 ± 800	390 ± 13	NM ± NM
MA9	2	3.2	338	2.3	2300 ± NM	4900 ± 500	14000 ± 3000	200 ± 26	400 ± 15	300 ± 16	400 ± 80	120 ± NM
MA10	1	48.1	109	5.2	NM ± NM	22 ± NM	cont. ± NM	cont ± NM	cont ± NM	cont ± NM	cont ± NM	NM ± NM
MA11	1	3.7	328	2.2	3100 ± NM	4400 ± NM	11900 ± NM	290 ± NM	210 ± NM	340 ± NM	650 ± NM	220 ± NM
MA12	2	2.9	350	2.3	2900 ± NM	4500 ± NM	12300 ± NM	310 ± NM	620 ± NM	300 ± NM	650 ± NM	170 ± NM
MA13	2	18.1	140	2.6	600 ± 260	6090 ± 50	2340 ± 50	200 ± 20	900 ± 500	17 ± 11	1500 ± NM	90 ± 13
MA14	2	2.6	319	2.3	900 ± 230	5600 ± 80	6730 ± 70	220 ± 12	500 ± 270	109 ± 1	1800 ± 100	280 ± 20
MA15	2	1.4	354	2.7	1600 ± 300	4400 ± 110	12500 ± 500	260 ± 60	320 ± 21	240 ± 13	390 ± 27	180 ± 15
MA16	2	2.1	364	2.7	2600 ± 400	4610 ± 18	14000 ± 300	250 ± 17	1100 ± 600	210 ± 7	500 ± 120	140 ± 11
MA17	2	8.0	362	2.8	1300 ± 600	3700 ± 120	13000 ± 2500	500 ± 130	560 ± 21	500 ± NM	700 ± 110	200 ± 9
MA18	2	12.8	300	2.7	1200 ± NM	4500 ± 110	11190 ± 27	260 ± NM	640 ± NM	160 ± 70	300 ± 300	130 ± 70
MA19	2	9.4	308	2.9	1600 ± 160	4500 ± 90	10980 ± 40	320 ± 50	840 ± NM	600 ± 160	534 ± 4	200 ± 22
MA20	2	2.7	344	2.6	1200 ± 20	5080 ± 60	11800 ± 300	200 ± 10	440 ± 50	170 ± 40	400 ± 110	150 ± 16
MA21	2	2.8	345	2.7	1100 ± 300	4360 ± 3	12200 ± 40	250 ± 11	340 ± 11	260 ± 50	400 ± 80	150 ± 40

Table 4B. Endmember Fluid Compositions (2 of 2)

Fluid	Number of Samples	min. Mg	max. T	min. pH	Mo	Ag	Cd	In	Sn	Sb	Au	Pb
		mmol/kg	°C	25°C	nmol/kg	nmol/kg	nmol/kg	nmol/kg	nmol/kg	nmol/kg	nmol/kg	nmol/kg
KM9	2	2.5	304	4.1	160 ± 10	52 ± 2	60 ± 28	NM ± NM	NM ± NM	1780 ± 19	0.12 ± NM	300 ± 100
TMo1	2	2.4	306	3.3	100 ± 40	40 ± 12	210 ± 20	NM ± NM	6 ± NM	40 ± 15	0.16 ± NM	530 ± NM
TMo2	2	1.0	298	3.9	90 ± 19	45 ± 4	120 ± 60	NM ± NM	6 ± NM	40 ± 10	0.12 ± NM	300 ± 200
TMo5	2	1.4	310	3.7	43 ± 6	26 ± 1	96 ± 1	NM ± NM	1 ± NM	28 ± 6	0.14 ± NM	58 ± 1
A10	1	2.1	317	4.4	41 ± NM	14 ± NM	31 ± NM	NM ± NM	3 ± NM	51 ± NM	0.04 ± NM	370 ± NM
A11	2	2.1	312	3.9	68 ± 4	6 ± 3	39 ± 7	NM ± NM	2 ± 0	19 ± 5	0.12 ± 0.03	200 ± 100
A13	2	2.3	283	4.3	1500 ± 170	50 ± 21	160 ± NM	50 ± 12	50 ± 40	59 ± NM	1600 ± 400	480 ± NM
A14	2	1.9	300	4.0	1400 ± NM	40 ± 40	600 ± NM	57 ± 3	90 ± 13	170 ± NM	820 ± NM	550 ± NM
A15	2	1.9	290	4.4	400 ± 400	51 ± NM	110 ± 21	30 ± 15	50 ± 13	100 ± NM	240 ± NM	900 ± 270
A16	2	1.7	263	4.5	900 ± 90	bdl ± NM	54 ± 4	40 ± 4	90 ± 50	44 ± 6	700 ± 400	600 ± 140
TM11	2	1.1	315	3.8	200 ± 110	20 ± 8	76 ± 7	NM ± NM	50 ± 40	36 ± 7	0 ± NM	900 ± 400
TM12	2	3.0	284	4.2	115 ± 4	33 ± 2	300 ± 220	NM ± NM	NM ± NM	40 ± 13	1 ± NM	2000 ± 900
TM13	2	3.6	262	3.9	1100 ± 200	14 ± 3	160 ± 24	45 ± NM	40 ± 4	49 ± 1	2100 ± 210	400 ± 300
TM14	2	1.5	290	3.9	1200 ± 250	16 ± 4	160 ± 11	50 ± 15	68 ± 3	60 ± 16	3000 ± 2985	1000 ± 210
TM15	1	22.0	269	5.0	cont ± NM	cont ± NM	cont ± NM	cont ± NM	cont ± NM	cont ± NM	cont ± NM	cont ± NM
TM16	2	5.5	251	3.9	2200 ± 140	120 ± NM	1600 ± 700	46 ± 2	60 ± 16	110 ± 50	2500 ± 600	2000 ± 1400
TM17	2	3.1	258	3.9	1260 ± 50	100 ± 30	1200 ± 120	44 ± 4	41 ± 5	120 ± 50	2700 ± 300	3300 ± 140
TM18	2	10.4	296	4.6	1400 ± NM	2 ± 1	1400 ± 600	56 ± NM	56 ± NM	80 ± 50	5000 ± 1000	1300 ± 230
TM19	1	3.0	232	4.2	1200 ± NM	520 ± NM	130 ± NM	50 ± NM	48 ± NM	460 ± NM	8700 ± NM	11500 ± NM
TM20	1	33.4	138	5.3	cont ± NM	20 ± NM	800 ± NM	cont ± NM	cont ± NM	130 ± NM	7600 ± NM	2200 ± NM
MA8	2	3.8	359	2.4	300 ± 80	50 ± 18	287 ± 0	NM ± NM	NM ± NM	1790 ± 14	1 ± NM	1100 ± 300
MA9	2	3.2	338	2.3	230 ± NM	66 ± NM	450 ± NM	NM ± NM	NM ± NM	1900 ± 900	1 ± NM	1200 ± NM
MA10	1	48.1	109	5.2	cont ± NM	cont ± NM	cont ± NM	NM ± NM	NM ± NM	280 ± NM	cont ± NM	cont ± NM
MA11	1	3.7	328	2.2	220 ± NM	59 ± NM	310 ± NM	NM ± NM	NM ± NM	1800 ± NM	1 ± NM	2500 ± NM
MA12	2	2.9	350	2.3	160 ± NM	96 ± NM	490 ± NM	NM ± NM	NM ± NM	98 ± NM	2 ± NM	5400 ± NM
MA13	2	18.1	140	2.6	1500 ± 300	51 ± NM	180 ± NM	61 ± 7	63 ± NM	100 ± 40	1800 ± 500	cont ± NM
MA14	2	2.6	319	2.3	700 ± 400	40 ± 28	1560 ± 40	160 ± 18	88 ± 28	140 ± 16	3000 ± 900	2000 ± 1000
MA15	2	1.4	354	2.7	1470 ± 70	60 ± 15	350 ± 15	90 ± 8	78 ± 2	110 ± 22	2000 ± 900	1400 ± 150
MA16	2	2.1	364	2.7	900 ± 270	50 ± 29	400 ± 150	84 ± 3	100 ± 40	170 ± NM	2400 ± 200	2200 ± 600
MA17	2	8.0	362	2.8	1300 ± 400	100 ± 14	400 ± 100	150 ± 28	90 ± 40	130 ± 70	28000 ± 2000	540 ± NM
MA18	2	12.8	300	2.7	1200 ± NM	100 ± NM	230 ± NM	110 ± 50	60 ± NM	140 ± NM	1500 ± NM	700 ± 300
MA19	2	9.4	308	2.9	1400 ± NM	90 ± 11	480 ± 28	240 ± 50	110 ± 3	360 ± 10	2200 ± NM	1200 ± NM
MA20	2	2.7	344	2.6	1200 ± 15	80 ± 40	400 ± 80	90 ± 14	55 ± 4	130 ± 30	2100 ± 600	1500 ± 500
MA21	2	2.8	345	2.7	1300 ± 260	50 ± 15	400 ± 90	100 ± 25	93 ± 23	160 ± 40	1100 ± 600	900 ± 150

Figures 4A to 4D. (A, B, and C) Results from this paper (gray diamonds) for maximum temperatures, pH (at 25°C), and zero-Mg endmember concentrations of Mn, Fe, Cu, Zn, Ag, Co, and Cd for hydrothermal vent fluids from the Kilo Moana (KM), TowCam (TC), Tahi Moana-1 (TMo), ABE (A), Tu'i Malila (TM), and Mariner (MA) vent fields in the Lau Basin are compared with those of Mottl et al. (2011) (white squares) for the same vent fields and those of Craddock (2009) (white circles) for hydrothermal vent fluids from the Vienna Woods (VW), PACMANUS (PAC), and SuSu Knolls (SuSu) vent fields in the Manus Basin. Vent fields in the PACMANUS area are separated into three groups based on differences in vent fluid temperature and pH: the Roger's and Roman Ruins vent fields (PAC-R), the Satanic Mills vent field (PAC-S), and the Fenway vent field (PAC-F). (D) Results from this paper (gray diamonds) for zero-Mg endmember concentrations of Cu, Fe, Zn, Co, Ni, Ga, In, and Pb for hydrothermal vent fluids from the Kilo Moana, Tahi Moana-1, ABE, Tu'i Malila, and Mariner vent fields in the Lau Basin are compared with those of Chapter 2 of this thesis for Cu, Fe, Zn, Pb in hydrothermal vent fluids from the Kilo Moana, TowCam, ABE, Tu'i Malila, and Mariner same vent fields (white squares). Uncertainties around results from this paper reflect those reported in Table 4A and 4B.

Figure 4A

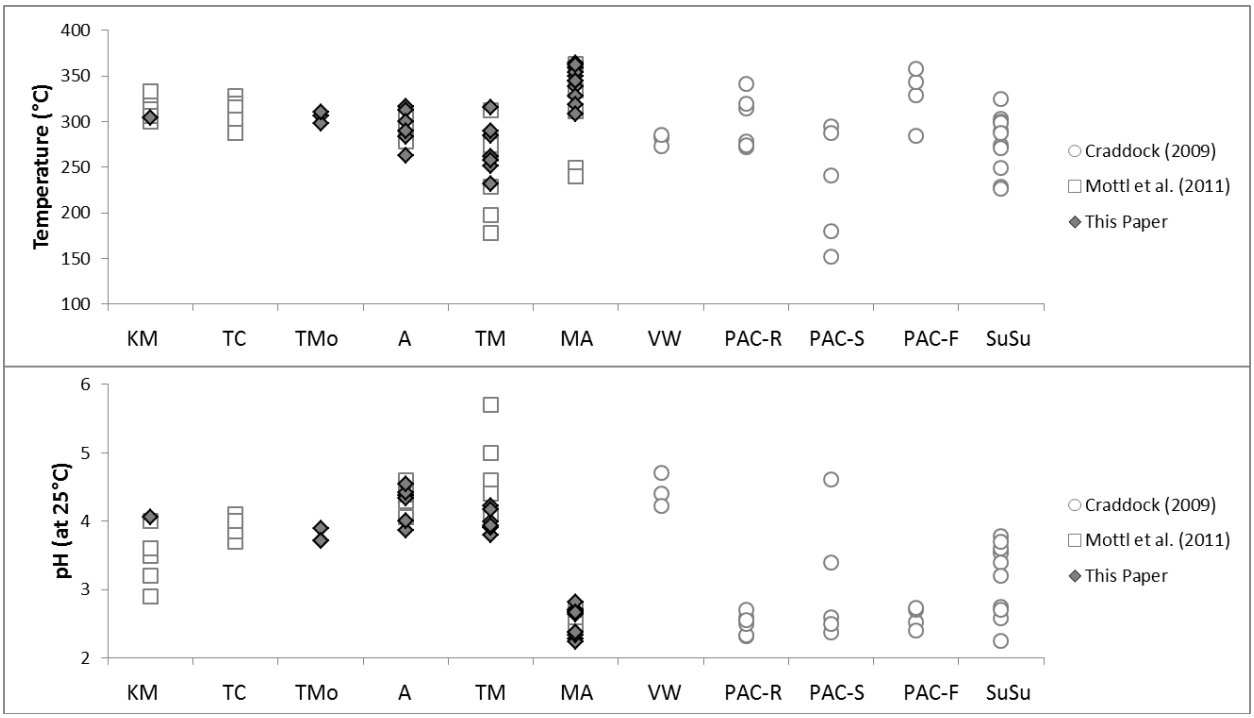

Figure 4B

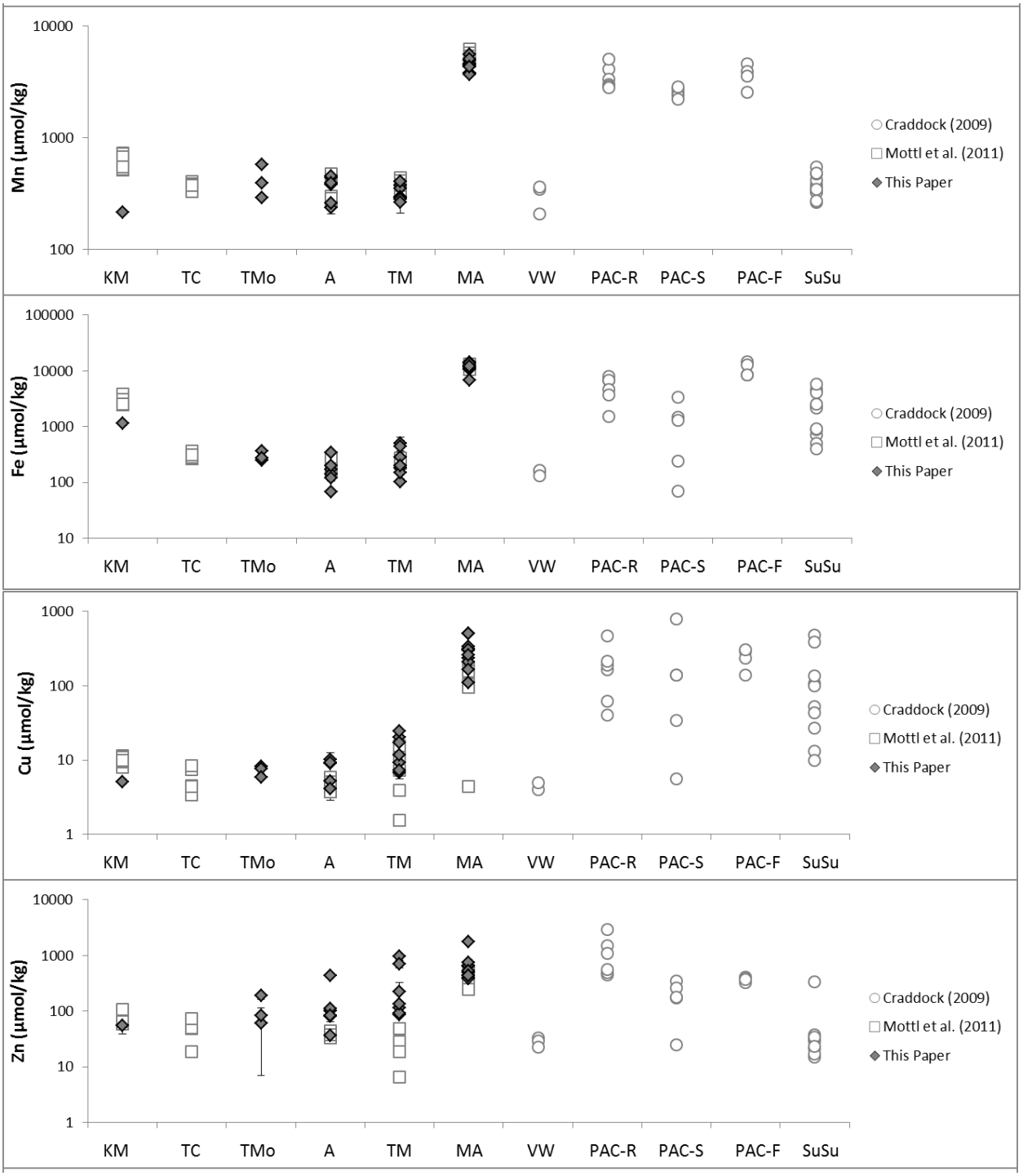
Mn (µmol/kg)
10000
1000
100
KM
TC
TMo
A
TM
MA
VW
PAC-R
PAC-S
PAC-F
SuSu
Craddock (2009)
Mottl et al. (2011)
This Paper
Fe (µmol/kg)
100000
10000
1000
100
10
Cu (µmol/kg)
1000
100
10
1
Zn (µmol/kg)
10000
1000
100
10
1

Figure 4C

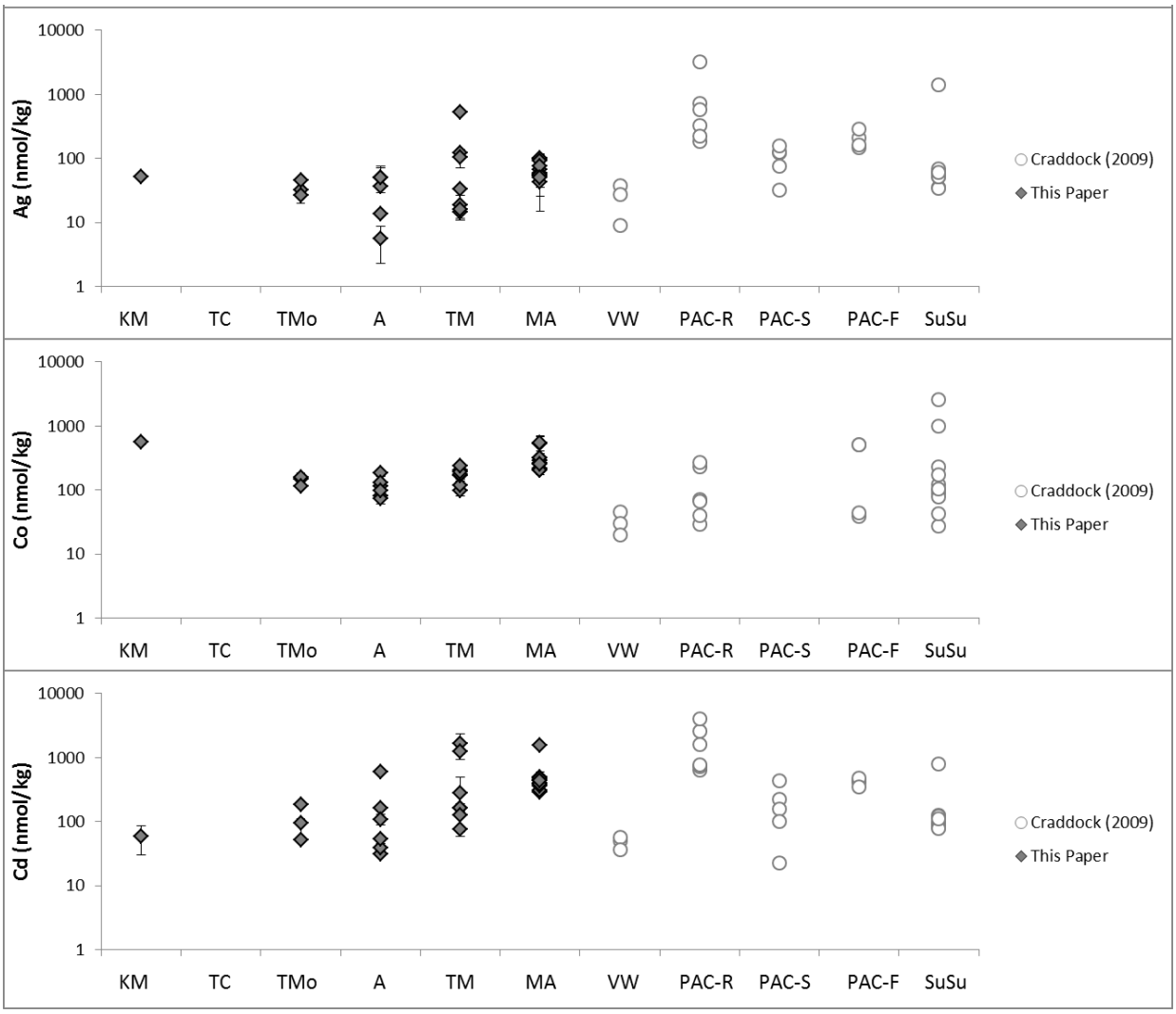
Ag (nmol/kg)
Co (nmol/kg)
Cd (nmol/kg)
10000
1000
100
10
1
KM
TC
TMo
A
TM
MA
VW
PAC-R
PAC-S
PAC-F
SuSu
Craddock (2009)
This Paper

Figure 4D

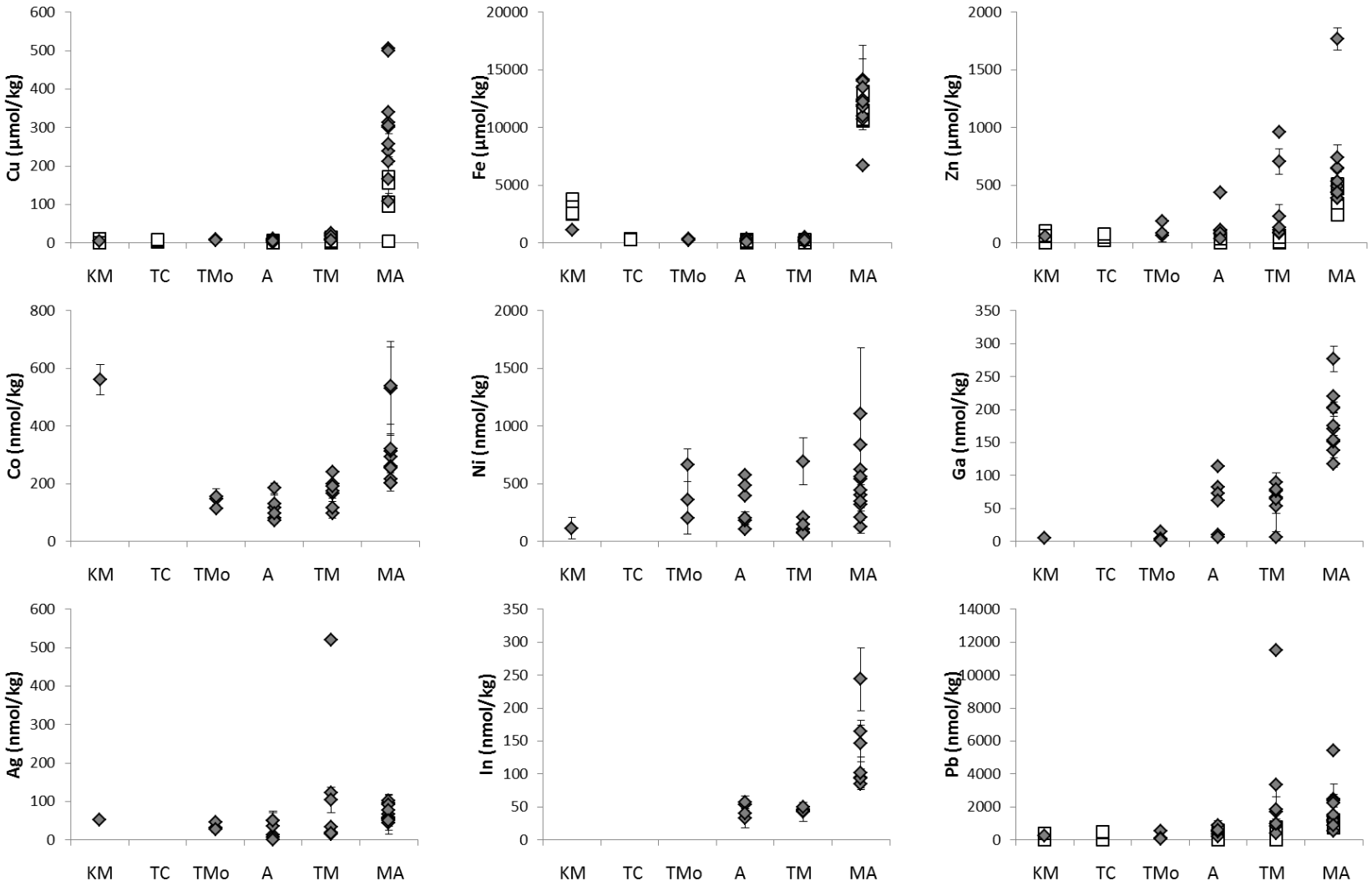
Cu (µmol/kg)
Fe (µmol/kg)
Zn (µmol/kg)
Co (nmol/kg)
Ni (nmol/kg)
Ga (nmol/kg)
Ag (nmol/kg)
In (nmol/kg)
Pb (nmol/kg)
KM
TC
TMo
A
TM
MA

Table 5. Temperature, pH (at 25°C), and elemental compositions of hydrothermal fluids used as inputs to the EQ3/6 model. These compositions represent fluids for which SIMS analyses of the chalcopyrite lining of a paired black smoker chimney are also available. Data for vent fluids from the Eastern Lau Spreading Center are from this paper and Chapter 2 of this thesis, data for vent fluids in the Manus Basin are from Craddock (2009), data for fluid Sully99 from the Main Endeavour Field are from Seyfried et al. (2003) and data for fluid BB5 from the Beebe / Piccard vent field are from McDermott (2015). Values listed in red for Ni, Ga, and In are estimated based on observed patterns between these elements and fluid pH. µM = µmol / L vent fluid; mm = mmol / kg vent fluid; µm = µmol / kg vent fluid; nm = nmol / kg vent fluid

Fluid ID	Temp.	pH	H_2	H_2S	Cl	Na	Ca	K	Mn	Fe	Cu	Co	Ni	Ag	Ga	In
	(°C)	(at 25°C)	µM	mm	mm	mm	mm	mm	µm	µm	µm	nm	nm	nm	nm	nm
Eastern Lau Spreading Center																
TMo5	310	3.7	114	3.3	555	405	64.4	19.2	400	280	6	120	360	26	2	50
A10	317	3.9	63	3.9	543	437	40.3	24.6	440	170	10	80	80	14	10	50
A11	306	4.0	114	2.7	552	446	40.2	24.9	380	140	9	73	180	6	6	50
A16	300	4.0	114	3.0	552	449	38.4	25.6	260	67	4	98	200	6	62	40
TM11	315	3.8	418	2.8	652	510	48.7	43.0	380	180	20	96	690	19	6	50
MA9	338	2.4	414	8.9	470	313	43.4	28.3	5200	12500	300	20	400	230	120	150
MA15	354	2.7	78	10.0	521	370	41.7	30.1	4400	12500	240	260	320	56	180	94
Manus Basin																
VW1	282	4.4	43	1.4	691	509	80.1	21.2	350	150	5	45	250	38	50	50
RGR1	320	2.7	20	3.6	648	489	27.1	81.1	3000	6900	200	35	250	200	150	150
RMR1	314	2.3	76	7.5	632	482	19.8	81.7	4000	5600	160	230	250	780	150	150
SM3	288	2.7	8	10.2	503	398	13.7	68.0	2300	1200	140	32	250	73	150	150
F3	358	2.7	407	18.8	562	407	22.3	76.1	3800	11800	140	520	250	600	150	150
NS3	300	3.4	82	3.4	673	541	30.6	65.0	430	2300	110	1000	250	44	50	50
SZ1	303	3.8	12	1.8	626	508	33.8	48.0	270	750	53	230	250	36	50	50
SZ2	274	3.6	7	1.8	684	533	49.4	49.2	370	780	27	100	250	53	50	50
Others																
Sully99	379	3.6	960	20.0	39	32	1.9	2.0	90	400	12	100	250	4	50	50
BB5	395	3.0	19200	12.3	352	313	6.1	11.5	560	6500	170	1000	250	50	50	50

Table 6. Temperature, pH (at 25°C), and EQ3/6 model outputs for *in situ* pH and log (base 10) of oxygen and sulfur fugacity at *in situ* conditions (temperature listed in second column, 250 bar pressure, closed system, mineral precipitation suppressed).

Fluid ID	Temp.	pH	pH	log fO2	log fS2
	(°C)	(at 25°C)	in situ		
Eastern Lau Spreading Center					
TMo5	310	3.7	4.6	-31.7	-10.0
A10	317	3.9	4.6	-31.6	-9.5
A11	306	4.0	5.2	-32.1	-10.3
A16	300	4.0	5.2	-32.7	-10.4
TM11	315	3.8	4.5	-32.4	-11.1
MA9	338	2.4	3.2	-30.2	-9.3
MA15	354	2.7	3.8	-27.4	-7.3
Manus Basin					
VW1	282	4.4	5.1	-33.7	-10.9
RGR1	320	2.7	4.0	-30.5	-9.4
RMR1	314	2.3	2.8	-29.9	-8.3
SM3	288	2.5	3.0	-31.7	-7.5
F3	358	2.7	3.9	-28.5	-8.1
NS3	300	3.4	3.9	-32.5	-10.0
SZ1	303	3.8	4.1	-35.7	-10.6
SZ2	274	3.6	4.0	-33.0	-9.4
Others					
Sully99	379	3.6	4.3	-28.0	-8.7
BB5	395	3.0	5.0	-28.7	-10.7

5. DISCUSSION

By examining paired samples of black smoker chimney linings and the hydrothermal fluids flowing through them at the time of collection, it is possible to directly investigate the effects of hydrothermal fluid chemistry on mineral chemistry and search for proxies of hydrothermal fluid chemistry based on mineral trace element contents. Additionally, analyses of the same elements in hydrothermal fluids and the chalcopyrite linings of black smoker chimneys allows for investigation of trace element partitioning between hydrothermal fluids and chalcopyrite.

5.1. Hydrothermal Fluid Chemistry

Similarities between the measured temperatures, pH, and zero-Mg endmember concentrations of major ions (Na, Li, K, Ca) and transition metals (Mn, Fe, Cu, Zn) of vent fluids collected from the ABE, Tu'i Malila and Mariner vent fields in 2005, 2009, and 2015 suggest that vent fluid temperature and chemistry have been relatively stable over this time period. Between 2005 and 2009, vent fluids from the Kilo Moana vent field exhibited a systematic decrease in temperature and transition metal concentrations and an increase in vent fluid pH (Chapter 2 of this thesis). No hydrothermal activity was observed at the Kilo Moana vent field in 2015 (J. Seewald, A-L. Reysenbach, pers. comm. 2015). Vent fluids at the Mariner vent field exhibit a bimodal range of chlorinity and H_2S contents associated with phase separation at the seafloor and in the shallow subsurface (Takai et al, 2008; Mottl et al., 2011). However, there is no indication of systematic changes in high chloride or low chloride Mariner vent fluids between 2005 and 2015. Black smoker chimneys from the Mariner vent field were collected as sample

pairs with the fluids flowing through them at the time of collection, allowing for comparison of the chemistry of black smoker chimney linings and hydrothermal fluids.

New analyses of Mn, Fe, Cu, and Zn for hydrothermal vent fluids collected from the ELSC in 2015 agree with concentrations measured in fluids collected in 2005 reported in Mottl et al. (2011) and fluids collected in 2009 reported in Chapter 2 of this thesis. Data are consistent with the conclusions of previous studies, that concentrations of Mn, Fe, Cu, and Zn in hydrothermal fluids are primarily controlled by the temperature- and pH-sensitive solubility of minerals in the subsurface (e.g., Mottl and Holland, 1978; Seyfried et al., 1984; Von Damm, 1995). Similarities in variabilities of concentrations with temperature and pH, as shown in plots of Ga, and In vs. hydrothermal fluid temperature and pH, suggest that these elements are likewise solubility controlled (Fig. 5A and 5B). Additionally, higher concentrations of Ga (and to a lesser extent, In) in the felsic-hosted ABE and Tu'i Malila vent fluids compared with similar temperature and pH vent fluids from the basalt-hosted Kilo Moana vent field and the Tahi Moana-1 vent field hosted in transitional lithology suggest some degree of lithologic control on Ga (and In) concentrations (Fig. 4C). In contrast to Ga and In, Co and Ni show significantly less difference in concentration as functions of temperature and pH than Mn, Fe, Cu, Zn, In, or Ga (Fig. 5A, 5B), while Ag concentrations do not correlate with temperature (Fig. 5B), and show some trend with pH (Fig. 5A), though some of that trend is due to local metal remobilization (e.g., RMR2, SZ5, RGR2) as opposed to reaction zone conditions (Craddock, 2009). For Co, higher concentrations in the Kilo Moana vent fluid KM9 compared with the higher temperature, lower pH vent fluids from Mariner vent field suggests that higher Co concentrations may be associated with basaltic as opposed to felsic lithology (Fig. 4C). Thus the shallower trends of Co

and Ni vs temperature and pH are hypothesized to reflect limited Co and Ni along the fluid-rock reaction path for back-arc basin fluids.

Previous studies of hydrothermal vent fluids from the Vai Lili vent field on the ELSC (Fouquet et al., 1993), the TAG hydrothermal mound on the Mid-Atlantic Ridge (Tivey et al., 1995) and the PACMANUS vent fields in the Manus Basin (Craddock, 2009) have demonstrated the sensitivity of Zn and Ag concentrations to near-surface remobilization of previously deposited Zn- and Ag-rich sulfide. Typical evidence for significant subsurface remobilization includes highly elevated concentrations of Zn, Cd, Ag, and Pb and low pH relative to high-temperature vent fluids from the same vent field (Fouquet et al., 1993; Tivey et al., 1995; Craddock, 2009). Such evidence is absent from the ELSC vent fluids analyzed here (but not for some of the Manus Basin vent fluids) and it is concluded that subsurface remobilization does not play a significant role in determining the metal concentrations of vent fluids from the Kilo Moana, Tahi Moana-1, ABE, Tu'i Malila or Mariner vent fields.

Figure 5A. Plots of hydrothermal fluid pH (at 25°C) vs. zero-Mg endmember concentrations of Mn, Fe, Cu, Zn, Co, Ag, Ni, Ga, In for hydrothermal fluids from the Lau Basin (this chapter and Mottl et al., 2011) and for hydrothermal fluids from the Manus Basin (Craddock, 2009).

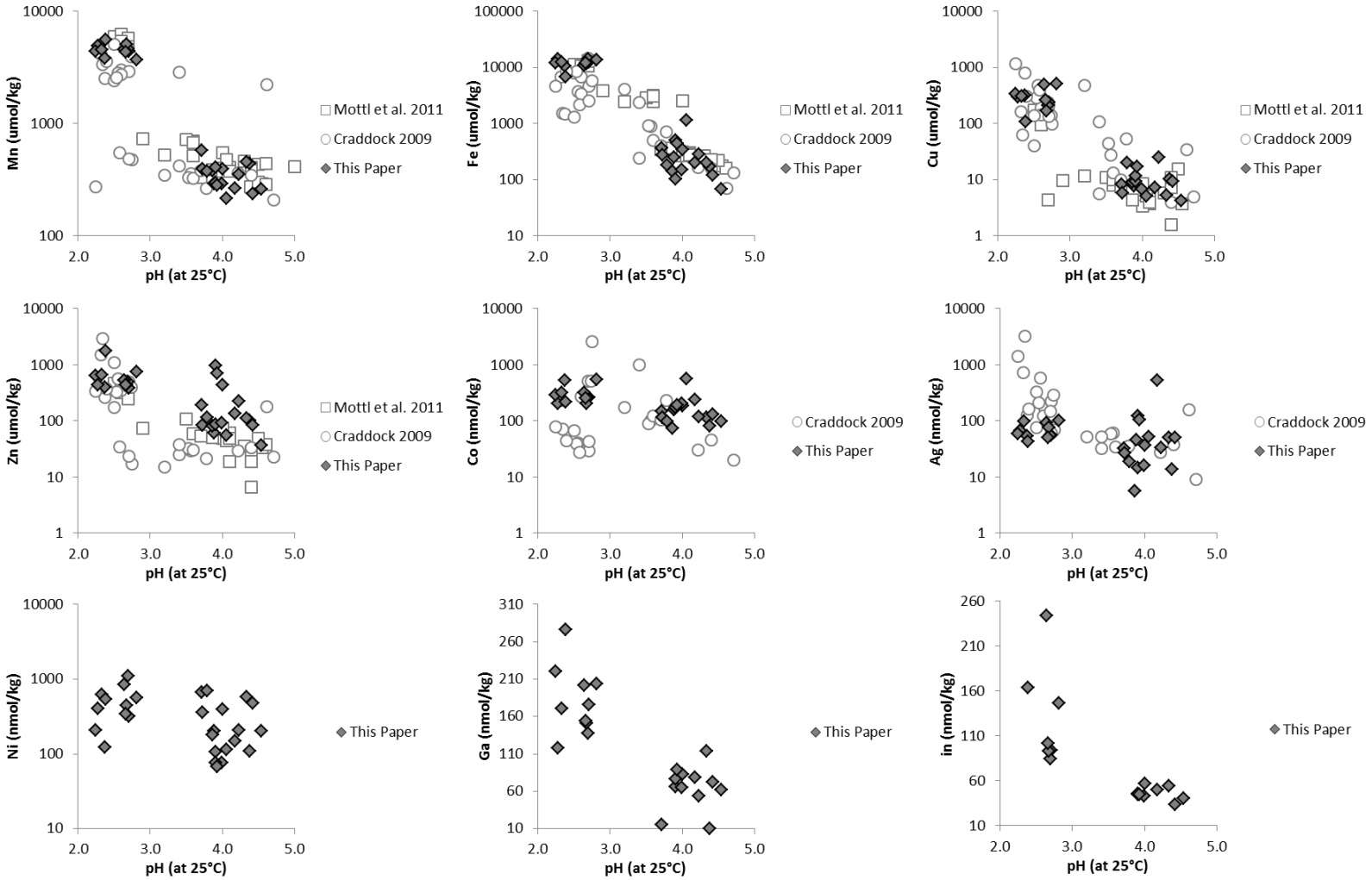

Figure 5B. Plots of hydrothermal fluid temperature (°C) vs. zero-Mg endmember concentrations of Mn, Fe, Cu, Zn, Co, Ag, Ni, Ga, In for hydrothermal fluids from the Lau Basin (this chapter and Mottl et al., 2011) and for hydrothermal fluids from the Manus Basin (Craddock, 2009).

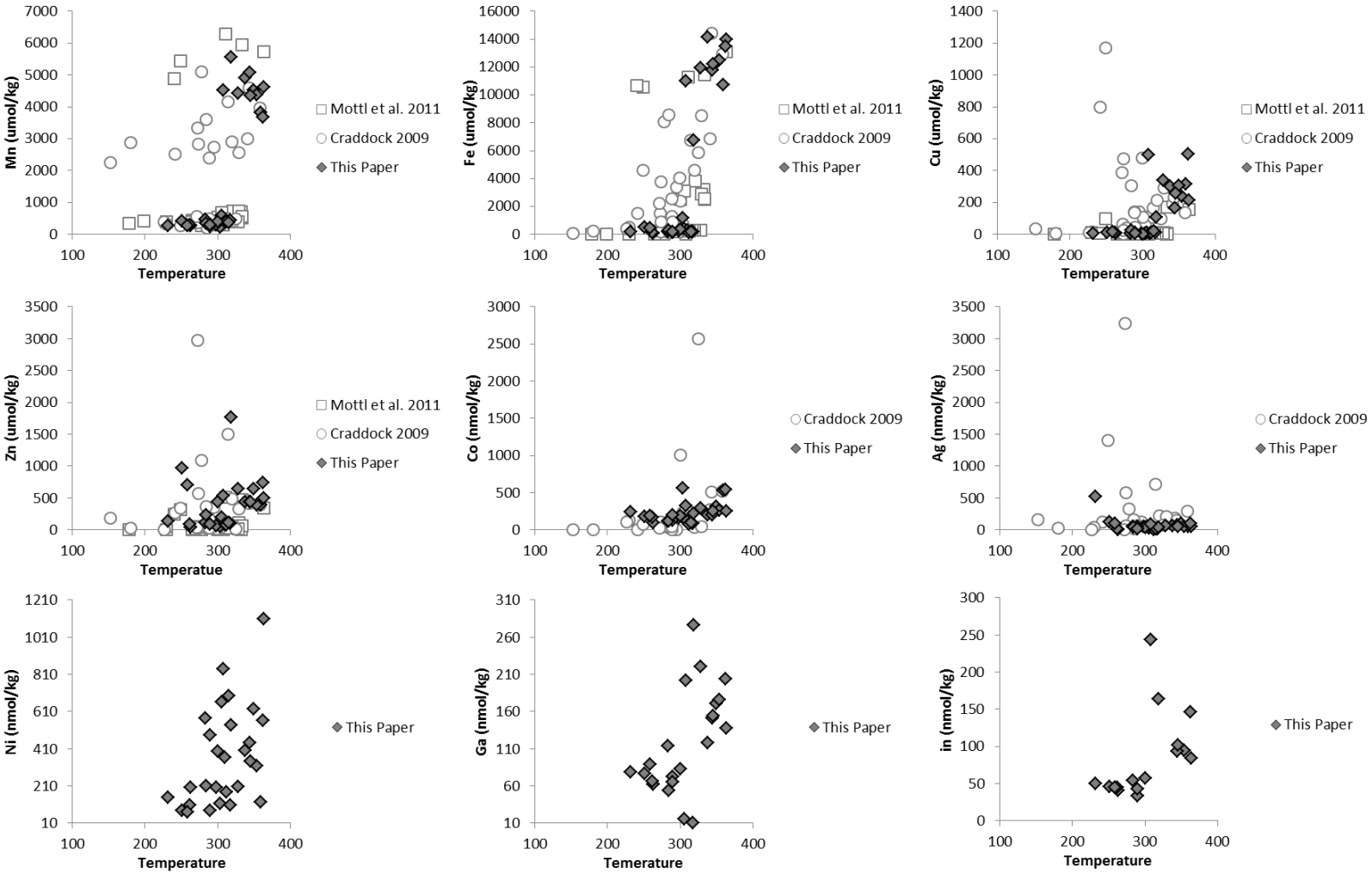

5.2. Comparison of Fluid and Mineral Chemistry

The analyses of Cu, Fe, Co, Ni, Ag, Ga, and In concentrations in ELSC hydrothermal vent fluids presented here can be compared with SIMS measurements of Co, Ni, Ag, Ga, and In concentrations in the chalcopyrite linings of black smoker chimney samples that were in contact with these fluids at the time of collection (Chapter 3 of this thesis). Additional SIMS analyses of black smoker chimney linings from the Manus Basin, Main Endeavour Field on the Juan de Fuca Ridge, and Mid-Cayman Rise (also in Chapter 3 of this thesis) may likewise be compared with published trace element analyses of hydrothermal fluid pairs from these vent fields. Because of uncertainties in the SIMS calibration curves, especially at low concentrations, SIMS count ratios are used for the comparison. The compositions of the relevant fluids are presented in Tables 4A and 4B. Selected results of SIMS analyses presented in Chapter 3 of this thesis are presented in Table 7A with conversions to concentration units provided in Table 7B.

5.2.1. Ag

Comparing the trace element contents of paired black smoker chimneys and fluids, the Ag content of chalcopyrite black smoker chimney linings correlates with the ratio of Ag to Cu in the corresponding fluid (Fig. 6A). This correlation is improved if the Ag contents of black smoker chimney linings are compared with the ratios of the activities of the free ions, Ag^+ and Cu^+ obtained through thermodynamic fluid modelling (Fig. 6B; see Appendix B).

Table 7A. Results of SIMS analyses of black smoker chimney linings presented in Chapter 3 of this thesis reported as counts ratios with 63Cu16O in the denominator. Uncertainties in the reported concentrations reflect standard errors (1σ) of multiple SIMS spots on the same sample. Details of these analyses can be found in Chapter 3 of this thesis.

Table 7A. Trace Element Contents of Chalcopyrite Lining Black Smoker Chimneys (Secondary Ion Intensity Ratios with $^{63}Cu^{16}O$)

Chimney	Fluid	59Co / 63Cu16O				60Ni / 63Cu16O				69Ga / 63Cu16O				109Ag / 63Cu16O				115In / 63Cu16O			
		n=	AVG	±	ASE	n=	AVG	±	ASE	n=	AVG	±	ASE	n=	AVG	±	ASE	n=	AVG	±	ASE
Eastern Lau Spreading Center																					
J2-450-3-R1	TMo5	18	6.39E-05	±	4.01E-05	3	1.18E-04	±	9.17E-06	3	6.85E-02	±	2.62E-02	18	6.60E-02	±	1.60E-02	18	5.26E+00	±	1.53E+00
J2-449-6-R1	A10	22	1.18E-02	±	1.15E-02	6	1.44E-05	±	4.26E-06	6	5.83E-02	±	1.63E-02	22	1.21E-02	±	5.35E-03	22	1.45E+00	±	1.01E+00
J2-449-5-R1	A11	20	2.65E-04	±	4.67E-04	8	4.86E-05	±	1.14E-05	8	1.00E-01	±	3.06E-02	20	2.34E-02	±	4.07E-03	20	1.04E-01	±	2.51E-02
J2-815-5-R1	A16	9	8.81E-04	±	1.08E-03	3	3.09E-05	±	9.18E-06	3	1.91E-01	±	1.47E-02	9	1.45E-02	±	1.90E-03	9	1.22E+00	±	5.68E-01
J2-442-4-R2	TM11	17	5.17E-03	±	4.72E-03	3	3.06E-05	±	8.65E-06	3	1.04E-02	±	2.85E-03	17	1.38E-02	±	2.07E-03	17	5.55E-01	±	4.95E-01
J2-437-3-R2	MA9	12	1.06E-04	±	2.44E-04	6	9.93E-05	±	1.54E-04	6	3.52E-01	±	1.04E-01	12	2.95E-03	±	2.00E-03	12	4.07E+00	±	1.74E+00
J2-817-4-R2	MA15	6	8.95E-04	±	3.88E-04		NM				NM			6	2.57E-03	±	4.32E-04	6	1.04E+00	±	1.23E-01
Manus Basin																					
J2-207-1-R1	VW1	88	1.21E-02	±	6.14E-03	21	5.60E-05	±	1.95E-05	21	2.31E-02	±	1.47E-02	88	9.56E-02	±	1.65E-02	88	1.32E-02	±	3.68E-02
J2-213-6-R1	RGR1	13	4.4E-05	±	5.4E-05	6	4.0E-05	±	2.6E-05	6	2.4E-01	±	1.6E-01	13	6.6E-03	±	7.6E-04	13	4.9E+00	±	1.1E+00
J2-208-1-R1	RMR1	24	7.28E-04	±	9.11E-04	6	1.24E-04	±	2.32E-05	6	2.62E+00	±	9.93E-01	24	3.25E-02	±	1.61E-02	11	2.45E+01	±	9.01E+00
J2-214-3-R1	SM3	27	1.18E-05	±	2.22E-05	8	1.67E-04	±	6.04E-05	8	1.07E+00	±	3.27E-01	27	1.55E-03	±	7.35E-03	27	2.83E+00	±	2.43E+00
J2-216-16-R1	F3	13	3.41E-02	±	1.26E-02	3	7.11E-04		2.21E-04	3	7.68E-01	±	7.97E-02	13	8.10E-03	±	6.32E-03	8	1.42E+00	±	5.22E-01
J2-223-1-R1	NS3	21	3.34E-01	±	1.01E-01	7	1.85E-02	±	3.87E-03	7	3.55E-01	±	1.22E-01	21	7.70E-03	±	2.64E-03	17	9.83E-01	±	4.54E-01
J2-217-2-R1	SZ1	13	1.57E-01	±	2.32E-02	3	5.64E-03	±	2.31E-04	3	5.10E-02	±	1.08E-02	13	6.44E-03	±	1.12E-03	8	7.69E-01	±	1.15E-01
J2-217-10-R1	SZ2	20	2.18E-02	±	1.05E-02	3	1.08E-03	±	1.50E-04	3	3.15E-01	±	5.28E-02	20	1.35E-02	±	5.01E-03	9	3.61E-01	±	1.67E-01
Others																					
Alv3474-3-1	Sully99	27	8.24E-01	±	1.19E-01	8	2.27E-02	±	1.24E-02	8	1.32E-02	±	7.94E-03	27	3.08E-03	±	5.55E-04	27	3.16E-01	±	9.05E-02
J2-613-16-R1	BB5	19	1.74E+01	±	5.77E+00	3	1.35E+00	±	6.62E-02	3	4.11E-02	±	1.91E-03	19	3.64E-03	±	2.18E-03	19	2.16E+00	±	8.56E-01

Table 7B. Trace Element in Chalcopyrite Lining Black Smoker Chimneys (μg/g)

Concentrations in μg/g were derived based on the SIMS calibration curves presented in Chapter 3 of this thesis. Uncertainties in the reported concentrations reflect standard errors (1σ) of multiple SIMS spots on the same sample. Details of these analyses can be found in Chapter 3 of this thesis.

Chimney	Fluid	Co	Ni	Ga	Ag	In
		mean ± 1σ	mean ± 1σ	mean ± 1σ	mean ± 1σ	mean ± 1σ
Eastern Lau Spreading Center						
J2-450-3-R1	TMo5	bdl ± bdl	bdl ± bdl	1.3 ± 0.5	2600 ± 600	60 ± 17
J2-449-6-R1	A10	0.5 ± 0.2	bdl ± bdl	1.1 ± 0.3	500 ± 210	20 ± 11
J2-449-5-R1	A11	bdl ± bdl	bdl ± bdl	1.8 ± 0.6	900 ± 160	1.1 ± 0.3
J2-815-5-R1	A16	bdl ± bdl	bdl ± bdl	3.5 ± 0.3	570 ± 70	13 ± 6
J2-442-4-R2	TM11	0.2 ± 0.2	bdl ± bdl	0.19 ± 0.05	540 ± 80	6 ± 5
J2-437-3-R2	MA9	bdl ± bdl	bdl ± bdl	6.4 ± 1.9	120 ± 80	40 ± 19
J2-817-4-R2	MA15	bdl ± bdl	NM	NM	100 ± 17	11 ± 1.3
Manus Basin						
J2-207-1-R1	VW1	0.5 ± 0.3	bdl ± bdl	0.4 ± 0.3	3800 ± 600	0.1 ± 0.4
J2-213-6-R1	RGR1	bdl ± bdl	bdl ± bdl	4.4 ± 2.9	260 ± 30	50 ± 12
J2-208-1-R1	RMR1	bdl ± bdl	bdl ± bdl	48 ± 18	1300 ± 600	50 ± 12
J2-214-3-R1	SM3	bdl ± bdl	bdl ± bdl	20 ± 6	100 ± 290	31 ± 26
J2-216-16-R1	F3	1.5 ± 0.6	15 ± 15	14.1 ± 1.5	300 ± 250	15 ± 6
J2-223-1-R1	NS3	15 ± 4	21 ± 16	6.5 ± 2.2	300 ± 100	11 ± 5
J2-217-2-R1	SZ1	6.9 ± 1.0	16 ± 15	0.93 ± 0.20	250 ± 40	8.3 ± 1.2
J2-217-10-R1	SZ2	1.0 ± 0.5	15 ± 15	5.8 ± 1.0	500 ± 200	3.9 ± 1.8
Others						
Alv3474-3-1	Sully99	36 ± 5	20 ± 19	0.2 ± 0.1	120 ± 22	3.4 ± 1.0
J2-613-16-R1	BB5	760 ± 250	480 ± 40	0.75 ± 0.04	140 ± 85	23 ± 9

Previous studies have posited that Ag^+ substitutes for Cu^+ in the chalcopyrite lattice ((Cu^+, Ag^+)$Fe^{3+}S_2$; e.g., Huston et al., 1995). Assuming that Ag regularly partitions into chalcopyrite according to the definition provided by McIntire (1963), the following equation may be applied:

$$D_{hf,cp} = \frac{\frac{\{Ag^+\}_{hf}}{\{Cu^+\}_{hf}}}{\frac{(Ag)_{cp}}{(Cu)_{cp}}}$$

where $D_{hf,cp}$ is the partitioning coefficient between hydrothermal fluid (hf) and chalcopyrite (cp) , the top term on the right hand side of the equation is the thermodynamic activity ratio of free (i.e. uncomplexed) Ag^+ to free Cu^+ in the hydrothermal fluid and the bottom term is the molar ratio of Ag to Cu in the corresponding chalcopyrite. By comparing the black smoker chimney linings and fluids investigated here, the partitioning coefficient is $D_{hf,cp} = 1.37 \pm 0.04$.

With the exception of a few samples from the PACMANUS vent fields of the Manus Basin, the concentration of Ag in black smoker chimney linings positively correlates with hydrothermal fluid pH (Fig. 7A). This correlation can be explained by regular partitioning of Ag into chalcopyrite combined with the relatively greater sensitivity of Cu concentrations in hydrothermal fluids to hydrothermal fluid pH. That is, vent fluid Cu concentrations are greatest when reaction zones are high temperature and low pH. While both Cu and Ag concentrations in hydrothermal fluids are greater at low pH, the Ag:Cu ratio is low at low pH and high at high pH, except in cases where there has been metal remobilization, for example at the Roman Ruin's vent field (Fig. 7B to 7D). The occurence of Ag-rich black smoker chimney lining associated with low pH hydrothermal fluids at the PACMANUS vent fields can be explained by elevated concentrations of Ag in these vent fields attributed to sub-surface dissolution and remobilization

of previously precipitated Zn- and Ag-rich massive sulfides that significantly enrich fluids in Zn, Cd, Ag, Pb, but not Cu (Craddock, 2009).

Figure 6A

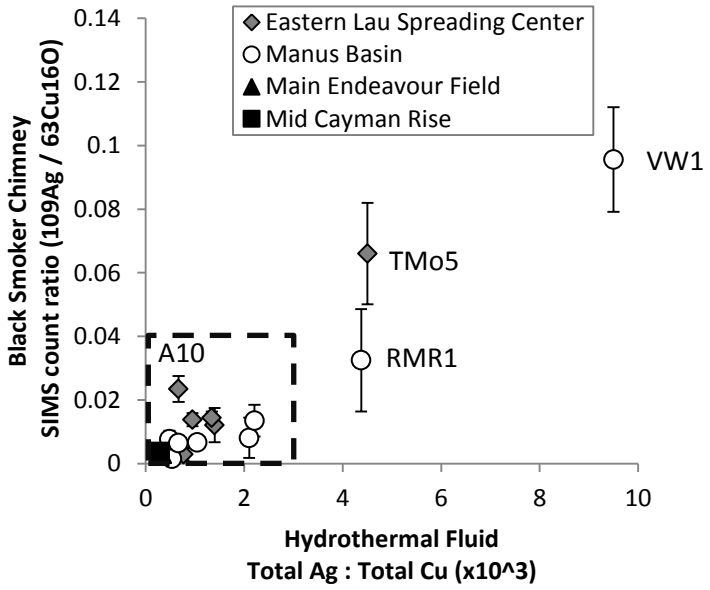

Figure 6B

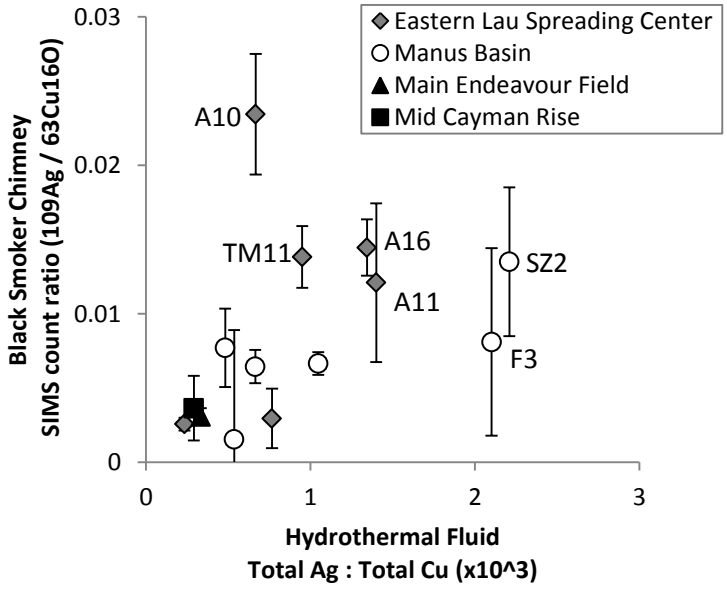

Figures 6A to 6D.

Plots of (A and B) the ratios of Ag:Cu total concentrations measured in hydrothermal fluids and (C and D) the ratios of Ag^{+}:Cu^{+} free ion activities as calculated by EQ3/6 modelling vs. the SIMS counts ratios of ^{109}Ag / $^{63}Cu^{16}O$ for chalcopyrite grains along the innermost linings of paired black smoker chimney samples. Dashed boxes in Fig. 6A and 6C are the extent of close-up views of the same plots in Fig. 6B and 6D. All SIMS data are from Chapter 3 of this thesis (Table 7A). Data for vent fluids from the Eastern Lau Spreading Center are from this paper, data for vent fluids in the Manus Basin are from Craddock (2009), data for fluid Sully99 from the Main Endeavour Field are from Seyfried et al. (2003) and data for fluid BB5 from the Beebe / Piccard vent field are from McDermott (2015) (Supplementary Table S6). Uncertainties in SIMS count ratios reflect standard errors (1σ) of multiple SIMS spots on the same sample. Details of these analyses can be found in Chapter 3 of this thesis.

Figure 6C

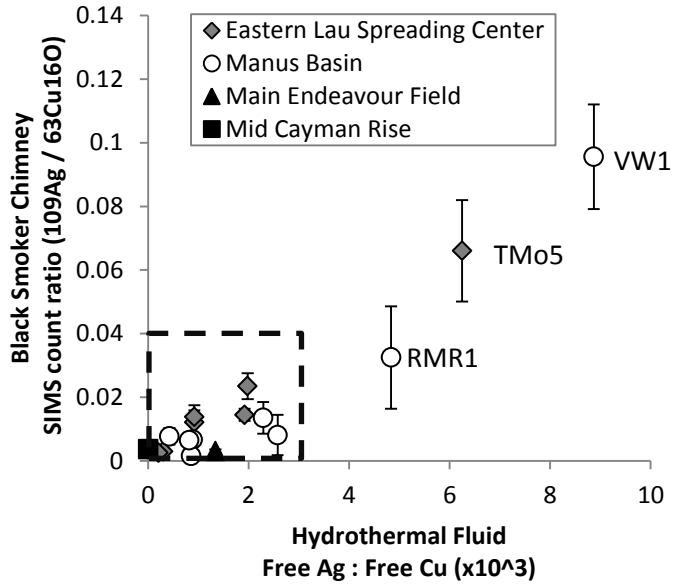

Figure 6D

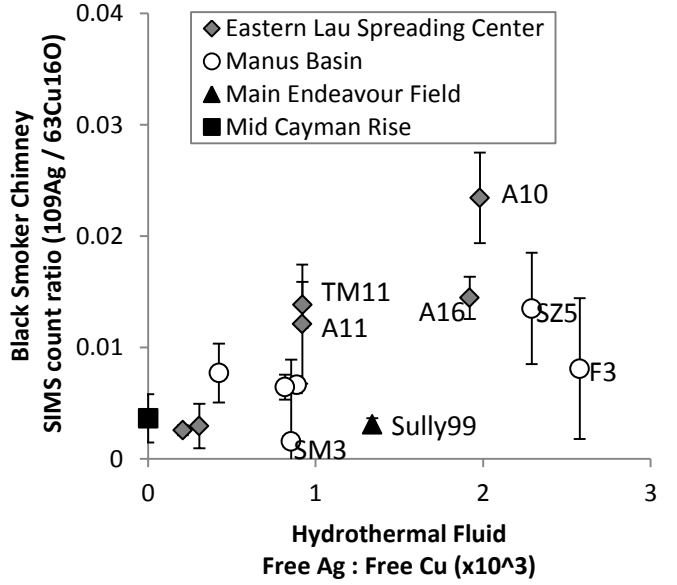

Figure 7A

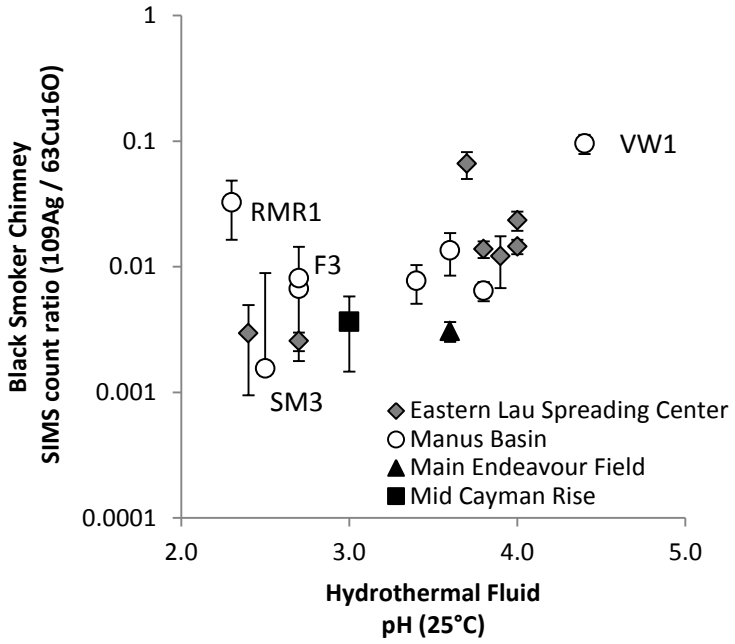

Figure 7B

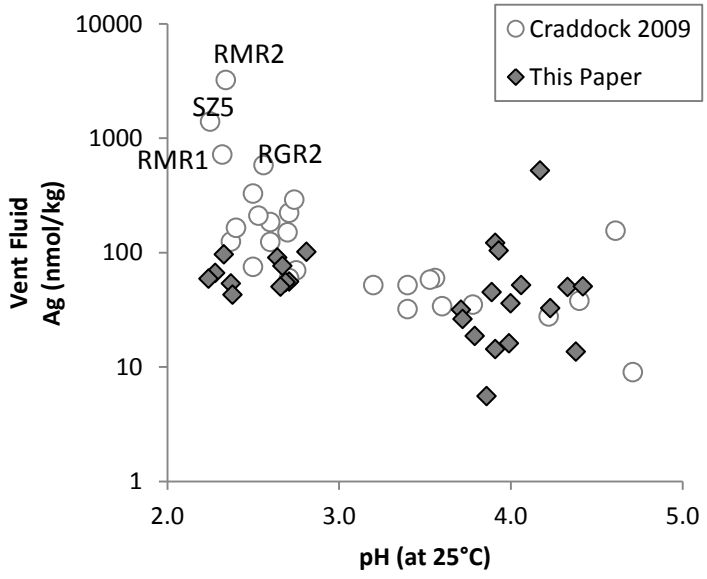

Figures 7A to 7D.

Plots of hydrothermal fluid pH (at 25°C) vs. (A) SIMS counts ratios of ^{109}Ag / $^{63}Cu^{16}O$ for chalcopyrite grains along the innermost linings of paired black smoker chimney samples, (B) the zero-Mg endmember Ag concentration of the fluid, (C) the zero-Mg endmember Cu concentration of the fluid, and (D) the total concentration ratio of Ag:Cu in the fluid. Data for vent fluids from the Eastern Lau Spreading Center are from this paper, data for vent fluids in the Manus Basin are from Craddock (2009) (Supplementary Table S7). SIMS data are from Chapter 3 of this thesis (Table7A). Uncertainties in SIMS count ratios reflect standard errors (1σ) of multiple SIMS spots on the same sample. Details of these analyses can be found in Chapter 3 of this thesis.

Figure 7C

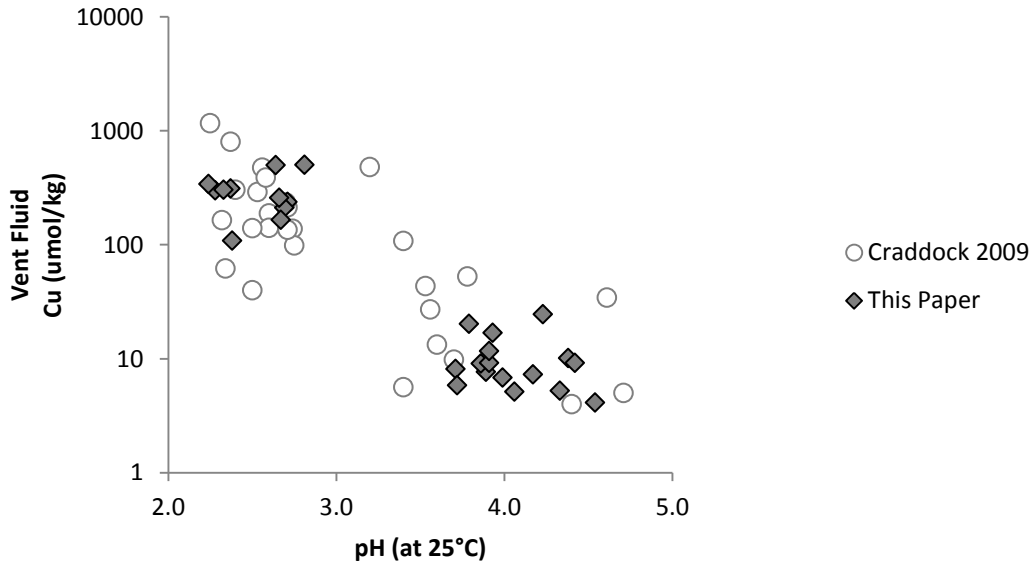

Figure 7D

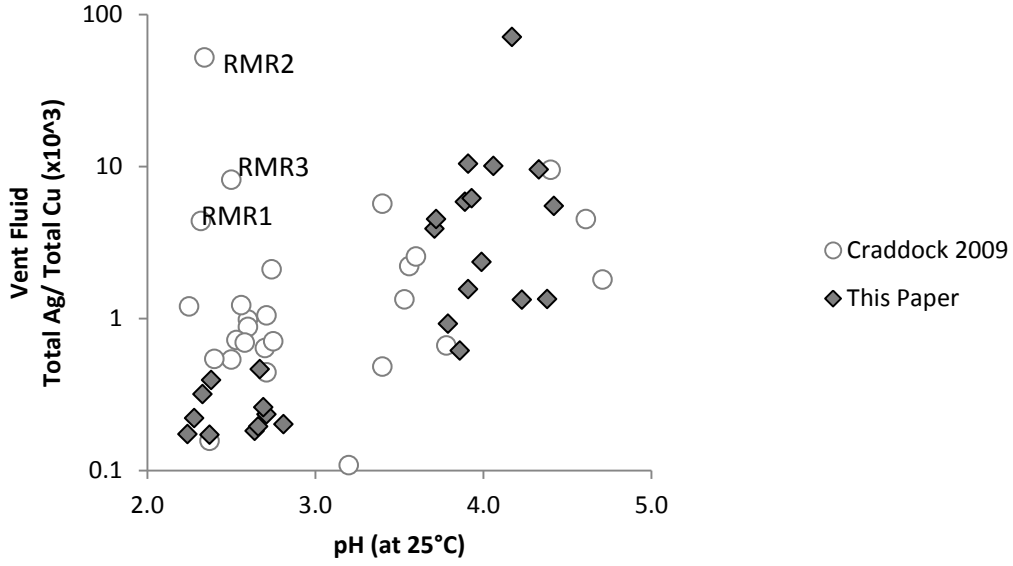

5.2.2 Ga and In

As discussed in Chapter 3 of this thesis, the Ga and In contents of chalcopyrite lining black smoker chimneys correlate with the pH of paired vent fluids (Fig. 8A and 8B), likely owing to the effect of hydroxide complexing (more prevalent at higher pH) on free Ga^{3+} and In^{3+} concentrations. Thermodynamic fluid modelling allows for a comparison of Ga and In contents of black smoker chimney linings with *in situ* fluid pH, which is likewise correlated (Fig. 8C and 8D). Compared with the lower-temperature, higher-pH vent fluids collected at the ABE and Tu'i Malila vent fields, total concentrations of Ga and In in the high-temperature, low-pH Mariner vent fluids are higher by a factor of 3 and 2, respectively. Data for Ga concentrations in paired hydrothermal fluids and black smoker chimney linings are only available for six samples from the Eastern Lau Spreading Center. The Ga concentrations of black smoker chimney linings for these samples correlate with free Ga^{3+} to free Fe^{2+} ratios calculated for paired hydrothermal fluids, but not the ratio of total Ga to total Fe (Fig. 9A, 9B). For In there are not enough data (data are only available for two fluid-chimney pairs) to examine trends.

Presumably, similar to Ag^{+} substituting for Cu^{+}, Ga^{3+} and In^{3+} are present in chalcopyrite as lattice substitutions for Fe^{3+}. If this is the case, then a possible explanation for the observed negative correlation between hydrothermal fluid pH and the Ga and In contents of paired black smoker chimney linings is complexing of Ga and In by OH^{-}, as discussed by Wood and Samson (2006). At higher pH, the activity of OH^{-} is high, Ga and In are predominantly complexed, and the activity of the free ions is low relative to the total concentrations of these elements. Hence, the Ga and In contents of paired black smoker chimney linings will be low at high pH and conversely higher at low pH. Thermodynamic fluid modelling performed here confirms that Ga is predominantly complexed as $Ga(OH)^{+2}$ while In is primarily complexed as $InCl^{+2}$ and

secondarily as $In(OH)^{+2}$ (see Appendix B). However, thermodynamic data for Ga and In complexes at the conditions of interest are highly uncertain (Woods and Samson, 2006). Figure 10A shows complexes of Ga at 200°C and 300°C at vapor saturated pressure as a function of pH (Wood and Samson, 2006). Figure 10B shows complexes of In as a functions of pH at 200°C and vapor saturated pressure (Charlotte Ashworth, pers. comm.). There are data for InCl complexes in a paper that is currently in review (Charlotte Ashworth, pers. comm.). In future there is a need to make more measurements of In and Ga on paired vent fluids and chalcopyrite linings, and to then model the free concentrations using additional updated thermodynamic data.

Figure 8A

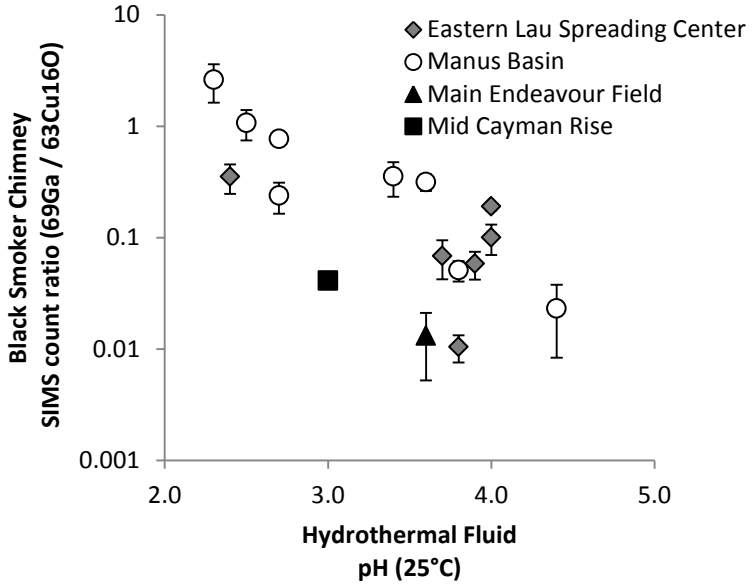

Figure 8B

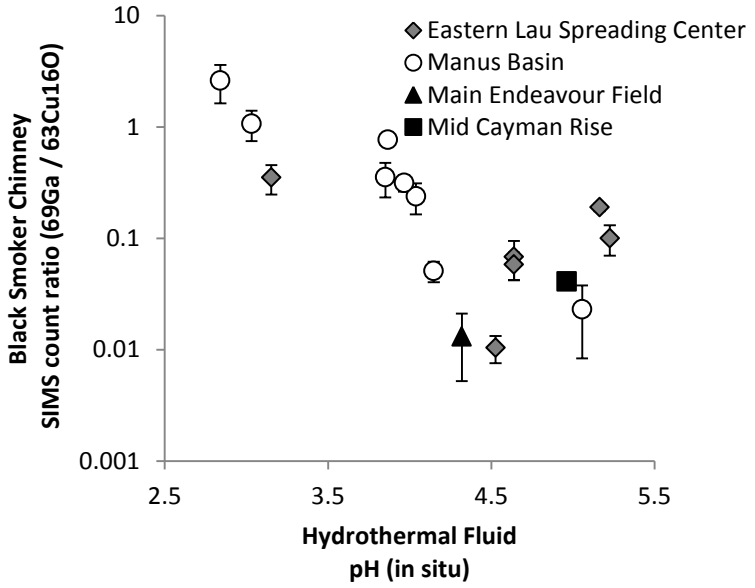

Figures 8A to 8D

Plots of (A) hydrothermal fluid pH (at 25°C) vs. SIMS counts ratios of ^{69}Ga / $^{63}Cu^{16}O$ (B) hydrothermal fluid pH (in situ) vs. SIMS counts ratios of ^{69}Ga / $^{63}Cu^{16}O$, (C) hydrothermal fluid pH (at 25°C) vs. SIMS counts ratios of ^{115}In / $^{63}Cu^{16}O$, and (D) hydrothermal fluid pH (in situ) vs. SIMS counts ratios of ^{115}In / $^{63}Cu^{16}O$ for sample pairs of black smoker fluids and chimney linings. All SIMS data are from Chapter 3 of this thesis (Table 7A). Data for vent fluids from the Eastern Lau Spreading Center are from this paper, data for vent fluids in the Manus Basin are from Craddock (2009), data for fluid Sully99 from the Main Endeavour Field are from Seyfried et al.(2003) and data for fluid BB5 from the Beebe / Piccard vent field are from McDermott (2015) (Supplementary Table S7). Uncertainties in SIMS count ratios reflect standard errors (1σ) of multiple SIMS spots on the same sample. Details of these analyses can be found in Chapter 3 of this thesis.

Figure 8C

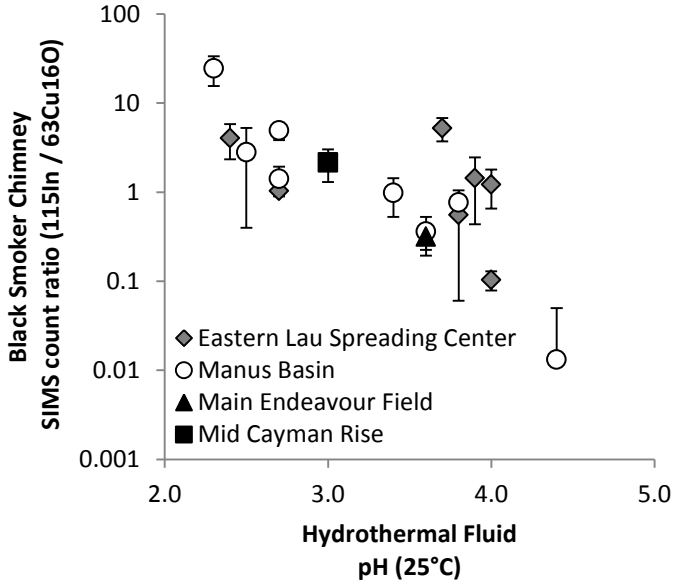

Figure 8D

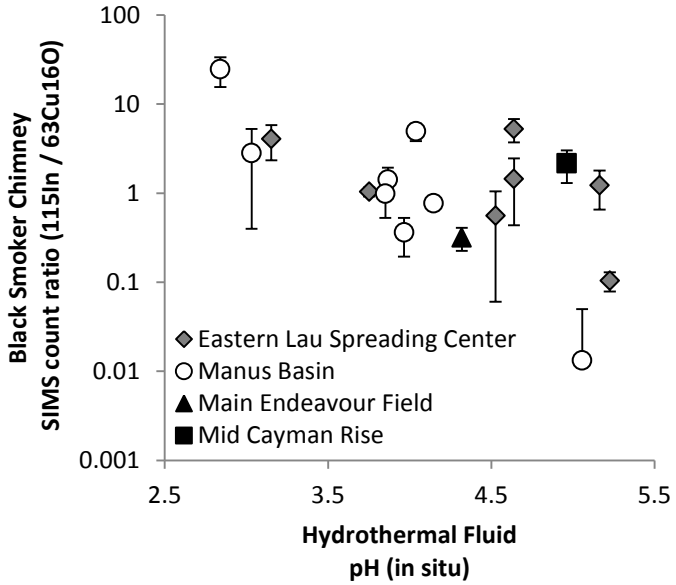

Figure 9. Plots of (A) the total Ga concentrations of hydrothermal fluids (Supplementary Table S7) and (B) the ratio of free Ga^{3+} to free Fe^{2+} calculated by EQ3/6 (Supplementary Table S7) vs. SIMS counts ratios of ^{69}Ga / $^{63}Cu^{16}O$ in chalcopyrite lining paired black smoker chimneys. SIMS data are from Chapter 3 of this thesis (Table 7A). Uncertainties in SIMS count ratios reflect standard errors (1σ) of multiple SIMS spots on the same sample. Details of these analyses can be found in Chapter 3 of this thesis.

Figure 9A

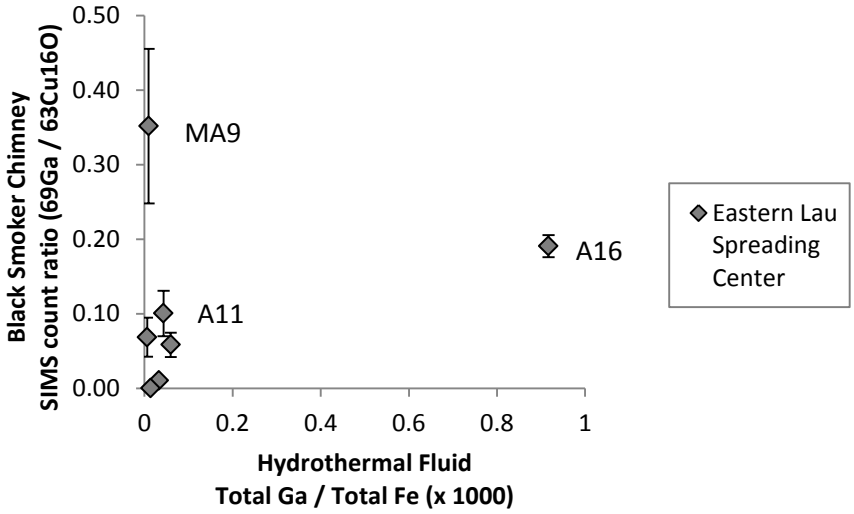

Figure 9B

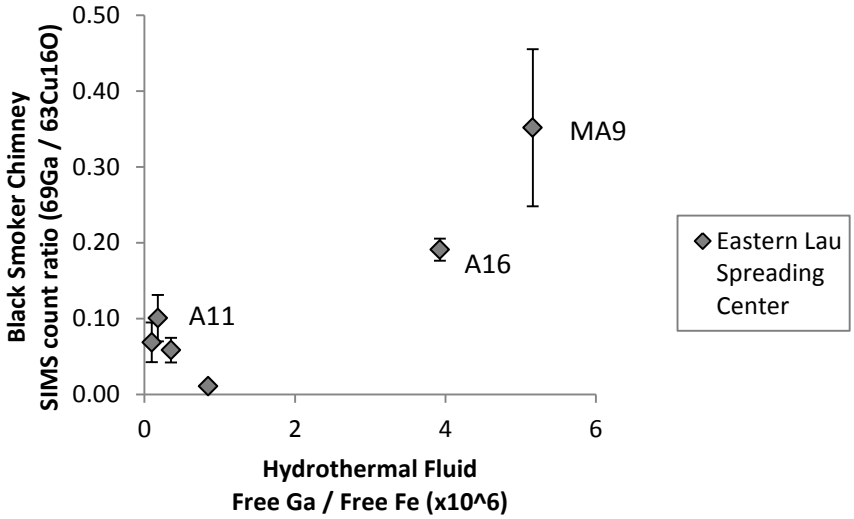

Figure 10. (A) Plots from Wood and Samson (2006) of pH vs. the log concentration of aqueous Ga complexes contributing to the solubility of GaOOH at 200°C and 300°C at vapor saturated pressures using the thermodynamic data of Benézéth et al. (1997) and (B) pH vs. the log concentration of aqueous In complexes contributing to the solubility of In_2S_3 at 20°C and 1M $NaClO_4$, total S = 0.01M using thermodynamic data from Tunaboylu and Schwarzenbach (1970). Red lines highlight the concentrations of free ions, Ga^{3+} and In^{3+}, as a function of pH. (C) Plot of pH vs. log concentration of In complexes at 200°C (Charlotte Ashworth, pers. comm.)

Figure 10A

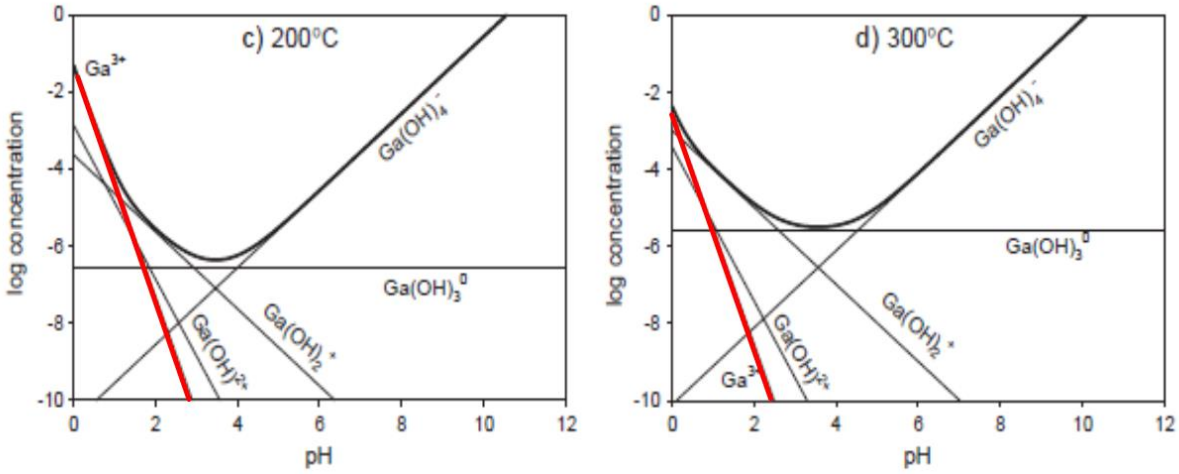

Figure 10B

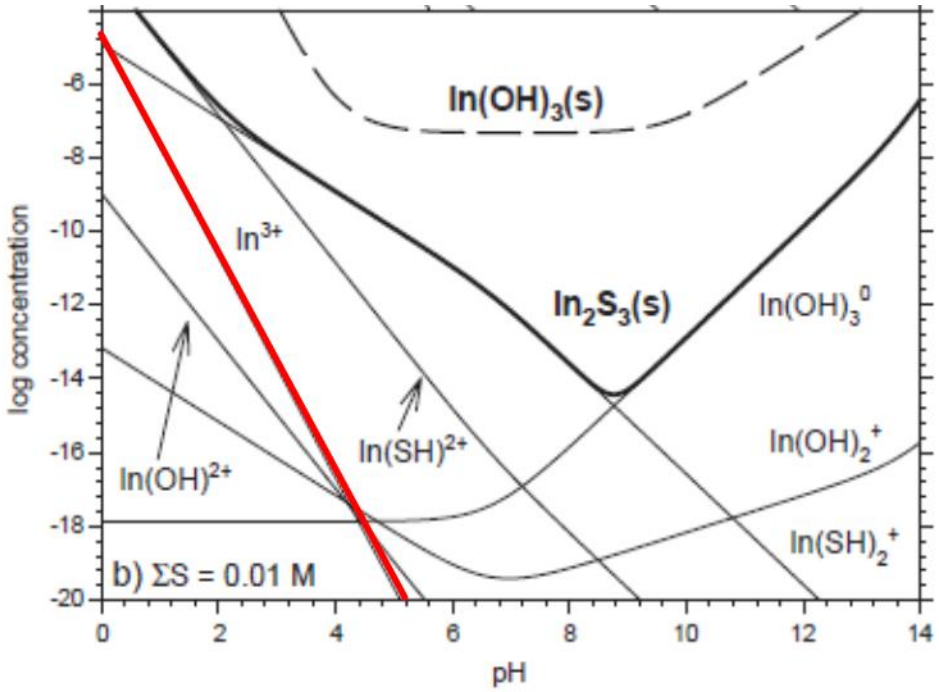

Figure 10C

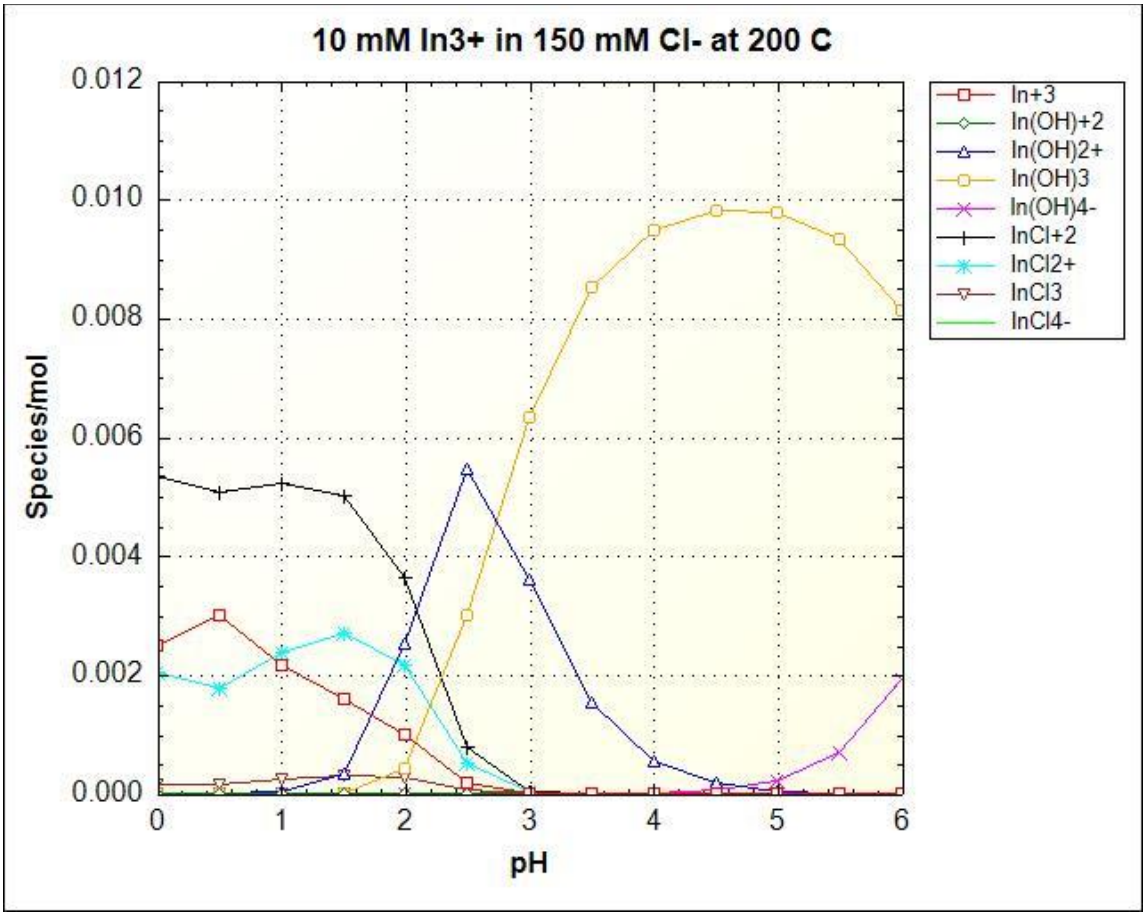

5.2.3. Co and Ni

No clear patterns or correlations were observed between the Co and Ni contents of black smoker chimney linings and the temperature, pH, fO_2, fS_2, free or total Co or Ni concentrations or ratios of these elements to Cu or Fe (Fig. 11). As discussed in Chapter 3 of this thesis, the Co and Ni contents of black smoker chimney linings correlate with each other except in more felsic hosted systems where concentrations of both Co and Ni are very low (Fig. 4A of Chapter 3). Additionally, data from basalt-hosted hydrothermal systems (discussed in Chapter 3) show correlations between hydrothermal fluid temperature and the Co and Ni contents of black smoker chimney linings, especially among samples from the southern East Pacific Rise. These black

smoker chimney samples are not considered in this chapter, because no Co and Ni data are available for the associated hydrothermal fluids. However, the lack of correlation between the Co content of black smoker chimney linings and the ratio of Co to Fe or Cu for fluids sampled from the Manus Basin, Mid-Cayman Rise, and Main Endeavour Field on the Juan de Fuca Ridge, which share the correlation between Co and Ni, suggest that Co (and likely Ni) concentrations in chimney linings are not primarily controlled by the Co content of hydrothermal fluids or the ratio of free Co^{2+} to free Cu^{+} or free Fe^{2+}.

Alternatively, crystal chemistry may play an important role in determining the Co content of black smoker chimney linings. The idea that more Fe-rich intermediate solid solutions (e.g., $CuFe_2S_3$, $CuFe_3S_4$) will host higher Co concentrations than chalcopyrite has been previously proposed (e.g., Rouxel et al., 2004). Such Fe-rich compositions are associated with lower sulfidation states which are in turn associated with more mafic lithologies (Kojima and Sugaki, 1985; Sack and Ebel, 2006; Einaudi, 2006). This hypothesis is supported by studies of metal valence in cubanite ($CuFe_2S_3$) that propose a valence structure of $Cu^{+}Fe^{2+}Fe^{3+}S_3$ (Greenwood and Whitfield, 1968; Goh et al., 2010). The presence of Fe^{2+} in the cubanite crystal lattice provides a substitution site for divalent Co^{2+} and Ni^{2+}, in contrast to the chalcopyrite valence structure, where Fe is trivalent (i.e., $Cu^{+}Fe^{3+}S_2$, Pearce et al., 2006). Electron microprobe analyses of samples J2-613-16-R1 from the Beebe/Piccard vent field on the Mid-Cayman Rise document intermediate composition between chalcopyrite ($CuFeS_2$) and isocubanite ($CuFe_2S_3$) (Fig. 12). Further testing of the effect of crystal chemistry on Co and Ni concentrations in black smoker chimney linings can be achieved by coordinating SIMS and electron microprobe studies of these samples.

Figure 11. Bivariate plots of vent fluid total Co over total Fe, vent fluid free Co over free Fe, vent fluid total Co over total Cu, and vent fluid free Co over free Cu vs. SIMS counts ratios of $^{59}Co/^{63}Cu^{16}O$. All SIMS data are from Chapter 3 of this thesis (Table 7A). Data for vent fluids from the Eastern Lau Spreading Center are from this paper, data for vent fluids in the Manus Basin are from Craddock (2009), data for fluid Sully99 from the Main Endeavour Field are from Seyfried et al.(2003) and data for fluid BB5 from the Beebe / Piccard vent field are from McDermott (2015) (Supplementary Table S7). Dotted line indicates SIMS detection limit = 5×10^{-5} counts per second / counts per second $^{63}Cu^{16}O$.

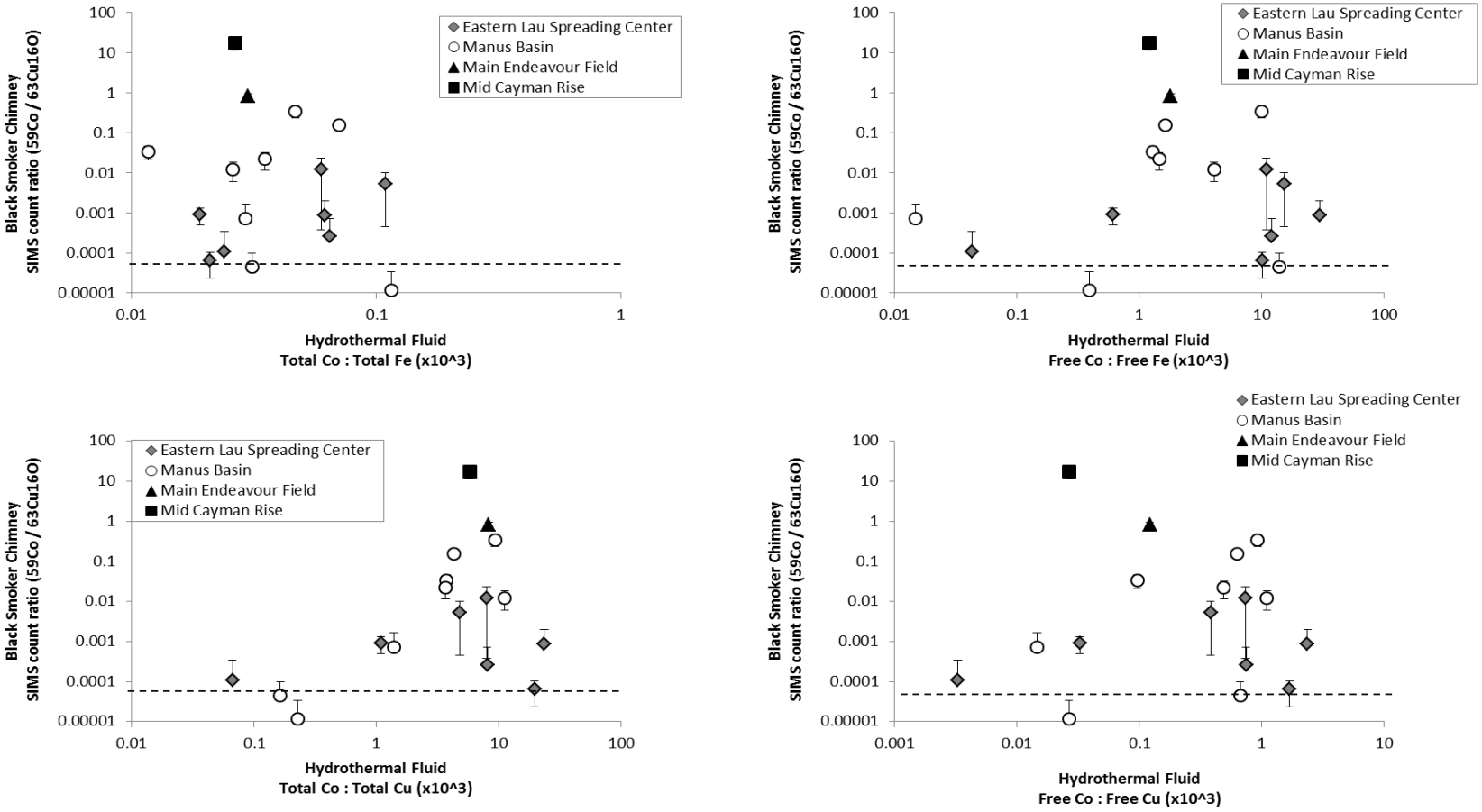

Figure 12. Plot of Cu and Fe in CuFe sulfide lining of sample J2-613-16-R1 from the Beebe/Piccard vent field on the Mid-Cayman Rise measured by electron microprobe. Also shown are compositions of chalcopyrite and cubanite chimney linings from vent fields in the Manus Basin (Craddock, 2009) and Eastern Lau Spreading Center (Chapter 2 of this thesis), likewise measured by electron microprobe. Results reported as weight percent normalized to total = Cu (wt%) + Fe (wt%) + S (wt%).

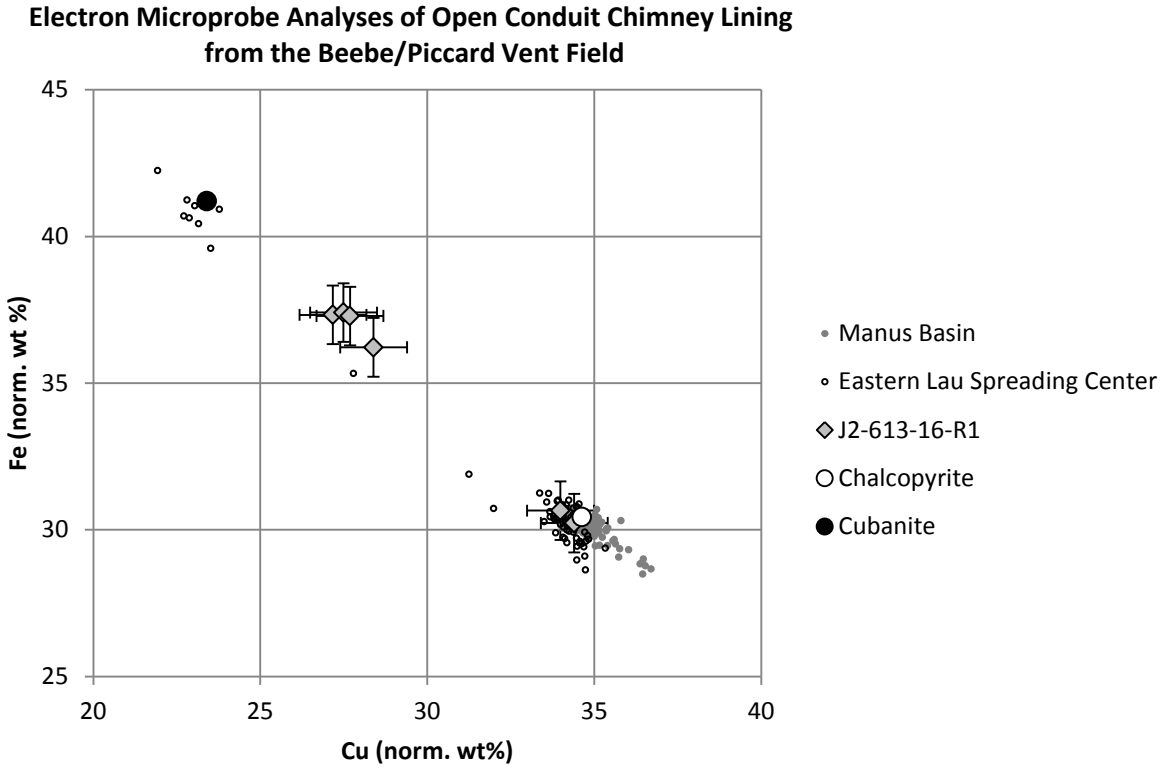

5.3. Trace element proxies of hydrothermal fluid pH and metal concentrations

The trace element content of black smoker chimney linings is controlled by the partitioning of trace elements between lining minerals and hydrothermal fluids (Fig. 13, marker A). For a given mineral, this partitioning is controlled by the free ion activity ratio of the trace element to the major (or "carrier") element it replaces in the crystal lattice (e.g., Ag^{+} for Cu^{+}, Ga^{3+} and In^{3+} for Fe^{3+}).

Figure 13. Schematic diagram of (A) partitioning between minerals in black smoker chimney linings and aqueous species in hydrothermal vent fluids and processes: (B) reaction zone conditions and (C) remobilization of previously deposited minerals that can affect element ratios in hydrothermal vent fluids.

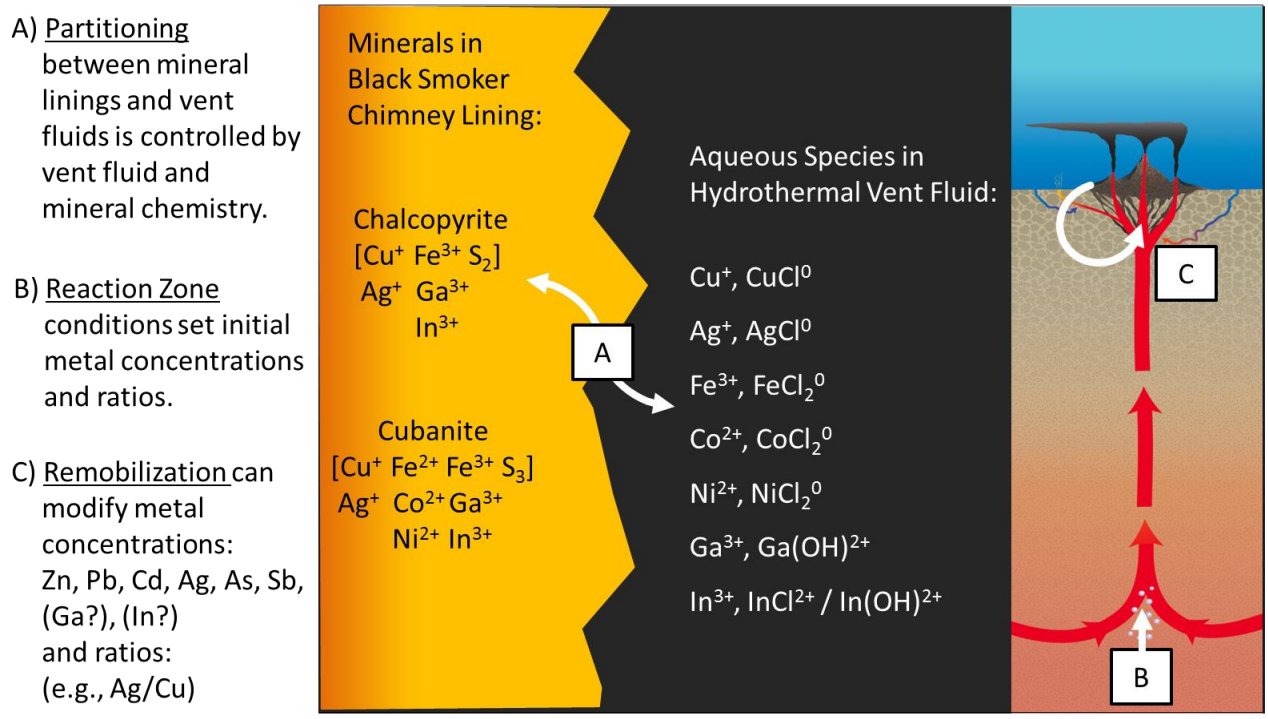

In the case of Ag replacing Cu, where both elements are similarly complexed by Cl- in high temperature vent fluids (e.g., Reed and Palandri, 2006), the free ion activity ratio of Ag^+/Cu^+ is primarily a reflection of the total Ag : total Cu concentration ratio (Fig. 6A to 6D). This ratio is initially set in the hydrothermal reaction zone (Fig. 13, marker B). Lower pH vent fluids, which can be caused by higher reaction zone temperatures or the influence of acidic magmatic volatiles, contain higher concentrations of Cu than higher pH vent fluids (Fig. 5A). Because the effect of pH on vent fluid Ag concentrations is less severe than the effect for Cu, lower pH vent fluids will tend to have a lower Ag/Cu ratio than higher pH vent fluids (Fig. 7D). Likewise, chalcopyrite formed from lower pH vent fluids will tend to contain lower

concentrations of Ag than chalcopyrite formed from high pH vent fluids (Fig. 7A). However, ratios of Ag to Cu in hydrothermal fluids can be additionally modified by remobilization of previously deposited metal sulfides in the subsurface (Fig. 13, marker C). Elevated concentrations of Ag in these fluids can lead to high Ag/Cu ratios despite low fluid pH (e.g., Fig. 7D, fluids RMR1, RMR2, and RMR3). Chalcopyrite formed from these fluids has correspondingly high concentrations of Ag (e.g., Fig. 6A, 6C, sample RMR1). Thus, high concentrations of Ag in the chalcopyrite linings of black smoker chimneys indicate either: 1) formation from higher-pH, Cu-poor vent fluids or 2) formation from Ag-rich vent fluids affected by remobilization of previously deposited Ag-rich metal sulfides in the subsurface.

In the case of Ga or In replacing Fe, the trace elements Ga and In are strongly complexed by OH^- in high-temperature hydrothermal fluids, while Fe is predominantly present as Cl^- complexes (Fig. 13, marker A). As a result, the dominant control on the free ion activity ratios of Ga/Fe and In/Fe is not the total concentration ratio of the trace and carrier elements, Ga/Fe and In/Fe, but rather the relative concentrations of the complexing ligands, Cl^- and OH^-. Among seafloor hydrothermal fluids associated with black smoker chimneys, the variation in Cl^- concentrations (here, 39 to 753 mmol/kg) is less than the variation in OH^- concentrations associated with pH (here, pH (in situ) = 3.2 to 5.2). Hence, the dominant control on the free ion activity ratios of Ga/Fe and In/Fe is pH and the Ga and In content of chalcopyrite lining black smoker chimney linings provides a proxy of vent fluid pH (Fig. 8A to 8D). When combined with Ag, the addition of Ga and In as indicators of hydrothermal fluid pH allows for a distinction to be made between Ag-rich chalcopyrite formed from higher-pH, Cu-poor vent fluids and similarly Ag-rich chalcopyrite lower-pH Ag-rich vent fluids. Specifically, high Ag concentrations, but low Ga and In concentrations in chalcopyrite are indicative of precipitation

from higher-pH, Cu-poor hydrothermal fluids while high Ag, Ga, and In concentrations in chalcopyrite are indicative of precipitation from low-pH, Ag- and Cu-rich hydrothermal fluids likely related to remobilization of Ag.

6. CONCLUSION

By analyzing the concentrations of trace elements, especially Co, Ni, Ga, Ag, and In, contained in the dregs, dissolved, and filter fractions of hydrothermal fluids from vent field along the Eastern Lau Spreading Center, this study expands previously published data on the chemistry of hydrothermal fluids from these vent fields. This study then makes use of these new data, in combination with previously published data on the trace element chemistry of hydrothermal fluids from the Manus Basin from Craddock (2009) and secondary ion mass spectrometry measurements of trace element (Co, Ni, Ga, Ag, In) concentrations in chalcopyrite from paired black smoker chimney linings presented in Chapter 3 of this thesis, to directly compare fluid and mineral trace element chemistry and thus identify potential proxies of hydrothermal fluid chemistry based on mineral trace element chemistry.

A significant result of this study is a linear correlation between the Ag content of black smoker chimney linings with the free ion activity ratio of Ag:Cu in the corresponding hydrothermal fluids, which supports regular partitioning of Ag into chalcopyrite as a lattice substitution for Cu, once aqueous complexing is considered. A partition coefficient of $D_{hf,cp}$ = 1.37 is calculated. When combined with the correlation between the Ga and In of black smoker chimney linings and hydrothermal fluid pH presented in Chapter 3 of this thesis, concentrations of Ag in chalcopyrite provide a proxy of Ag and Cu concentrations in hydrothermal fluids.

Specifically, chalcopyrite linings containing high concentrations of Ag, but low concentrations of Ga and In are indicative of formation from higher-pH, Cu-poor fluids; chalcopyrite linings containing low concentrations of Ag, but high concentrations of Ga and In are indicative of formation from low-pH fluids; and chalcopyrite linings containing high concentrations of Ag, Ga, and In are indicative of formation from low-pH fluids in which Ag is highly enriched, likely as a result of subsurface remobilization of previously deposited sulfide minerals. Also highlighted in this study is the need for additional data on the concentrations of trace elements such as Ga and In in hydrothermal fluids and the need to refine understandings of the thermodynamic properties of aqueous Ga and In complexes at elevated temperatures and pressures.

REFERENCES

Benézéth, P., Diakonov, I. I., Pokrovski, G. S., Dandurand, J. L., Schott, J., and Khodakovsky, I. L. (1997) Gallium speciation in aqueous solution. Experimental study and modelling: Part 2. Solubility of α-GaOOH in acidic solutions from 150 to 250 C and hydrolysis constants of gallium (III) to 300 C. *Geochim. Cosmochim. Acta*, **61(7)**, 1345-1357.

Bézos, A., Escrig, S., Langmuir, C. H., Michael, P. J., and Asimow, P. D. (2009) Origins of chemical diversity of back- arc basin basalts: A segment- scale study of the Eastern Lau Spreading Center. *J. Geophys. Res.: Solid Earth*, **114**, *B06212, doi:*10.1029/2008JB005924

Binns, R. A. and Scott, S. D. (1993) Actively forming polymetallic sulfide deposits associated with felsic volcanic rocks in the eastern Manus back-arc basin, Papua New Guinea. *Econ. Geol.*, *88*(8), 2226-2236.

Both, R., Crook, K., Taylor, B., Brogan, S., Chappell, B., Frankel, E., Liu, L., Sinton, J., and Tiffin, D. (1986) Hydrothermal chimneys and associated fauna in the Manus Back- Arc Basin, Papua New Guinea. *Eos, Transactions American Geophysical Union*, **67(21)**, 489-490.

Craddock, P. R. (2009) Geochemical tracers of processes affecting the formation of seafloor hydrothermal fluids and deposits in the Manus back-arc basin. Ph.D. Thesis, MIT/WHOI Joint Program in Oceanography.

Davies, H. L., Honza, E., Tiffin, D. L., Lock, J., Okuda, Y., Keene, J. B., Murakami, F., and Kisimoto, K. (1987) Regional setting and structure of the western Solomon Sea. *Geo-Marine Letters*, ***7*(3)**, 153-160.

Einaudi, M. T., Hedenquist, J. W., and Inan, E. E. (2003) Sulfidation state of fluids in active and extinct hydrothermal systems: transitions from porphyry to epithermal environments. In Special Publication-Society of Economic Geologists, **10** (eds. S.F. Simmons, I. Graham). Society of Economic Geologists, 285-314.

Elthon, D., Ross, D.K., Meen, J.K. (1995) Compositional variations of basaltic glasses from the Mid-Cayman Rise spreading center. *J. Geophys. Res.: Solid Earth*, **100**, 12497-12512.

Escrig, S., Bézos, A., *Goldstein*, S. L., Langmuir, C. H., and Michael, P. J. (2009*)* Mantle source variations beneath the Eastern Lau Spreading Center and the nature of subduction components in the Lau basin–Tonga arc system, *Geochem. Geophys. Geosys.*, **10**, *Q04014, doi:*10.1029/2008GC002281.

Fouquet, Y., von Stackelberg, U., Charlou, J. L., Erzinger, J., Herzig, P. M., Mühe, R., and Wiedicke, M. (1993) Metallogenesis in back-arc environments: the Lau Basin example. *Econ. Geol.*, **88(8)**, 2154-2181.

Frenzel, G., Mühe, R., and Stoffers, P. (1990) Petrology of the volcanic rocks from the Lau Basin, southwest Pacific. *Geologisches Jahrbuch*, **92**, 395-479.

Fretzdorff, S., Schwarz- Schampera, U., Gibson, H. L., Garbe- Schönberg, C. D., Hauff, F., and Stoffers, P. (2006) Hydrothermal activity and magma genesis along a propagating back-arc basin: Valu Fa Ridge (southern Lau Basin). *J. Geophys. Res.: Solid Earth*, **111(B8)**.

Huston, D. L., Sie, S. H., Suter, G. F., Cooke, D. R., and Both, R. A. (1995) Trace elements in sulfide minerals from eastern Australian volcanic-hosted massive sulfide deposits; Part I, Proton microprobe analyses of pyrite, chalcopyrite, and sphalerite, and Part II, Selenium levels in pyrite; comparison with delta 34 S values and implications for the source of sulfur in volcanogenic hydrothermal systems. *Econ. Geol.*, **90(5)**, 1167-1196.

Jenner, G. A., Cawood, P. A., Rautenschlein, M., and White, W. M. (1987) Composition of back-arc basin volcanics, Valu Fa Ridge, Lau Basin: evidence for a slab-derived component in their mantle source. *J. Volcanol. Geotherm. Res.*, **32(1-3)**, 209-222.

Johnson, J. W., Oelkers, E. H., and Helgeson, H. C. (1992) SUPCRT92: A software package for calculating the standard molal thermodynamic properties of minerals, gases, aqueous species, and reactions from 1 to 5000 bar and 0 to 1000 C. *Computers Geosci.*, **18(7)**, 899-947.

Johnson, H. P., Hutnak, M., Dziak, R. P., Fox, C. G., Urcuyo, I., Cowen, J. P., Nabelek, J., and Fisher, C. (2000) Earthquake-induced changes in a hydrothermal system on the Juan de Fuca mid-ocean ridge. *Nature*, **407(6801)**, 174-177.

Kamenetsky, V. S., Binns, R. A., Gemmell, J. B., Crawford, A. J., Mernagh, T. P., Maas, R., and Steele, D. (2001) Parental basaltic melts and fluids in eastern Manus backarc basin: Implications for hydrothermal mineralization. *Earth Planet. Sci. Lett.*, **184(3)**, 685-702.

Karsten, J. L., Delaney, J. R., Rhodes, J. M., and Liias, R. A. (1990) Spatial and temporal evolution of magmatic systems beneath the Endeavour Segment, Juan de Fuca Ridge: Tectonic and petrologic constraints. *J. Geophys. Res.: Solid Earth*, **95(B12)**, 19235-19256.

Krasnov, S., Poroshina, I., Cherkashev, G., Mikhalsky, E., and Maslov, M. (1997) Morphotectonics, volcanism and hydrothermal activity on the East Pacific Rise between 21 12′ S and 22 40′ S. *Marine Geophysical Researches*, **19(4)**, 287-317.

Kojima, S., and Sugaki, A. (1985) Phase relations in the Cu-Fe-Zn-S system between 500 degrees and 300 degrees C under hydrothermal conditions. Econ. Geol., **80(1)**, 158-171.

Langmuir, C., Humphris, S., Fornari, D., Van Dover, C., Von Damm, K. L., Tivey, M. K., Colodner, D., Charlou, J. –L. Desonie, D., Wilson, C., and Fouquet, Y. (1997) Hydrothermal vents near a mantle hot spot: the Lucky Strike vent field at 37 N on the Mid-Atlantic Ridge. *Earth Planet. Sci. Lett.*, **148(1-2)**, 69-91.

Langmuir, C. H., Bézos, A., Escrig, S., and Parman, S. W. (2006) Chemical systematics and hydrous melting of the mantle in back-arc basins. In *Back-Arc Spreading Systems: Geological, Biological, Chemical, and Physical Interactions* (eds. D. M. Christie, C. R. Fisher, S.-M. Lee, and S. Givens) Geophysical Monograph Series, vol. 166, American Geophysical Union, Washington, DC. pp. 87–146.

Martinez, F., and Taylor, B. (1996) Backarc spreading, rifting, and microplate rotation, between transform faults in the Manus Basin. *Marine Geophysical Research*, **18(2),** 203-224.

Martinez, F. and Taylor, B. (2002) Mantle wedge control on back-arc crustal accretion. *Nature*. **416**, 417-420.

McDermott, J. M. (2015) Geochemistry of deep-sea hydrothermal vent fluids from the Mid-Cayman Rise, Caribbean Sea. Ph.D. Thesis, MIT/WHOI Joint Program in Oceanography.

McIntire, W. L. (1963) Trace element partition coefficients—a review of theory and applications to geology. *Geochim. Cosmochim. Acta*, **27(12)**, 1209-1264.

Metz, S., and Trefry, J. H. (2000) Chemical and mineralogical influences on concentrations of trace metals in hydrothermal fluids. *Geochim. Cosmochim. Acta*, **64(13)**, 2267-2279.

Moore, W. S. and Stakes, D. (1990) Ages of barite-sulfide chimneys from the Mariana Trough. *Earth Planet. Sci. Let.*, **100(1)**, 265-274.

Mottl, M. J. and Holland, H. D. (1978) Chemical exchange during hydrothermal alteration of basalt by seawater. I. Experimental results for major and minor components of seawater. *Geochim. Cosmochim. Acta*, **42**, 1103-1115.

Mottl, M. J., Seewald, J. S., Wheat, C. G., Tivey, M. K., Michael, P. J., Proskurowski, G., McCollom, M., Reeves, E., Sharkey, S., You, C.-F., Chan, L.-H., and Pichler, T. (2011) Chemistry of hot springs along the Eastern Lau Spreading Center. *Geochim Cosmochim. Acta*, **75(4)**, 1013-1038.

Pearce, C. I., Pattrick, R. A. D., Vaughan, D. J., Henderson, C. M. B., and Van der Laan, G. (2006) Copper oxidation state in chalcopyrite: Mixed Cu d 9 and d 10 characteristics. Geochim. Cosmochim. Acta, **70(18)**, 4635-4642.

Reed, M. H., and Palandri, J. (2006) Sulfide mineral precipitation from hydrothermal fluids. In *Reviews in mineralogy and geochemistry*, **61(1)** (ed. D.J. Vaughan). Geochemical Society and Mineralogical Society of America. 609-631.

Reeves, E. P., Seewald, J. S., Saccocia, P., Bach, W., Craddock, P. R., Shanks, W. C., Sylva. S., Walsh, E., Pichler, T., and Rosner, M. (2011) Geochemistry of hydrothermal fluids from the PACMANUS, Northeast Pual and Vienna Woods hydrothermal fields, Manus Basin, Papua New Guinea. *Geochim. Cosmochim. Acta*, **75(4)**, 1088-1123.

Rouxel, O., Fouquet, Y., and Ludden, J. N. (2004) Copper isotope systematics of the Lucky Strike, Rainbow, and Logatchev sea-floor hydrothermal fields on the Mid-Atlantic Ridge. *Econ. Geol.*, **99(3)**, 585-600.

Sack, R. O., and Ebel, D. S. (2006) Thermochemistry of sulfide mineral solutions. In Reviews in mineralogy and geochemistry, **61(1)** (ed. D.J. Vaughan). Geochemical Society and Mineralogical Society of America. pp. 265-364.

Seewald, J. S. (2017) Chemical composition of hydrothermal fluids collected on RV/Roger Revelle RR1507 in the Eastern Lau Spreading Center and Valu Fa Ridge, April-May 2015 (Functional microbial dynamics of vent deposits project) Biological and Chemical Oceanography Data Management Office (BCO-DMO) Dataset version 2017-01-13 http://lod.bco-dmo.org/id/dataset/674750 (accessed, May 2017).

Seewald, J. S., Doherty, K. W., Hammar, T. R., and Liberatore, S. P. (2002) A new gas-tight isobaric sampler for hydrothermal fluids. *Deep Sea Research Part I: Oceanographic Research Papers*, **49(1),** 189-196.

Seewald, J. S., Reeves, E. P., Bach, W., Saccocia, P. J., Craddock, P. R., Shanks, W. C., Sylva, S. P., Pichler, T., Rosner, M., and Walsh, E. (2015) Submarine venting of magmatic volatiles in the Eastern Manus Basin, Papua New Guinea. *Geochim. Cosmochim. Acta*, **163**, 178-199.

Seyfried, W. E., Janecky, D. R., and Mottl, M. J. (1984) Alteration of the oceanic crust: implications for geochemical cycles of lithium and boron. *Geochim. Cosmochim. Acta*, **48(3)**, 557-569.

Seyfried, W. E., Seewald, J. S., Berndt, M. E., Ding, K., and Foustoukos, D. I. (2003) Chemistry of hydrothermal vent fluids from the Main Endeavour Field, northern Juan de Fuca Ridge: Geochemical controls in the aftermath of June 1999 seismic events. *J. Geophys. Res.: Solid Earth*, **108(B9)**.

Shock, E. L., Sassani, D. C., Willis, M., and Sverjensky, D. A. (1997) Inorganic species in geologic fluids: correlations among standard molal thermodynamic properties of aqueous ions and hydroxide complexes. *Geochim. Cosmochim. Acta*, **61(5)**, 907-950.

Sinton, J. M., Ford, L. L., Chappell, B., and McCulloch, M. T. (2003) Magma genesis and mantle heterogeneity in the Manus back-arc basin, Papua New Guinea. *J. Petrol.*, **44(1)**, 159-195.

Sleeper, J. D., and Martinez, F. (2014) Controls on segmentation and morphology along the back- arc Eastern Lau Spreading Center and Valu Fa Ridge. *J. Geophys. Res.: Solid Earth*, **119(3)**, 1678-1700.

Sverjensky, D. A., Shock, E. L., and Helgeson, H. C. (1997) Prediction of the thermodynamic properties of aqueous metal complexes to 1000 C and 5 kb. *Geochim. Cosmochim. Acta*, **61(7)**, 1359-1412.

Takai, K., Nunoura, T., Ishibashi, J.-I., Lupton, J., Suzuki, R., Hamasaki, H., Ueno, Y., Kawagucci, S., Gamo, T., Suzuki, Y., Hirayama, H., and Horikoshi, K. (2008) Variability in the microbial communities and hydrothermal fluid chemistry at the newly discovered Mariner hydrothermal field, southern Lau Basin. J. *Geophys. Res.*, **113**, *G02031, doi:*10.1029/2007JG000636.

Taylor, B. (1979) Bismarck Sea: Evolution of a back-arc basin. *Geology*, ***7*(4)**, 171-174.

Taylor, B. (2006) Swath Bathymetry Compilation. accessed through GeoMapAhttp://www.geomapapp.org

Tivey, M. K. (1995) The influence of hydrothermal fluid composition and advection rates on black smoker chimney mineralogy: Insights from modeling transport and reaction. *Geochim. Cosmochim. Acta*, **59(10)**, 1933-1949.

Tivey, M.K. (2004) Environmental conditions within active seafloor vent structures: sensitivity to vent fluid composition and fluid flow. In Wilcock, W., Cary, C., DeLong, E., Kelley, D., Baross, J. (Eds.) Subseafloor Biosphere at Mid-Ocean Ridges, Geophysical Monograph Series, No. 144. American Geophysical Union, Washington, DC, 137-152.

Trefry, J. H., Butterfield, D. B., Metz, S., Massoth, G. J., Trocine, R. P., and Feely R. A. (1994) Trace metals in hydrothermal solutions from Cleft segment on the southern Juan de Fuca Ridge. *J. Geophys. Res.***99**, 4925–4935.

Tunaboylu, K., Schwarzenbach, G., 1970. Die Löslichkeit von Indiumsulfid. *Chimia* (Switzerland) **24**, 424– 427.

Vallier, T. L., Jenner, G. A., Frey, F. A., Gill, J. B., Davis, A. S., Volpe, A. M., Hawkins, J. W., Morris, J.D., Cawood, P.A., Morton, J. L., Scholl, D.W., Rautenschlein, M., White, Williams, W.M., Stevenson, A.J., White, L.D. (1991) Subalkaline andesite from Valu Fa Ridge, a back-arc spreading center in southern Lau Basin: petrogenesis, comparative chemistry, and tectonic implications. *Chem. Geol.*, **91(3)**, 227-256.

Von Damm, K. L. (1995) Controls on the chemistry and temporal variability of seafloor hydrothermal fluids. In *Seafloor Hydrothermal Systems: Physical, Chemical, Biological, and Geological Interactions* (eds. S. E. Humphris, R. A. Zierenberg, L. S. Mullineaux, and R. E. Thomson), American Geophysical Union, Washington, D. C., pp. 222-247.

Von Damm, K. L., Edmond, J. M., Grant, B., Measures, C. I., Walden, B., and Weiss, R. F. (1985) Chemistry of submarine hydrothermal solutions at 21° N, East Pacific Rise. *Geochim. Cosmochim. Acta*, **49(11)**, 2197-2220.

Wolery, T. J. (1992) EQ3/6: A software package for geochemical modeling of aqueous systems: package overview and installation guide (version 7.0) Livermore, CA: Lawrence Livermore National Laboratory.

Wood, S. A. and Samson, I. M. (2006) The aqueous geochemistry of gallium, germanium, indium and scandium. *Ore Geology Reviews*, ***28*(1)**, 57-102.

Appendix A.

Bivariate plots of fluid Mg measured by ion chromatography vs. metals and metalloids measured by inductively coupled plasma mass spectrometry (ICP-MS). Concentrations of the dissolved fraction are marked in white. Concentrations of the total fluid samples (total = dregs + dissolved + filter fractions) are marked in black. Samples thought to be contaminated are marked in red. Also shown are sample regression lines to zero-Mg hydrothermal endmember.

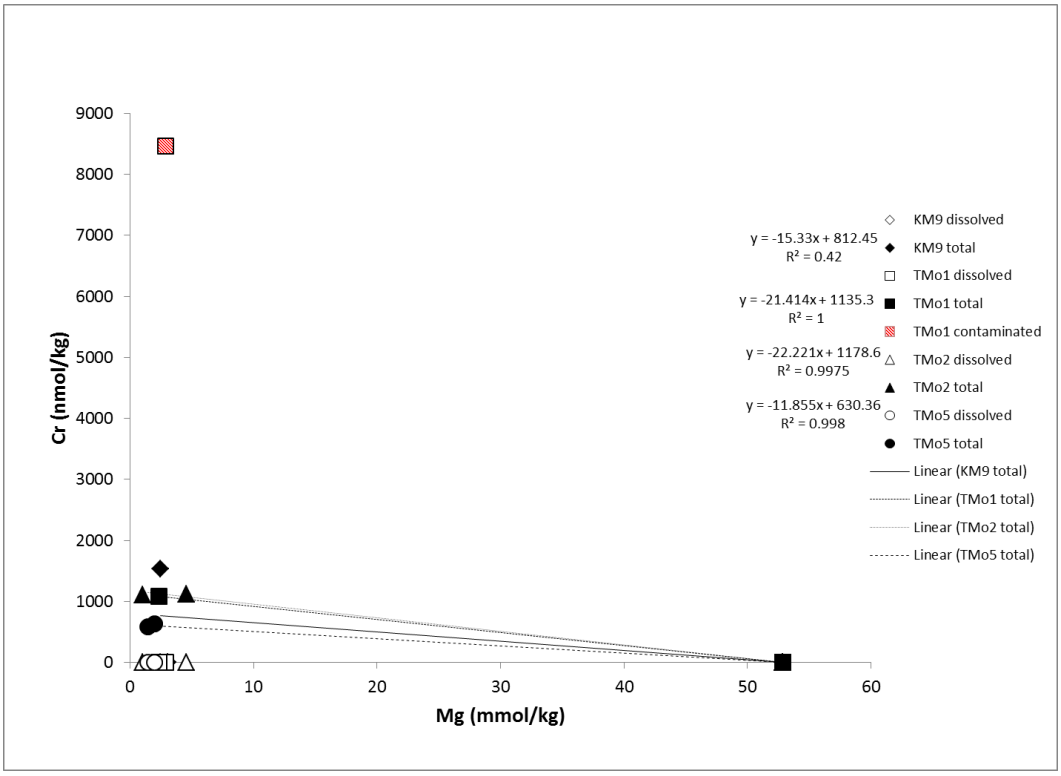

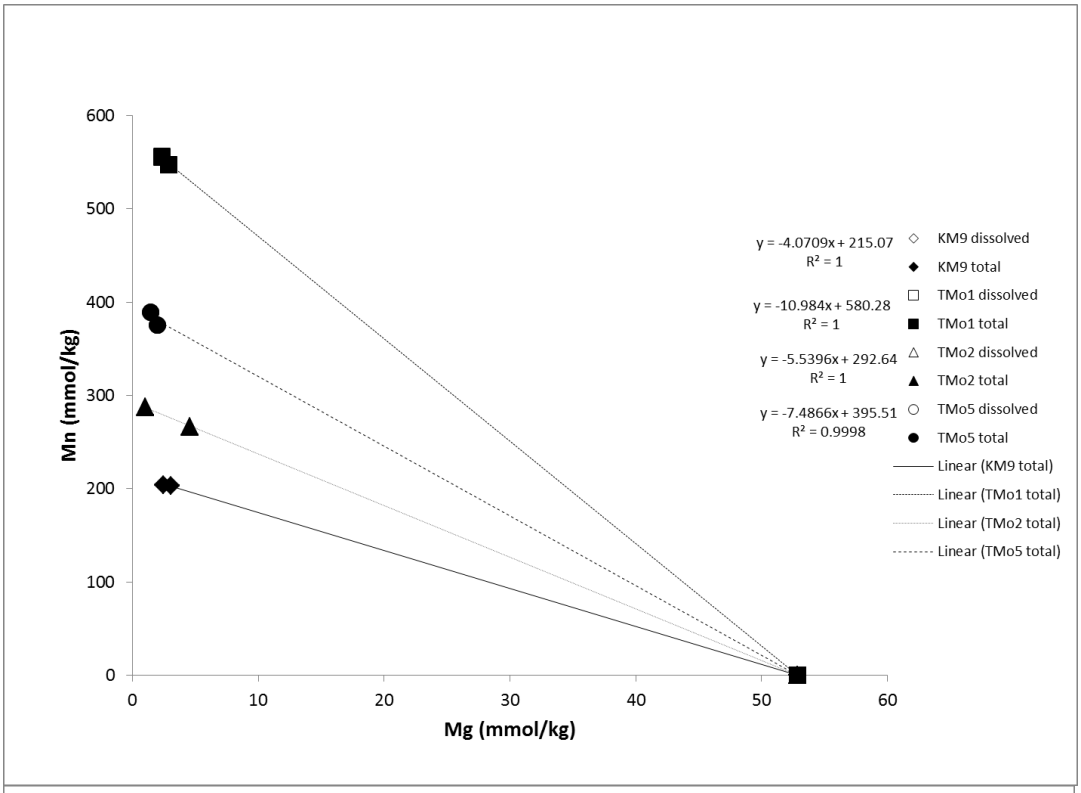
600
500
400
300
200
100
0
0
10
20
30
40
50
60
Mn (mmol/kg)
Mg (mmol/kg)
y = -4.0709x + 215.07
R² = 1
y = -10.984x + 580.28
R² = 1
y = -5.5396x + 292.64
R² = 1
y = -7.4866x + 395.51
R² = 0.9998
KM9 dissolved
KM9 total
TMo1 dissolved
TMo1 total
TMo2 dissolved
TMo2 total
TMo5 dissolved
TMo5 total
Linear (KM9 total)
Linear (TMo1 total)
Linear (TMo2 total)
Linear (TMo5 total)

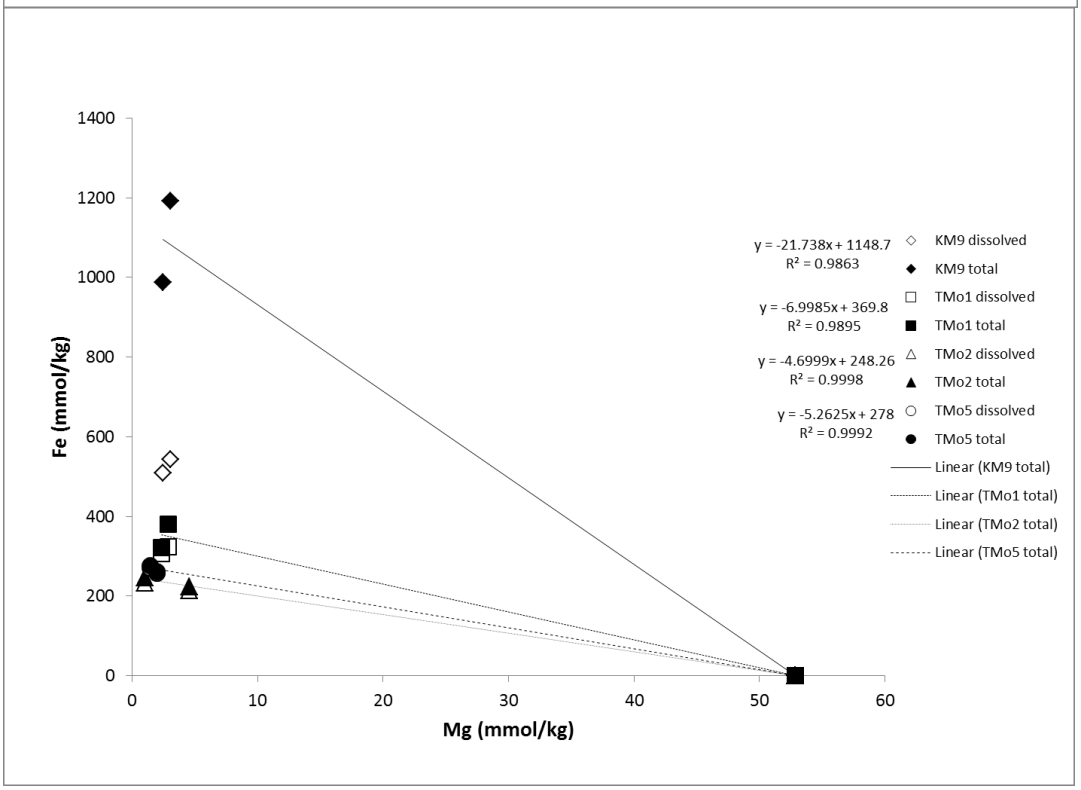
1400
1200
1000
800
600
400
200
0
0
10
20
30
40
50
60
Fe (mmol/kg)
Mg (mmol/kg)
y = -21.738x + 1148.7
R² = 0.9863
y = -6.9985x + 369.8
R² = 0.9895
y = -4.6999x + 248.26
R² = 0.9998
y = -5.2625x + 278
R² = 0.9992
KM9 dissolved
KM9 total
TMo1 dissolved
TMo1 total
TMo2 dissolved
TMo2 total
TMo5 dissolved
TMo5 total
Linear (KM9 total)
Linear (TMo1 total)
Linear (TMo2 total)
Linear (TMo5 total)

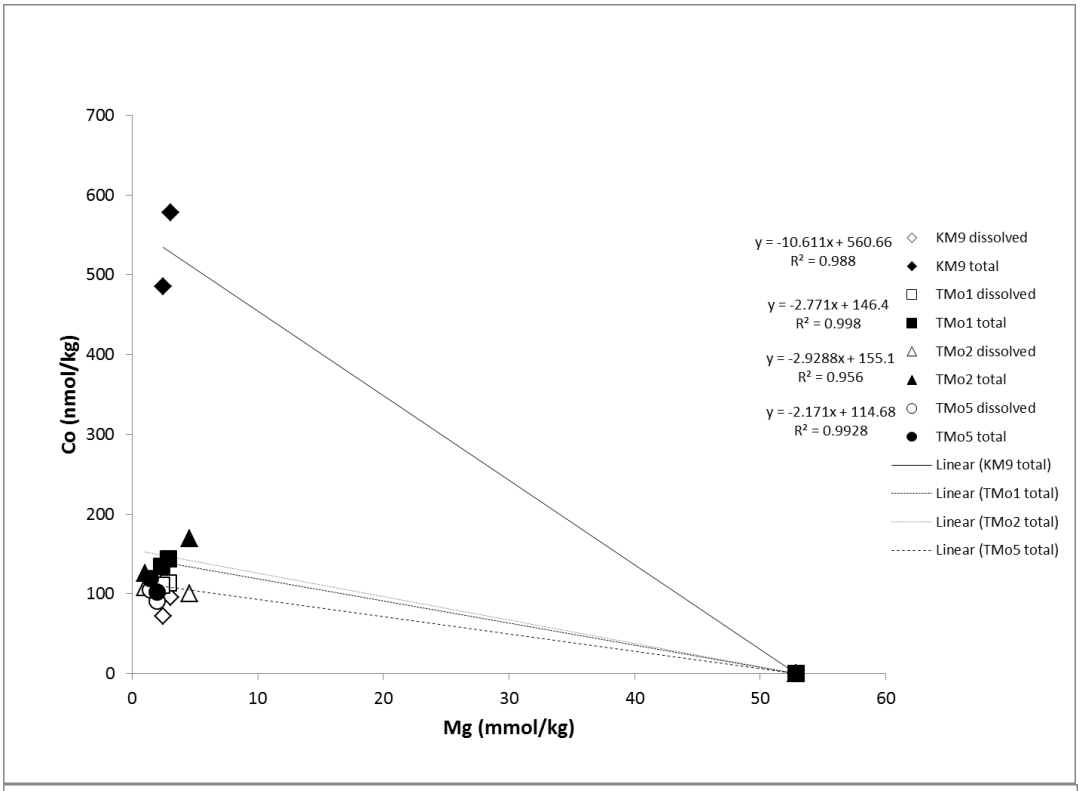
Co (nmol/kg)
Mg (mmol/kg)
y = -10.611x + 560.66
R² = 0.988
y = -2.771x + 146.4
R² = 0.998
y = -2.9288x + 155.1
R² = 0.956
y = -2.171x + 114.68
R² = 0.9928
KM9 dissolved
KM9 total
TMo1 dissolved
TMo1 total
TMo2 dissolved
TMo2 total
TMo5 dissolved
TMo5 total
Linear (KM9 total)
Linear (TMo1 total)
Linear (TMo2 total)
Linear (TMo5 total)

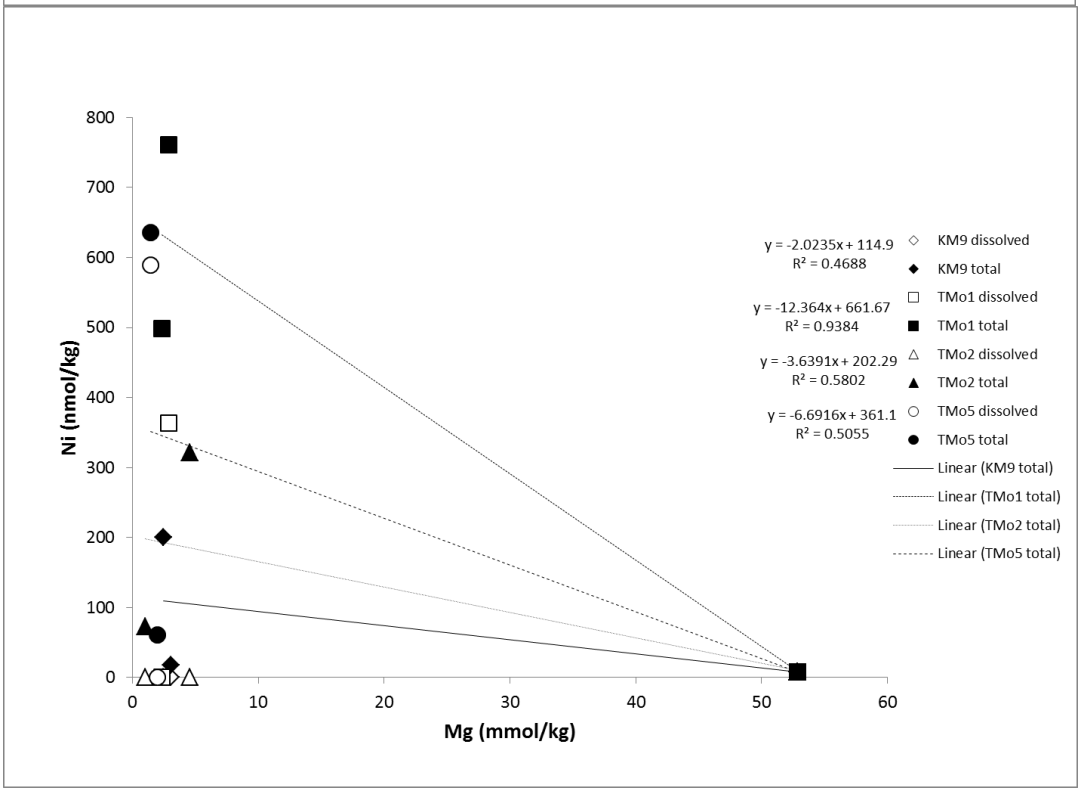
Ni (nmol/kg)
Mg (mmol/kg)
y = -2.0235x + 114.9
R² = 0.4688
y = -12.364x + 661.67
R² = 0.9384
y = -3.6391x + 202.29
R² = 0.5802
y = -6.6916x + 361.1
R² = 0.5055
KM9 dissolved
KM9 total
TMo1 dissolved
TMo1 total
TMo2 dissolved
TMo2 total
TMo5 dissolved
TMo5 total
Linear (KM9 total)
Linear (TMo1 total)
Linear (TMo2 total)
Linear (TMo5 total)

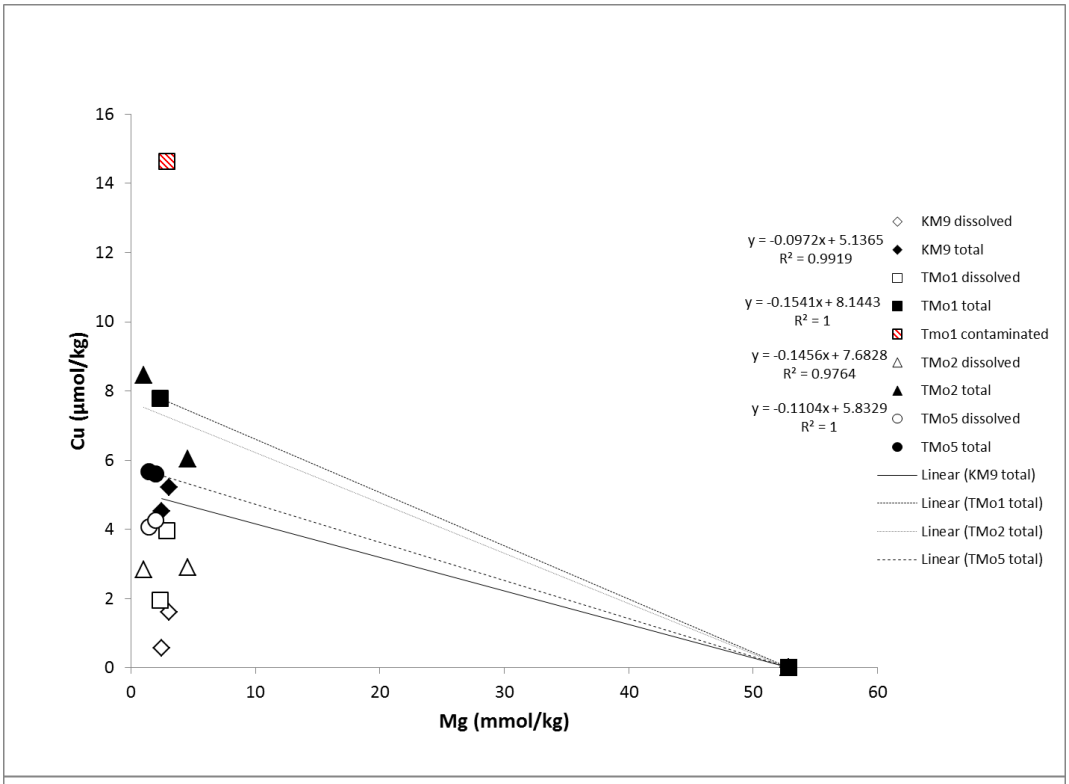
Cu (µmol/kg)
Mg (mmol/kg)
y = -0.0972x + 5.1365
R² = 0.9919
y = -0.1541x + 8.1443
R² = 1
y = -0.1456x + 7.6828
R² = 0.9764
y = -0.1104x + 5.8329
R² = 1
KM9 dissolved
KM9 total
TMo1 dissolved
TMo1 total
Tmo1 contaminated
TMo2 dissolved
TMo2 total
TMo5 dissolved
TMo5 total
Linear (KM9 total)
Linear (TMo1 total)
Linear (TMo2 total)
Linear (TMo5 total)

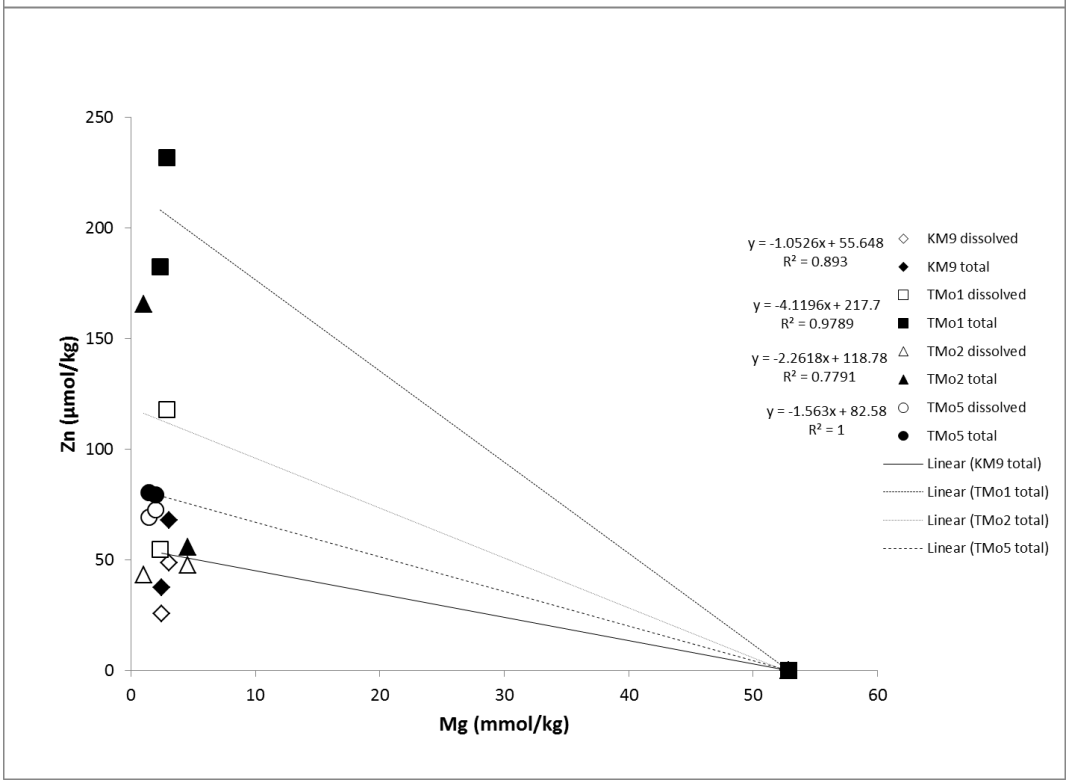
Zn (µmol/kg)
Mg (mmol/kg)
y = -1.0526x + 55.648
R² = 0.893
y = -4.1196x + 217.7
R² = 0.9789
y = -2.2618x + 118.78
R² = 0.7791
y = -1.563x + 82.58
R² = 1
KM9 dissolved
KM9 total
TMo1 dissolved
TMo1 total
TMo2 dissolved
TMo2 total
TMo5 dissolved
TMo5 total
Linear (KM9 total)
Linear (TMo1 total)
Linear (TMo2 total)
Linear (TMo5 total)

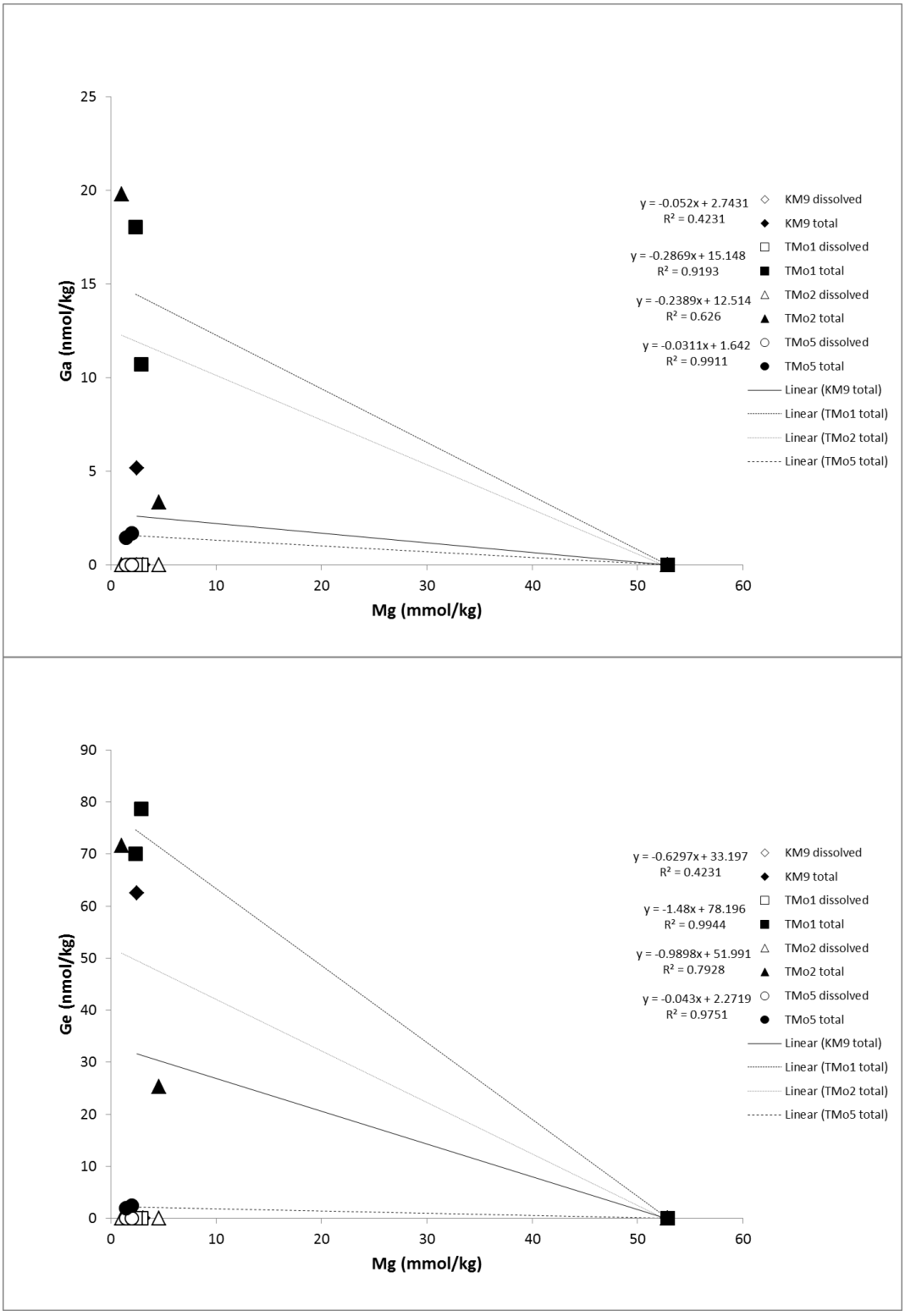
Ga (nmol/kg)
Mg (mmol/kg)
y = -0.052x + 2.7431
R² = 0.4231
y = -0.2869x + 15.148
R² = 0.9193
y = -0.2389x + 12.514
R² = 0.626
y = -0.0311x + 1.642
R² = 0.9911
KM9 dissolved
KM9 total
TMo1 dissolved
TMo1 total
TMo2 dissolved
TMo2 total
TMo5 dissolved
TMo5 total
Linear (KM9 total)
Linear (TMo1 total)
Linear (TMo2 total)
Linear (TMo5 total)
Ge (nmol/kg)
Mg (mmol/kg)
y = -0.6297x + 33.197
R² = 0.4231
y = -1.48x + 78.196
R² = 0.9944
y = -0.9898x + 51.991
R² = 0.7928
y = -0.043x + 2.2719
R² = 0.9751
KM9 dissolved
KM9 total
TMo1 dissolved
TMo1 total
TMo2 dissolved
TMo2 total
TMo5 dissolved
TMo5 total
Linear (KM9 total)
Linear (TMo1 total)
Linear (TMo2 total)
Linear (TMo5 total)

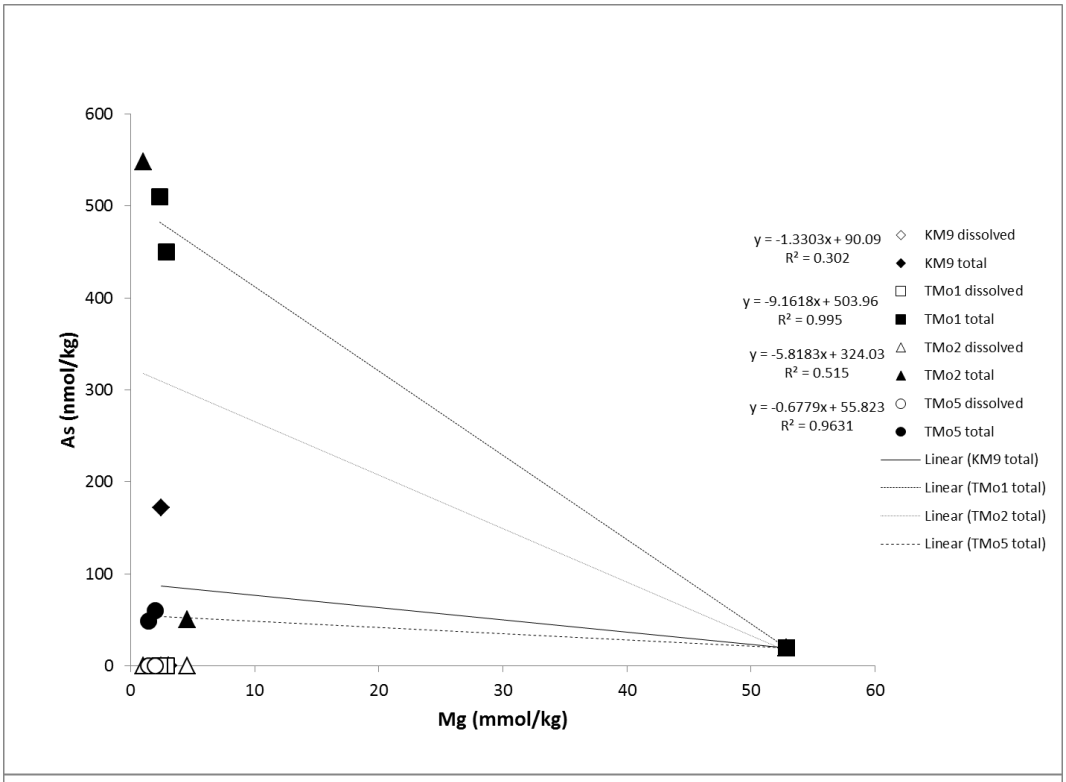
As (nmol/kg)
Mg (mmol/kg)
y = -1.3303x + 90.09
R² = 0.302
y = -9.1618x + 503.96
R² = 0.995
y = -5.8183x + 324.03
R² = 0.515
y = -0.6779x + 55.823
R² = 0.9631
KM9 dissolved
KM9 total
TMo1 dissolved
TMo1 total
TMo2 dissolved
TMo2 total
TMo5 dissolved
TMo5 total
Linear (KM9 total)
Linear (TMo1 total)
Linear (TMo2 total)
Linear (TMo5 total)

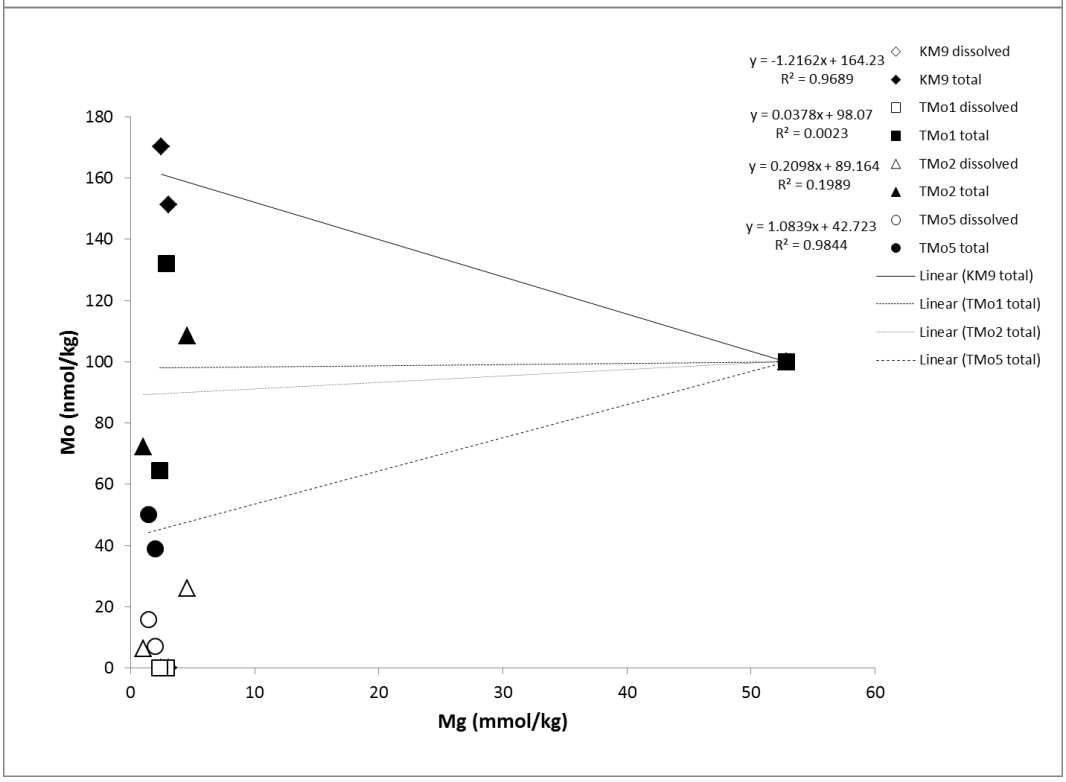
Mo (nmol/kg)
Mg (mmol/kg)
y = -1.2162x + 164.23
R² = 0.9689
y = 0.0378x + 98.07
R² = 0.0023
y = 0.2098x + 89.164
R² = 0.1989
y = 1.0839x + 42.723
R² = 0.9844
KM9 dissolved
KM9 total
TMo1 dissolved
TMo1 total
TMo2 dissolved
TMo2 total
TMo5 dissolved
TMo5 total
Linear (KM9 total)
Linear (TMo1 total)
Linear (TMo2 total)
Linear (TMo5 total)

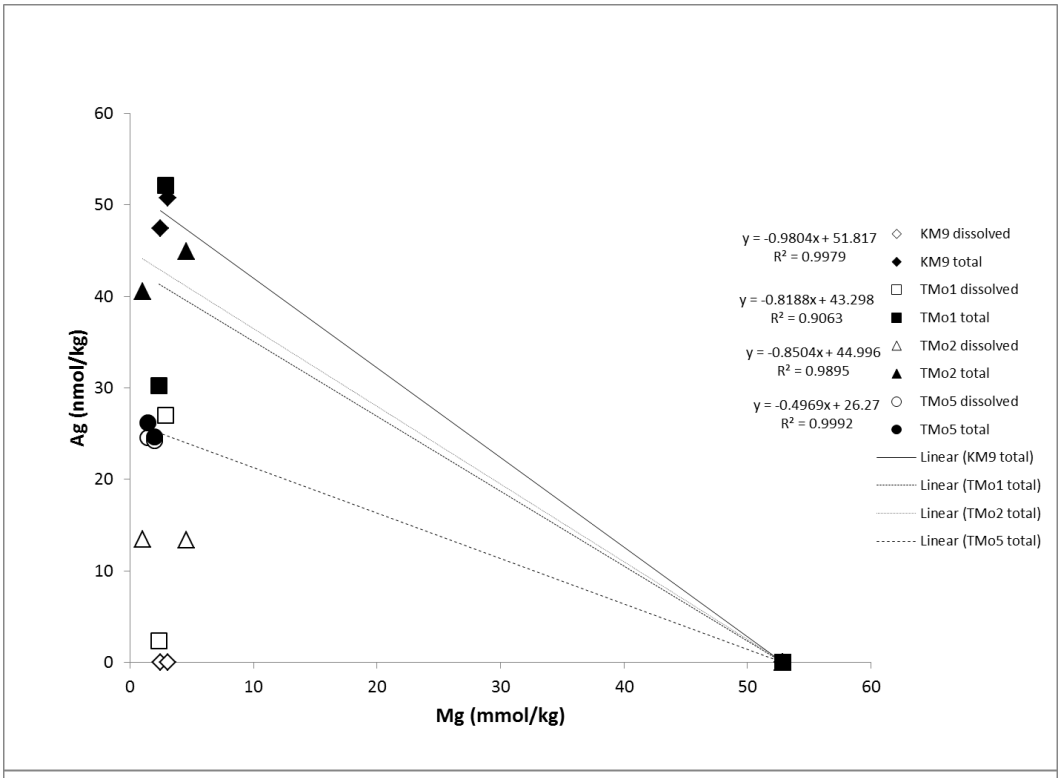
Ag (nmol/kg)
Mg (mmol/kg)
0
10
20
30
40
50
60
y = -0.9804x + 51.817
R² = 0.9979
y = -0.8188x + 43.298
R² = 0.9063
y = -0.8504x + 44.996
R² = 0.9895
y = -0.4969x + 26.27
R² = 0.9992
KM9 dissolved
KM9 total
TMo1 dissolved
TMo1 total
TMo2 dissolved
TMo2 total
TMo5 dissolved
TMo5 total
Linear (KM9 total)
Linear (TMo1 total)
Linear (TMo2 total)
Linear (TMo5 total)

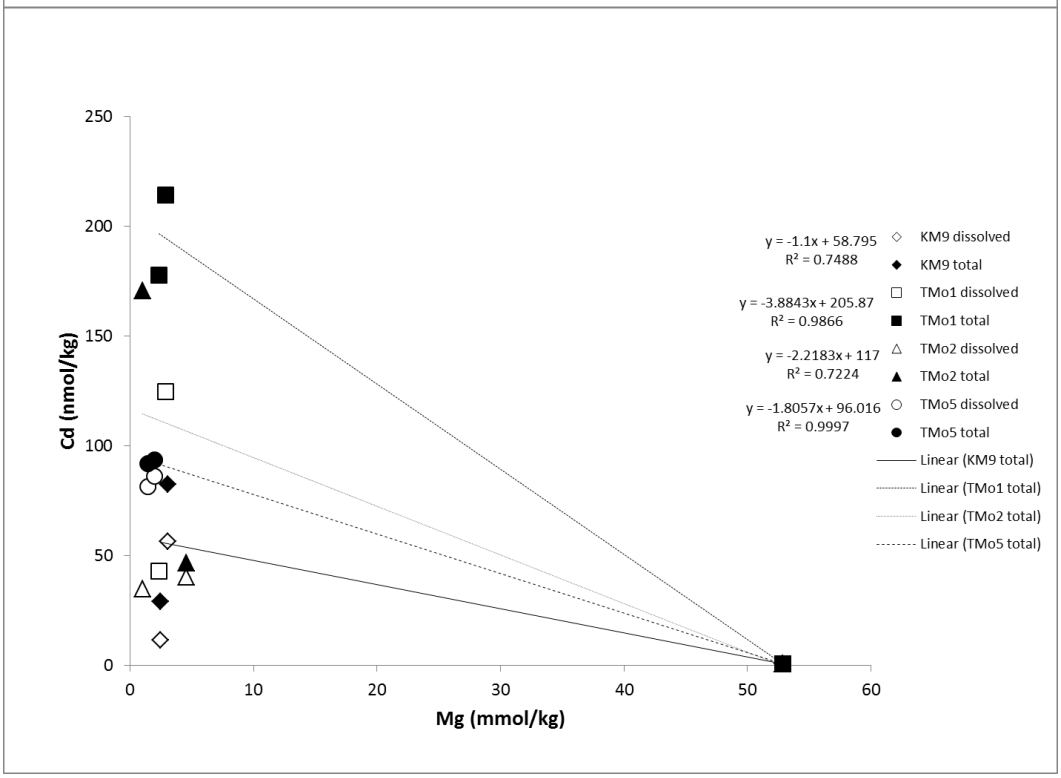
Cd (nmol/kg)
Mg (mmol/kg)
0
50
100
150
200
250
0
10
20
30
40
50
60
y = -1.1x + 58.795
R² = 0.7488
y = -3.8843x + 205.87
R² = 0.9866
y = -2.2183x + 117
R² = 0.7224
y = -1.8057x + 96.016
R² = 0.9997
KM9 dissolved
KM9 total
TMo1 dissolved
TMo1 total
TMo2 dissolved
TMo2 total
TMo5 dissolved
TMo5 total
Linear (KM9 total)
Linear (TMo1 total)
Linear (TMo2 total)
Linear (TMo5 total)

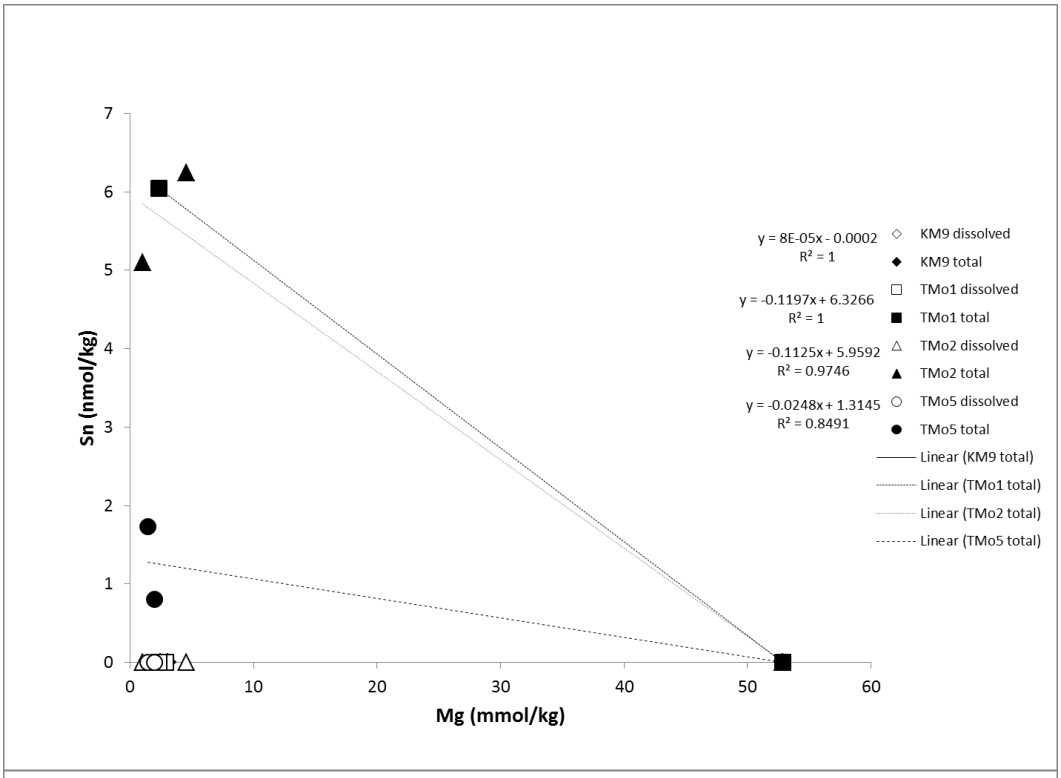
Sn (nmol/kg)
Mg (mmol/kg)
y = 8E-05x - 0.0002
R² = 1
y = -0.1197x + 6.3266
R² = 1
y = -0.1125x + 5.9592
R² = 0.9746
y = -0.0248x + 1.3145
R² = 0.8491
KM9 dissolved
KM9 total
TMo1 dissolved
TMo1 total
TMo2 dissolved
TMo2 total
TMo5 dissolved
TMo5 total
Linear (KM9 total)
Linear (TMo1 total)
Linear (TMo2 total)
Linear (TMo5 total)

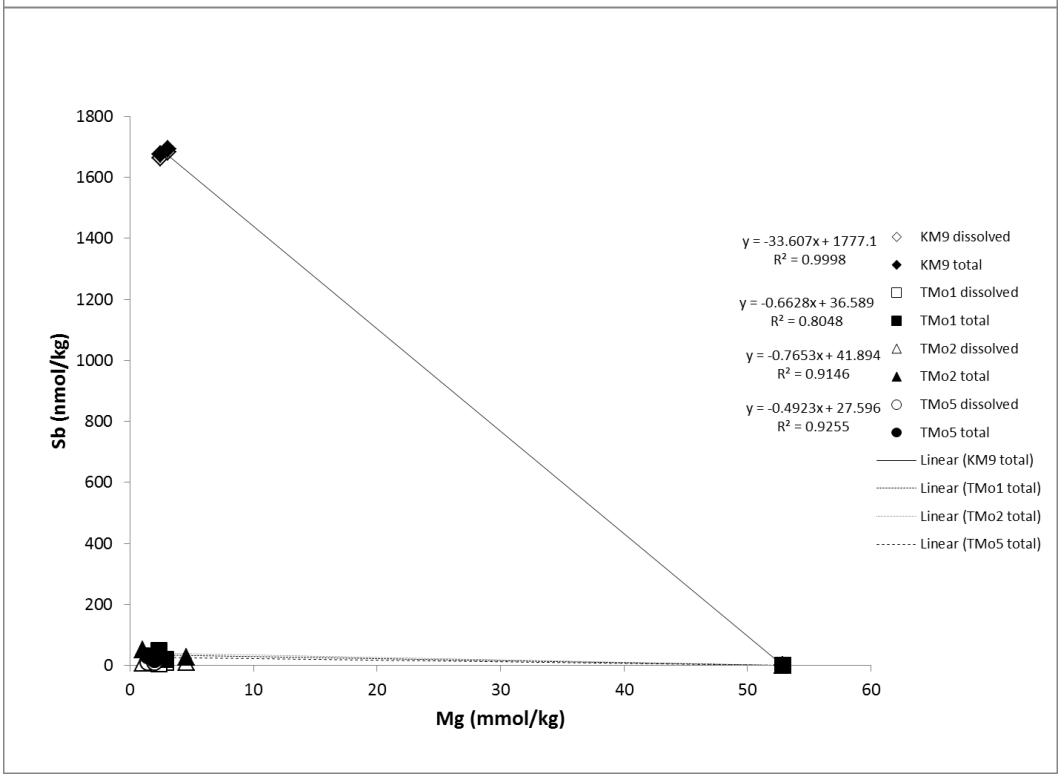
Sb (nmol/kg)
Mg (mmol/kg)
y = -33.607x + 1777.1
R² = 0.9998
y = -0.6628x + 36.589
R² = 0.8048
y = -0.7653x + 41.894
R² = 0.9146
y = -0.4923x + 27.596
R² = 0.9255
KM9 dissolved
KM9 total
TMo1 dissolved
TMo1 total
TMo2 dissolved
TMo2 total
TMo5 dissolved
TMo5 total
Linear (KM9 total)
Linear (TMo1 total)
Linear (TMo2 total)
Linear (TMo5 total)

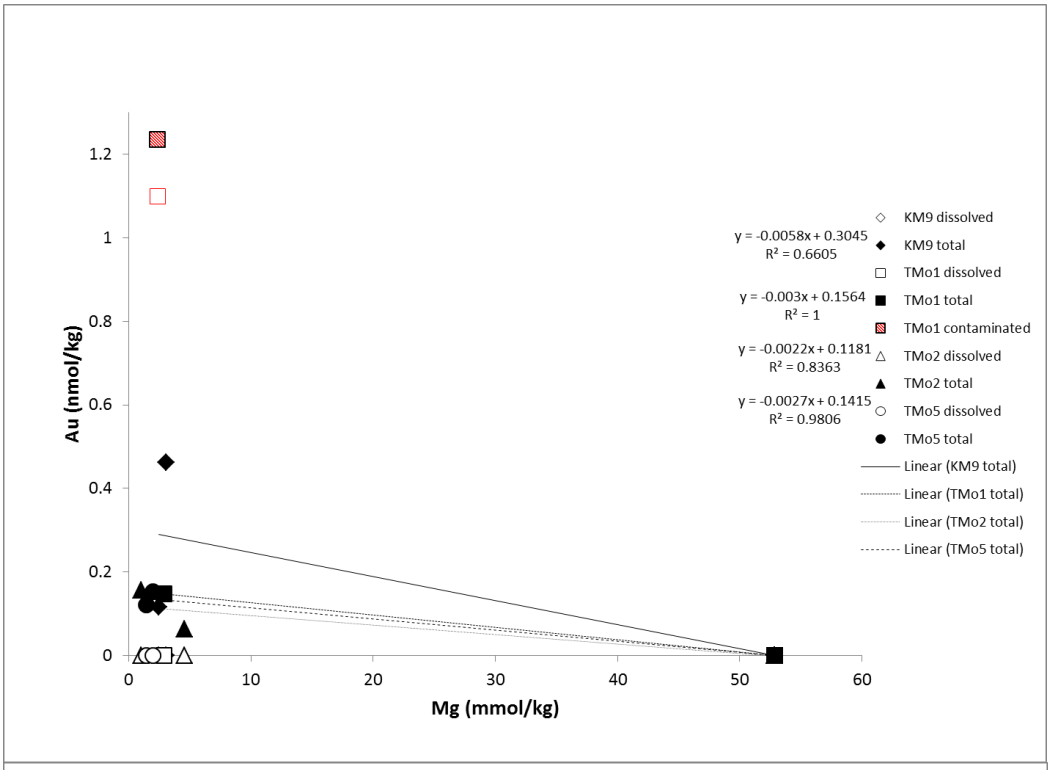
Au (nmol/kg)
Mg (mmol/kg)
y = -0.0058x + 0.3045
R² = 0.6605
y = -0.003x + 0.1564
R² = 1
y = -0.0022x + 0.1181
R² = 0.8363
y = -0.0027x + 0.1415
R² = 0.9806
KM9 dissolved
KM9 total
TMo1 dissolved
TMo1 total
TMo1 contaminated
TMo2 dissolved
TMo2 total
TMo5 dissolved
TMo5 total
Linear (KM9 total)
Linear (TMo1 total)
Linear (TMo2 total)
Linear (TMo5 total)

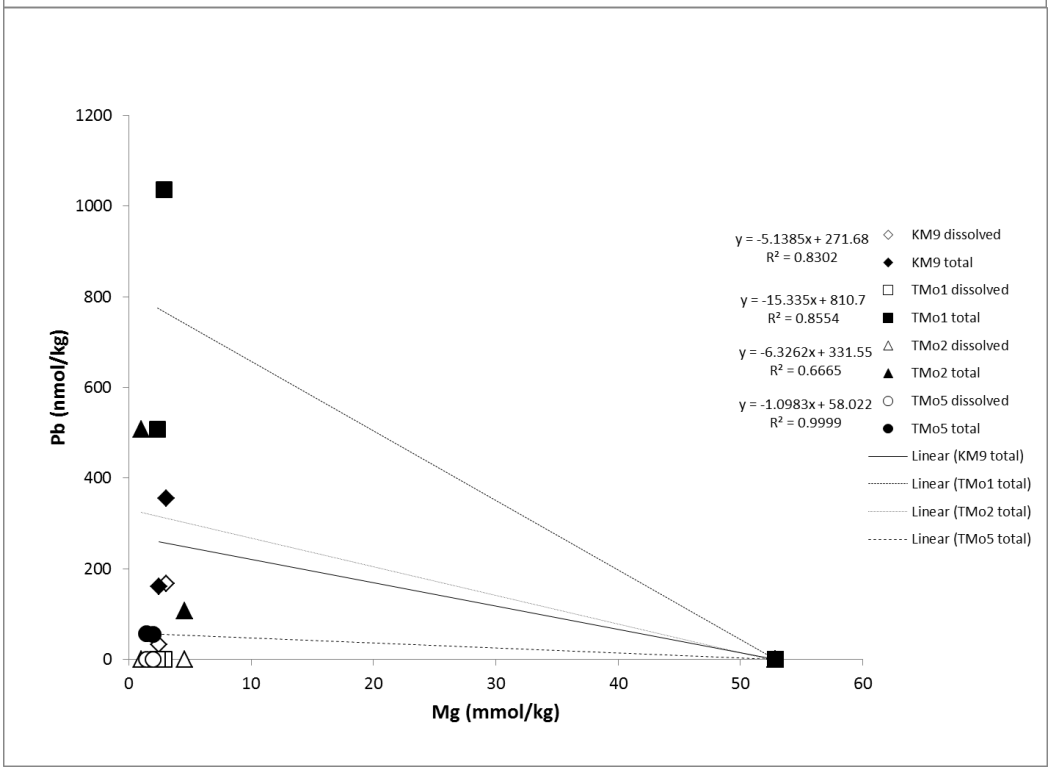
Pb (nmol/kg)
Mg (mmol/kg)
y = -5.1385x + 271.68
R² = 0.8302
y = -15.335x + 810.7
R² = 0.8554
y = -6.3262x + 331.55
R² = 0.6665
y = -1.0983x + 58.022
R² = 0.9999
KM9 dissolved
KM9 total
TMo1 dissolved
TMo1 total
TMo2 dissolved
TMo2 total
TMo5 dissolved
TMo5 total
Linear (KM9 total)
Linear (TMo1 total)
Linear (TMo2 total)
Linear (TMo5 total)

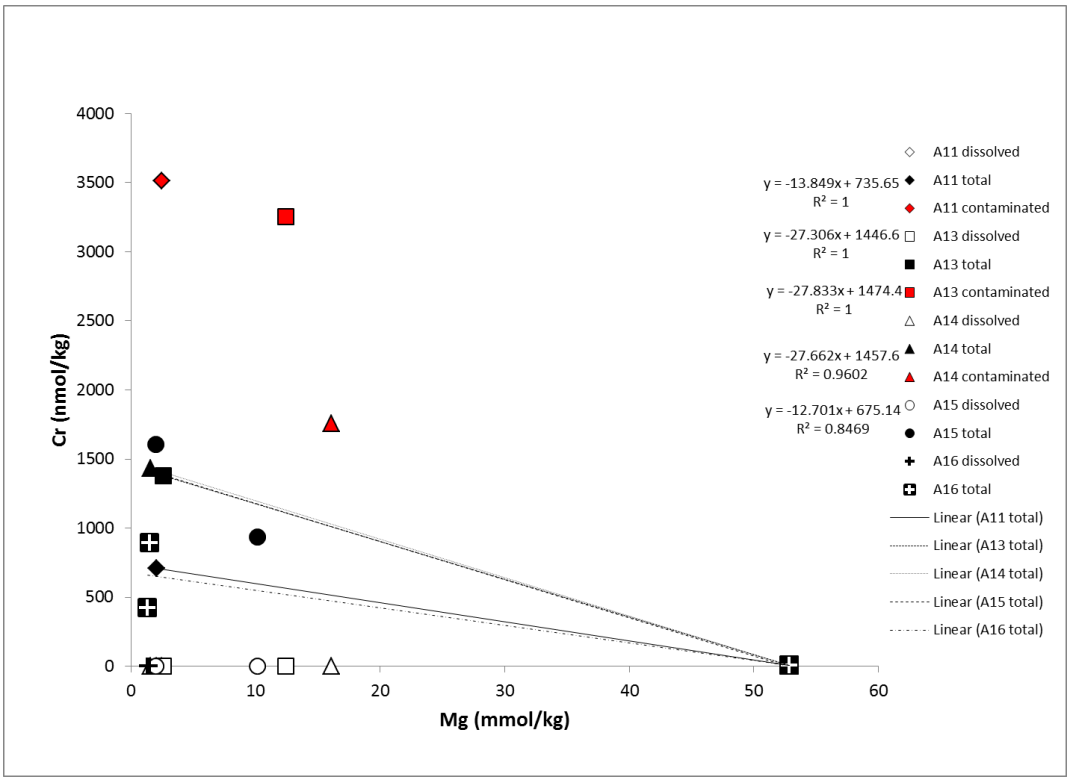
Cr (nmol/kg)
Mg (mmol/kg)
y = -13.849x + 735.65
R² = 1
y = -27.306x + 1446.6
R² = 1
y = -27.833x + 1474.4
R² = 1
y = -27.662x + 1457.6
R² = 0.9602
y = -12.701x + 675.14
R² = 0.8469
A11 dissolved
A11 total
A11 contaminated
A13 dissolved
A13 total
A13 contaminated
A14 dissolved
A14 total
A14 contaminated
A15 dissolved
A15 total
A16 dissolved
A16 total
Linear (A11 total)
Linear (A13 total)
Linear (A14 total)
Linear (A15 total)
Linear (A16 total)

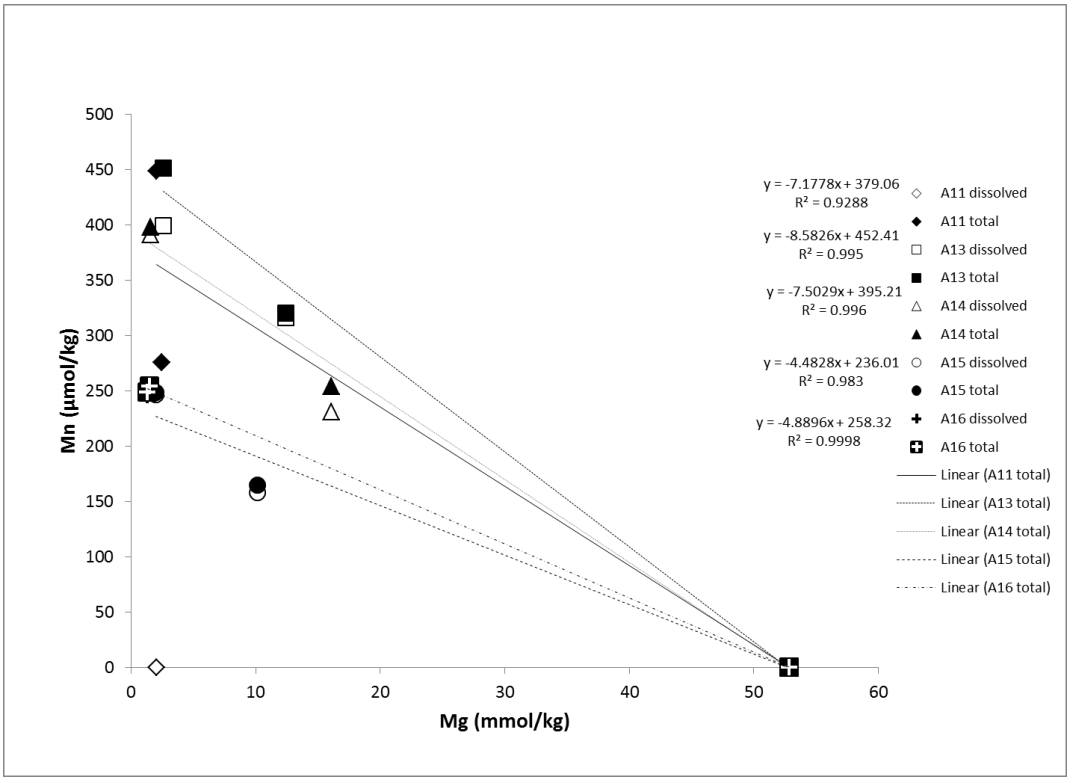
Mn (µmol/kg)
Mg (mmol/kg)
y = -7.1778x + 379.06
R² = 0.9288
y = -8.5826x + 452.41
R² = 0.995
y = -7.5029x + 395.21
R² = 0.996
y = -4.4828x + 236.01
R² = 0.983
y = -4.8896x + 258.32
R² = 0.9998
A11 dissolved
A11 total
A13 dissolved
A13 total
A14 dissolved
A14 total
A15 dissolved
A15 total
A16 dissolved
A16 total
Linear (A11 total)
Linear (A13 total)
Linear (A14 total)
Linear (A15 total)
Linear (A16 total)

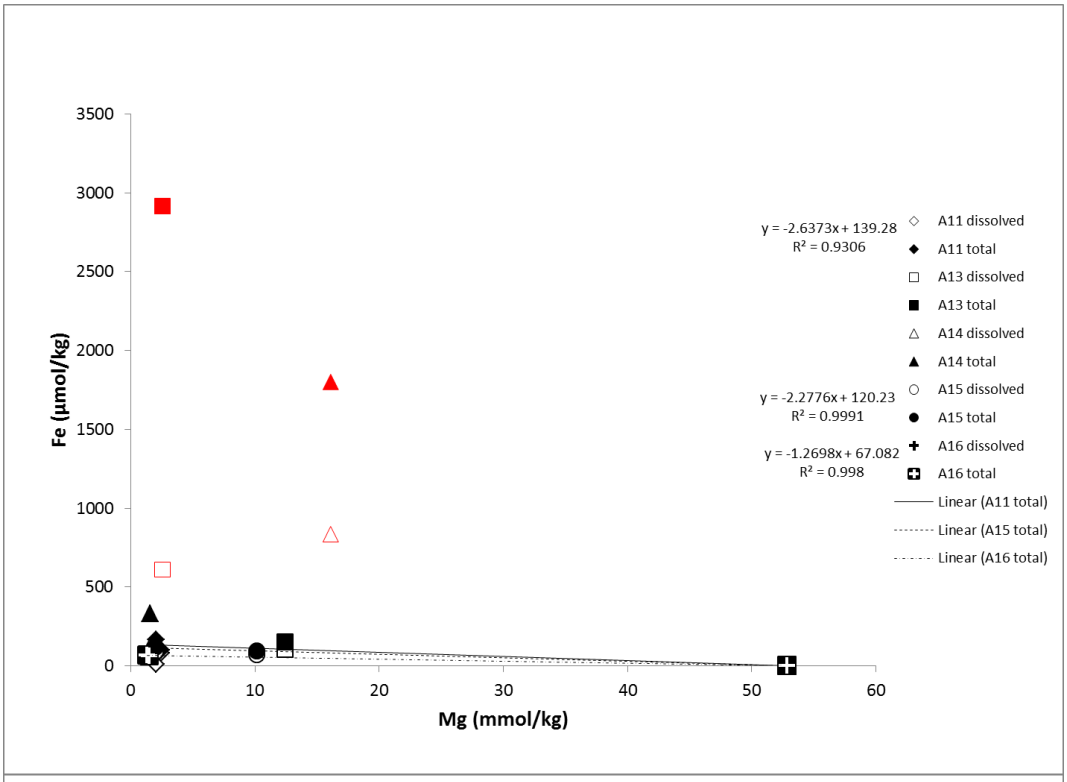
3500
3000
2500
2000
1500
1000
500
0
Fe (µmol/kg)
0
10
20
30
40
50
60
Mg (mmol/kg)
y = -2.6373x + 139.28
R² = 0.9306
y = -2.2776x + 120.23
R² = 0.9991
y = -1.2698x + 67.082
R² = 0.998
A11 dissolved
A11 total
A13 dissolved
A13 total
A14 dissolved
A14 total
A15 dissolved
A15 total
A16 dissolved
A16 total
Linear (A11 total)
Linear (A15 total)
Linear (A16 total)

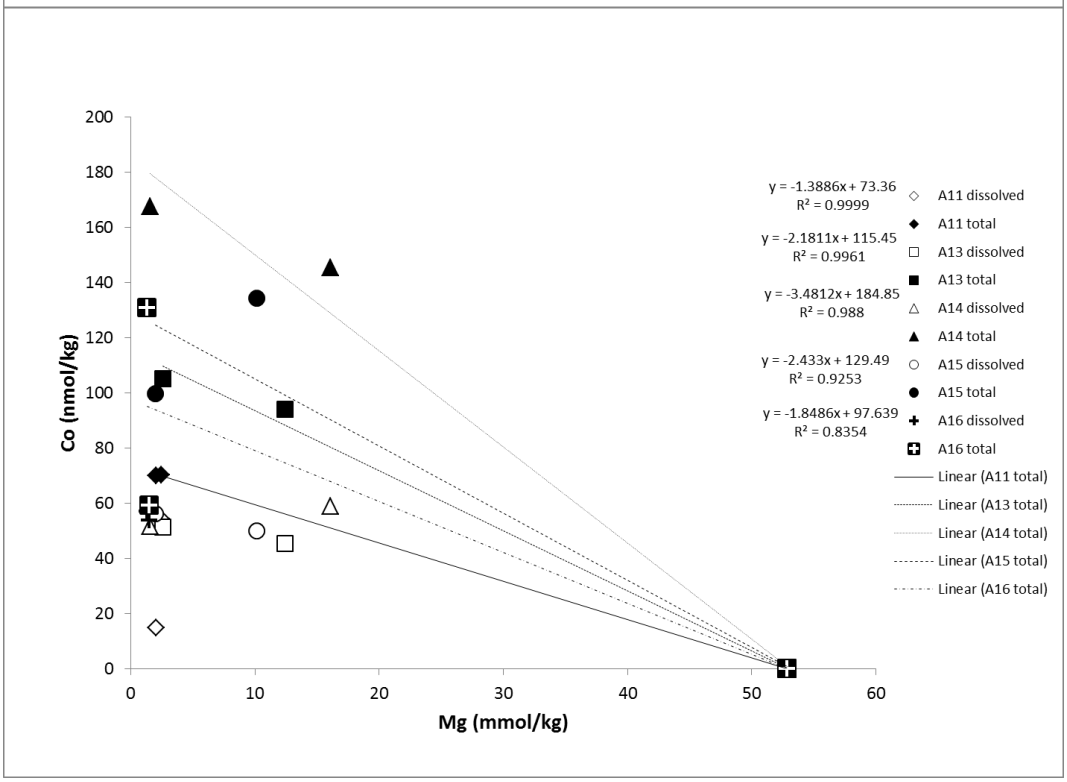
200
180
160
140
120
100
80
60
40
20
0
Co (nmol/kg)
0
10
20
30
40
50
60
Mg (mmol/kg)
y = -1.3886x + 73.36
R² = 0.9999
y = -2.1811x + 115.45
R² = 0.9961
y = -3.4812x + 184.85
R² = 0.988
y = -2.433x + 129.49
R² = 0.9253
y = -1.8486x + 97.639
R² = 0.8354
A11 dissolved
A11 total
A13 dissolved
A13 total
A14 dissolved
A14 total
A15 dissolved
A15 total
A16 dissolved
A16 total
Linear (A11 total)
Linear (A13 total)
Linear (A14 total)
Linear (A15 total)
Linear (A16 total)

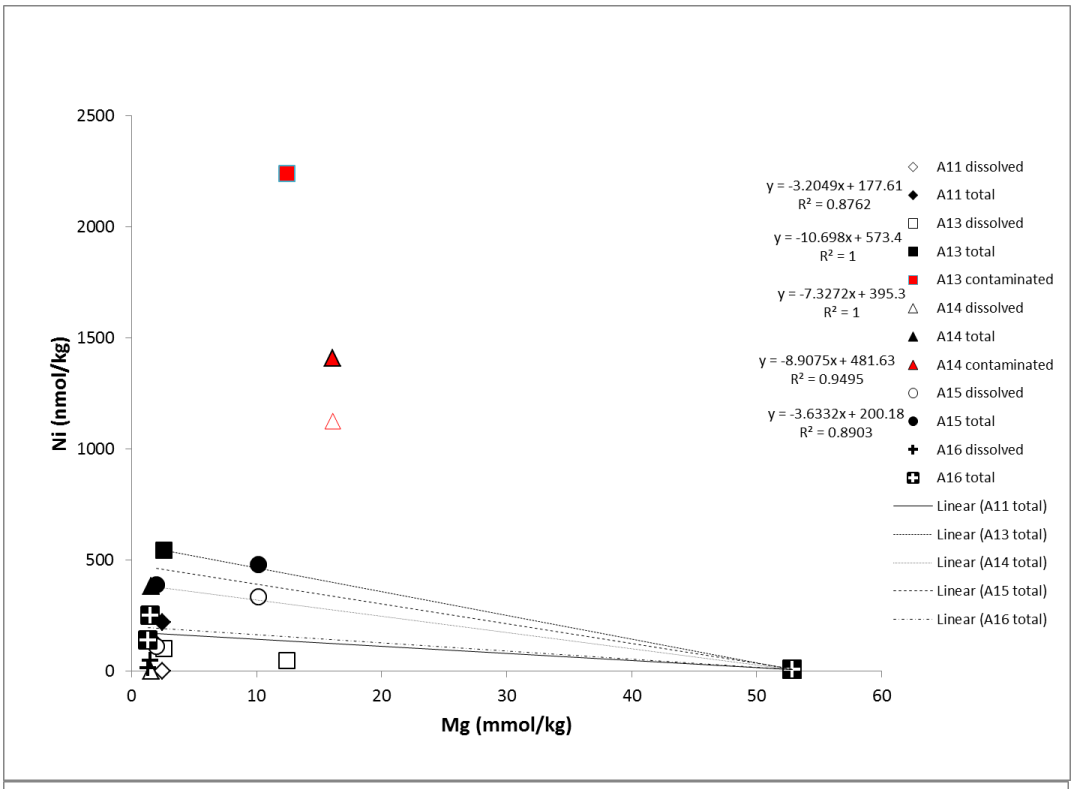
Ni (nmol/kg)
Mg (mmol/kg)
y = -3.2049x + 177.61
R² = 0.8762
y = -10.698x + 573.4
R² = 1
y = -7.3272x + 395.3
R² = 1
y = -8.9075x + 481.63
R² = 0.9495
y = -3.6332x + 200.18
R² = 0.8903
A11 dissolved
A11 total
A13 dissolved
A13 total
A13 contaminated
A14 dissolved
A14 total
A14 contaminated
A15 dissolved
A15 total
A16 dissolved
A16 total
Linear (A11 total)
Linear (A13 total)
Linear (A14 total)
Linear (A15 total)
Linear (A16 total)

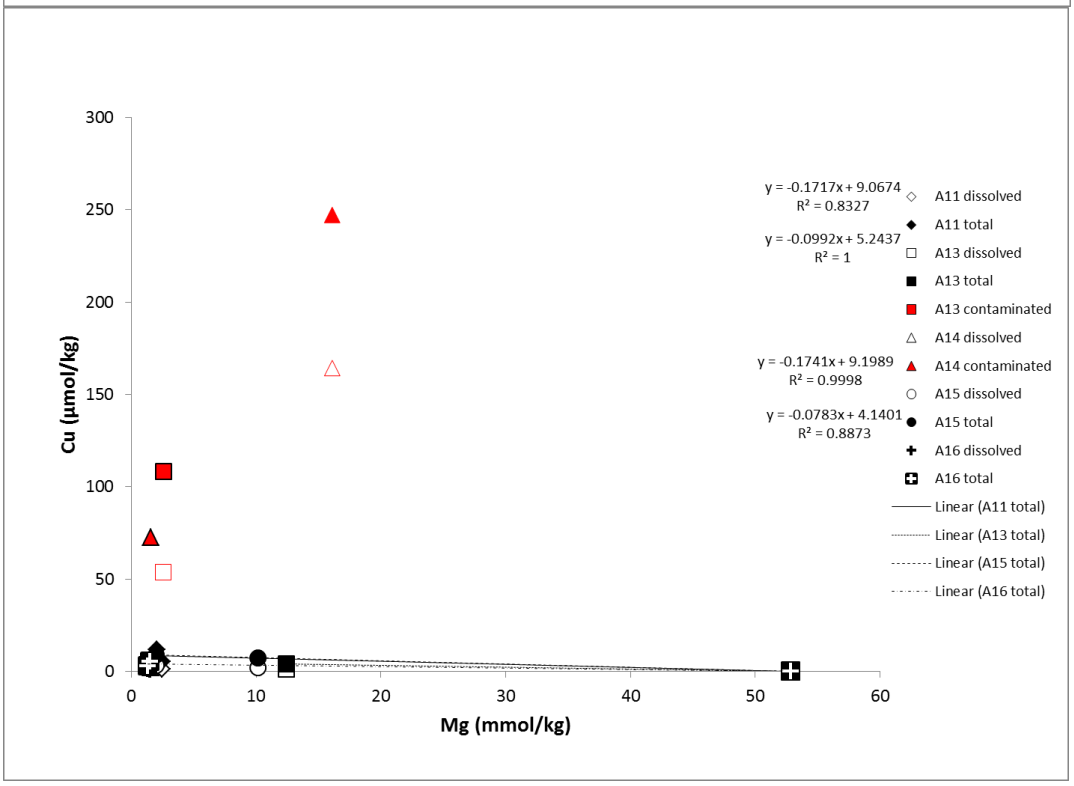
Cu (µmol/kg)
Mg (mmol/kg)
y = -0.1717x + 9.0674
R² = 0.8327
y = -0.0992x + 5.2437
R² = 1
y = -0.1741x + 9.1989
R² = 0.9998
y = -0.0783x + 4.1401
R² = 0.8873
A11 dissolved
A11 total
A13 dissolved
A13 total
A13 contaminated
A14 dissolved
A14 contaminated
A15 dissolved
A15 total
A16 dissolved
A16 total
Linear (A11 total)
Linear (A13 total)
Linear (A15 total)
Linear (A16 total)

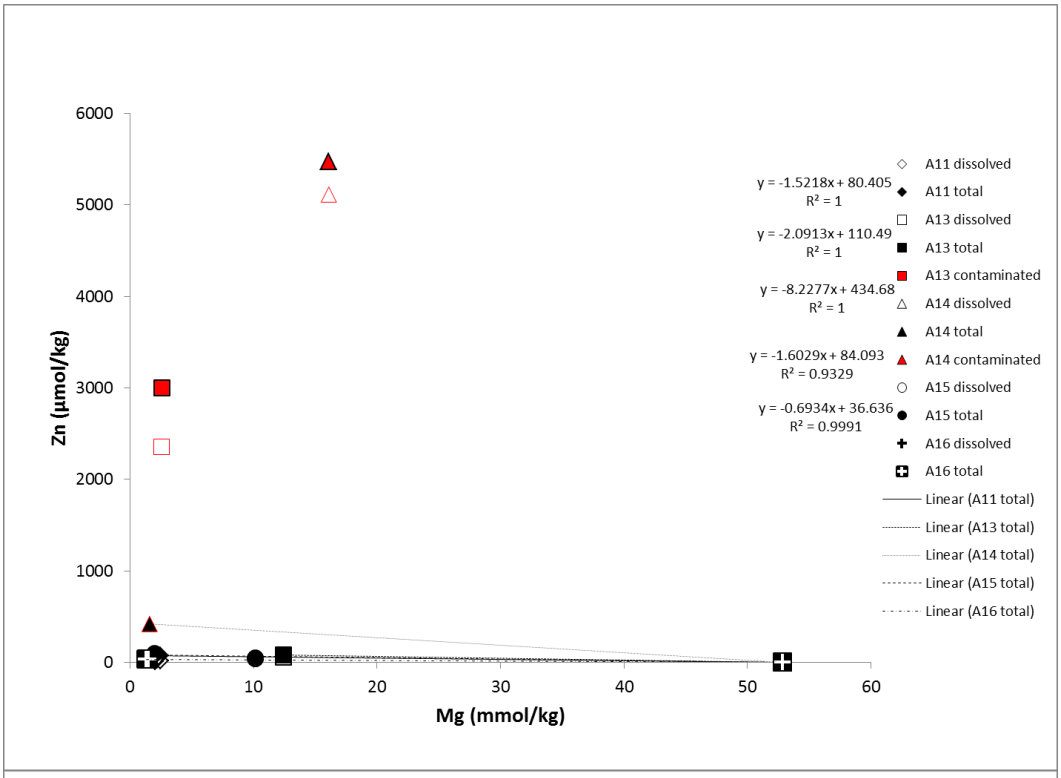
6000
5000
4000
3000
2000
1000
0
Zn (µmol/kg)
0
10
20
30
40
50
60
Mg (mmol/kg)
y = -1.5218x + 80.405
R² = 1
y = -2.0913x + 110.49
R² = 1
y = -8.2277x + 434.68
R² = 1
y = -1.6029x + 84.093
R² = 0.9329
y = -0.6934x + 36.636
R² = 0.9991
A11 dissolved
A11 total
A13 dissolved
A13 total
A13 contaminated
A14 dissolved
A14 total
A14 contaminated
A15 dissolved
A15 total
A16 dissolved
A16 total
Linear (A11 total)
Linear (A13 total)
Linear (A14 total)
Linear (A15 total)
Linear (A16 total)

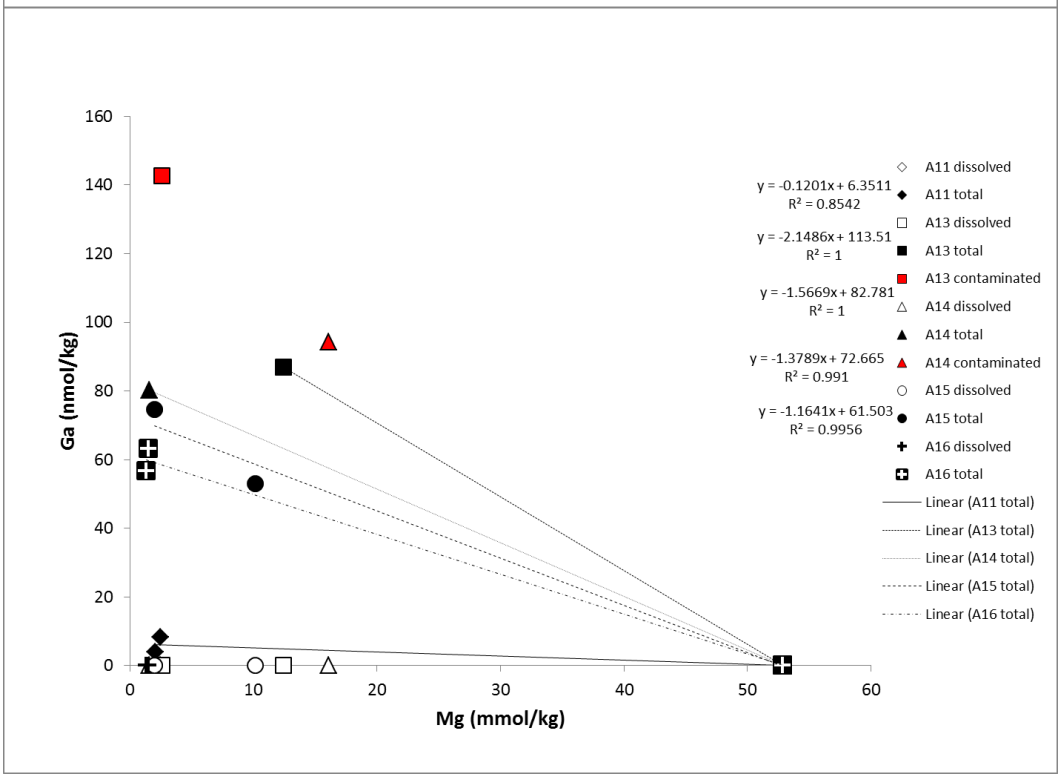
160
140
120
100
80
60
40
20
0
Ga (nmol/kg)
0
10
20
30
40
50
60
Mg (mmol/kg)
y = -0.1201x + 6.3511
R² = 0.8542
y = -2.1486x + 113.51
R² = 1
y = -1.5669x + 82.781
R² = 1
y = -1.3789x + 72.665
R² = 0.991
y = -1.1641x + 61.503
R² = 0.9956
A11 dissolved
A11 total
A13 dissolved
A13 total
A13 contaminated
A14 dissolved
A14 total
A14 contaminated
A15 dissolved
A15 total
A16 dissolved
A16 total
Linear (A11 total)
Linear (A13 total)
Linear (A14 total)
Linear (A15 total)
Linear (A16 total)

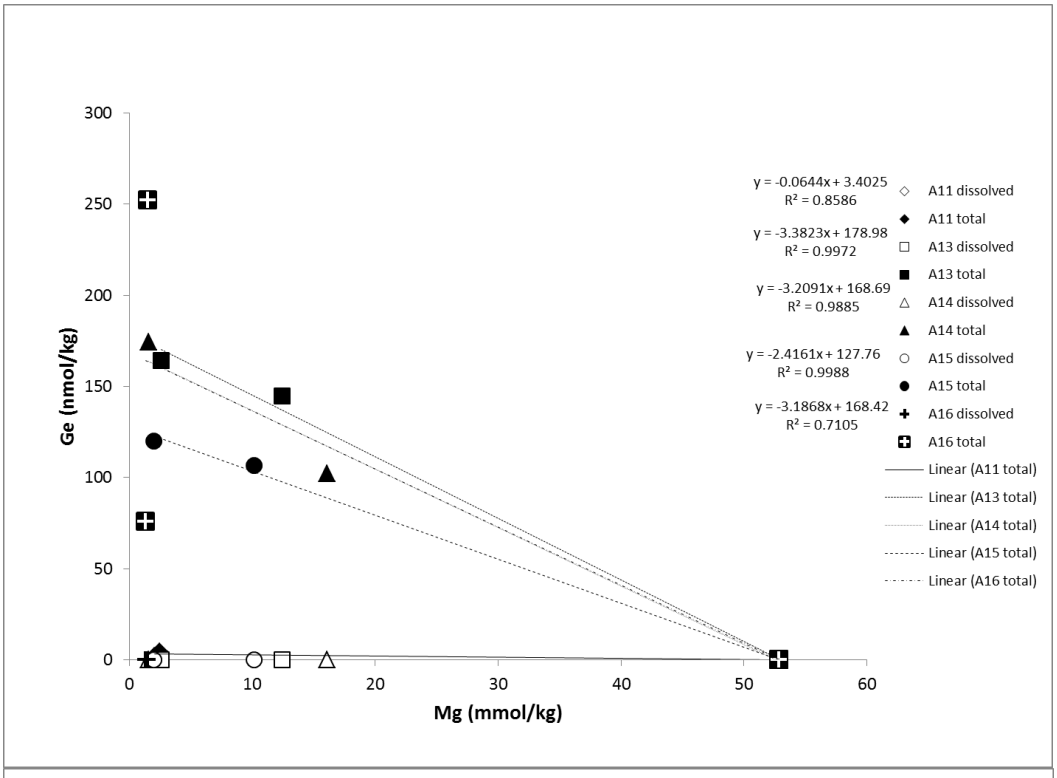
Ge (nmol/kg)
Mg (mmol/kg)
y = -0.0644x + 3.4025
R² = 0.8586
y = -3.3823x + 178.98
R² = 0.9972
y = -3.2091x + 168.69
R² = 0.9885
y = -2.4161x + 127.76
R² = 0.9988
y = -3.1868x + 168.42
R² = 0.7105
A11 dissolved
A11 total
A13 dissolved
A13 total
A14 dissolved
A14 total
A15 dissolved
A15 total
A16 dissolved
A16 total
Linear (A11 total)
Linear (A13 total)
Linear (A14 total)
Linear (A15 total)
Linear (A16 total)

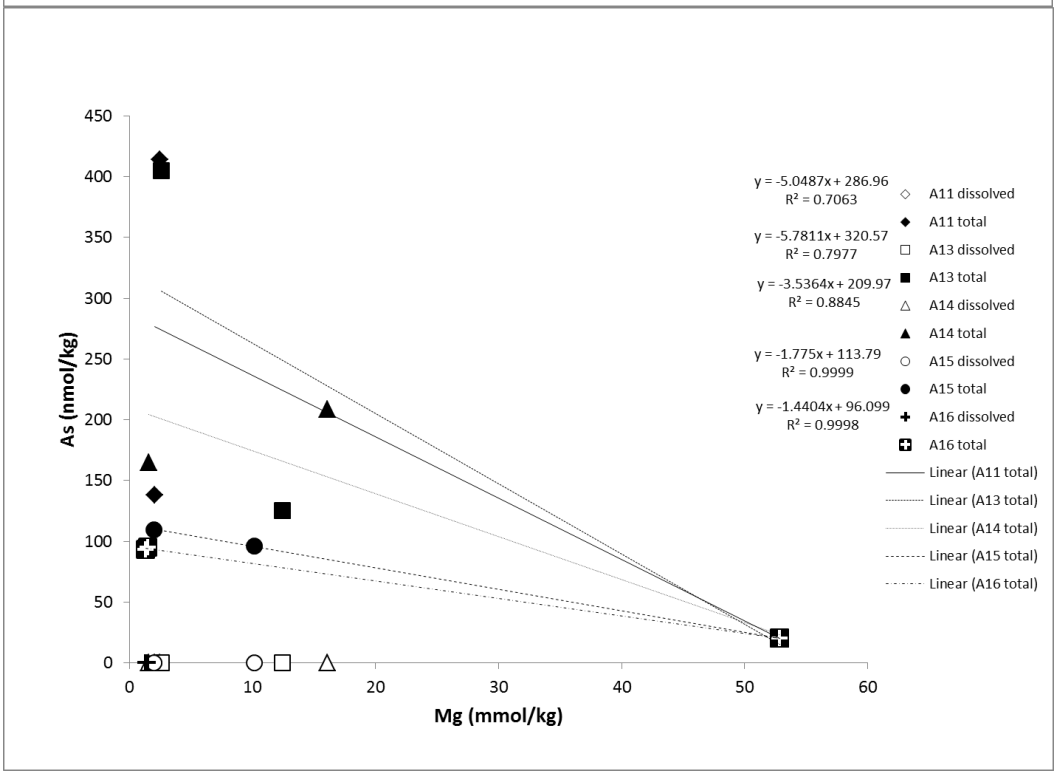
As (nmol/kg)
Mg (mmol/kg)
y = -5.0487x + 286.96
R² = 0.7063
y = -5.7811x + 320.57
R² = 0.7977
y = -3.5364x + 209.97
R² = 0.8845
y = -1.775x + 113.79
R² = 0.9999
y = -1.4404x + 96.099
R² = 0.9998
A11 dissolved
A11 total
A13 dissolved
A13 total
A14 dissolved
A14 total
A15 dissolved
A15 total
A16 dissolved
A16 total
Linear (A11 total)
Linear (A13 total)
Linear (A14 total)
Linear (A15 total)
Linear (A16 total)

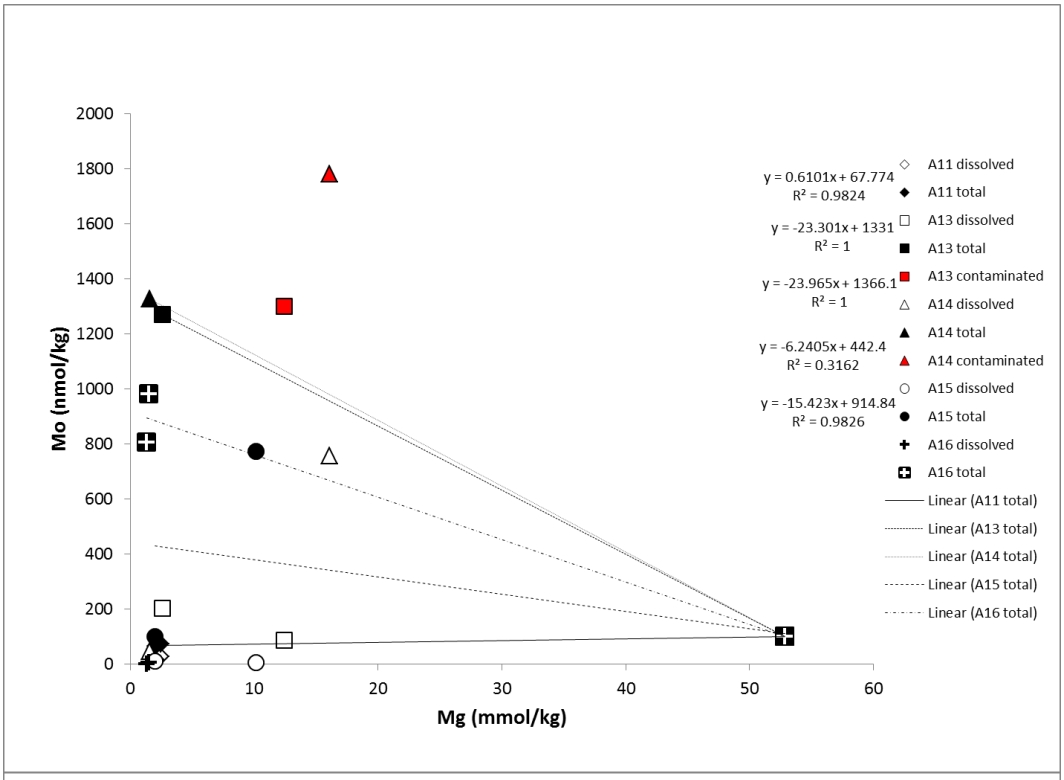
Mo (nmol/kg)
Mg (mmol/kg)
y = 0.6101x + 67.774
R² = 0.9824
y = -23.301x + 1331
R² = 1
y = -23.965x + 1366.1
R² = 1
y = -6.2405x + 442.4
R² = 0.3162
y = -15.423x + 914.84
R² = 0.9826
A11 dissolved
A11 total
A13 dissolved
A13 total
A13 contaminated
A14 dissolved
A14 total
A14 contaminated
A15 dissolved
A15 total
A16 dissolved
A16 total
Linear (A11 total)
Linear (A13 total)
Linear (A14 total)
Linear (A15 total)
Linear (A16 total)

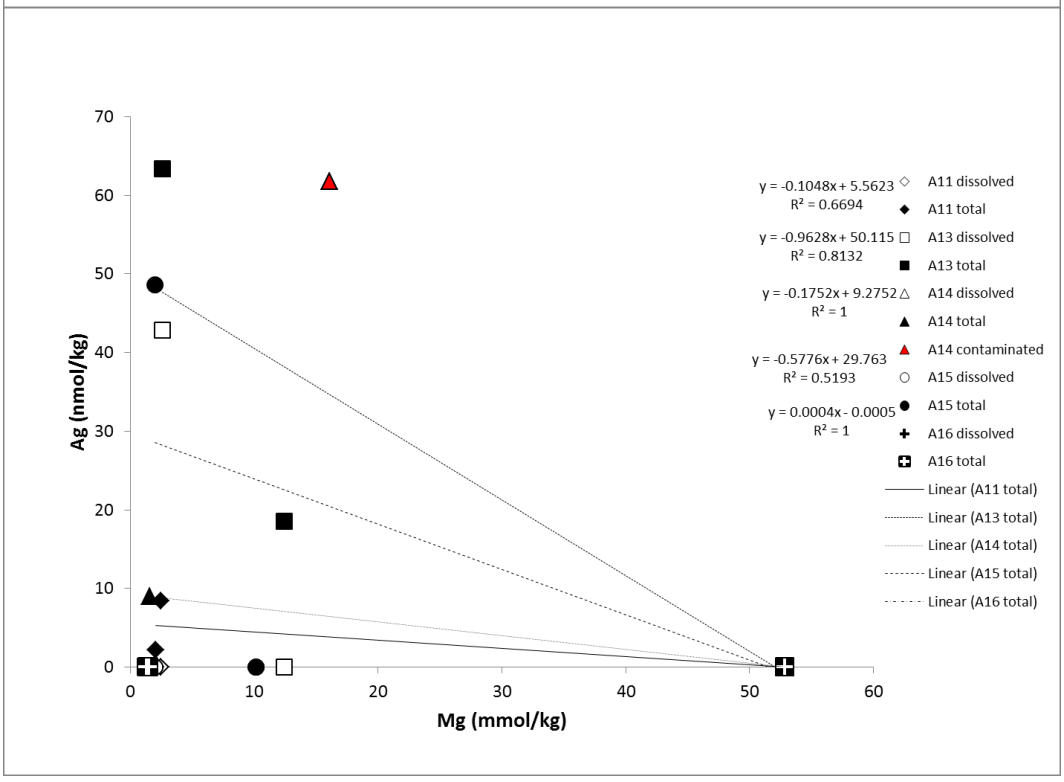
Ag (nmol/kg)
Mg (mmol/kg)
y = -0.1048x + 5.5623
R² = 0.6694
y = -0.9628x + 50.115
R² = 0.8132
y = -0.1752x + 9.2752
R² = 1
y = -0.5776x + 29.763
R² = 0.5193
y = 0.0004x - 0.0005
R² = 1
A11 dissolved
A11 total
A13 dissolved
A13 total
A14 dissolved
A14 total
A14 contaminated
A15 dissolved
A15 total
A16 dissolved
A16 total
Linear (A11 total)
Linear (A13 total)
Linear (A14 total)
Linear (A15 total)
Linear (A16 total)

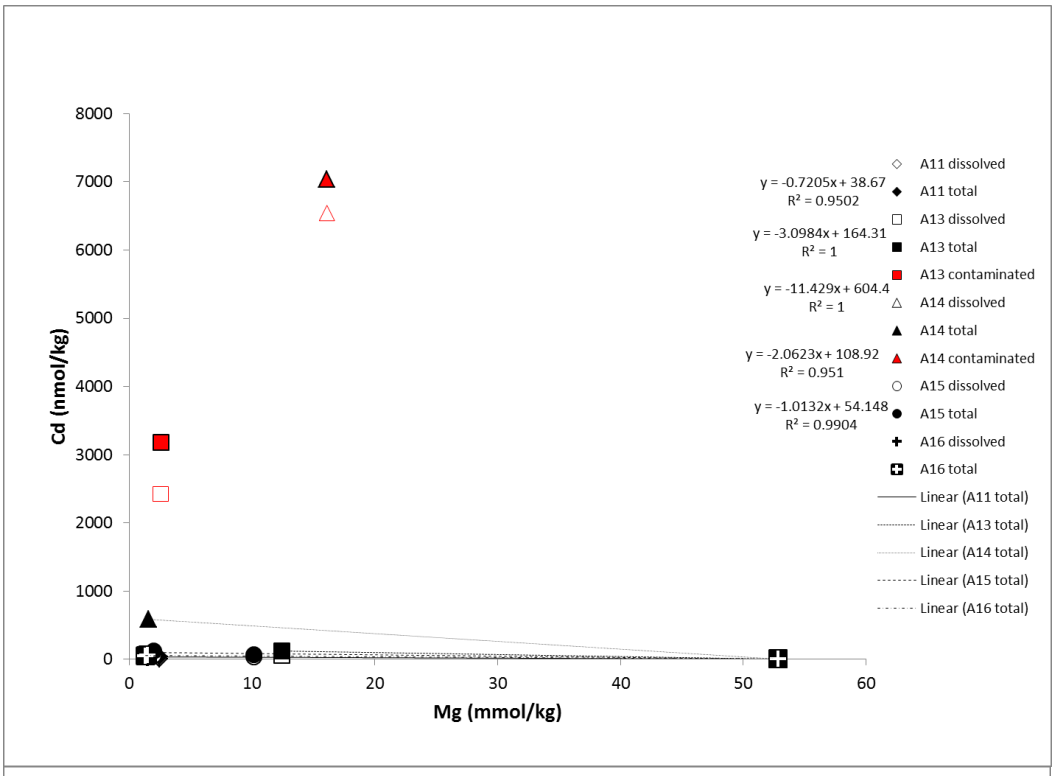
8000
7000
6000
5000
4000
3000
2000
1000
0
Cd (nmol/kg)
0
10
20
30
40
50
60
Mg (mmol/kg)
y = -0.7205x + 38.67
R² = 0.9502
y = -3.0984x + 164.31
R² = 1
y = -11.429x + 604.4
R² = 1
y = -2.0623x + 108.92
R² = 0.951
y = -1.0132x + 54.148
R² = 0.9904
A11 dissolved
A11 total
A13 dissolved
A13 total
A13 contaminated
A14 dissolved
A14 total
A14 contaminated
A15 dissolved
A15 total
A16 dissolved
A16 total
Linear (A11 total)
Linear (A13 total)
Linear (A14 total)
Linear (A15 total)
Linear (A16 total)

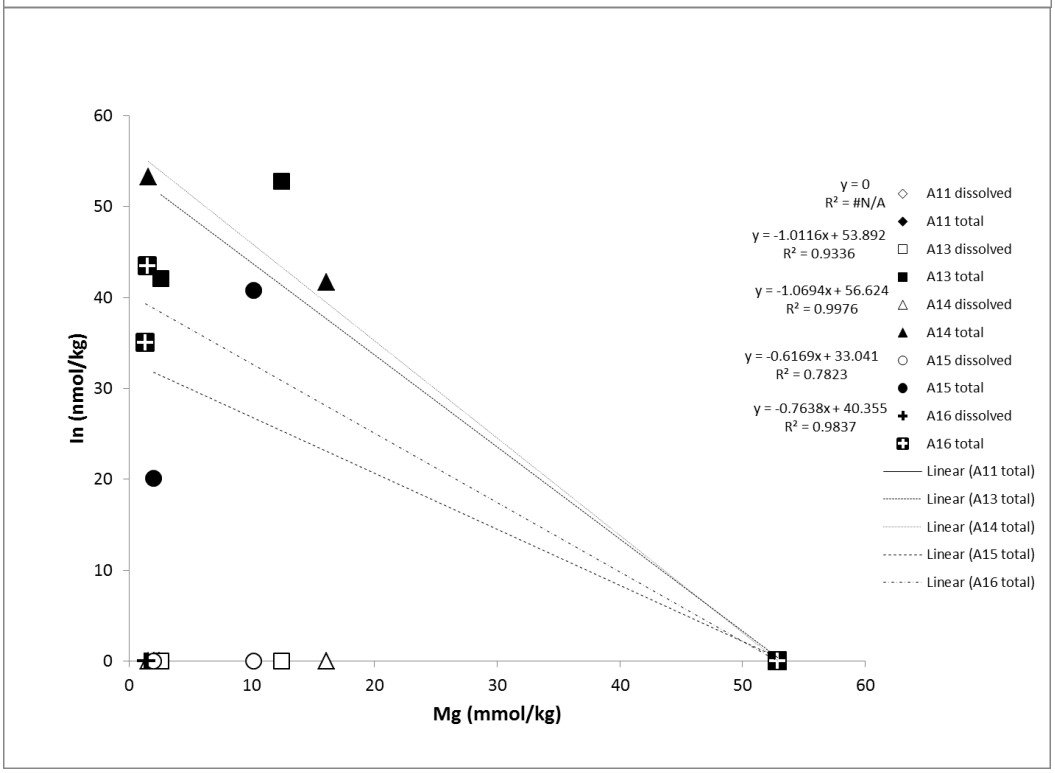
60
50
40
30
20
10
0
ln (nmol/kg)
0
10
20
30
40
50
60
Mg (mmol/kg)
y = 0
R² = #N/A
y = -1.0116x + 53.892
R² = 0.9336
y = -1.0694x + 56.624
R² = 0.9976
y = -0.6169x + 33.041
R² = 0.7823
y = -0.7638x + 40.355
R² = 0.9837
A11 dissolved
A11 total
A13 dissolved
A13 total
A14 dissolved
A14 total
A15 dissolved
A15 total
A16 dissolved
A16 total
Linear (A11 total)
Linear (A13 total)
Linear (A14 total)
Linear (A15 total)
Linear (A16 total)

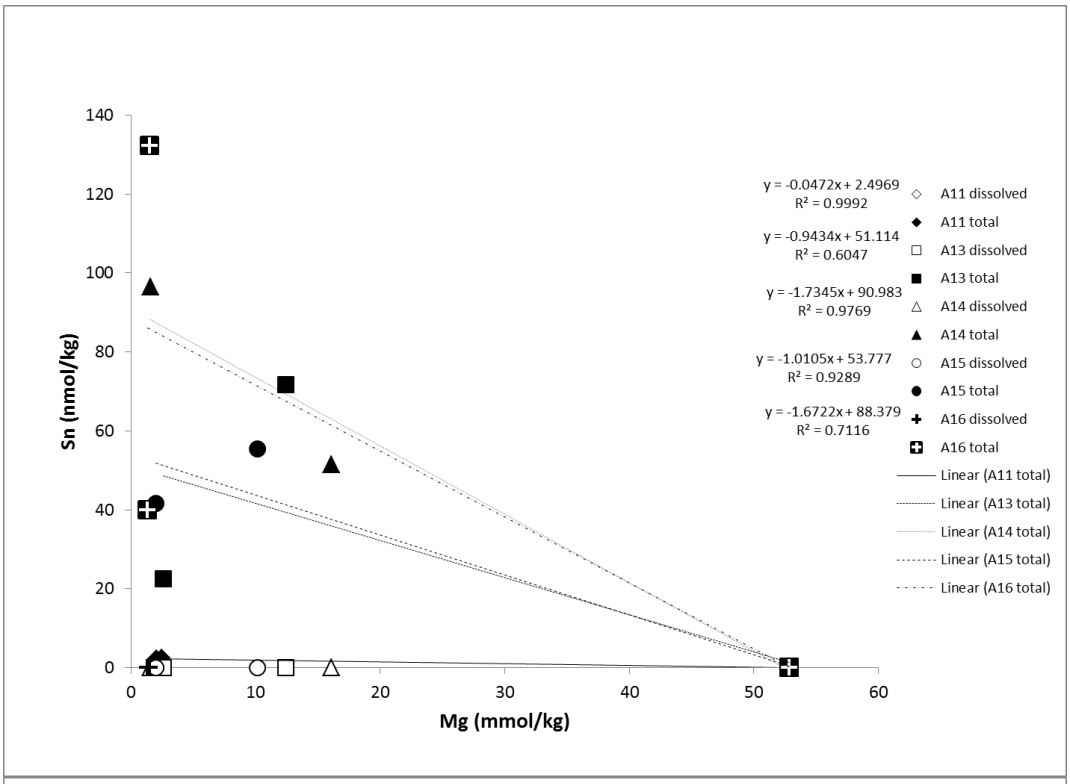
Sn (nmol/kg)
Mg (mmol/kg)
y = -0.0472x + 2.4969
R² = 0.9992
y = -0.9434x + 51.114
R² = 0.6047
y = -1.7345x + 90.983
R² = 0.9769
y = -1.0105x + 53.777
R² = 0.9289
y = -1.6722x + 88.379
R² = 0.7116
A11 dissolved
A11 total
A13 dissolved
A13 total
A14 dissolved
A14 total
A15 dissolved
A15 total
A16 dissolved
A16 total
Linear (A11 total)
Linear (A13 total)
Linear (A14 total)
Linear (A15 total)
Linear (A16 total)

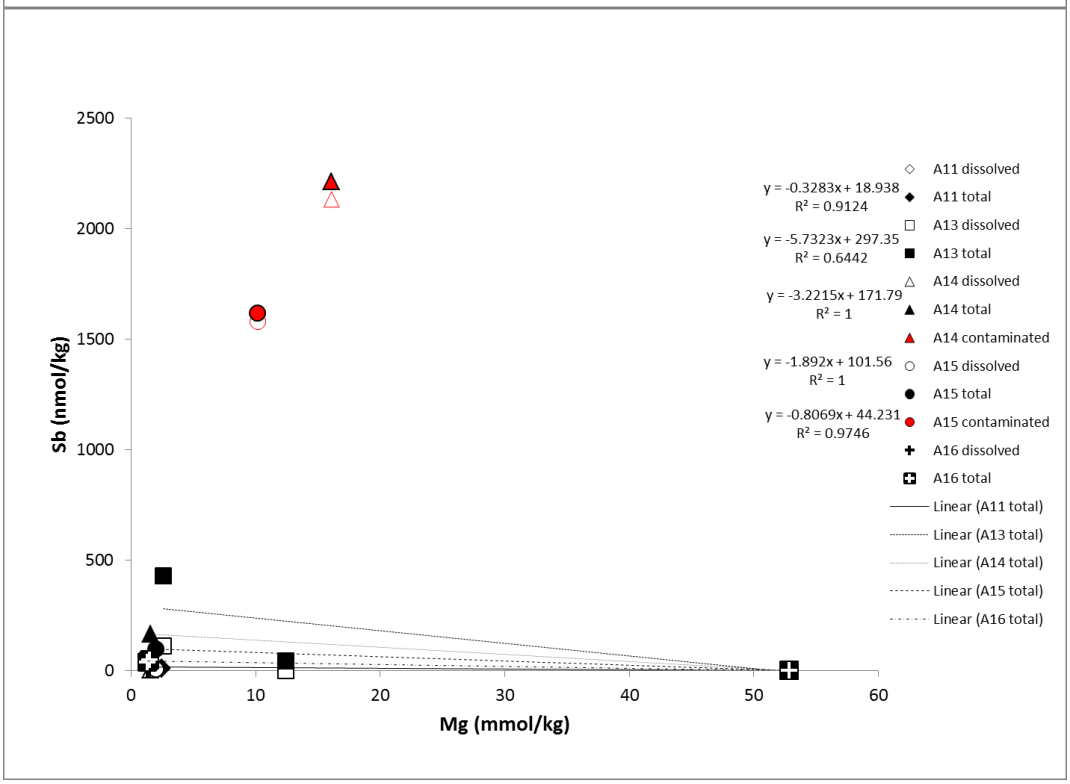
Sb (nmol/kg)
Mg (mmol/kg)
y = -0.3283x + 18.938
R² = 0.9124
y = -5.7323x + 297.35
R² = 0.6442
y = -3.2215x + 171.79
R² = 1
y = -1.892x + 101.56
R² = 1
y = -0.8069x + 44.231
R² = 0.9746
A11 dissolved
A11 total
A13 dissolved
A13 total
A14 dissolved
A14 total
A14 contaminated
A15 dissolved
A15 total
A15 contaminated
A16 dissolved
A16 total
Linear (A11 total)
Linear (A13 total)
Linear (A14 total)
Linear (A15 total)
Linear (A16 total)

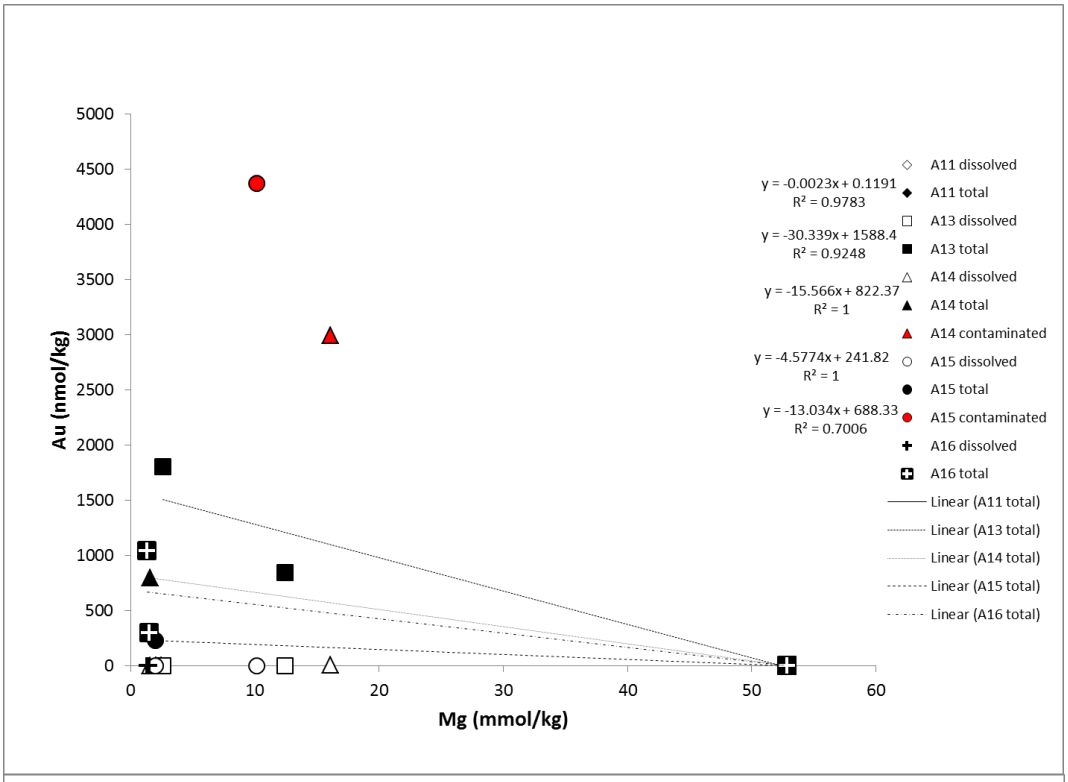
Au (nmol/kg)
Mg (mmol/kg)
y = -0.0023x + 0.1191
R² = 0.9783
y = -30.339x + 1588.4
R² = 0.9248
y = -15.566x + 822.37
R² = 1
y = -4.5774x + 241.82
R² = 1
y = -13.034x + 688.33
R² = 0.7006
A11 dissolved
A11 total
A13 dissolved
A13 total
A14 dissolved
A14 total
A14 contaminated
A15 dissolved
A15 total
A15 contaminated
A16 dissolved
A16 total
Linear (A11 total)
Linear (A13 total)
Linear (A14 total)
Linear (A15 total)
Linear (A16 total)

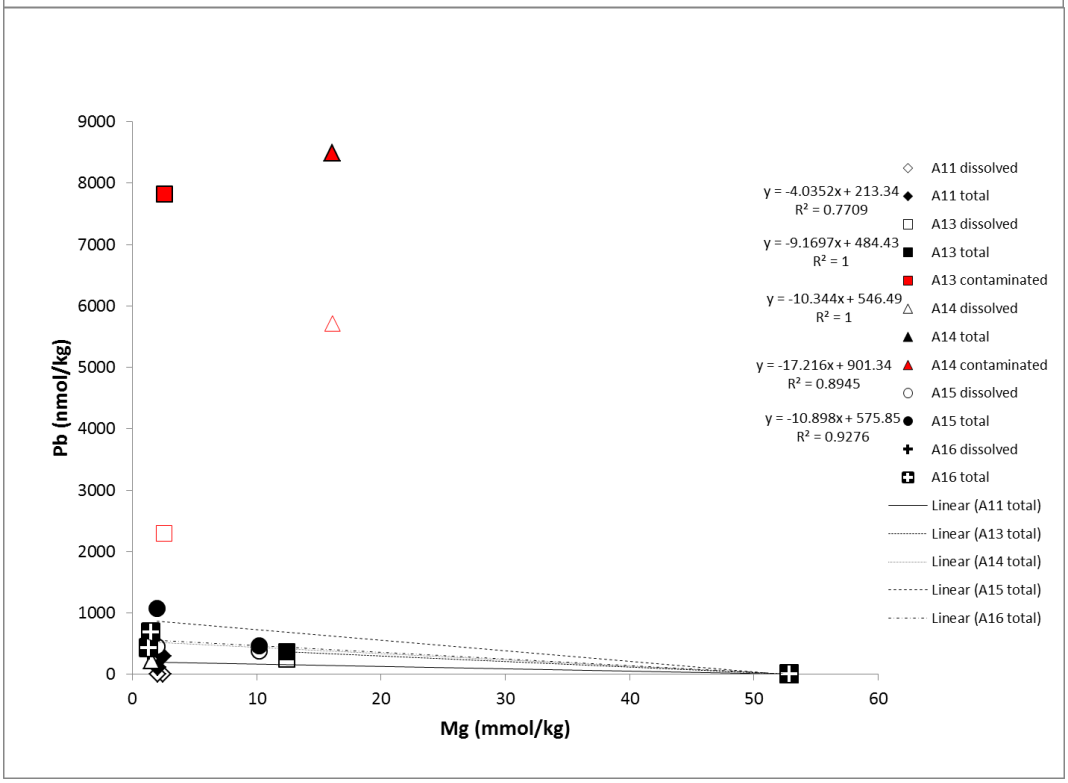
Pb (nmol/kg)
Mg (mmol/kg)
y = -4.0352x + 213.34
R² = 0.7709
y = -9.1697x + 484.43
R² = 1
y = -10.344x + 546.49
R² = 1
y = -17.216x + 901.34
R² = 0.8945
y = -10.898x + 575.85
R² = 0.9276
A11 dissolved
A11 total
A13 dissolved
A13 total
A13 contaminated
A14 dissolved
A14 total
A14 contaminated
A15 dissolved
A15 total
A16 dissolved
A16 total
Linear (A11 total)
Linear (A13 total)
Linear (A14 total)
Linear (A15 total)
Linear (A16 total)

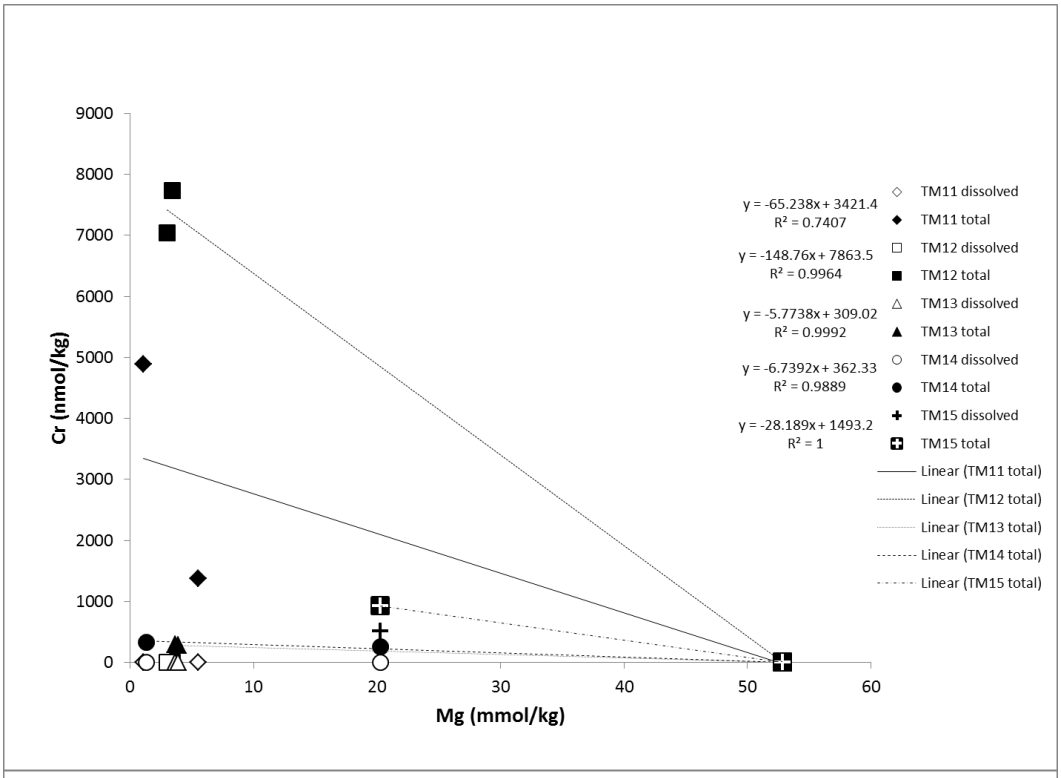
Cr (nmol/kg)
Mg (mmol/kg)
y = -65.238x + 3421.4
R² = 0.7407
y = -148.76x + 7863.5
R² = 0.9964
y = -5.7738x + 309.02
R² = 0.9992
y = -6.7392x + 362.33
R² = 0.9889
y = -28.189x + 1493.2
R² = 1
TM11 dissolved
TM11 total
TM12 dissolved
TM12 total
TM13 dissolved
TM13 total
TM14 dissolved
TM14 total
TM15 dissolved
TM15 total
Linear (TM11 total)
Linear (TM12 total)
Linear (TM13 total)
Linear (TM14 total)
Linear (TM15 total)

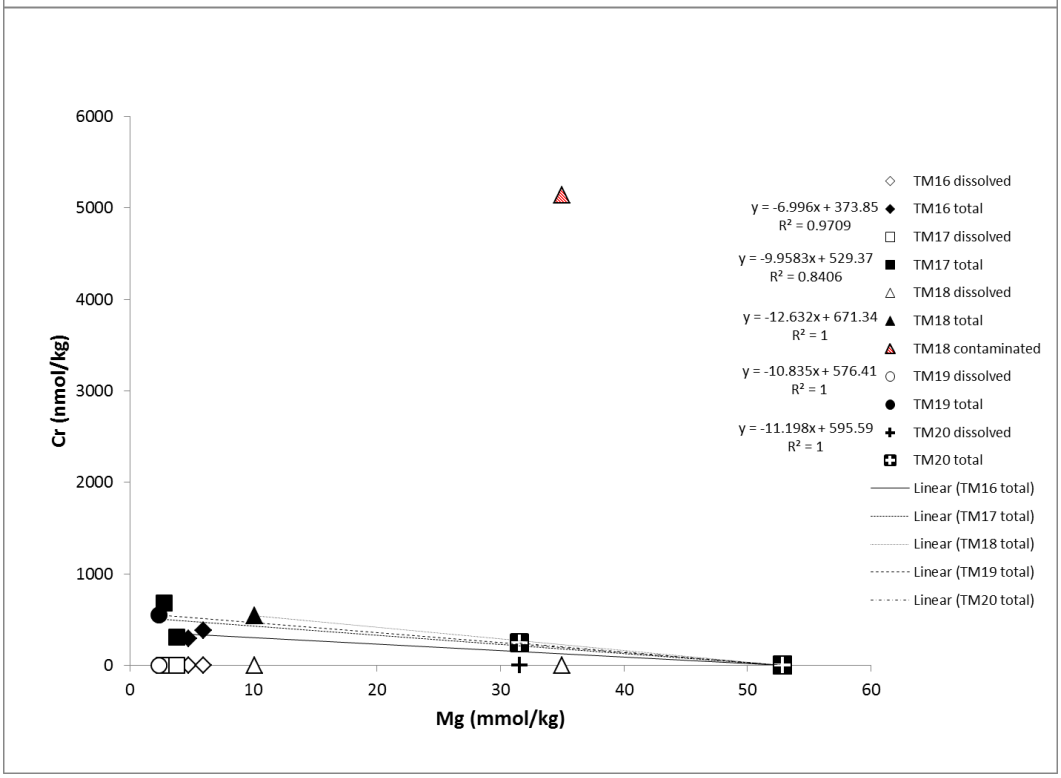
Cr (nmol/kg)
Mg (mmol/kg)
y = -6.996x + 373.85
R² = 0.9709
y = -9.9583x + 529.37
R² = 0.8406
y = -12.632x + 671.34
R² = 1
y = -10.835x + 576.41
R² = 1
y = -11.198x + 595.59
R² = 1
TM16 dissolved
TM16 total
TM17 dissolved
TM17 total
TM18 dissolved
TM18 total
TM18 contaminated
TM19 dissolved
TM19 total
TM20 dissolved
TM20 total
Linear (TM16 total)
Linear (TM17 total)
Linear (TM18 total)
Linear (TM19 total)
Linear (TM20 total)

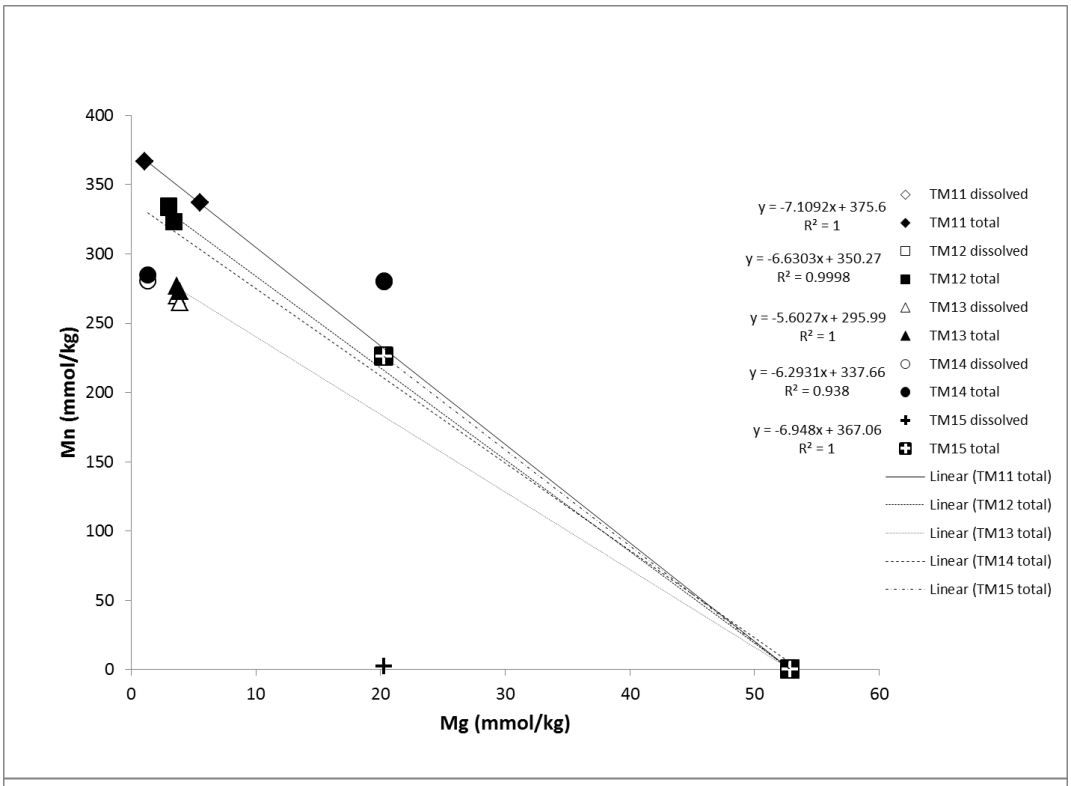
Mn (mmol/kg)
Mg (mmol/kg)
y = -7.1092x + 375.6
R² = 1
y = -6.6303x + 350.27
R² = 0.9998
y = -5.6027x + 295.99
R² = 1
y = -6.2931x + 337.66
R² = 0.938
y = -6.948x + 367.06
R² = 1
TM11 dissolved
TM11 total
TM12 dissolved
TM12 total
TM13 dissolved
TM13 total
TM14 dissolved
TM14 total
TM15 dissolved
TM15 total
Linear (TM11 total)
Linear (TM12 total)
Linear (TM13 total)
Linear (TM14 total)
Linear (TM15 total)

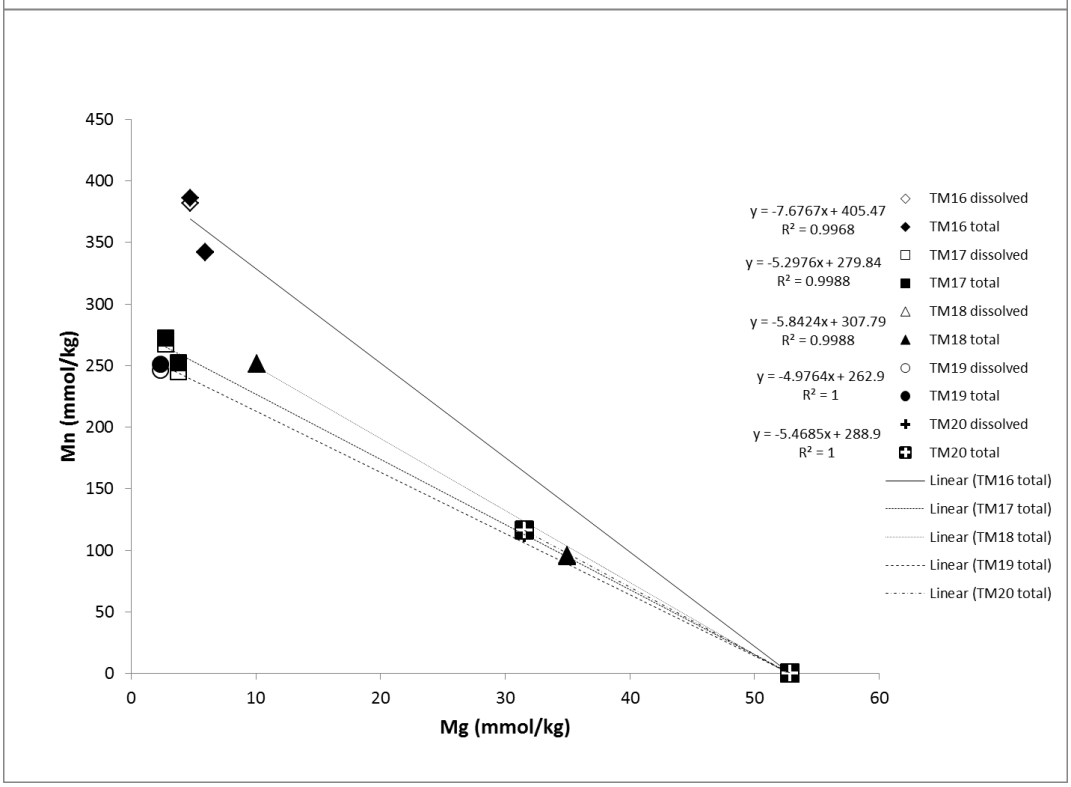
Mn (mmol/kg)
Mg (mmol/kg)
y = -7.6767x + 405.47
R² = 0.9968
y = -5.2976x + 279.84
R² = 0.9988
y = -5.8424x + 307.79
R² = 0.9988
y = -4.9764x + 262.9
R² = 1
y = -5.4685x + 288.9
R² = 1
TM16 dissolved
TM16 total
TM17 dissolved
TM17 total
TM18 dissolved
TM18 total
TM19 dissolved
TM19 total
TM20 dissolved
TM20 total
Linear (TM16 total)
Linear (TM17 total)
Linear (TM18 total)
Linear (TM19 total)
Linear (TM20 total)

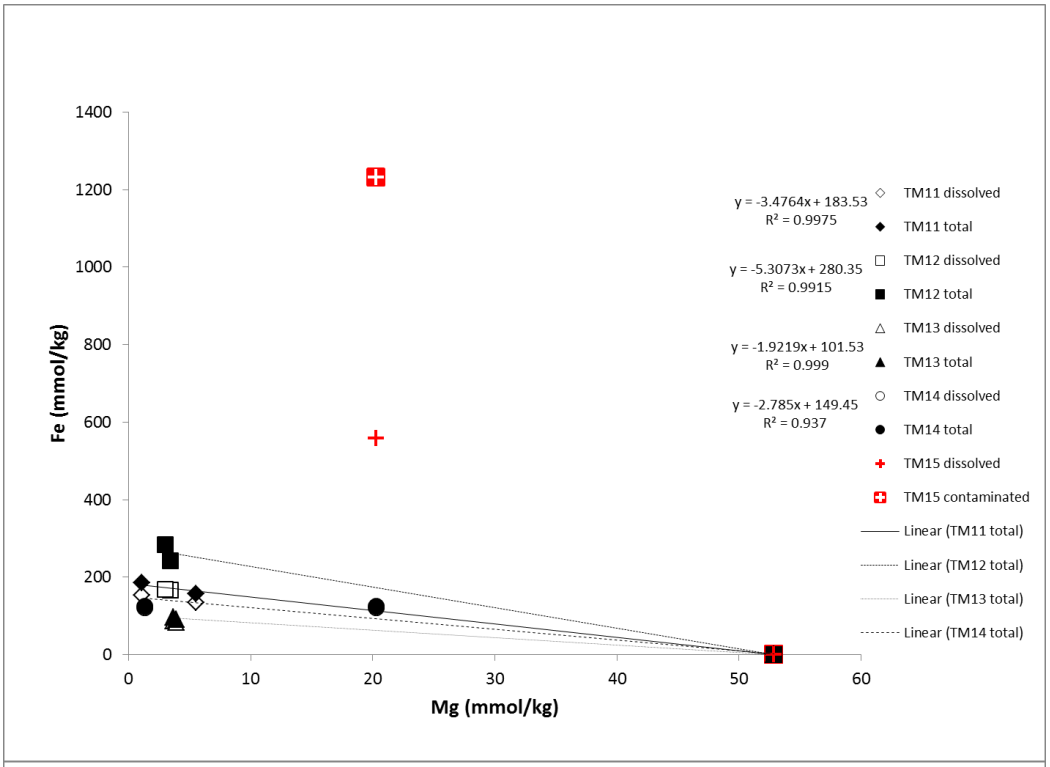
Fe (mmol/kg)
Mg (mmol/kg)
y = -3.4764x + 183.53
R² = 0.9975
y = -5.3073x + 280.35
R² = 0.9915
y = -1.9219x + 101.53
R² = 0.999
y = -2.785x + 149.45
R² = 0.937
TM11 dissolved
TM11 total
TM12 dissolved
TM12 total
TM13 dissolved
TM13 total
TM14 dissolved
TM14 total
TM15 dissolved
TM15 contaminated
Linear (TM11 total)
Linear (TM12 total)
Linear (TM13 total)
Linear (TM14 total)

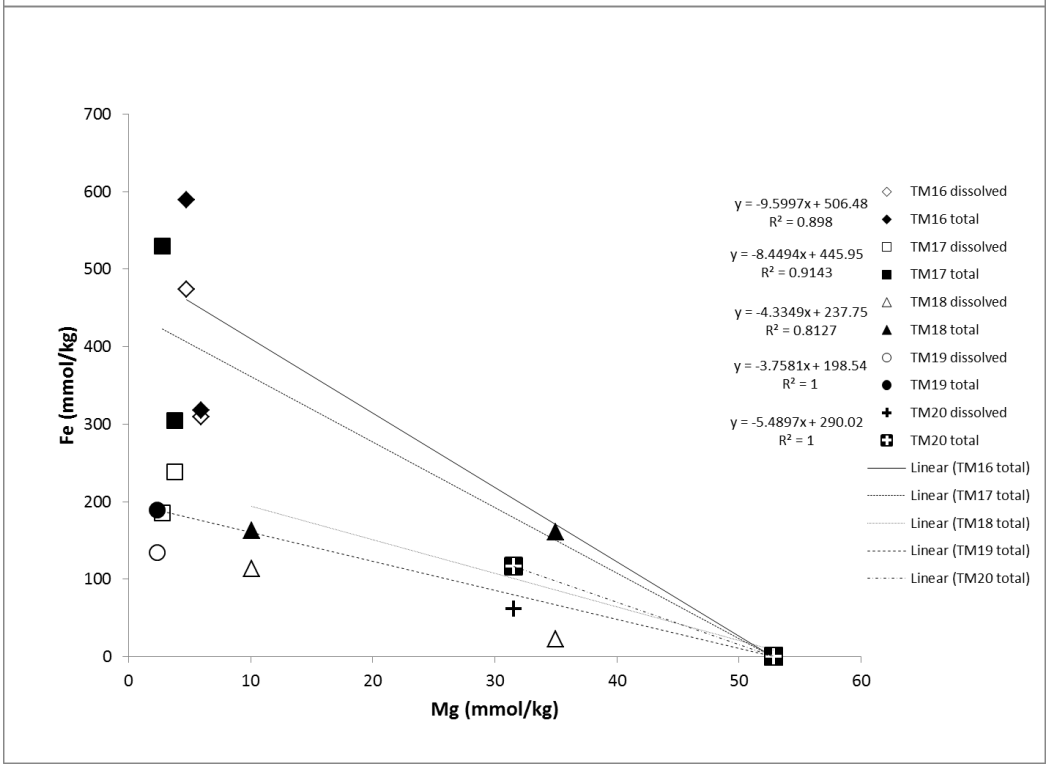
Fe (mmol/kg)
Mg (mmol/kg)
y = -9.5997x + 506.48
R² = 0.898
y = -8.4494x + 445.95
R² = 0.9143
y = -4.3349x + 237.75
R² = 0.8127
y = -3.7581x + 198.54
R² = 1
y = -5.4897x + 290.02
R² = 1
TM16 dissolved
TM16 total
TM17 dissolved
TM17 total
TM18 dissolved
TM18 total
TM19 dissolved
TM19 total
TM20 dissolved
TM20 total
Linear (TM16 total)
Linear (TM17 total)
Linear (TM18 total)
Linear (TM19 total)
Linear (TM20 total)

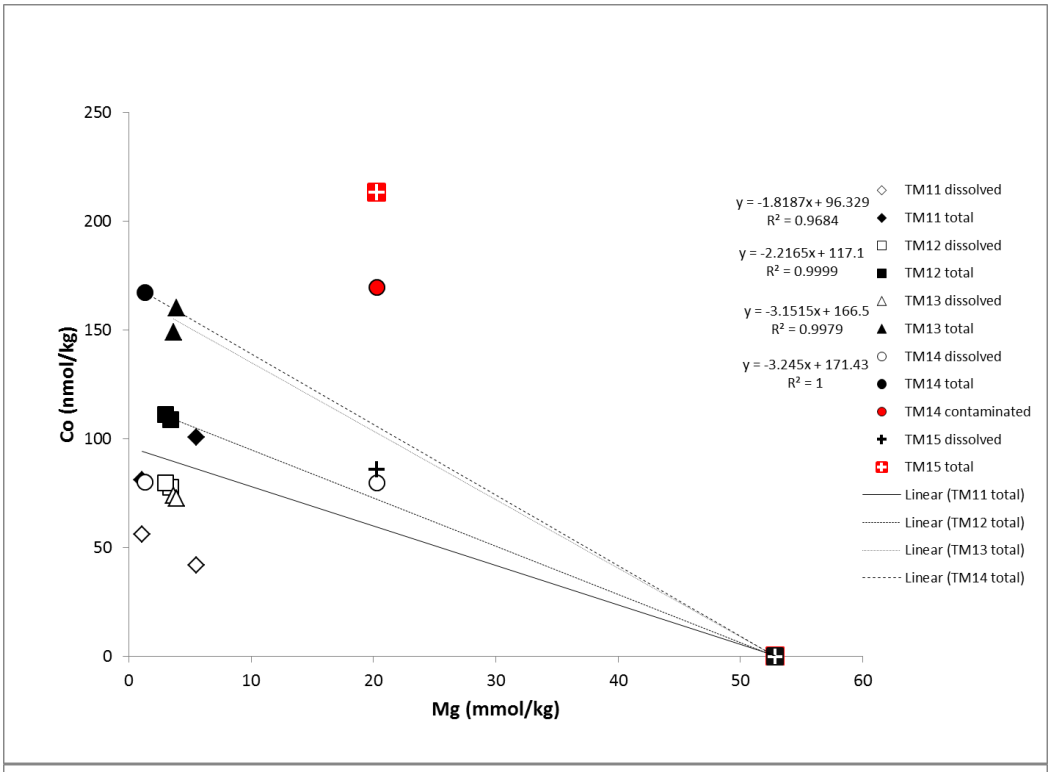
Co (nmol/kg)
Mg (mmol/kg)
y = -1.8187x + 96.329
R² = 0.9684
y = -2.2165x + 117.1
R² = 0.9999
y = -3.1515x + 166.5
R² = 0.9979
y = -3.245x + 171.43
R² = 1
TM11 dissolved
TM11 total
TM12 dissolved
TM12 total
TM13 dissolved
TM13 total
TM14 dissolved
TM14 total
TM14 contaminated
TM15 dissolved
TM15 total
Linear (TM11 total)
Linear (TM12 total)
Linear (TM13 total)
Linear (TM14 total)

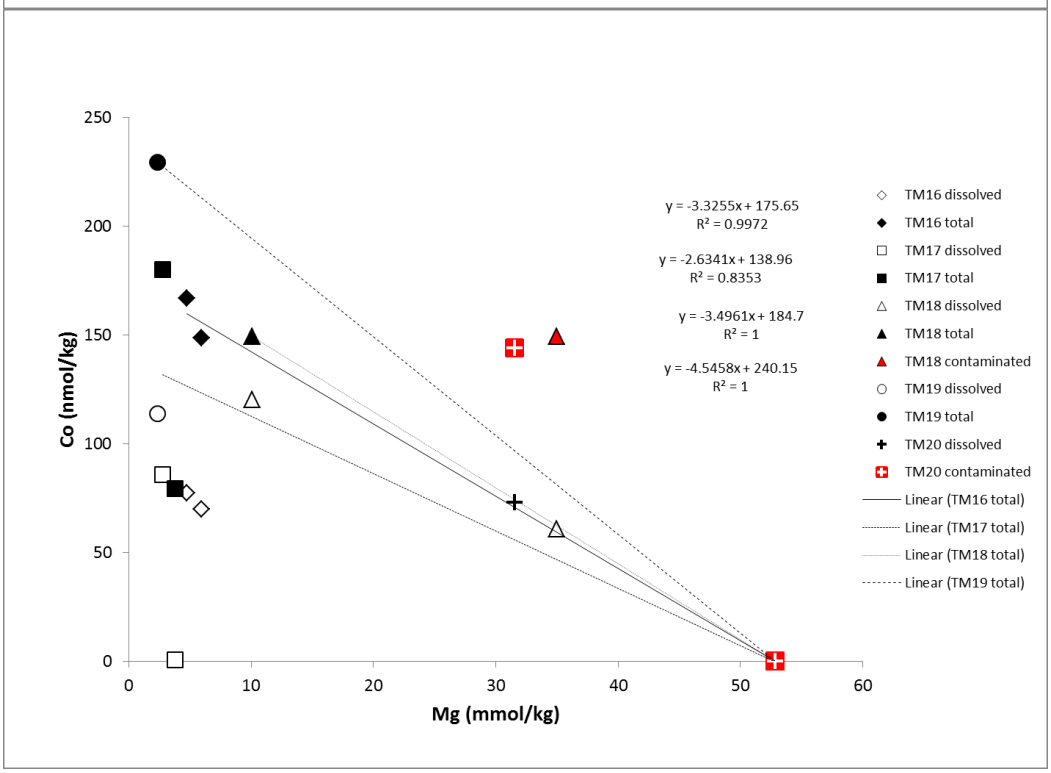
Co (nmol/kg)
Mg (mmol/kg)
y = -3.3255x + 175.65
R² = 0.9972
y = -2.6341x + 138.96
R² = 0.8353
y = -3.4961x + 184.7
R² = 1
y = -4.5458x + 240.15
R² = 1
TM16 dissolved
TM16 total
TM17 dissolved
TM17 total
TM18 dissolved
TM18 total
TM18 contaminated
TM19 dissolved
TM19 total
TM20 dissolved
TM20 contaminated
Linear (TM16 total)
Linear (TM17 total)
Linear (TM18 total)
Linear (TM19 total)

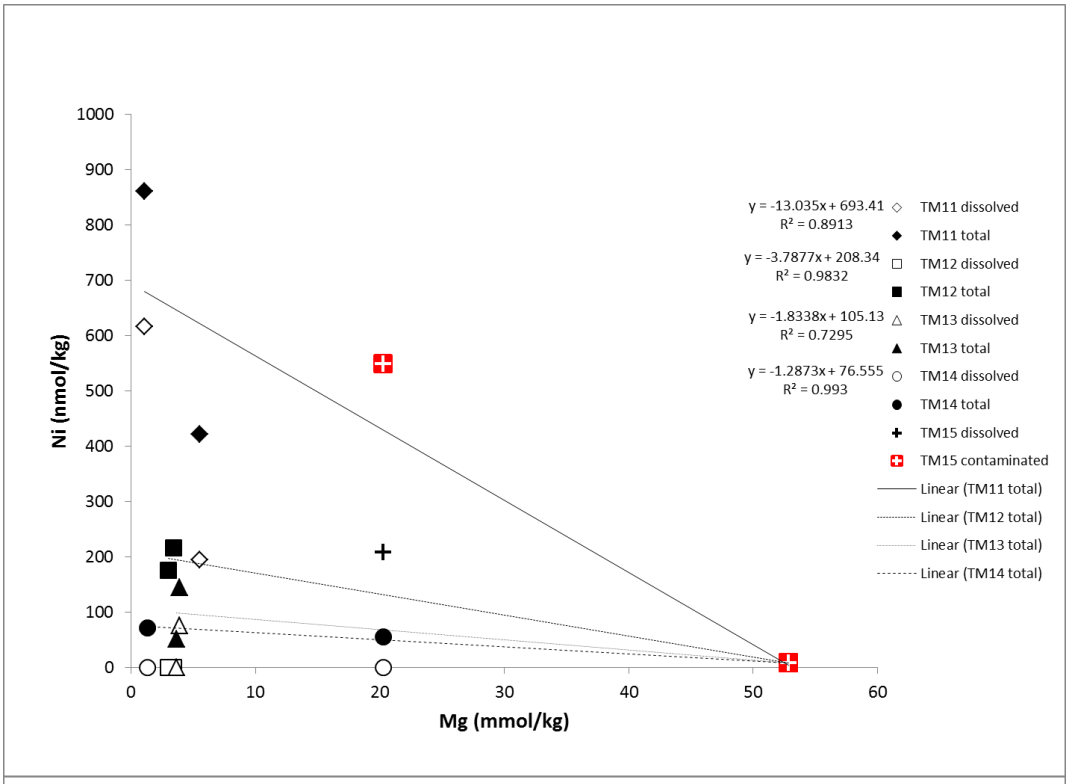
Ni (nmol/kg)
Mg (mmol/kg)
y = -13.035x + 693.41
R² = 0.8913
y = -3.7877x + 208.34
R² = 0.9832
y = -1.8338x + 105.13
R² = 0.7295
y = -1.2873x + 76.555
R² = 0.993
TM11 dissolved
TM11 total
TM12 dissolved
TM12 total
TM13 dissolved
TM13 total
TM14 dissolved
TM14 total
TM15 dissolved
TM15 contaminated
Linear (TM11 total)
Linear (TM12 total)
Linear (TM13 total)
Linear (TM14 total)

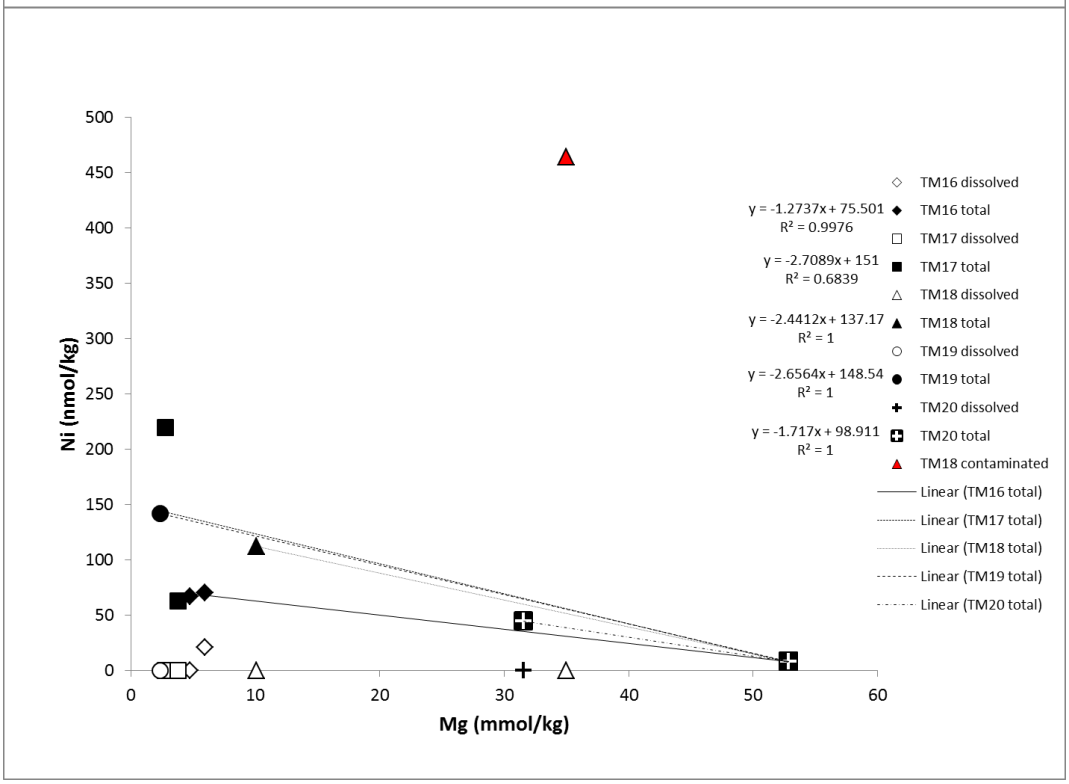
Ni (nmol/kg)
Mg (mmol/kg)
y = -1.2737x + 75.501
R² = 0.9976
y = -2.7089x + 151
R² = 0.6839
y = -2.4412x + 137.17
R² = 1
y = -2.6564x + 148.54
R² = 1
y = -1.717x + 98.911
R² = 1
TM16 dissolved
TM16 total
TM17 dissolved
TM17 total
TM18 dissolved
TM18 total
TM19 dissolved
TM19 total
TM20 dissolved
TM20 total
TM18 contaminated
Linear (TM16 total)
Linear (TM17 total)
Linear (TM18 total)
Linear (TM19 total)
Linear (TM20 total)

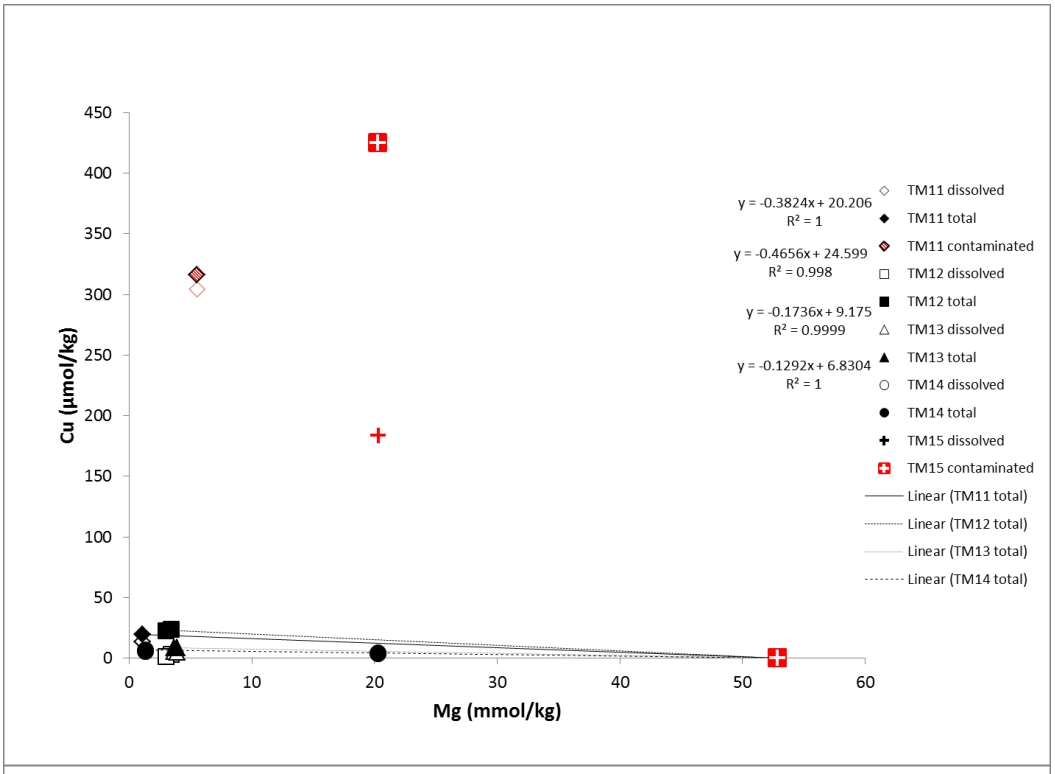
Cu (µmol/kg)
Mg (mmol/kg)
y = -0.3824x + 20.206
R² = 1
y = -0.4656x + 24.599
R² = 0.998
y = -0.1736x + 9.175
R² = 0.9999
y = -0.1292x + 6.8304
R² = 1
TM11 dissolved
TM11 total
TM11 contaminated
TM12 dissolved
TM12 total
TM13 dissolved
TM13 total
TM14 dissolved
TM14 total
TM15 dissolved
TM15 contaminated
Linear (TM11 total)
Linear (TM12 total)
Linear (TM13 total)
Linear (TM14 total)

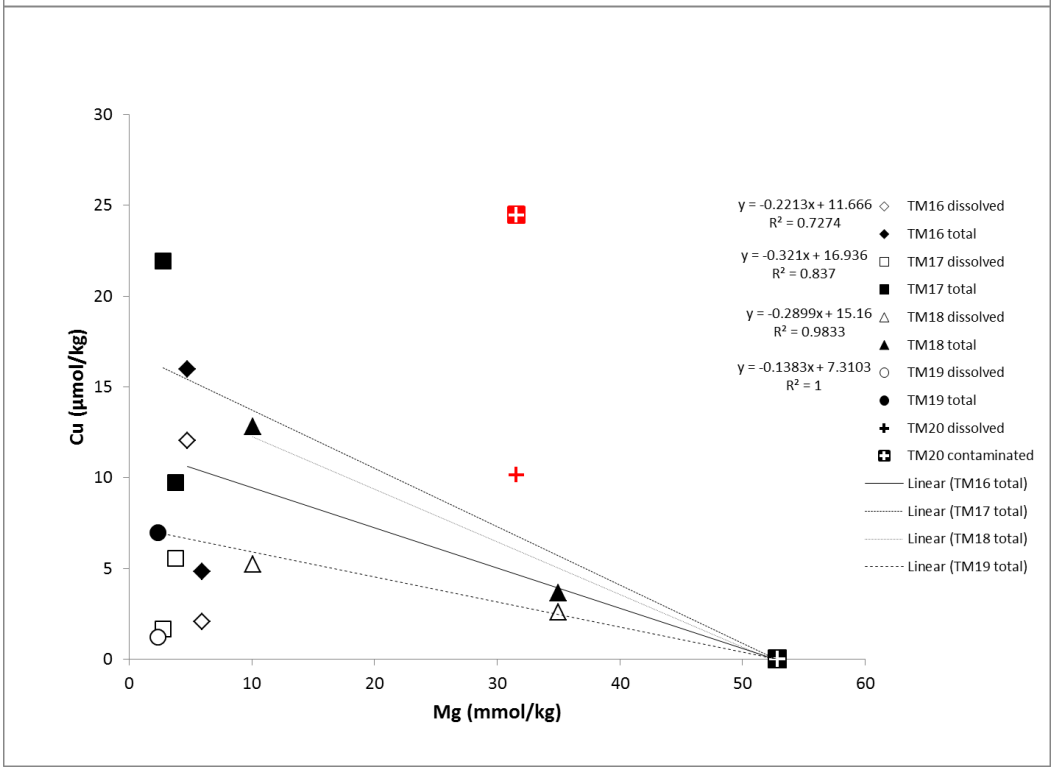
Cu (µmol/kg)
Mg (mmol/kg)
y = -0.2213x + 11.666
R² = 0.7274
y = -0.321x + 16.936
R² = 0.837
y = -0.2899x + 15.16
R² = 0.9833
y = -0.1383x + 7.3103
R² = 1
TM16 dissolved
TM16 total
TM17 dissolved
TM17 total
TM18 dissolved
TM18 total
TM19 dissolved
TM19 total
TM20 dissolved
TM20 contaminated
Linear (TM16 total)
Linear (TM17 total)
Linear (TM18 total)
Linear (TM19 total)

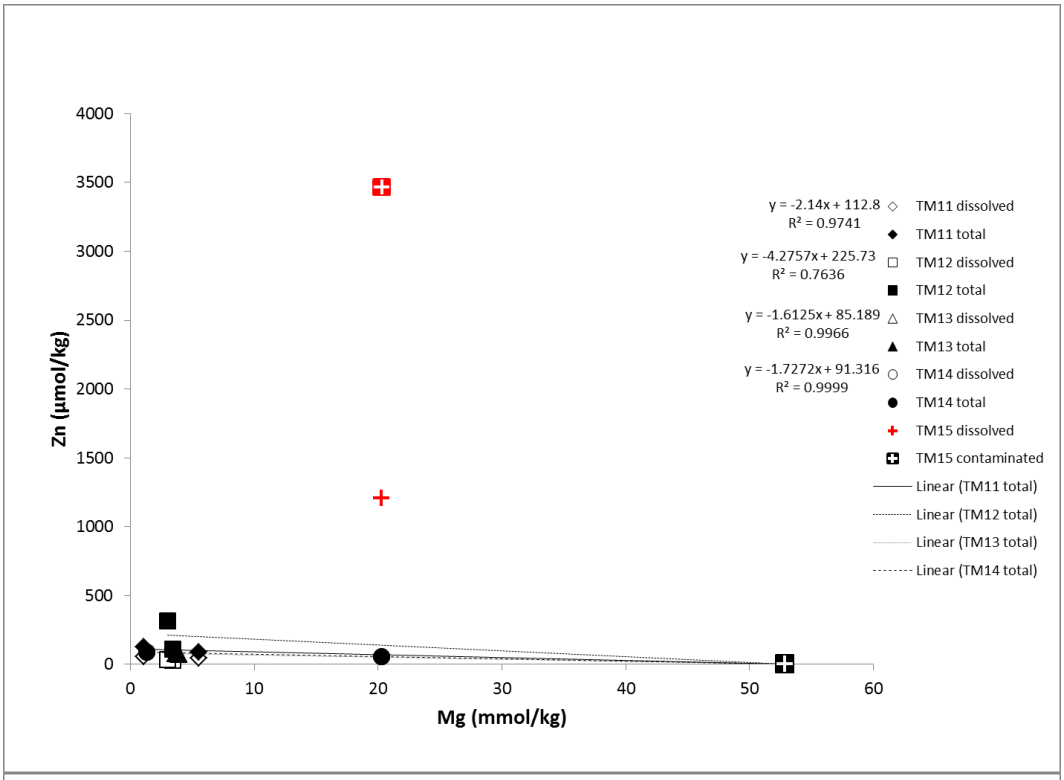
Zn (µmol/kg)
Mg (mmol/kg)
y = -2.14x + 112.8
R² = 0.9741
y = -4.2757x + 225.73
R² = 0.7636
y = -1.6125x + 85.189
R² = 0.9966
y = -1.7272x + 91.316
R² = 0.9999
TM11 dissolved
TM11 total
TM12 dissolved
TM12 total
TM13 dissolved
TM13 total
TM14 dissolved
TM14 total
TM15 dissolved
TM15 contaminated
Linear (TM11 total)
Linear (TM12 total)
Linear (TM13 total)
Linear (TM14 total)

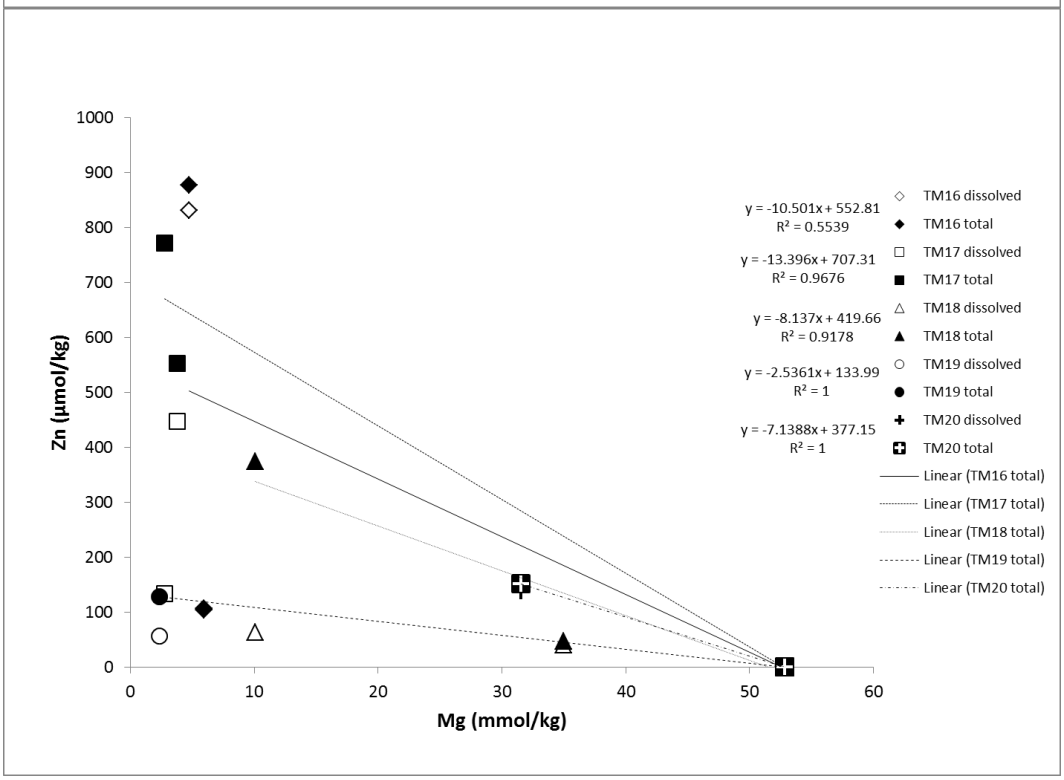
Zn (µmol/kg)
Mg (mmol/kg)
y = -10.501x + 552.81
R² = 0.5539
y = -13.396x + 707.31
R² = 0.9676
y = -8.137x + 419.66
R² = 0.9178
y = -2.5361x + 133.99
R² = 1
y = -7.1388x + 377.15
R² = 1
TM16 dissolved
TM16 total
TM17 dissolved
TM17 total
TM18 dissolved
TM18 total
TM19 dissolved
TM19 total
TM20 dissolved
TM20 total
Linear (TM16 total)
Linear (TM17 total)
Linear (TM18 total)
Linear (TM19 total)
Linear (TM20 total)

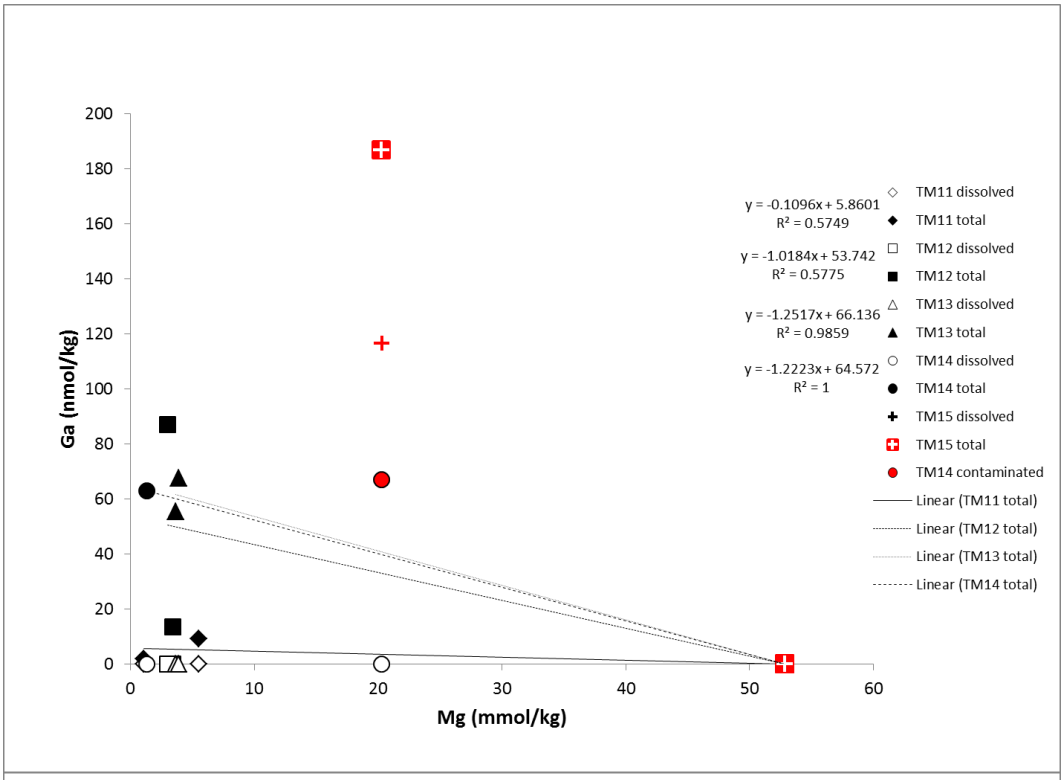
Ga (nmol/kg)
Mg (mmol/kg)
y = -0.1096x + 5.8601
R² = 0.5749
y = -1.0184x + 53.742
R² = 0.5775
y = -1.2517x + 66.136
R² = 0.9859
y = -1.2223x + 64.572
R² = 1
TM11 dissolved
TM11 total
TM12 dissolved
TM12 total
TM13 dissolved
TM13 total
TM14 dissolved
TM14 total
TM15 dissolved
TM15 total
TM14 contaminated
Linear (TM11 total)
Linear (TM12 total)
Linear (TM13 total)
Linear (TM14 total)

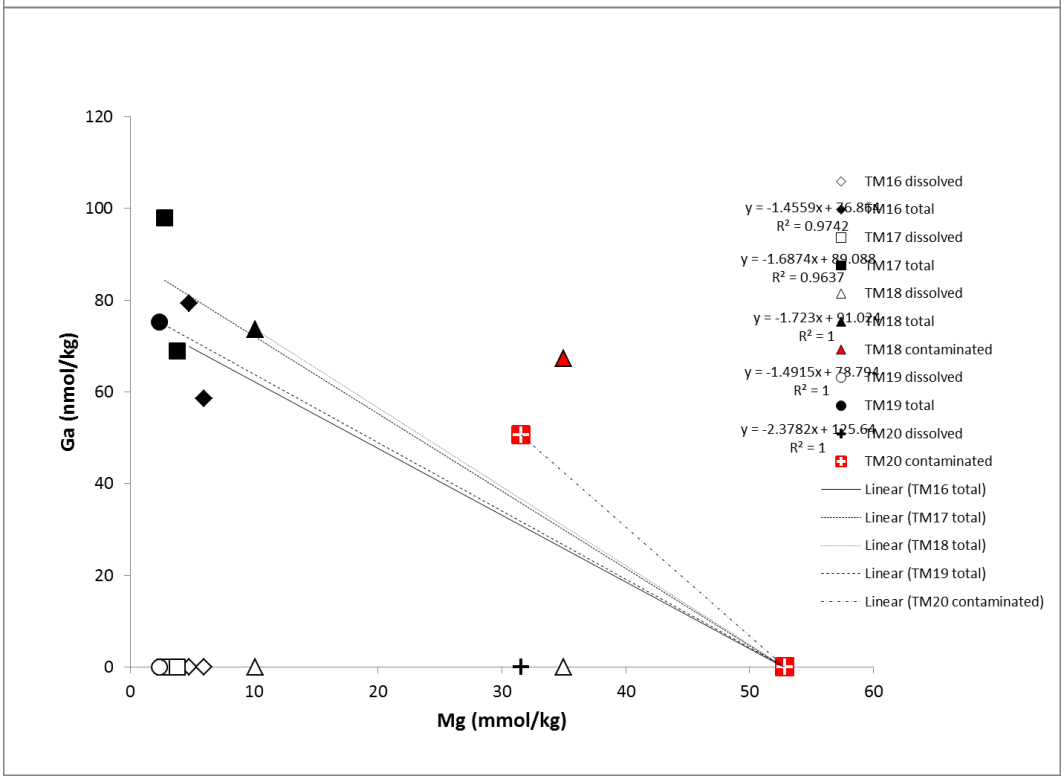
Ga (nmol/kg)
Mg (mmol/kg)
y = -1.4559x + 76.864
R² = 0.9742
y = -1.6874x + 89.088
R² = 0.9637
y = -1.723x + 91.024
R² = 1
y = -1.4915x + 78.794
R² = 1
y = -2.3782x + 125.64
R² = 1
TM16 dissolved
TM16 total
TM17 dissolved
TM17 total
TM18 dissolved
TM18 total
TM18 contaminated
TM19 dissolved
TM19 total
TM20 dissolved
TM20 contaminated
Linear (TM16 total)
Linear (TM17 total)
Linear (TM18 total)
Linear (TM19 total)
Linear (TM20 contaminated)

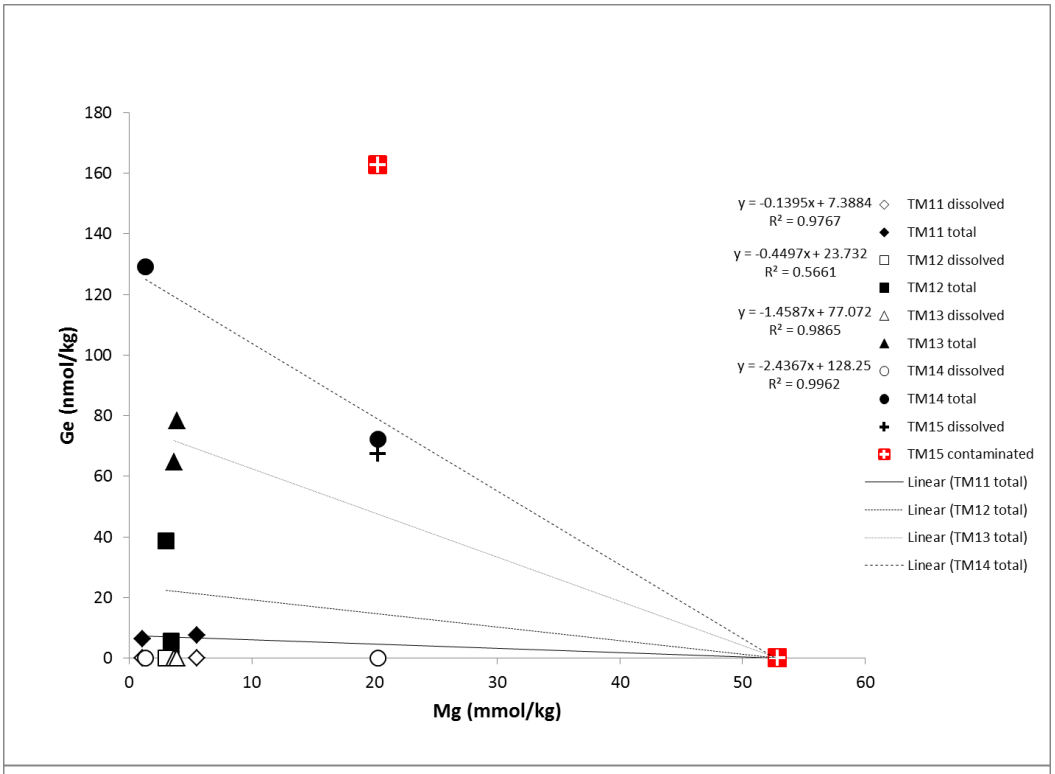
Ge (nmol/kg)
Mg (mmol/kg)
0
20
40
60
80
100
120
140
160
180
0
10
20
30
40
50
60
y = -0.1395x + 7.3884
R² = 0.9767
y = -0.4497x + 23.732
R² = 0.5661
y = -1.4587x + 77.072
R² = 0.9865
y = -2.4367x + 128.25
R² = 0.9962
TM11 dissolved
TM11 total
TM12 dissolved
TM12 total
TM13 dissolved
TM13 total
TM14 dissolved
TM14 total
TM15 dissolved
TM15 contaminated
Linear (TM11 total)
Linear (TM12 total)
Linear (TM13 total)
Linear (TM14 total)

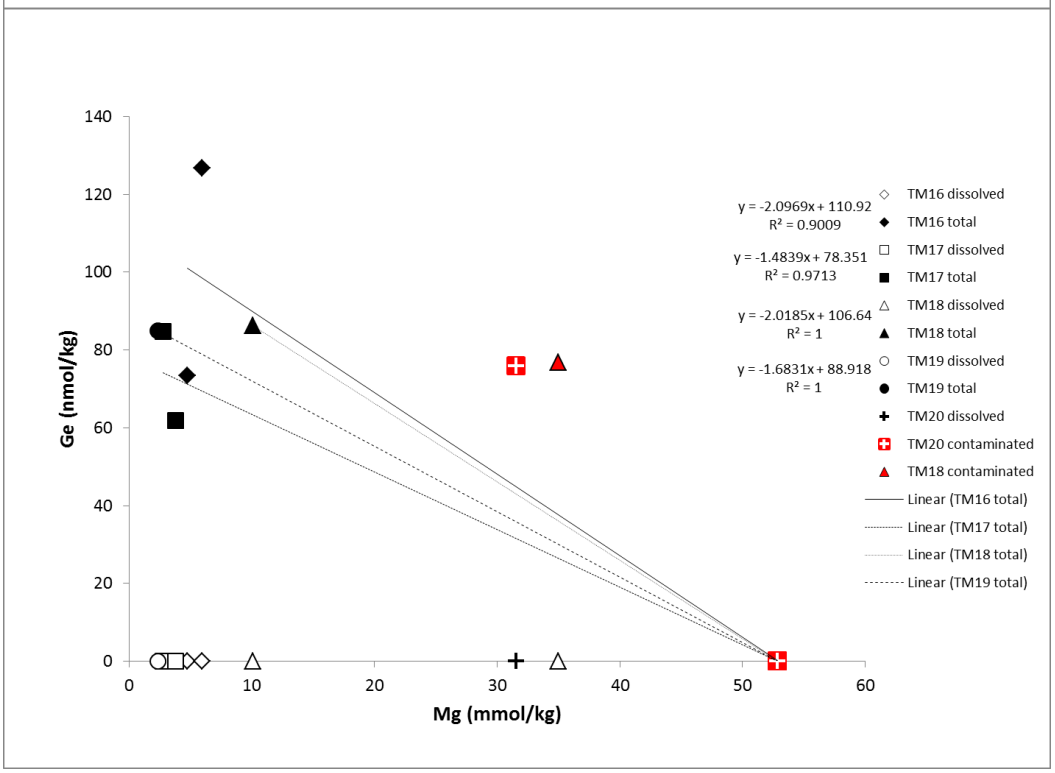
Ge (nmol/kg)
Mg (mmol/kg)
0
20
40
60
80
100
120
140
0
10
20
30
40
50
60
y = -2.0969x + 110.92
R² = 0.9009
y = -1.4839x + 78.351
R² = 0.9713
y = -2.0185x + 106.64
R² = 1
y = -1.6831x + 88.918
R² = 1
TM16 dissolved
TM16 total
TM17 dissolved
TM17 total
TM18 dissolved
TM18 total
TM19 dissolved
TM19 total
TM20 dissolved
TM20 contaminated
TM18 contaminated
Linear (TM16 total)
Linear (TM17 total)
Linear (TM18 total)
Linear (TM19 total)

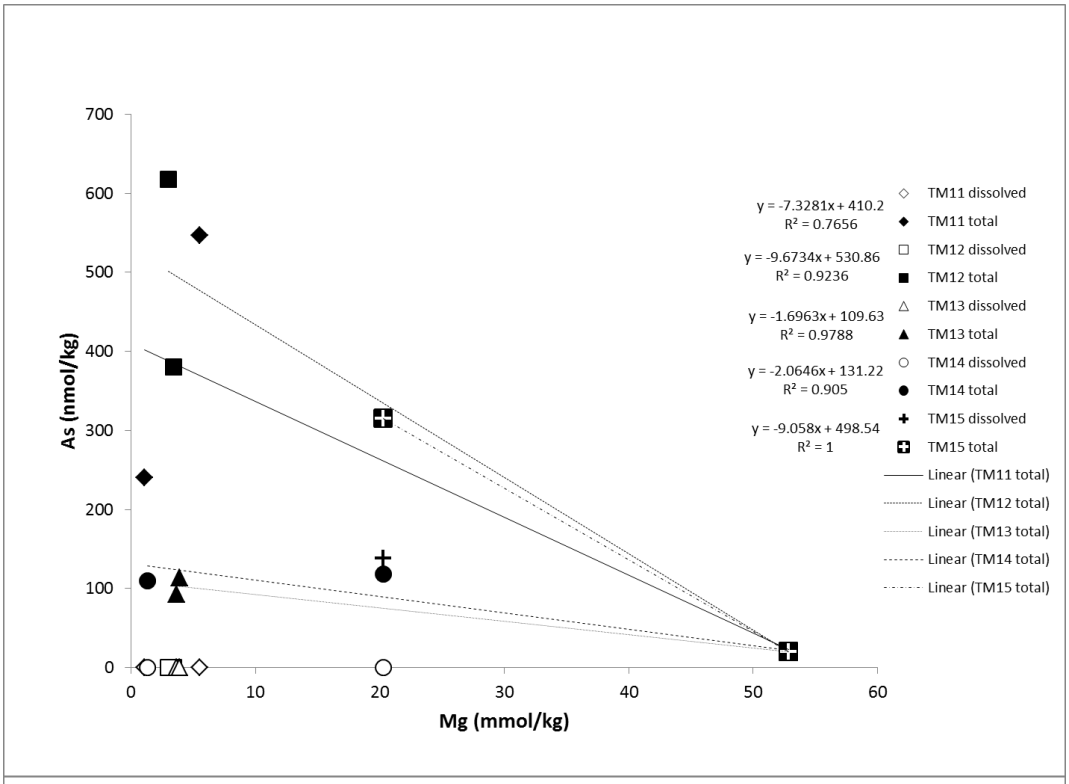
As (nmol/kg)
Mg (mmol/kg)
y = -7.3281x + 410.2
R² = 0.7656
y = -9.6734x + 530.86
R² = 0.9236
y = -1.6963x + 109.63
R² = 0.9788
y = -2.0646x + 131.22
R² = 0.905
y = -9.058x + 498.54
R² = 1
TM11 dissolved
TM11 total
TM12 dissolved
TM12 total
TM13 dissolved
TM13 total
TM14 dissolved
TM14 total
TM15 dissolved
TM15 total
Linear (TM11 total)
Linear (TM12 total)
Linear (TM13 total)
Linear (TM14 total)
Linear (TM15 total)

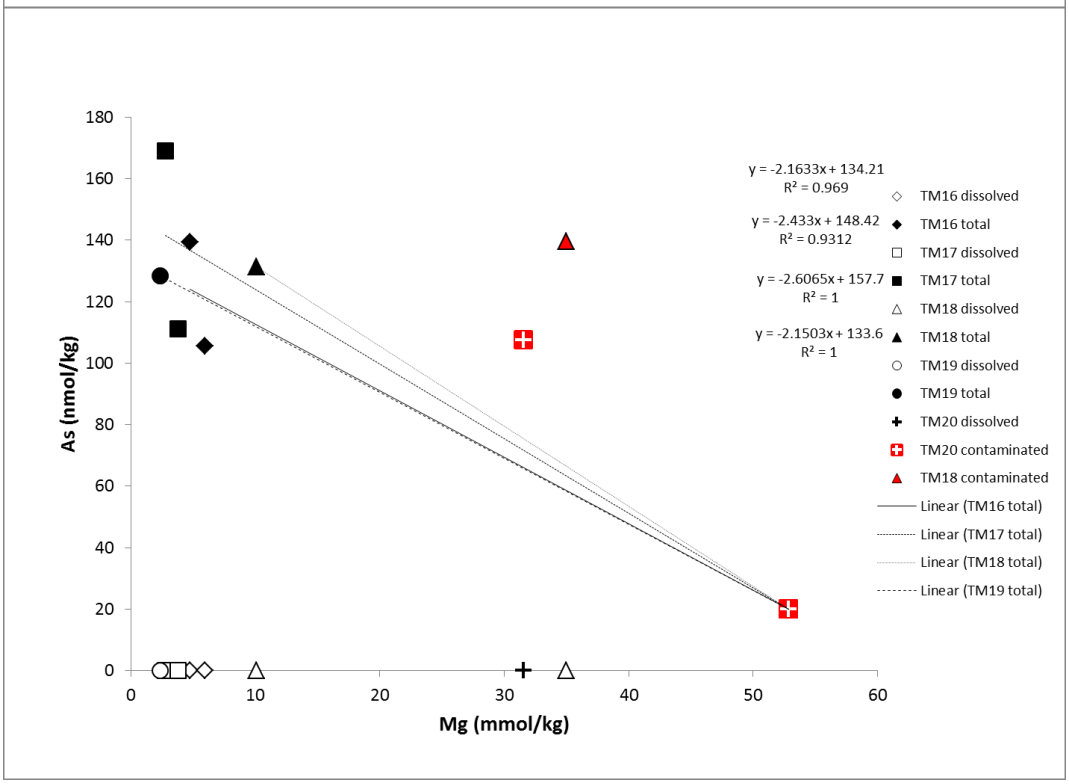
As (nmol/kg)
Mg (mmol/kg)
y = -2.1633x + 134.21
R² = 0.969
y = -2.433x + 148.42
R² = 0.9312
y = -2.6065x + 157.7
R² = 1
y = -2.1503x + 133.6
R² = 1
TM16 dissolved
TM16 total
TM17 dissolved
TM17 total
TM18 dissolved
TM18 total
TM19 dissolved
TM19 total
TM20 dissolved
TM20 contaminated
TM18 contaminated
Linear (TM16 total)
Linear (TM17 total)
Linear (TM18 total)
Linear (TM19 total)

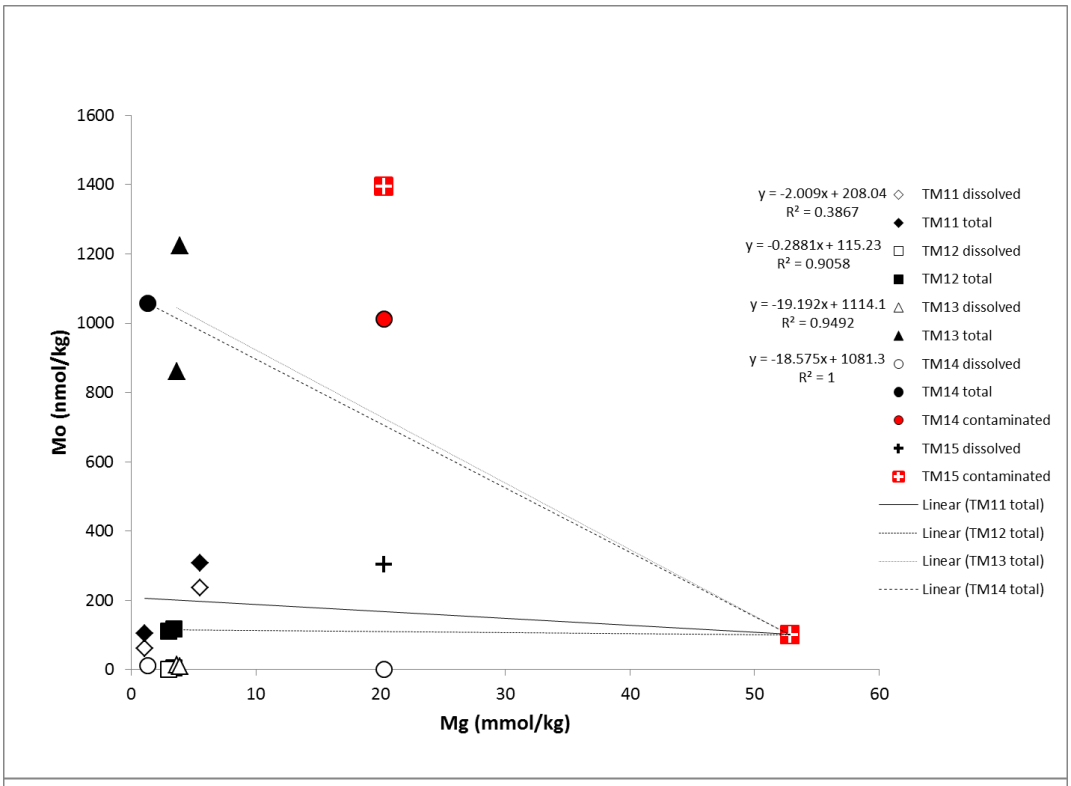
Mo (nmol/kg)
Mg (mmol/kg)
y = -2.009x + 208.04
R² = 0.3867
y = -0.2881x + 115.23
R² = 0.9058
y = -19.192x + 1114.1
R² = 0.9492
y = -18.575x + 1081.3
R² = 1
TM11 dissolved
TM11 total
TM12 dissolved
TM12 total
TM13 dissolved
TM13 total
TM14 dissolved
TM14 total
TM14 contaminated
TM15 dissolved
TM15 contaminated
Linear (TM11 total)
Linear (TM12 total)
Linear (TM13 total)
Linear (TM14 total)

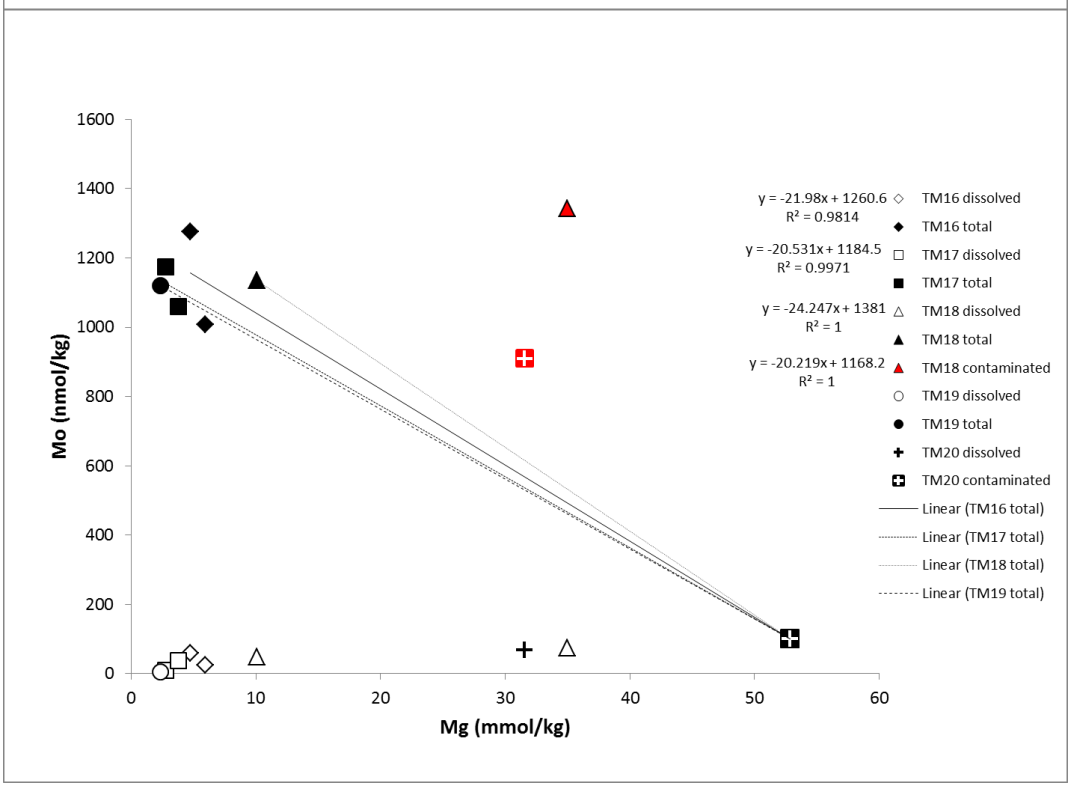
Mo (nmol/kg)
Mg (mmol/kg)
y = -21.98x + 1260.6
R² = 0.9814
y = -20.531x + 1184.5
R² = 0.9971
y = -24.247x + 1381
R² = 1
y = -20.219x + 1168.2
R² = 1
TM16 dissolved
TM16 total
TM17 dissolved
TM17 total
TM18 dissolved
TM18 total
TM18 contaminated
TM19 dissolved
TM19 total
TM20 dissolved
TM20 contaminated
Linear (TM16 total)
Linear (TM17 total)
Linear (TM18 total)
Linear (TM19 total)

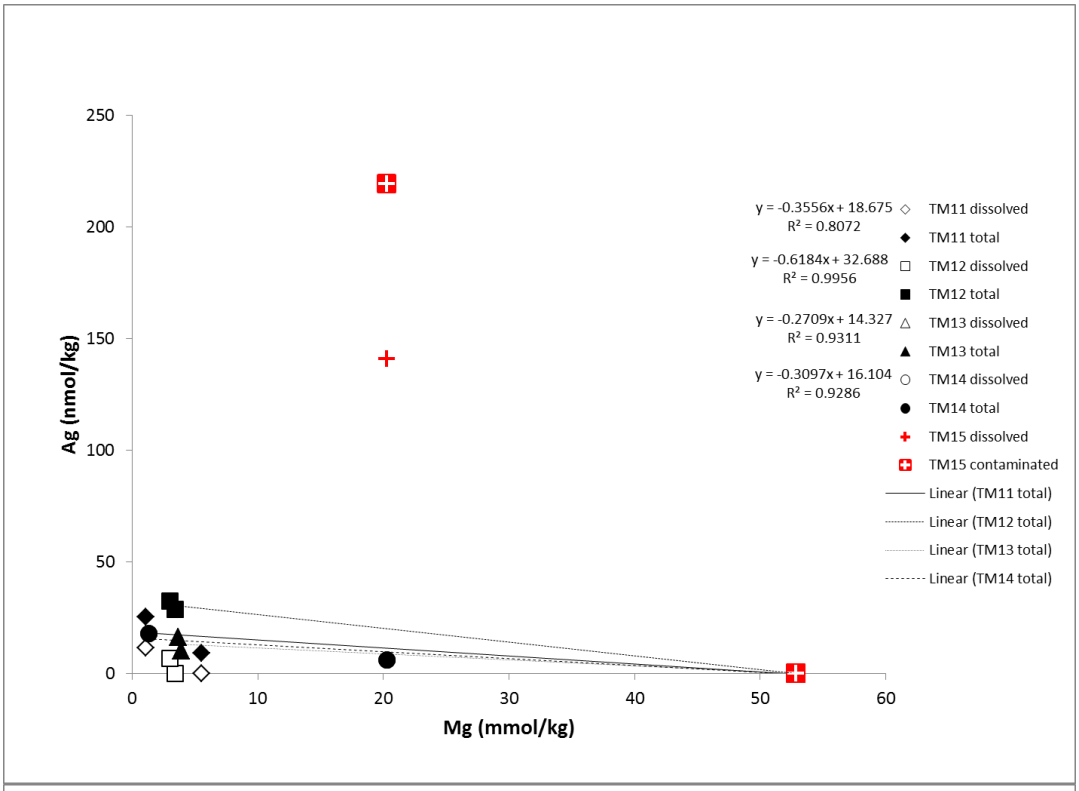
Ag (nmol/kg)
Mg (mmol/kg)
0
50
100
150
200
250
0
10
20
30
40
50
60
y = -0.3556x + 18.675
R² = 0.8072
y = -0.6184x + 32.688
R² = 0.9956
y = -0.2709x + 14.327
R² = 0.9311
y = -0.3097x + 16.104
R² = 0.9286
TM11 dissolved
TM11 total
TM12 dissolved
TM12 total
TM13 dissolved
TM13 total
TM14 dissolved
TM14 total
TM15 dissolved
TM15 contaminated
Linear (TM11 total)
Linear (TM12 total)
Linear (TM13 total)
Linear (TM14 total)

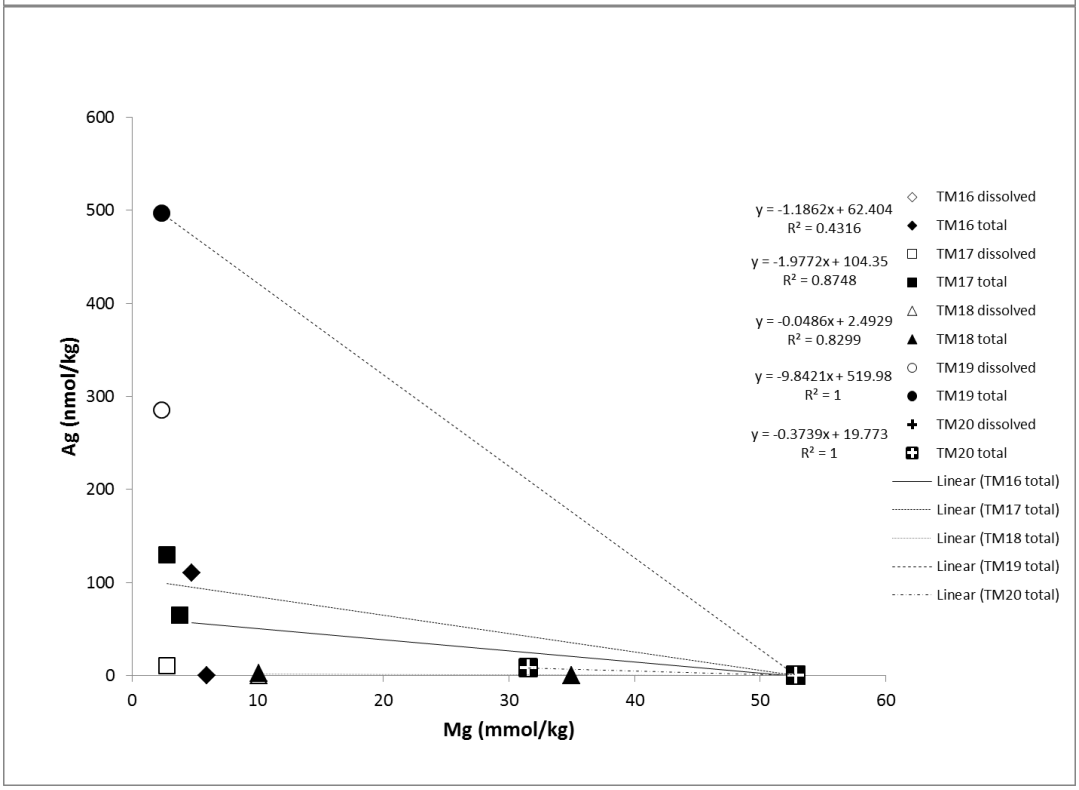
Ag (nmol/kg)
Mg (mmol/kg)
0
100
200
300
400
500
600
0
10
20
30
40
50
60
y = -1.1862x + 62.404
R² = 0.4316
y = -1.9772x + 104.35
R² = 0.8748
y = -0.0486x + 2.4929
R² = 0.8299
y = -9.8421x + 519.98
R² = 1
y = -0.3739x + 19.773
R² = 1
TM16 dissolved
TM16 total
TM17 dissolved
TM17 total
TM18 dissolved
TM18 total
TM19 dissolved
TM19 total
TM20 dissolved
TM20 total
Linear (TM16 total)
Linear (TM17 total)
Linear (TM18 total)
Linear (TM19 total)
Linear (TM20 total)

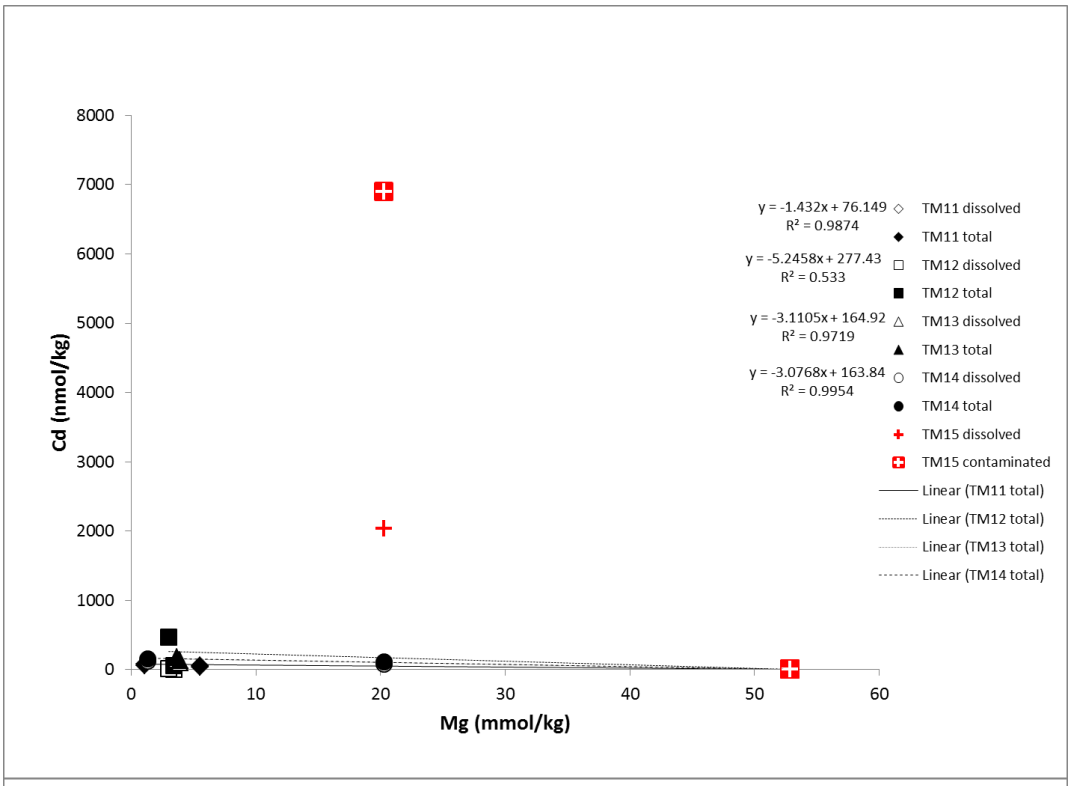
8000
7000
6000
5000
4000
3000
2000
1000
0
Cd (nmol/kg)
0
10
20
30
40
50
60
Mg (mmol/kg)
y = -1.432x + 76.149
R² = 0.9874
y = -5.2458x + 277.43
R² = 0.533
y = -3.1105x + 164.92
R² = 0.9719
y = -3.0768x + 163.84
R² = 0.9954
TM11 dissolved
TM11 total
TM12 dissolved
TM12 total
TM13 dissolved
TM13 total
TM14 dissolved
TM14 total
TM15 dissolved
TM15 contaminated
Linear (TM11 total)
Linear (TM12 total)
Linear (TM13 total)
Linear (TM14 total)

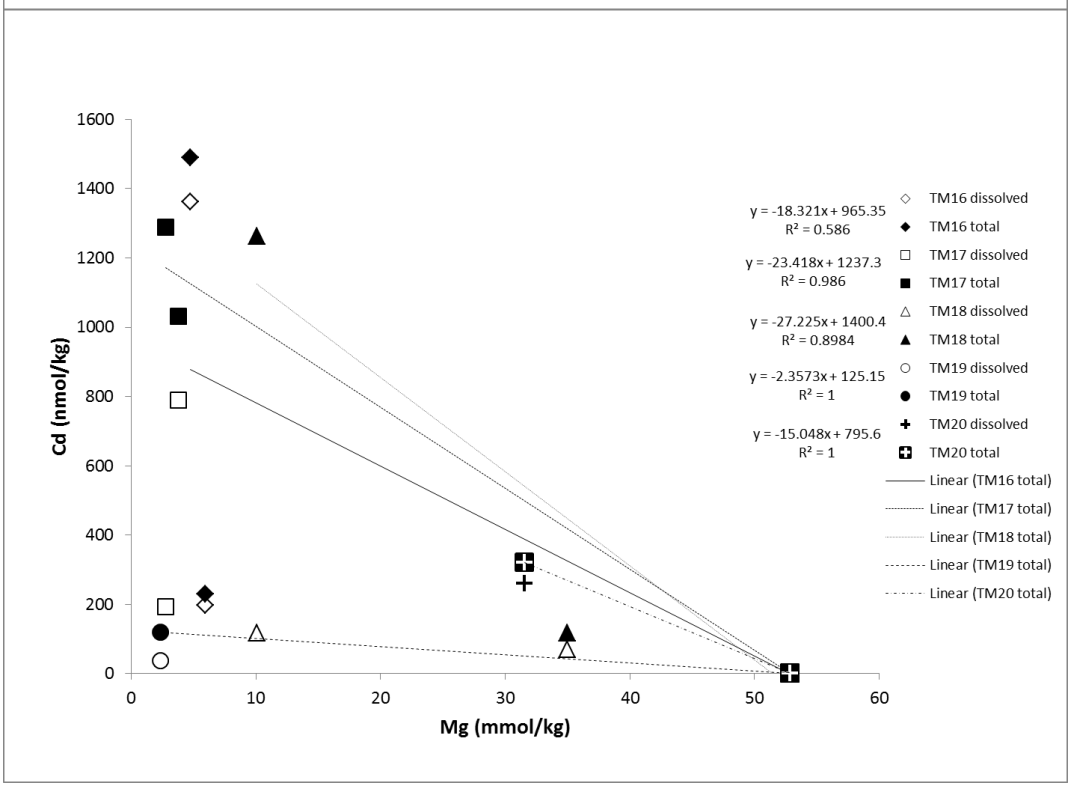
1600
1400
1200
1000
800
600
400
200
0
Cd (nmol/kg)
0
10
20
30
40
50
60
Mg (mmol/kg)
y = -18.321x + 965.35
R² = 0.586
y = -23.418x + 1237.3
R² = 0.986
y = -27.225x + 1400.4
R² = 0.8984
y = -2.3573x + 125.15
R² = 1
y = -15.048x + 795.6
R² = 1
TM16 dissolved
TM16 total
TM17 dissolved
TM17 total
TM18 dissolved
TM18 total
TM19 dissolved
TM19 total
TM20 dissolved
TM20 total
Linear (TM16 total)
Linear (TM17 total)
Linear (TM18 total)
Linear (TM19 total)
Linear (TM20 total)

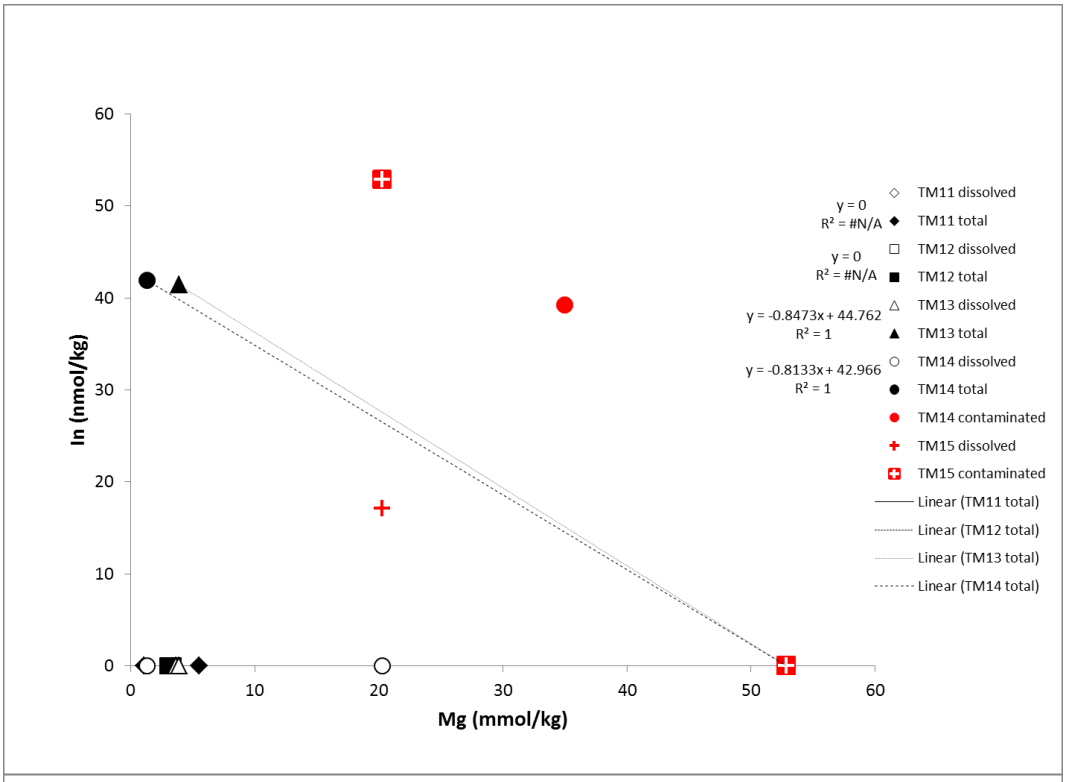
ln (nmol/kg)
Mg (mmol/kg)
y = 0
R² = #N/A
y = 0
R² = #N/A
y = -0.8473x + 44.762
R² = 1
y = -0.8133x + 42.966
R² = 1
TM11 dissolved
TM11 total
TM12 dissolved
TM12 total
TM13 dissolved
TM13 total
TM14 dissolved
TM14 total
TM14 contaminated
TM15 dissolved
TM15 contaminated
Linear (TM11 total)
Linear (TM12 total)
Linear (TM13 total)
Linear (TM14 total)

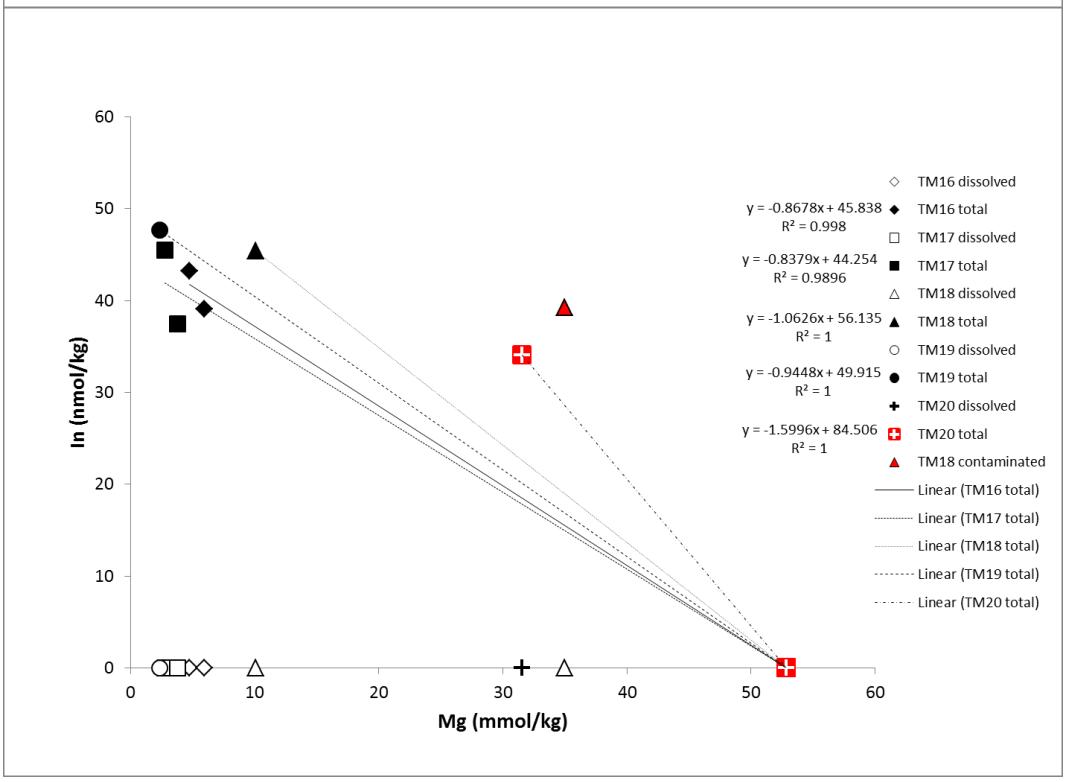
ln (nmol/kg)
Mg (mmol/kg)
y = -0.8678x + 45.838
R² = 0.998
y = -0.8379x + 44.254
R² = 0.9896
y = -1.0626x + 56.135
R² = 1
y = -0.9448x + 49.915
R² = 1
y = -1.5996x + 84.506
R² = 1
TM16 dissolved
TM16 total
TM17 dissolved
TM17 total
TM18 dissolved
TM18 total
TM19 dissolved
TM19 total
TM20 dissolved
TM20 total
TM18 contaminated
Linear (TM16 total)
Linear (TM17 total)
Linear (TM18 total)
Linear (TM19 total)
Linear (TM20 total)

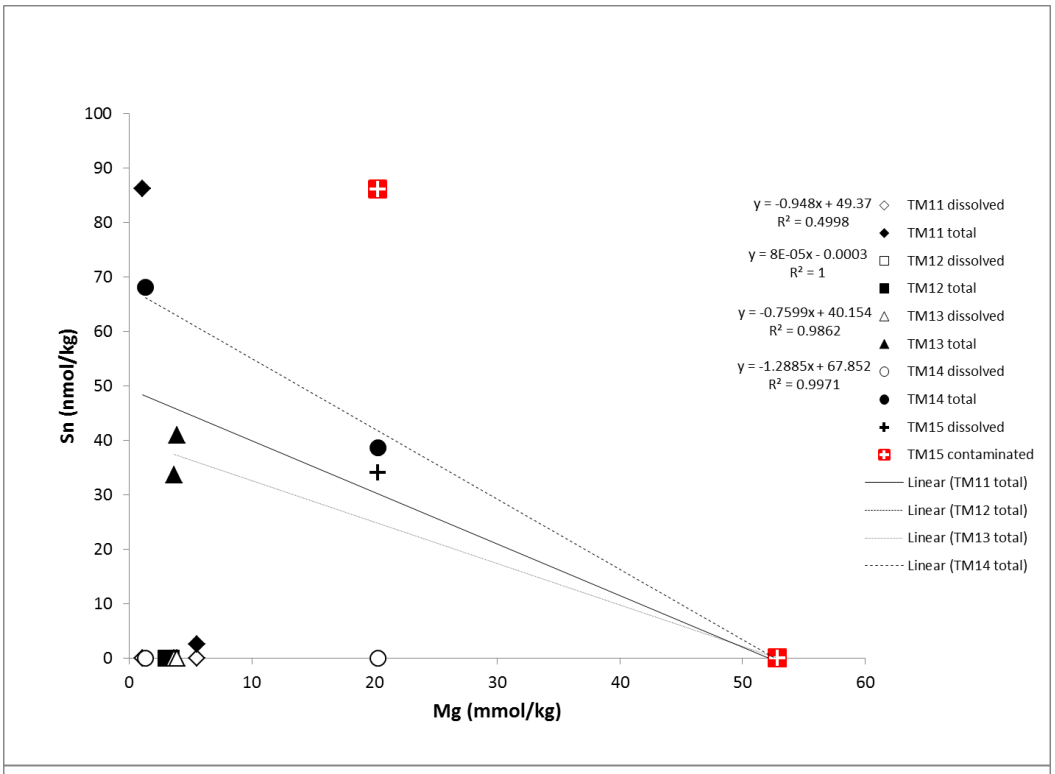
Sn (nmol/kg)
Mg (mmol/kg)
y = -0.948x + 49.37
R² = 0.4998
y = 8E-05x - 0.0003
R² = 1
y = -0.7599x + 40.154
R² = 0.9862
y = -1.2885x + 67.852
R² = 0.9971
TM11 dissolved
TM11 total
TM12 dissolved
TM12 total
TM13 dissolved
TM13 total
TM14 dissolved
TM14 total
TM15 dissolved
TM15 contaminated
Linear (TM11 total)
Linear (TM12 total)
Linear (TM13 total)
Linear (TM14 total)

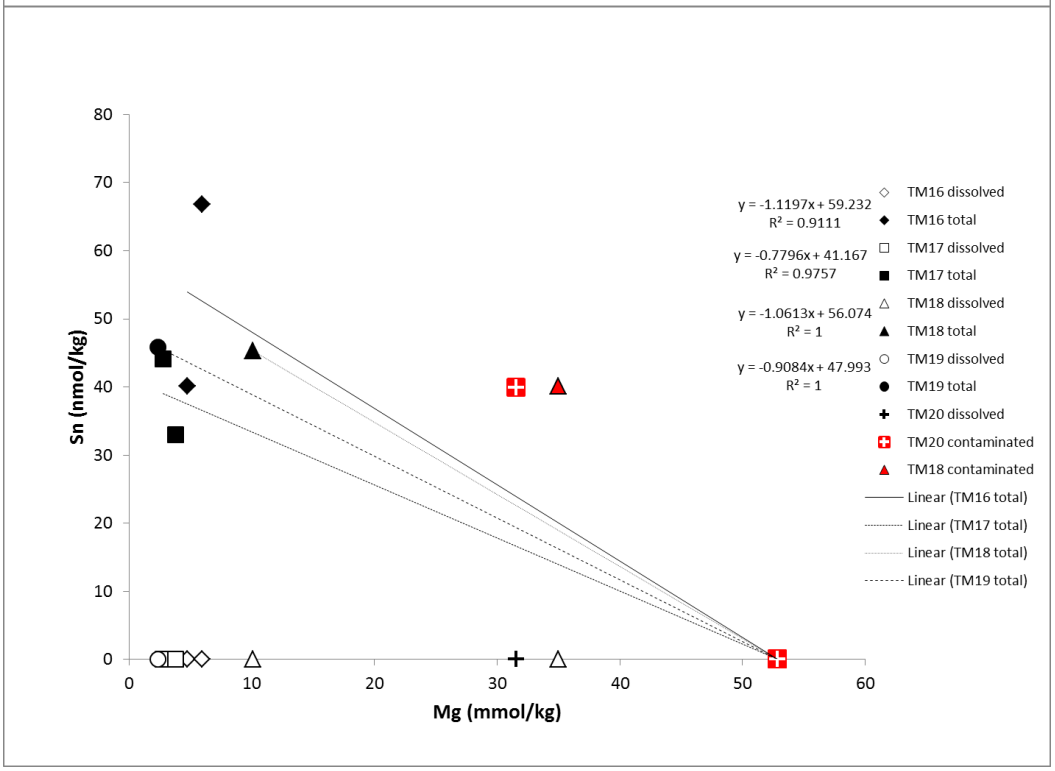
Sn (nmol/kg)
Mg (mmol/kg)
y = -1.1197x + 59.232
R² = 0.9111
y = -0.7796x + 41.167
R² = 0.9757
y = -1.0613x + 56.074
R² = 1
y = -0.9084x + 47.993
R² = 1
TM16 dissolved
TM16 total
TM17 dissolved
TM17 total
TM18 dissolved
TM18 total
TM19 dissolved
TM19 total
TM20 dissolved
TM20 contaminated
TM18 contaminated
Linear (TM16 total)
Linear (TM17 total)
Linear (TM18 total)
Linear (TM19 total)

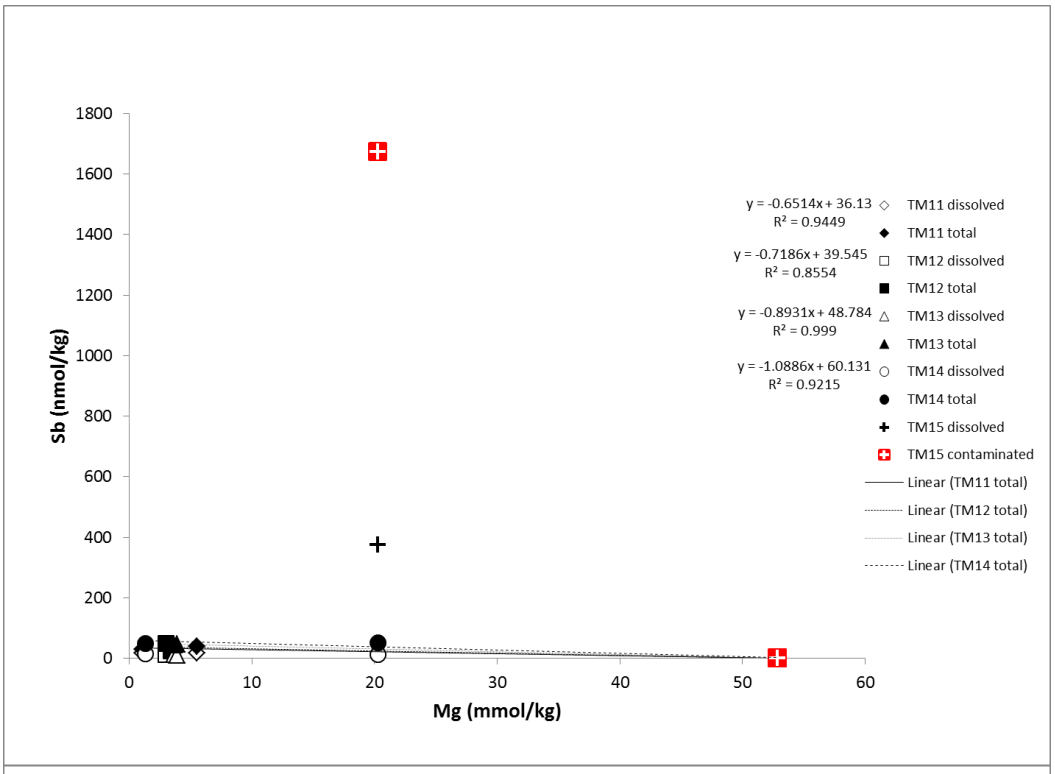
Sb (nmol/kg)
Mg (mmol/kg)
y = -0.6514x + 36.13
R² = 0.9449
y = -0.7186x + 39.545
R² = 0.8554
y = -0.8931x + 48.784
R² = 0.999
y = -1.0886x + 60.131
R² = 0.9215
TM11 dissolved
TM11 total
TM12 dissolved
TM12 total
TM13 dissolved
TM13 total
TM14 dissolved
TM14 total
TM15 dissolved
TM15 contaminated
Linear (TM11 total)
Linear (TM12 total)
Linear (TM13 total)
Linear (TM14 total)

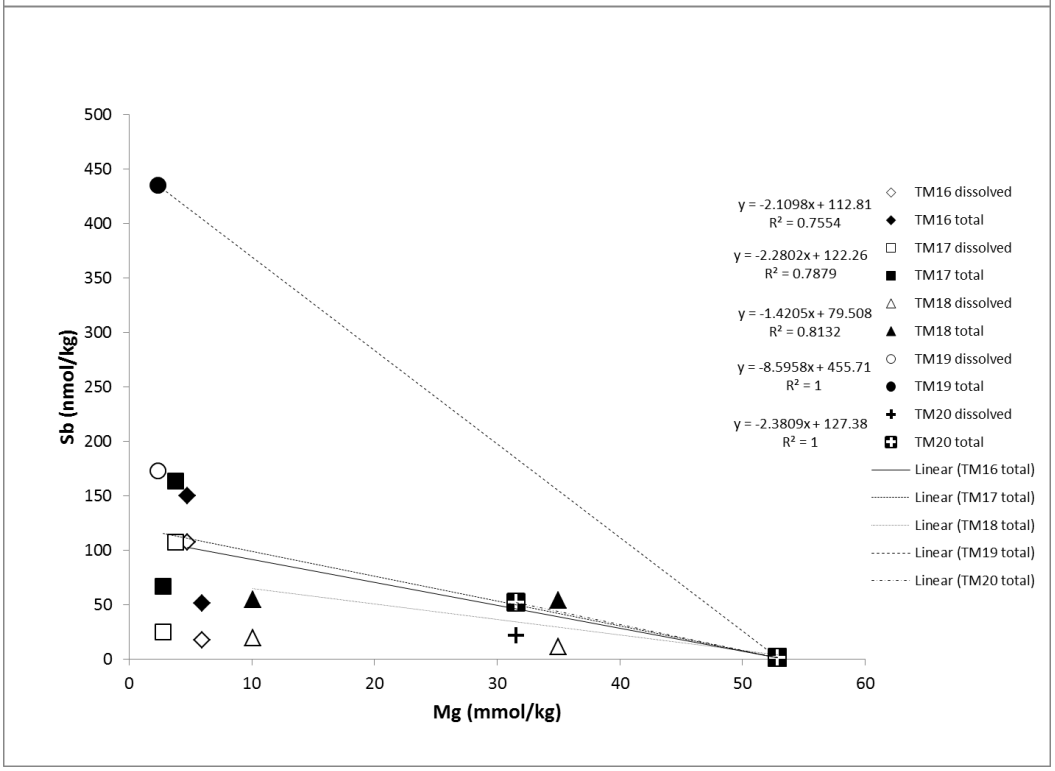
Sb (nmol/kg)
Mg (mmol/kg)
y = -2.1098x + 112.81
R² = 0.7554
y = -2.2802x + 122.26
R² = 0.7879
y = -1.4205x + 79.508
R² = 0.8132
y = -8.5958x + 455.71
R² = 1
y = -2.3809x + 127.38
R² = 1
TM16 dissolved
TM16 total
TM17 dissolved
TM17 total
TM18 dissolved
TM18 total
TM19 dissolved
TM19 total
TM20 dissolved
TM20 total
Linear (TM16 total)
Linear (TM17 total)
Linear (TM18 total)
Linear (TM19 total)
Linear (TM20 total)

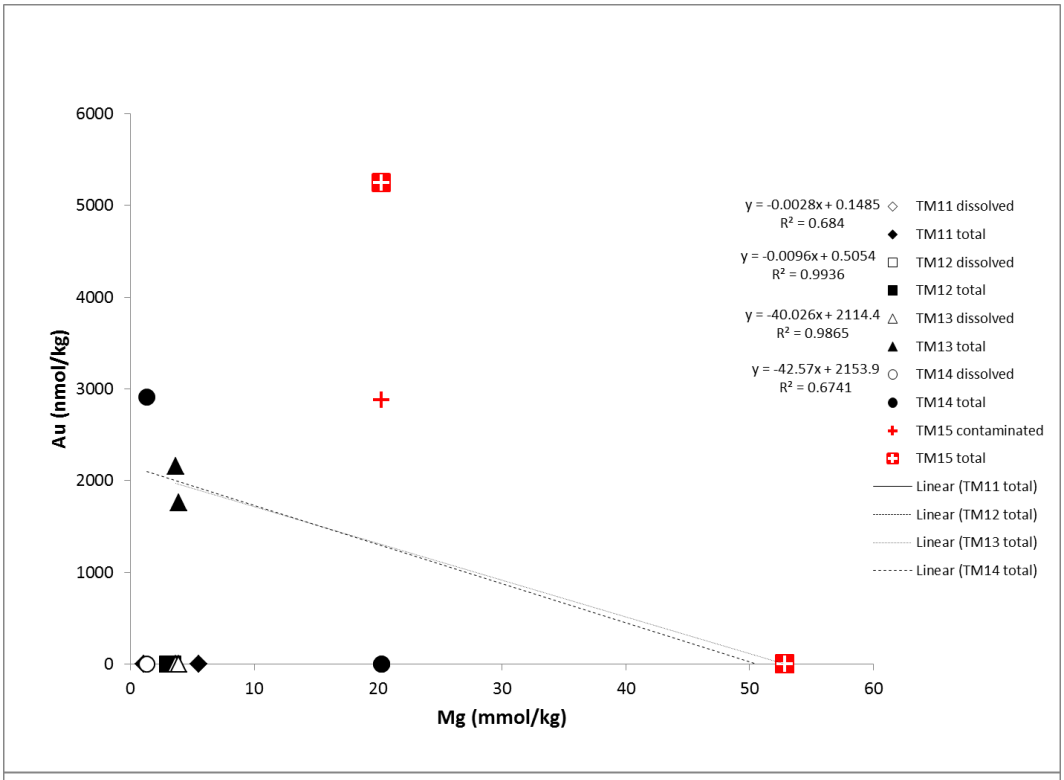
6000
5000
4000
3000
2000
1000
0
Au (nmol/kg)
0
10
20
30
40
50
60
Mg (mmol/kg)
y = -0.0028x + 0.1485
R² = 0.684
y = -0.0096x + 0.5054
R² = 0.9936
y = -40.026x + 2114.4
R² = 0.9865
y = -42.57x + 2153.9
R² = 0.6741
TM11 dissolved
TM11 total
TM12 dissolved
TM12 total
TM13 dissolved
TM13 total
TM14 dissolved
TM14 total
TM15 contaminated
TM15 total
Linear (TM11 total)
Linear (TM12 total)
Linear (TM13 total)
Linear (TM14 total)

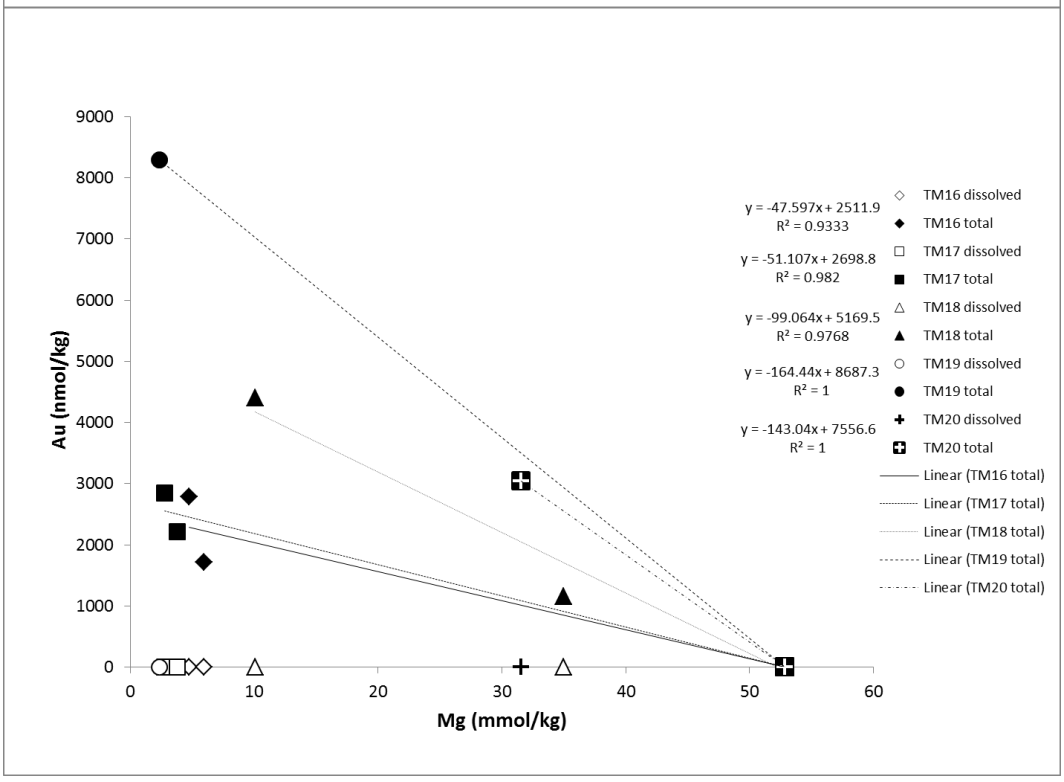
9000
8000
7000
6000
5000
4000
3000
2000
1000
0
Au (nmol/kg)
0
10
20
30
40
50
60
Mg (mmol/kg)
y = -47.597x + 2511.9
R² = 0.9333
y = -51.107x + 2698.8
R² = 0.982
y = -99.064x + 5169.5
R² = 0.9768
y = -164.44x + 8687.3
R² = 1
y = -143.04x + 7556.6
R² = 1
TM16 dissolved
TM16 total
TM17 dissolved
TM17 total
TM18 dissolved
TM18 total
TM19 dissolved
TM19 total
TM20 dissolved
TM20 total
Linear (TM16 total)
Linear (TM17 total)
Linear (TM18 total)
Linear (TM19 total)
Linear (TM20 total)

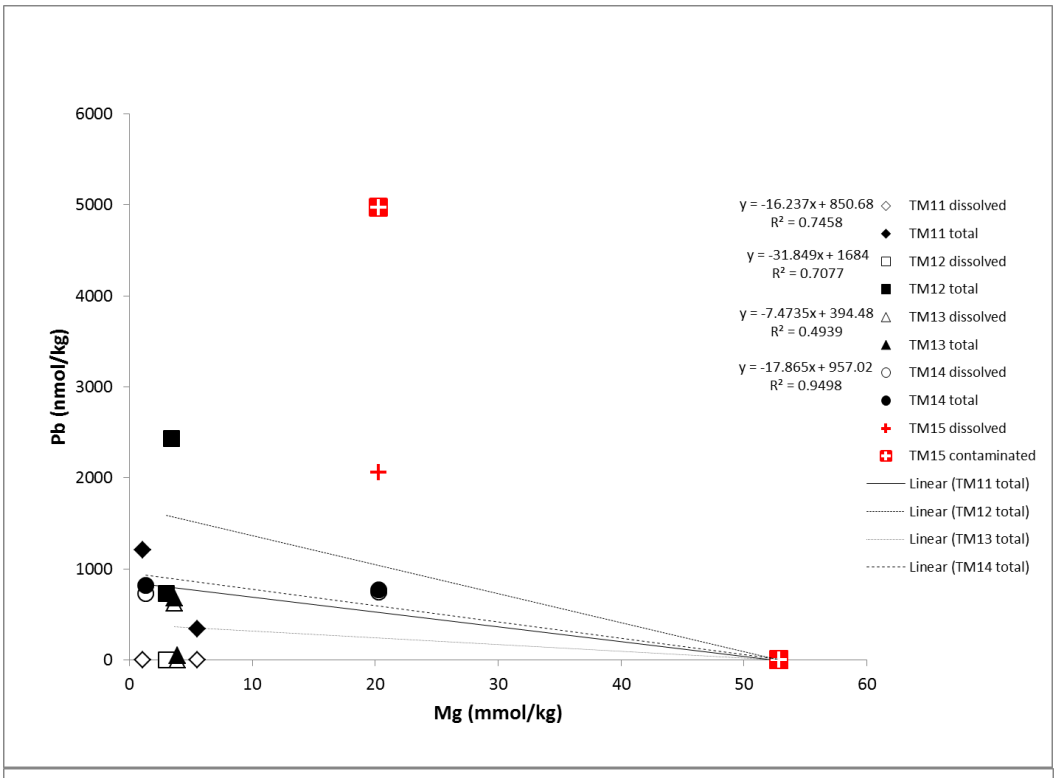
Pb (nmol/kg)
Mg (mmol/kg)
y = -16.237x + 850.68
R² = 0.7458
y = -31.849x + 1684
R² = 0.7077
y = -7.4735x + 394.48
R² = 0.4939
y = -17.865x + 957.02
R² = 0.9498
TM11 dissolved
TM11 total
TM12 dissolved
TM12 total
TM13 dissolved
TM13 total
TM14 dissolved
TM14 total
TM15 dissolved
TM15 contaminated
Linear (TM11 total)
Linear (TM12 total)
Linear (TM13 total)
Linear (TM14 total)

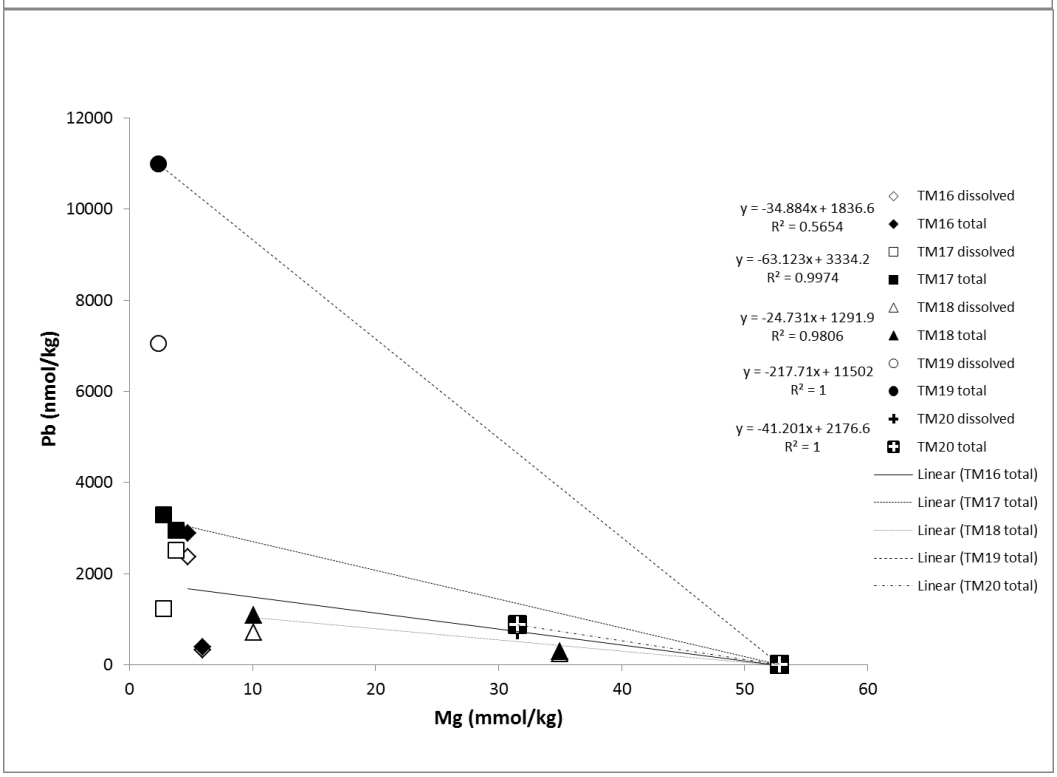
Pb (nmol/kg)
Mg (mmol/kg)
y = -34.884x + 1836.6
R² = 0.5654
y = -63.123x + 3334.2
R² = 0.9974
y = -24.731x + 1291.9
R² = 0.9806
y = -217.71x + 11502
R² = 1
y = -41.201x + 2176.6
R² = 1
TM16 dissolved
TM16 total
TM17 dissolved
TM17 total
TM18 dissolved
TM18 total
TM19 dissolved
TM19 total
TM20 dissolved
TM20 total
Linear (TM16 total)
Linear (TM17 total)
Linear (TM18 total)
Linear (TM19 total)
Linear (TM20 total)

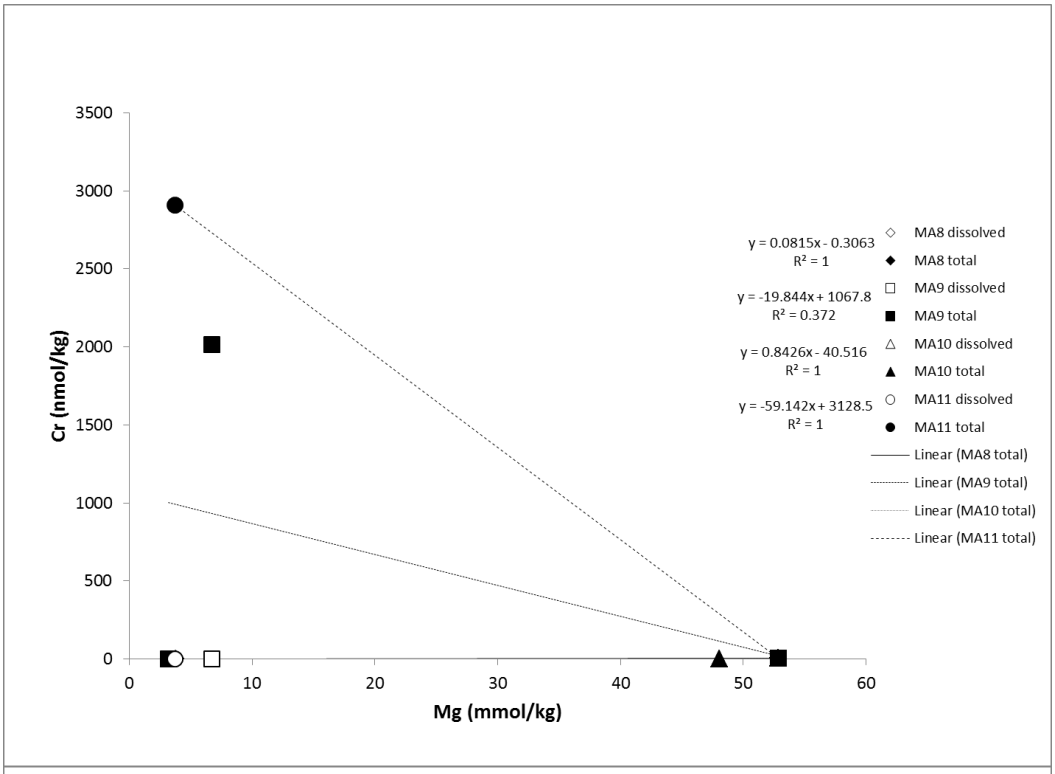
3500
3000
2500
2000
1500
1000
500
0
Cr (nmol/kg)
0
10
20
30
40
50
60
Mg (mmol/kg)
y = 0.0815x - 0.3063
R² = 1
y = -19.844x + 1067.8
R² = 0.372
y = 0.8426x - 40.516
R² = 1
y = -59.142x + 3128.5
R² = 1
MA8 dissolved
MA8 total
MA9 dissolved
MA9 total
MA10 dissolved
MA10 total
MA11 dissolved
MA11 total
Linear (MA8 total)
Linear (MA9 total)
Linear (MA10 total)
Linear (MA11 total)

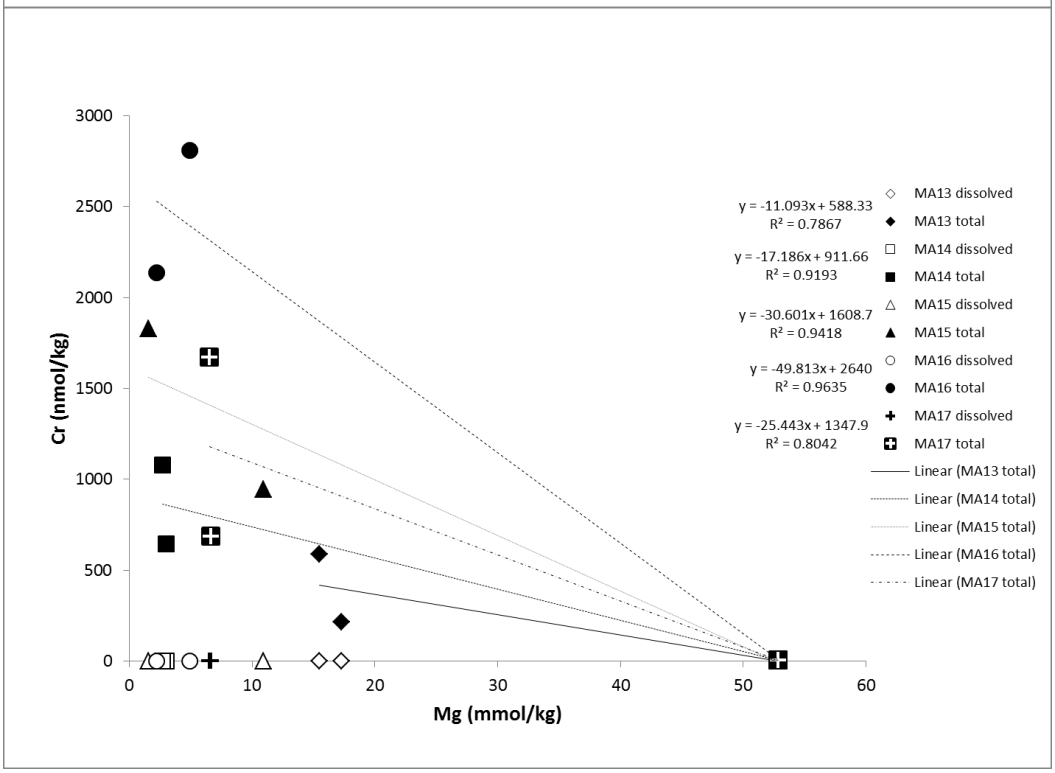
3000
2500
2000
1500
1000
500
0
Cr (nmol/kg)
0
10
20
30
40
50
60
Mg (mmol/kg)
y = -11.093x + 588.33
R² = 0.7867
y = -17.186x + 911.66
R² = 0.9193
y = -30.601x + 1608.7
R² = 0.9418
y = -49.813x + 2640
R² = 0.9635
y = -25.443x + 1347.9
R² = 0.8042
MA13 dissolved
MA13 total
MA14 dissolved
MA14 total
MA15 dissolved
MA15 total
MA16 dissolved
MA16 total
MA17 dissolved
MA17 total
Linear (MA13 total)
Linear (MA14 total)
Linear (MA15 total)
Linear (MA16 total)
Linear (MA17 total)

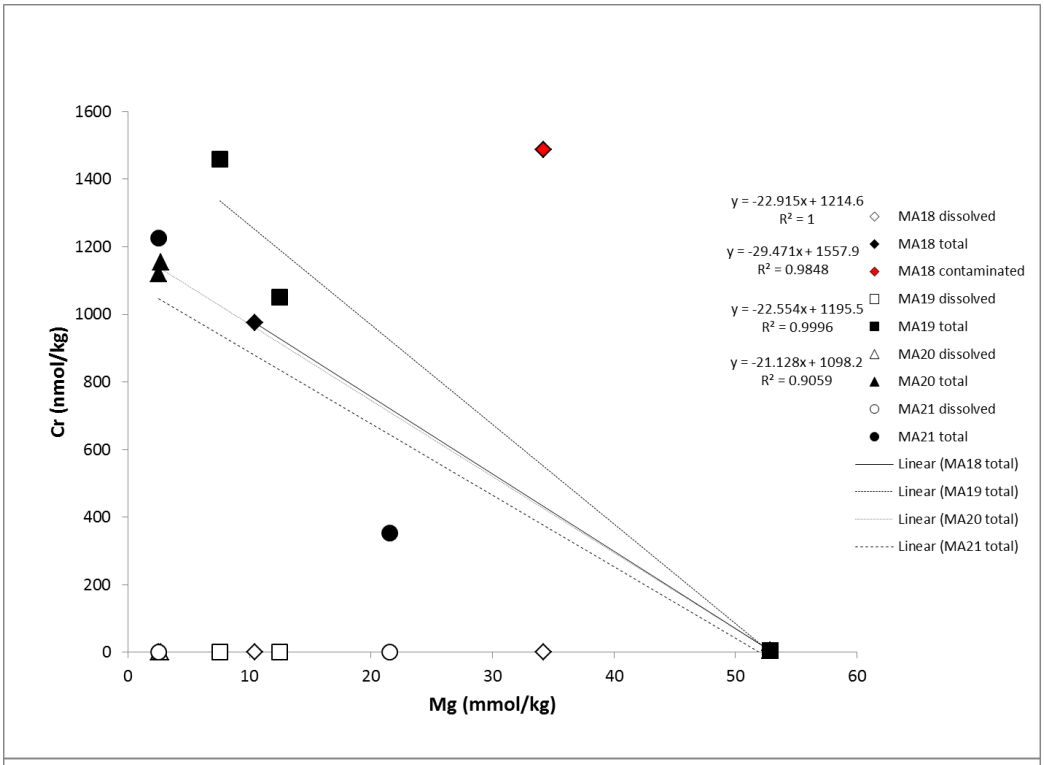
Cr (nmol/kg)
Mg (mmol/kg)
y = -22.915x + 1214.6
R² = 1
y = -29.471x + 1557.9
R² = 0.9848
y = -22.554x + 1195.5
R² = 0.9996
y = -21.128x + 1098.2
R² = 0.9059
MA18 dissolved
MA18 total
MA18 contaminated
MA19 dissolved
MA19 total
MA20 dissolved
MA20 total
MA21 dissolved
MA21 total
Linear (MA18 total)
Linear (MA19 total)
Linear (MA20 total)
Linear (MA21 total)

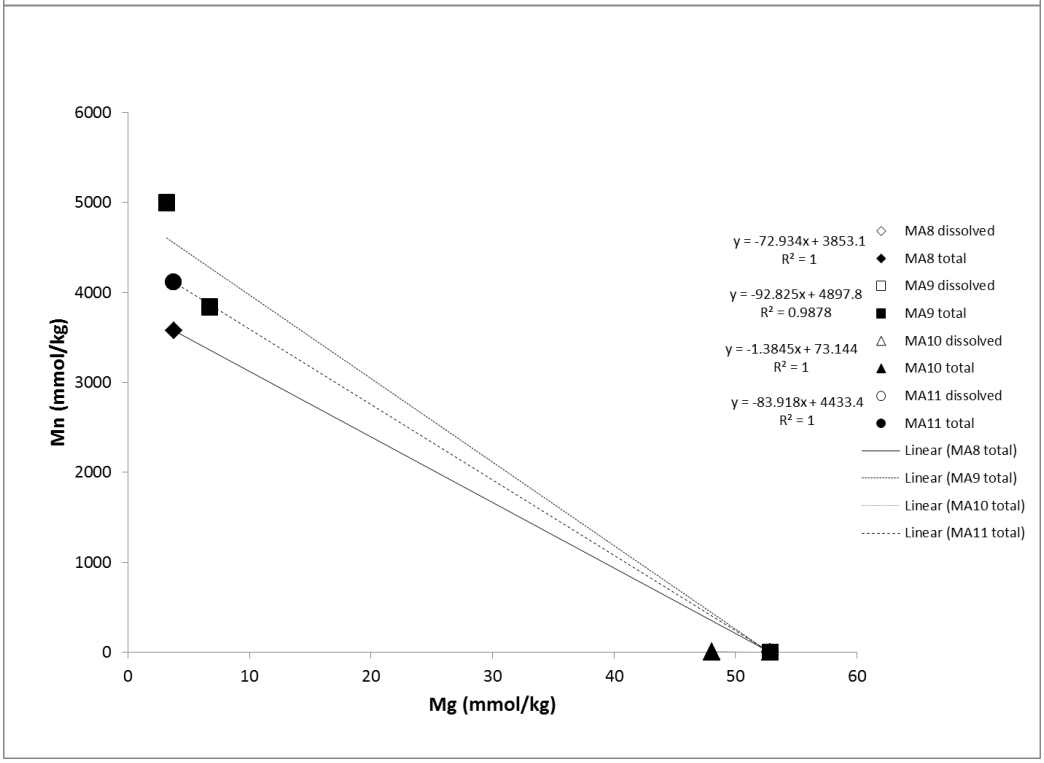
Mn (mmol/kg)
Mg (mmol/kg)
y = -72.934x + 3853.1
R² = 1
y = -92.825x + 4897.8
R² = 0.9878
y = -1.3845x + 73.144
R² = 1
y = -83.918x + 4433.4
R² = 1
MA8 dissolved
MA8 total
MA9 dissolved
MA9 total
MA10 dissolved
MA10 total
MA11 dissolved
MA11 total
Linear (MA8 total)
Linear (MA9 total)
Linear (MA10 total)
Linear (MA11 total)

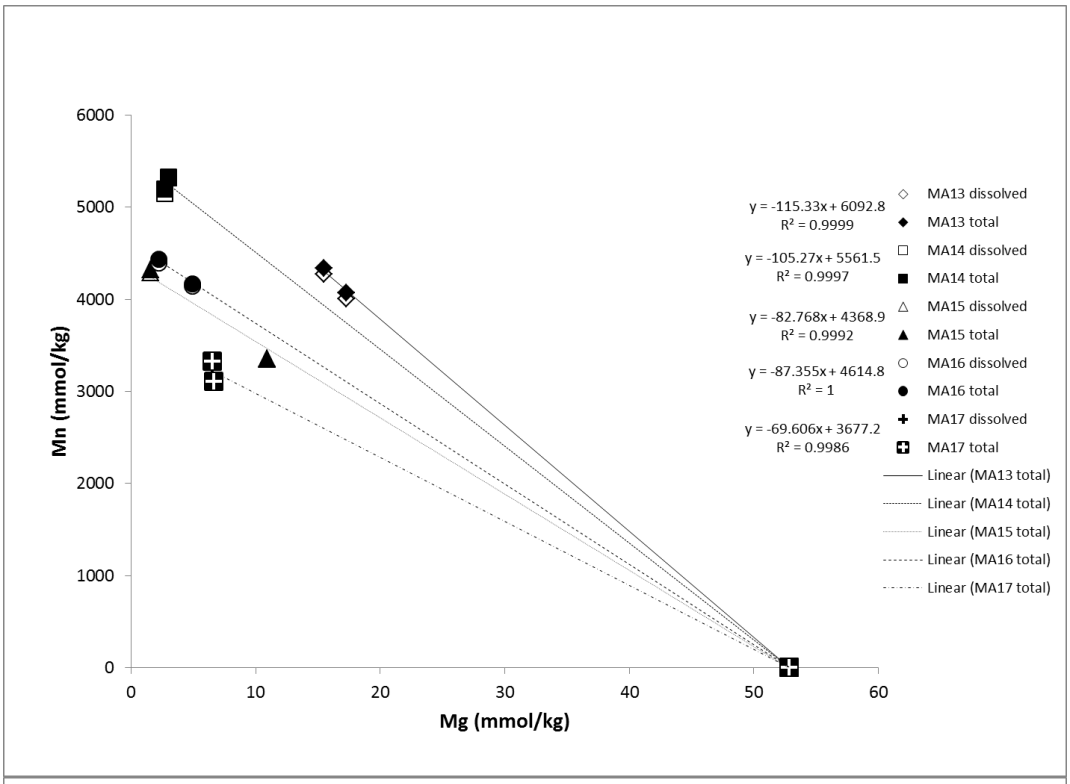
Mn (mmol/kg)
Mg (mmol/kg)
y = -115.33x + 6092.8
R² = 0.9999
y = -105.27x + 5561.5
R² = 0.9997
y = -82.768x + 4368.9
R² = 0.9992
y = -87.355x + 4614.8
R² = 1
y = -69.606x + 3677.2
R² = 0.9986
MA13 dissolved
MA13 total
MA14 dissolved
MA14 total
MA15 dissolved
MA15 total
MA16 dissolved
MA16 total
MA17 dissolved
MA17 total
Linear (MA13 total)
Linear (MA14 total)
Linear (MA15 total)
Linear (MA16 total)
Linear (MA17 total)

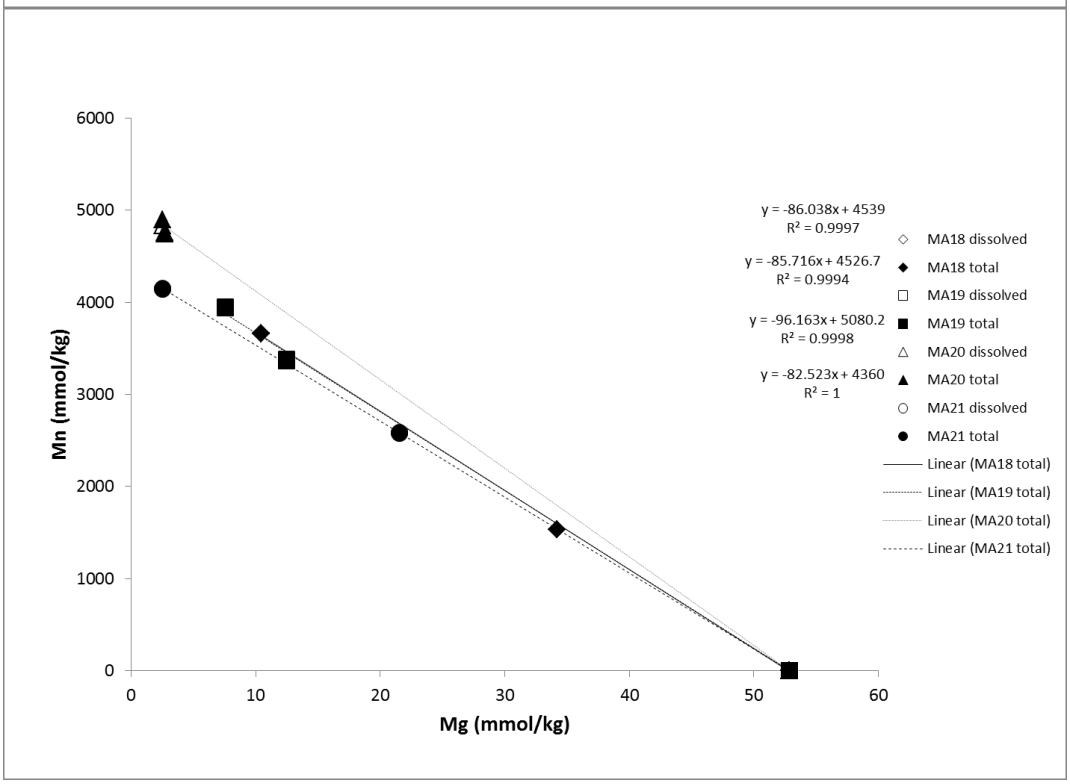
Mn (mmol/kg)
Mg (mmol/kg)
y = -86.038x + 4539
R² = 0.9997
y = -85.716x + 4526.7
R² = 0.9994
y = -96.163x + 5080.2
R² = 0.9998
y = -82.523x + 4360
R² = 1
MA18 dissolved
MA18 total
MA19 dissolved
MA19 total
MA20 dissolved
MA20 total
MA21 dissolved
MA21 total
Linear (MA18 total)
Linear (MA19 total)
Linear (MA20 total)
Linear (MA21 total)

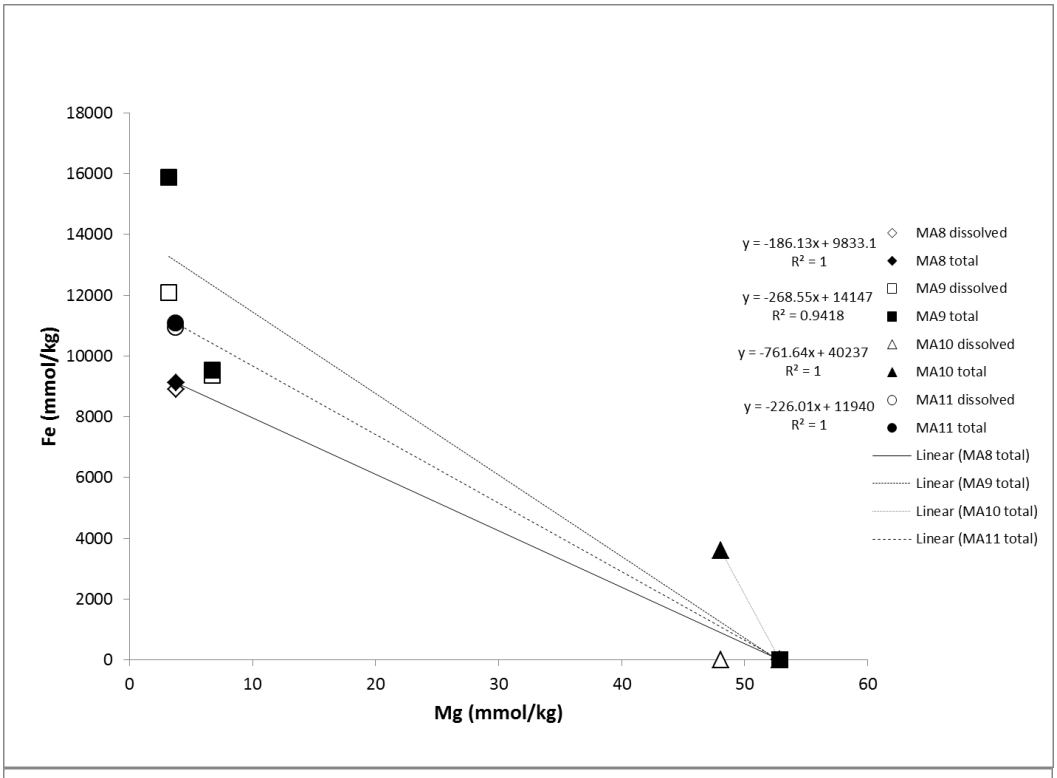
18000
16000
14000
12000
10000
8000
6000
4000
2000
0
0
10
20
30
40
50
60
Fe (mmol/kg)
Mg (mmol/kg)
y = -186.13x + 9833.1
R² = 1
y = -268.55x + 14147
R² = 0.9418
y = -761.64x + 40237
R² = 1
y = -226.01x + 11940
R² = 1
MA8 dissolved
MA8 total
MA9 dissolved
MA9 total
MA10 dissolved
MA10 total
MA11 dissolved
MA11 total
Linear (MA8 total)
Linear (MA9 total)
Linear (MA10 total)
Linear (MA11 total)

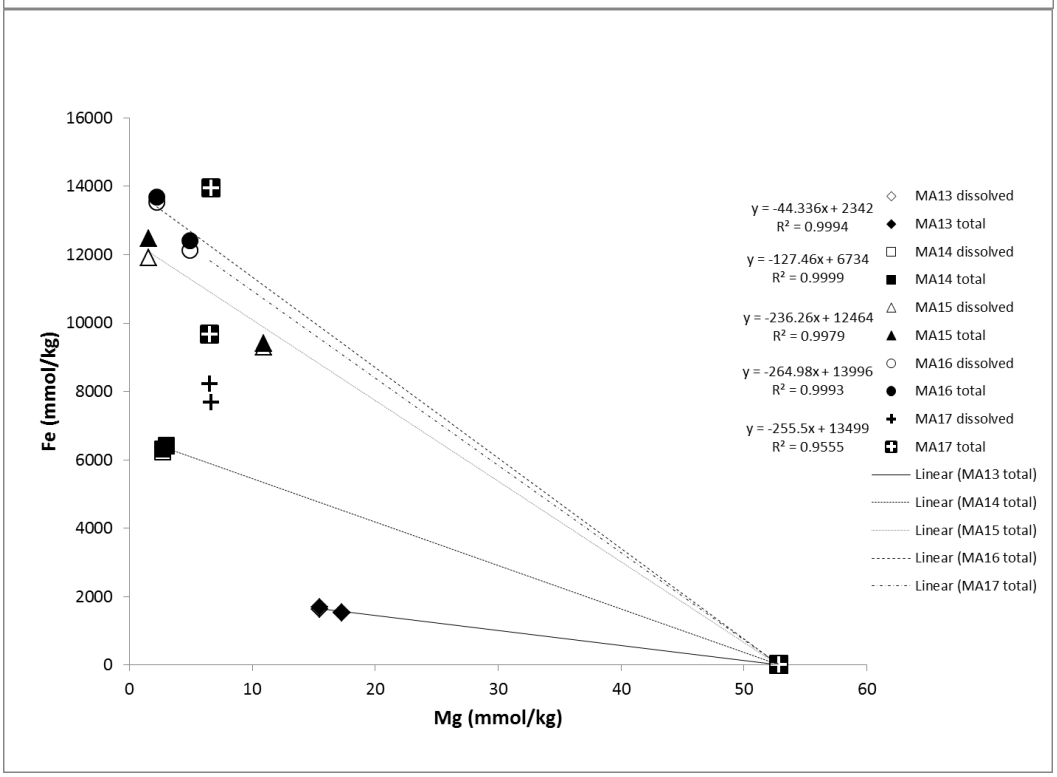
16000
14000
12000
10000
8000
6000
4000
2000
0
0
10
20
30
40
50
60
Fe (mmol/kg)
Mg (mmol/kg)
y = -44.336x + 2342
R² = 0.9994
y = -127.46x + 6734
R² = 0.9999
y = -236.26x + 12464
R² = 0.9979
y = -264.98x + 13996
R² = 0.9993
y = -255.5x + 13499
R² = 0.9555
MA13 dissolved
MA13 total
MA14 dissolved
MA14 total
MA15 dissolved
MA15 total
MA16 dissolved
MA16 total
MA17 dissolved
MA17 total
Linear (MA13 total)
Linear (MA14 total)
Linear (MA15 total)
Linear (MA16 total)
Linear (MA17 total)

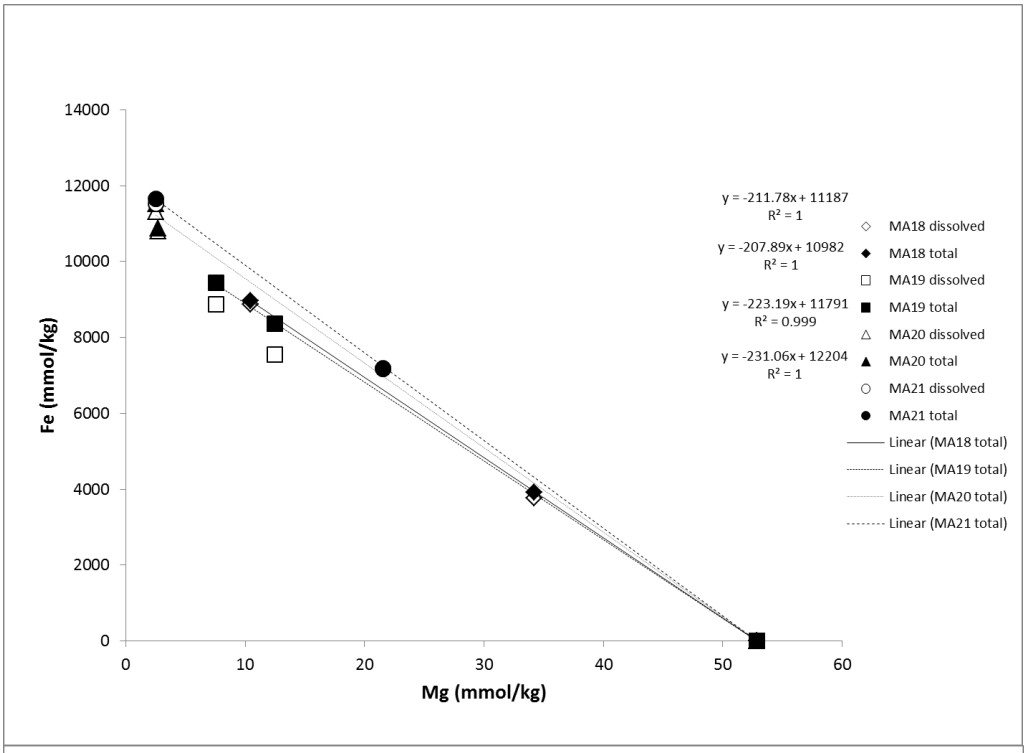
14000
12000
10000
8000
6000
4000
2000
0
Fe (mmol/kg)
0
10
20
30
40
50
60
Mg (mmol/kg)
y = -211.78x + 11187
R² = 1
y = -207.89x + 10982
R² = 1
y = -223.19x + 11791
R² = 0.999
y = -231.06x + 12204
R² = 1
MA18 dissolved
MA18 total
MA19 dissolved
MA19 total
MA20 dissolved
MA20 total
MA21 dissolved
MA21 total
Linear (MA18 total)
Linear (MA19 total)
Linear (MA20 total)
Linear (MA21 total)

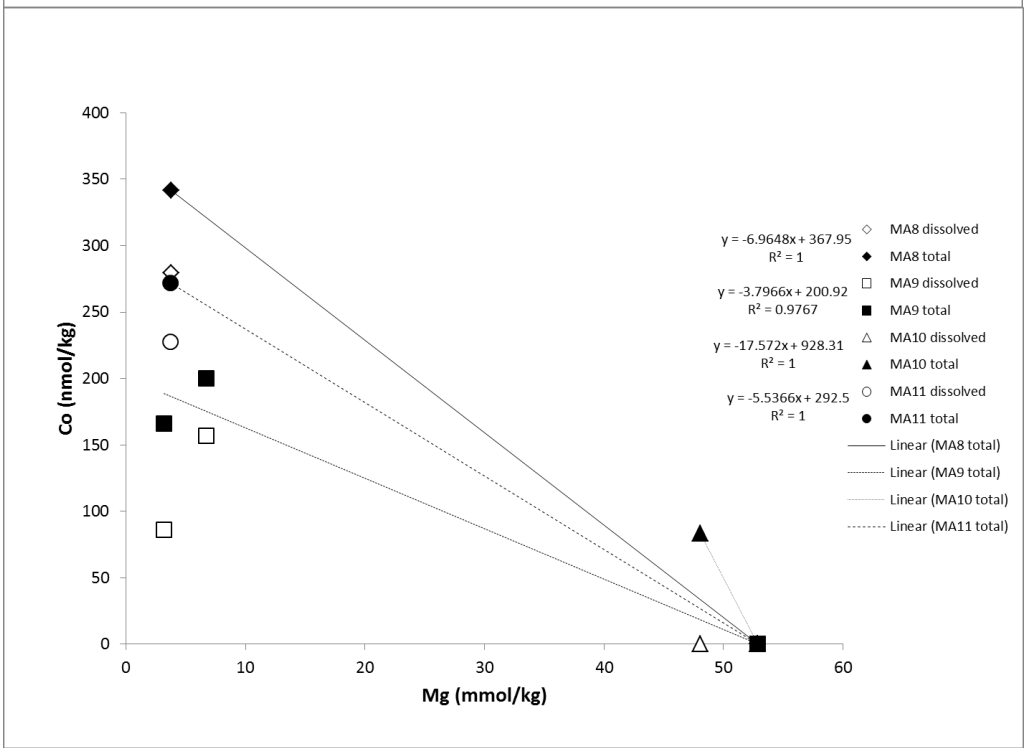
400
350
300
250
200
150
100
50
0
Co (nmol/kg)
0
10
20
30
40
50
60
Mg (mmol/kg)
y = -6.9648x + 367.95
R² = 1
y = -3.7966x + 200.92
R² = 0.9767
y = -17.572x + 928.31
R² = 1
y = -5.5366x + 292.5
R² = 1
MA8 dissolved
MA8 total
MA9 dissolved
MA9 total
MA10 dissolved
MA10 total
MA11 dissolved
MA11 total
Linear (MA8 total)
Linear (MA9 total)
Linear (MA10 total)
Linear (MA11 total)

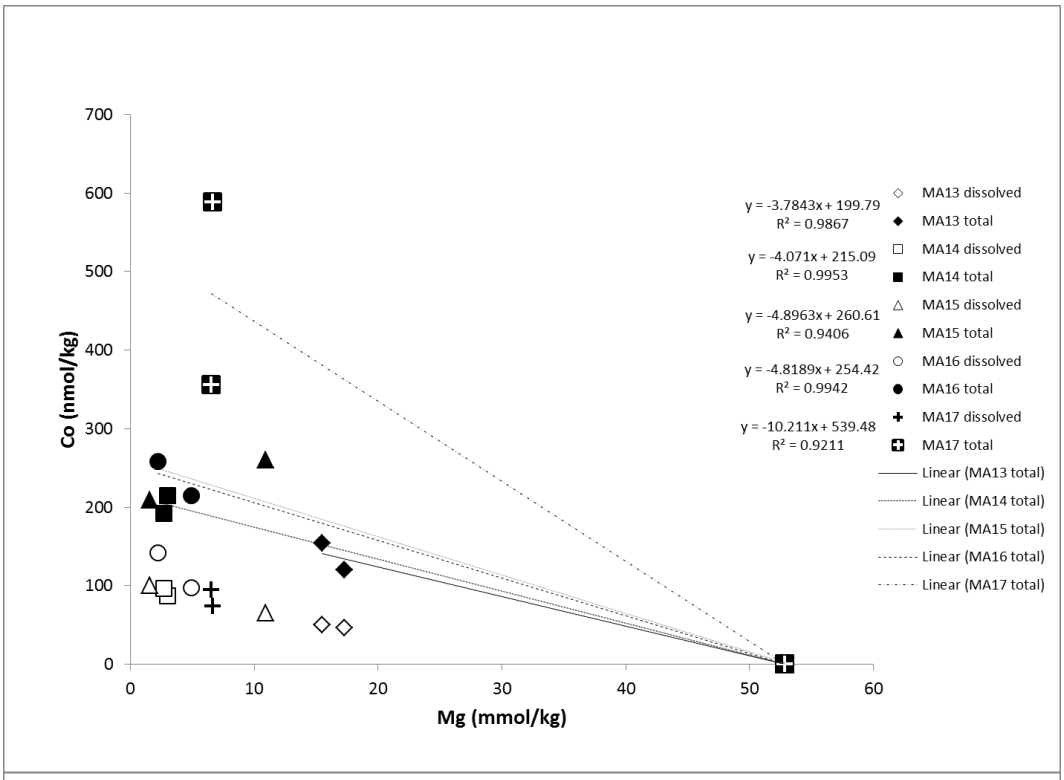
Co (nmol/kg)
Mg (mmol/kg)
y = -3.7843x + 199.79
R² = 0.9867
y = -4.071x + 215.09
R² = 0.9953
y = -4.8963x + 260.61
R² = 0.9406
y = -4.8189x + 254.42
R² = 0.9942
y = -10.211x + 539.48
R² = 0.9211
MA13 dissolved
MA13 total
MA14 dissolved
MA14 total
MA15 dissolved
MA15 total
MA16 dissolved
MA16 total
MA17 dissolved
MA17 total
Linear (MA13 total)
Linear (MA14 total)
Linear (MA15 total)
Linear (MA16 total)
Linear (MA17 total)

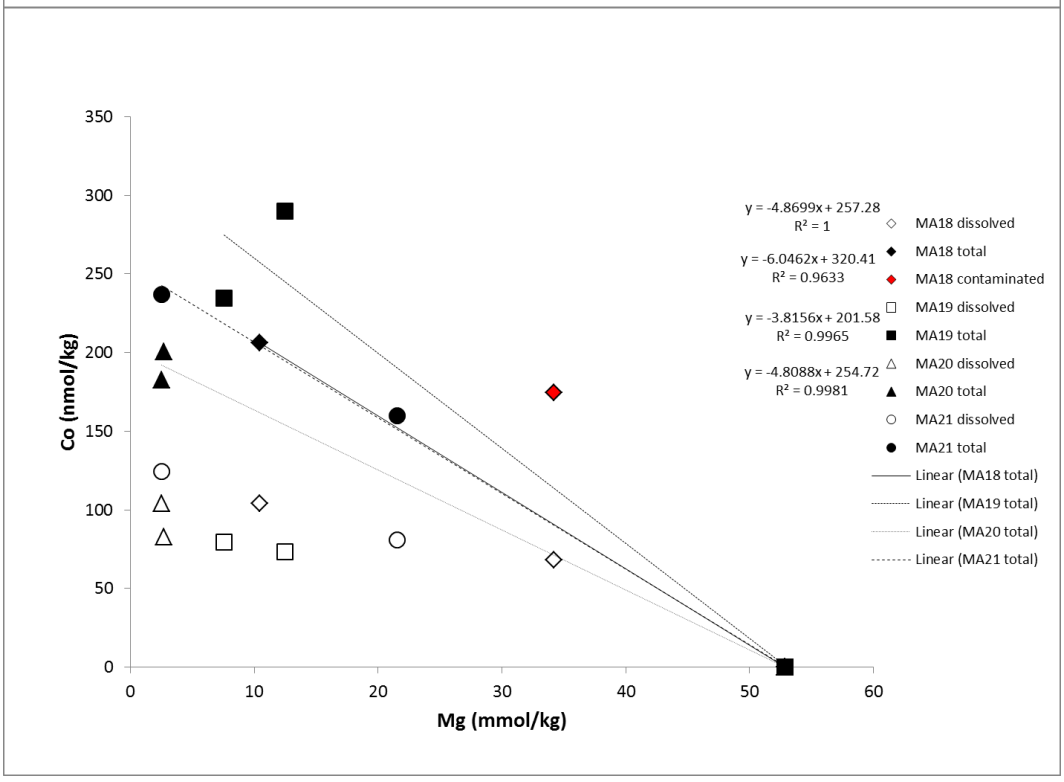
Co (nmol/kg)
Mg (mmol/kg)
y = -4.8699x + 257.28
R² = 1
y = -6.0462x + 320.41
R² = 0.9633
y = -3.8156x + 201.58
R² = 0.9965
y = -4.8088x + 254.72
R² = 0.9981
MA18 dissolved
MA18 total
MA18 contaminated
MA19 dissolved
MA19 total
MA20 dissolved
MA20 total
MA21 dissolved
MA21 total
Linear (MA18 total)
Linear (MA19 total)
Linear (MA20 total)
Linear (MA21 total)

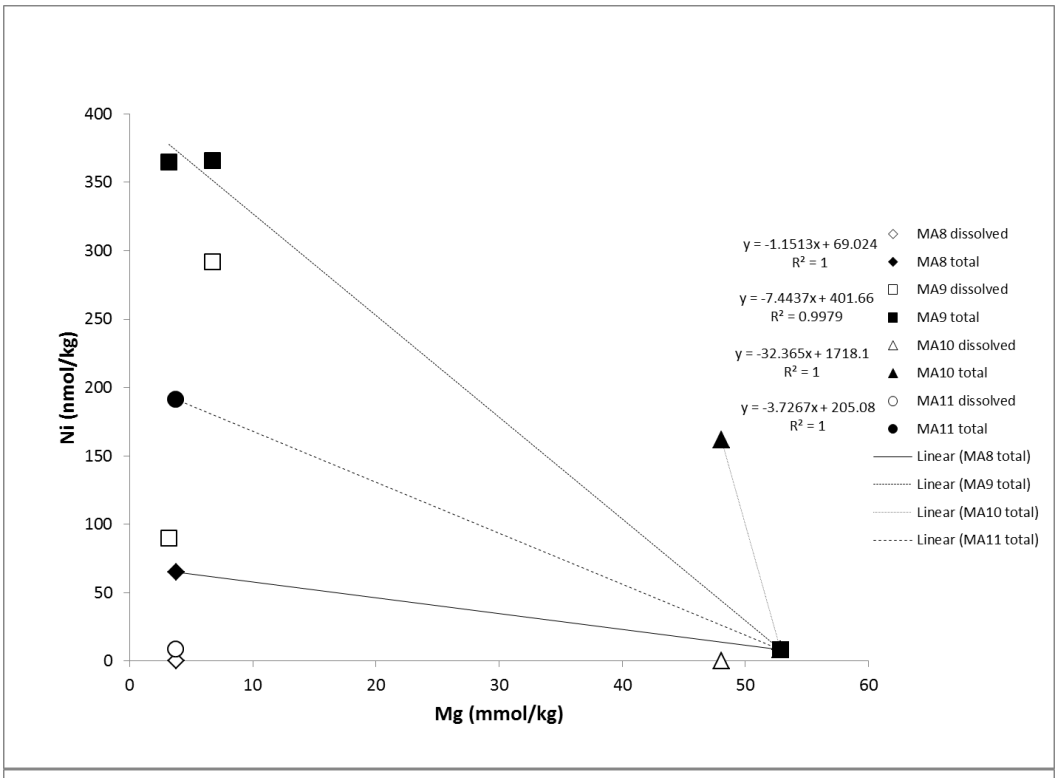
Ni (nmol/kg)
Mg (mmol/kg)
y = -1.1513x + 69.024
R² = 1
y = -7.4437x + 401.66
R² = 0.9979
y = -32.365x + 1718.1
R² = 1
y = -3.7267x + 205.08
R² = 1
MA8 dissolved
MA8 total
MA9 dissolved
MA9 total
MA10 dissolved
MA10 total
MA11 dissolved
MA11 total
Linear (MA8 total)
Linear (MA9 total)
Linear (MA10 total)
Linear (MA11 total)

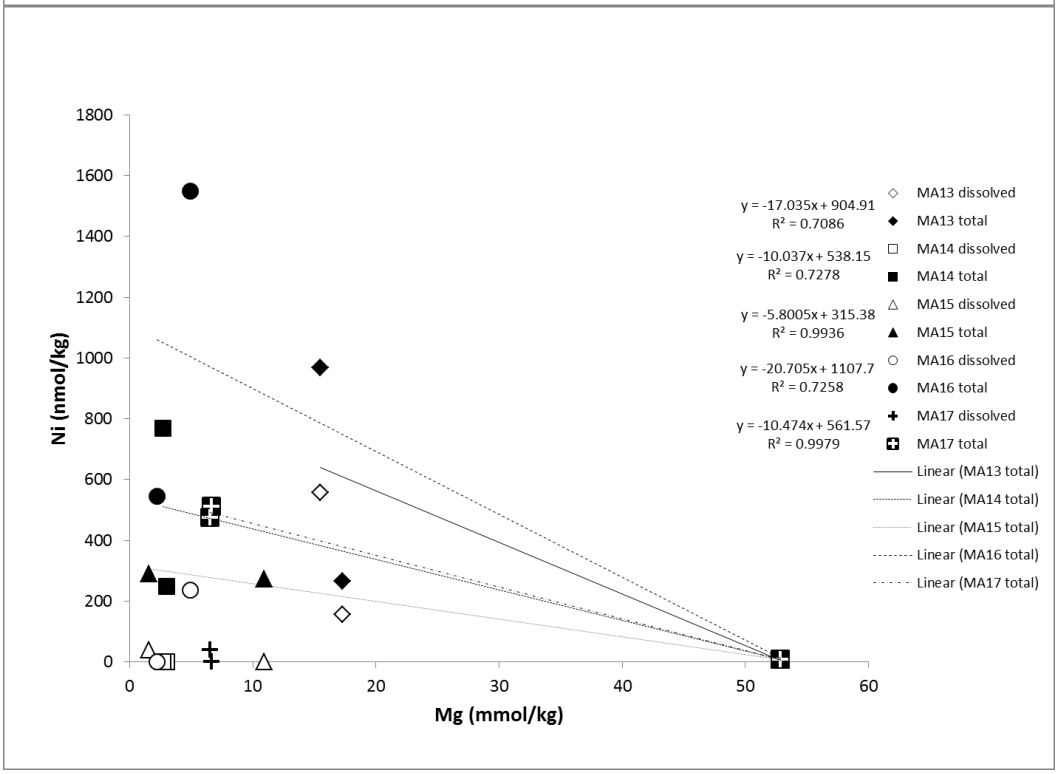
Ni (nmol/kg)
Mg (mmol/kg)
y = -17.035x + 904.91
R² = 0.7086
y = -10.037x + 538.15
R² = 0.7278
y = -5.8005x + 315.38
R² = 0.9936
y = -20.705x + 1107.7
R² = 0.7258
y = -10.474x + 561.57
R² = 0.9979
MA13 dissolved
MA13 total
MA14 dissolved
MA14 total
MA15 dissolved
MA15 total
MA16 dissolved
MA16 total
MA17 dissolved
MA17 total
Linear (MA13 total)
Linear (MA14 total)
Linear (MA15 total)
Linear (MA16 total)
Linear (MA17 total)

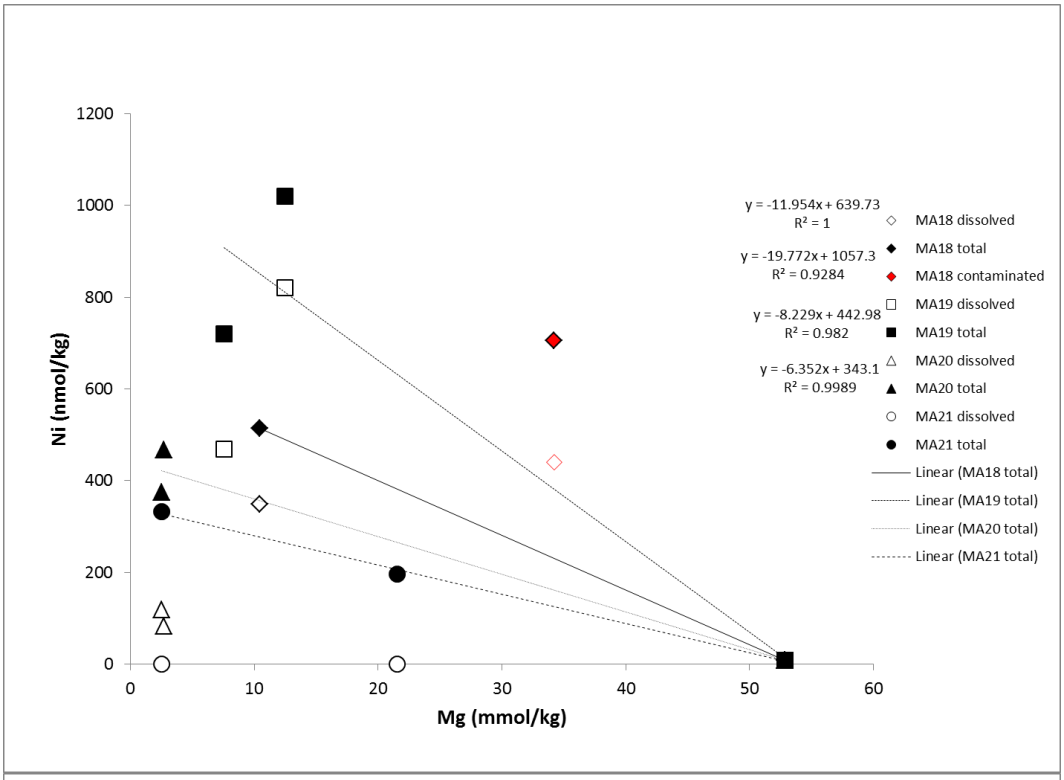
Ni (nmol/kg)
Mg (mmol/kg)
y = -11.954x + 639.73
R² = 1
y = -19.772x + 1057.3
R² = 0.9284
y = -8.229x + 442.98
R² = 0.982
y = -6.352x + 343.1
R² = 0.9989
MA18 dissolved
MA18 total
MA18 contaminated
MA19 dissolved
MA19 total
MA20 dissolved
MA20 total
MA21 dissolved
MA21 total
Linear (MA18 total)
Linear (MA19 total)
Linear (MA20 total)
Linear (MA21 total)

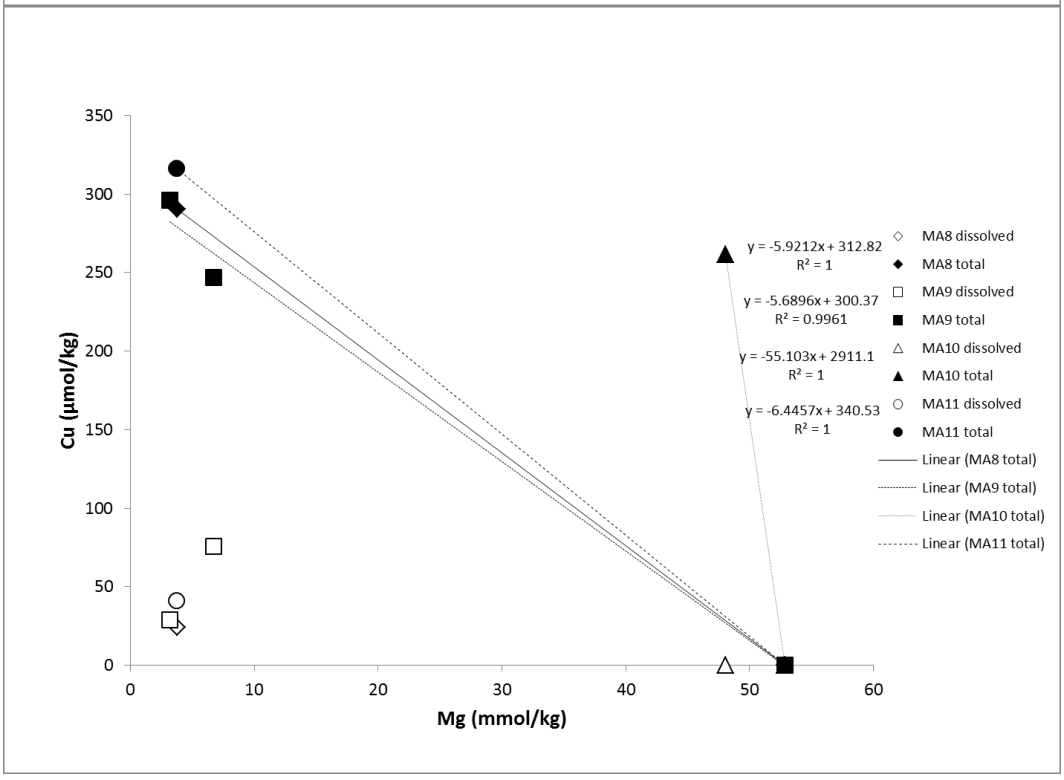
Cu (µmol/kg)
Mg (mmol/kg)
y = -5.9212x + 312.82
R² = 1
y = -5.6896x + 300.37
R² = 0.9961
y = -55.103x + 2911.1
R² = 1
y = -6.4457x + 340.53
R² = 1
MA8 dissolved
MA8 total
MA9 dissolved
MA9 total
MA10 dissolved
MA10 total
MA11 dissolved
MA11 total
Linear (MA8 total)
Linear (MA9 total)
Linear (MA10 total)
Linear (MA11 total)

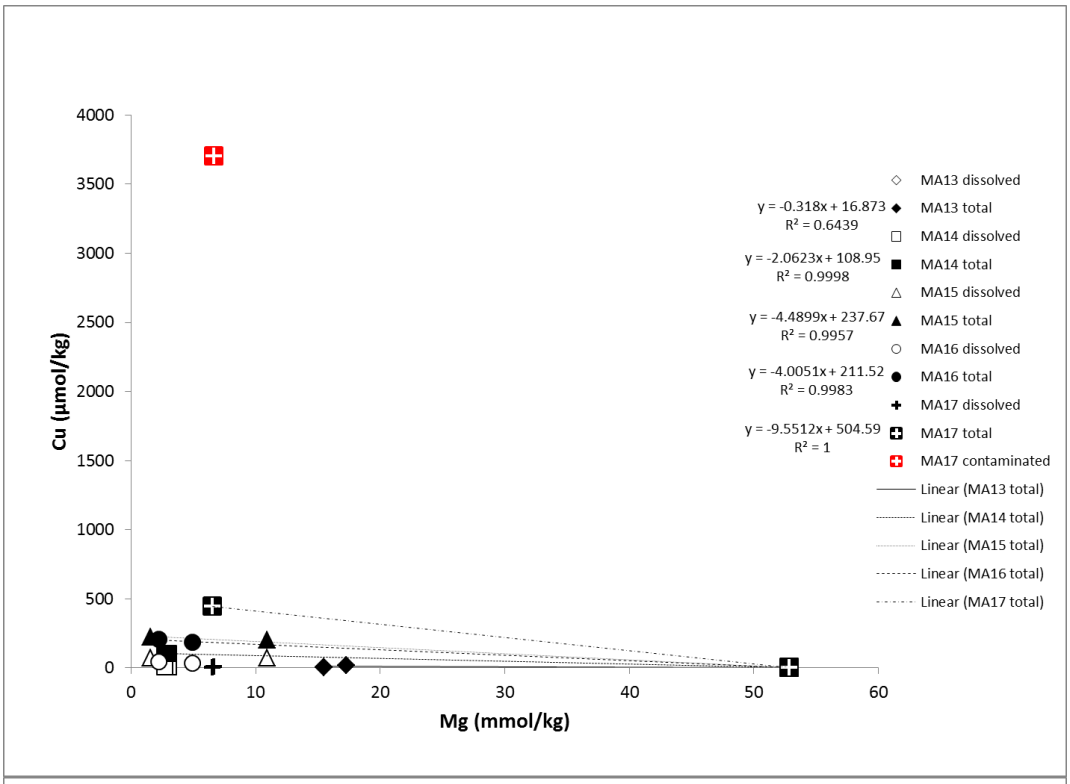
Cu (µmol/kg)
Mg (mmol/kg)
y = -0.318x + 16.873
R² = 0.6439
y = -2.0623x + 108.95
R² = 0.9998
y = -4.4899x + 237.67
R² = 0.9957
y = -4.0051x + 211.52
R² = 0.9983
y = -9.5512x + 504.59
R² = 1
MA13 dissolved
MA13 total
MA14 dissolved
MA14 total
MA15 dissolved
MA15 total
MA16 dissolved
MA16 total
MA17 dissolved
MA17 total
MA17 contaminated
Linear (MA13 total)
Linear (MA14 total)
Linear (MA15 total)
Linear (MA16 total)
Linear (MA17 total)

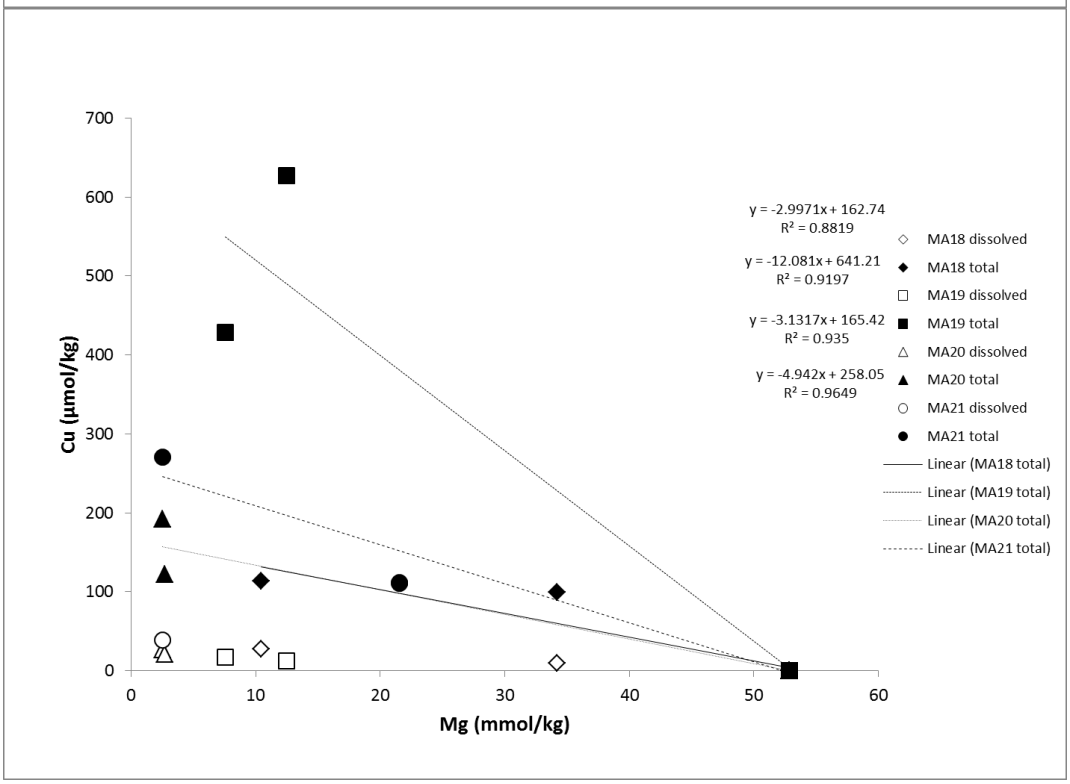
Cu (µmol/kg)
Mg (mmol/kg)
y = -2.9971x + 162.74
R² = 0.8819
y = -12.081x + 641.21
R² = 0.9197
y = -3.1317x + 165.42
R² = 0.935
y = -4.942x + 258.05
R² = 0.9649
MA18 dissolved
MA18 total
MA19 dissolved
MA19 total
MA20 dissolved
MA20 total
MA21 dissolved
MA21 total
Linear (MA18 total)
Linear (MA19 total)
Linear (MA20 total)
Linear (MA21 total)

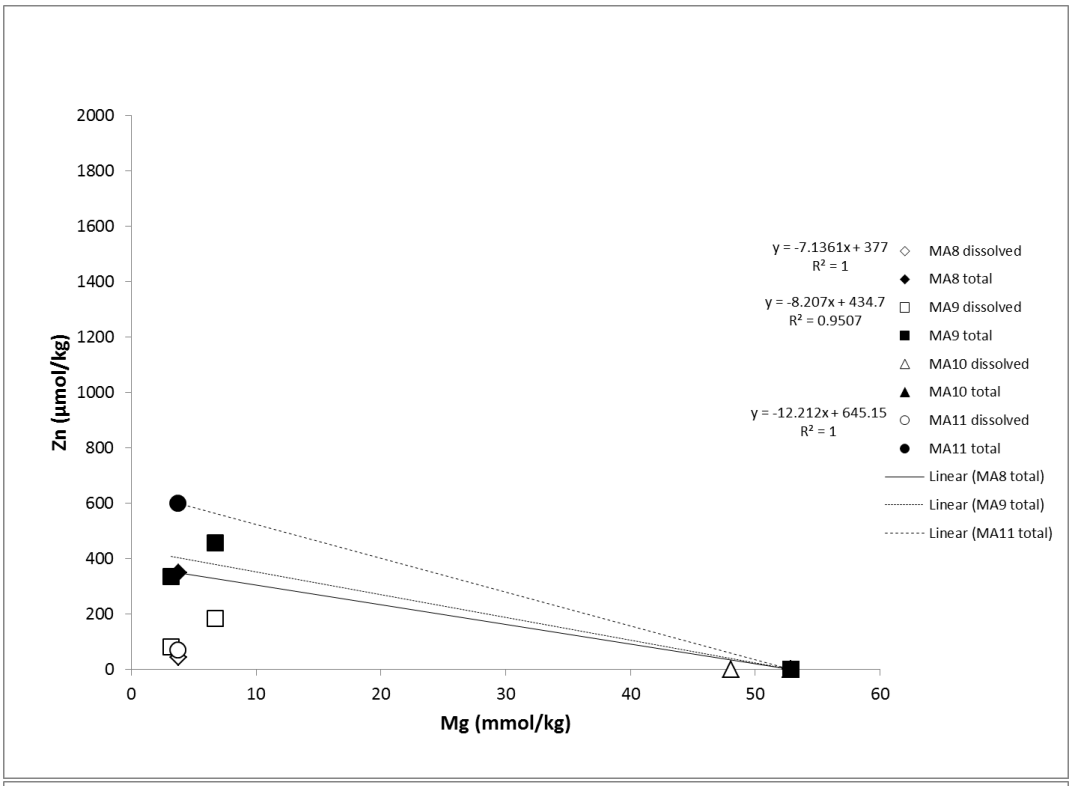
Zn (µmol/kg)
Mg (mmol/kg)
y = -7.1361x + 377
R² = 1
y = -8.207x + 434.7
R² = 0.9507
y = -12.212x + 645.15
R² = 1
MA8 dissolved
MA8 total
MA9 dissolved
MA9 total
MA10 dissolved
MA10 total
MA11 dissolved
MA11 total
Linear (MA8 total)
Linear (MA9 total)
Linear (MA11 total)

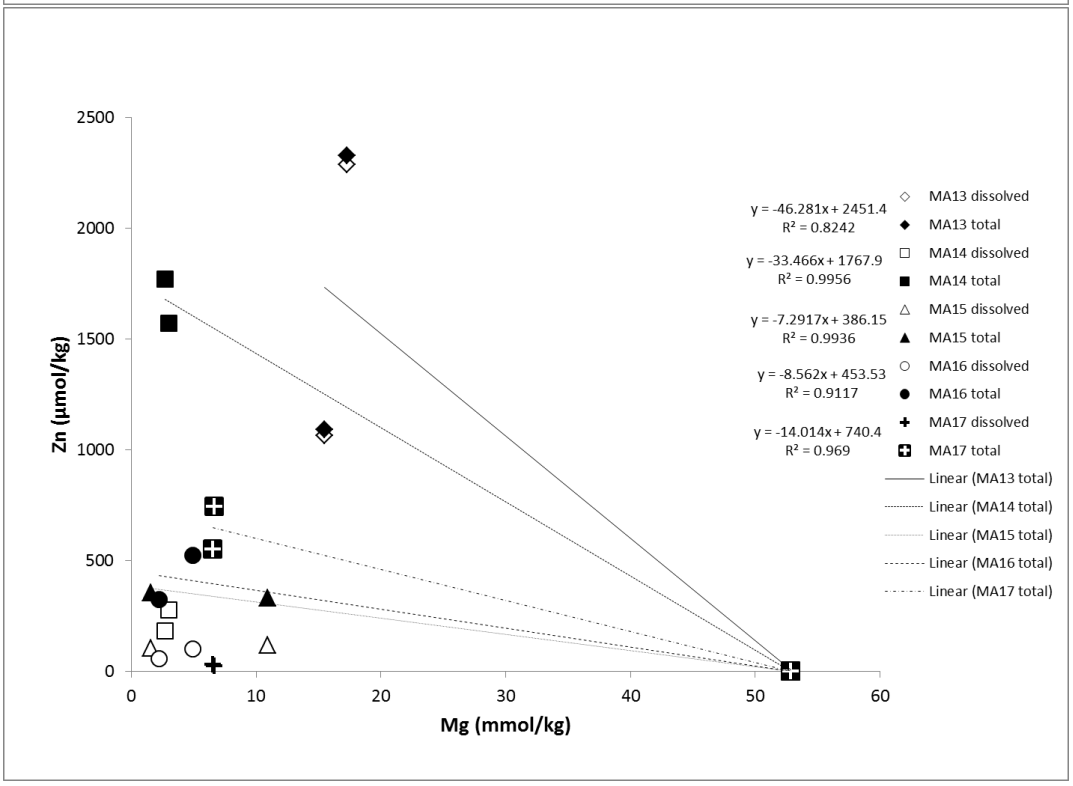
Zn (µmol/kg)
Mg (mmol/kg)
y = -46.281x + 2451.4
R² = 0.8242
y = -33.466x + 1767.9
R² = 0.9956
y = -7.2917x + 386.15
R² = 0.9936
y = -8.562x + 453.53
R² = 0.9117
y = -14.014x + 740.4
R² = 0.969
MA13 dissolved
MA13 total
MA14 dissolved
MA14 total
MA15 dissolved
MA15 total
MA16 dissolved
MA16 total
MA17 dissolved
MA17 total
Linear (MA13 total)
Linear (MA14 total)
Linear (MA15 total)
Linear (MA16 total)
Linear (MA17 total)

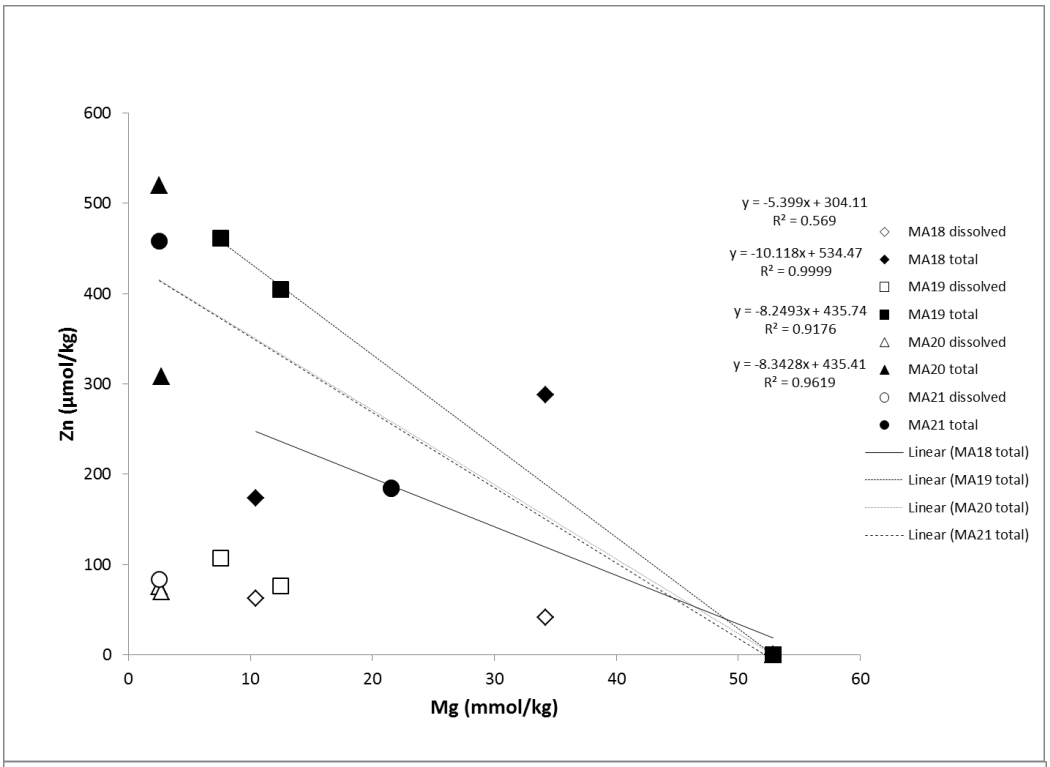
600
500
400
300
200
100
0
Zn (µmol/kg)
0
10
20
30
40
50
60
Mg (mmol/kg)
y = -5.399x + 304.11
R² = 0.569
y = -10.118x + 534.47
R² = 0.9999
y = -8.2493x + 435.74
R² = 0.9176
y = -8.3428x + 435.41
R² = 0.9619
MA18 dissolved
MA18 total
MA19 dissolved
MA19 total
MA20 dissolved
MA20 total
MA21 dissolved
MA21 total
Linear (MA18 total)
Linear (MA19 total)
Linear (MA20 total)
Linear (MA21 total)

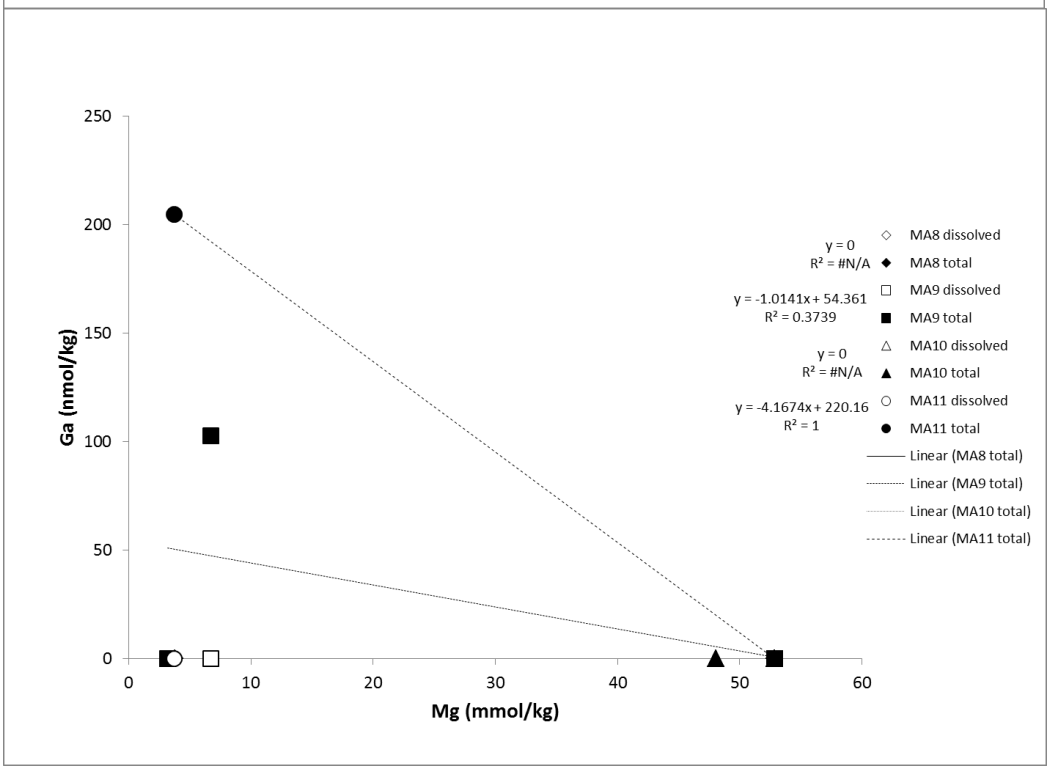
250
200
150
100
50
0
Ga (nmol/kg)
0
10
20
30
40
50
60
Mg (mmol/kg)
y = 0
R² = #N/A
y = -1.0141x + 54.361
R² = 0.3739
y = 0
R² = #N/A
y = -4.1674x + 220.16
R² = 1
MA8 dissolved
MA8 total
MA9 dissolved
MA9 total
MA10 dissolved
MA10 total
MA11 dissolved
MA11 total
Linear (MA8 total)
Linear (MA9 total)
Linear (MA10 total)
Linear (MA11 total)

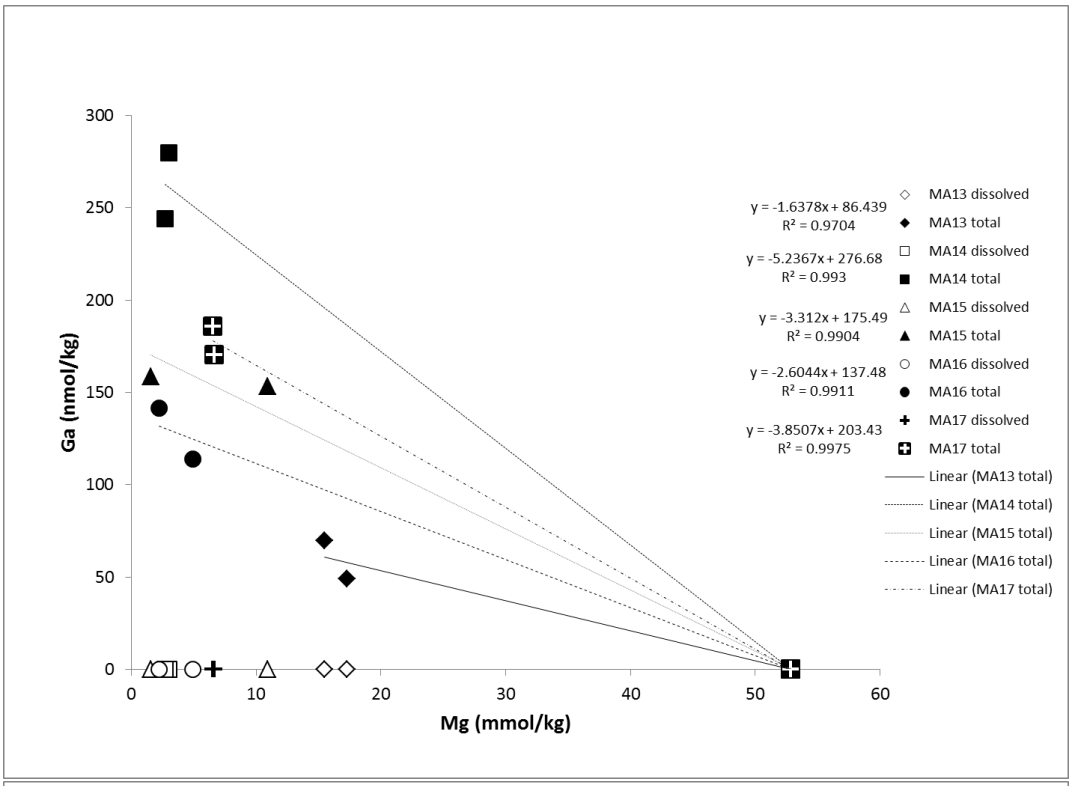
Ga (nmol/kg)
Mg (mmol/kg)
y = -1.6378x + 86.439
R² = 0.9704
y = -5.2367x + 276.68
R² = 0.993
y = -3.312x + 175.49
R² = 0.9904
y = -2.6044x + 137.48
R² = 0.9911
y = -3.8507x + 203.43
R² = 0.9975
MA13 dissolved
MA13 total
MA14 dissolved
MA14 total
MA15 dissolved
MA15 total
MA16 dissolved
MA16 total
MA17 dissolved
MA17 total
Linear (MA13 total)
Linear (MA14 total)
Linear (MA15 total)
Linear (MA16 total)
Linear (MA17 total)

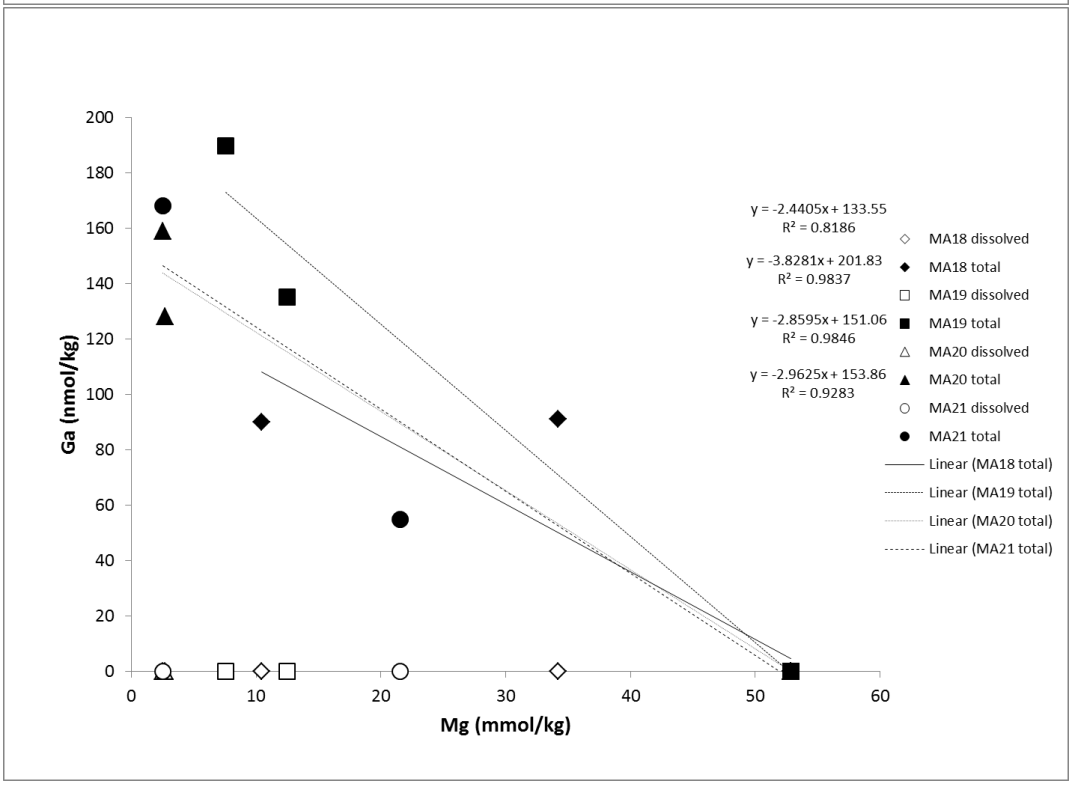
Ga (nmol/kg)
Mg (mmol/kg)
y = -2.4405x + 133.55
R² = 0.8186
y = -3.8281x + 201.83
R² = 0.9837
y = -2.8595x + 151.06
R² = 0.9846
y = -2.9625x + 153.86
R² = 0.9283
MA18 dissolved
MA18 total
MA19 dissolved
MA19 total
MA20 dissolved
MA20 total
MA21 dissolved
MA21 total
Linear (MA18 total)
Linear (MA19 total)
Linear (MA20 total)
Linear (MA21 total)

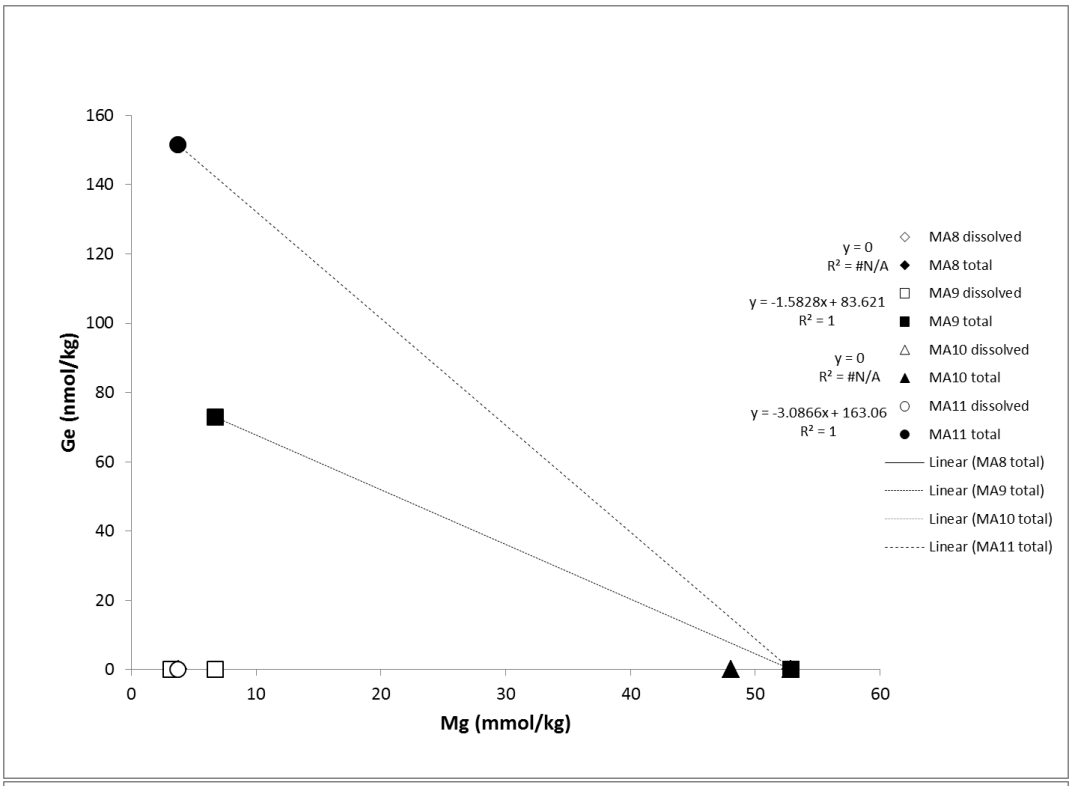
160
140
120
100
80
60
40
20
0
0
10
20
30
40
50
60
Ge (nmol/kg)
Mg (mmol/kg)
y = 0
R² = #N/A
y = -1.5828x + 83.621
R² = 1
y = 0
R² = #N/A
y = -3.0866x + 163.06
R² = 1
MA8 dissolved
MA8 total
MA9 dissolved
MA9 total
MA10 dissolved
MA10 total
MA11 dissolved
MA11 total
Linear (MA8 total)
Linear (MA9 total)
Linear (MA10 total)
Linear (MA11 total)

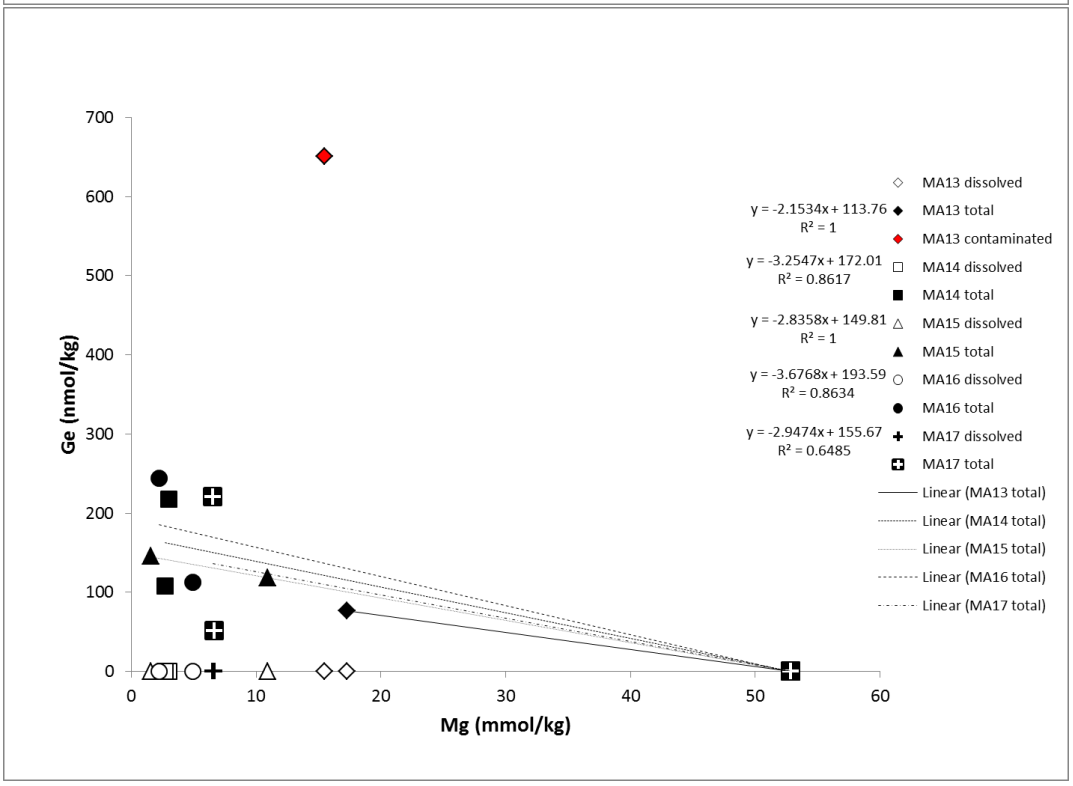
700
600
500
400
300
200
100
0
0
10
20
30
40
50
60
Ge (nmol/kg)
Mg (mmol/kg)
y = -2.1534x + 113.76
R² = 1
y = -3.2547x + 172.01
R² = 0.8617
y = -2.8358x + 149.81
R² = 1
y = -3.6768x + 193.59
R² = 0.8634
y = -2.9474x + 155.67
R² = 0.6485
MA13 dissolved
MA13 total
MA13 contaminated
MA14 dissolved
MA14 total
MA15 dissolved
MA15 total
MA16 dissolved
MA16 total
MA17 dissolved
MA17 total
Linear (MA13 total)
Linear (MA14 total)
Linear (MA15 total)
Linear (MA16 total)
Linear (MA17 total)

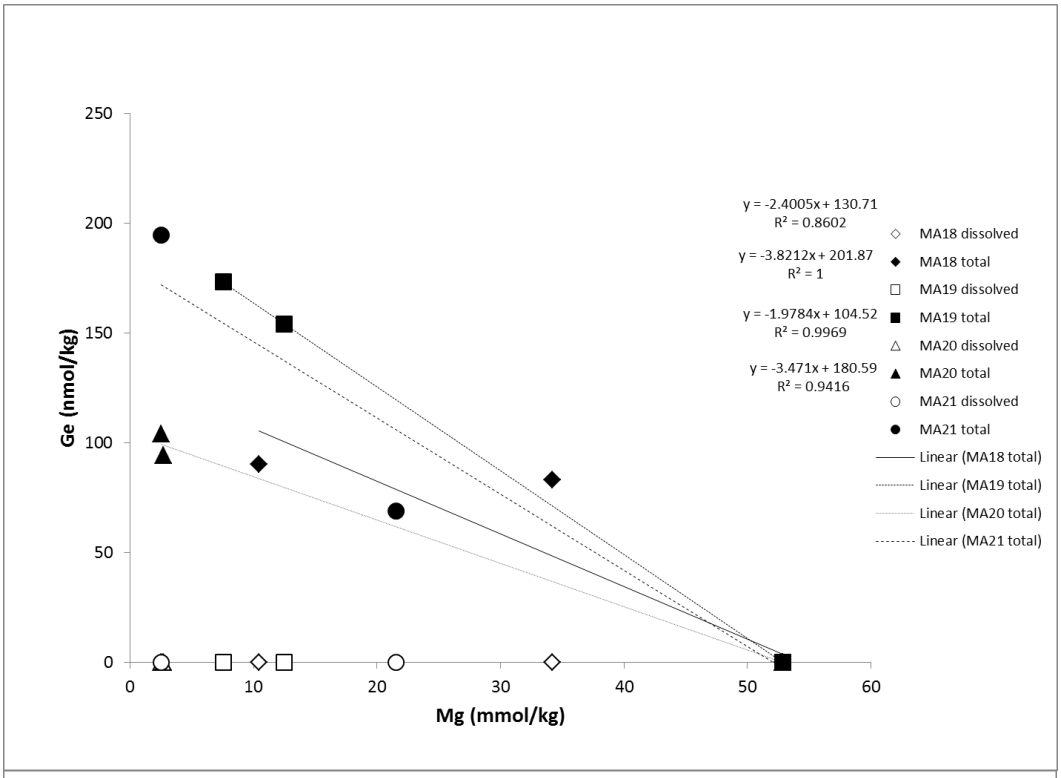
y = -2.4005x + 130.71
R² = 0.8602
y = -3.8212x + 201.87
R² = 1
y = -1.9784x + 104.52
R² = 0.9969
y = -3.471x + 180.59
R² = 0.9416
MA18 dissolved
MA18 total
MA19 dissolved
MA19 total
MA20 dissolved
MA20 total
MA21 dissolved
MA21 total
Linear (MA18 total)
Linear (MA19 total)
Linear (MA20 total)
Linear (MA21 total)
Ge (nmol/kg)
Mg (mmol/kg)
0
50
100
150
200
250
0
10
20
30
40
50
60

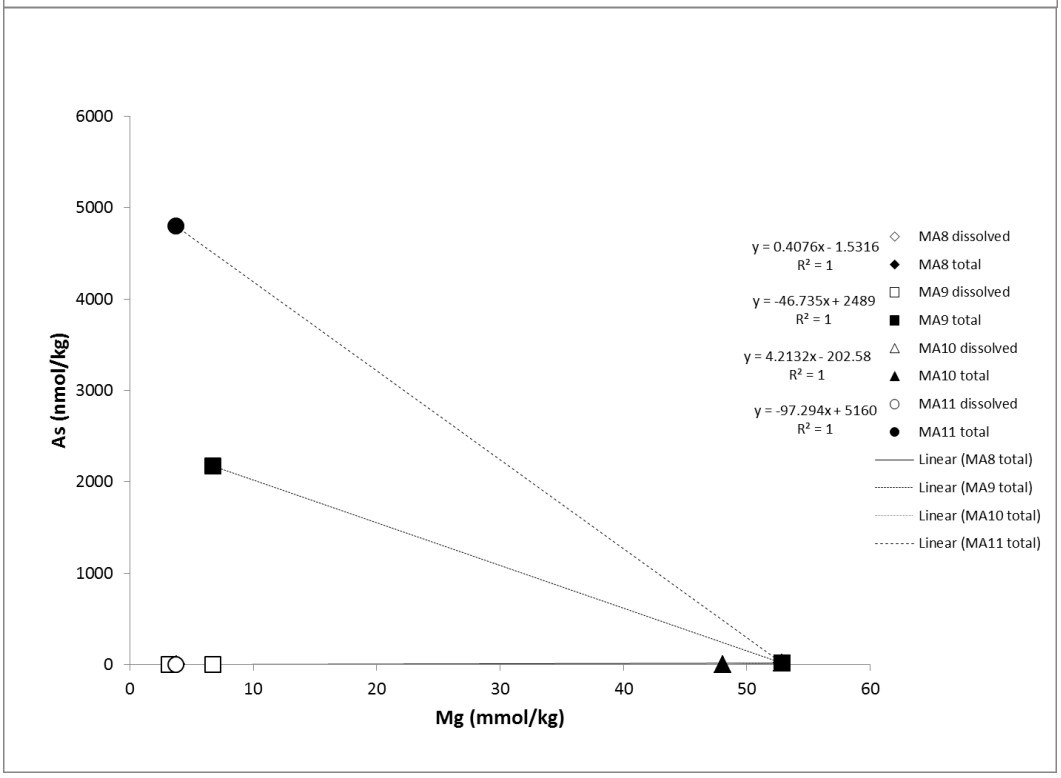
y = 0.4076x - 1.5316
R² = 1
y = -46.735x + 2489
R² = 1
y = 4.2132x - 202.58
R² = 1
y = -97.294x + 5160
R² = 1
MA8 dissolved
MA8 total
MA9 dissolved
MA9 total
MA10 dissolved
MA10 total
MA11 dissolved
MA11 total
Linear (MA8 total)
Linear (MA9 total)
Linear (MA10 total)
Linear (MA11 total)
As (nmol/kg)
Mg (mmol/kg)
0
1000
2000
3000
4000
5000
6000
0
10
20
30
40
50
60

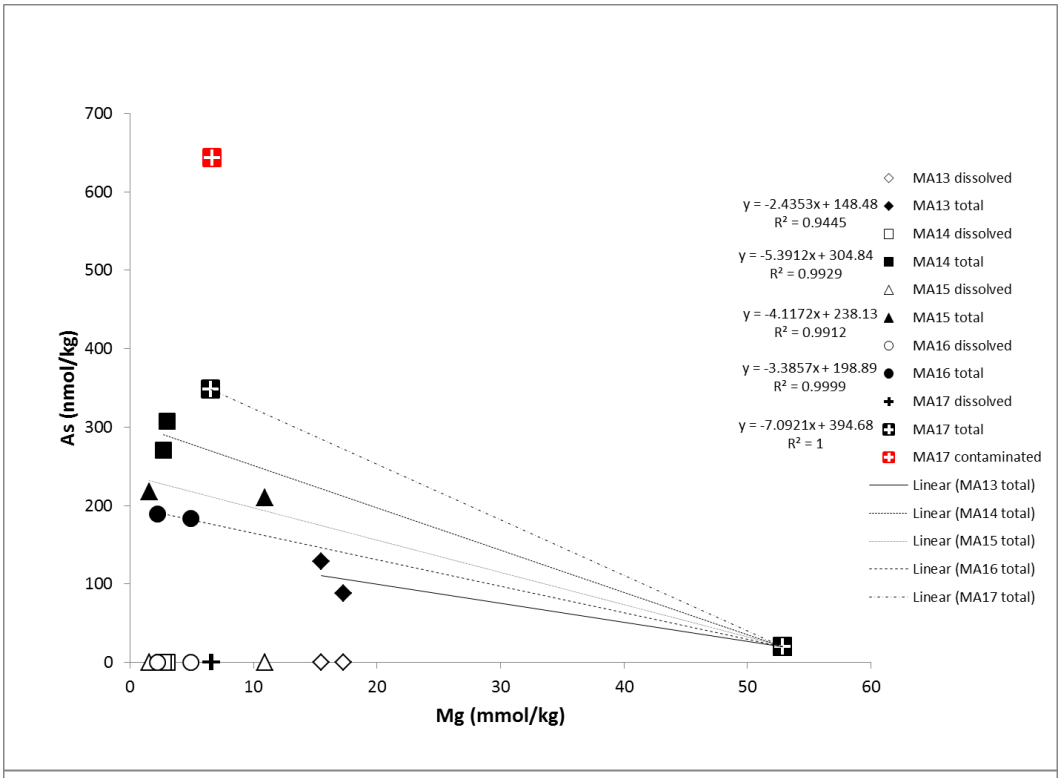
As (nmol/kg)
Mg (mmol/kg)
y = -2.4353x + 148.48
R² = 0.9445
y = -5.3912x + 304.84
R² = 0.9929
y = -4.1172x + 238.13
R² = 0.9912
y = -3.3857x + 198.89
R² = 0.9999
y = -7.0921x + 394.68
R² = 1
MA13 dissolved
MA13 total
MA14 dissolved
MA14 total
MA15 dissolved
MA15 total
MA16 dissolved
MA16 total
MA17 dissolved
MA17 total
MA17 contaminated
Linear (MA13 total)
Linear (MA14 total)
Linear (MA15 total)
Linear (MA16 total)
Linear (MA17 total)

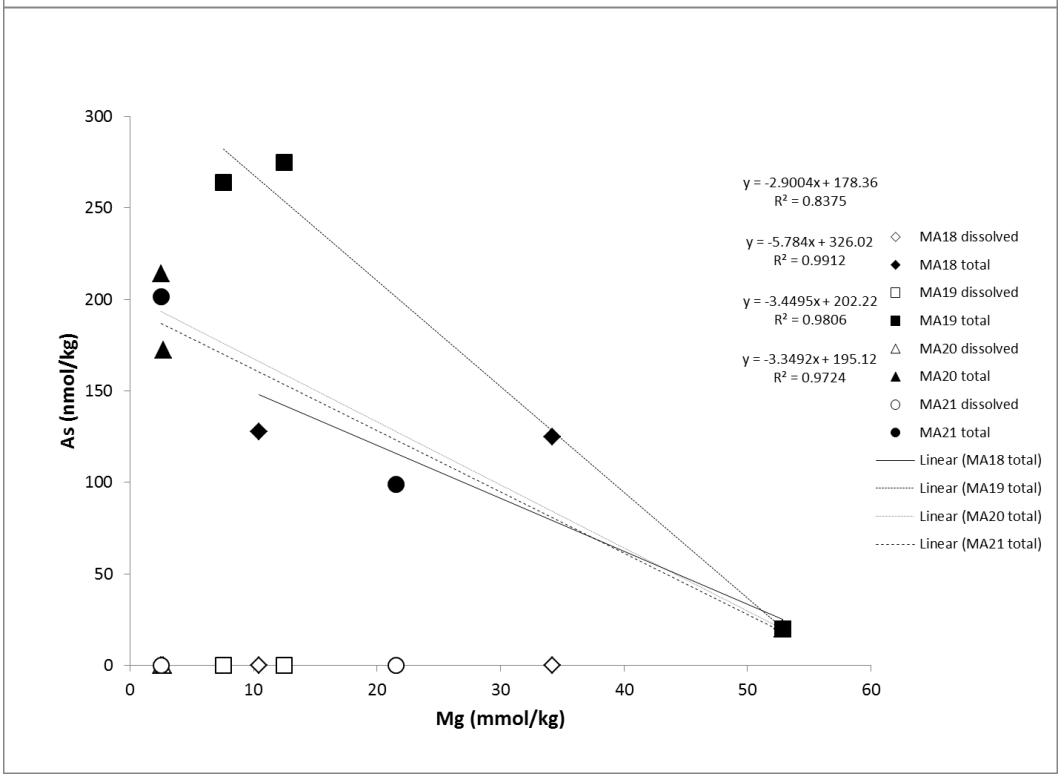
As (nmol/kg)
Mg (mmol/kg)
y = -2.9004x + 178.36
R² = 0.8375
y = -5.784x + 326.02
R² = 0.9912
y = -3.4495x + 202.22
R² = 0.9806
y = -3.3492x + 195.12
R² = 0.9724
MA18 dissolved
MA18 total
MA19 dissolved
MA19 total
MA20 dissolved
MA20 total
MA21 dissolved
MA21 total
Linear (MA18 total)
Linear (MA19 total)
Linear (MA20 total)
Linear (MA21 total)

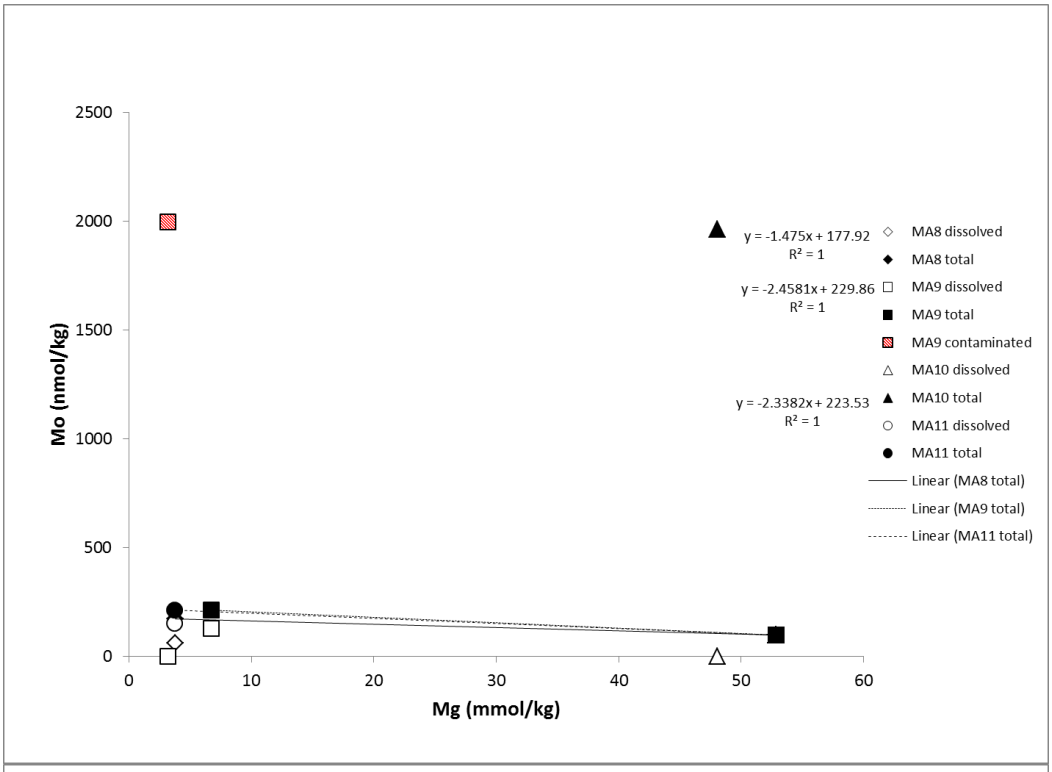
2500
2000
1500
1000
500
0
0
10
20
30
40
50
60
Mo (nmol/kg)
Mg (mmol/kg)
y = -1.475x + 177.92
R² = 1
y = -2.4581x + 229.86
R² = 1
y = -2.3382x + 223.53
R² = 1
MA8 dissolved
MA8 total
MA9 dissolved
MA9 total
MA9 contaminated
MA10 dissolved
MA10 total
MA11 dissolved
MA11 total
Linear (MA8 total)
Linear (MA9 total)
Linear (MA11 total)

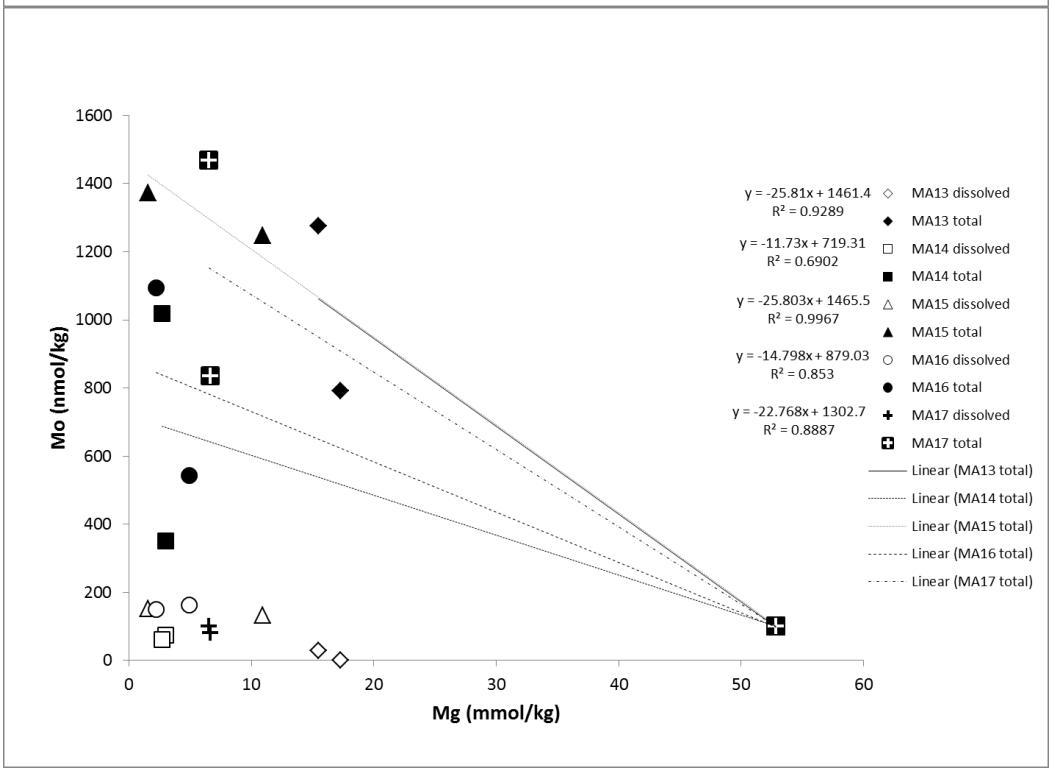
1600
1400
1200
1000
800
600
400
200
0
0
10
20
30
40
50
60
Mo (nmol/kg)
Mg (mmol/kg)
y = -25.81x + 1461.4
R² = 0.9289
y = -11.73x + 719.31
R² = 0.6902
y = -25.803x + 1465.5
R² = 0.9967
y = -14.798x + 879.03
R² = 0.853
y = -22.768x + 1302.7
R² = 0.8887
MA13 dissolved
MA13 total
MA14 dissolved
MA14 total
MA15 dissolved
MA15 total
MA16 dissolved
MA16 total
MA17 dissolved
MA17 total
Linear (MA13 total)
Linear (MA14 total)
Linear (MA15 total)
Linear (MA16 total)
Linear (MA17 total)

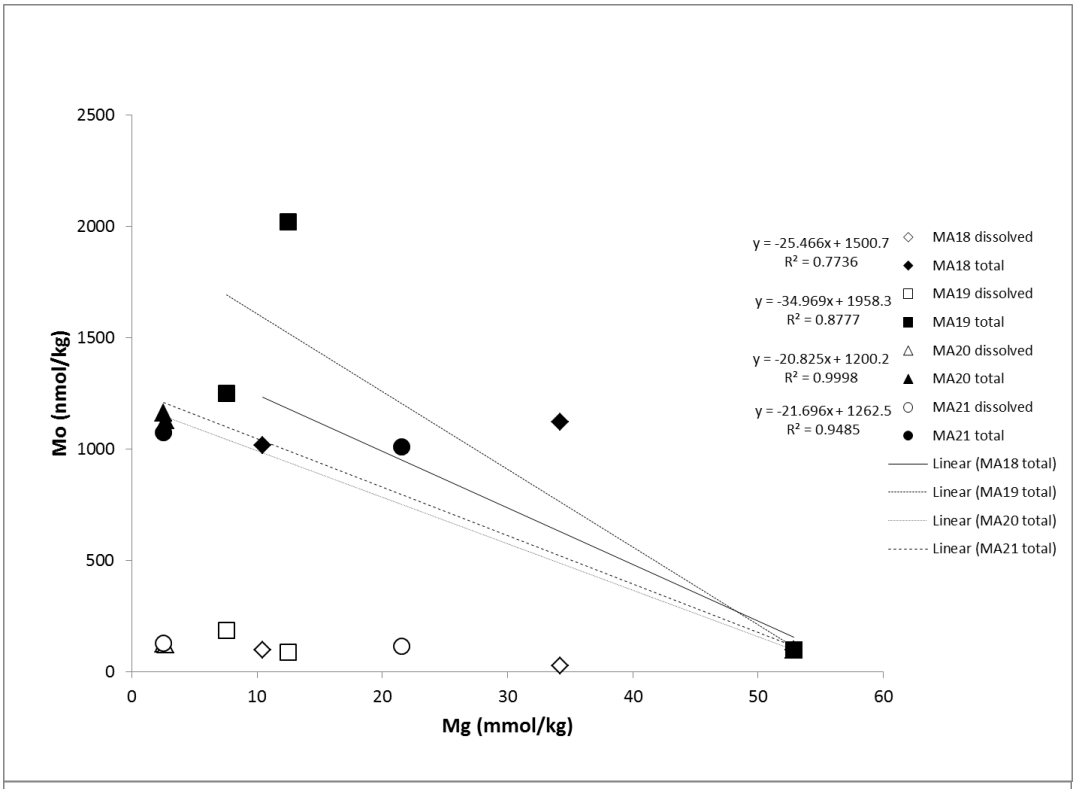
Mo (nmol/kg)
Mg (mmol/kg)
y = -25.466x + 1500.7
R² = 0.7736
y = -34.969x + 1958.3
R² = 0.8777
y = -20.825x + 1200.2
R² = 0.9998
y = -21.696x + 1262.5
R² = 0.9485
MA18 dissolved
MA18 total
MA19 dissolved
MA19 total
MA20 dissolved
MA20 total
MA21 dissolved
MA21 total
Linear (MA18 total)
Linear (MA19 total)
Linear (MA20 total)
Linear (MA21 total)

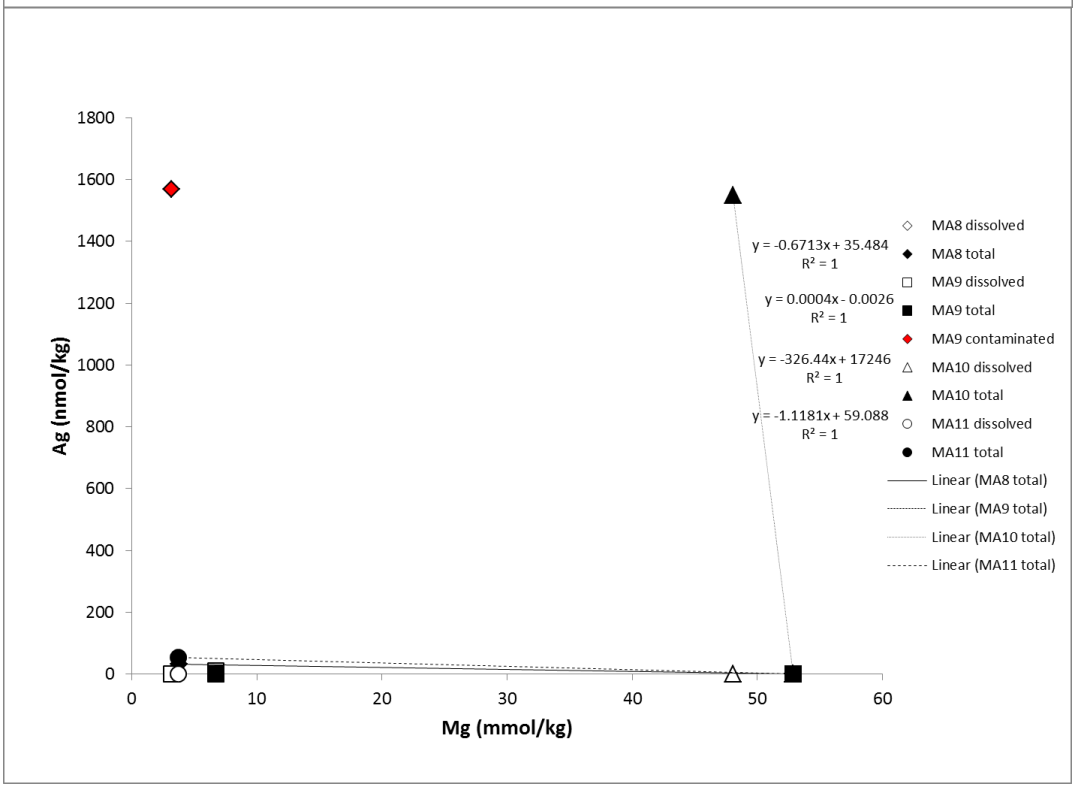
Ag (nmol/kg)
Mg (mmol/kg)
y = -0.6713x + 35.484
R² = 1
y = 0.0004x - 0.0026
R² = 1
y = -326.44x + 17246
R² = 1
y = -1.1181x + 59.088
R² = 1
MA8 dissolved
MA8 total
MA9 dissolved
MA9 total
MA9 contaminated
MA10 dissolved
MA10 total
MA11 dissolved
MA11 total
Linear (MA8 total)
Linear (MA9 total)
Linear (MA10 total)
Linear (MA11 total)

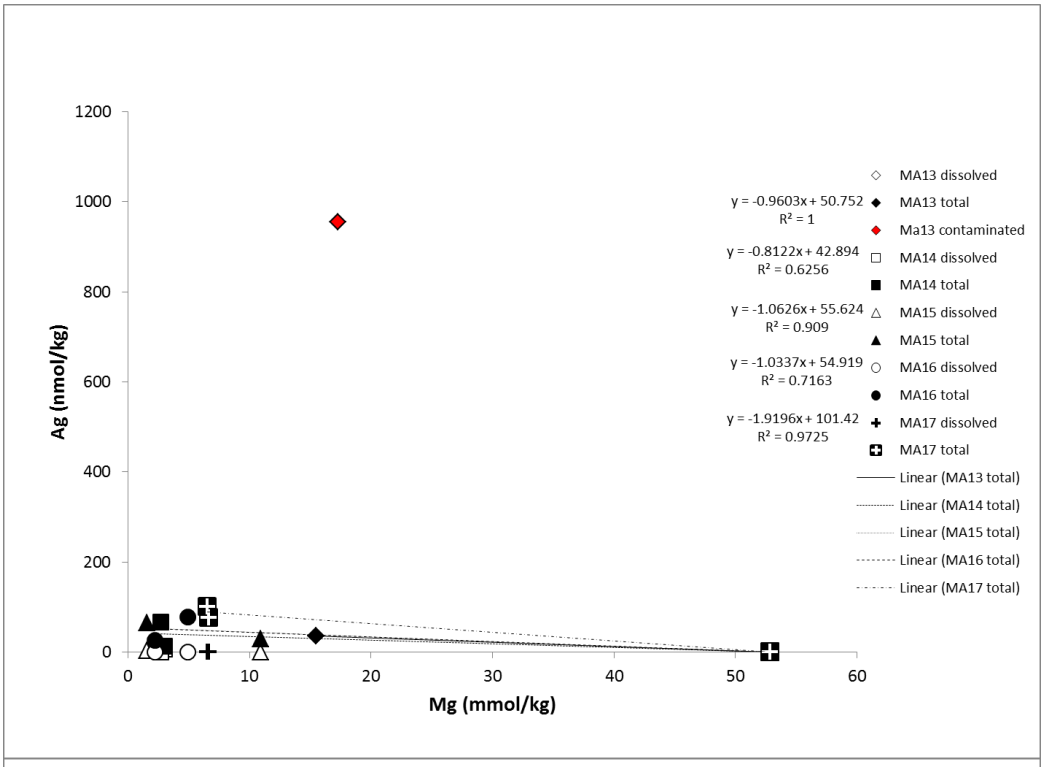
Ag (nmol/kg)
Mg (mmol/kg)
0
200
400
600
800
1000
1200
0
10
20
30
40
50
60
y = -0.9603x + 50.752
R² = 1
y = -0.8122x + 42.894
R² = 0.6256
y = -1.0626x + 55.624
R² = 0.909
y = -1.0337x + 54.919
R² = 0.7163
y = -1.9196x + 101.42
R² = 0.9725
MA13 dissolved
MA13 total
Ma13 contaminated
MA14 dissolved
MA14 total
MA15 dissolved
MA15 total
MA16 dissolved
MA16 total
MA17 dissolved
MA17 total
Linear (MA13 total)
Linear (MA14 total)
Linear (MA15 total)
Linear (MA16 total)
Linear (MA17 total)

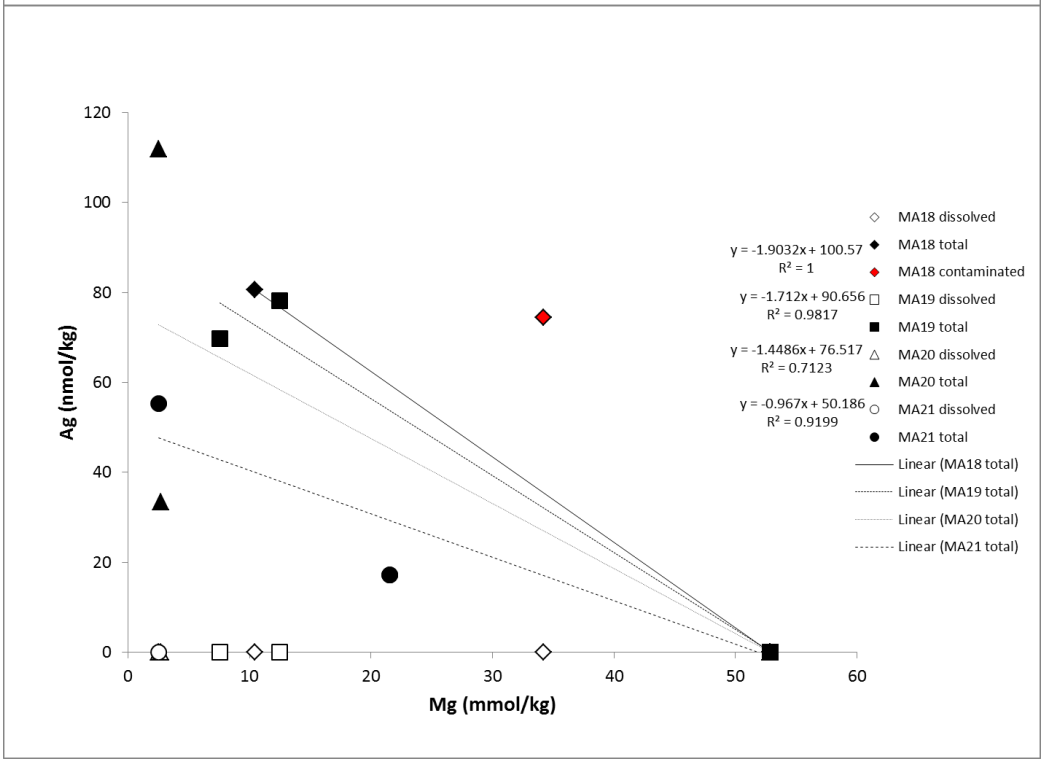
Ag (nmol/kg)
Mg (mmol/kg)
0
20
40
60
80
100
120
0
10
20
30
40
50
60
y = -1.9032x + 100.57
R² = 1
y = -1.712x + 90.656
R² = 0.9817
y = -1.4486x + 76.517
R² = 0.7123
y = -0.967x + 50.186
R² = 0.9199
MA18 dissolved
MA18 total
MA18 contaminated
MA19 dissolved
MA19 total
MA20 dissolved
MA20 total
MA21 dissolved
MA21 total
Linear (MA18 total)
Linear (MA19 total)
Linear (MA20 total)
Linear (MA21 total)

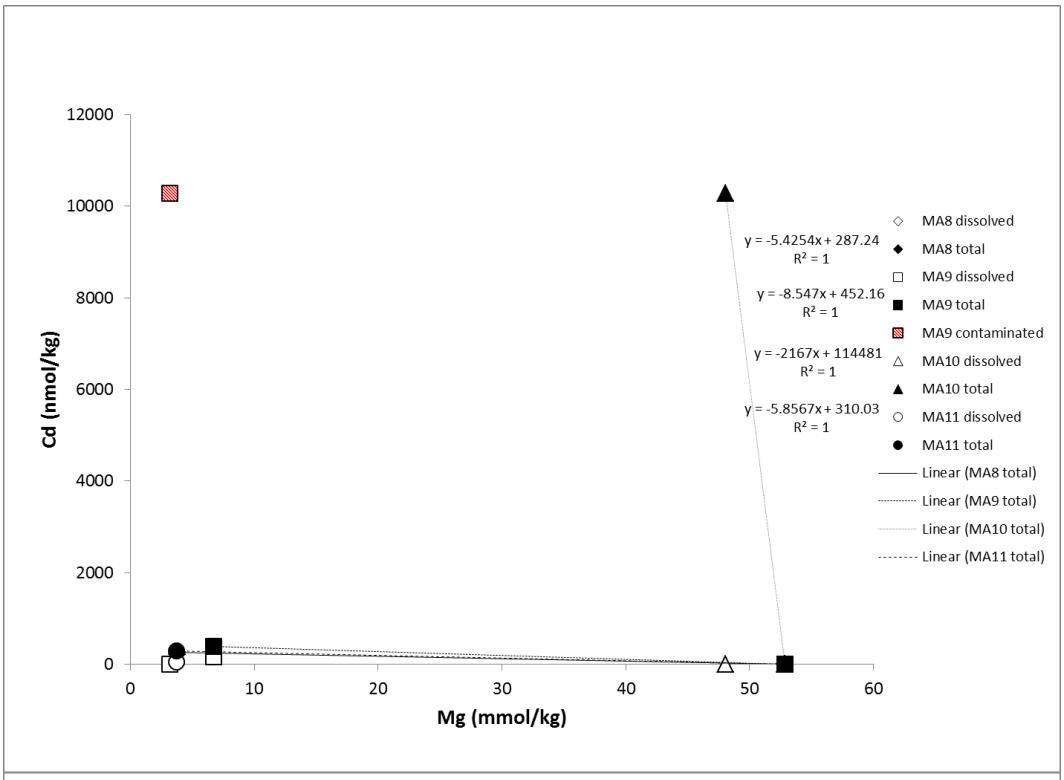
12000
10000
8000
6000
4000
2000
0
Cd (nmol/kg)
0
10
20
30
40
50
60
Mg (mmol/kg)
y = -5.4254x + 287.24
R² = 1
y = -8.547x + 452.16
R² = 1
y = -2167x + 114481
R² = 1
y = -5.8567x + 310.03
R² = 1
MA8 dissolved
MA8 total
MA9 dissolved
MA9 total
MA9 contaminated
MA10 dissolved
MA10 total
MA11 dissolved
MA11 total
Linear (MA8 total)
Linear (MA9 total)
Linear (MA10 total)
Linear (MA11 total)

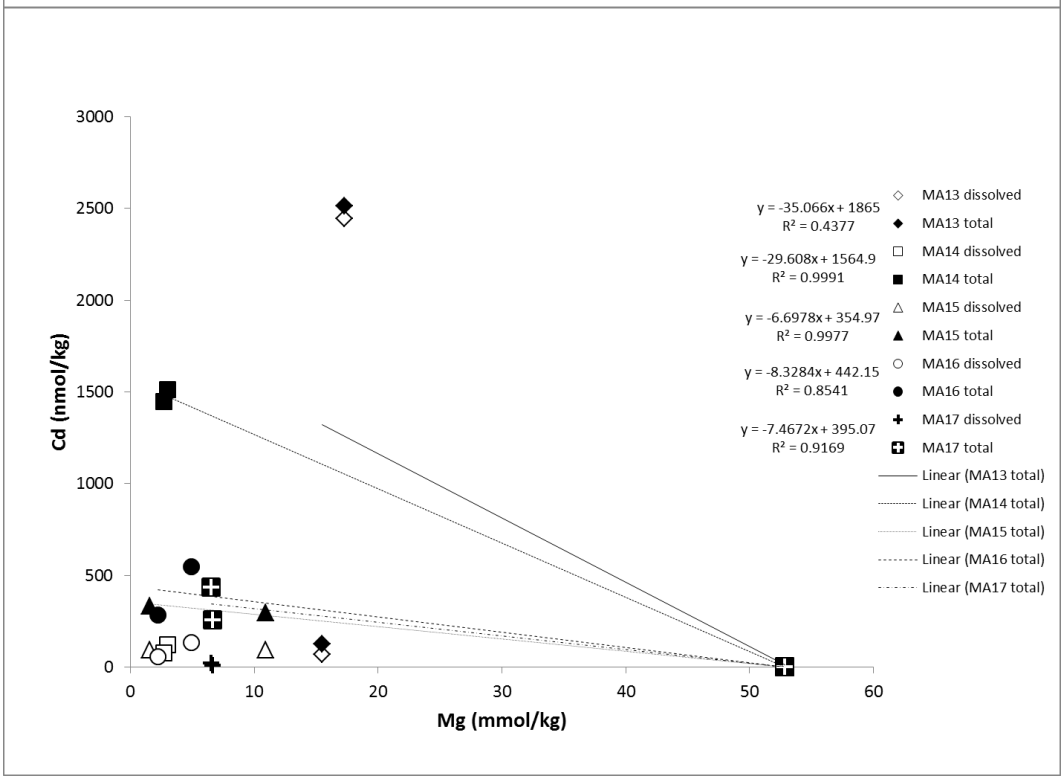
3000
2500
2000
1500
1000
500
0
Cd (nmol/kg)
0
10
20
30
40
50
60
Mg (mmol/kg)
y = -35.066x + 1865
R² = 0.4377
y = -29.608x + 1564.9
R² = 0.9991
y = -6.6978x + 354.97
R² = 0.9977
y = -8.3284x + 442.15
R² = 0.8541
y = -7.4672x + 395.07
R² = 0.9169
MA13 dissolved
MA13 total
MA14 dissolved
MA14 total
MA15 dissolved
MA15 total
MA16 dissolved
MA16 total
MA17 dissolved
MA17 total
Linear (MA13 total)
Linear (MA14 total)
Linear (MA15 total)
Linear (MA16 total)
Linear (MA17 total)

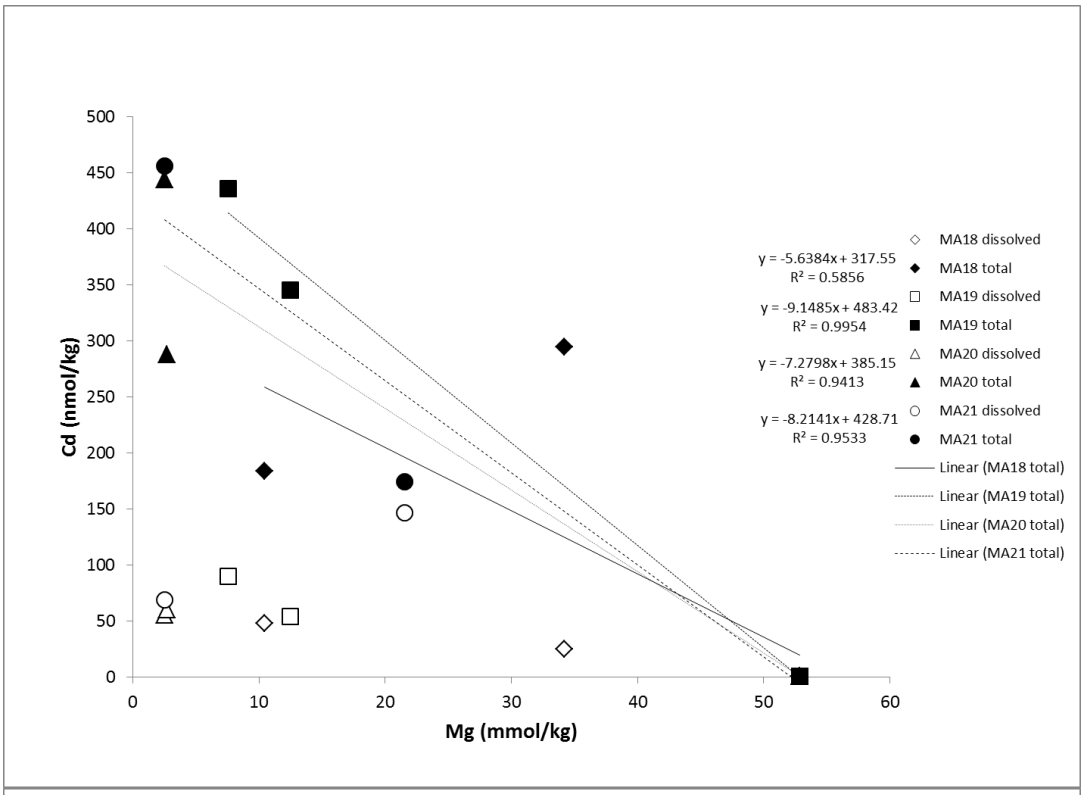
Cd (nmol/kg)
Mg (mmol/kg)
y = -5.6384x + 317.55
R² = 0.5856
y = -9.1485x + 483.42
R² = 0.9954
y = -7.2798x + 385.15
R² = 0.9413
y = -8.2141x + 428.71
R² = 0.9533
MA18 dissolved
MA18 total
MA19 dissolved
MA19 total
MA20 dissolved
MA20 total
MA21 dissolved
MA21 total
Linear (MA18 total)
Linear (MA19 total)
Linear (MA20 total)
Linear (MA21 total)

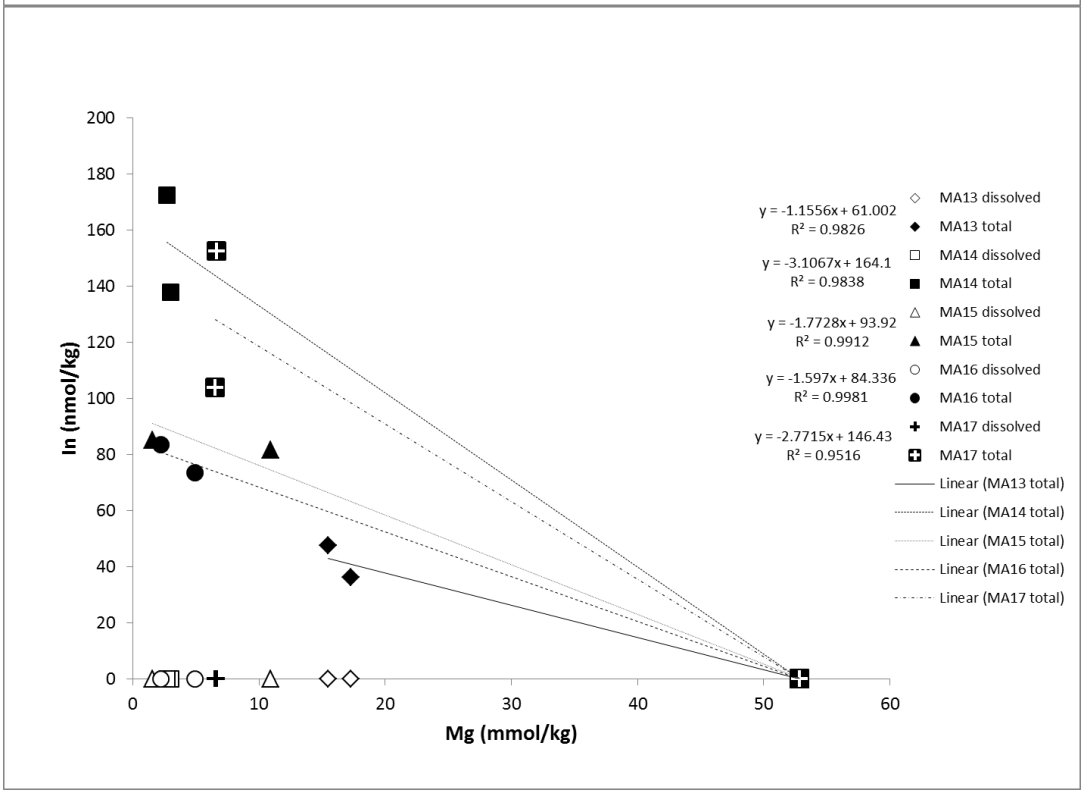
In (nmol/kg)
Mg (mmol/kg)
y = -1.1556x + 61.002
R² = 0.9826
y = -3.1067x + 164.1
R² = 0.9838
y = -1.7728x + 93.92
R² = 0.9912
y = -1.597x + 84.336
R² = 0.9981
y = -2.7715x + 146.43
R² = 0.9516
MA13 dissolved
MA13 total
MA14 dissolved
MA14 total
MA15 dissolved
MA15 total
MA16 dissolved
MA16 total
MA17 dissolved
MA17 total
Linear (MA13 total)
Linear (MA14 total)
Linear (MA15 total)
Linear (MA16 total)
Linear (MA17 total)

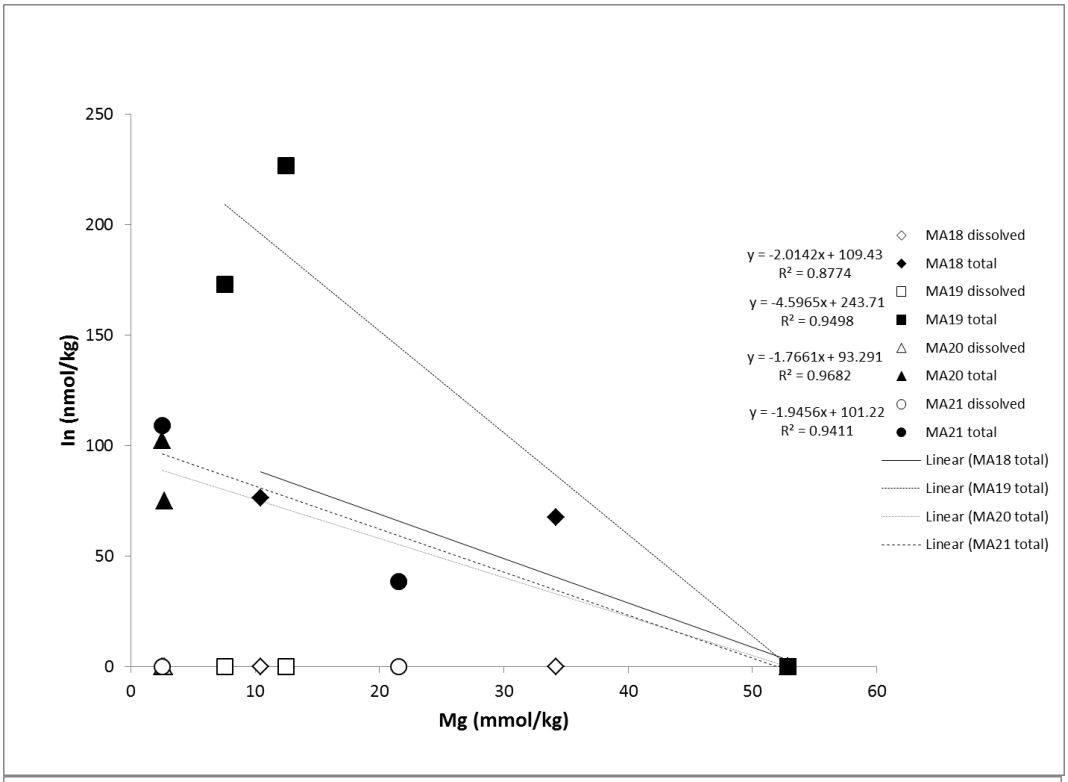
In (nmol/kg)
Mg (mmol/kg)
y = -2.0142x + 109.43
R² = 0.8774
y = -4.5965x + 243.71
R² = 0.9498
y = -1.7661x + 93.291
R² = 0.9682
y = -1.9456x + 101.22
R² = 0.9411
MA18 dissolved
MA18 total
MA19 dissolved
MA19 total
MA20 dissolved
MA20 total
MA21 dissolved
MA21 total
Linear (MA18 total)
Linear (MA19 total)
Linear (MA20 total)
Linear (MA21 total)

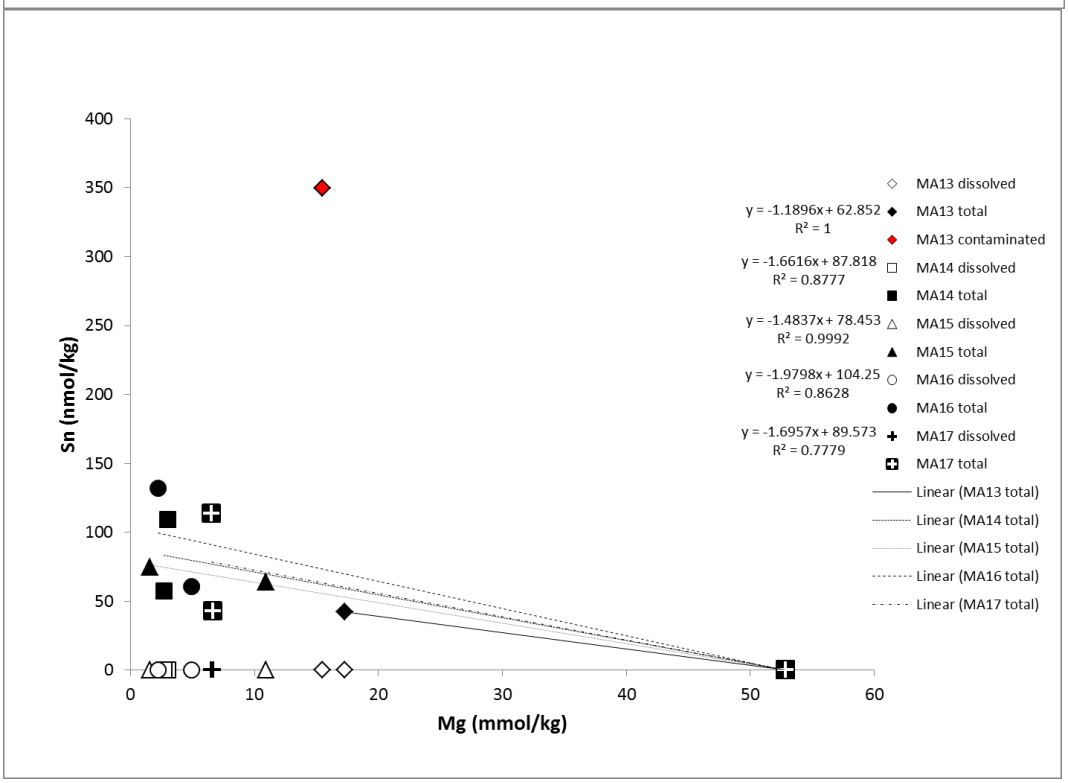
Sn (nmol/kg)
Mg (mmol/kg)
y = -1.1896x + 62.852
R² = 1
y = -1.6616x + 87.818
R² = 0.8777
y = -1.4837x + 78.453
R² = 0.9992
y = -1.9798x + 104.25
R² = 0.8628
y = -1.6957x + 89.573
R² = 0.7779
MA13 dissolved
MA13 total
MA13 contaminated
MA14 dissolved
MA14 total
MA15 dissolved
MA15 total
MA16 dissolved
MA16 total
MA17 dissolved
MA17 total
Linear (MA13 total)
Linear (MA14 total)
Linear (MA15 total)
Linear (MA16 total)
Linear (MA17 total)

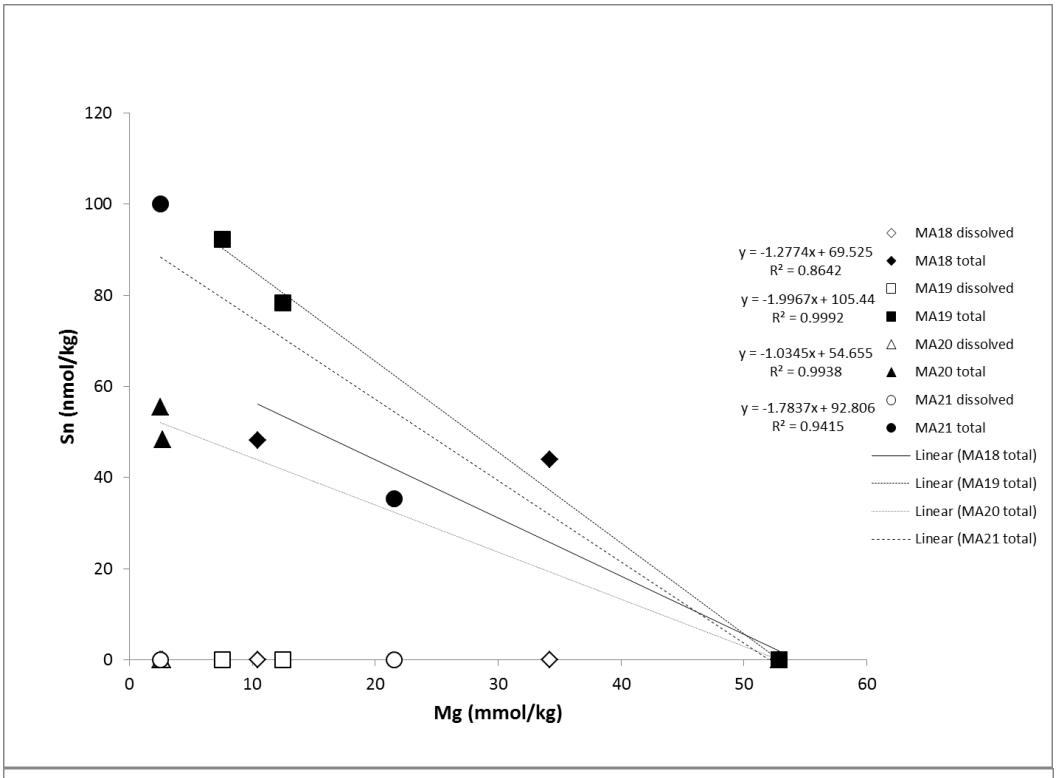
120
100
80
60
40
20
0
Sn (nmol/kg)
0
10
20
30
40
50
60
Mg (mmol/kg)
y = -1.2774x + 69.525
R² = 0.8642
y = -1.9967x + 105.44
R² = 0.9992
y = -1.0345x + 54.655
R² = 0.9938
y = -1.7837x + 92.806
R² = 0.9415
MA18 dissolved
MA18 total
MA19 dissolved
MA19 total
MA20 dissolved
MA20 total
MA21 dissolved
MA21 total
Linear (MA18 total)
Linear (MA19 total)
Linear (MA20 total)
Linear (MA21 total)

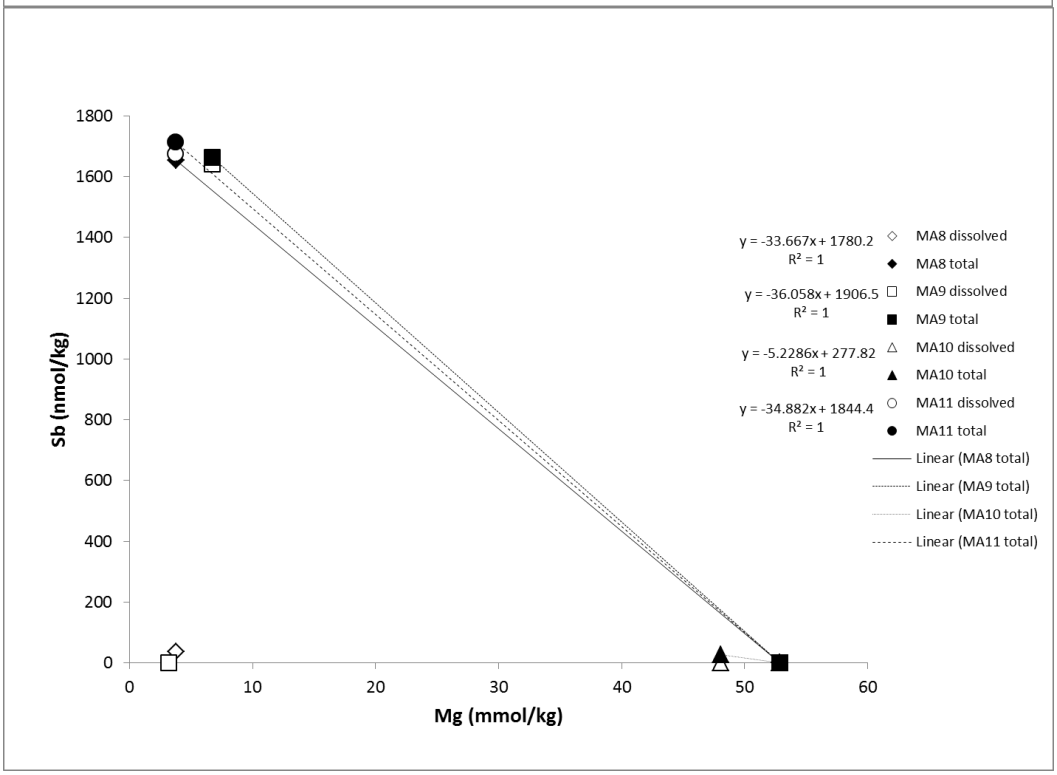
1800
1600
1400
1200
1000
800
600
400
200
0
Sb (nmol/kg)
0
10
20
30
40
50
60
Mg (mmol/kg)
y = -33.667x + 1780.2
R² = 1
y = -36.058x + 1906.5
R² = 1
y = -5.2286x + 277.82
R² = 1
y = -34.882x + 1844.4
R² = 1
MA8 dissolved
MA8 total
MA9 dissolved
MA9 total
MA10 dissolved
MA10 total
MA11 dissolved
MA11 total
Linear (MA8 total)
Linear (MA9 total)
Linear (MA10 total)
Linear (MA11 total)

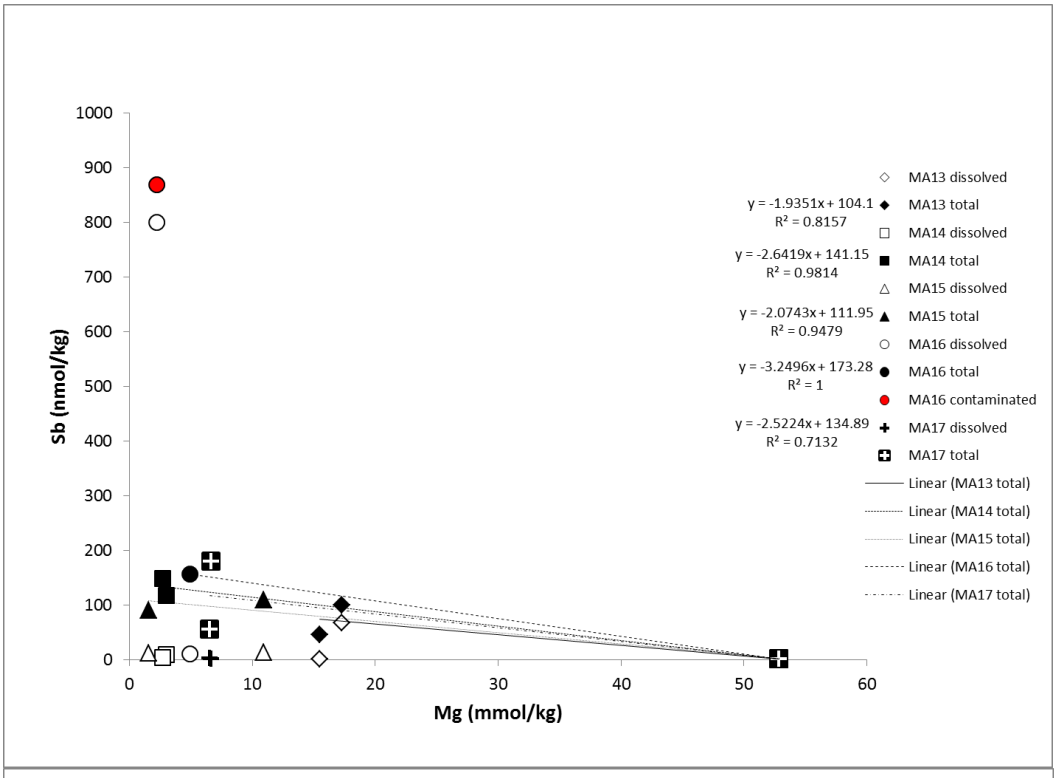
Sb (nmol/kg)
Mg (mmol/kg)
0
100
200
300
400
500
600
700
800
900
1000
0
10
20
30
40
50
60
y = -1.9351x + 104.1
R² = 0.8157
y = -2.6419x + 141.15
R² = 0.9814
y = -2.0743x + 111.95
R² = 0.9479
y = -3.2496x + 173.28
R² = 1
y = -2.5224x + 134.89
R² = 0.7132
MA13 dissolved
MA13 total
MA14 dissolved
MA14 total
MA15 dissolved
MA15 total
MA16 dissolved
MA16 total
MA16 contaminated
MA17 dissolved
MA17 total
Linear (MA13 total)
Linear (MA14 total)
Linear (MA15 total)
Linear (MA16 total)
Linear (MA17 total)

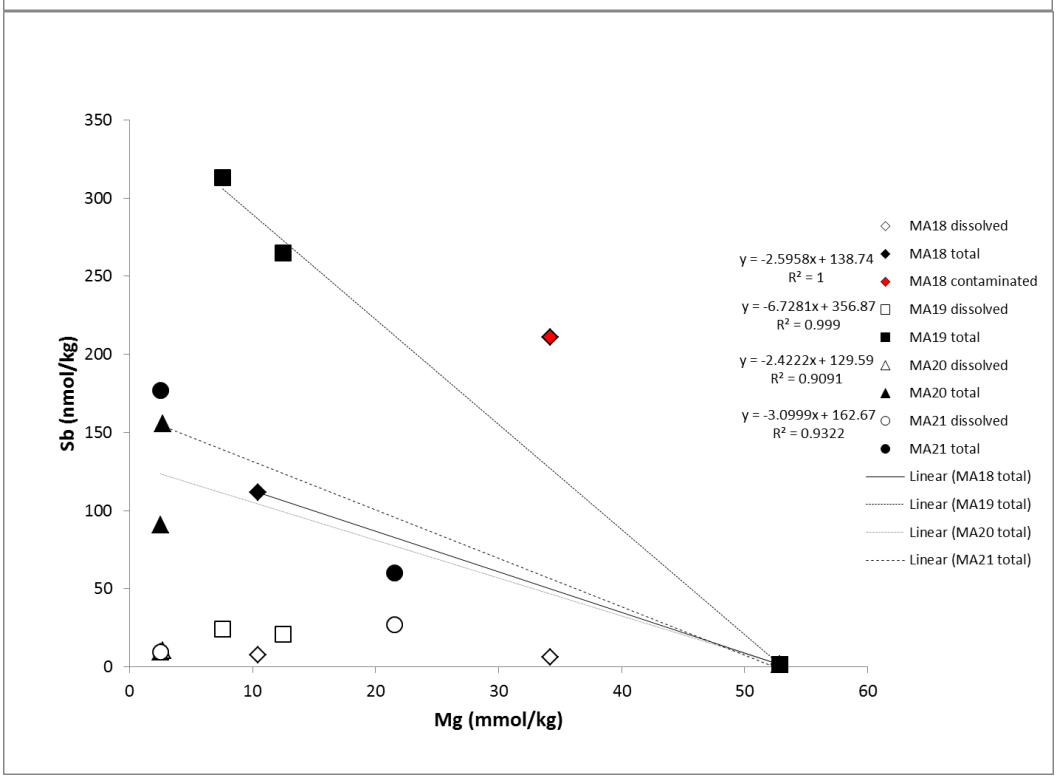
Sb (nmol/kg)
Mg (mmol/kg)
0
50
100
150
200
250
300
350
0
10
20
30
40
50
60
y = -2.5958x + 138.74
R² = 1
y = -6.7281x + 356.87
R² = 0.999
y = -2.4222x + 129.59
R² = 0.9091
y = -3.0999x + 162.67
R² = 0.9322
MA18 dissolved
MA18 total
MA18 contaminated
MA19 dissolved
MA19 total
MA20 dissolved
MA20 total
MA21 dissolved
MA21 total
Linear (MA18 total)
Linear (MA19 total)
Linear (MA20 total)
Linear (MA21 total)

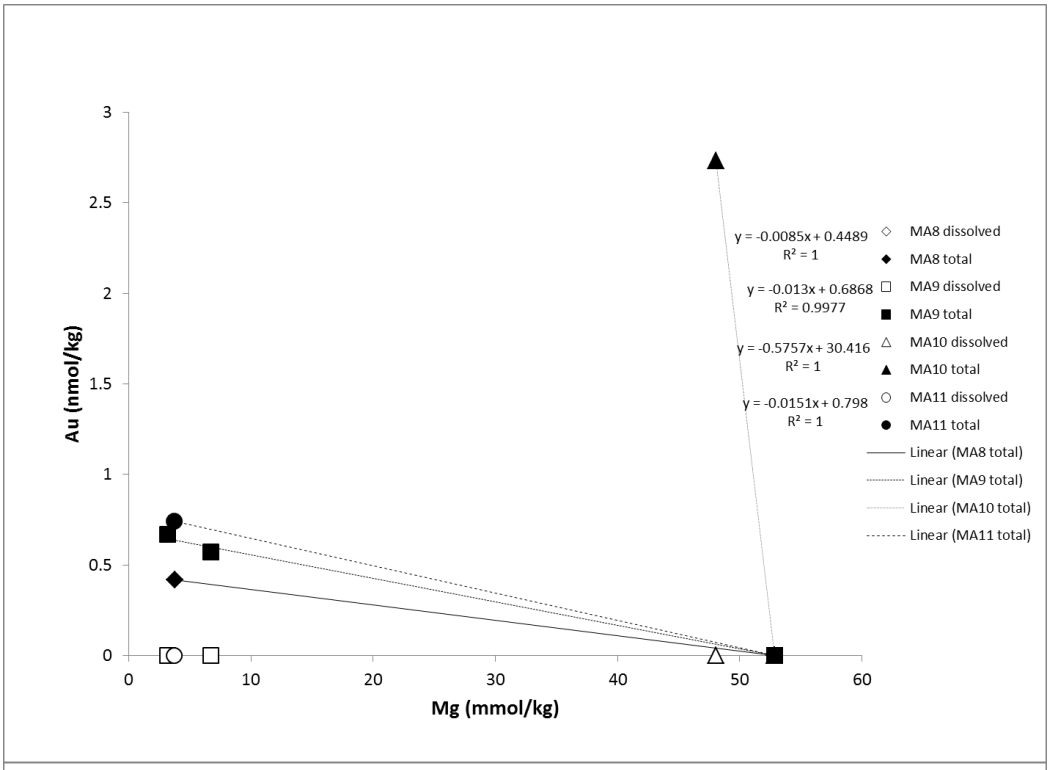
Au (nmol/kg)
Mg (mmol/kg)
y = -0.0085x + 0.4489
R² = 1
y = -0.013x + 0.6868
R² = 0.9977
y = -0.5757x + 30.416
R² = 1
y = -0.0151x + 0.798
R² = 1
MA8 dissolved
MA8 total
MA9 dissolved
MA9 total
MA10 dissolved
MA10 total
MA11 dissolved
MA11 total
Linear (MA8 total)
Linear (MA9 total)
Linear (MA10 total)
Linear (MA11 total)

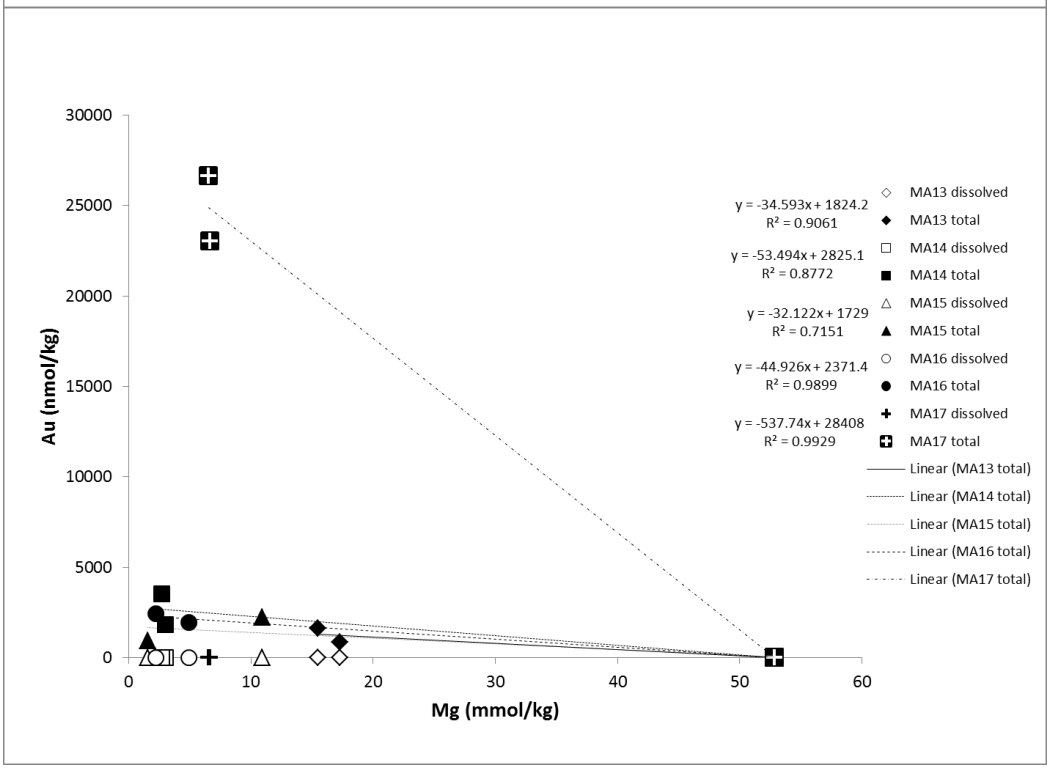
Au (nmol/kg)
Mg (mmol/kg)
y = -34.593x + 1824.2
R² = 0.9061
y = -53.494x + 2825.1
R² = 0.8772
y = -32.122x + 1729
R² = 0.7151
y = -44.926x + 2371.4
R² = 0.9899
y = -537.74x + 28408
R² = 0.9929
MA13 dissolved
MA13 total
MA14 dissolved
MA14 total
MA15 dissolved
MA15 total
MA16 dissolved
MA16 total
MA17 dissolved
MA17 total
Linear (MA13 total)
Linear (MA14 total)
Linear (MA15 total)
Linear (MA16 total)
Linear (MA17 total)

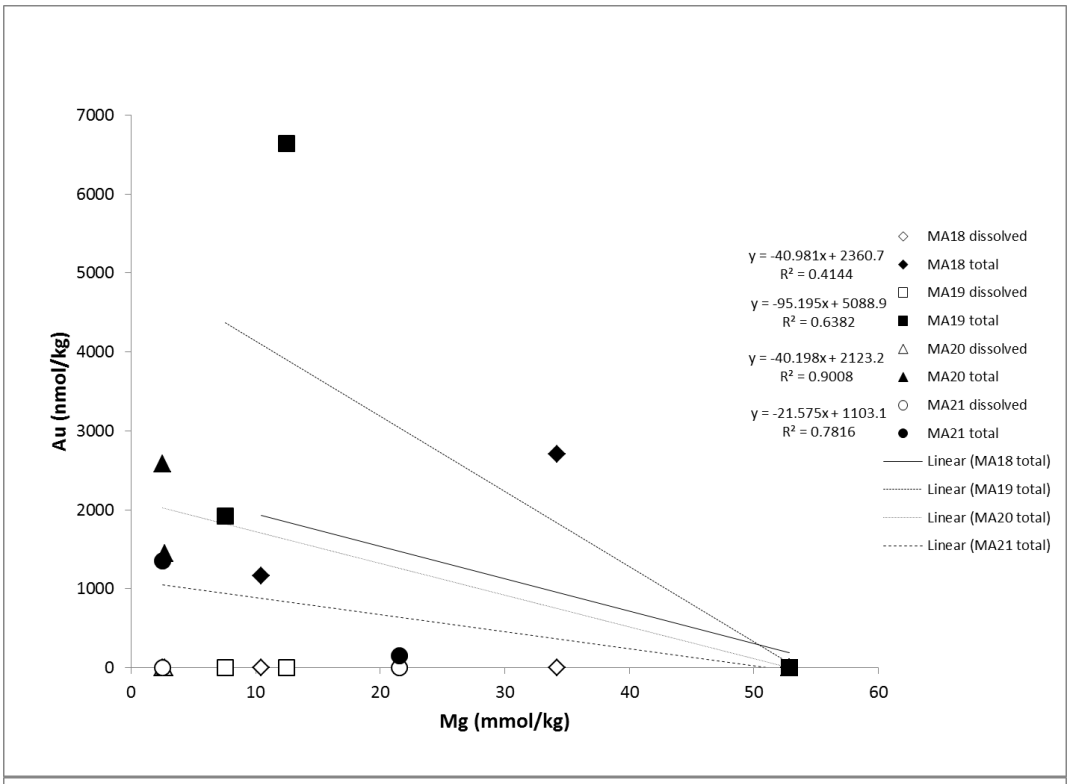
Au (nmol/kg)
Mg (mmol/kg)
y = -40.981x + 2360.7
R² = 0.4144
y = -95.195x + 5088.9
R² = 0.6382
y = -40.198x + 2123.2
R² = 0.9008
y = -21.575x + 1103.1
R² = 0.7816
MA18 dissolved
MA18 total
MA19 dissolved
MA19 total
MA20 dissolved
MA20 total
MA21 dissolved
MA21 total
Linear (MA18 total)
Linear (MA19 total)
Linear (MA20 total)
Linear (MA21 total)

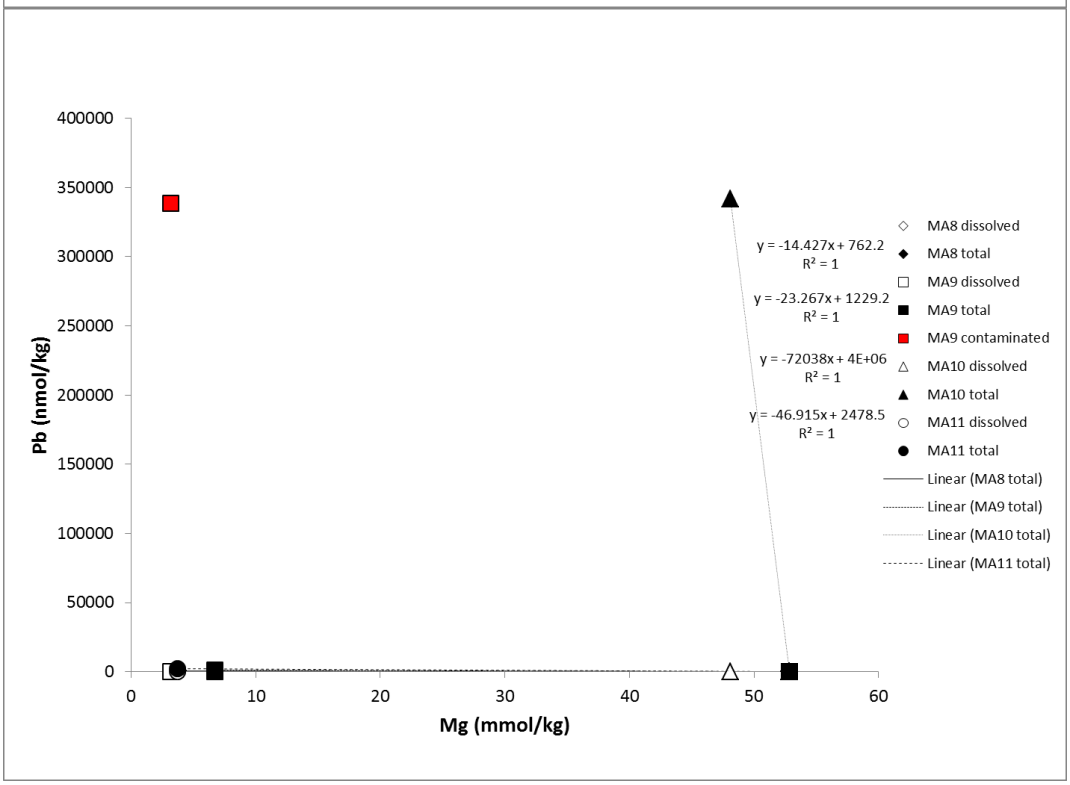
Pb (nmol/kg)
Mg (mmol/kg)
y = -14.427x + 762.2
R² = 1
y = -23.267x + 1229.2
R² = 1
y = -72038x + 4E+06
R² = 1
y = -46.915x + 2478.5
R² = 1
MA8 dissolved
MA8 total
MA9 dissolved
MA9 total
MA9 contaminated
MA10 dissolved
MA10 total
MA11 dissolved
MA11 total
Linear (MA8 total)
Linear (MA9 total)
Linear (MA10 total)
Linear (MA11 total)

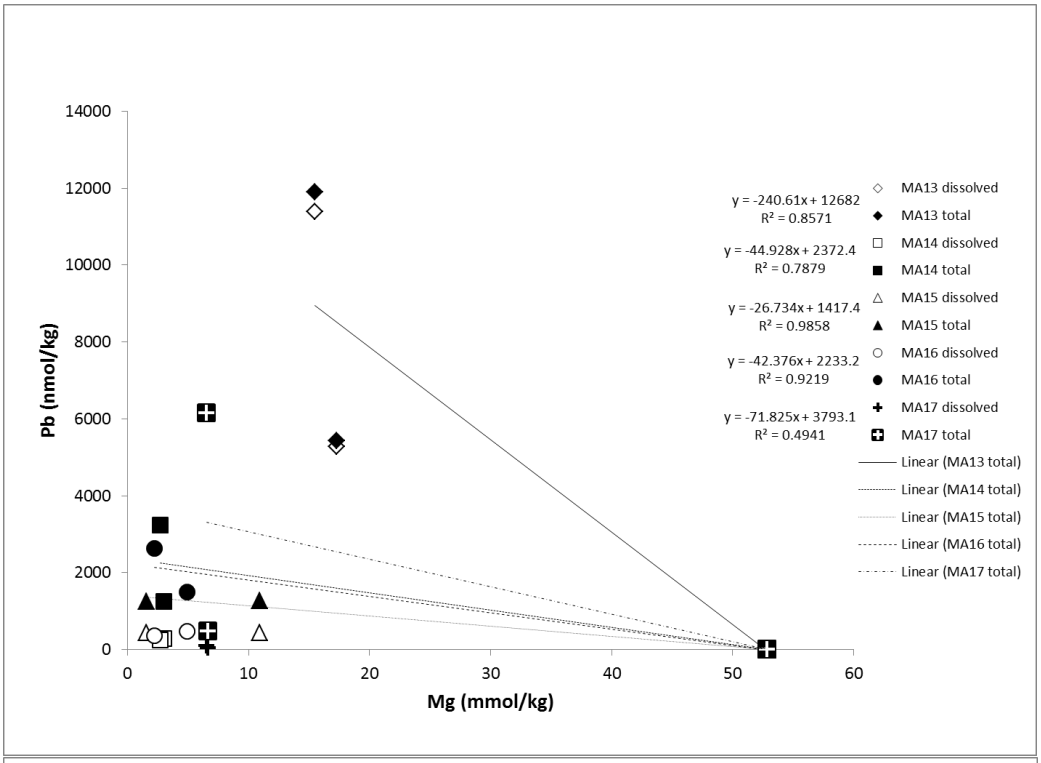
14000
12000
10000
8000
6000
4000
2000
0
0
10
20
30
40
50
60
Pb (nmol/kg)
Mg (mmol/kg)
y = -240.61x + 12682
R² = 0.8571
y = -44.928x + 2372.4
R² = 0.7879
y = -26.734x + 1417.4
R² = 0.9858
y = -42.376x + 2233.2
R² = 0.9219
y = -71.825x + 3793.1
R² = 0.4941
MA13 dissolved
MA13 total
MA14 dissolved
MA14 total
MA15 dissolved
MA15 total
MA16 dissolved
MA16 total
MA17 dissolved
MA17 total
Linear (MA13 total)
Linear (MA14 total)
Linear (MA15 total)
Linear (MA16 total)
Linear (MA17 total)

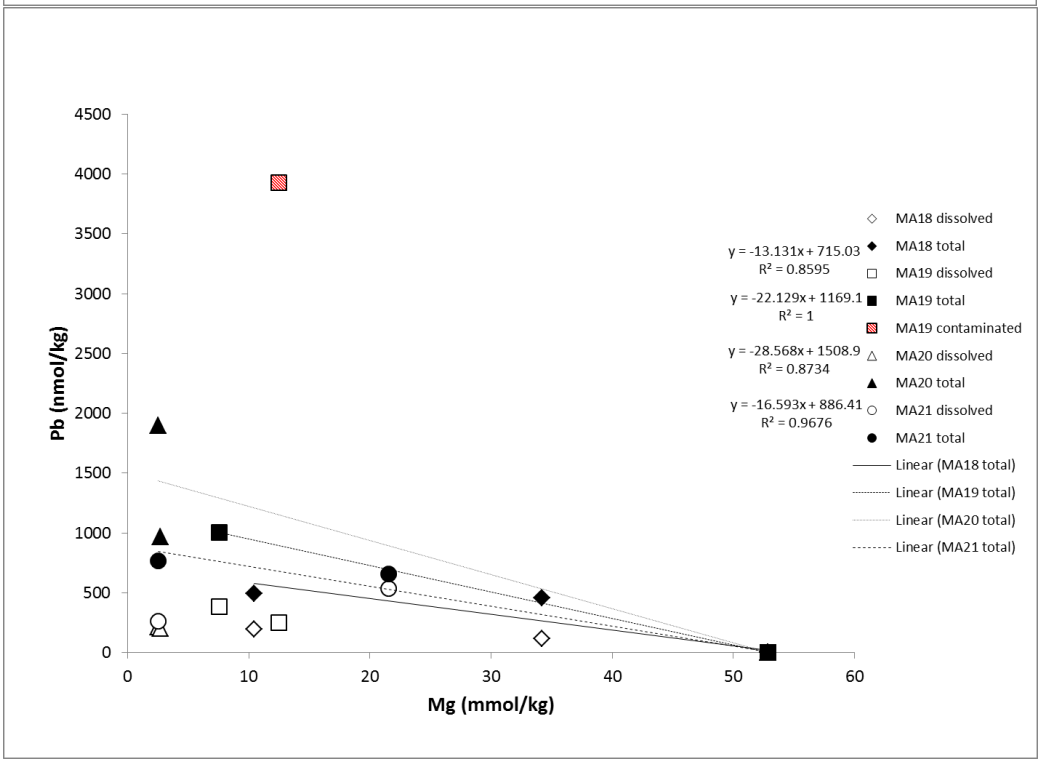
4500
4000
3500
3000
2500
2000
1500
1000
500
0
0
10
20
30
40
50
60
Pb (nmol/kg)
Mg (mmol/kg)
y = -13.131x + 715.03
R² = 0.8595
y = -22.129x + 1169.1
R² = 1
y = -28.568x + 1508.9
R² = 0.8734
y = -16.593x + 886.41
R² = 0.9676
MA18 dissolved
MA18 total
MA19 dissolved
MA19 total
MA19 contaminated
MA20 dissolved
MA20 total
MA21 dissolved
MA21 total
Linear (MA18 total)
Linear (MA19 total)
Linear (MA20 total)
Linear (MA21 total)

Appendix B. Calculated aqueous speciation of hydrothermal fluids: VW1, A10, SM3, and F3.

Fluid VW1 from the Vienna Woods vent field in the Manus Basin
Temperature = 282°C; pH(at 25°C) = 4.4; pH(at 282°C) = 5.1

--- Distribution of Aqueous Solute Species ---

Species	Molality	Log Molality	Log Gamma	Log Activity
Cl-	4.7634E-01	-0.3221	-0.3573	-0.6794
Na+	3.6773E-01	-0.4345	-0.3905	-0.8249
NaCl,aq	1.4086E-01	-0.8512	0.0000	-0.8512
Ca+2	3.0957E-02	-1.5092	-1.2014	-2.7107
CaCl+	2.8313E-02	-1.5480	-0.3905	-1.9385
CaCl2,aq	2.0771E-02	-1.6825	0.0000	-1.6825
K+	1.7981E-02	-1.7452	-0.4435	-2.1887
SiO2,aq	1.4944E-02	-1.8255	0.0000	-1.8255
CO2,aq	4.2307E-03	-2.3736	0.0963	-2.2772
KCl,aq	3.2192E-03	-2.4923	0.0000	-2.4923
H2S,aq	1.3457E-03	-2.8710	0.0000	-2.8710
MnCl+	3.4968E-04	-3.4563	-0.3905	-3.8468
FeCl2,aq	1.4876E-04	-3.8275	0.0000	-3.8275
Ca(HCO3)+	5.8991E-05	-4.2292	-0.3905	-4.6197
H2,aq	4.3000E-05	-4.3665	0.0963	-4.2702
HS-	2.2308E-05	-4.6515	-0.3573	-5.0088
ZnCl+	1.9368E-05	-4.7129	-0.3905	-5.1034
H+	1.5636E-05	-4.8059	-0.2509	-5.0568
HCO3-	9.8192E-06	-5.0079	-0.3043	-5.3122
HCl,aq	9.5498E-06	-5.0200	0.0000	-5.0200
ZnCl2,aq	7.2224E-06	-5.1413	0.0000	-5.1413
ZnCl4-2	6.1101E-06	-5.2140	-1.3216	-6.5356
NaHSiO3,aq	4.3629E-06	-5.3602	0.0000	-5.3602
CuCl,aq	4.0768E-06	-5.3897	0.0000	-5.3897
FeCl+	3.9786E-06	-5.4003	-0.3905	-5.7907
HSiO3-	2.6357E-06	-5.5791	-0.3043	-5.8834
OH-	2.2412E-06	-5.6495	-0.3573	-6.0068
Mn+2	1.3181E-06	-5.8801	-1.2014	-7.0815
Fe+2	1.2637E-06	-5.8984	-1.2014	-7.0998
CuCl3-2	4.7623E-07	-6.3222	-1.3216	-7.6438
CuCl2-	4.4622E-07	-6.3505	-0.3043	-6.6547
ZnCl3-	2.9898E-07	-6.5244	-0.3043	-6.8287
Ni+2	1.9222E-07	-6.7162	-1.4074	-8.1236
PbCl2,aq	1.3109E-07	-6.8824	0.0000	-6.8824
PbCl4-2	1.1291E-07	-6.9473	-1.3216	-8.2689
PbCl3-	8.4021E-08	-7.0756	-0.3043	-7.3799
NiCl+	5.7779E-08	-7.2382	-0.3905	-7.6287
Ca(CO3),aq	5.5810E-08	-7.2533	0.0000	-7.2533

Ga(OH)+2	4.9988E-08	-7.3011	-1.4074	-8.7085
InCl+2	3.8756E-08	-7.4117	-1.4074	-8.8191
CoCl+	3.6668E-08	-7.4357	-0.3905	-7.8262
CdCl2,aq	3.3909E-08	-7.4697	0.0000	-7.4697
AgCl2-	2.2801E-08	-7.6420	-0.3043	-7.9463
PbCl+	2.1672E-08	-7.6641	-0.3905	-8.0545
In(OH)+2	1.1217E-08	-7.9501	-1.4074	-9.3575
CdCl+	9.2661E-09	-8.0331	-0.3905	-8.4236
AgCl4-3	9.1314E-09	-8.0395	-3.0459	-11.0854
Co+2	8.3316E-09	-8.0793	-1.4074	-9.4867
CdCl3-	6.5505E-09	-8.1837	-0.3043	-8.4880
AgCl3-2	5.2505E-09	-8.2798	-1.3216	-9.6014
Zn+2	1.0282E-09	-8.9879	-1.2014	-10.1893
AgCl,aq	7.4500E-10	-9.1278	0.0000	-9.1278
Cu+	7.2473E-10	-9.1398	-0.3905	-9.5303
Pb+2	3.0349E-10	-9.5179	-1.3308	-10.8487
Cd+2	1.6453E-10	-9.7838	-1.4074	-11.1912
CdCl4-2	1.1017E-10	-9.9579	-1.3216	-11.2796
AsO2-	1.0000E-10	-10.0000	-0.3043	-10.3043
HSe-	1.0000E-10	-10.0000	-0.3043	-10.3043
Au(HS)2-	9.9761E-11	-10.0010	-0.3043	-10.3053
BaCl+	7.7660E-11	-10.1098	-0.3905	-10.5003
CO3-2	7.5825E-11	-10.1202	-1.1585	-11.2787
Ag(HS)2-	6.4403E-11	-10.1911	-0.3043	-10.4954
In+3	2.6379E-11	-10.5787	-2.0487	-12.6274
Ba+2	2.2340E-11	-10.6509	-1.3308	-11.9817
Ga+3	1.1944E-11	-10.9228	-2.0487	-12.9715
Ag+	7.2612E-12	-11.1390	-0.4435	-11.5825
AuCl2-	1.2882E-13	-12.8900	-0.3043	-13.1943
AuCl3-2	9.0855E-14	-13.0417	-1.3216	-14.3633
AuCl,aq	1.9253E-14	-13.7155	0.0000	-13.7155
Cu+2	7.3523E-17	-16.1336	-1.2014	-17.3350
Ba(CO3),aq	7.0185E-18	-17.1538	0.0000	-17.1538
Au+	1.0627E-18	-17.9736	-0.3905	-18.3640
MgCl+	8.7060E-19	-18.0602	-0.3905	-18.4506
H2AsO3-	2.7475E-19	-18.5611	-0.3043	-18.8654
Mg+2	1.2903E-19	-18.8893	-1.0092	-19.8985
Fe+3	3.1805E-20	-19.4975	-2.0487	-21.5462

Species Accounting for 99% or More of Aqueous Ga+3

Species	Factor	Molality	Per Cent
Ga(OH)+2	1.00	4.9988E-08	99.98

Species Accounting for 99% or More of Aqueous In+3

Species	Factor	Molality	Per Cent
InCl+2	1.00	3.8756E-08	77.51
In(OH)+2	1.00	1.1217E-08	22.43

Fluid A10 from the ABE vent field in the Lau Basin
Temperature = 317°C; pH(at 25°C) = 3.9; pH(at 317°C) = 4.6

--- Distribution of Aqueous Solute Species ---

Species	Molality	Log Molality	Log Gamma	Log Activity
Cl-	3.5038E-01	-0.4555	-0.3694	-0.8249
Na+	2.9390E-01	-0.5318	-0.4074	-0.9392
NaCl,aq	1.4282E-01	-0.8452	0.0000	-0.8452
CO2,aq	6.6837E-02	-1.1750	0.0798	-1.0952
K+	2.0005E-02	-1.6989	-0.4573	-2.1562
SiO2,aq	1.5593E-02	-1.8071	0.0000	-1.8071
CaCl+	1.4981E-02	-1.8244	-0.4074	-2.2319
CaCl2,aq	1.4620E-02	-1.8350	0.0000	-1.8350
Ca+2	1.0401E-02	-1.9829	-1.2558	-3.2388
KCl,aq	4.5886E-03	-2.3383	0.0000	-2.3383
H2S,aq	3.7423E-03	-2.4269	0.0000	-2.4269
MnCl+	4.3515E-04	-3.3614	-0.4074	-3.7688
Ca(HCO3)+	3.0180E-04	-3.5203	-0.4074	-3.9277
FeCl2,aq	1.6441E-04	-3.7841	0.0000	-3.7841
HCO3-	6.6900E-05	-4.1746	-0.3195	-4.4941
H2,aq	6.1641E-05	-4.2101	0.0798	-4.1303
ZnCl+	5.8232E-05	-4.2348	-0.4074	-4.6423
HS-	3.4658E-05	-4.4602	-0.3694	-4.8296
ZnCl2,aq	2.7019E-05	-4.5683	0.0000	-4.5683
HCl,aq	1.6843E-05	-4.7736	0.0000	-4.7736
H+	1.6046E-05	-4.7946	-0.2708	-5.0655
ZnCl4-2	1.5864E-05	-4.7996	-1.3624	-6.1620
BaCl+	1.1066E-05	-4.9560	-0.4074	-5.3635
CuCl,aq	8.6181E-06	-5.0646	0.0000	-5.0646
NaHSiO3,aq	3.2118E-06	-5.4933	0.0000	-5.4933
FeCl+	2.9789E-06	-5.5259	-0.4074	-5.9334
Ba+2	1.9340E-06	-5.7135	-1.3818	-7.0954
OH-	1.9050E-06	-5.7201	-0.3694	-6.0895
HSiO3-	1.7819E-06	-5.7491	-0.3195	-6.0686
ZnCl3-	8.8352E-07	-6.0538	-0.3195	-6.3733
Mn+2	8.4721E-07	-6.0720	-1.2558	-7.3278
CuCl2-	7.2718E-07	-6.1384	-0.3195	-6.4579
CuCl3-2	6.5345E-07	-6.1848	-1.3624	-7.5472
Fe+2	6.0986E-07	-6.2148	-1.2558	-7.4706
Ca(CO3),aq	2.1820E-07	-6.6612	0.0000	-6.6612
PbCl2,aq	1.4723E-07	-6.8320	0.0000	-6.8320
PbCl4-2	1.0828E-07	-6.9654	-1.3624	-8.3279
PbCl3-	8.9414E-08	-7.0486	-0.3195	-7.3681
CoCl+	6.9400E-08	-7.1586	-0.4074	-7.5661
Ni+2	5.5459E-08	-7.2560	-1.4556	-8.7116
InCl+2	3.8838E-08	-7.4107	-1.4556	-8.8663

NiCl+	2.4540E-08	-7.6101	-0.4074	-8.0176
CdCl2,aq	2.2658E-08	-7.6448	0.0000	-7.6448
PbCl+	1.9895E-08	-7.7013	-0.4074	-8.1087
In(OH)+2	1.1141E-08	-7.9531	-1.4556	-9.4086
Co+2	1.0599E-08	-7.9747	-1.4556	-9.4303
Ga(OH)+2	9.9982E-09	-8.0001	-1.4556	-9.4557
AgCl2-	8.6249E-09	-8.0642	-0.3195	-8.3838
CdCl+	4.4579E-09	-8.3509	-0.4074	-8.7583
CdCl3-	3.7825E-09	-8.4222	-0.3195	-8.7417
AgCl4-3	3.4581E-09	-8.4612	-3.1299	-11.5911
AgCl3-2	1.5466E-09	-8.8106	-1.3624	-10.1731
Cu+	1.2815E-09	-8.8923	-0.4074	-9.2997
Zn+2	1.2748E-09	-8.8945	-1.2558	-10.1504
AgCl,aq	3.1277E-10	-9.5048	0.0000	-9.5048
CO3-2	2.8052E-10	-9.5520	-1.2060	-10.7580
Pb+2	1.8173E-10	-9.7406	-1.3818	-11.1224
Ag(HS)2-	5.4692E-11	-10.2621	-0.3195	-10.5816
Cd+2	5.3850E-11	-10.2688	-1.4556	-11.7244
CdCl4-2	4.7753E-11	-10.3210	-1.3624	-11.6834
Au(HS)2-	3.9942E-11	-10.3986	-0.3195	-10.7181
In+3	2.1037E-11	-10.6770	-2.1644	-12.8414
Ba(CO3),aq	6.9781E-12	-11.1563	0.0000	-11.1563
Ag+	2.8466E-12	-11.5457	-0.4573	-12.0030
Ga+3	1.7360E-12	-11.7604	-2.1644	-13.9248
AuCl2-	3.3650E-14	-13.4730	-0.3195	-13.7925
AuCl3-2	1.8189E-14	-13.7402	-1.3624	-15.1026
AuCl,aq	6.0150E-15	-14.2208	0.0000	-14.2208
Cu+2	1.0324E-16	-15.9861	-1.2558	-17.2420
MgCl+	9.1437E-19	-18.0389	-0.4074	-18.4463
Au+	4.2470E-19	-18.3719	-0.4074	-18.7794
Mg+2	8.2198E-20	-19.0851	-1.0655	-20.1507
Ag(CO3)-	3.5153E-20	-19.4540	-0.3195	-19.7736
Fe+3	1.8430E-20	-19.7345	-2.1644	-21.8988

Species Accounting for 99% or More of Aqueous Ga+3

Species	Factor	Molality	Per Cent
Ga(OH)+2	1.00	9.9982E-09	99.98

Species Accounting for 99% or More of Aqueous In+3

Species	Factor	Molality	Per Cent
InCl+2	1.00	3.8838E-08	77.68
In(OH)+2	1.00	1.1141E-08	22.28

Fluid SM3 from the Satanic Mills vent field in the Manus Basin
Temperature = 288°C; pH(at 25°C) = 2.5; pH(at 288°C) = 3.0

--- Distribution of Aqueous Solute Species ---

Species	Molality	Log Molality	Log Gamma	Log Activity
Cl-	3.6753E-01	-0.4347	-0.3398	-0.7745
Na+	2.9031E-01	-0.5371	-0.3720	-0.9092
CO2,aq	2.6773E-01	-0.5723	0.0771	-0.4952
NaCl,aq	1.0711E-01	-0.9702	0.0000	-0.9702
K+	5.7850E-02	-1.2377	-0.4183	-1.6560
SiO2,aq	1.4755E-02	-1.8311	0.0000	-1.8311
KCl,aq	1.0149E-02	-1.9936	0.0000	-1.9936
H2S,aq	9.9658E-03	-2.0015	0.0000	-2.0015
Ca+2	5.1838E-03	-2.2854	-1.1565	-3.4419
CaCl+	4.9652E-03	-2.3041	-0.3720	-2.6761
CaCl2,aq	3.5449E-03	-2.4504	0.0000	-2.4504
MnCl+	2.3071E-03	-2.6369	-0.3720	-3.0089
H+	1.6355E-03	-2.7863	-0.2454	-3.0318
FeCl2,aq	1.1752E-03	-2.9299	0.0000	-2.9299
HCl,aq	1.0033E-03	-2.9986	0.0000	-2.9986
CuCl,aq	1.2152E-04	-3.9153	0.0000	-3.9153
ZnCl+	1.1436E-04	-3.9417	-0.3720	-4.3137
ZnCl2,aq	4.0871E-05	-4.3886	0.0000	-4.3886
FeCl+	3.0540E-05	-4.5151	-0.3720	-4.8871
ZnCl4-2	2.0419E-05	-4.6900	-1.2615	-5.9514
AsO2-	1.6100E-05	-4.7932	-0.2936	-5.0868
CuCl2-	1.0339E-05	-4.9855	-0.2936	-5.2791
Fe+2	9.2963E-06	-5.0317	-1.1565	-6.1882
H2,aq	8.4000E-06	-5.0757	0.0771	-4.9986
CuCl3-2	8.1131E-06	-5.0908	-1.2615	-6.3523
Mn+2	7.8812E-06	-5.1034	-1.1565	-6.2599
Ca(HCO3)+	6.0772E-06	-5.2163	-0.3720	-5.5883
HCO3-	4.4637E-06	-5.3503	-0.2936	-5.6439
PbCl2,aq	2.0959E-06	-5.6786	0.0000	-5.6786
ZnCl3-	1.3445E-06	-5.8715	-0.2936	-6.1650
HS-	1.2988E-06	-5.8865	-0.3398	-6.2263
PbCl4-2	1.1221E-06	-5.9500	-1.2615	-7.2115
PbCl3-	1.1146E-06	-5.9529	-0.2936	-6.2465
PbCl+	3.6270E-07	-6.4405	-0.3720	-6.8125
Ni+2	1.8875E-07	-6.7241	-1.3417	-8.0658
CdCl2,aq	1.5262E-07	-6.8164	0.0000	-6.8164
InCl+2	1.4942E-07	-6.8256	-1.3417	-8.1673
Ga(OH)+2	1.4657E-07	-6.8340	-1.3417	-8.1756
NiCl+	6.1247E-08	-7.2129	-0.3720	-7.5849
AgCl2-	5.1334E-08	-7.2896	-0.2936	-7.5832
CdCl+	4.2395E-08	-7.3727	-0.3720	-7.7447

NaHSiO3,aq	3.2523E-08	-7.4878	0.0000	-7.4878
CoCl+	2.6434E-08	-7.5778	-0.3720	-7.9499
CdCl3-	2.3999E-08	-7.6198	-0.2936	-7.9134
Cu+	2.2451E-08	-7.6488	-0.3720	-8.0208
HSiO3-	2.1467E-08	-7.6682	-0.2936	-7.9618
OH-	1.9567E-08	-7.7085	-0.3398	-8.0483
AgCl4-3	1.1067E-08	-7.9560	-2.9008	-10.8568
AgCl3-2	8.5317E-09	-8.0690	-1.2615	-9.3304
Co+2	5.5660E-09	-8.2545	-1.3417	-9.5961
Zn+2	5.1960E-09	-8.2843	-1.1565	-9.4408
Pb+2	4.7580E-09	-8.3226	-1.2733	-9.5959
Ga+3	3.4300E-09	-8.4647	-1.9966	-10.4613
Au(HS)2-	2.1911E-09	-8.6593	-0.2936	-8.9529
AgCl,aq	2.0455E-09	-8.6892	0.0000	-8.6892
Cd+2	6.9997E-10	-9.1549	-1.3417	-10.4966
AuCl2-	6.5502E-10	-9.1837	-0.2936	-9.4773
In(OH)+2	4.6987E-10	-9.3280	-1.3417	-10.6697
AuCl3-2	3.3217E-10	-9.4786	-1.2615	-10.7401
CdCl4-2	2.8830E-10	-9.5402	-1.2615	-10.8016
AuCl,aq	1.2172E-10	-9.9146	0.0000	-9.9146
In+3	1.1081E-10	-9.9554	-1.9966	-11.9520
HSe-	1.0000E-10	-10.0000	-0.2936	-10.2936
BaCl+	7.9086E-11	-10.1019	-0.3720	-10.4739
Ca(CO3),aq	5.3184E-11	-10.2742	0.0000	-10.2742
Ag+	2.1318E-11	-10.6713	-0.4183	-11.0895
Ba+2	2.0913E-11	-10.6796	-1.2733	-11.9529
Ag(HS)2-	6.9173E-13	-12.1601	-0.2936	-12.4536
Cu+2	5.0841E-13	-12.2938	-1.1565	-13.4503
CO3-2	2.5761E-13	-12.5890	-1.1164	-13.7055
Au+	7.8945E-15	-14.1027	-0.3720	-14.4747
H2AsO3-	1.2249E-15	-14.9119	-0.2936	-15.2055
Fe+3	5.9857E-17	-16.2229	-1.9966	-18.2195

Species Accounting for 99% or More of Aqueous Ga+3

Species	Factor	Molality	Per Cent
Ga(OH)+2	1.00	1.4657E-07	97.71
Ga+3	1.00	3.4300E-09	2.29

Species Accounting for 99% or More of Aqueous In+3

Species	Factor	Molality	Per Cent
InCl+2	1.00	1.4942E-07	99.61

Fluid F3 from the Fenway vent field in the Manus Basin
Temperature = 358°C; pH(at 25°C) = 2.7; pH(at 358°C) = 3.9

--- Distribution of Aqueous Solute Species ---
--- Distribution of Aqueous Solute Species ---

Species	Molality	Log Molality	Log Gamma	Log Activity
NaCl,aq	2.5209E-01	-0.5984	0.0000	-0.5984
Cl-	2.0805E-01	-0.6818	-0.4563	-1.1381
Na+	1.5429E-01	-0.8117	-0.4683	-1.2800
CO2,aq	5.4818E-02	-1.2611	0.0593	-1.2017
K+	4.3792E-02	-1.3586	-0.5212	-1.8798
KCl,aq	3.2308E-02	-1.4907	0.0000	-1.4907
H2S,aq	1.8369E-02	-1.7359	0.0000	-1.7359
CaCl2,aq	1.7155E-02	-1.7656	0.0000	-1.7656
SiO2,aq	1.1921E-02	-1.9237	0.0000	-1.9237
FeCl2,aq	1.1587E-02	-1.9360	0.0000	-1.9360
CaCl+	4.4595E-03	-2.3507	-0.4683	-2.8190
MnCl+	3.7989E-03	-2.4203	-0.4683	-2.8886
HCl,aq	2.4602E-03	-2.6090	0.0000	-2.6090
Ca+2	6.8451E-04	-3.1646	-1.5036	-4.6682
H2,aq	4.0701E-04	-3.3904	0.0593	-3.3311
H+	2.8089E-04	-3.5515	-0.3150	-3.8665
FeCl+	2.0316E-04	-3.6922	-0.4683	-4.1605
ZnCl2,aq	1.7613E-04	-3.7542	0.0000	-3.7542
ZnCl+	1.1966E-04	-3.9220	-0.4683	-4.3903
CuCl,aq	1.1108E-04	-3.9544	0.0000	-3.9544
ZnCl4-2	8.9951E-05	-4.0460	-1.6843	-5.7303
CuCl2-	1.4829E-05	-4.8289	-0.4034	-5.2323
CuCl3-2	1.4077E-05	-4.8515	-1.6843	-6.5358
H2AsO3-	1.3692E-05	-4.8635	-0.4034	-5.2670
PbCl4-2	1.3521E-05	-4.8690	-1.6843	-6.5533
PbCl2,aq	1.2933E-05	-4.8883	0.0000	-4.8883
PbCl3-	9.9548E-06	-5.0020	-0.4034	-5.4054
Fe+2	9.5098E-06	-5.0218	-1.5036	-6.5254
ZnCl3-	4.2568E-06	-5.3709	-0.4034	-5.7744
HS-	1.5658E-06	-5.8053	-0.4563	-6.2616
Mn+2	1.0628E-06	-5.9735	-1.5036	-7.4771
Ca(HCO3)+	8.1863E-07	-6.0869	-0.4683	-6.5552
PbCl+	5.8909E-07	-6.2298	-0.4683	-6.6981
CoCl+	4.9948E-07	-6.3015	-0.4683	-6.7698
CdCl2,aq	4.2163E-07	-6.3751	0.0000	-6.3751
HCO3-	3.2491E-07	-6.4882	-0.4034	-6.8917
AgCl4-3	2.9320E-07	-6.5328	-3.8408	-10.3736
AgCl2-	2.5875E-07	-6.5871	-0.4034	-6.9906
NiCl+	1.6032E-07	-6.7950	-0.4683	-7.2633
Ga(OH)+2	1.4977E-07	-6.8246	-1.7245	-8.5491

InCl+2	1.4875E-07	-6.8275	-1.7245	-8.5521
Ni+2	8.9677E-08	-7.0473	-1.7245	-8.7718
NaHSiO3,aq	6.2469E-08	-7.2043	0.0000	-7.2043
CdCl3-	5.8521E-08	-7.2327	-0.4034	-7.6361
OH-	4.1202E-08	-7.3851	-0.4563	-7.8414
AgCl3-2	3.9229E-08	-7.4064	-1.6843	-9.0907
Co+2	2.0516E-08	-7.6879	-1.7245	-9.4124
CdCl+	1.9167E-08	-7.7175	-0.4683	-8.1858
HSiO3-	1.8260E-08	-7.7385	-0.4034	-8.1420
Cu+	1.1805E-08	-7.9279	-0.4683	-8.3962
AgCl,aq	8.7821E-09	-8.0564	0.0000	-8.0564
H2AsO4-	7.7371E-09	-8.1114	-0.4034	-8.5149
Pb+2	1.2363E-09	-8.9079	-1.6437	-10.5516
In(OH)+2	1.2184E-09	-8.9142	-1.7245	-10.6387
CdCl4-2	6.1801E-10	-9.2090	-1.6843	-10.8933
AuCl2-	5.8491E-10	-9.2329	-0.4034	-9.6364
Au(HS)2-	5.4372E-10	-9.2646	-0.4034	-9.6681
AuCl3-2	2.6070E-10	-9.5839	-1.6843	-11.2682
Zn+2	2.3593E-10	-9.6272	-1.5036	-11.1308
Ga+3	2.3306E-10	-9.6325	-2.6559	-12.2884
AuCl,aq	1.1066E-10	-9.9560	0.0000	-9.9560
HSe-	1.0000E-10	-10.0000	-0.4034	-10.4035
BaCl+	9.6510E-11	-10.0154	-0.4683	-10.4837
Cd+2	6.2997E-11	-10.2007	-1.7245	-11.9252
Ag+	3.4350E-11	-10.4641	-0.5212	-10.9852
In+3	2.6988E-11	-10.5688	-2.6559	-13.2247
Ca(CO3),aq	1.9963E-11	-10.6998	0.0000	-10.6998
Ba+2	3.4902E-12	-11.4572	-1.6437	-13.1009
Ag(HS)2-	2.5315E-12	-11.5966	-0.4034	-12.0001
HAsO4-2	3.6647E-13	-12.4360	-1.6843	-14.1203
AsO2-	5.6709E-14	-13.2463	-0.4034	-13.6498
CO3-2	1.4623E-14	-13.8350	-1.5140	-15.3490
Cu+2	6.4039E-15	-14.1936	-1.5036	-15.6971
Au+	6.1448E-15	-14.2115	-0.4683	-14.6798
Fe+3	4.6136E-18	-17.3360	-2.6559	-19.9919
ClO4-	1.8151E-75	-74.7411	-0.4563	-75.1974

Species Accounting for 99% or More of Aqueous Ga+3

Species	Factor	Molality	Per Cent
Ga(OH)+2	1.00	1.4977E-07	99.84

Species Accounting for 99% or More of Aqueous In+3

Species	Factor	Molality	Per Cent
InCl+2	1.00	1.4875E-07	99.17

Supplementary Table S1. Elemental Concentrations in Dissolved Fractions of Hydrothermal Fluids

Vent Field	Year	Fluid	Sample	max T	pH	Mg	Mn	Fe	Co	Ni	Cu	Zn	Mo	Ag	Cd	Sb	Au	Pb
				°C	25°C	mmol/kg	umol/kg	umol/kg	nmol/kg	nmol/kg	umol/kg	umol/kg	nmol/kg	nmol/kg	nmol/kg	nmol/kg	nmol/kg	nmol/kg
Kilo Moana	2009	KM9	J2-434-IGT1	301	4.1	2.5		490	72	bdl	0.6	26	bdl	bdl	12	1700	bdl	33
Kilo Moana	2009	KM9	J2-434-IGT4	304	5.0	3.0	180	520	96	bdl	1.6	49	NM	bdl	57	1700	bdl	170
Tahi Moana 1	2009	TMo1	J2-444-IGT1	297	3.3	2.9	600	320	110	360	4.0	120	bdl	27	120	10	bdl	NM
Tahi Moana 1	2009	TMo1	J2-444-IGT6	306	3.7	2.4	520	310	110	bdl	2.0	55	bdl	2.4	43	4.3	1.1	NM
Tahi Moana 1	2009	TMo2	J2-444-IGT3	298	4.4	4.6	280	210	100	bdl	2.9	48	26	13	40	9.8	bdl	NM
Tahi Moana 1	2009	TMo2	J2-444-IGT4	297	3.9	1.0	290	230	110	bdl	2.8	43	6.3	13	35	7.9	bdl	NM
Tahi Moana 1	2009	TMo5	J2-450-IGT4	309	3.7	1.4	340	240	110	590	4.1	69	16	25	82	9.6	bdl	NM
Tahi Moana 1	2009	TMo5	J2-450-IGT6	310	3.8	2.0	330	240	91	bdl	4.3	73	7.1	24	86	9.6	bdl	NM
ABE	2009	A10	J2-449-IGT5	317	4.4	2.1	350	140	54	bdl	1.9	18	bdl	bdl	bdl	2.0	bdl	NM
ABE	2009	A11	J2-449-IGT1	306	4.0	2.5	270	76	54	bdl	1.1	19	27	bdl	bdl	6.5	bdl	NM
ABE	2009	A11	J2-449-IGT6	312	3.9	2.1	400	150	15	120	5.5	13	18	bdl	33	16	bdl	NM
ABE	2015	A13	J2-815-IGT7	283	5.0	12.8	320	100	45	48	1.3	61	86	bdl	55	2.0	0.5	240
ABE	2015	A13	J2-815-IGT8	283	4.3	2.3	400	610	52	100	54	2400	200	43	2400	110	0.0	2300
ABE	2015	A14	J2-815-IGT1	288	5.1	16.8	230	840	59	1100	160	5100	760	62	6500	2100	6.2	5700
ABE	2015	A14	J2-815-IGT3	300	4.0	1.9	390	120	52	bdl	2.3	57	48	bdl	49	4.0	0.2	230
ABE	2015	A15	J2-815-IGT2	290	4.9	8.1	160	71	50	340	2.2	43	4.7	bdl	33	1600	1.2	380
ABE	2015	A15	J2-815-IGT4	279	4.4	1.9	250	93	56	110	3.2	60	11	bdl	53	8.8	bdl	450
ABE	2015	A16	J2-815-IGT5	262	4.6	1.7	250	51	54	48	1.0	30	6.2	bdl	14	6.2	bdl	620
ABE	2015	A16	J2-815-IGT6	263	4.5	1.7	250	58	57	16	1.4	34	bdl	bdl	21	1.1	bdl	370
Tu'i Malila	2009	TM11	J2-442-IGT3	313	4.1	5.5	370	130	42	190	300	42	240	bdl	30	18	bdl	NM
Tu'i Malila	2009	TM11	J2-442-IGT4	315	3.8	1.1	330	150	56	620	14	55	61	12	57	17	bdl	NM
Tu'i Malila	2009	TM12	J2-442-IGT1	284	4.3	3.4	290	170	78	bdl	3.3	30	5.9	bdl	0.7	14	bdl	NM
Tu'i Malila	2009	TM12	J2-442-IGT6	268	4.2	3.0	280	170	80	bdl	1.4	32	bdl	6.7	9.5	12	bdl	NM
Tu'i Malila	2015	TM13	J2-819-IGT6	260	3.9	4.3	270	87	74	bdl	5.8	79	14	16	140	13	bdl	630
Tu'i Malila	2015	TM13	J2-819-IGT8	262	3.9	3.6	270	83	73	75	5.2	71	9.4	10	98	11	bdl	NM
Tu'i Malila	2015	TM14	J2-819-IGT4	214	4.0	1.5	280	120	80	bdl	3.5	56	bdl	6.1	78	12	bdl	750
Tu'i Malila	2015	TM14	J2-819-IGT5	290	3.9	1.7	280	120	80	bdl	5.5	86	11.1	18	120	14	bdl	730
Tu'i Malila	2015	TM15	J2-819-IGT2	269	5.0	22.0	220	190	55	260	26	1500	110	14	3200	1100	bdl	1700
Tu'i Malila	2015	TM16	J2-819-IGT3	251	3.9	5.5	380	470	78	bdl	12	830	60	110	1400	110	bdl	2400
Tu'i Malila	2015	TM16	J2-819-IGT7	242	4.2	6.7	340	310	70	21	2.1	100	24	bdl	200	18	bdl	320
Tu'i Malila	2015	TM17	J2-819-IGT4B	258	3.9	3.1	270	190	86	bdl	1.7	130	9.8	11	190	25	bdl	1200
Tu'i Malila	2015	TM17	J2-819-IGT5B	257	4.0	4.4	240	240	0.69	bdl	5.6	450	38	65	790	110	bdl	2500
Tu'i Malila	2015	TM18	J2-819-IGT2B	296	4.6	10.4	95	23	61	bdl	2.6	41	74	bdl	69	12	bdl	250
Tu'i Malila	2015	TM18	J2-819-IGT7B	232	5.4	36.9	250	110	120	bdl	5.2	63	47	bdl	120	20	bdl	710
Tu'i Malila	2015	TM19	J2-819-IGT6B	232	4.2	3.0	250	130	110	bdl	1.2	57	4.4	290	36	170	bdl	7100
Tu'i Malila	2015	TM20	J2-819-IGT3B	138	5.3	33.4	110	61	73	bdl	10	140	66	8.0	260	22	bdl	730

Supplementary Table S1 cont. Elemental Concentrations in Dissolved Fractions of Hydrothermal Fluids

Vent Field	Year	Fluid	Sample	max T	pH	Mg	Mn	Fe	Co	Ni	Cu	Zn	Mo	Ag	Cd	Sb	Au	Pb
				°C	25°C	mmol/kg	umol/kg	umol/kg	nmol/kg	nmol/kg	umol/kg	umol/kg	nmol/kg	nmol/kg	nmol/kg	nmol/kg	nmol/kg	nmol/kg
Mariner	2009	MA8	J2-437-IGT1	359	2.6	5.6	3500	8500	280	bdl	24	45	63	33	220	38	0.4	580
Mariner	2009	MA8	J2-437-IGT3	359	2.4	3.8	NM	NM	70	bdl	16	43	110	bdl	20	1600	bdl	120
Mariner	2009	MA9	J2-437-IGT5	338	2.4	6.7	4500	10800	160	290	76	180	130	11	170	1600	bdl	NM
Mariner	2009	MA9	J2-437-IGT6	336	2.3	3.2	4900	11900	86	90	29	82	NM	NM	NM	NM	bdl	280
Mariner	2009	MA10	J2-439-IGT1	109	5.2	48.1	570	340	NM	NM	NM	NM	NM	NM	NM	NM	NM	NM
Mariner	2009	MA11	J2-439-IGT6	328	2.2	3.7	4100	10700	230	9	41	71	150	bdl	49	1700	bdl	310
Mariner	2009	MA12	J2-446-IGT3	350	2.3	2.9	48	130	bdl	bdl	3.1	11	bdl	bdl	bdl	1.6	0.5	NM
Mariner	2009	MA12	J2-446-IGT6	350	2.3	3.5	4200	11200	210	bdl	99	190	bdl	34	130	21	0.9	NM
Mariner	2015	MA13	J2-816-IGT5	140	2.6	20.4	4000	1500	47	160	17	2300	bdl	950	2400	68	0.9	5300
Mariner	2015	MA13	J2-816-IGT6	78	2.6	18.1	4300	1600	51	560	1.2	1100	29	36	69	2.1	bdl	11400
Mariner	2015	MA14	J2-817-IGT5	318	2.4	2.6	5300	6400	87	bdl	7.7	280	74	6.9	120	9.8	bdl	290
Mariner	2015	MA14	J2-817-IGT6	319	2.3	2.8	5200	6200	97	bdl	6.0	180	62	bdl	77	3.7	bdl	250
Mariner	2015	MA15	J2-817-IGT2	354	3.0	12.7	3300	9300	65	bdl	69	120	130	1.0	93	13	1.0	450
Mariner	2015	MA15	J2-817-IGT4	345	2.7	1.4	4300	11900	100	40	69	100	150	3.0	93	12	bdl	440
Mariner	2015	MA16	J2-817-IGT1	363	5.8	6.8	4100	12100	97	240	32	100	160	bdl	130	11	1.3	470
Mariner	2015	MA16	J2-817-IGT8	364	2.7	2.1	4400	13500	140	bdl	47	58	150	bdl	57	800	bdl	370
Mariner	2015	MA17	J2-817-IGT5B	360	2.9	8.0	3100	7700	74	bdl	4.6	23	79	bdl	8.4	1.8	bdl	39
Mariner	2015	MA17	J2-817-IGT6B	362	2.8	8.1	3300	8200	95	39	2.3	32	99	bdl	22	2.4	bdl	97
Mariner	2015	MA18	J2-818-IGT4	300	2.7	12.8	3700	8900	100	350	27	63	99	bdl	48	7.8	bdl	200
Mariner	2015	MA18	J2-818-IGT5	300	4.3	35.5	1500	3800	68	440	10	41	28	bdl	25	6.4	bdl	120
Mariner	2015	MA19	J2-818-IGT2	308	2.9	15.6	3400	7500	73	820	13	77	89	bdl	54	21	bdl	250
Mariner	2015	MA19	J2-818-IGT3	297	2.6	9.4	3900	8900	80	470	17	110	190	bdl	90	24	bdl	380
Mariner	2015	MA20	J2-818-IGT6	344	2.6		4800	11300	100	120	26	75	130	bdl	55	9.5	bdl	220
Mariner	2015	MA20	J2-818-IGT8	342	2.7	2.7	4700	10800	83	84	21	70	120	bdl	61	11	bdl	200
Mariner	2015	MA21	J2-818-IGT7	345	2.7	2.8	4100	11500	120	bdl	39	83	130	bdl	69	9.5	bdl	260
Mariner	2015	MA21	J2-818-M1		3.4	22.8	2600	7200	81	bdl	110	180	110	17	150	27	bdl	540
Vai Lili	2015	VL4	J2-817-IGT3	109	5.2	28.1	1000	28	57	bdl	0.4	25	40	bdl	13	3.2	bdl	18
Vai Lili	2015	VL4	J2-817-IGT7	116	5.2	29.3	960	32	32	300	1.1	41	18	bdl	40	4.4	bdl	480

Supplementary Table S2 . Elemental Concentrations in Filters Fractions of Hydrothermal Fluids

Vent Field	Year	Fluid	Sample	Cr	Mn	Fe	Co	Ni	Cu	Zn	Ga
				nmol/kg	umol/kg	umol/kg	nmol/kg	nmol/kg	umol/kg	umol/kg	nmol/kg
ABE	2015	A13	J2-815-IGT7	1600	3.4	36	41	2000	0.9	bdl	77
ABE	2015	A13	J2-815-IGT8	480	47	2000	8.2	170	20	57	120
ABE	2015	A14	J2-815-IGT1	1800	23	970	87	280	83	360	94
ABE	2015	A14	J2-815-IGT3	330	4.9	21	81	140	2.7	4.3	59
ABE	2015	A15	J2-815-IGT2	930	6.6	24	84	140	5.1	6.7	53
ABE	2015	A15	J2-815-IGT4	450	1.1	3.5	bdl	80	2.5	3.1	63
ABE	2015	A16	J2-815-IGT5	520	1.2	8.1	bdl	130	3.0	2.7	54
ABE	2015	A16	J2-815-IGT6	420	2.6	9.4	74	120	1.5	2.2	57
Tu'i Malila	2015	TM13	J2-819-IGT6	290	7.0	9.7	75	52	2.8	3.9	55
Tu'i Malila	2015	TM13	J2-819-IGT8	280	7.9	8.3	87	69	3.2	3.6	67
Tu'i Malila	2015	TM14	J2-819-IGT4	260	0.1	2.7	90	55	0.7	1.0	67
Tu'i Malila	2015	TM14	J2-819-IGT5	330	4.7	4.4	87	72	1.2	2.3	63
Tu'i Malila	2015	TM15	J2-819-IGT2	410	4.3	480	73	83	220	780	70
Tu'i Malila	2015	TM16	J2-819-IGT3	290	4.5	120	89	67	3.9	46	79
Tu'i Malila	2015	TM16	J2-819-IGT7	380	0.3	8.3	79	49	2.7	2.5	59
Tu'i Malila	2015	TM17	J2-819-IGT4B	220	2.8	35	29	34	1.8	110	65
Tu'i Malila	2015	TM17	J2-819-IGT5B	310	7.2	66	79	63	4.2	110	69
Tu'i Malila	2015	TM18	J2-819-IGT2B	5100	1.5	140	90	460	1.1	6.8	67
Tu'i Malila	2015	TM18	J2-819-IGT7B	340	0.4	4.6	17	53	1.3	19	61
Tu'i Malila	2015	TM19	J2-819-IGT6B	280	4.2	8.6	85	50	0.8	2.3	57
Tu'i Malila	2015	TM20	J2-819-IGT3B	240	3.4	56	71	45	14.3	14	51
Mariner	2015	MA13	J2-816-IGT5	210	64	33	74	110	1.4	42	49
Mariner	2015	MA13	J2-816-IGT6	590	62	68	100	410	3.6	25	70
Mariner	2015	MA14	J2-817-IGT5	230	5.7	8.6	91	110	0.6	0.4	82
Mariner	2015	MA14	J2-817-IGT6	740	49	69	75	93	0.7	2.1	61
Mariner	2015	MA15	J2-817-IGT2	200	10	42	88	140	0.8	0.3	67
Mariner	2015	MA15	J2-817-IGT4	730	29	92	82	91	1.0	2.8	60
Mariner	2015	MA16	J2-817-IGT1	1200	26	85	52	93	1.6	1.6	56
Mariner	2015	MA16	J2-817-IGT8	920	38	69	86	110	1.1	3.2	66
Mariner	2015	MA17	J2-817-IGT5B	110	3.9	11	280	260	0.6	0.8	0.1
Mariner	2015	MA17	J2-817-IGT6B	1100	29	93	95	200	1.3	13	72
Mariner	2015	MA18	J2-818-IGT4	740	4.6	17	81	100	2.2	1.2	67
Mariner	2015	MA18	J2-818-IGT5	580	1.0	5.1	70	59	0.6	0.3	54
Mariner	2015	MA19	J2-818-IGT2	370	9.8	29	180	98	4.1	0.6	66
Mariner	2015	MA19	J2-818-IGT3	880	11	33	120	140	0.7	1.3	64
Mariner	2015	MA20	J2-818-IGT6	340	66	140	59	67	1.1	1.4	67
Mariner	2015	MA20	J2-818-IGT8	330	12	23	88	280	1.2	1.0	59
Mariner	2015	MA21	J2-818-IGT7	410	3.3	13	81	60	1.9	0.4	66
Mariner	2015	MA21	J2-818-M1	350	4.9	15	79	200	0.7	0.5	55

Supplementary Table S2 cont . Elemental Concentrations in Filters Fractions of Hydrothermal Fluids

Vent Field	Year	Fluid	Sample	Mo	Ag	Cd	In	Sn	Sb	Au	Pb
				nmol/kg	nmol/kg	nmol/kg	nmol/kg	nmol/kg	nmol/kg	nmol/kg	nmol/kg
ABE	2015	A13	J2-815-IGT7	990	bdl	37	47	64	23	490	55
ABE	2015	A13	J2-815-IGT8	720	bdl	75	37	10	44	1100	4200
ABE	2015	A14	J2-815-IGT1	1000	bdl	490	42	52	80	3000	2800
ABE	2015	A14	J2-815-IGT3	980	bdl	33	41	76	40	NM	52
ABE	2015	A15	J2-815-IGT2	770	bdl	35	41	56	38	4400	87
ABE	2015	A15	J2-815-IGT4	37	43	58	NM	21	89	230	250
ABE	2015	A16	J2-815-IGT5	740	bdl	31	38	120	34	300	44
ABE	2015	A16	J2-815-IGT6	810	bdl	27	35	40	36	1000	59
Tu'i Malila	2015	TM13	J2-819-IGT6	850	bdl	31	NM	34	31	2200	54
Tu'i Malila	2015	TM13	J2-819-IGT8	1200	bdl	33	41	41	35	1800	51
Tu'i Malila	2015	TM14	J2-819-IGT4	1000	bdl	32	44	39	40	0.4	27
Tu'i Malila	2015	TM14	J2-819-IGT5	1000	bdl	33	42	68	36	2900	94
Tu'i Malila	2015	TM15	J2-819-IGT2	980	64	1700	36	52	210	2400	1200
Tu'i Malila	2015	TM16	J2-819-IGT3	1200	bdl	130	43	40	43	2800	520
Tu'i Malila	2015	TM16	J2-819-IGT7	980	bdl	33	39	67	34	1700	64
Tu'i Malila	2015	TM17	J2-819-IGT4B	960	bdl	110	39	36	41	1600	280
Tu'i Malila	2015	TM17	J2-819-IGT5B	1000	bdl	240	37	33	56	2200	440
Tu'i Malila	2015	TM18	J2-819-IGT2B	1300	bdl	50	39	40	43	1200	53
Tu'i Malila	2015	TM18	J2-819-IGT7B	940	bdl	61	39	35	35	2200	110
Tu'i Malila	2015	TM19	J2-819-IGT6B	980	bdl	31	41	38	45	3900	250
Tu'i Malila	2015	TM20	J2-819-IGT3B	840	bdl	62	34	40	30	3000	150
Mariner	2015	MA13	J2-816-IGT5	790	bdl	69	36	42	32	880	140
Mariner	2015	MA13	J2-816-IGT6	1200	bdl	58	48	350	44	1600	520
Mariner	2015	MA14	J2-817-IGT5	bdl	bdl	32	45	94	38	110	25
Mariner	2015	MA14	J2-817-IGT6	660	bdl	26	36	42	31	550	22
Mariner	2015	MA15	J2-817-IGT2	850	bdl	30	42	46	36	270	56
Mariner	2015	MA15	J2-817-IGT4	850	bdl	29	39	52	34	600	37
Mariner	2015	MA16	J2-817-IGT1	NM	bdl	26	35	44	33	540	34
Mariner	2015	MA16	J2-817-IGT8	620	bdl	31	41	110	36	770	110
Mariner	2015	MA17	J2-817-IGT5B	0.9	21	0.7	39	24	160	4.3	1.2
Mariner	2015	MA17	J2-817-IGT6B	990	bdl	33	42	83	NM	530	38
Mariner	2015	MA18	J2-818-IGT4	750	bdl	28	40	40	37	350	27
Mariner	2015	MA18	J2-818-IGT5	800	bdl	25	33	32	30	390	24
Mariner	2015	MA19	J2-818-IGT2	1300	bdl	33	46	42	39	340	31
Mariner	2015	MA19	J2-818-IGT3	770	bdl	31	43	67	38	170	27
Mariner	2015	MA20	J2-818-IGT6	730	bdl	30	41	41	36	1100	26
Mariner	2015	MA20	J2-818-IGT8	830	bdl	27	38	39	39	530	24
Mariner	2015	MA21	J2-818-IGT7	720	bdl	28	40	37	33	400	25
Mariner	2015	MA21	J2-818-M1	900	bdl	28	39	35	33	150	120

Supplementary Table S3 . Elemental Concentrations in Dregs Fractions of Hydrothermal Fluids

Vent Field	Year	Fluid	Sample	Cr	Mn	Fe	Co	Ni	Cu	Zn	Ga
NM = not measured; NS = no sample											
				nmol/kg	umol/kg	umol/kg	nmol/kg	nmol/kg	umol/kg	umol/kg	nmol/kg
Kilo Moana	2009	KM9	J2-434-IGT1	1500	0.8	480	410	200	4.0	12	5.2
Kilo Moana	2009	KM9	J2-434-IGT4	NM	0.7	650	480	17	3.6	19	NM
Tahi Moana 1	2009	TMo1	J2-444-IGT1	8500	0.3	57	30	400	11	110	11
Tahi Moana 1	2009	TMo1	J2-444-IGT6	1100	0.6	16	24	500	5.8	130	18
Tahi Moana 1	2009	TMo2	J2-444-IGT3	1100	0.3	10	69	320	3.1	8.2	3.3
Tahi Moana 1	2009	TMo2	J2-444-IGT4	1100	0.4	13	19	72	5.6	120	20
Tahi Moana 1	2009	TMo5	J2-450-IGT4	590	0.2	6.7	14	46	1.6	11	1.5
Tahi Moana 1	2009	TMo5	J2-450-IGT6	630	0.2	3.9	11	60	1.3	6.5	1.7
ABE	2009	A10	J2-449-IGT5	4200	0.5	25	23	100	7.9	80	9.7
ABE	2009	A11	J2-449-IGT1	3500	0.3	22	16	220	4.2	58	8.2
ABE	2009	A11	J2-449-IGT6	710	448.6	160	55	bdl	6.5	64	4.0
ABE	2015	A13	J2-815-IGT7	1600	0.2	14	7.6	150	1.8	24	9.8
ABE	2015	A13	J2-815-IGT8	900	4.2	280	45	270	34	590	24
ABE	2015	A14	J2-815-IGT1	NS	NS	NS	NS	NS	NS	NS	NS
ABE	2015	A14	J2-815-IGT3	1100	1.8	190	34	240	68	360	21
ABE	2015	A15	J2-815-IGT2	NS	NS	NS	NS	NS	NS	NS	NS
ABE	2015	A15	J2-815-IGT4	1200	0.7	22	43	200	3.2	33	11
ABE	2015	A16	J2-815-IGT5	370	0.1	3.1	5.2	76	1.2	1.8	9.5
ABE	2015	A16	J2-815-IGT6	NS	NS	NS	NS	NS	NS	NS	NS
Tu'i Malila	2009	TM11	J2-442-IGT3	1400	0.3	23	59	230	12	44	9.4
Tu'i Malila	2009	TM11	J2-442-IGT4	4900	0.4	34	25	250	6.0	70	2.0
Tu'i Malila	2009	TM12	J2-442-IGT1	7700	0.4	75	31	220	21	81	14
Tu'i Malila	2009	TM12	J2-442-IGT6	7000	0.7	120	32	180	21	280	87
Tu'i Malila	2015	TM13	J2-819-IGT6	NS	NS	NS	NS	NS	NS	NS	NS
Tu'i Malila	2015	TM13	J2-819-IGT8	NS	NS	NS	NS	NS	NS	NS	NS
Tu'i Malila	2015	TM14	J2-819-IGT4	NS	NS	NS	NS	NS	NS	NS	NS
Tu'i Malila	2015	TM14	J2-819-IGT5	NS	NS	NS	NS	NS	NS	NS	NS
Tu'i Malila	2015	TM15	J2-819-IGT2	520	2.2	560	86	210	180	1200	120
Tu'i Malila	2015	TM16	J2-819-IGT3	NS	NS	NS	NS	NS	NS	NS	NS
Tu'i Malila	2015	TM16	J2-819-IGT7	NS	NS	NS	NS	NS	NS	NS	NS
Tu'i Malila	2015	TM17	J2-819-IGT4B	460	2.4	310	65	190	18	520	32
Tu'i Malila	2015	TM17	J2-819-IGT5B	NS	NS	NS	NS	NS	NS	NS	NS
Tu'i Malila	2015	TM18	J2-819-IGT2B	NS	NS	NS	NS	NS	NS	NS	NS
Tu'i Malila	2015	TM18	J2-819-IGT7B	200	0.5	44	12	59	6.3	290	13
Tu'i Malila	2015	TM19	J2-819-IGT6B	270	0.6	47	30	91.9	5.0	69	18
Tu'i Malila	2015	TM20	J2-819-IGT3B	NS	NS	NS	NS	NS	NS	NS	NS

Supplementary Table S3 cont. Elemental Concentrations in Dregs Fractions of Hydrothermal Fluids

Vent Field	Year	Fluid	Sample	Cr	Mn	Fe	Co	Ni	Cu	Zn	Ga
NM = not measured; NS = no sample											
Mariner	2009	MA8	J2-437-IGT1	NM	0.7	220	62	65	270	310	NM
Mariner	2009	MA8	J2-437-IGT3	NM	1.7	2100	570	170	1800	330	NM
Mariner	2009	MA9	J2-437-IGT5	2000	1.0	160	43	74	170	270	100
Mariner	2009	MA9	J2-437-IGT6	NM	6.9	3800	80	270	270	250	NM
Mariner	2009	MA10	J2-439-IGT1	NM	6.6	3600	83	160	260	17600	NM
Mariner	2009	MA11	J2-439-IGT6	2900	0.6	160	44	180	280	530	200
Mariner	2009	MA12	J2-446-IGT3	600	0.8	20	14	76	56	130	41.4
Mariner	2009	MA12	J2-446-IGT6	2700	0.7	240	87	580	180	420	160
Mariner	2015	MA13	J2-816-IGT5	NS	NS	NS	NS	NS	NS	NS	NS
Mariner	2015	MA13	J2-816-IGT6	NS	NS	NS	NS	NS	NS	NS	NS
Mariner	2015	MA14	J2-817-IGT5	420	0.6	bdl	36	141.2	93	1300	200
Mariner	2015	MA14	J2-817-IGT6	340	0.9	27	20	676.3	98	1600	180
Mariner	2015	MA15	J2-817-IGT2	750	0.6	58	110	130.8	130	210	86
Mariner	2015	MA15	J2-817-IGT4	1100	1.1	480	27	158.4	150	250	99
Mariner	2015	MA16	J2-817-IGT1	1600	1.7	190	66	1222.2	150	420	58
Mariner	2015	MA16	J2-817-IGT8	1200	0.5	81	30	430.7	160	260	76
Mariner	2015	MA17	J2-817-IGT5B	580	5.7	6300	240	248.0	3700	720	170
Mariner	2015	MA17	J2-817-IGT6B	550	0.8	1400	170	236.1	440	510	110
Mariner	2015	MA18	J2-818-IGT4	240	0.3	88	21	63.0	85	110	23
Mariner	2015	MA18	J2-818-IGT5	910	0.9	150	36	205.8	89	250	37
Mariner	2015	MA19	J2-818-IGT2	680	2.2	780	33	101.8	610	330	69
Mariner	2015	MA19	J2-818-IGT3	580	0.9	540	36	113.1	410	350	130
Mariner	2015	MA20	J2-818-IGT6	780	0.5	67	19	189.3	170	440	92
Mariner	2015	MA20	J2-818-IGT8	820	0.6	59	30	104.2	99	240	69
Mariner	2015	MA21	J2-818-IGT7	810	0.9	110	32	273.1	230	370	100
Mariner	2015	MA21	J2-818-M1	NS	NS	NS	NS	NS	NS	NS	NS

Supplementary Table S3 cont. Elemental Concentrations in Dregs Fractions of Hydrothermal Fluids

Vent Field	Year	Fluid	Sample	Mo	Ag	Cd	In	Sn	Sb	Au	Pb
NM = not measured; NS = no sample											
				nmol/kg	nmol/kg	nmol/kg	nmol/kg	nmol/kg	nmol/kg	nmol/kg	nmol/kg
Kilo Moana	2009	KM9	J2-434-IGT1	170	47	18	NM	NM	11	0.1	130
Kilo Moana	2009	KM9	J2-434-IGT4	150	51	26	NM	NM	10	0.5	190
Tahi Moana 1	2009	TMo1	J2-444-IGT1	130	25	89	NM	NM	10	0.1	1000
Tahi Moana 1	2009	TMo1	J2-444-IGT6	65	28	130	NM	6.0	44	0.1	510
Tahi Moana 1	2009	TMo2	J2-444-IGT3	82	32	6.4	NM	6.2	18	0.1	110
Tahi Moana 1	2009	TMo2	J2-444-IGT4	66	27	140	NM	5.1	43	0.2	510
Tahi Moana 1	2009	TMo5	J2-450-IGT4	34	1.5	11	NM	1.7	23	0.1	57
Tahi Moana 1	2009	TMo5	J2-450-IGT6	32	0.4	7.7	NM	0.8	11	0.2	55
ABE	2009	A10	J2-449-IGT5	43	13	30	NM	3.0	47	0.0	350
ABE	2009	A11	J2-449-IGT1	46	8.5	30	NM	2.4	7.2	0.1	300
ABE	2009	A11	J2-449-IGT6	48	2.2	12	NM	2.3	7.0	0.1	110
ABE	2015	A13	J2-815-IGT7	230	19	34	5.4	7.9	21	350	73
ABE	2015	A13	J2-815-IGT8	340	20	680	5.4	13	270	700	1300
ABE	2015	A14	J2-815-IGT1	NS	NS	NS	NS	NS	NS	NS	NS
ABE	2015	A14	J2-815-IGT3	300	9.0	500	12.7	21	120	800	250
ABE	2015	A15	J2-815-IGT2	NS	NS	NS	NS	NS	NS	NS	NS
ABE	2015	A15	J2-815-IGT4	51	5.9	11	20	20	NM	NM	370
ABE	2015	A16	J2-815-IGT5	240	bdl	12	5.5	8.2	8.2	0.1	31
ABE	2015	A16	J2-815-IGT6	NS	NS	NS	NS	NS	NS	NS	NS
Tu'i Malila	2009	TM11	J2-442-IGT3	72	9.1	31	NM	2.6	21	0.2	350
Tu'i Malila	2009	TM11	J2-442-IGT4	43	14	24	NM	86	12	0.1	1200
Tu'i Malila	2009	TM12	J2-442-IGT1	110	29	52	NM	NM	11	0.5	2400
Tu'i Malila	2009	TM12	J2-442-IGT6	110	26	460	NM	NM	37	0.4	730
Tu'i Malila	2015	TM13	J2-819-IGT6	NS	NS	NS	NS	NS	NS	NS	NS
Tu'i Malila	2015	TM13	J2-819-IGT8	NS	NS	NS	NS	NS	NS	NS	NS
Tu'i Malila	2015	TM14	J2-819-IGT4	NS	NS	NS	NS	NS	NS	NS	NS
Tu'i Malila	2015	TM14	J2-819-IGT5	NS	NS	NS	NS	NS	NS	NS	NS
Tu'i Malila	2015	TM15	J2-819-IGT2	300	140	2000	17	34	380	2900	2100
Tu'i Malila	2015	TM16	J2-819-IGT3	NS	NS	NS	NS	NS	NS	NS	NS
Tu'i Malila	2015	TM16	J2-819-IGT7	NS	NS	NS	NS	NS	NS	NS	NS
Tu'i Malila	2015	TM17	J2-819-IGT4B	210	120	990	6.5	7.7	NM	1200	1800
Tu'i Malila	2015	TM17	J2-819-IGT5B	NS	NS	NS	NS	NS	NS	NS	NS
Tu'i Malila	2015	TM18	J2-819-IGT2B	NS	NS	NS	NS	NS	NS	NS	NS
Tu'i Malila	2015	TM18	J2-819-IGT7B	150	2.3	1100	6.3	10	NM	2200	280
Tu'i Malila	2015	TM19	J2-819-IGT6B	130	210	52	6.3	8.3	220	4400	3700
Tu'i Malila	2015	TM20	J2-819-IGT3B	NS	NS	NS	NS	NS	NS	NS	NS

Supplementary Table S3 cont. Elemental Concentrations in Dregs Fractions of Hydrothermal Fluids

Vent Field	Year	Fluid	Sample	Mo	Ag	Cd	In	Sn	Sb	Au	Pb
NM = not measured; NS = no sample											
Mariner	2009	MA8	J2-437-IGT1	110	bdl	44	NM	NM	1600	bdl	130
Mariner	2009	MA8	J2-437-IGT3	210	67	250	NM	NM	57	1.3	1200
Mariner	2009	MA9	J2-437-IGT5	84	47	230	NM	NM	23	0.6	1100
Mariner	2009	MA9	J2-437-IGT6	2000	1600	10300	NM	NM	25	0.7	338100
Mariner	2009	MA10	J2-439-IGT1	2000	1500	10300	NM	NM	26	2.7	342000
Mariner	2009	MA11	J2-439-IGT6	63	55	240	NM	NM	37	0.7	2000
Mariner	2009	MA12	J2-446-IGT3	35	10	72	NM	6.2	48	0.5	710
Mariner	2009	MA12	J2-446-IGT6	160	56	330	NM	NM	70	0.7	5100
Mariner	2015	MA13	J2-816-IGT5	NS	NS	NS	NS	NS	NS	NS	NS
Mariner	2015	MA13	J2-816-IGT6	NS	NS	NS	NS	NS	NS	NS	NS
Mariner	2015	MA14	J2-817-IGT5	280	7.0	1400	93	15	69.7	1700	930
Mariner	2015	MA14	J2-817-IGT6	290	67	1300	140	16	114.2	3000	3000
Mariner	2015	MA15	J2-817-IGT2	260	28	170	39	18	60.5	2000	760
Mariner	2015	MA15	J2-817-IGT4	370	63	210	46	23	45.0	370	780
Mariner	2015	MA16	J2-817-IGT1	380	78	390	38	16	113.7	1400	990
Mariner	2015	MA16	J2-817-IGT8	330	26	200	43	22	32.4	1700	2200
Mariner	2015	MA17	J2-817-IGT5B	760	55	250	110	19	14.7	23000	430
Mariner	2015	MA17	J2-817-IGT6B	370	100	380	62	31	53.6	26100	6000
Mariner	2015	MA18	J2-818-IGT4	170	81	110	36	8.2	66.3	820	270
Mariner	2015	MA18	J2-818-IGT5	290	74	240	34	12	174.3	2300	320
Mariner	2015	MA19	J2-818-IGT2	660	78	260	180	36	204.8	6300	3600
Mariner	2015	MA19	J2-818-IGT3	290	70	310	130	26	251.2	1800	590
Mariner	2015	MA20	J2-818-IGT6	310	110	360	61	14	45.8	1500	1700
Mariner	2015	MA20	J2-818-IGT8	180	33	200	37	8.9	106.4	920	740
Mariner	2015	MA21	J2-818-IGT7	230	55	360	69	63	134.8	950	480
Mariner	2015	MA21	J2-818-M1	NS	NS	NS	NS	NS	NS	NS	NS

Supplementary Table S4. Selected ELSC Hydrothermal Fluid Data

Selected Hydrothermal Fluid Data from Mottl et al. (2011) and Chapter 2 of this thesis.

Fluid_ID	FieldCode	max T	pH	Mn	Fe	Cu	Zn	Pb
		°C	25°C	umol/kg	umol/kg	umol/kg	umol/kg	nmol/kg
KM1	1	333	3.6	511	2485	8	58	272
KM2	1	332	3.6	694	3202	...	...	312
KM3	1	321	2.9	733	3836	9	74	312
KM4	1	300	3.2	524	2473	11	...	226
KM5	1	329	3.5	717	2898	11	108	...
KM6	1	306	3.6	675	3116	10	60	402
KM8	1	333	4.0	553	2557	...	64	390
TC1	2	328	4.1	388	305	4	19	369
TC3	2	320	4.0	398	267	3	49	430
TC4	2	316	4.1	407	282	5	61	498
TC5	2	302	3.7	329	343	7	53	...
TC6	2	288	3.9	389	368	4	50	427
TC7	2	288	4.0	375	313	8	74	515
A1	4	309	4.3	461	268	6	36	387
A2	4	309	4.1	476	264	5	44	385
A4	4	278	4.4	273	...	...	...	...
A5	4	290	4.5	289	174	4	33	380
A8	4	308	4.5	301	...	...	...	...
A9	4	295	4.6	286	159	...	37	573
TM1	5	279	4.5	432	219	16	48	532
TM2	5	312	4.4	406	218	7	28	571
TM4	5	178	5.7	332	...	...	...	...
TM5	5	265	4.6	439	...	...	...	...
TM6	5	265	4.4	399	227	2	18	564
TM7	5	198	5.0	413	...			
TM8	5	229	4.4	380	...	11	7	786
TM10	5	274	4.1	378	271	4	49	...
MA1	6	334	2.5	5938	11417	171	467	862
MA2	6	311	2.6	6275	11265	105	514	751
MA3	6	363	2.7	5728	13122	156	336	1135
MA5	6	249	2.6	5440	10547	96	321	858
MA6	6	240	2.7	4875	10684	4	242	1200

Supplementary Table S5. Selected Manus Basin Hydrothermal Fluid Data

Selected Hydrothermal Fluid Data from Craddock (2009)

Fluid_ID	FieldCode	max T	pH	Mn	Fe	Cu	Zn	Pb	Co	Ag	Cd	Ag/Cu
		°C	25°C	umol/kg	umol/kg	umol/kg	umol/kg	nmol/kg	nmol/kg	nmol/kg	nmol/kg	x1000
VW1	7	282	4.4	349	159	4	33	0.35	45	38	50	9.50
VW2	7	273	4.2	365	165	(—)	30	0.30	30	28	57	
VW3	7	285	4.7	209	130	5	23	0.25	20	9	36	1.80
RMR1	8	314	2.3	4155	6731	165	1499	22.0	234	720	2600	4.38
RMR2	8	272	2.3	3345	1509	62	2970	137.0	71	3233	4000	52.15
RMR3	8	278	2.5	5089	8079	40	1095	24.0	67	328	1620	8.20
RMR4	8	341	2.6	3005	6829	188	453	8.6	272	185	634	0.98
RGR1	8	320	2.7	2906	4610	213	490	4.0	29	223	720	1.05
RGR2	8	274	2.6	2822	3740	475	566	2.9	41	580	770	1.22
SM1	9	295	2.6	2745	3370	141	350	7.0	(90)	124	440	0.88
SM2	9	241	2.4	2520	1475	800	265	4.0	(35)	125	220	0.16
SM3	9	288	2.5	2394	1298	140	175	5.0	10	75	155	0.54
SC1	9	152	4.6	2240	70	34	179	31.0	(58)	155	100	4.51
SC2	9	180	3.4	2880	241	6	25	2.0	(50)	32	23	5.69
F1	10	329	2.5	2570	8500	291	330	6.0	39	210	410	0.72
F2	10	343	2.7	4600	14400	235	410	5.2	508	150	430	0.64
F3	10	358	2.7	3962	12950	138	390	18.0	517	290	480	2.10
F4	10	284	2.4	3599	8549	305	367	2.6	45	165	353	0.54
SZ1	11	303	3.8	265	720	53	22	1.7	230	35	85	0.66
SZ2	11	274	3.6	360	880	27	29	3.4	101	60	96	2.21
SZ3	11	290	3.5	329	916	44	32	2.4	89	58	125	1.33
SZ4	11	229	3.6	324	495	13	31	2.7	122	34	93	2.56
SZ5	11	249	2.3	271	4571	1170	340	15.5	79	1400	800	1.20
SZ6	11	226	3.7	382	405	10	(35)	2.0	105	(25)	124	
NS3	11	300	3.4	421	2390	108	38	1.4	1003	52	99	0.48
NS5	11	299	3.2	349	4021	480	15	1.8	173	52	82	0.11
NS6	11	325	2.8	479	5858	99	17	2.9	2570	70	79	0.71
SS1	11	271	2.6	550	2194	390	34	1.2	28	270	(160)	0.69
SS2	11	288	2.7	485	2562	136	23	2.4	42	60	110	0.44

Supplementary Table S6

Data for Figure 6

Fluid ID		109Ag/63Cu16O		Ag / Cu	Ag+ / Cu+
		Counts Ratio	Counts Ratio	total element concentration	activity ratio
	n	Average	Error	ratio (x1000)	(x1000)
Eastern Lau Spreading Center					
TMo5	18	6.60E-02	1.60E-02	4.50	6.25
A10	22	1.21E-02	5.35E-03	1.40	0.92
A11	20	2.34E-02	4.07E-03	0.67	1.98
A16	9	1.45E-02	1.90E-03	1.34	1.92
TM11	17	1.38E-02	2.07E-03	0.95	0.92
MA9	12	2.95E-03	2.00E-03	0.77	0.31
MA15	6	2.57E-03	4.32E-04	0.23	0.21
Manus Basin					
VW1	88	9.56E-02	1.65E-02	9.50	8.87
RGR1	28	8.71E-02	9.91E-02	1.05	0.89
RMR1	24	3.25E-02	1.61E-02	4.38	4.83
SM3	27	1.55E-03	7.35E-03	0.54	0.85
F3	13	8.10E-03	6.32E-03	2.10	2.58
NS3	21	7.70E-03	2.64E-03	0.48	0.42
SZ1	13	6.44E-03	1.12E-03	0.66	0.82
SZ2	20	1.35E-02	5.01E-03	2.21	2.29
Others					
Sully99	27	3.08E-03	5.55E-04	0.33	1.34
BB5	19	3.64E-03	2.18E-03	0.29	0.00

Supplementary Table S7

Data for Figures 7, 8, and 9

Fluid ID	Temp.	pH	pH	Cu	Ag	Ag/Cu	Ga	Ga+3/Fe+2
	(°C)	(at 25°C)	in situ	µmol/kg	nmol/kg	x1000	nmol/kg	x10^6
Eastern Lau Spreading Center								
TMo5	310	3.7	4.6	6	26	4.50	2	0.10
A10	317	3.9	4.6	10	14	1.40	10	0.35
A11	306	4.0	5.2	9	6	0.67	6	0.18
A16	300	4.0	5.2	4	6	1.34E+00	62	3.93
TM11	315	3.8	4.5	20	19	9.50E-01	6	0.85
MA9	338	2.4	3.2	300	230	0.77	118	5.16
MA15	354	2.7	3.8	238	56	0.23	175	2.39
Manus Basin								
VW1	282	4.4	5.1	4	38	9.50	50	1.34
RGR1	320	2.7	4.0	213	223	1.05	150	1.91
RMR1	314	2.3	2.8	165	720	4.38	150	1.08
SM3	288	2.5	3.0	140	75	0.54	150	53.32
F3	358	2.7	3.9	138	290	2.10	150	1.73
NS3	300	3.4	3.9	108	52	0.48	50	1.93
SZ1	303	3.8	4.1	53	35	0.66	50	1.03
SZ2	274	3.6	4.0	27	60	2.21	50	2.81
Others								
Sully99	379	3.6	4.3	12	4	0.33	50	2.14
BB5	395	3.0	5.0	172	50	0.29	50	0.06

Chapter 5

Summary and Conclusions

1. Summary of Findings

The studies presented in this thesis investigate the relationships between active seafloor massive sulfide (SMS) deposits and the hydrothermal fluids from which they form. Particular attention is given to the linings of black smoker chimneys, which are shown to provide mineral and trace element indicators of the temperature, sulfur fugacity, pH, and trace metal content of hydrothermal fluids. Specifically, the Ga and In contents of chalcopyrite chimney linings are identified as proxies for hydrothermal fluid pH while Ag contents closely reflect the ratios of free Ag^+ to free Cu^+ in paired hydrothermal fluids.

Chapter 2

Chapter 2 examines the morphology, mineralogy, and geochemistry of SMS deposits along the Eastern Lau Spreading Center (ELSC), and demonstrates how SMS deposits reflect the temperature and composition of hydrothermal fluids influenced by the nearby Tonga Subduction Zone. Closer to the Tonga Subduction Zone, SMS deposits exhibit higher concentrations of Ba, Pb, As, and Sb and mineral assemblages contain higher modal abundances of barite ($BaSO_4$) and galena (PbS), consistent with elevated concentrations of these elements in more felsic host rocks. The precipitation of barite also influences deposit morphology, contributing to the formation of horizontal flanges and squat terraces.

The stability of minerals present along open conduit chimneys linings and, where wurtzite is present, the mole% FeS in (Zn,Fe)S, closely reflect the temperature and sulfur fugacity of hydrothermal fluids. Additionally, the presence of co-precipitated wurtzite and chalcopyrite is associated with higher pH (pH (at 25°C) ~4) vent fluids. Bulk geochemical data also provide an indicator of pH, with Zn and Ag positively correlated in deposits associated with hydrothermal systems that vent fluids of minimum pH (at 25°C) < 3.3, but not in deposits associated with hydrothermal systems that vent fluids of minimum pH (at 25°C) > 3.3.

Chapter 3

Chapter 3 focuses on the development of secondary ion mass spectrometry (SIMS) as a method for measuring trace element concentrations in the chalcopyrite linings of black smoker chimneys. Advantages of this technique include small (~40 μm diameter) spot sizes and low (~0.1 ppb) detection limits. A key aspect of this study is the construction of SIMS calibration curves for Co, Ni, Ga, Ag, and In. This was done by comparing SIMS measurements of selected black smoker chimney linings with analyses of digested chalcopyrite grains picked from the linings of the same samples. Picked grains are analyzed by inductively coupled plasma mass spectrometry (ICP-MS) calibrated against serial dilutions of standard reference solutions. Another key aspect of this study is the use of SIMS to measure concentrations of Co, Ni, Ga, Ag, and In in black smoker chimney samples representing a variety of geologic settings (e.g., fast-, intermediate-, slow-, and ultraslow-spreading mid-ocean ridges, and back-arc spreading centers) and hydrothermal fluid conditions (e.g., pH (at 25°C) = 2.3 to 4.4 and temperature = 274°C to 395°C).

Chapter 3 advances the use of SIMS as a technique for measuring Co, Ni, Ga, Ag, and In concentrations in chalcopyrite and identifies patterns between the concentrations of these elements and hydrothermal fluid parameters. Specific patterns for trace metal concentrations in the mineral chalcopyrite include:

1) covariation of Co and Ni concentrations
2) association of high Co and Ni concentrations with high-temperature vent fluids from basalt-hosted mid-ocean ridges
3) a negative correlation between Ga and In concentrations and the pH of hydrothermal fluids

This third pattern is particularly intriguing as it provides a potential trace element proxy for hydrothermal fluid pH. Complexing of Ga and In by OH^- and the inverse relationship between OH^- and H^+ activity (i.e., pH) is proposed as a possible explanatory mechanism. Overall, this study demonstrates the potential of SIMS to quantitatively measure Co, Ni, Ga, Ag, and In in chalcopyrite and identifies several natural chalcopyrite samples that are homogeneous with respect to these and possibly other trace elements, making them potentially useful as calibration standards in geochemical analyses.

Chapter 4

Chapter 4 builds on the findings of Chapter 3 and compares the Co, Ni, Ga, Ag, and In concentrations of black smoker chimney linings with those of the hydrothermal fluids that were flowing through them at the time of collection. This comparison is aided by thermodynamic modelling of fluid speciation at *in situ* conditions. A significant result of Chapter 4 is the observation of a strong linear correlation between the Ag content of black smoker chimney

linings with the free ion activity ratio of Ag:Cu in the corresponding hydrothermal fluids. This correlation supports partitioning of Ag into chalcopyrite as a lattice substitution for Cu, once aqueous complexing is considered. When combined with the correlation identified in Chapter 3 between the Ga and In concentrations of black smoker chimneys and hydrothermal fluid pH, the Ag concentrations of black smoker chimney linings provide the following proxies of hydrothermal fluid chemistry:

1) low Ag concentration and high Ga and In concentrations indicate formation from low-pH fluids.
2) high Ag concentration and low Ga and In concentrations indicate formation from higher-pH, Cu-poor fluids.
3) high Ag concentration and high Ga and In concentrations indicate formation from low-pH fluids in which Ag is highly enriched, likely as a result of subsurface remobilization

The correlation between the Ga and In concentrations of black smoker chimney linings and hydrothermal pH is investigated further with measurements of the Ga and In concentrations of some hydrothermal fluids and thermodynamic modelling of fluid speciation, including pH and the activities of Ga and In free ions and complexes at *in situ* conditions (temperatures, pressures, fluid composition). These calculations generally support OH^- complexing as an explanatory mechanism for the observed correlation between Ga and In and hydrothermal fluid pH. Additionally, results of species distributions at *in situ* conditions support regular partitioning of Ga for Fe. However, there is a need for additional analyses of Ga and In in hydrothermal fluids as well as a need to refine thermodynamic data concerning Ga and In complexes at hydrothermal conditions to better quantify these relationships.

2. Significance of Findings

This thesis investigates trace element proxies and mineral indicators of hydrothermal fluid pH and metal content based on careful study of actively forming SMS deposits. Because studies focus on actively forming SMS deposits, and especially black smoker chimney linings, the correspondence between mineral samples and collected hydrothermal fluid samples is straightforward and well constrained.

Chapters 3 and 4 propose new proxies of hydrothermal fluid chemistry (Ga and In as a proxy for pH, Ag as a proxy for free ion activity ratio of Ag:Cu and indicator of subsurface remobilization). These elements are thought to occur as stoichiometric lattice substitutions in chalcopyrite (Ag^{+} for Cu^{+}, Ga^{3+} and In^{3+} for Fe^{3+}). Elements that occur as lattice substitutions are less likely to be remobilized by hydrothermal recrystallization than elements that occur as inclusions or nonstoichiometric lattice inclusions (Huston et al., 1995). Thus, proxies based on these elements are more likely to be geologically preserved and thereby useful for the study of inactive or fossil deposits. Moreover, the proxies and indicators of hydrothermal fluid temperature and chemistry presented in this thesis are based on the mineralogy and trace element contents of ore minerals (e.g., chalcopyrite, wurtzite, sphalerite) rather than the associated gangue minerals. This means that it is not necessary to assume that both ore and gangue minerals were co-precipitated under the same temperature and chemical conditions and from the same source fluid. Future studies should investigate the applicability of pH proxies based on the Ga and In concentrations in chalcopyrite and proxies of Ag and Cu concentrations based on combined knowledge from Ga, In, and Ag concentrations in chalcopyrite to fossilized SMS deposits.

A second contribution of this thesis is the identification of black smoker chimney linings that are homogeneous with respect to Co, Ni, Ga, Ag, In, and likely other trace elements. Such samples may be useful as analytical standards from which to derive calibration curves for other elements or microanalytical techniques or as matrix-matched materials (for chalcopyrite) by which to validate the performance of proposed non-matrix matched standards. Previous work by McDermott et al. (2015) demonstrated that the innermost chalcopyrite linings of black smoker chimneys are in equilibrium with hydrothermal fluids with respect to sulfur isotopes. Together with the work presented in this thesis, these results suggest that black smoker chimney linings very closely reflect the hydrothermal fluids from which they form provided that careful picking or microanalysis allows for analysis of only the innermost linings. Future work should seek to combine trace element and isotopic studies particularly with the aim of better understanding remobilization and zone refinement processes. It should also be noted that several of the black smoker chimney samples investigated in this study contain intergrown chalcopyrite and wurtzite or chalcopyrite and pyrite. Such samples provide an excellent basis from which to quantify trace element partitioning between different metal sulfide minerals under well constrained, but difficult to engineer, geochemical conditions.

Third, the trace element proxies presented in Chapters 3 and 4 highlight the importance of aqueous complexing in determining the trace element contents of chalcopyrite and present a strategy by which to search for additional trace element proxies based on isovalent lattice substitutions. In cases such as Ag and Cu, where elements are predominantly complexed by the same ion in the hydrothermal fluid (i.e. Cl^-), trace element concentrations primarily reflect the ratio of the concentration of the trace element to that of the major element it replaces. More precisely, trace element concentrations are controlled by the activity ratio of the free ions, which

can be calculated through thermodynamic modelling provided that major fluid parameters are known or can be accurately estimated. Alternatively, in cases where there are major differences in the complexing behavior of the trace element and the major element it replaces, mineral trace element concentrations reflect the activities of the relevant ligands. For example, complexing of Ga and In by OH^- contrasts with the predominance of Cl^- complexing for Fe. This contrast in aqueous complexing behavior provides an explanatory mechanism for the observed correlation between hydrothermal fluid pH and concentrations of Ga and In in the associated black smoker chimney linings. Future studies should identify pairs of trace element and carrier elements that exhibit contrasting complexing behavior as a strategy for identifying additional proxies of hydrothermal fluid pH. Additionally, a better understanding is needed of possible crystal chemical controls on trace element partitioning. This is particularly true of divalent ions (e.g., Co^{2+}, Ni^{2+}), which may partition more readily into more Fe-rich copper iron sulfide minerals containing divalent Fe than into chalcopyrite, where Fe is trivalent.

3. Future Directions

This thesis has identified several trace element proxies and mineral indicators of hydrothermal fluid pH and metal content (i.e. Ag:Cu ratio) and developed SIMS as a technique for measuring Co, Ni, Ga, Ag, and In in chalcopyrite. Future directions for this research can be divided into short term, medium term, and long term goals.

Short Term

In the immediate short term, efforts can be made to refine the techniques used in this thesis and to expand their use to include additional samples and scientific applications. In

particular, SIMS analyses of trace elements (Co, Ni, Ga, Ag, In) in chalcopyrite can be improved by refining the SIMS calibration curves constructed in Chapter 3. Specific improvements include validation of the Ag calibration curve and reduction of the uncertainties surrounding measurements of Ni at low concentrations. Validation of the Ag calibration curve can be achieved through electron microprobe analyses of black smoker chimney samples containing high concentrations of Ag (> 1000 μg/g). In order to obtain better ICP-MS measurements of Ni in digested picked grains of chalcopyrite, analyses should be repeated using Pt rather than Ni cones. In order to identify possible effects of major element ratios on trace element concentrations, electron microprobe analyses of black smoker chimney linings should be conducted. Additionally, elements that were not considered in this thesis, but which offer potential for expanded use of SIMS measurements in the near term, include Sn, Se, and Te. Measurements of Se and Te can be obtained by switching from a O_2^- to a Cs^+ ion beam and by modifying the digestion of picked grains to avoid volatilization of Se.

The sample suite examined in this thesis is heavily biased toward samples from back-arc basins. One possibility for expanding the current sample suite would be to focus on samples from mid-ocean ridges (of various spreading rate) to more closely reflect the full population of actively forming SMS deposits. A second possibility would be to focus on samples from volcanic arcs or marginal basins which are more likely to be geologically preserved as volcanogenic massive sulfide (VMS) deposits. Yet a third possibility would be to focus on vent sites such as those along the Endeavour segment of the Juan de Fuca Ridge, where analyses of black smoker chimney linings can be integrated with detailed monitoring of hydrothermal fluid chemistry and changes in hydrothermal venting related to volcanic and tectonic activity. Alternatively, data presented here concerning the bulk geochemistry of SMS deposits and the

trace element contents of hydrothermal fluids at the ABE, Tu'i Malila and Mariner vent fields can be integrated using the known locations of SMS deposit and hydrothermal fluid samples to directly track and estimate the efficiency of trace element incorporation into SMS deposits from hydrothermal fluids.

Medium Term

Coincident with the desire to conduct trace element analyses of additional black smoker chimney samples is the desire to obtain additional data for these elements in paired hydrothermal fluids, particularly for Ga, Ag, and In. While relatively straightforward given the techniques used in this thesis, detailed sampling and analysis of paired black smoker chimneys and hydrothermal fluid samples likely requires sampling cruises where this is a priority. As such, this is a medium term rather than short term goal

An additional direction in which to apply SIMS measurements of trace elements would be to investigate grains along a transect from the interior to the exterior of a black smoker chimney wall. Several models have been proposed regarding the temperature and chemical conditions within black smoker chimney walls (e.g., Janecky and Seyfried, 1984; Tivey, 1995; La Rowe at al., 2014), but results vary widely in predictions of H_2 and H_2S concentrations (collectively sulfur fugacity) and fluid pH. Because estimates of temperature alone are better constrained and easier to calculate than estimates of fluid chemistry, geochemical proxies of sulfur fugacity and pH such as those presented in this thesis could be useful in helping to discriminate between the various model predictions. Because models need to be implemented and studies would likely benefit from the integration of thermodynamic data for Ga and In complexes into these models, this is also a medium term rather than short term goal.

Long term

Long term, there is a desire to obtain a better understanding of the incorporation of trace elements into sulfide minerals. Specific deficits in understanding concern the spatial distributions of trace elements within sulfide mineral grains precipitated under various chemical conditions, the valence states of the incorporated trace elements, trace element partitioning between mineral pairs, and trace element behavior during solid-phase solution and dissolution processes (e.g., the formation of dissolution lamellae). Answering these questions will likely involve the use of additional analytical techniques including line scans and/or spot analyses using microsecond or femtosecond laser ablation inductively coupled plasma mass spectrometry and, in the case of investigating valence states, synchrotron techniques such as x-ray absorption near edge structure (XANES).

Additionally, there is a desire to integrate these studies with studies of ocean chemistry and mined ore deposits. With respect to ocean chemistry, better understandings of the trace element contents of hydrothermal vent fluids will lead to better estimates of hydrothermal fluxes of these elements into the ocean and the efficiency with which various elements are precipitated and removed from the ocean as sedimentary particles. With respect to mined ore deposits, many questions remain regarding the pH and metal contents of ore-formation fluids as well as the processes responsible for observed differences between various deposits. While modern SMS deposits are imperfect analogues for mined VMS deposits, insights into the partitioning of trace elements into metal sulfide minerals derived from SMS deposits studies can nevertheless be useful in helping to interpret the observed mineralogy and geochemistry of VMS deposits. Expansion of investigated samples to include additional types of hydrothermal (e.g., porphyry

copper, iron oxide copper gold, Mississippi Valley Type) and magmatic sulfide occurrences is also desired.

References

Huston, D. L., Sie, S. H., Suter, G. F., Cooke, D. R., and Both, R. A. (1995). Trace elements in sulfide minerals from eastern Australian volcanic-hosted massive sulfide deposits; Part I, Proton microprobe analyses of pyrite, chalcopyrite, and sphalerite, and Part II, Selenium levels in pyrite; comparison with delta 34 S values and implications for the source of sulfur in volcanogenic hydrothermal systems. *Econ. Geol.*, **90(5)**, 1167-1196.

Janecky, D. R. and Seyfried, W. E. (1984). Formation of massive sulfide deposits on oceanic ridge crests: Incremental reaction models for mixing between hydrothermal solutions and seawater. *Geochim. Cosmochim. Acta*, **48(12)**, 2723-2738.

La Rowe, D. E., Dale, A. W., Aguilera, D. R., L'Heureux, I., Amend, J. P., and Regnier, P. (2014). Modeling microbial reaction rates in a submarine hydrothermal vent chimney wall. *Geochim. Cosmochim. Acta*, **124**, 72-97.

McDermott, J. M., Ono, S., Tivey, M. K., Seewald, J. S., Shanks, W. C., and Solow, A. R. (2015). Identification of sulfur sources and isotopic equilibria in submarine hot-springs using multiple sulfur isotopes. *Geochim. Cosmochim. Acta*, **160**, 169-187.

Tivey, M. K. (1995) The influence of hydrothermal fluid composition and advection rates on black smoker chimney mineralogy: Insights from modeling transport and reaction. *Geochim. Cosmochim. Acta*, **59(10)**, 1933-1949.